frontiers | Research Topics

Bioinspired superwettable materials from design, fabrication to application

Edited by
Jingxin Meng, Hongliang Liu, Jun-Bing Fan, Pengchao Zhang, Tailin Xu and Feilong Zhang

Published in
Frontiers in Bioengineering and Biotechnology

ISSN 1664-8714
ISBN 978-2-8325-2401-5
DOI 10.3389/978-2-8325-2401-5

About Frontiers

Frontiers is more than just an open access publisher of scholarly articles: it is a pioneering approach to the world of academia, radically improving the way scholarly research is managed. The grand vision of Frontiers is a world where all people have an equal opportunity to seek, share and generate knowledge. Frontiers provides immediate and permanent online open access to all its publications, but this alone is not enough to realize our grand goals.

Frontiers journal series

The Frontiers journal series is a multi-tier and interdisciplinary set of open-access, online journals, promising a paradigm shift from the current review, selection and dissemination processes in academic publishing. All Frontiers journals are driven by researchers for researchers; therefore, they constitute a service to the scholarly community. At the same time, the *Frontiers journal series* operates on a revolutionary invention, the tiered publishing system, initially addressing specific communities of scholars, and gradually climbing up to broader public understanding, thus serving the interests of the lay society, too.

Dedication to quality

Each Frontiers article is a landmark of the highest quality, thanks to genuinely collaborative interactions between authors and review editors, who include some of the world's best academicians. Research must be certified by peers before entering a stream of knowledge that may eventually reach the public - and shape society; therefore, Frontiers only applies the most rigorous and unbiased reviews. Frontiers revolutionizes research publishing by freely delivering the most outstanding research, evaluated with no bias from both the academic and social point of view. By applying the most advanced information technologies, Frontiers is catapulting scholarly publishing into a new generation.

What are Frontiers Research Topics?

Frontiers Research Topics are very popular trademarks of the *Frontiers journals series*: they are collections of at least ten articles, all centered on a particular subject. With their unique mix of varied contributions from Original Research to Review Articles, Frontiers Research Topics unify the most influential researchers, the latest key findings and historical advances in a hot research area.

Find out more on how to host your own Frontiers Research Topic or contribute to one as an author by contacting the Frontiers editorial office: frontiersin.org/about/contact

Bioinspired superwettable materials from design, fabrication to application

Topic editors

Jingxin Meng — Technical Institute of Physics and Chemistry, Chinese Academy of Sciences (CAS), China

Hongliang Liu — Yantai University, China

Jun-Bing Fan — Southern Medical University, China

Pengchao Zhang — Wuhan University of Technology, China

Tailin Xu — Shenzhen University, China

Feilong Zhang — Nanyang Technological University, Singapore

Citation

Meng, J., Liu, H., Fan, J.-B., Zhang, P., Xu, T., Zhang, F., eds. (2023). *Bioinspired superwettable materials from design, fabrication to application*. Lausanne: Frontiers Media SA. doi: 10.3389/978-2-8325-2401-5

Table of contents

frontiers | Frontiers in Bioengineering and Biotechnology

TYPE Editorial
PUBLISHED 28 April 2023
DOI 10.3389/fbioe.2023.1204607

OPEN ACCESS

EDITED AND REVIEWED BY
Hasan Uludag,
University of Alberta, Canada

*CORRESPONDENCE
Jingxin Meng,
mengjx628@mail.ipc.ac.cn
Hongliang Liu,
liuhongliang@ytu.edu.cn
Jun-Bing Fan,
fjb2012@smu.edu.cn
Pengchao Zhang,
pczhang@whut.edu.cn,
Tailin Xu,
xutailin@szu.edu.cn
Feilong Zhang,
flzhang@ntu.edu.sg

RECEIVED 12 April 2023
ACCEPTED 24 April 2023
PUBLISHED 28 April 2023

CITATION
Meng J, Liu H, Fan J-B, Zhang P, Xu T and Zhang F (2023), Editorial: Bioinspired superwettable materials from design, fabrication to application.
Front. Bioeng. Biotechnol. 11:1204607.
doi: 10.3389/fbioe.2023.1204607

Editorial: Bioinspired superwettable materials from design, fabrication to application

Jingxin Meng[1,2]*, Hongliang Liu[3,4]*, Jun-Bing Fan[5]*, Pengchao Zhang[6]*, Tailin Xu[7]* and Feilong Zhang[8]*

[1]Technical Institute of Physics and Chemistry, Chinese Academy of Sciences (CAS), Beijing, China, [2]Binzhou Institute of Technology, Weiqiao-UCAS Science and Technology Park, Binzhou, China, [3]School of Chemistry and Chemical Engineering, Yantai University, Yantai, China, [4]Shandong Laboratory of Yantai Advanced Materials and Green Manufacturing, Yantai, China, [5]Southern Medical University, Guangzhou, China, [6]State Key Laboratory of Advanced Technology for Materials Synthesis and Processing, School of Materials Science and Engineering, Wuhan University of Technology, Wuhan, China, [7]Shenzhen University, Shenzhen, China, [8]Nanyang Technological University, Singapore, Singapore

KEYWORDS

antifouling, biosensing, bioseparation, specific adhesion, bioinspired

Editorial on the Research Topic
Bioinspired superwettable materials from design, fabrication to application

Due to the combination of surface micro/nanostructure and surface chemical modification, superwettable interfacial materials have exhibited remarkable functions in muti-fields, such as anti-fouling, sensor detection, materials manufacture and medical treatment. The most advantageous strategy to construct and prepare superwetting materials and expand their probable applications is deeply investigating the potential mechanisms of superwetting biological organisms. During the last 2 decades, superwetting biological organisms with superhydrophobicity, superhydrophilicity, directional liquid-transportation, and multifunctional composite surfaces integrating superwettability with other physicochemical properties have brought great enlightenment to the development of superwettable materials. With further research of more unique biological phenomena, more practical superwetting materials will be utilized for a wider range of applications in the near future.

The primary task of this Research Topic is to compile high-level researches on bioinspired superwettable materials for the solution of actual scientific problems. In this Research Topic, we present ten original articles and seven review articles, aiming to highlight the recent progress of bioinspired superwetting materials in the fields as diverse as controlled preparation of functional materials, anti-fouling, biosensing and biomedicine, etc.

The deposition of unwanted objects (e.g., ice, wax and bacteria) has been caused significant Research Topic in both daily life and industrial production. As a result, there has been an increased interest in the development of superwetting interfacial materials that offer efficient and sustainable resistance to deposition. Zhang et al. prepared a cheap superwetting micro/nanostructured surfaces with excellent anti-icing properties and promising applications scenarios in low-temperature environments. The surface was fabricated by the combination of deep reactive ion etching, glancing angle deposition, and fluorocarbon deposition. Based on classical heterogeneous nucleation theory, Li et al. roughened and fluorization-modified an Al substrate for preparing the superhydrophobic surfaces. The water vapor condensation experiment finally confirmed that only

superhydrophobic surfaces with coral-like micro/nano-structures showed excellent anti-condensation properties, the droplets appear slowly and the number of droplets is rare. Due to a higher nuclear barrier caused by the smaller nanostructure, most of the superhydrophobic materials areas remained dry. This research offers a new avenue for the practical application of advanced superhydrophobic materials in anti-solid and anti-liquid fouling. Biofilms, which are the primary cause of most oral diseases, originate from the attachment of salivary proteins and pioneer bacteria. Natural antifouling surfaces inspire new antibacterial strategies. Zhang et al. summarized the mechanisms and fabrication strategies of bio-inspired superwetting materials to prevent the adhesion of bacteria, and highlighted their applications in dentistry. These novel strategies provide a solid foundation for oral antimicrobial application and improving the efficacy of anti-bacteria. The reason why bio-inspired superhydrophobic preparation means has received intense attention in recent years is that it has been widely applied in anti-fouling, liquid-liquid separation, and other applications. Ge-Zhang et al. expounded the basic principle of superhydrophobic surface through different superhydrophobic models, summarized the structural features of biological superhydrophobic surfaces (e.g., lotus leaves), and detailly introduced the characteristics differences and applications of various surfaces. Finally, the challenges and future development directions of bionic superhydrophobic surfaces were discussed. However, the poor durability of bio inspired superhydrophobic materials limits their practical application. In addition to elucidating five typical superhydrophobic models, Luo et al. summarized the improvement of superhydrophobic surfaces in terms of wear resistance and chemical corrosion resistance, and discussed the testing measure of durability such as tape-peeling methods and electchemical corrosion. They also demonstrated the application of stable superhydrophobic interfacial materials in anti-fouling, mixture separation, membrane distillation, and electrochemical process.

With the advancement in the field of nanotechnology, nanomaterials or bionic nano platforms of different scales have been applied in related fields such as reverse electrodialysis, clinical analysis, etc. These materials have selective separation and recognition functions. Inspired by the electric eel, ions can be selectively transferred by their unique ion channels for generating electricity, Yao et al., performed a composite membrane based on metal-organic framework, thereby achieving high-effective power production from salinity difference of sea water and river water. The composite membrane has a dense structure and exhibits long-term stability in saline. This study provides a guiding path for producing the high-effective salinity-gradient power generation systems based on selective transportation of anion. To effectively separate phosphopeptides and glycopeptides, Shang et al. constructed silica microspheres modified with polyhistidine. The combination of hydrophilic and hydrogen bonding interactions endow silica microspheres with high selectivity and coverage, benefiting for the Research Topic of phosphopeptides and glycopeptides at the same time, . Furthermore, this strategy allows sequential elution of phosphopeptides and glycopeptides, showing significant potential in co-analysis of protein in clinical medicine. For the patients with chronic kidney disease, cardiac surgery-associated acute kidney injury (CSA-AKI) may increase the mortality rates of the disease. Bai et al. used Gemini C_{18} column and high-resolution mass spectrometry to analysis the proteomic of urine samples from six CSA-AKI patients, aimed to investigate the possible correlation between changes in urine proteomics and CSA-AKI. The Gemini C_{18} silica microspheres can be enhanced the protein recognition rate to achieve highly precious resources for the urinary differential expressed proteins of AKI. This analysis provides indispensable foundation about urinary proteome biomarkers and valuable resources for deeper study of AKI. Additionally, Wu et al. concluded the various bio-inspired nanoparticles (e.g., metallic nanoparticles, polymeric nanoparticles and nanovesicles) in biomedical fields and discussed the progress of bioinspired nanotechnology in biomedicine. Then, they highlighted the importance of fabricating nanoparticles through the bioinspired route. Finally, the preparation of new nanoparticles and their applications in the field of biomedicine are prospected.

Superwettable surfaces have also been extensively studied for use in fabricating sensors (e.g., electrochemical immunosensor and non-enzymatic sensors) in medical field. As one of the neurodegenerative disease, Alzheimer's disease (AD) is caused by the injury of brain neurons, which severely affect human normal life and health. Based on the superwetting microdroplet array, Huang et al. reported an sensing platform by electrochemical way for detecting various AD biological markers in blood. In comparison, this superwetting sensor has excellent properties such as large specific surface area, excellent conductivity and prominent biocompatibility. In addition to health detection, Chen et al. developed a non-enzyme sensor with the liquid-solid-air triphase interfacial electrode for electrochemical applications. The sensor collaboratively utilizes the property of electrocatalytic glucose oxidation to promote the formation of local alkalinity production. The high local pH value is obtained through the oxidation reaction at the three-phase interface, thus realizing the electrochemical detection of glucose at neutral solution. For acquiring deep insight into the biosensors, Yang et al. clearly introduced the sensing methods of superwetting biosensors for disease detection by biomarkers, which mainly introduces disease analysis by fluorescence analysis, electrochemistry display, surface enhancement Raman scattering assay and visional means. The author further systematically introduces the applications of super-wettable biosensors in the field of biomarkers, and finally gives suggestions on the future challenges and development of sensors.

As one of the superwettable materials, interestingly, superwetting materials can enhance the ability of cartilage regeneration. Inspired by the mussel-adhesive phenomenon, Chi et al. proposed a simple preparation method for osteoconductive and osteoinductive nanomaterials utilizing material extrusion techniques and surface modification strategies. By adding polydopamine and hydroxyapatite nanoparticles on the surface of the composite material, the 3D printed porous scaffold with enhanced osteogenesis was prepared. The physical and chemical properties of the scaffold such as surface wettability, roughness, mechanical performance, and biodegradability was studied to demonstrate the enhanced osteogenesis ability. The superwetting material will inevitably endure the impact of the bone, Liu et al. investigated the impact resistance and energy dissipation of multilayer bioinspired composites based on the fiber periodic helical structure of fibers. Under the same material component and property parameters, adjusting the fiber spiral angle of the fiber can effectively improve

the stress concentration of the bioinspired materials caused by external impact. In conclusion, the mineralized collagen fibers based on the periodic spiral structure in osteons can effectively improve the impact resistance property of cortical bone. The research results have guiding significance for the design and preparation of high performance biomimetic osteogenic superwetting materials. Inducing cartilage reproduction can cure temporomandibular disorders with biomaterials. However, the wettability of bone-filled biomaterials was not satisfactory. For addressing this problem, Yang et al. placed mesenchymal stem cells with wetting properties on the surface of TGF-β-loaded gelatin methacryl microspheres, resulting in active wetting of biomaterials. Modified gelatin-MSCs microspheres can more effectively localize bone defect repair sites, expediting the healing of temporomandibular joint defect area caused by releasing cytokines at specific sites. This method provides a new strategy for the development of cartilage regeneration materials through the addition of infiltrating factors. Therefore, superwetting materials will play a great role in bioengineering and medical remediation. As one of the bioinspired superhydrophilic materials, hydrogels have excellent properties such as biocompatibility, biodegradability and strong crosslinking. The above excellent physical and chemical properties will make hydrogels promising to be a new delivery platform and unconventional therapy for repairing endometrial damage. Many works on bioinspired-hydrogels for subcavity endometrial repair was discussed. For example, As the post-operative physical barrier and therapeutic delivery platform, Dong et al. discussed recent developments in hydrogel delivery platforms for endometrial repair. In addition, the development status, application limitations and future development of hydrogels are discussed in detail. Liquid-infused surfaces (LIS) also have unique prospects in the fields of biological engineering, medical equipment, and biosensor. LIS also play an important role in the fields of bioengineering, medical devices and biosensing. Yang et al. focused on the influence of liquid layers on the properties of medical materials. At the same time, the development trend of information system in the future is forecasted.

Overall, this Research Topic cover several cutting-edge fields in bio-inspired materials with superwettability, such as anti-adhesive materials, sensing detection systems, life medical treatments, etc., which help readers understand the application progress of bio-inspired materials with superwettability. Despite the encouraging results mentioned above, more research is still needed to gain a deeper understanding of the mechanisms for applications and to develop more superwetting materials that can be applied more quickly.

Author contributions

All authors listed have made a substantial, direct, and intellectual contribution to the work, and approved it for publication.

Funding

JM also appreciates the support of the Strategic Priority Research Program of the Chinese Academy of Sciences (XDB 0470000), State Key Laboratory of Advanced Technology for Materials Synthesis and Processing (Wuhan University of Technology), National Natural Science Foundation of China (22275203). HL appreciates the Taishan Young Scholar Program (tsqn202103053) and the Fundamental Research Projects of Science and Technology Innovation and Development Plan in Yantai City (2022YTJC06002541). PZ appreciates the support of the National Basic Research Program of China (2021YFA0715700) and the National Natural Science Foundation of China (22202157).

Acknowledgments

The editors appreciate the contributions of all the authors to this Research Topic, the constructive comments of all the reviewers, and the editorial support from Frontiers throughout the publication process.

Conflict of interest

The authors declare that the research was conducted in the absence of any commercial or financial relationships that could be construed as a potential conflict of interest.

Publisher's note

frontiers in Bioengineering and Biotechnology

ORIGINAL RESEARCH
published: 21 March 2022
doi: 10.3389/fbioe.2022.872268

Bio-Inspired Hierarchical Micro/Nanostructured Surfaces for Superhydrophobic and Anti-Ice Applications

Lansheng Zhang[1†], *Paul C. Uzoma*[1†], *Chu Xiaoyang*[1], *Oleksiy V. Penkov*[1] *and Huan Hu*[1,2*]

[1]ZJU-UIUC Institute, International Campus, Zhejiang University, Haining, China, [2]State Key Laboratory of Fluidic Power and Mechanical Systems, Zhejiang University, Hangzhou, China

We report a scalable and cost-effective fabrication approach for constructing bio-inspired micro/nanostructured surfaces. It involves silicon microstructure etching using a deep reactive ion etch (DRIE) method, nanowires deposition *via* glancing angle deposition (GLAD) process, and fluorocarbon thin film deposition. Compared with the smooth, microstructured, and nanostructured surfaces, the hierarchical micro/nanostructured surfaces obtained *via* this method showed the highest water contact angle of ~161° and a low sliding angle of <10°. It also offered long ice delay times of 2313 s and 1658 s at −5°C and −10°C respectively, more than 10 times longer than smooth surfaces indicating excellent anti-icing properties and offering promising applications in low-temperature environments. These analyses further proved that the surface structures have a significant influence on surface wettability and anti-icing behavior. Hence, the GLAD process which is versatile and cost-effective offers the freedom of constructing nanostructures on top of microstructures to achieve the required objective in the fabrication of micro/nanostructured surfaces when compared to other fabrication techniques.

Keywords: hierarchical micro/nanostructures, superhydrophobic, anti-icing, GLAD, deep reactive ion etching

OPEN ACCESS

Edited by:
Tailin Xu,
Shenzhen University, China

Reviewed by:
Likun Zhu,
Indiana University, Purdue University Indianapolis, United States
Ke Du,
Rochester Institute of Technology, United States

***Correspondence:**
Huan Hu
huanhu@intl.zju.edu.cn

[†]*These authors have contributed equally to this work and share first authorship*

Specialty section:
This article was submitted to Bionics and Biomimetics, a section of the journal Frontiers in Bioengineering and Biotechnology

Received: *09 February 2022*
Accepted: *01 March 2022*
Published: *21 March 2022*

Citation:
Zhang L, Uzoma PC, Xiaoyang C, Penkov OV and Hu H (2022) Bio-Inspired Hierarchical Micro/Nanostructured Surfaces for Superhydrophobic and Anti-Ice Applications. Front. Bioeng. Biotechnol. 10:872268. doi: 10.3389/fbioe.2022.872268

INTRODUCTION

The formation of ice on artificial surfaces causes significant problems to industries and human life qualities. Ice accretion on the wings of an aircraft's cab alters the aerodynamic characteristic of aircraft leading to flight stability and safety issues (Cao et al., 2015); icing on blades of wind turbines causes reduced energy generation efficiencies, degradation of the aerodynamic performance, and even flight accidents (Kraj and Bibeau, 2010; Dong et al., 2020); icing on thermal exchanger surfaces such as those in refrigerators increases the thermal resistance between the refrigerant and the surrounding air thus reduce the heat exchange efficiency (Malik et al., 2020); icing on walls of tall buildings and towers pose a serious threat to people and properties on the ground (Carter and Stangl, 2012); ice stack on the antenna, camera, solar panels also lead to a drop in output efficiency and durability (Rahmatmand et al., 2018). These challenges and more are behind the drive to design and construct durable icephobic surfaces to suppress icing and protect surfaces from being covered with ice.

Existing solutions to icing problems fall into active and passive categories. Active approaches use external energy sources such as heating wires, hot airs, mechanical vibration, or ultrasonic to remove

ice (Tian et al., 2015; Gao et al., 2019; Liu et al., 2020a; Shan et al., 2020), which are efficient but costly, require complex piping systems, and is demanding high energy. Passive approaches use a combination of physical and chemical methods such as slippery liquid-infused porous surface (SLIPS), coating, electrochemical deposition, etching, self-assembly technique, etc. (Kumar et al., 2019; Latthe et al., 2019). Passive approaches are preferred in situations where human operation is difficult like in tall buildings, power towers, etc. In passive approaches, adding a layer of icephobic coating is the most common method. For example, Wu et al. prepared an anti-icing coating on concrete using fluorinated silicon-based copolymer adhesive and nano-silica (Wu et al., 2020). Paul et al. reported the use of functionalized nanodiamonds and acrylic resin to design an icephobic coating on an aluminum substrate (Uzoma et al., 2021). Also, Huang et al. has proposed the use of hydrogels to design anti-icing coatings on various kinds of substrates (Huang et al., 2020). Interestingly, most of the reported icephobic coatings also exhibit superhydrophobic properties. However, the anti-icing ability by coating a substrate with a thin superhydrophobic film is not sufficient to satisfy the end-use requirements because they easily fail under the conditions of mechanical abrasion, high humidity, and heavy snowfall (Kreder et al., 2016; Latthe et al., 2019).

Inspired by Nature, scientists have designed superhydrophobic surfaces for many crucial applications such as anti-icing (Onda et al., 1996; Lin et al., 2011; Latthe et al., 2019), biosensing (Xu et al., 2017; He et al., 2018; Song et al., 2018; Xu et al., 2018; Xu et al., 2019), energy storage (Sun et al., 2019), and surface-enhanced Raman scattering (SERS) (Chen et al., 2018). The hierarchically structured surface was found to be one of the key factors for the superhydrophobic property because it provides a composite surface consisting of both solid surfaces as well as air pockets, thereby increasing the contact angle and rendering more repellent surfaces for water (Feng et al., 2002; Liu et al., 2020b; Wu et al., 2021). Hence, water droplet from rains or snow, or condensed water droplet can roll off the surface before it forms ice.

Wenzel and Cassie's models have been used to effectively describe the behavior of droplets on a surface (Wenzel, 1936; Cassie and Baxter, 1944). A droplet on a solid surface can either spread or contract till the contact angle with the surface gets to a certain value. The value of the angle is known to depend on the parity between the interfacial contact to reduce the surface free energy. On a rough surface, Wenzel proved that there is an increase in the contributions of the solid-liquid and solid-vapor areas to the surface free energy. His equation also suggests that the surface texture affects the essential wetness behavior because it assumes that the liquid remains in contact with the solid surface at all points within the projected droplet's contact area. Hence, in Wenzel's state, the water will fill into the micro/nanostructure of a textured surface. On the other hand, Cassie described a situation where the drop is suspended by air pockets trapped inside the textured surface suggesting that the liquid-gas interface replaced some of the liquid-solid interface (Cassie and Baxter, 1944; Uzoma et al., 2019). Within the structured surface approach, hierarchical micro/nanostructured (MN) surfaces achieve larger contact angles and smaller sliding angles for water droplets therefore potentially enhancing anti-icing properties (Guo et al., 2012; Guo et al., 2014). Shirtcliffe et al. have shown an increase in the superhydrophobic properties of hierarchical MN surfaces when the microstructure is in the Wenzel state and the nanostructure is in the Cassie state (Shirtcliffe et al., 2004). They suggested that for surfaces with dual-length scale roughness, the upward part of the surface tension of a water drop suspended between two short pillars could contribute to the influence of smaller scale roughness at the base of the pillars permitting the suspension of the water drop on the smaller scale roughness. This will make a micro/nanostructured surface show a large water contact angle while possessing relatively lower surface roughness. Also combining a rough base with smooth pillars can protect the rough surface against wear. Peng and co-workers demonstrated that MN surfaces can impact durable anti-icing property more than surfaces with only nanostructure, microstructure, or smooth surface (Guo et al., 2012). Bhushan et al. proved that hierarchical MN surfaces can overcome scale-dependent contact angle hence creating stable superhydrophobic states (Michael and Bhushan, 2007). (Wang et al., 2022) recently design MN surfaces that can spontaneously transition from Wenzel to Cassie state during the icing/deicing cycle. The surface was fabricated using the ultrafast laser ablation method.

MN surfaces are not straightforward to produce because a single fabrication approach is difficult to produce both microstructures and nanostructures. Du et al. used a combination of laser interference lithography, reactive ion etching, and e-beam deposition techniques to fabricate MN surface (nanoporous trilayer composite films) (Du et al., 2013). Electron beam lithography was applied to fabricate hierarchical micro/nanostructures but suffers from high cost and small area (Feng et al., 2011; Pattantyus-Abraham et al., 2013; Kumar et al., 2019). Normally, fabricating these types of surfaces requires a combination of a microfabrication process and a nanofabrication process. For example, microfabrication consisting of a UV lithography and etching as well as metal-assisted chemical etching was used to produce monolithic silicon hierarchical MN surfaces (Hu et al., 2014), but this method is only applicable to single-crystal silicon. Others use CVD-grown ZnO nanowires on top of microstructures, but normally require high temperature and furnaces to prepare (Bhujel et al., 2019; Choi et al., 2021). The machining process has also been employed to produce micro-rachets together with nano hairs prepared by crystal growth (Guo et al., 2012).

Here, we report a new process of producing hierarchical MN surfaces with a large contact angle of ~161° and a small sliding angle of ˂10°. Moreover, we demonstrated a long icing delay time (IDT) of 1658 s and 2313 s at −5°C and −10°C respectively, both are more than 10 times longer than the IDT on smooth surfaces without MN structures. Furthermore, we showed the fabrication of MN surfaces on a 4-inch wafer scale in a low-cost fashion, which is very promising in practical applications.

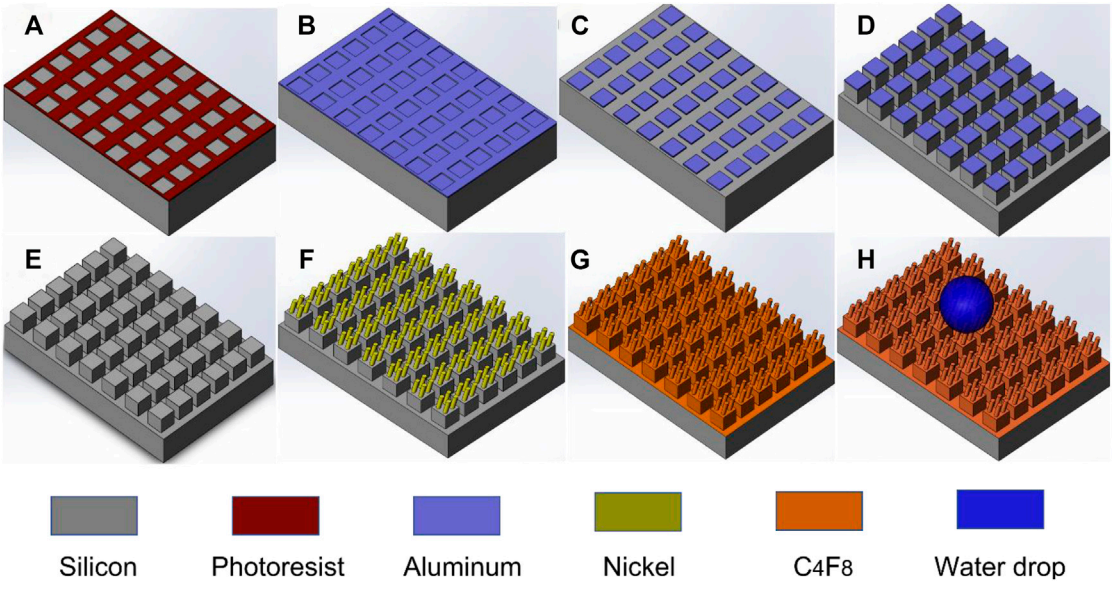

FIGURE 1 | Schematic illustration of the major fabrication processes of micro/nano hierarchical structure. **(A)** UV photolithography; **(B)** Aluminum deposition; **(C)** Aluminum lift-off process; **(D)** Deep reactive ion etch; **(E)** Removal of aluminum; **(F)** GLAD nickel nanowires; **(G)** C_4F_8 deposition; **(H)** A water drop on the surface.

EXPERIMENT

Fabrication Process

The fabrication of the hierarchical micro/nanostructured surface involves three main processes: silicon microstructure fabrication, nanowires deposition, and fluorocarbon C_4F_8 thin film deposition as described in **Figure 1**. The substrate used is a p-type <100> silicon. A micro-pattern of photoresist was designed *via* UV photolithography (step a), followed by the deposition of 300 nm thick aluminum (step b), and thereafter, applied the lift-off process to produce an aluminum metal mask (step c). Deep reactive ion etch (DRIE) was employed to etch silicon using the aluminum pattern as a mask (step d). Then aluminum etchants were used to etch aluminum to produce micro silicon pillar arrays (step e). Following these steps, the GLAD process was used to produce nickel nanowires on the micropillar's surface (step f). Finally, 20 nm thick amorphous fluorocarbon film was deposited on the surface to reduce the surface energy and improve water resistance (step g). Step h shows a schematic diagram of water drop on the hierarchical micro/nanostructured surface.

Glancing Angle Deposition Process

The nickel nanowires (step f) were fabricated using a custom-designed electron-beam evaporation system. The source materials for evaporation were nickel pellets (Ni 13,301, Φ: 3 mm × 3 mm, purity: 99.9%) obtained from Zhong Nuo Advanced Material Technology Co., Limited. The incident angle was fixed at 86° degrees to allow the self-formation of nanopillars, and the vacuum pressure was 4×10^{-6} Torr. The deposition rate was maintained at 0.2 nm/s. Nickel is used because of its good wear and corrosion resistance, and ductility which is particularly useful in anti-icing applications (Bassford et al., 1998).

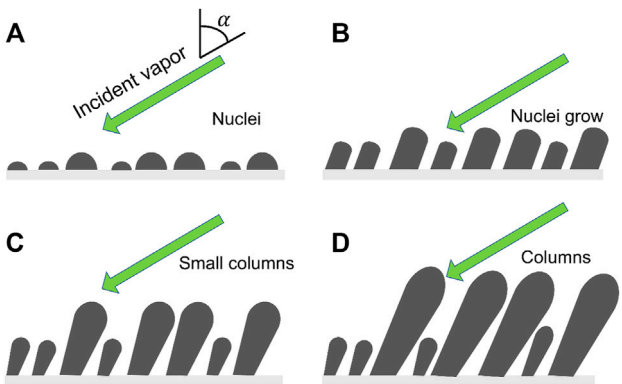

FIGURE 2 | Schematic view of GLAD nanowires growth. **(A)** Vapor flux at an angle α produces a random distribution of nuclei on a substrate surface, **(B)** nuclei grow; **(C)** the nuclei develop into columns, some smaller columns were shadowed and stopped their growth; **(D)** columns growth and the further growth is restricted to the top of columns.

Figure 2 shows the growing process of nanowires using GLAD. It starts with the formation of the diverse sizes of the deposited random islands followed by the gradual amplification of the surface topography via ballistic shadowing. Hence a planar substrate will roughen through Volmer–Weber mode growth (Taschuk et al., 2010) and the resultant defects will also accelerate surface roughening. The initial stage of GLAD nanowires growth is shown in **Figure 2A**. The nuclei grow into columns and develop shadows as shown in **Figure 2B**. The columns and shadows screen the neighboring nuclei from

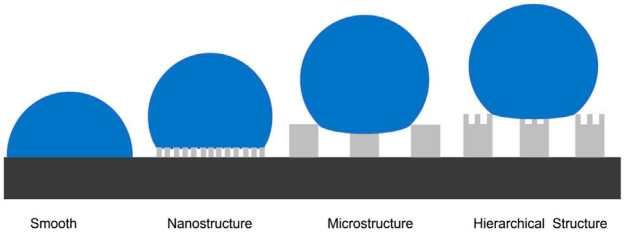

FIGURE 3 | Schematic illustration of the water droplet on the differently structured surfaces.

incoming vapor flux thereby suppressing their growth (**Figure 2C**). The smaller nuclei and columns are completely shadowed and stop growing as seen in **Figure 2D**. Eventually, nanowires are formed without using nanotemplate or other expensive nanolithography techniques.

The key factors to have the nanowires successfully on surfaces are that the incident evaporation vapor is not blocked by other micropillars and the incident evaporation vapor has a certain angle with the surface similarly like with the top surfaces. When the evaporation vapor is almost vertical to the front sidewall surface as the normal evaporation, a thin film is formed instead of nanowires. When the sidewalls are not able to be touched by the evaporation source, no films or nanowires can be formed. When the sidewalls are almost parallel to the evaporation vapor forming a very small angle, nanowires are formed. Most areas on the bottom surfaces have nanowires except areas that are shadowed by micropillars. **Supplementary Figure S1** in supplementary materials shows the surfaces on different sidewalls of micropillars as well as on the bottom surfaces. **Supplementary Figure S2** illustrates the effects of the wafer size and position of the substrate on the heights of the nanowires.

The equilibrium contact angle (CA) is widely used to characterize the wetting behavior of a surface. The well-known Cassie–Baxter theory describes the equilibrium CA of a composite surface where vapor pockets are trapped underneath the liquid as expressed by the following equation (Cassie and Baxter, 1944):

$$cos\theta^{*} = f\left(cos\theta_{y} + 1\right) - 1 \quad (1)$$

Where θ* represents the apparent CA. It is the sum of all the contributions of the liquid-solid and liquid-vapor interfaces as expressed in the Cassie-Baxter equation which is obtained using the contact angle goniometer and the ImageJ software., f is the area fraction of the solid that is in contact with the liquid, θ_y is the equilibrium CA of the liquid droplet on a smooth surface of the same substrate material. From this equation, we can adjust f and θ_y to increase the equilibrium CA. f is reduced by controlling the surface roughness and θy is increased by the addition of low-surface-energy materials. In this paper, the surface roughness was increased by the fabrication of microstructure, nanostructure, and hierarchical structure (microstructure and nanostructure) on the surface and the reduction of the surface energy *via* the deposition of fluorocarbons (C_4F_8) on the surface. **Figure 3** shows the schematic of the wetting behavior of a water drop on the differently structured surfaces. MN structures enable even smaller contact area of solid-liquid than only nanostructured or microstructured surfaces.

In order to determine the contributions of different surface structures to superhydrophobicity, we prepared four types of sample sets: hierarchical micro/nanostructured surface, microstructured surface, nanostructured surface, and smooth surface. These four surfaces were coated with an amorphous fluorocarbon (C_4F_8) film. The image of the droplet was taken by using a water drop shape imaging system and the water contact angle was measured by the ImageJ software. The sliding angle was measured by tilting the sample stage and recording when the droplet began to slide. All the droplets were generated by a micro-injector. Three duplicate measurements were taken for all the samples under normal laboratory ambient conditions.

Anti-Icing Properties Measurements

Icing delay time (IDT) measurement was used to characterize the anti-icing ability of the four samples with different surface structures. The ice formation platform was designed using a Peltier thermoelectric generator sandwiched between a copper plate and a water-cooling unit as shown in **Supplementary Figure S3**. A digital temperature controller was attached to the platform to regulate the temperature. A 5 μL water droplet was used on a 1 cm × 1 cm sample area, and the time taken for the water droplet to turn into ice was recorded. When the ice was formed, the droplet lost its transparency easily as captured by image analysis. Three duplicate measurements were taken for all the samples at normal laboratory ambient conditions (22°C and 24% relative humidity).

RESULTS AND DISCUSSION

Micro/nanostructured Surface Features

Figure 4 shows three different hierarchical micro/nanostructured surfaces from the above-described fabrication process in **Figure 1** (steps a–h). As seen in **Figure 4**, images a, b, and c have three different silicon microstructures (cylinder, regular pentagon columns, and rectangular columns) fabricated by the DRIE process and the same nickel nanostructures fabricated by the GLAD process (a3, b3, c3). The dimensions of these three different microstructures are outlined in **Table 1**.

Figure 4 (a3, b3, c3) shows the nickel nanowires produced using the GLAD process while **Figure 5** describes the statistics of nanowires' top width and height. 100 nanowires were measured in order. The average height of the nanowires is 101 nm with a higher concentration between 80 and 120 nm. The pillar top width concentrated between 10 and 14 nm with a 12 nm average. The evaporation time and metal thickness are used in controlling the height of the nanowires. Interestingly, the 3 MN structures in **Figure 4** offered approximately the same CA value of 161° (a = 161.1 ± 0.5; b = 160.7 ± 0.8; c = 160.7 ± 0.6). This might be because the three structures possess the same unit distance as seen in **Table 1** and the same area fraction as discussed in the next

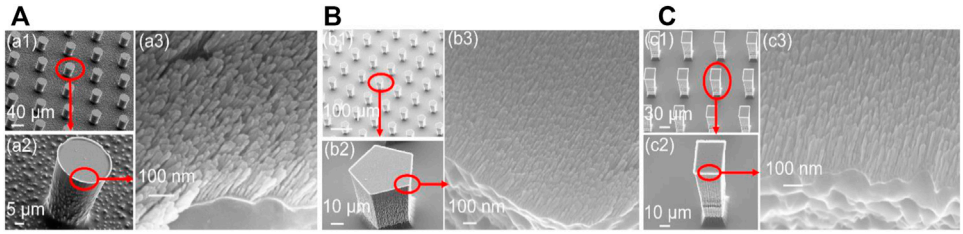

FIGURE 4 | Three hierarchical micro/nanostructured surfaces with different microstructures, **(A)** cylinder, **(B)** regular pentagon columns, **(C)** rectangular columns

TABLE 1 | Dimensions of three microstructures.

Microstructures	Diameter or length of side (μm)	Height (μm)	Unit distance (μm)
Cylinder	35.6	42	99
Regular pentagon columns	24.1	42	99
Rectangular columns	31.6	61	99

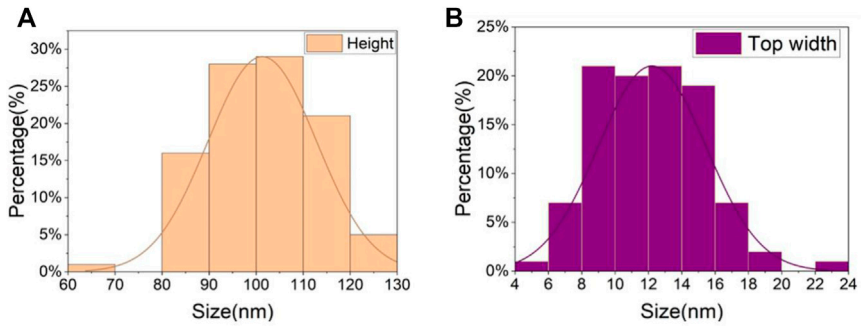

FIGURE 5 | The measured statistic data of the nickel nanowire sizes. **(A)** height of nanowires, **(B)** top width of nickel nanowires.

section. It suggests that the CA is less dependent on the shape of the microstructure.

Wettability Analysis

Figure 6 shows the equilibrium water CA of the four different structured surfaces which are smooth (S), microstructured (M), nanostructured (N), and hierarchical micro/nanostructured (MN) surfaces. The obtained results are plotted on the theoretical Cassie state curve. The equilibrium water CA of the S surface with fluorocarbon film is 110° and the area fraction obtained using **Eq. 1** is ~1. The CA of the N surface is 117° and the same *f* value of 0.79 was obtained using **Eq. 1** and **Figure 4** (a3, b3, c3). This indicates that the nanopillars on the surface are close-knit, and there is a good agreement between the experimental and theoretical results. The equilibrium CA of the M surface is 153°, the experimented *f* value is 0.15, and the *f* value obtained from **Figure 4** (a1, b1, c1) is 0.1 which is within the permitted error margin. For the MN surface, the equilibrium CA is 161° and the *f* value is 0.12 which is approximately close to the theoretical *f* value of 0.08. From the results, it is shown that the water droplet had a Wenzel wetting state contact with the S and N surfaces but showed a Cassie state contact with the M and MN surface. This can be attributed to the composite nature of the M and MN surfaces made of solid materials and trapped air. Also, the highest CA value seen in the MN surface is because of the hierarchical nature of the surface. These findings also prove that superhydrophobicity is largely dependent on multi-scale structures as seen in nature such as lotus leaves (Darmanin and Guittard, 2015; Neinhuis and Barthlott, 1997). Besides, the results are in concordance with literature; MN structured surfaces were shown both experimentally and theoretically that the presence of submicron and nanostructures can decrease the threshold of micropillar height to attain superhydrophobicity (Patankar, 2004; Sui et al., 2021). In cases of extremely small droplets, the nanostructures can prevent them from accessing the groves (Liu et al., 2011). The water contact angle hysteresis of M and MN surfaces are 9° and 15° respectively as shown in **Supplementary Figure S4**, indicating that the

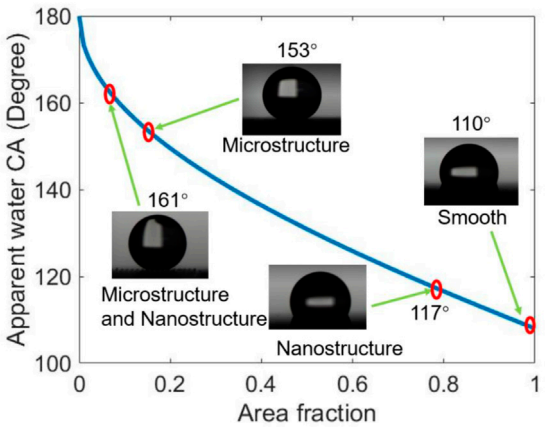

FIGURE 6 | The equilibrium water contact angle of the various structured surfaces compared with the theoretical Cassie state curve. The apparent CA is the sum of all the contributions of the liquid-solid and liquid-vapor interfaces and is also the contact angle we measured using the goniometer and ImageJ software. And the area fraction is the fraction of the solid in contact with the liquid as described in the Cassie–Baxter equation.

droplet is more likely to adhere to the M surface than the MN surface. Furthermore, **Supplementary Video S1** proved that water droplets can easily roll off the MN surface at a very low tilt angle (< 10°). The low contact angle hysteresis and low sliding angle of the superhydrophobic surface are very essential for self-cleaning applications (Neinhuis and Barthlott, 1997; Yilbas et al., 2018). It is interesting to note that M structured surfaces have been reported to show good application potential (Song et al., 2020a; Song et al., 2020b; Fan et al., 2021).

Anti-Icing Analysis

The icing delay time (IDT) of 5 μL water droplets on the S, N, M, and MN surfaces at −5°C and −10°C temperatures were measured, and the results are shown in **Figure 7**. The initial temperature of the droplet is 20°C, and the images in **Figure 7** show the gradual transformation of the droplet from liquid to ice. The droplet on the S surface shows the least IDT of 180 and 110 s at −5°C and −10°C respectively, suggesting that normal smooth silicon surfaces do not have anti-icing properties. The icing times for the droplet on the N surface at −5°C and −10 °C are 959 and 282 s respectively, while the times to form ice for the droplet on the M surface at −5°C and −10°C are 1620 and 1151 s. The hierarchical MN surface offered the highest IDT of 2313 and 1658 s at −5°C and −10°C respectively, indicating that it has improved anti-icing properties compared to the other structured surfaces. Furthermore, the results showed a reduction in the IDT as the temperature decreases from −5°C to −10°C; the different surfaces S, N, M, and MN exhibited 39, 70, 29, and 28% respective decrease in the IDT values. This proves that the ice delay time is strongly influenced by the substrate's temperature because decreasing the substrate's temperature could alter the CA of the water droplet and eventually lead to the Cassie-Wenzel transition (Su et al., 2016; Li and Guo, 2018). MN surface is the least affected by the temperature change suggesting improved Cassie state stability. Besides, there are no observable changes in the SEM images of the MN surfaces after 10 cycles of icing/deicing as shown in

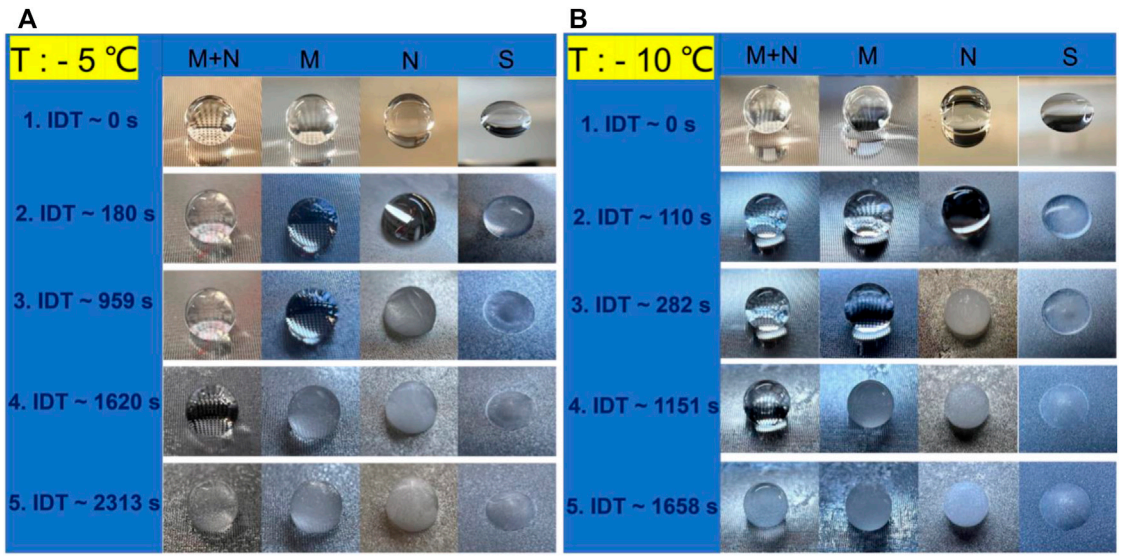

FIGURE 7 | Observations of ice formation on the differently structured surfaces at −5°C and −10°C cooling temperatures. From right to left are the photos of the droplets on the surfaces of S, N, M, and MN, respectively. **(A)** Record of ice formation and IDT at −5°C: Frame 1 (IDT ~0 s) shows the water drop on the surface prior to the experiment; Frame 2, the droplet on S surface freezes at ~180 s IDT; Frame 3, the droplet on N surface freezes at ~959 s; Frame 4, the droplet on M surface freezes at ~ 620 s IDT; Frame 5, the droplet on MN freezes at ~2313 s IDT. **(B)** Record of ice formation and IDT at −10°C with each frame showing a similar trend as **(A)**.

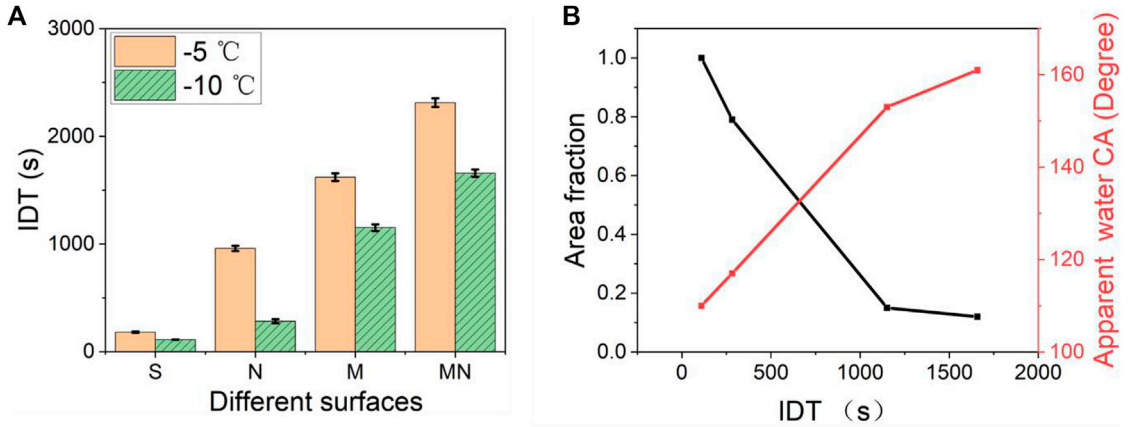

FIGURE 8 | (A) Shows the contrast on the IDT of the various structured surfaces at −5°C and −10°C. The MN surface shows the longest DT of 2313 ± 40 s while the S surface shows the shortest IDT of 180 ± 6 s **(B)** Shows the relationship between the area fraction, apparent water contact angle, and the IDT at −10°. The apparent water contact angle is the sum of all the contributions of the liquid-solid and liquid-vapor interfaces as expressed in the Cassie–Baxter equation which is obtained using the contact angle goniometer and the ImageJ software.

Supplementary Figure S5 signifying that the ice formation did not destroy the MN surfaces.

Figure 8A shows the statistical contrasting column plots of the IDT of the various surfaces at −5°C and −10°C. **Supplementary Video S2** recorded the whole process of water droplets' transition from the liquid state to the ice state for the S and MN surfaces. The high IDT values obtained from the superhydrophobic surfaces can be attributed to the fact that heat transfer proceeds majorly over the contact area between ice and the structured pillars. Since the water droplet sits atop the air pockets on the superhydrophobic surfaces, and due to the low thermal conductivity of air, the structured pillars served as the primary mode of heat transfer in the vertical direction between the cold silicon substrate and the water droplet. The pockets of air between neighboring structured pillars and the water droplet interface act as a thermal absorbing layer (heat block) leading to decreased heat transfer efficiency. Furthermore, the classical nucleation theory suggests that the larger the CA of the substrate, the greater the free-energy barrier required for the ice nucleus formation, and the smaller the rate of nucleation, making the ice formation more difficult and slower (Varanasi et al., 2009; Varanasi et al., 2010). As seen in **Figure 8B**, the smaller the apparent contact area, the lower the heat transfer efficiency resulting in increased IDT. MN surface which has the largest CA with the least area fraction showed the longest IDT signifying excellent anti-icing behavior. Similar observations have been reported elsewhere (Li and Guo, 2018; Nguyen et al., 2018). In practice, a reduced ice nucleation temperature will enable more equipment and devices to be safely and effectively employed in environments of lower temperatures thereby generating greater productivity and profitability. Likewise, a longer IDT will increase the chances of water removal from the surface before the ice formation.

To further increase the anti-ice properties, both microstructures and nanostructures can be optimized. The micropillar gap, area fractions, heights can be easily defined by the UV-lithography and the DRIE etching step. The nanowire heights, material type can be optimized in the GLAD step by changing the deposition time and using more thermally insulative target materials such as titanium oxide (TiO2) (Fresno et al., 2021) and tin oxide (SnO2) (Chetri and Dhar, 2019). The gap of the GLAD nanowires is more difficult to change mostly determined by the initial nucleation but can be controlled in certain degrees using a prefabricated seed layer (Dick et al., 2003). The advantages of our fabrication approach are the scalability and cost-effectiveness, essential for the application of anti-ice applications.

CONCLUSION

A new scalable and cost-effective method of fabricating hierarchical MN surfaces consisting of a standard microfabrication process and GLAD was demonstrated. The exciting advantage of GLAD lies in its versatility in the control and design of different types of nanostructures. The wettability analysis test results show that the contact angle of liquid droplets depends on the area fraction and is not affected by the shape of the microstructure (M surface). The obtained hierarchical MN surface offered a large water contact angle of ~161° and sliding angle of <10° indicating good self-cleaning potentials. In addition, the surface showed an excellent icing delay time of 2313 s and 1658 s at −5°C and −10°C respectively, both are more than 10 times the icing delay time of smooth surfaces. This high icing delay time was attributed to the larger CA of the surface contributing to a higher energy barrier for ice nucleation. Besides, the CA and the IDT of the three different MN surfaces showed good consistency due to the standardization of the fabrication process.

DATA AVAILABILITY STATEMENT

The raw data supporting the conclusion of this article will be made available by the authors, without undue reservation.

AUTHOR CONTRIBUTIONS

LZ performed the fabrication and characterization; PU contributed to the data analysis and led the writing; CX contributed to the characterization setup and test; OP contributed to the concept formation and revised the manuscript; HH formed the concept, revised the manuscript, and led the whole project.

FUNDING

This work was led by the HH. The work was also funded by the NSFC normal grant (Grant No. 61974128), Natural Science Foundation of Zhejiang Province (Grant No. LY19F040007), the Center of Pathogen Detection in the Dynamic Research Enterprise for Multidisciplinary Engineering Sciences (DREMES), Cyrus Tang Foundation, Li Dak Sum and Yip Yio Chin Development Fund for Regenerative Medicine of Zhejiang University.

ACKNOWLEDGMENTS

We thank the facility of micro/nanofabrication in the nanofabrication facility in ZJUI and the microfabrication facility in the International Polymer Center.

SUPPLEMENTARY MATERIAL

The Supplementary Material for this article can be found online at: https://www.frontiersin.org/articles/10.3389/fbioe.2022.872268/full#supplementary-material.

REFERENCES

Bassford, T. H., and Hosier, J. (1998). "Nickel and its Alloys," in *Mechanical Engineer's Handbook*. Editor M. Kutz (Huntington, West Virginia: John Wiley & Sons), 71–89.

Bhujel, R., Rai, S., and Swain, B. P. (2019). Spectroscopic Characterization of CVD Grown Zinc Oxide Nanowires. *Mater. Sci. Semiconductor Process.* 102, 104592. doi:10.1016/j.mssp.2019.104592

Cao, Y., Wu, Z., Su, Y., and Xu, Z. (2015). Aircraft Flight Characteristics in Icing Conditions. *Prog. Aerospace Sci.* 74, 62–80. doi:10.1016/j.paerosci.2014.12.001

Carter, M., and Stangl, R. (2012). Increasing Problems of Falling Ice and Snow on Modern Tall Buildings. *CTBUH J.* (IV), 24–28. Available at: https://global.ctbuh.org/resources/papers/download/271-increasing-problems-of-falling-ice-and-snow-on-modern-tall-buildings.pdf.

Cassie, A. B. D., and Baxter, S. (1944). Wettability of Porous Surfaces. *Trans. Faraday Soc.* 40 (0), 546–551. doi:10.1039/tf9444000546

Chen, X., Wen, J., Zhou, J., Zheng, Z., An, D., Wang, H., et al. (2018). Superhydrophobic SERS Substrates Based on Silicon Hierarchical Nanostructures. *J. Opt.* 20 (2), 024012. doi:10.1088/2040-8986/aaa100

Chetri, P., and Dhar, J. C. (2019). Au/GLAD-SnO2 Nanowire Array-Based Fast Response Schottky UV Detector. *Appl. Phys. a-Materials Sci. Process.* 125 (5), 286–293. doi:10.1007/s00339-019-2590-0

Choi, S. C., Lee, D. K., and Sohn, S. H. (2021). Nano/Micro-Structured ZnO Rods Synthesized by Thermal Chemical Vapor Deposition with Perpendicular Configuration. *Nanomaterials* 11 (10), 2518. doi:10.3390/nano11102518

Darmanin, T., and Guittard, F. (2015). Superhydrophobic and Superoleophobic Properties in Nature. *Mater. Today* 18 (5), 273–285. doi:10.1016/j.mattod.2015.01.001

Dick, B., Brett, M. J., and Smy, T. (2003). Controlled Growth of Periodic Pillars by Glancing Angle Deposition. *J. Vac. Sci. Technol. B* 21 (1), 23–28. doi:10.1116/1.1529652

Dong, X., Gao, D., Li, J., Jincao, Z., and Zheng, K. (2020). Blades Icing Identification Model of Wind Turbines Based on SCADA Data. *Renew. Energ.* 162, 575–586. doi:10.1016/j.renene.2020.07.049

Du, K., Liu, Y., Wathuthanthri, I., and Choi, C.-H. (2013). Fabrication of Hierarchical Nanostructures Using Free-Standing Trilayer Membrane. *J. Vacuum Sci. Techn. B, Nanotechnology Microelectronics: Mater. Process. Meas. Phenomena* 31 (6), 06FF04. doi:10.1116/1.4821655

Fan, C., Luo, Y., Xu, T., Song, Y., and Zhang, X. (2021). On-demand Mixing and Dispersion in Mini-Pillar Based Microdroplets. *Nanoscale* 13 (2), 739–745. doi:10.1039/d0nr08011j

Feng, J., Tuominen, M. T., and Rothstein, J. P. (2011). Hierarchical Superhydrophobic Surfaces Fabricated by Dual-Scale Electron-Beam-Lithography with Well-Ordered Secondary Nanostructures. *Adv. Funct. Mater.* 21 (19), 3715–3722. doi:10.1002/adfm.201100665

Feng, L., Li, S., Li, Y., Li, H., Zhang, L., Zhai, J., et al. (2002). Super-Hydrophobic Surfaces: From Natural to Artificial. *Adv. Mater.* 14 (24), 1857–1860. doi:10.1002/adma.200290020

Fresno, F., González, M. U., Martinez, L., Castro, M. F., Barawi, M., Villar-García, I. J., et al. (2021). Photo-Induced Self-Cleaning and Wettability in TiO2 Nanocolumn Arrays Obtained by Glancing-Angle Deposition with Sputtering. *Adv. Sustain. Syst.* 5 (11), 2100071. doi:10.1002/adsu.202100071

Gao, L., Liu, Y., Ma, L., and Hu, H. (2019). A Hybrid Strategy Combining Minimized Leading-Edge Electric-Heating and Superhydro-/ice-Phobic Surface Coating for Wind Turbine Icing Mitigation. *Renew. Energ.* 140, 943–956. doi:10.1016/j.renene.2019.03.112

Guo, P., Wen, M., Wang, L., and Zheng, Y. (2014). Strong Anti-ice Ability of Nanohairs over Micro-ratchet Structures. *Nanoscale* 6 (8), 3917–3920. doi:10.1039/c3nr04061e

Guo, P., Zheng, Y., Wen, M., Song, C., Lin, Y., and Jiang, L. (2012). Icephobic/Anti-Icing Properties of Micro/Nanostructured Surfaces. *Adv. Mater.* 24 (19), 2642–2648. doi:10.1002/adma.201104412

He, X., Xu, T., Gao, W., Xu, L.-P., Pan, T., and Zhang, X. (2018). Flexible Superwettable Tapes for On-Site Detection of Heavy Metals. *Anal. Chem.* 90 (24), 14105–14110. doi:10.1021/acs.analchem.8b04536

Hu, H., Swaminathan, V. V., Farahani, M. R. Z., Mensing, G., Yeom, J., Shannon, M. A., et al. (2014). Hierarchically Structured Re-entrant Microstructures for Superhydrophobic Surfaces with Extremely Low Hysteresis. *J. Micromech. Microeng.* 24 (9), 095023. doi:10.1088/0960-1317/24/9/095023

Huang, B., Jiang, S., Diao, Y., Liu, X., Liu, W., Chen, J., et al. (2020). Hydrogels as Durable Anti-icing Coatings Inhibit and Delay Ice Nucleation. *Molecules* 25 (15), 3378. doi:10.3390/molecules25153378

Kraj, A. G., and Bibeau, E. L. (2010). Phases of Icing on Wind Turbine Blades Characterized by Ice Accumulation. *Renew. Energ.* 35 (5), 966–972. doi:10.1016/j.renene.2009.09.013

Kreder, M. J., Alvarenga, J., Kim, P., and Aizenberg, J. (2016). Design of Anti-icing Surfaces: Smooth, Textured or Slippery? *Nat. Rev. Mater.* 1 (1), 15003. doi:10.1038/natrevmats.2015.3

Kumar, A., and Nanda, D. (2019). "Methods and Fabrication Techniques of Superhydrophobic Surfaces," in *Superhydrophobic Polymer Coatings*. Editors S. K. Samal, S. Mohanty, and S. K. Nayak (Amsterdam, Netherlands: Elsevier), 43–75. doi:10.1016/b978-0-12-816671-0.00004-7

Latthe, S. S., Sutar, R. S., Bhosale, A. K., Nagappan, S., Ha, C.-S., Sadasivuni, K. K., et al. (2019). Recent Developments in Air-Trapped Superhydrophobic and Liquid-Infused Slippery Surfaces for Anti-icing Application. *Prog. Org. Coat.* 137, 105373. doi:10.1016/j.porgcoat.2019.105373

Li, Q., and Guo, Z. (2018). Fundamentals of Icing and Common Strategies for Designing Biomimetic Anti-icing Surfaces. *J. Mater. Chem. A.* 6 (28), 13549–13581. doi:10.1039/c8ta03259a

Lin, J., Cai, Y., Wang, X., Ding, B., Yu, J., and Wang, M. (2011). Fabrication of Biomimetic Superhydrophobic Surfaces Inspired by lotus Leaf and Silver Ragwort Leaf. *Nanoscale* 3 (3), 1258–1262. doi:10.1039/c0nr00812e

Liu, C., Li, Y., Lu, C., Liu, Y., Feng, S., and Liu, Y. (2020). Robust Slippery Liquid-Infused Porous Network Surfaces for Enhanced Anti-icing/Deicing Performance. *ACS Appl. Mater. Inter.* 12 (22), 25471–25477. doi:10.1021/acsami.0c05954

Liu, H. H., Zhang, H. Y., and Li, W. (2011). Thermodynamic Analysis on Wetting Behavior of Hierarchical Structured Superhydrophobic Surfaces. *Langmuir* 27 (10), 6260–6267. doi:10.1021/la200028x

Liu, M., Li, M.-T., Xu, S., Yang, H., and Sun, H.-B. (2020). Bioinspired Superhydrophobic Surfaces via Laser-Structuring. *Phys. Chem. Chem. Phys.* 8, 835. doi:10.3389/fchem.2020.00835

Malik, A. N., Khan, S. A., and Lazoglu, I. (2020). A Novel Hybrid Frost Detection and Defrosting System for Domestic Refrigerators. *Int. J. Refrigeration* 117, 256–268. doi:10.1016/j.ijrefrig.2020.05.016

Michael, N., and Bhushan, B. (2007). Hierarchical Roughness Makes Superhydrophobic States Stable. *Microelectronic Eng.* 84 (3), 382–386. doi:10.1016/j.mee.2006.10.054

Neinhuis, C., and Barthlott, W. (1997). Characterization and Distribution of Water-Repellent, Self-Cleaning Plant Surfaces. *Ann. Bot.* 79 (6), 667–677. doi:10.1006/anbo.1997.0400

Nguyen, T.-B., Park, S., and Lim, H. (2018). Effects of Morphology Parameters on Anti-icing Performance in Superhydrophobic Surfaces. *Appl. Surf. Sci.* 435, 585–591. doi:10.1016/j.apsusc.2017.11.137

Onda, T., Shibuichi, S., Satoh, N., and Tsujii, K. (1996). Super-water-repellent Fractal Surfaces. *Langmuir* 12 (9), 2125–2127. doi:10.1021/la950418o

Patankar, N. A. (2004). Transition between Superhydrophobic States on Rough Surfaces. *Langmuir* 20 (17), 7097–7102. doi:10.1021/la049329e

Pattantyus-Abraham, A., Krahn, J., and Menon, C. (2013). Recent Advances in Nanostructured Biomimetic Dry Adhesives. *Front. Bioeng. Biotechnol.* 1, 22. doi:10.3389/fbioe.2013.00022

Rahmatmand, A., Harrison, S. J., and Oosthuizen, P. H. (2018). An Experimental Investigation of Snow Removal from Photovoltaic Solar Panels by Electrical Heating. *Solar Energy* 171, 811–826. doi:10.1016/j.solener.2018.07.015

Shan, L., Yang, H., Tian, D., and Tan, Y. (2020). Evaluation of Anti-icing Emulsified Asphalt Binders. *Front. Mater.* 7. doi:10.3389/fmats.2020.00257

Shirtcliffe, N. J., McHale, G., Newton, M. I., Chabrol, G., and Perry, C. C. (2004). Dual-Scale Roughness Produces Unusually Water-Repellent Surfaces. *Adv. Mater.* 16 (21), 1929–1932. doi:10.1002/adma.200400315

Song, Y., Xu, T., Song, X., and Zhang, X. (2020). Integrated Microdroplets Array for Intelligent Electrochemical Fabrication. *Adv. Funct. Mater.* 30 (13), 1910329. doi:10.1002/adfm.201910329

Song, Y., Xu, T., Xu, L.-P., and Zhang, X. (2018). Superwettable Nanodendritic Gold Substrates for Direct miRNA SERS Detection. *Nanoscale* 10 (45), 20990–20994. doi:10.1039/c8nr07348a

Song, Y., Xu, T., Zhu, Q., and Zhang, X. (2020). Integrated Individually Electrochemical Array for Simultaneously Detecting Multiple Alzheimer's Biomarkers. *Biosens. Bioelectron.* 162, 112253. doi:10.1016/j.bios.2020.112253

Su, B., Tian, Y., and Jiang, L. (2016). Bioinspired Interfaces with Superwettability: From Materials to Chemistry. *J. Am. Chem. Soc.* 138 (6), 1727–1748. doi:10.1021/jacs.5b12728

Sui, X., Wang, Y., Sun, Y., Liang, W., Xue, Y., and Bonsu, A. O. (2021). Superhydrophobic Behavior of cylinder Dual-Scale Hierarchical Nanostructured Surfaces. *Colloids Surf. A: Physicochemical Eng. Aspects* 629, 127406. doi:10.1016/j.colsurfa.2021.127406

Sun, K., Liu, H., Wang, X., and Wu, D. (2019). Innovative Design of Superhydrophobic thermal Energy-Storage Materials by Microencapsulation of N-Docosane with Nanostructured ZnO/SiO2 Shell. *Appl. Energ.* 237, 549–565. doi:10.1016/j.apenergy.2019.01.043

Taschuk, M. T., Hawkeye, M. M., and Brett, M. J. (2010). "Glancing Angle Deposition," in *Handbook of Deposition Technologies for Films and Coatings*. Editor P. M. Martin. Third Edition (Boston: William Andrew Publishing), 621–678. doi:10.1016/b978-0-8155-2031-3.00013-2

Tian, B., Zhu, C., Miao, B., Li, K., and Zhu, C. (2015). Vibration De-icing Method with Piezoelectric Actuators. *J. Vibroengineering* 17 (1), 61–73. Available at: https://www.jvejournals.com/article/15322.

Uzoma, P. C., Liu, F., Xu, L., Zhang, Z., Han, E.-H., Ke, W., et al. (2019). Superhydrophobicity, Conductivity and Anticorrosion of Robust Siloxane-Acrylic Coatings Modified with Graphene Nanosheets. *Prog. Org. Coat.* 127, 239–251. doi:10.1016/j.porgcoat.2018.11.018

Uzoma, P. C., Wang, Q., Zhang, W., Gao, N., Li, J., Okonkwo, P. C., et al. (2021). Anti-bacterial, Icephobic, and Corrosion protection Potentials of Superhydrophobic Nanodiamond Composite Coating. *Colloids Surf. A: Physicochemical Eng. Aspects* 630, 127532. doi:10.1016/j.colsurfa.2021.127532

Varanasi, K. K., Deng, T., Smith, J. D., Hsu, M., and Bhate, N. (2010). Frost Formation and Ice Adhesion on Superhydrophobic Surfaces. *Appl. Phys. Lett.* 97 (23), 234102. doi:10.1063/1.3524513

Varanasi, K. K., Hsu, M., Bhate, N., Yang, W., and Deng, T. (2009). Spatial Control in the Heterogeneous Nucleation of Water. *Appl. Phys. Lett.* 95 (9), 094101. doi:10.1063/1.3200951

Wang, L., Tian, Z., Jiang, G., Luo, X., Chen, C., Hu, X., et al. (2022). Spontaneous Dewetting Transitions of Droplets during Icing & Melting Cycle. *Nat. Commun.* 13 (1), 378. doi:10.1038/s41467-022-28036-x

Wenzel, R. N. (1936). Resistance of Solid Surfaces to Wetting by Water. *Ind. Eng. Chem.* 28 (8), 988–994. doi:10.1021/ie50320a024

Wu, Y.-l., She, W., Shi, D., Jiang, T., Hao, T.-h., Liu, J., et al. (2020). An Extremely Chemical and Mechanically Durable Siloxane Bearing Copolymer Coating with Self-Crosslinkable and Anti-icing Properties. *Composites B: Eng.* 195, 108031. doi:10.1016/j.compositesb.2020.108031

Wu, Y., Zhao, W., Wu, X., Gan, J., Zhang, H., and Cai, Y. (2021). A Superhydrophobic Moso Bamboo Cellulose Nano-Fibril Film Modified by Dopamine Hydrochloride. *Front. Bioeng. Biotechnol.* 9, 756839. doi:10.3389/fbioe.2021.756839

Xu, T., Shi, W., Huang, J., Song, Y., Zhang, F., Xu, L. P., et al. (2017). Superwettable Microchips as a Platform toward Microgravity Biosensing. *ACS Nano* 11 (1), 621–626. doi:10.1021/acsnano.6b06896

Xu, T., Song, Y., Gao, W., Wu, T., Xu, L.-P., Zhang, X., et al. (2018). Superwettable Electrochemical Biosensor toward Detection of Cancer Biomarkers. *ACS Sens.* 3 (1), 72–78. doi:10.1021/acssensors.7b00868

Xu, T., Xu, L.-P., Zhang, X., and Wang, S. (2019). Bioinspired Superwettable Micropatterns for Biosensing. *Chem. Soc. Rev.* 48 (12), 3153–3165. doi:10.1039/c8cs00915e

Yilbas, B. S., Hassan, G., Al-Sharafi, A., Ali, H., Al-Aqeeli, N., and Al-Sarkhi, A. (2018). Water Droplet Dynamics on a Hydrophobic Surface in Relation to the Self-Cleaning of Environmental Dust. *Sci. Rep.* 8 (1), 2984. doi:10.1038/s41598-018-21370-5

Conflict of Interest: The authors declare that the research was conducted in the absence of any commercial or financial relationships that could be construed as a potential conflict of interest.

Publisher's Note: All claims expressed in this article are solely those of the authors and do not necessarily represent those of their affiliated organizations, or those of the publisher, the editors and the reviewers. Any product that may be evaluated in this article, or claim that may be made by its manufacturer, is not guaranteed or endorsed by the publisher.

frontiers in Bioengineering and Biotechnology

MINI REVIEW
published: 28 March 2022
doi: 10.3389/fbioe.2022.872984

Superwettable Biosensor for Disease Biomarker Detection

Yun Jun Yang[1] *and Zhong Feng Gao*[2]*

[1]Advanced Research Institute for Multidisciplinary Science, Qilu University of Technology (Shandong Academy of Sciences), Jinan, China, [2]Advanced Materials Institute, Qilu University of Technology (Shandong Academy of Sciences), Jinan, China

Bioinspired superwettable materials have aroused wide interests in recent years for their promising application fields from service life to industry. As one kind of emerging application, the superwettable surfaces used to fabricate biosensors for the detection of disease biomarkers, especially tumor biomarkers, have been extensively studied. In this mini review, we briefly summarized the sensing strategy for disease biomarker detection based on superwettable biosensors, including fluorescence, electrochemistry, surface-enhanced Raman scattering, and visual assays. Finally, the challenges and direction for future development of superwettable biosensors are also discussed.

Keywords: biosensing, superwettability, bioinspired material, interface, detecting technologies

OPEN ACCESS

Edited by:
Hongliang Liu,
Yantai University, China

Reviewed by:
Tailin Xu,
Shenzhen University, China
Shenshan Zhan,
Chinese Academy of Agricultural Sciences (CAAS), China
Xiaoqing Yi,
Gannan Medical University, China

***Correspondence:**
Zhong Feng Gao
zfgao1024@hotmail.com

Specialty section:
This article was submitted to Bionics and Biomimetics, a section of the journal Frontiers in Bioengineering and Biotechnology

Received: *10 February 2022*
Accepted: *01 March 2022*
Published: *28 March 2022*

Citation:
Yang YJ and Gao ZF (2022) Superwettable Biosensor for Disease Biomarker Detection. Front. Bioeng. Biotechnol. 10:872984. doi: 10.3389/fbioe.2022.872984

INTRODUCTION

The detection of potential disease biomarkers in patient samples is an important factor for screening and early diagnosis of diseases, such as cancer (Karachaliou et al., 2015; Wu and Qu, 2015). The abnormal expression of genes, proteins, tumor-related mRNA, exosomes, and circulating tumor cells is closely associated with the occurrence of tumor and has been generally considered specific biomarkers to evaluate the development stage of cancer (Hanahan and Weinberg, 2000; Meng et al., 2021). Recently, tremendous efforts in the field of the disease biomarker biosensing method provide rich diagnostic and prognostic information for disease management (Seferos et al., 2007; Gong et al., 2021; Liu et al., 2022). Among them, the use of superwettable property-based biosensors is an emerging research field. Superwettable surfaces, such as lotus leaf-inspired superhydrophobic surface, Namib Desert beetles-inspired patterned superwettable surface, and *Nepenthes* pitcher plant-inspired slippery surface, are commonly used for the development of novel superwettable biosensors. These bioinspired surfaces exert unique liquid-repellent performance with large contact angle, decreasing the contact area between the droplet and surface (Dong et al., 2018; Sun et al., 2021). The remarkable wetting behavior brings several merits, such as remarkable evaporation-enrichment effect and new insights into visual biosensing. Superhydrophobic and slippery surfaces provide an effective and simple strategy to concentrate the analyte inside the droplet and improve spot homogeneity, promising for the fabrication of sensitive biosensor. The patterned superwettable surface has the feature to anchor the droplet, which holds the potential for the high-throughput biosensor.

It is reported that worldwide *in vitro* diagnostics market investments are growing every year, implying that biomedical diagnostic tools are playing key roles in disease diagnosis and human health assessment (Sassolas et al., 2008; Collins et al., 2021). The eventual aim of these endeavors is the development of point-of-care testing (POCT) devices with high selectivity, sensitivity, accuracy, and real-time detection for real sample analysis. Compared to the conventional methods using solution systems, the superwettable biosensing strategy used the droplet as the reaction system, which is promising for POCT applications due to their flexibility, easy-to-use, portability, and short

sample processing time (Chen et al., 2020; He et al., 2021; Zhu et al., 2021). To realize this goal, researchers developed various versatile and robust superwettable biosensors that meet the requirement of clinical patient sample assays. In recent years, biosensing methods including fluorescence, electrochemical, surface-enhanced Raman scattering (SERS), colorimetry, and visual assays are widely employed in analytical chemistry. Integrations between these biosensing strategies and superwettable surfaces have been put forward by researchers in quest of biomarker detection.

In this mini review, we summarized the recent progress of biosensing applications based on bioinspired superwettable surfaces, such as superhydrophobic surfaces, patterned wettable surfaces, and slippery surfaces. Various detecting techniques, including fluorescence, electrochemical, SERS, colorimetric, and visual methods are combined, respectively, with different superwettable surfaces. The application in the field of biomarker detection is described in detail. By introducing the commonly used biosensing methods, such as fluorescence, electrochemistry, SERS, and visual assays, the superwettable biosensors have been demonstrated to be a useful platform in the field of disease biomarker detection (**Figure 1**). Finally, the highlights and challenges of superwettable biosensors for biomarker detection were discussed.

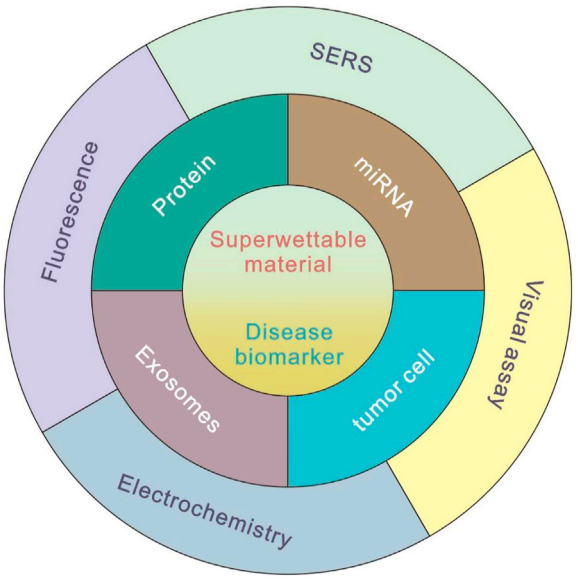

FIGURE 1 | Commonly used methods of superwettable biosensors for disease biomarker detection.

DIFFERENT TYPES OF SUPERWETTABLE BIOSENSORS

Fluorescence-Based Superwettable Biosensor

Fluorescent methods have attracted increasing attention because they do not require costly or sophisticated equipment and have been widely used in portable, *in situ*, and rapid detection (Hou et al., 2015). However, it has been reported that the detecting targets are dispersed in large volumes with the weak signal and low signal-to-noise ratio which cannot be detected effectively (Yan et al., 2014; Zhan et al., 2015). To solve this problem, droplet evaporation enrichment was developed to concentrate the targets from highly diluted solution to an area-confined domain to increase the effective contact frequency between the signal probes and targets (Gao et al., 2009).

Zhang et al. pioneered such an approach that the superhydrophobic TiO_2 surface was designed with spotting superhydrophilic microwells (Xu et al., 2015). By the silane chemistry process, the capture probe was attached onto the superhydrophilic microwell. As the miRNA-141, a biomarker of prostate cancer, and FAM-labeled probe were introduced subsequently, the probes could be enriched and specifically recognized by the immobilized capture probe, resulting in the formation of the sandwich structure and exponential enhanced fluorescence intensity. This superwettable biosensor was realized for sensitive and selective detection of miRNA-141 with a low limit of detection (LOD) of 88 pM (Xu et al., 2018). This strategy has been applied for ultrasensitive detection of different cancer biomarkers, such as free prostate-specific antigen (PSA) (Chen et al., 2018) and mRNA (Hu et al., 2017). For a comprehensive understanding of the development and biosensing application of superwettable micropatterns, several high-quality reviews can be found in the literature (Xu et al., 2019; Wang et al., 2021).

With the signal probe condensed after droplet evaporation, the aggregation-induced quenching effect might present, leading to the inaccurate analysis and even false-positive results. To address this problem, Lou et al. proposed an aggregation-induced emission (AIE) luminogen-based fluorescent method for the detection of matrix metalloproteinase-2 (MMP-2) tumor marker on slippery lubricant-infused porous substrates (SLIPSs) (**Figure 2A**). This SLIPS method obtained a low LOD of 3.7 ng/ml, which has been successfully used for detecting the MMP-2 secreted by tumor cells directly (Wu et al., 2021).

Based on the aforementioned discussion, fluorescence-based superwettable biosensors offer sensitive and accurate features to concentrate the sample and amplify the fluorescent signal, making them promising for the sensitive biomarker detection. However, the current methods mainly rely on the fluorescent microscope for laboratory measurements, which is cumbersome and not suitable for POCT application. The future direction should focus on the development of a portable fluorescent method, especially the smartphone-based superwettable biosensing method.

Electrochemistry-Based Superwettable Biosensor

As an ultrasensitive and universal analytical method, electrochemical assays have significant advantages including low cost, rapid response, simple operation, and high sensitivity, and they have been widely considered the powerful

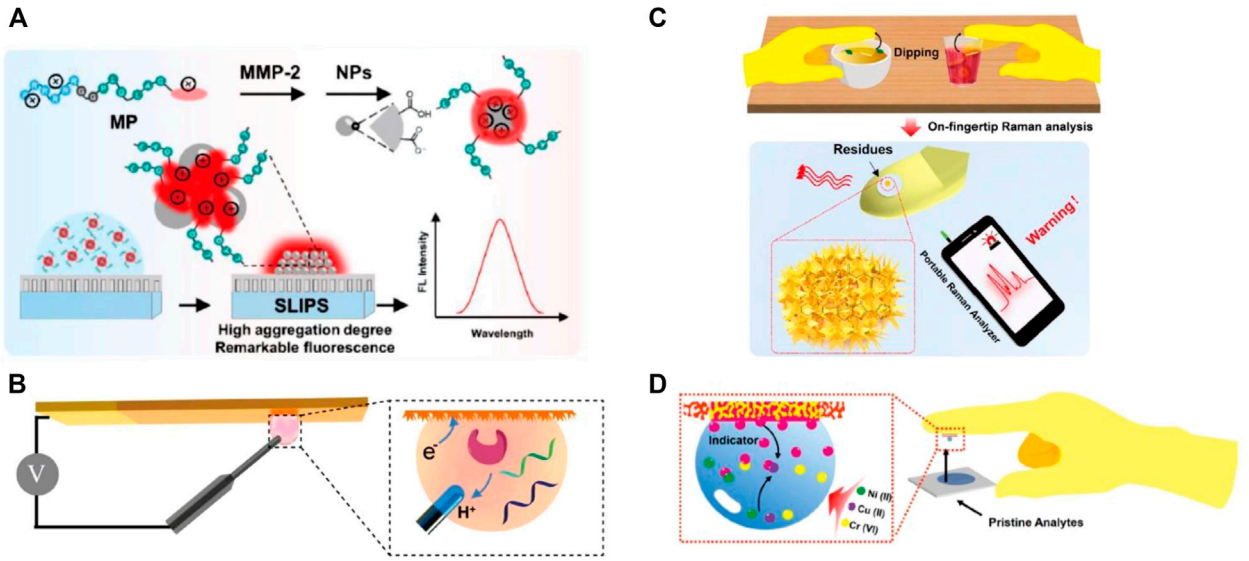

FIGURE 2 | (A) Sensing process of peptide-conjugated AIEgen for quantitative detection of MMP-2 secreted from cells on the slippery surface (Wu et al., 2021). **(B)** Superwettable electrochemical microchip toward PSA detection (Xu et al., 2018). **(C)** Tape-based SERS superwettable sensors for the detection of food contaminants in an on-hand way (He et al., 2020b). **(D)** Design of the superwettable tapes for the colorimetric monitoring of heavy metals (He et al., 2018).

tool for biosensing (Hasanzadeh et al., 2017; Mani et al., 2021). Combining the characteristics of the superwettable surface with the merits of the electrochemical system, prominent performances have been realized in the following examples.

Xu et al. reported a nanodendritic electrochemical biosensor based on superhydrophilic microwells on a superwettable microchip for the selective and sensitive determination of prostate cancer biomarkers such as miRNA-141 (LODs = 0.8 nM), miRNA-375 (LODs = 0.8 nM), and PSA (LOD = 1.0 pM) (Xu et al., 2018) (**Figure 2B**). Li's group developed a refreshable electrochemical biosensor with an excellent self-cleaning property by casting superhydrophobic conductive polydimethylsiloxane (PDMS) and multiwalled carbon nanotubes nanocomposite onto a glassy carbon electrode (Zhu et al., 2017). By recording HRP-dependent electrochemical signals, a tumor marker, namely, carcinoembryonic antigen has been successfully detected by this method with a wide dynamic range from 0.1 to 100 mg/ml, and the detection limit is as low as 0.041 ng/ml. To meet the requirement for personal healthcare management at home, Zhang's group developed several portable electrochemical micro-workstation platforms for detecting biomarkers of disease, such as glucose (Song et al., 2020b), miRNA (Song et al., 2019), and multiple Alzheimer's disease biomarkers (Song et al., 2020c; Liu et al., 2022). These smart electrochemical biosensors demonstrated significant performance on cloud data management and multichannel detection, indicating great potential for remote detection and portable high-throughput biomedical applications in future.

These current electrochemical methods based on the superwettable surface demonstrate a great perspective in biosensing. The current superwettable biosensor cannot be reused. To overcome this problem, nucleic acid probes with regenerated conformation can be considered to construct sensitive superwettable biosensors.

SERS-Based Superwettable Biosensor

Due to the significant advantages including small testing volume, rapid output, and high sensitivity, the SERS has been widely applied in various research fields such as sensing, bioimaging, food analysis, and environmental monitoring (Cardinal et al., 2017; Lin and He, 2019; Gao et al., 2021; Lin et al., 2021). To achieve significant performance, the SERS substrate incorporated with superwettability become an ideal candidate to access not only abundant hot spots for acquiring excellent sensitivity but also equally distributed hot spots for generating a stable signal.

Di Fabrizio et al. reported an interesting example for the direct detection of exosomes by SERS with a superhydrophobic array of silicon micropillars decorated with silver nanostructures (Tirinato et al., 2012). They found that exosomes from tumor colon cells show a high presence of RNA, whereas exosomes obtained from healthy colon cells display a high presence of lipid signals. Suarasan and coworkers also reported a superhydrophobic plasmonic biosensor for SERS-sensitive detection of exosomes with only 0.5 μL testing sample. PDMS was used to fabricate the superhydrophobic substrate with nanobowl and microbowl structures by the soft lithography method. Then, silver nanoparticles were grown *in situ* to impart SERS-enhancing properties (Suarasan et al., 2020). Yang et al. synthesized Fe_3O_4/Au/Ag nanocomposites and proposed a magnetically assisted SERS method to detect

adenosine traces in clinical urine samples from lung cancer patients (Yang et al., 2014). This label-free method showed excellent sensitivity down to 1×10^{-10} M. Feng et al. developed an automatic deep learning-based superhydrophobic SERS platform for label-free detection of 695 clinical serum samples including 321 breast cancer patients, 77 leukemia M5 patients, 94 hepatitis B virus patients, and 203 healthy volunteers. This method demonstrated a high diagnostic accuracy (98.6%), which is promising for rapid, high-throughput, and label-free screening for cancer (Lin et al., 2021). With various designs of the superhydrophobic substrate, SERS-based superwettable biosensors have also been used to detect diverse cancer biomarkers, such as miRNA (Song et al., 2018; Song X. et al., 2020), extracellular vesicles (Suarasan et al., 2020), and peptides (Perozziello et al., 2014). These methods provide enormous potential to construct POCT devices for the early diagnosis of cancer. In addition, Zhang et al. proposed Au nanodendrites-functionalized superwettable microwells on the conductive carbon tape surface (He et al., 2020b). This sensor realized early-warning SERS detection of various food contaminants, such as thiabendazole, thiram, and Sudan-1, from real samples (**Figure 2C**).

These investigations provided a sensitive and accurate solution for coupling superwettable surface with SERS biosensing. However, the aggregation of targets is accompanied by the aggregation of contaminants during the droplet evaporation process, which is not desired in biosensing. To address this issue, pretreatment of samples is necessary before detection.

Colorimetric/Visual Method-Based Superwettable Biosensor

There have been extensive endeavors dedicated to the development of a quantitative visual method in the context of cancer biomarker assays. Colorimetric assay is a classic visual strategy for detection due to its equipment-free, simple, and rapid advantages (Sabela et al., 2017; Xu et al., 2017). As superwettable behaviors, such as contact angle and rolling/sliding angle performance, are the most obvious and direct characteristics of the superwettability, they have been emerged as a novel visual strategy for biosensing.

Superwettability is typically used to develop paper-based analytical devices (PADs) with superhydrophilic microwells on a hydrophobic wax substrate. Whitesides et al. pioneered the first PADs, leading the trend of PADs for diverse applications (Martinez et al., 2007). For example, Chen et al. reported a highly sensitive colorimetric method for prostate-specific antigen (PSA) diagnosis using gold nanoparticles labeled with biotinylated poly (adenine) ssDNA sequences and streptavidin–horseradish peroxidase for enzymatic signal enhancement (Huang et al., 2018). They realized a detection limit down to 10 pg/ml for PSA detection within 15 min of experimental operation. Hou et al. reported a disposable colorimetric assay based on droplet array that has been constructed from diverse chemo-responsive colorants. This rapid, small, inexpensive, non-invasive, and visualized droplet array achieved an accuracy of at least 90% and can be used as a powerful tool for early screening of lung cancer (Zhong et al., 2018). Using flexible tapes, Zhang's group established a superwettable colorimetric biosensor for on-site heavy metals monitoring (He et al., 2018). They achieved quantitative colorimetric detection of multiplex heavy metal ions including copper, chromium, and nickel by the naked eye (**Figure 2D**). Furthermore, they applied a smartphone to acquire colorimetric signals for semiquantitative detection of routine urine biomarkers (glucose, nitrite, protein, and phenylpyruvate) (He et al., 2020a) and sweat biomarkers (pH, chloride, glucose, and calcium) (He et al., 2019). The tape-based superwettable biosensors show significant merits including user-friendly, POCT potential, and favorable screening for the early disease warning toward the clinical patients. We presented a contact angle-based visual biosensing method based on the pH-responsive superhydrophobic surface. PSA can be detected with a low LOD of 3.2 pg/ml by analyzing the contact angle (Gao et al., 2019). The contact angle-based method is suitable for color-blind and color-weak individuals. Another method suitable for color-blind and color-weak individuals is sliding angle-based visual detection, in which by tuning the hydrophobic interaction between DNA and organogel, miRNA 21 can be detected by analyzing the sliding angle (Gao et al., 2020). As the superwettable performance of these biosensors was hardly influenced by temperature, elevation, and even droplet color, it has significant potential to numerous users, especially to those color-blind/weak people.

These current wetting behavior-based visual assays have direct implications for developing simple, rapid, and low-cost strategies for biomarker detection. However, the small changes of contact angle and rolling/sliding angle cannot be discriminated by the naked eye. Thus, it is desirable to develop a smartphone-based digital method for the visual detection.

CONCLUSION

In summary, the recent progresses in superwettable biosensors for the detection of different biomarkers are briefly summarized, including the strategies of fluorescence, electrochemical, SERS, and visual assays. With continuing interdisciplinary technology and research progress, endless bioinspired nanomaterials and detection strategies will be introduced in the biosensing platforms. To note, several challenges also remain to be addressed in future developments. First, as almost applications presented in this review are mainly single target detection, developing a high-throughput superwettable biosensor with a multifunctional testing area would be more challenging and practical for future application. Second, the external stimulations including contamination and destruction may influence the wettability of the surface, leading to poor repeatability and credibility of such superwettable biosensors. Thus, long-surviving wettable surfaces are urgently required for practical application under extreme and complex biomedical conditions. Finally, the specificity of superwettable biosensing should be highlighted. Because the superwettable surfaces are

preferred to interact with nonspecific targets by hydrophobic interaction and electrostatic interaction in complex environments such as cell matrix and blood, leading to the conformational change, recombination, and even oxidation of surface molecules. To avoid false-positive results, it is necessary to address the specificity for detection. We hope that this mini review will provide current insights and inspire researchers to investigate toward solving these existing problems and explore the superwettable biosensors as simple and commercialized devices for disease biomarker detection.

AUTHOR CONTRIBUTIONS

YY wrote the manuscript. ZG reviewed and edited the manuscript. All authors revised the manuscript.

FUNDING

This work was financially supported by the National Natural Science Foundation of China (22176080 and 31800829).

REFERENCES

Cardinal, M. F., Vander Ende, E., Hackler, R. A., McAnally, M. O., Stair, P. C., Schatz, G. C., et al. (2017). Expanding Applications of SERS through Versatile Nanomaterials Engineering. *Chem. Soc. Rev.* 46 (13), 3886–3903. doi:10.1039/C7CS00207F

Chen, Y., Li, K., Zhang, S., Qin, L., Deng, S., Ge, L., et al. (2020). Bioinspired Superwettable Microspine Chips with Directional Droplet Transportation for Biosensing. *ACS Nano* 14 (4), 4654–4661. doi:10.1021/acsnano.0c00324

Chen, Y., Xu, L.-P., Meng, J., Deng, S., Ma, L., Zhang, S., et al. (2018). Superwettable Microchips with Improved Spot Homogeneity toward Sensitive Biosensing. *Biosens. Bioelectron.* 102, 418–424. doi:10.1016/j.bios.2017.11.036

Collins, F. S., Schwetz, T. A., Tabak, L. A., and Lander, E. S. (2021). ARPA-H: Accelerating Biomedical Breakthroughs. *Science* 373 (6551), 165–167. doi:10.1126/science.abj8547

Dong, Z., Schumann, M. F., Hokkanen, M. J., Chang, B., Welle, A., Zhou, Q., et al. (2018). Superoleophobic Slippery Lubricant-Infused Surfaces: Combining Two Extremes in the Same Surface. *Adv. Mater.* 30 (45), 1803890. doi:10.1002/adma.201803890

Gao, J. B., Sann, E. E., Wang, X. Y., Ye, C., Liu, R., and Gao, Z. F. (2019). Visual Detection of the Prostate Specific Antigen via a sandwich Immunoassay and by Using a Superwettable Chip Coated with pH-Responsive Silica Nanoparticles. *Microchim. Acta* 186 (8), 550. doi:10.1007/s00604-019-3662-8

Gao, J., Gu, H., and Xu, B. (2009). Multifunctional Magnetic Nanoparticles: Design, Synthesis, and Biomedical Applications. *Acc. Chem. Res.* 42 (8), 1097–1107. doi:10.1021/ar9000026

Gao, Z. F., Li, Y. X., Dong, L. M., Zheng, L. L., Li, J. Z., Shen, Y., et al. (2021). Photothermal-induced Partial Leidenfrost Superhydrophobic Surface as Ultrasensitive Surface-Enhanced Raman Scattering Platform for the Detection of Neonicotinoid Insecticides. *Sensors Actuators B: Chem.* 348, 130728. doi:10.1016/j.snb.2021.130728

Gao, Z. F., Liu, R., Wang, J., Dai, J., Huang, W.-H., Liu, M., et al. (2020). Manipulating the Hydrophobicity of DNA as a Universal Strategy for Visual Biosensing. *Nat. Protoc.* 15 (2), 316–337. doi:10.1038/s41596-019-0235-6

Gong, S., Zhang, S., Lu, F., Pan, W., Li, N., and Tang, B. (2021). CRISPR/Cas-Based *In Vitro* Diagnostic Platforms for Cancer Biomarker Detection. *Anal. Chem.* 93 (35), 11899–11909. doi:10.1021/acs.analchem.1c02533

Hanahan, D., and Weinberg, R. A. (2000). The Hallmarks of Cancer. *Cell* 100, 57–70. doi:10.1016/S0092-8674(00)81683-9

Hasanzadeh, M., Shadjou, N., and de la Guardia, M. (2017). Early Stage Screening of Breast Cancer Using Electrochemical Biomarker Detection. *Trac Trends Anal. Chem.* 91, 67–76. doi:10.1016/j.trac.2017.04.006

He, X., Pei, Q., Xu, T., and Zhang, X. (2020a). Smartphone-based Tape Sensors for Multiplexed Rapid Urinalysis. *Sensors Actuators B: Chem.* 304, 127415. doi:10.1016/j.snb.2019.127415

He, X., Xu, T., Gao, W., Xu, L.-P., Pan, T., and Zhang, X. (2018). Flexible Superwettable tapes for On-Site Detection of Heavy Metals. *Anal. Chem.* 90 (24), 14105–14110. doi:10.1021/acs.analchem.8b04536

He, X., Xu, T., Gu, Z., Gao, W., Xu, L.-P., Pan, T., et al. (2019). Flexible and Superwettable Bands as a Platform toward Sweat Sampling and Sensing. *Anal. Chem.* 91 (7), 4296–4300. doi:10.1021/acs.analchem.8b05875

He, X., Yang, S., Xu, T., Song, Y., and Zhang, X. (2020b). Microdroplet-captured tapes for Rapid Sampling and SERS Detection of Food Contaminants. *Biosens. Bioelectron.* 152, 112013. doi:10.1016/j.bios.2020.112013

He, Z., Li, S., Zeng, Y., Zhang, J., Li, Q., Gao, B., et al. (202121014). Photo-Adjustable TiO 2 -Paper as a Smart Substrate for Paper-Based Analytical Devices. *Adv. Mater. Inter* 9, 2101450. doi:10.1002/admi.202101450

Hou, J., Zhang, H., Yang, Q., Li, M., Jiang, L., and Song, Y. (2015). Hydrophilic-Hydrophobic Patterned Molecularly Imprinted Photonic Crystal Sensors for High-Sensitive Colorimetric Detection of Tetracycline. *Small* 11 (23), 2738–2742. doi:10.1002/smll.201403640

Hu, X., Wang, Y., Liu, H., Wang, J., Tan, Y., Wang, F., et al. (2017). Naked Eye Detection of Multiple Tumor-Related mRNAs from Patients with Photonic-crystal Micropattern Supported Dual-Modal Upconversion Bioprobes. *Chem. Sci.* 8 (1), 466–472. doi:10.1039/c6sc03401b

Huang, J.-Y., Lin, H.-T., Chen, T.-H., Chen, C.-A., Chang, H.-T., and Chen, C.-F. (2018). Signal Amplified Gold Nanoparticles for Cancer Diagnosis on Paper-Based Analytical Devices. *ACS Sens.* 3 (1), 174–182. doi:10.1021/acssensors.7b00823

Karachaliou, N., Mayo-de-Las-Casas, C., Molina-Vila, M. A., and Rosell, R. (2015). Real-time Liquid Biopsies Become a Reality in Cancer Treatment. *Ann. Transl. Med.* 3, 36. doi:10.3978/j.issn.2305-5839.2015.01.16

Lin, X., Lin, D., Chen, Y., Lin, J., Weng, S., Song, J., et al. (2021). High Throughput Blood Analysis Based on Deep Learning Algorithm and Self-Positioning Super-Hydrophobic SERS Platform for Non-Invasive Multi-Disease Screening. *Adv. Funct. Mater.* 31 (51), 2103382. doi:10.1002/adfm.202103382

Lin, Z., and He, L. (2019). Recent advance in SERS Techniques for Food Safety and Quality Analysis: A Brief Review. *Curr. Opin. Food Sci.* 28, 82–87. doi:10.1016/j.cofs.2019.10.001

Liu, Y., Huang, Z., Xu, Q., Zhang, L., Liu, Q., and Xu, T. (2022). Portable Electrochemical Micro-workstation Platform for Simultaneous Detection of Multiple Alzheimer's Disease Biomarkers. *Microchim. Acta* 189 (3), 1–9. doi:10.1007/s00604-022-05199-4

Mani, V., Beduk, T., Khushaim, W., Ceylan, A. E., Timur, S., Wolfbeis, O. S., et al. (2021). Electrochemical Sensors Targeting Salivary Biomarkers: A Comprehensive Review. *Trac Trends Anal. Chem.* 135, 116164. doi:10.1016/j.trac.2020.116164

Martinez, A. W., Phillips, S. T., Butte, M. J., and Whitesides, G. M. (2007). Patterned Paper as a Platform for Inexpensive, Low-Volume, Portable Bioassays. *Angew. Chem.* 119 (8), 1340–1342. doi:10.1002/ange.200603817

Meng, X., Yang, F., Dong, H., Dou, L., and Zhang, X. (2021). Recent Advances in Optical Imaging of Biomarkers *In Vivo*. *Nano Today* 38, 101156. doi:10.1016/j.nantod.2021.101156

Perozziello, G., Candeloro, P., Gentile, F., Nicastri, A., Perri, A., Coluccio, M. L., et al. (2014). Microfluidics & Nanotechnology: towards Fully Integrated Analytical Devices for the Detection of Cancer Biomarkers. *RSC Adv.* 4 (98), 55590–55598. doi:10.1039/C4RA10486B

Sabela, M., Balme, S., Bechelany, M., Janot, J.-M., and Bisetty, K. (2017). A Review of Gold and Silver Nanoparticle-Based Colorimetric Sensing Assays. *Adv. Eng. Mater.* 19 (12), 1700270. doi:10.1002/adem.201700270

Sassolas, A., Leca-Bouvier, B. D., and Blum, L. J. (2008). DNA Biosensors and Microarrays. *Chem. Rev.* 108, 109–139. doi:10.1021/cr0684467

Seferos, D. S., Giljohann, D. A., Hill, H. D., Prigodich, A. E., and Mirkin, C. A. (2007). Nano-flares: Probes for Transfection and mRNA Detection in Living Cells. *J. Am. Chem. Soc.* 129, 15477–15479. doi:10.1021/ja0776529

Song, X., Xu, T., Song, Y., He, X., Wang, D., Liu, C., et al. (2020a). Droplet Array for Open-Channel High-Throughput SERS Biosensing. *Talanta* 218, 121206. doi:10.1016/j.talanta.2020.121206

Song, Y., Xu, T., Xiu, J., and Zhang, X. (2020b). Mini-pillar Microarray for Individually Electrochemical Sensing in Microdroplets. *Biosens. Bioelectron.* 149, 111845. doi:10.1016/j.bios.2019.111845

Song, Y., Xu, T., Xu, L.-P., and Zhang, X. (2019). Nanodendritic Gold/graphene-Based Biosensor for Tri-mode miRNA Sensing. *Chem. Commun.* 55 (12), 1742–1745. doi:10.1039/c8cc09586h

Song, Y., Xu, T., Xu, L.-P., and Zhang, X. (2018). Superwettable Nanodendritic Gold Substrates for Direct miRNA SERS Detection. *Nanoscale* 10 (45), 20990–20994. doi:10.1039/C8NR07348A

Song, Y., Xu, T., Zhu, Q., and Zhang, X. (2020c). Integrated Individually Electrochemical Array for Simultaneously Detecting Multiple Alzheimer's Biomarkers. *Biosens. Bioelectron.* 162, 112253. doi:10.1016/j.bios.2020.112253

Suarasan, S., Liu, J., Imanbekova, M., Rojalin, T., Hilt, S., Voss, J. C., et al. (2020). Superhydrophobic Bowl-like SERS Substrates Patterned from CMOS Sensors for Extracellular Vesicle Characterization. *J. Mater. Chem. B* 8 (38), 8845–8852. doi:10.1039/D0TB00889C

Sun, L., Guo, J., Chen, H., Zhang, D., Shang, L., Zhang, B., et al. (2021). Tailoring Materials with Specific Wettability in Biomedical Engineering. *Adv. Sci.* 8 (19), 2100126. doi:10.1002/advs.202100126

Tirinato, L., Gentile, F., Di Mascolo, D., Coluccio, M. L., Das, G., Liberale, C., et al. (2012). SERS Analysis on Exosomes Using Super-hydrophobic Surfaces. *Microelectronic Eng.* 97, 337–340. doi:10.1016/j.mee.2012.03.022

Wang, Y., Liu, F., Yang, Y., and Xu, L.-P. (2021). Droplet Evaporation-Induced Analyte Concentration toward Sensitive Biosensing. *Mater. Chem. Front.* 5 (15), 5639–5652. doi:10.1039/d1qm00500f

Wu, F., Huang, Y., Yang, X., Hu, J.-J., Lou, X., Xia, F., et al. (2021). Tunning Intermolecular Interaction of Peptide-Conjugated AIEgen in Nano-Confined Space for Quantitative Detection of Tumor Marker Secreted from Cells. *Anal. Chem.* 93 (48), 16257–16263. doi:10.1021/acs.analchem.1c04422

Wu, L., and Qu, X. (2015). Cancer Biomarker Detection: Recent Achievements and Challenges. *Chem. Soc. Rev.* 44, 2963–2997. doi:10.1039/C4CS00370E

Xu, L.-P., Chen, Y., Yang, G., Shi, W., Dai, B., Li, G., et al. (2015). Ultratrace DNA Detection Based on the Condensing-Enrichment Effect of Superwettable Microchips. *Adv. Mater.* 27 (43), 6878–6884. doi:10.1002/adma.201502982

Xu, T., Shi, W., Huang, J., Song, Y., Zhang, F., Xu, L.-P., et al. (2017). Superwettable Microchips as a Platform toward Microgravity Biosensing. *ACS Nano* 11 (1), 621–626. doi:10.1021/acsnano.6b06896

Xu, T., Song, Y., Gao, W., Wu, T., Xu, L.-P., Zhang, X., et al. (2018). Superwettable Electrochemical Biosensor toward Detection of Cancer Biomarkers. *ACS Sens.* 3 (1), 72–78. doi:10.1021/acssensors.7b00868

Xu, T., Xu, L.-P., Zhang, X., and Wang, S. (2019). Bioinspired Superwettable Micropatterns for Biosensing. *Chem. Soc. Rev.* 48 (12), 3153–3165. doi:10.1039/c8cs00915e

Yan, F., Zou, Y., Wang, M., Mu, X., Yang, N., and Chen, L. (2014). Highly Photoluminescent Carbon Dots-Based Fluorescent Chemosensors for Sensitive and Selective Detection of Mercury Ions and Application of Imaging in Living Cells. *Sensors Actuators B: Chem.* 192, 488–495. doi:10.1016/j.snb.2013.11.041

Yang, T., Guo, X., Wu, Y., Wang, H., Fu, S., Wen, Y., et al. (2014). Facile and Label-free Detection of Lung Cancer Biomarker in Urine by Magnetically Assisted Surface-Enhanced Raman Scattering. *ACS Appl. Mater. Inter.* 6 (23), 20985–20993. doi:10.1021/am5057536

Zhan, S., Xu, H., Zhan, X., Wu, Y., Wang, L., Lv, J., et al. (2015). Determination of Silver(I) Ion Based on the Aggregation of Gold Nanoparticles Caused by Silver-specific DNA, and its Effect on the Fluorescence of Rhodamine B. *Microchim. Acta* 182 (7), 1411–1419. doi:10.1007/s00604-015-1462-3

Zhong, X., Li, D., Du, W., Yan, M., Wang, Y., Huo, D., et al. (2018). Rapid Recognition of Volatile Organic Compounds with Colorimetric Sensor Arrays for Lung Cancer Screening. *Anal. Bioanal. Chem.* 410 (16), 3671–3681. doi:10.1007/s00216-018-0948-3

Zhu, H., Huang, Y., Lou, X., and Xia, F. (2021). Bioinspired Superwetting Surfaces for Biosensing. *View* 2 (1), 20200053. doi:10.1002/VIW.20200053

Zhu, X., Chen, Y., Feng, C., Wang, W., Bo, B., Ren, R., et al. (2017). Assembly of Self-Cleaning Electrode Surface for the Development of Refreshable Biosensors. *Anal. Chem.* 89 (7), 4131–4138. doi:10.1021/acs.analchem.6b05177

Conflict of Interest: The authors declare that the research was conducted in the absence of any commercial or financial relationships that could be construed as a potential conflict of interest.

Publisher's Note: All claims expressed in this article are solely those of the authors and do not necessarily represent those of their affiliated organizations, or those of the publisher, the editors, and the reviewers. Any product that may be evaluated in this article, or claim that may be made by its manufacturer, is not guaranteed or endorsed by the publisher.

frontiers | Frontiers in Bioengineering and Biotechnology

ORIGINAL RESEARCH
published: 21 April 2022
doi: 10.3389/fbioe.2022.901507

Bio-Inspired Salinity-Gradient Power Generation With UiO-66-NH_2 Metal-Organic Framework Based Composite Membrane

Lu Yao[1], *Qi Li*[2], *Shangfa Pan*[2], *Junmei Cheng*[1]* *and Xueli Liu*[3]*

[1]Key Laboratory of Rubber-Plastics, Ministry of Education, Qingdao University of Science and Technology, Qingdao, China, [2]Qingdao Institute of Bioenergy and Bioprocess Technology, Chinese Academy of Sciences, Qingdao, China, [3]College of Materials Science and Engineering, Institute of Marine Biobased Materials, Qingdao University, Qingdao, China

Salinity-gradient directed osmotic energy between seawater and river water has been widely considered as a promising clean and renewable energy source, as there are numerous river estuaries on our planet. In the past few decades, reverse electrodialysis (RED) technique based on cation-selective membranes has been used as the key strategy to convert osmotic energy into electricity. From this aspect, developing high-efficiency anion-selective membranes will also have great potential for capturing osmotic energy, however, remains systematically unexplored. In nature, electric eels can produce electricity from ionic gradients by using their "sub-nanoscale" protein ion channels to transport ions selectively. Inspired by this, here we developed a UiO-66-NH_2 metal-organic framework (MOF) based anion-selective composite membrane with sub-nanochannels, and achieved high-performance salinity-gradient power generation by mixing artificial seawater (0.5 M NaCl) and river water (0.01 M NaCl). The UiO-66-NH_2 metal-organic framework based composite membranes can be easily and economically fabricated with dense structure and long-term working stability in saline, and its performance of power generation can also be adjusted by pH to enhance the surface charge density of the MOF sub-nanochannels. This study will inspire the exploitation of MOFs for investigating the sub-nanochannel directed high-performance salinity-gradient energy harvesting systems based on anion-selective ion transport.

Keywords: biomimetics, energy conversion, salinity gradient, nanofluidic, metal-organic frameworks, ion transport

OPEN ACCESS

Edited by:
Feilong Zhang,
Nanyang Technological University, Singapore

Reviewed by:
Kai Xiao,
Southern University of Science and Technology, China
Xiang-Yu Kong,
Technical Institute of Physics and Chemistry (CAS), China

***Correspondence:**
Junmei Cheng
junmei_cheng@126.com
Xueli Liu
liuxl@qdu.edu.cn

Specialty section:
This article was submitted to Bionics and Biomimetics, a section of the journal Frontiers in Bioengineering and Biotechnology

Received: *22 March 2022*
Accepted: *05 April 2022*
Published: *21 April 2022*

Citation:
Yao L, Li Q, Pan S, Cheng J and Liu X (2022) Bio-Inspired Salinity-Gradient Power Generation With UiO-66-NH_2 Metal-Organic Framework Based Composite Membrane. Front. Bioeng. Biotechnol. 10:901507. doi: 10.3389/fbioe.2022.901507

INTRODUCTION

Due to the serious shortage and pollution of traditional energy sources and the increasing human demand for energy, the development of sustainable, abundant, and clean sources of energy is urgent for both the environment and human society (van Ruijven et al., 2019; Sadeghi, 2022). In the past few decades, salinity-gradient generated osmotic energy, which can be derived from ambient environments by mixing river water with salty seawater, has been recognized as a sustainable source of "blue energy" (Yip et al., 2016). Various efforts have been focusing on the development of highly-efficient salinity-gradient osmotic energy harvesting systems (Zhang et al., 2015; Xiao et al., 2019; Tawalbeh et al., 2021). Among these systems, reverse electrodialysis (RED) has been widely studied because of that electricity could be generated directly through ion transport driven by salinity

gradients (Siria et al., 2017; Liu et al., 2020). An important component of the RED system is ion-selective membranes, as the permselectivity of membrane directly determines the energy conversion performance. Till now, extensive studies have been conducted, focusing on the high permselectivity of cation-selective membranes in RED systems (Zhang et al., 2015; Zhang et al., 2017; Xiao et al., 2019; Xin et al., 2019; Xin et al., 2020; Man et al., 2021). However, little research has been made on anion-selective membranes, which is to say, ignoring the possibility of energy generation with anion gradients. We consider that the use of anion-selective membranes could also be an efficient approach for salinity-gradient osmotic energy harvesting.

For achieving a high efficiency during the RED based power generation, people have learned a lot from the nature. The highly-selective ion transport thorough the sub-nanochannels of transmembrane proteins is one of the essential and fundamental activity for almost all life processes of living species (Montenegro et al., 2013; Gao et al., 2017; Ren et al., 2019; Xiao et al., 2019). For example, electric eels can produce high-voltage electricity from ionic gradients by using their "sub-nanoscale" protein ion channels (Schroeder et al., 2017; Liu et al., 2021). Inspired by that, artificial nanofluidic ion channels have been extensively investigated for their potential applications in energy conversion (Zhang et al., 2015; Gao et al., 2017; Xiao et al., 2019). Because of the unique nanoconfinement effect, the ion transport in nanofluidic channels is largely governed by the surface properties of channel walls, leading to excellent ion selectivity and high ionic throughput (Sun et al., 2020; Teng et al., 2021; Yang et al., 2021). Therefore, a variety of nanofluidic RED systems have been proposed for salinity-gradient osmotic energy harvesting. Firstly, one-dimensional (1D) single-nanopore and multi-nanopore based ion-selective membranes have been developed for the capture of osmotic energy (Gao et al., 2019; Xiao et al., 2019). However, the scalability of these nanochannels or nanopores is very hard to realize for the further commercialization, making these systems more suitable for fundamental research. As the research continues, nanofluidic heterogeneous membranes have shown their advantage for improving the power generation efficiency, thanks to their unique ionic diode effect to rectify ion transport and prohibit the flow back of current (Gao et al., 2014; Zhang et al., 2015). In addition, two-dimensional (2D) nanofluidic systems, mainly based on the stacking of 2D nanomaterials such as graphene and MXene, have also been exploited during the recent years (Zhao et al., 2015; Lao et al., 2018; Zhang et al., 2019; Ding et al., 2020; Lao et al., 2020), showing their potential in the facile fabrication of high-efficiency osmotic energy devices. However, despite of the prosperous study of nanochannel and nanopore based nanofludic RED system, ion-selective membranes based on sub-nanometer channels remain systematically unexplored for salinity-gradient osmotic energy generation, although it is sub-nanometer ion channels that are used in nature for ion transport and highly-efficient life processes.

In the respect of material selection for ion-selective membrane with sub-nanometer channels, metal-organic frameworks (MOFs) have shown their potential usage as MOFs owns three-dimensional and interconnected sub-nm-sized channels. Through the combination of variable metal clusters and ligands, MOFs have been applied to various fields such as catalysis, sensing and gas storage, thanks to their highly ordered porosity, high surface area and adjustable surface properties (Kadhom and Deng, 2018; Kirchon et al., 2018; Zhao et al., 2020; Cai et al., 2021). Recently, MOF based ion-selective membranes have also been explored for RED osmotic energy harvesting (Rice et al., 2019; Jiang et al., 2020; Tan et al., 2021). The sub-nm-sized three-dimensional interconnected channels of MOFs can provide more rigid nanoconfinements than conventional nanochannel membranes, allowing the possibility for faster and more efficient selective ion transport. This property offers new opportunities for manufacturing high-performance salinity-gradient osmotic energy generation (Lu et al., 2021), however, has not been systematically investigated till now. Particularly, UiO-66-based MOFs with tailorable surface chemistry have recently been used for ion transport (Wan et al., 2017; Li et al., 2019; Ruan et al., 2021). The channels of UiO-66-based MOFs comprise angstrom-sized windows and nm-sized cavities that comparable to most hydrated ions in water, showing great potential for highly efficient harvesting of osmotic energy. For example, a UiO-66-NH_2 MOF based heterogeneous membrane have been fabricated for highly selective anion ion transport, and achieved highly efficient osmotic power generation under a 100-fold KBr gradient (Liu et al., 2021). Therefore, it is worthful to further explore the potential usage of UiO-66-NH_2 MOFs as anion-selective membrane toward high-performance salinity-gradient power generator as well as other applications.

Here, based on the previous study and inspired by the sub-nanochannel based ion-transport of living systems in nature, we report an UiO-66-NH_2 based composite membranes fabricated by a secondary-growth approach using porous anodic aluminum oxide (AAO) support, and achieved efficient anion-selective salinity-gradient power generation. The channels of the prepared UiO-66-NH_2 MOF comprise sub-1-nanometer sized windows and nm-sized cavities with a positive surface charge because of the NH_2 functional group. The thickness of a UiO-66-NH_2 layer is of the submicron scale (~710 nm). These characteristics allow the UiO-66-NH_2 membranes to achieve rapid ion transport with low fluid resistance. The proposed UiO-66-NH_2 membranes can achieve a maximum power density up to 1.47 W/m^2 under 50-fold sodium chloride (NaCl) gradient (0.5 M/0.01 M), which is higher than those produced by typical commercial membranes. This UiO-66-NH_2 based composite membranes was fabricated economically and simply without complex synthesis and expensive scientific equipment. Moreover, the membrane kept their continuous and dense structures after immersion in deionized water for 1 month, and their power density exhibited no obvious change within 1 week. Therefore, we considered that the membranes showed long-term stability. The current work can inspire research for

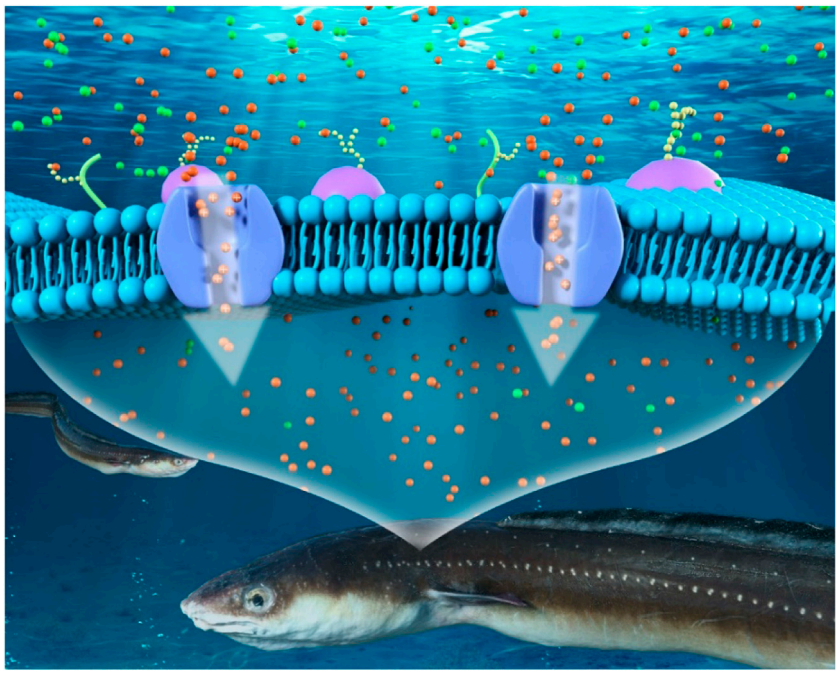

FIGURE 1 | Schematic illustration of the sub-nanometer protein ion channels of an electric ell.

designing anion-selective MOF based membranes, to provide more possibilities for realizing high-performance salinity-gradient osmotic power harvesting systems.

MATERIALS AND METHODS

Materials

Zirconium (IV) chloride ($ZrCl_4$), 2-aminoterephthalic acid (BDC-NH_2), dimethylformamide (DMF), and sodium chloride (NaCl) were purchased from Sigma-Aldrich (Shanghai, China). Highly ordered porous AAO membranes (160–200 nm) were obtained from Puyuan nano (Anhui, China).

Preparation of Single-Growth UiO-66-NH_2 Composite Membrane

For preparing single-growth UiO-66-NH_2 membrane, 0.116 g of $ZrCl_4$ and 0.0906 g of BDC-NH_2 were firstly ultrasonically dissolved in 30 mL of DMF, and then the resulting solution was transferred into a 50 mL Teflon-lined stainless-steel autoclave. The AAO membrane was then placed vertically in the reaction solution by using a Teflon holder, which ensured that the generated UiO-66-NH_2 layers were grown on both sides of the AAO membrane. The autoclave reactor was then placed in an oven and heated at 120°C for 1–5 days. After cooling to room temperature, the resulting solution (of a 1-day reaction) was collected for further use. Meanwhile, the single-growth UiO-66-NH_2 based composite membranes were taken out and washed consecutively three times with ethanol and DMF. This was followed by drying overnight at room temperature.

Preparation of Secondary-Growth UiO-66-NH_2 Composite Membrane

The reaction solution collected during the single-growth procedure was transferred into another 50 mL Teflon-lined stainless-steel autoclave for seed growth of UiO-66-NH_2 MOF on a new AAO support. The autoclave was placed in an oven and heated at 120°C for 24 h. After cooling to room temperature, the old reaction solution was removed, and a new mixture solution (0.116 g $ZrCl_4$ and 0.0906 g BDC-NH_2 in 30 mL of DMF) was transferred into the Teflon container. The autoclave was placed in the oven again and heated at 120°C for 24 h. After cooling to room temperature, the secondary-growth membrane was washed with ethanol and DMF for three times, followed by drying overnight at room temperature.

RESULTS AND DISCUSSION

Fabrication of UiO-66-NH_2 Composite Membranes

Inspired by the sub-nanometer protein ion-transporting channels of electric ell (**Figure 1**), we synthesized the UiO-66-NH_2 MOF based composite membranes for salinity-gradient osmotic energy conversion. The synthesis of the continuous and ultrathin UiO-66-NH_2 membranes using a seeded secondary-growth method is shown in **Figure 2A**. In

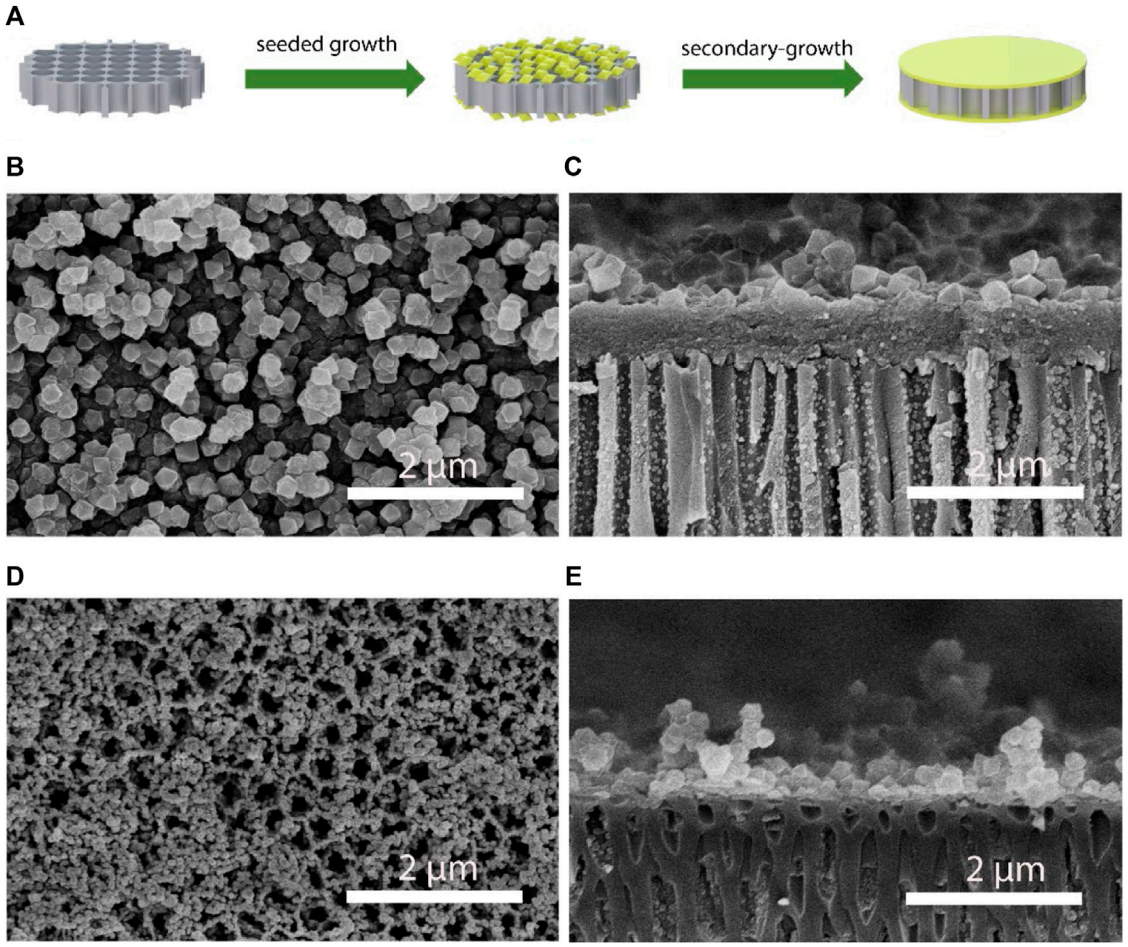

FIGURE 2 | Preparation and characterization of the UiO-66-NH_2 composite membranes. **(A)** The fabrication process for the UiO-66-NH_2 composite membranes. Representative **(B)** top and **(C)** cross-sectional SEM images of the secondary-growth UiO-66-NH_2 membrane. Representative **(D)** top and **(E)** cross-sectional SEM images of the single-growth UiO-66-NH_2 membrane.

the first step, nm-sized UiO-66-NH_2 crystals, left in the reaction solution during the single-growth procedure, were used to deposit a seed layer on both surfaces of a porous AAO substrate. The seeded AAO support was then exposed to a UiO-66-NH_2 precursor solution for secondary growth to form a dense UiO-66-NH_2 membrane. Scanning electron microscopy (SEM) characterization showed a continuous and dense UiO-66-NH_2 layer on the AAO support (**Figure 2B**). The samples exhibited clear octahedral shapes, which suggested high crystallinity. The thickness of the UiO-66-NH_2 layers was ~0.71 μm (**Figure 2C**). Furthermore, it is important to compare the influence of seeds to the single-growth and secondary-growth UiO-66-NH_2 membranes. The single-growth UiO-66-NH_2 has a small particle size and numerous defects (**Figures 2D,E**), while the introduction of a seed layer yields a larger particle size of UiO-66-NH_2 membranes (**Figures 2B,C**). In addition, the seeding step was found to be very crucial for forming a continuous MOF membrane. Without a seed layer, a discontinuous and defective layer was observed even when the single-growth period was extended to more than 5 days (**Supplementary Figure S1**). The X-ray diffraction (XRD) patterns of the UiO-66-NH_2 crystals were consistent with the reported calculated XRD patterns obtained from simulation (**Supplementary Figure S2**), confirming the successful synthesis of the UiO-66-NH_2 MOFs. Moreover, the as-prepared UiO-66-NH_2 owns a Brunauer–Emmett–Teller surface areas of 520 m^2/g, sub-1 nanometer size window apertures, and 1.2 nm cavities of MOF channels, as calculated from N_2 adsorption/desorption isotherm profiles (**Supplementary Figure S3**). These channel structures were comparable to most hydrated ions in water, therefore proved the potential of UiO-66-NH_2 membranes for harvesting osmotic energy. The positive framework charge originated from NH_2 functional groups was demonstrated by the positive zeta potential value, showing the ability of the as-prepared UiO-66-NH_2 membranes to transport anions selectively (**Supplementary Figure S4**). The contact angle results show that the composite membrane obtained high hydrophilicity after MOF deposition, and therefore can

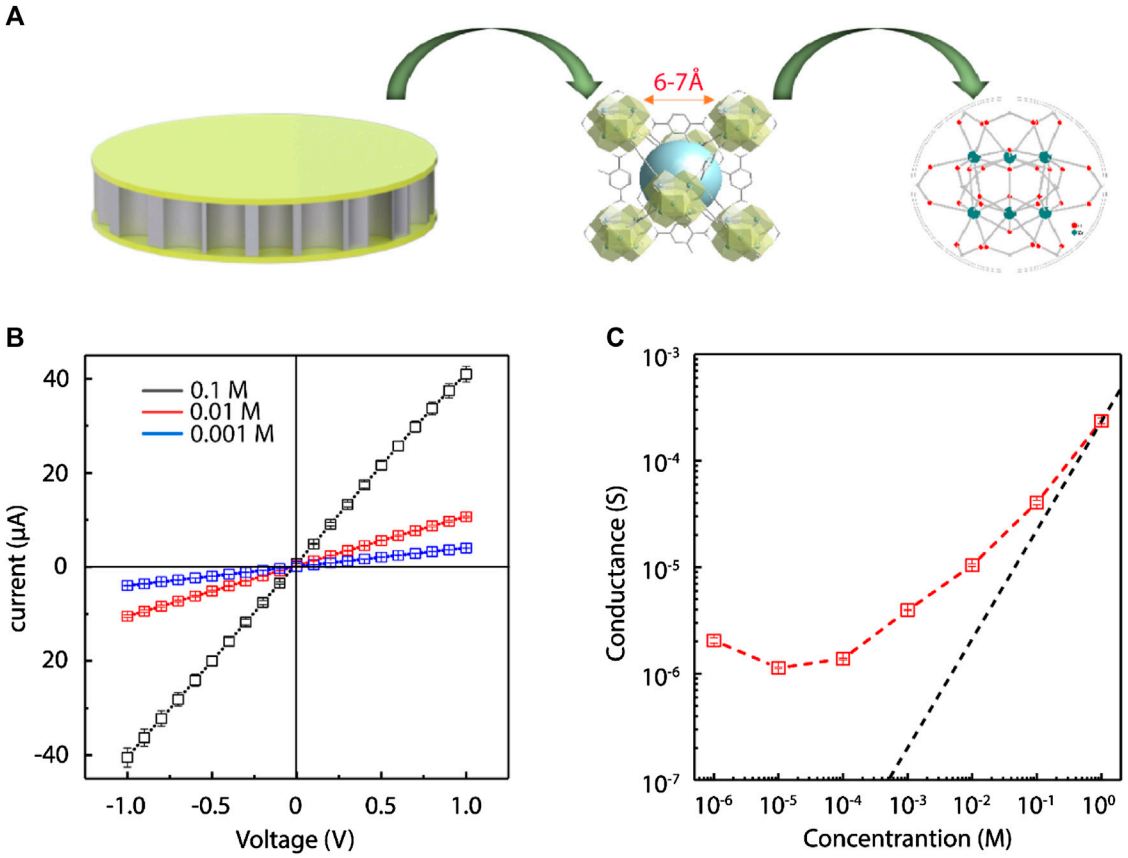

FIGURE 3 | Surface charge-governed ion transport in UiO-66-NH_2 composite membrane. **(A)** Schematic illustration of the UiO-66-NH_2 composite membrane with sub-nanometer sized channels. **(B)** Representative *I-V* curves obtained with three different NaCl concentration. **(C)** Ionic conductance of the UiO-66-NH_2 membranes at different electrolyte concentration. When the salt concentrations were <1 M, the ionic conductance values of the UiO-66-NH_2 membranes (red square) deviate significantly from the bulk value (black curve), demonstrating the surface charge governed ion transport behavior.

realize fast and low-resistance fluid transport (**Supplementary Figure S5**).

Surface Charge-Governed Ion Transport

The positively charged framework and sub-1 nanometer apertures of the UiO-66-NH_2 composite membranes (**Figure 3A**) suggest that it should have surface charged-governed ion transport at low electrolyte concentration. To demonstrate, we measured the ionic conductivity of the UiO-66-NH_2 membranes by changing NaCl electrolyte concentration. Two Ag/AgCl electrodes were inserted on either side of the custom-made electrochemical cell (**Supplementary Figure S6**) to record the current generated by sweeping voltages from −1 V to +1 V. *I–V* curves at different NaCl concentrations were firstly recorded, and *I–V* curves at three representative concentrations are shown in **Figure 3B**. As MOF layers were deposited on both sides of the AAO support, the ion transport of the composite membrane showed a symmetric behavior. Then, the conductance was calculated from the *I–V* slopes (**Figure 3C**). At high concentrations, the ionic conductance values of the UiO-66-NH_2 membranes were similar to that of the bulk phase. However, the ionic conductance started to deviate from the bulk value tendency, and was considerably higher than the bulk value when the salt concentration was below 1 M. When the salt concentration was <0.1 M, the Debye lengths were larger than the window apertures of UiO-66-NH_2 MOFs. Thus, the anions were the dominant charge carriers, and their concentrations were determined by the surface charge densities of the UiO-66-NH_2 sub-nanochannels. The result that the conductance of as-prepared composite membrane is larger than that of the bulk phase at low electrolyte concentration demonstrated that ionic transport is controlled by surface charge, which also sheds light on the further application of the as-prepared MOF composite membrane for harvesting salinity-gradient osmotic energy through selective anion transport.

Evaluation of Electrochemical Properties

The performance of the UiO-66-NH_2 composite membranes for salinity-gradient osmotic energy conversion was further studied by using asymmetric NaCl electrolyte solutions in the electrochemical cell (**Figure 4A**). The high concentration solution was standard artificial seawater (0.5 M NaCl), while the low concentration solution ranged from 0.0001

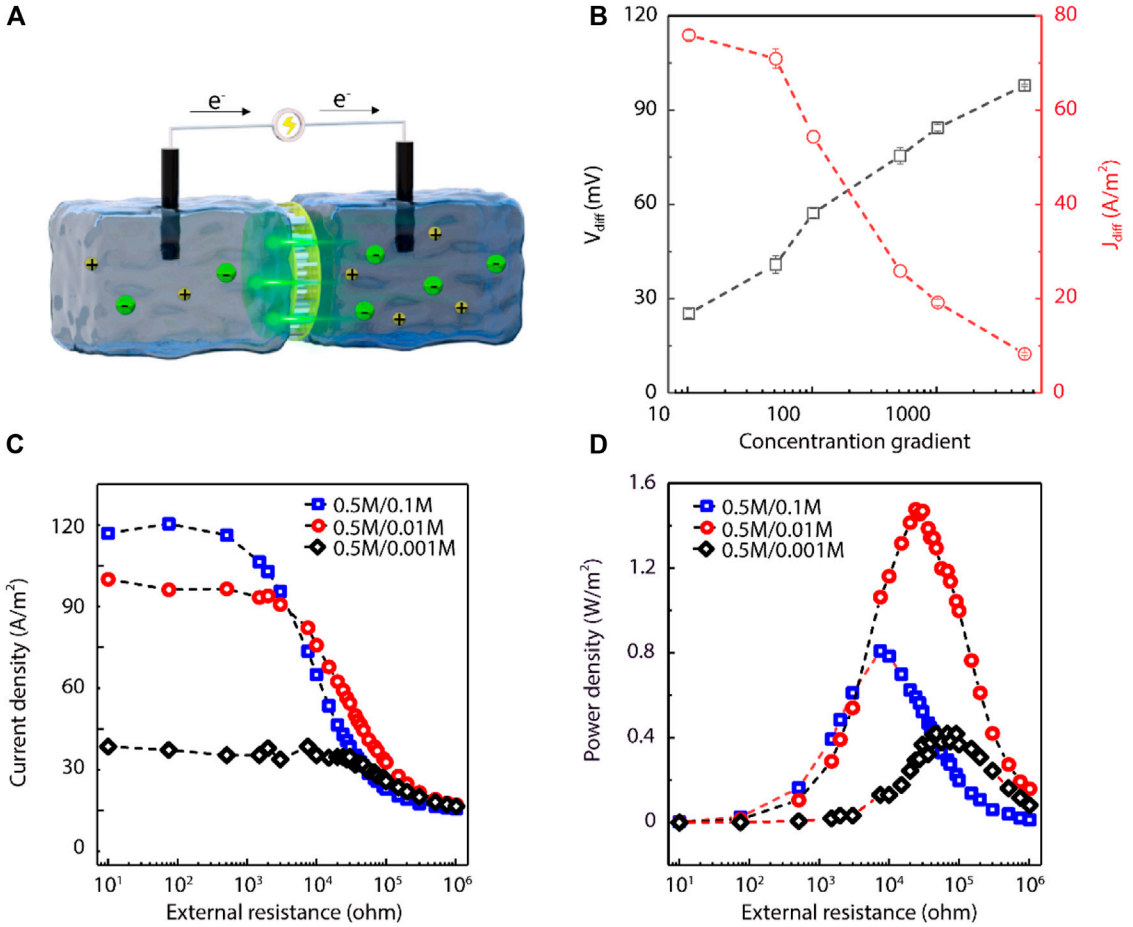

FIGURE 4 | UiO-66-NH_2 composite membranes for salinity-gradient osmotic energy conversion. **(A)** Schematic illustration of the proposed energy harvesting device. **(B)** As the concentration gradient was increased, the V_{diff} gradually increased and the J_{diff} gradually decreased. The high NaCl concentration was fixed at 0.5 M. **(C)** Current density and **(D)** power density of the as-prepared UiO-66-NH_2 composite membranes as a function of the external resistance under three different NaCl concentration gradients. For three salinity gradients, the measured current densities all gradually decrease with increasing external resistance. The maximum power density values were ~0.8, 1.47, and 0.42 W/m^2 for 5-, 50-, and 500-fold NaCl concentration gradients, respectively.

to 0.05 M NaCl. The salinity gradient was converted into electrical energy by the positively charged UiO-66-NH_2 composite membranes to transport anions selectively. We firstly recorded the current generated by sweeping voltages. The quadrant of the *I-V* curve under a 50-fold NaCl concentration gradient further indicated the positive charge of the UiO-66-NH_2 MOF (**Supplementary Figure S7**). During the osmotic energy conversion with asymmetric electrolytes, we eliminated the imbalance in electrode potentials by using a pair of salt bridges. The results showed that the V_{diff} values increased as the salinity gradient increased. However, the J_{diff} values decreased as the concentration gradient increased (**Figure 4B**). The reason of V_{diff} and J_{diff} changing in the opposite ways is that the increase in salinity gradient produces higher osmotic pressure and increases the resistance of the system. In a 50-fold salinity gradient, the V_{diff} and J_{diff} values of the UiO-66-NH_2 composite membranes were 40.85 mV and 70.91 A/m^2, respectively. However, the V_{diff} and J_{diff} of the single-growth UiO-66-NH_2 membranes were about 15.69 mV and 70 A/m^2 respectively (**Supplementary Figure S8**), which V_{diff} was smaller than that of the secondary-growth UiO-66-NH_2 membranes. In addition, the performance of the single-growth UiO-66-NH_2 composite membrane did not change obviously with the single-growth period (**Supplementary Figure S8**), showing the necessity of this seeded secondary-growth procedure for high-performance power-generation UiO-66-NH_2 composite membrane. Under the 50-fold salinity gradient, the corresponding energy conversion efficiency of the UiO-66-NH_2 composite membranes was 8.8% (**Supplementary Table S1**).

The actual power generation performance of the UiO-66-NH_2 membranes was further investigated by using an external circuit resistor (R_L). *I–t* curves under different external resistances were recorded, where *I* denotes the measured current. Then, the output power density was calculated as $P = I^2 \times R_L$. Under three salinity gradients, the current density decreased as the external resistance

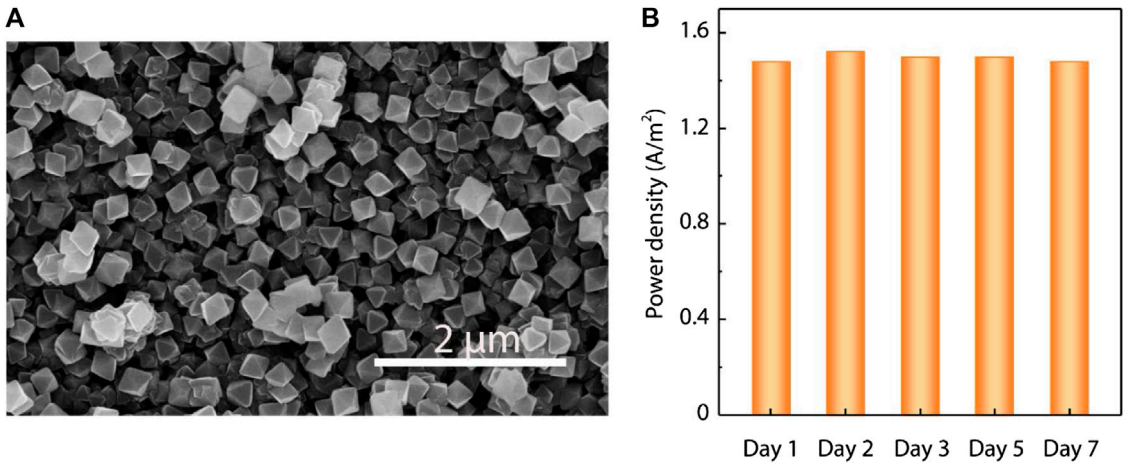

FIGURE 5 | Long-term stability of the as-prepared UiO-66-NH_2 composite membranes. **(A)** Representative SEM images of the UiO-66-NH_2 composite membranes, showing no obvious change after immersion in deionized water for 1 month. **(B)** Under 50-fold NaCl concentration gradient, the output power density of the UiO-66-NH_2 composite membranes showed strong stability examined in 1 week.

increased because the V_{diff} is the same at the same concentration (**Figure 4C**). However, the output power density increased firstly and then decreased with the increase of resistance, and reached a maximum value when the internal and external resistances were equal (**Figure 4D**). Moreover, a larger concentration gradient means a comparatively lower concentration on the low salt concentration side, which leads to an increase in the internal resistance of the system. Due to that, the power density of 500-fold salinity gradient turned smaller than that of the 50-fold salinity gradient. The resultant power density values were 0.80, 1.47, and 0.42 W/m^2 under 5-, 50-, and 500-fold NaCl gradients, respectively, indicating the practical application merits in estuaries with different concentration gradients. In contrast, the power density of the AAO support itself at the 50-fold NaCl concentration gradient was only 0.07 W/m^2, much less than that of the UiO-66-NH_2 composite membrane (**Supplementary Figure S9**), further indicating that the power generation performance of the composite membrane was ascribed to the MOF layer with sub-nanometer channels. It is worth noting that the power density measured here is not low compared with other MOF based materials (**Supplementary Table S2**).

Membranes with another two different thickness of MOF layer have also been fabricated (**Supplementary Figure S10**), to investigate the influence of MOF thickness to energy conversion. The results demonstrated that under the 50-fold NaCl concentration gradient, the power density values decreased from 1.47 to 0.42 W/m^2 due to the increased internal resistance caused by the increase in MOF layer thickness (**Supplementary Figure S11**). Furthermore, to prove that the UiO-66-NH_2 membranes can be applied to different fields, we measured the current density and power density of the UiO-66-NH_2 membranes at different pH conditions (**Supplementary Figure S12**). Under the 50-fold NaCl concentration gradient, the power density values decreased from 3.2 to 1.2 W/m^2 when the pH values of the solutions increased from 2 to 11. This is because of that positively charged materials have a higher surface charge density under more acidic condition, therefore exhibiting better ion-transport performance and higher power generation capability. The related zeta potential results also proved this explanation (**Supplementary Figure S13**). The external resistance values corresponding to the maximum value of power densities were close even under different pH conditions, indicating that the internal resistance was independent of pH at the same concentration gradient. These results demonstrated that the ion transport behaviour of the UiO-66-NH_2 membranes can be modulated by adjusting pH values, and therefore high performance of salinity-gradient osmotic energy generation can be achieved by further tailoring the surface charge properties of UiO-66-NH_2 MOF, as we expected.

Stability of the UiO-66-NH_2 Composite Membranes

More importantly, we demonstrated the long-term stability of the proposed UiO-66-NH_2 composite membranes. The UiO-66-NH_2 membranes maintained their continuous and dense structures after immersion in deionized water for 1 month (**Figure 5A**; **Supplementary Figure S14**). XRD patterns also indicate that there is no obvious change of the MOF crystal structure (**Supplementary Figure S15**). The long-term power generation stability of the UiO-66-NH_2 membrane was also confirmed, as the output power density was found maintained for at least 1 week (**Figure 5B**). This further suggests the good application viability of the MOF membranes in practical osmotic energy harvesting.

CONCLUSION

In summary, we prepared positively charged UiO-66-NH_2 MOF based composite membrane with sub-1-nm windows through a simple seed-assisted secondary growth method, and achieved successful capture of salinity-gradient osmotic energy by anion-

selective ion transport. The secondary-growth MOF membrane showed better structure and properties than the single-growth membrane. The as-prepared UiO-66-NH_2 composite membrane was also practical based on the results of power density under different salinity gradients and pH conditions and their long-term stability of structure and performance. We note that by adjusting the physical structures and the surface chemistry of the composite membrane, the power generation capability can be further improved. The current work suggests the potential of the UiO-66-NH_2 composite membrane in various practical applications, and provides inspirations for designing anion-selective and sub-nanochannel based membranes towards high-performance osmotic energy harvesting.

DATA AVAILABILITY STATEMENT

The original contributions presented in the study are included in the article/**Supplementary Material,** further inquiries can be directed to the corresponding authors.

AUTHOR CONTRIBUTIONS

XL and JC conceived and designed the project. XL and JC supervised the project. LY, QL, and SP conducted the experiments. All authors contributed to data analysis and manuscript drafting.

FUNDING

This work was supported by the Postdoctoral Applied Research Project of Qingdao.

SUPPLEMENTARY MATERIAL

The Supplementary Material for this article can be found online at: https://www.frontiersin.org/articles/10.3389/fbioe.2022.901507/full#supplementary-material

REFERENCES

Cai, P., Xu, M., Meng, S. S., Lin, Z., Yan, T., Drake, H. F., et al. (2021). Precise Spatial-Designed Metal-Organic-Framework Nanosheets for Efficient Energy Transfer and Photocatalysis. *Angew. Chem. Int. Ed.* 60 (52), 27258–27263. doi:10.1002/anie.202111594

Ding, L., Xiao, D., Lu, Z., Deng, J., Wei, Y., Caro, J., et al. (2020). Oppositely Charged Ti 3 C 2 T X MXene Membranes with 2D Nanofluidic Channels for Osmotic Energy Harvesting. *Angew. Chem. Int. Ed.* 59 (22), 8720–8726. doi:10.1002/anie.201915993

Gao, J., Feng, Y., Guo, W., and Jiang, L. (2017). Nanofluidics in Two-Dimensional Layered Materials: Inspirations from Nature. *Chem. Soc. Rev.* 46 (17), 5400–5424. doi:10.1039/c7cs00369b

Gao, J., Guo, W., Feng, D., Wang, H., Zhao, D., and Jiang, L. (2014). High-Performance Ionic Diode Membrane for Salinity Gradient Power Generation. *J. Am. Chem. Soc.* 136 (35), 12265–12272. doi:10.1021/ja503692z

Gao, J., Liu, X., Jiang, Y., Ding, L., Jiang, L., and Guo, W. (2019). Understanding the Giant Gap between Single-Pore- and Membrane-Based Nanofluidic Osmotic Power Generators. *Small* 15 (11), 1804279. doi:10.1002/smll.201804279

Jiang, Y., Ma, W., Qiao, Y., Xue, Y., Lu, J., Gao, J., et al. (2020). Metal-Organic Framework Membrane Nanopores as Biomimetic Photoresponsive Ion Channels and Photodriven Ion Pumps. *Angew. Chem. Int. Ed.* 59 (31), 12795–12799. doi:10.1002/anie.202005084

Kadhom, M., and Deng, B. (2018). Metal-Organic Frameworks (MOFs) in Water Filtration Membranes for Desalination and Other Applications. *Appl. Mater. Today* 11, 219–230. doi:10.1016/j.apmt.2018.02.008

Kirchon, A., Feng, L., Drake, H. F., Joseph, E. A., and Zhou, H.-C. (2018). From Fundamentals to Applications: A Toolbox for Robust and Multifunctional MOF Materials. *Chem. Soc. Rev.* 47 (23), 8611–8638. doi:10.1039/c8cs00688a

Lao, J., Lv, R., Gao, J., Wang, A., Wu, J., and Luo, J. (2018). Aqueous Stable Ti3C2 MXene Membrane with Fast and Photoswitchable Nanofluidic Transport. *ACS Nano* 12 (12), 12464–12471. doi:10.1021/acsnano.8b06708

Lao, J., Wu, S., Gao, J., Dong, A., Li, G., and Luo, J. (2020). Electricity Generation Based on a Photothermally Driven Ti3C2Tx MXene Nanofluidic Water Pump. *Nano Energy* 70, 104481. doi:10.1016/j.nanoen.2020.104481

Li, X., Zhang, H., Wang, P., Hou, J., Lu, J., Easton, C. D., et al. (2019). Fast and Selective Fluoride Ion Conduction in Sub-1-nanometer Metal-Organic Framework Channels. *Nat. Commun.* 10, 2490. doi:10.1038/s41467-019-10420-9

Liu, X., He, M., Calvani, D., Qi, H., Gupta, K. B. S. S., de Groot, H. J. M., et al. (2020). Power Generation by Reverse Electrodialysis in A Single-Layer Nanoporous Membrane Made from Core-Rim Polycyclic Aromatic Hydrocarbons. *Nat. Nanotechnol.* 15 (4), 307–312. doi:10.1038/s41565-020-0641-5

Liu, Y.-C., Yeh, L.-H., Zheng, M.-J., and Wu, K. C.-W. (2021). Highly Selective and High-Performance Osmotic Power Generators in Subnanochannel Membranes Enabled by Metal-Organic Frameworks. *Sci. Adv.* 7 (10), eabe9924. doi:10.1126/sciadv.abe9924

Lu, J., Zhang, H., Hu, X., Qian, B., Hou, J., Han, L., et al. (2021). Ultraselective Monovalent Metal Ion Conduction in a Three-Dimensional Sub-1 Nm Nanofluidic Device Constructed by Metal-Organic Frameworks. *ACS Nano* 15 (1), 1240–1249. doi:10.1021/acsnano.0c08328

Man, Z., Safaei, J., Zhang, Z., Wang, Y., Zhou, D., Li, P., et al. (2021). Serosa-Mimetic Nanoarchitecture Membranes for Highly Efficient Osmotic Energy Generation. *J. Am. Chem. Soc.* 143 (39), 16206–16216. doi:10.1021/jacs.1c07392

Montenegro, J., Ghadiri, M. R., and Granja, J. R. (2013). Ion Channel Models Based on Self-Assembling Cyclic Peptide Nanotubes. *Acc. Chem. Res.* 46 (12), 2955–2965. doi:10.1021/ar400061d

Ren, C., Chen, F., Ye, R., Ong, Y. S., Lu, H., Lee, S. S., et al. (2019). Molecular Swings as Highly Active Ion Transporters. *Angew. Chem. Int. Ed.* 58 (24), 8034–8038. doi:10.1002/anie.201901833

Rice, A. M., Leith, G. A., Ejegbavwo, O. A., Dolgopolova, E. A., and Shustova, N. B. (2019). Heterometallic Metal-Organic Frameworks (MOFs): The Advent of Improving the Energy Landscape. *ACS Energ. Lett.* 4 (8), 1938–1946. doi:10.1021/acsenergylett.9b00874

Ruan, H., Pan, N., Wang, C., Yu, L., Liao, J., and Shen, J. (2021). Functional UiO-66 Series Membranes with High Perm Selectivity of Monovalent and Bivalent Anions for Electrodialysis Applications. *Ind. Eng. Chem. Res.* 60 (10), 4086–4096. doi:10.1021/acs.iecr.0c05992

Sadeghi, G. (2022). Energy Storage on Demand: Thermal Energy Storage Development, Materials, Design, and Integration Challenges. *Energ. Storage Mater.* 46, 192–222. doi:10.1016/j.ensm.2022.01.017

Schroeder, T. B. H., Guha, A., Lamoureux, A., VanRenterghem, G., Sept, D., Shtein, M., et al. (2017). An Electric-Eel-Inspired Soft Power Source from Stacked Hydrogels. *Nature* 552, 214–218. doi:10.1038/nature24670

Siria, A., Bocquet, M.-L., and Bocquet, L. (2017). New Avenues for the Large-Scale Harvesting of Blue Energy. *Nat. Rev. Chem.* 1 (11), 0091. doi:10.1038/s41570-017-0091

Sun, Y., Dong, T., Lu, C., Xin, W., Yang, L., Liu, P., et al. (2020). Tailoring A Poly(ether Sulfone) Bipolar Membrane: Osmotic-Energy Generator with High Power Density. *Angew. Chem. Int. Ed.* 59 (40), 17423–17428. doi:10.1002/anie.202006320

Tan, H., Zhou, Y., Qiao, S.-Z., and Fan, H. J. (2021). Metal Organic Framework (MOF) in Aqueous Energy Devices. *Mater. Today* 48, 270–284. doi:10.1016/j.mattod.2021.03.011

Tawalbeh, M., Al-Othman, A., Abdelwahab, N., Alami, A. H., and Olabi, A. G. (2021). Recent Developments in Pressure Retarded Osmosis for Desalination and Power Generation. *Renew. Sustainable Energ. Rev.* 138, 110492. doi:10.1016/j.rser.2020.110492

Teng, Y., Kong, X.-Y., Liu, P., Qian, Y., Hu, Y., Fu, L., et al. (2021). A Universal Functionalization Strategy for Biomimetic Nanochannel via External Electric Field Assisted Non-covalent Interaction. *Nano Res.* 14 (5), 1421–1428. doi:10.1007/s12274-020-3192-z

van Ruijven, B. J., De Cian, E., and Sue Wing, I. (2019). Amplification of Future Energy Demand Growth Due to Climate Change. *Nat. Commun.* 10, 2762. doi:10.1038/s41467-019-10399-3

Wan, L., Zhou, C., Xu, K., Feng, B., and Huang, A. (2017). Synthesis of Highly Stable UiO-66-NH2 Membranes with High Ions Rejection for Seawater Desalination. *Microporous Mesoporous Mater.* 252, 207–213. doi:10.1016/j.micromeso.2017.06.025

Xiao, K., Jiang, L., and Antonietti, M. (2019). Ion Transport in Nanofluidic Devices for Energy Harvesting. *Joule* 3 (10), 2364–2380. doi:10.1016/j.joule.2019.09.005

Xin, W., Xiao, H., Kong, X.-Y., Chen, J., Yang, L., Niu, B., et al. (2020). Biomimetic Nacre-like Silk-Crosslinked Membranes for Osmotic Energy Harvesting. *ACS Nano* 14 (8), 9701–9710. doi:10.1021/acsnano.0c01309

Xin, W., Zhang, Z., Huang, X., Hu, Y., Zhou, T., Zhu, C., et al. (2019). High-Performance Silk-Based Hybrid Membranes Employed for Osmotic Energy Conversion. *Nat. Commun.* 10, 3876. doi:10.1038/s41467-019-11792-8

Yang, L., Liu, P., Zhu, C., Zhao, Y., Yuan, M., Kong, X.-Y., et al. (2021). Ion Transport Regulation through Triblock Copolymer/PET Asymmetric Nanochannel Membrane: Model System Establishment and Rectification Mapping. *Chin. Chem. Lett.* 32 (2), 822–825. doi:10.1016/j.cclet.2020.04.047

Yip, N. Y., Brogioli, D., Hamelers, H. V. M., and Nijmeijer, K. (2016). Salinity Gradients for Sustainable Energy: Primer, Progress, and Prospects. *Environ. Sci. Technol.* 50 (22), 12072–12094. doi:10.1021/acs.est.6b03448

Zhang, Z., Kong, X.-Y., Xiao, K., Liu, Q., Xie, G., Li, P., et al. (2015). Engineered Asymmetric Heterogeneous Membrane: A Concentration-Gradient-Driven Energy Harvesting Device. *J. Am. Chem. Soc.* 137 (46), 14765–14772. doi:10.1021/jacs.5b09918

Zhang, Z., Sui, X., Li, P., Xie, G., Kong, X.-Y., Xiao, K., et al. (2017). Ultrathin and Ion-Selective Janus Membranes for High-Performance Osmotic Energy Conversion. *J. Am. Chem. Soc.* 139 (26), 8905–8914. doi:10.1021/jacs.7b02794

Zhang, Z., Yang, S., Zhang, P., Zhang, J., Chen, G., and Feng, X. (2019). Mechanically Strong MXene/Kevlar Nanofiber Composite Membranes as High-Performance Nanofluidic Osmotic Power Generators. *Nat. Commun.* 10, 2920. doi:10.1038/s41467-019-10885-8

Zhao, F., Cheng, H., Zhang, Z., Jiang, L., and Qu, L. (2015). Direct Power Generation from a Graphene Oxide Film under Moisture. *Adv. Mater.* 27 (29), 4351–4357. doi:10.1002/adma.201501867

Zhao, Y., Wei, Y., Lyu, L., Hou, Q., Caro, J., and Wang, H. (2020). Flexible Polypropylene-Supported ZIF-8 Membranes for Highly Efficient Propene/Propane Separation. *J. Am. Chem. Soc.* 142 (50), 20915–20919. doi:10.1021/jacs.0c07481

Conflict of Interest: The authors declare that the research was conducted in the absence of any commercial or financial relationships that could be construed as a potential conflict of interest.

Publisher's Note: All claims expressed in this article are solely those of the authors and do not necessarily represent those of their affiliated organizations, or those of the publisher, the editors and the reviewers. Any product that may be evaluated in this article, or claim that may be made by its manufacturer, is not guaranteed or endorsed by the publisher.

frontiers | Frontiers in Bioengineering and Biotechnology

ORIGINAL RESEARCH
published: 26 April 2022
doi: 10.3389/fbioe.2022.887902

"Anti-Condensation" Aluminum Superhydrophobic Surface by Smaller Nanostructures

Kangning Li[1,2], *Ying Zhao*[1], *Jintao Yang*[1] *and Jie Feng*[1]*

[1]College of Materials Science and Engineering, Zhejiang University of Technology, Hangzhou, China, [2]Jinhua Polytechnic, Jinhua, China

According to classical heterogeneous nucleation theory, the free energy barrier (ΔG_C) of heterogeneous nucleation of vapor condensation ascends dramatically as the substrate nanostructure diameter (R_S) decreases. Based on this idea, we fabricated two types of superhydrophobic surfaces (SHSs) on an aluminum substrate by different roughening processes and the same fluorization treatment. Water vapor condensation trials by optical microscope and ESEM confirmed that on SHSs with submicron rectangle structures, a typical self-propelled motion of condensates or jumping condensation occurred. However, on SHS with coral-like micro/nano-structures, vapor nucleation occurred tardily, randomly, and sparsely, and the subsequent condensation preferentially occurred on the nuclei formed earlier, e.g., the condensation on such SHS typically followed the Matthew effect. Higher vapor-liquid nucleation energy barrier caused by smaller fluorinated nanostructures should be responsible for such a unique "anti-condensation" property. This study would be helpful in designing new SHSs and moving their application in anti-icing, anti-fogging, air humidity control, and so on.

Keywords: aluminum, superhydrophobic surface, anti-condensation, microscopic mechanism, smaller nanostructures

OPEN ACCESS

Edited by:
Feilong Zhang,
Nanyang Technological University, Singapore

Reviewed by:
Chao-Hua Xue,
Shaanxi University of Science and Technology, China
Zhen Gu,
University of Science and Technology Beijing, China

***Correspondence:**
Jie Feng
fengjie@zjut.edu.cn

Specialty section:
This article was submitted to Bionics and Biomimetics, a section of the journal Frontiers in Bioengineering and Biotechnology

Received: *02 March 2022*
Accepted: *23 March 2022*
Published: *26 April 2022*

Citation:
Li K, Zhao Y, Yang J and Feng J (2022) "Anti-Condensation" Aluminum Superhydrophobic Surface by Smaller Nanostructures. Front. Bioeng. Biotechnol. 10:887902. doi: 10.3389/fbioe.2022.887902

INTRODUCTION

Many plants exhibit remarkable water repellency owing to their rough surface. The textured surface traps air underneath water droplets and the air cushioning gives rise to superhydrophobicity (Barthlott and Neinhuis, 1997; Neinhuis and Barthlott, 1997). However, biomimetic superhydrophobic surfaces (SHSs) generally do not retain water repellency when exposed to a condensing environment (Zhao and Yang, 2017; Chen et al., 2018; Zhao et al., 2018; Orejon et al., 2019). Water condensates proceeding from nanoscale nuclei tend to penetrate into the surface texture and displace the trapped air, forfeiting the superhydrophobicity. Along with the condensation proceeds, arrays of visible, glittering, transparent, and adhesive large Wenzel drops (3–5 mm in diameter) cover the SHSs gradually. This seriously limits their applications in sustained dropwise condensation (Hao et al., 2018; Wang et al., 2020), water collection (Zheng et al., 2010), anti-icing (Kreder et al., 2016; Caldona et al., 2017; Zhu et al., 2020), and anti-corrosion (Xue et al., 2020). In some cases, these SHSs even represent a worse performance than general hydrophobic surfaces do such as increasing ice adhesion strength once the ice forms (Kreder et al., 2016; Caldona et al., 2017).

Recently, the self-propelled motion of condensate drops on some SHSs has attracted increasing attention due to its potential applications in delaying frost growth (Hao et al., 2014; Jiang et al., 2020; Mohammadian et al., 2020), enhancing condensation heat transfer (Hao et al., 2018; Sarode et al., 2020),

stronger self-cleaning (Geyer et al., 2020), and breathable anti-condensation coating on buildings (Wu et al., 2021). Wang et al. (2021) demonstrated that the vapor molecules can be intercepted by oblique nanowires and preferentially nucleate at near-surface locations, avoiding the penetration of vapor into the microscale gaps.

In our earlier studies (Feng et al., 2012a; Feng et al., 2012b), we have confirmed that nuclei formed within the nanogaps of SHSs would grow and coalesce into micro-droplets. Then the micro-droplets derive themselves upwards and form into Cassie droplets. It is such a Cassie state that causes the spontaneous motion of drops after coalescence. A nanostructure with sufficiently narrow spacing and high perpendicularity is favorable to form such a Cassie condensation. According to classical heterogeneous nucleation theory (Liu, 1999), the free energy barrier (ΔG_c) of heterogeneous nucleation of vapor condensation ascends dramatically as the substrate nanostructure's diameter (R_s) decreases. No nucleation would bring none condensation. Based on this principle, new types of SHS with a more obvious anti-condensation property may be created by designing fine nanostructures.

In this study, we fabricated two types of SHSs on an aluminum substrate by two different roughening processes and the same fluorization treatment. One was only by HCl etching and the other was by HCl etching and by further immersing in hot water. Water vapor condensation trials confirmed that although both two surfaces were superhydrophobic and supported Cassie condensation, only SHS by HCl etching and further by hot water treatment showed an obvious anti-condensation property, e.g., the condensate droplets appeared tardily, randomly, and sparsely on it. Most of the SHS areas appeared dry. A much higher nucleation energy barrier caused by much smaller nanostructures should be responsible for such phenomena. This study opens a new door for designing new SHSs and moving their applications in fields such as anti-icing, anti-fogging, anti-corrosion, and air humidity control.

EXPERIMENTAL SECTION

Superhydrophobic Surfaces Preparation

The aluminum foils with size of 6 cm × 5 cm × 0.5 mm (purity 99.99%) were ultrasonically washed in acetone and ethanol to get rid of organic contamination. The cleaned aluminum foils were etched in 9 wt% HCl aqueous solution for 12 min at room temperature. After being rinsed with deionized water, a part of the samples were further immersed in deionized water (50°C) for 40 min and subsequently dried with nitrogen. Then the two batches of samples were incubated in a 0.5 wt% hexane solution of 1H, 1H, 2H, and 2H-perfluorodecyltriethoxysilane (FAS17, Sigma) at room temperature for 1 h, followed by drying at 120°C for 1 h.

Morphology and Wettability of the Superhydrophobic Surfaces

The morphologies of as-prepared aluminum surfaces were characterized by field emission scanning electron microscopy (FE-SEM, S4700, Hitachi, Japan). For each surface, its nanostructure parameters such as the diameter or width/length and gap space were measured and calculated statistically from the SEM images. The water contact angles (CAs) and slide angles (SAs) were measured by using a Dataphysics OCA35 contact-angle system with a temperature control stage. This stage can precisely maintain the temperature of SHS from -30–160°C. The volume of the water droplet used for the CA measurements is 4 μL. The CAs were obtained by averaging five measurement results.

Condensation Under Ambient Condition

Condensation experiments were performed in a closed room with an area of 25 m^2 and a height of 3 m. The ambient temperature was controlled at 28 ± 1°C and the relative humidity (RH) was adjusted at 80 ± 2%. The surface superhydrophobilized aluminum foils with a size of 3 cm × 3 cm × 0.5 mm were placed on a horizontally orientated Peltier cooling stage with the hot side cooled by recirculating water. The sample surface was maintained at 0–1°C. The spontaneous motion of condensate droplets was observed and visualized by an optical microscope (Nikon LV 150) with a ×10 objective and charge-coupled device camera (CCD) at 25 fps. The phenomena were quantified by analyzing 2 min representative videos. Four short periods of time (only 1 s) spacing 30 s, all together 5 × 25 pieces of snapshots were used to quantify the average numbers of distinguishable drop location changes in 1 s videos (here named as "spontaneous motion frequency") (Feng et al., 2012a; Feng et al., 2012b).

Condensation Dynamics in ESEM

The microscale dynamics of vapor condensation on the sample surfaces were *in situ* visualized using an environmental scanning electron microscopy (ESEM, FEI Quanta 200 FEG) with a Peltier cooling stage. The sample was placed on a stainless steel sample holder that was rested on the Peltier cooling stage. The drop condensation was imaged using a gaseous secondary electron detector. The electron beam voltage was set at ~30 keV in order to ensure better contrast for image visualization. The condensation process can be triggered by precisely controlling the stage temperature and the water vapor pressure in the chamber. In this experiment, the temperature of the Peltier cooling stage was fixed at ~1°C. The vapor pressure was gradually increased to ~800 Pa, at which the vapor started to nucleate on the sample surface, and then maintained at ~800 Pa during imaging. The images were taken every 1.6 s.

RESULTS AND DISCUSSION

Morphology and Superhydrophobicity of as-Fabricated Surfaces

Similar to the results of Yin et al. (2012) and Z. Zhang Yang et al. (2011), rectangle-shaped submicron-structure (**Figure 1A1–3**) and coral-like micro/nano-hierarchical structures (**Figure 1B1–3**) were obtained on the aluminum surface after HCl etching and HCl etching combined with hot water treatment,

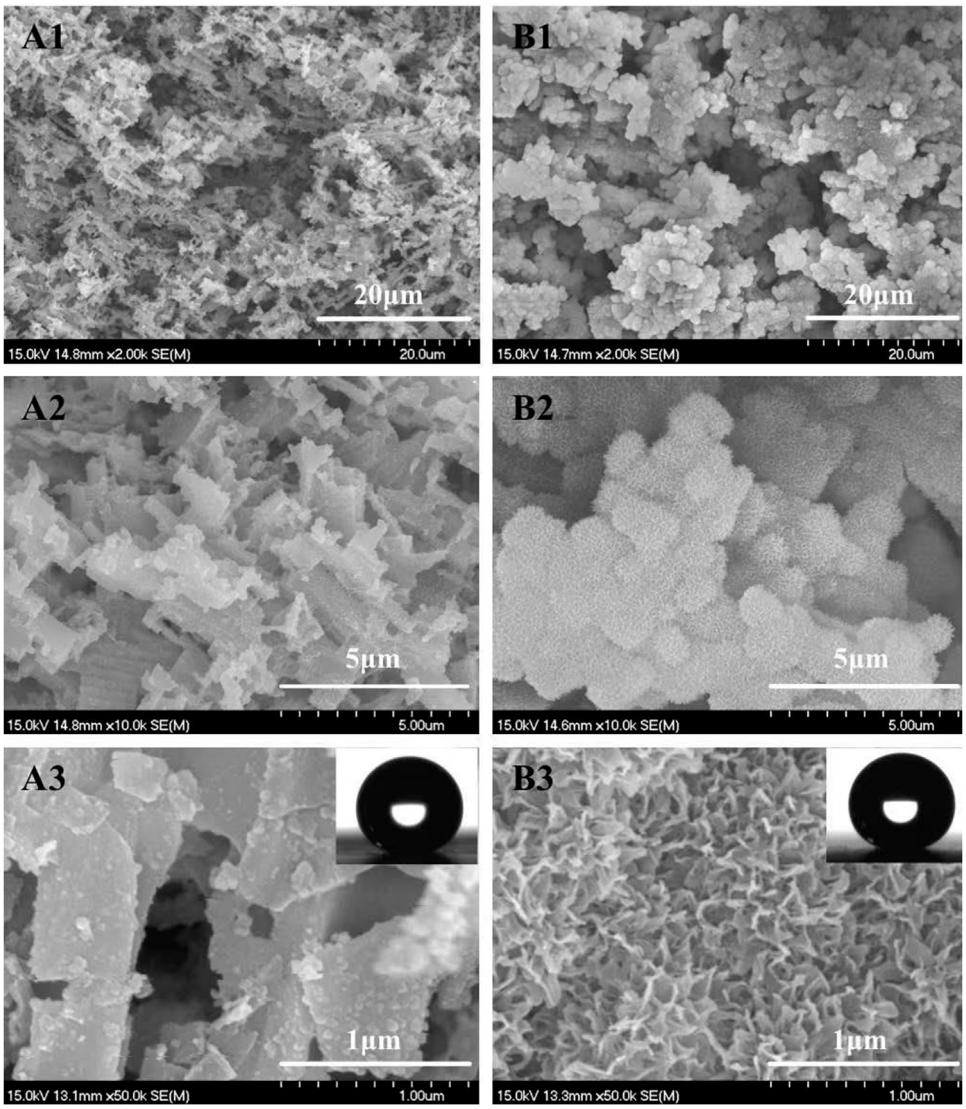

FIGURE 1 | FESEM images of the textured aluminum surface obtained by 12 min HCl etching (9 wt%) at 20°C **(A)** and further immersing in 50°C water for 40 min **(B)**. Magnification from A1 to A3 or B1 to B3 is increased. The insets were profiles of 4 μL water droplets showing WCA both at ~155°.

respectively. Vulnerable dislocation sites inside the crystalline aluminum should be responsible for such a submicron rectangle structure (~0.5–1 μm) (Yin et al., 2012). While the reaction of aluminum with hot water starting from the dissolution of aluminum and followed by the deposition of aluminum hydroxide colloidal particles on the aluminum surface should be responsible for the coral like micro/nano-hierarchical structures (He et al., 2012). The average width of nano-flakes is ~10 nm and the average space is ~100 nm (**Figure 1B3**).

CAs and SAs measurement showed that the sessile CAs of two types of as-prepared surfaces were both larger than 150° (**Figure 1**, insets) and the SAs were both less than 2°. This demonstrated that both two types of surfaces were typical superhydrophobic and the intrinsic surface energy was sufficiently low. The latter is one of two key factors affecting the vapor condensation nucleation energy barrier (Liu, 1999). Compared with the anodization method, simple hot water immersing supplied a facile process in creating dense nanostructures and narrow nanogaps on the aluminum substrate, which is necessary for forming larger upward Laplace pressure to the droplets condensed within the gaps (if they could form there) and thus bringing Cassie condensation and rapid self-propelled motion phenomenon to condensate droplets (Feng et al., 2012a; Feng et al., 2012b).

Condensation Under Ambient Condition

Figure 2 shows the time-lapse top-view optical images of dropwise condensation on aluminum surfaces prepared by two different etching methods. It clearly demonstrates that different surface structures do bring different condensation behaviors. On

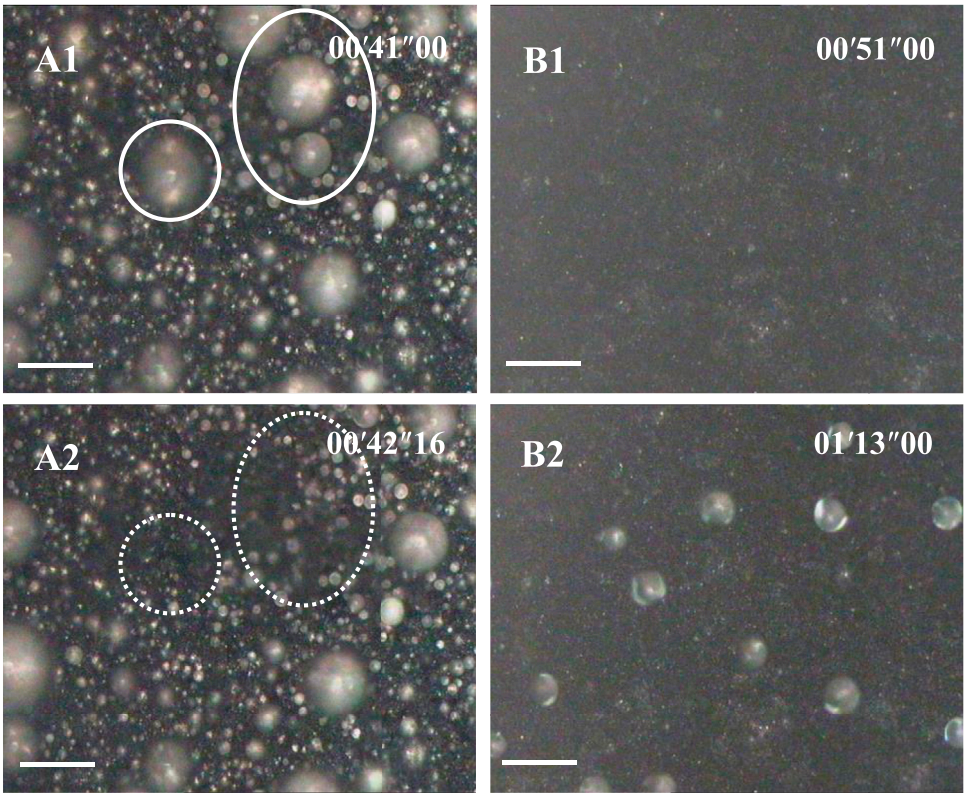

FIGURE 2 | Water vapor condensation behavior on SHS with submicron rectangle microstructures **(A)** series (implying Cassie or jumping condensation), and on SHS with coral- like micro/nano-structures **(B)** series, implying an anti-condensation character). The scale bar is 60 μm. The temperature of SHSs was 0–1°C. The environmental RH was 80 ± 2% (28 ± 1°C). The time scale in the images is minute, second, and millisecond.**Supplementary Video S1,S2** corresponding to A and B are available in the Supporting Information.

a rectangle submicron structured SHS, condensate droplets appeared in a classical self-propelled motion or "jumping" behavior, e g., condensation, is continuously, covering all areas and homogeneous (**Figure 2A**). The spontaneous motion frequency began at the high level (>100 drops/s), changed a little in 1 min and then gradually decreased, and finally balanced at 70 drops/s. Re-nucleation and growth of condensate droplets appeared on any region of the SHS especially including bare areas caused by droplet move-away. However, on coral-like micro/nano-structured SHS, condensate droplets appeared slowly (~50 s delay), dispersedly, and sparsely in the whole condensation procedure. Most of SHS was always bare and dry. Primary nucleation occurred randomly and the subsequent nucleation occurred preferentially on the droplets formed by these former nuclei. Because the distance between the droplets was so far, the coalescence opportunity was so low that no self-propelled motion or "jumping" appeared throughout the condensation process (**Figure 2B**).

Condensation in ESEM

To better understand the aforementioned preferential condensation phenomenon, we further apply ESEM to observe the condensation dynamics on both types of SHSs. **Figure 3** shows time-lapse images of condensation on the SHSs with submicron rectangle microstructures and coral like micro/nano-structures, respectively. It clearly proved the results of the microscopy video: both SHSs presented spherical Cassie state condensate droplets, however, only SHS with coral-like micro/nano-structures appeared to have an obvious anti-condensation property. That is, on SHSs with submicron rectangle microstructures, spherical droplets emerged continuously and coalesced successively thus forming droplets with dispersed diameters (**Figure 3A**). However, on SHS with coral-like micro/nano-structures, vapor nucleation occurred tardily, randomly, and sparsely, and the subsequent condensation preferentially occurred on these earlier formed nuclei. In the microscopy visual field, only several large drops grew up through their growth and asymmetric coalescence, while most areas were always dry (**Figure 3B**).

Anti-Condensation Mechanism Analysis

As it showed in **Figures 2B**, **3B**, when homogeneous dropwise condensation continuously occurred on SHS with submicron rectangle microstructures, no condensate droplets appeared on most districts of SHS with coral-like micro/nano-structures. This phenomenon can be explained by the classical nucleation theory. Essentially, vapor condensation at least includes the process of

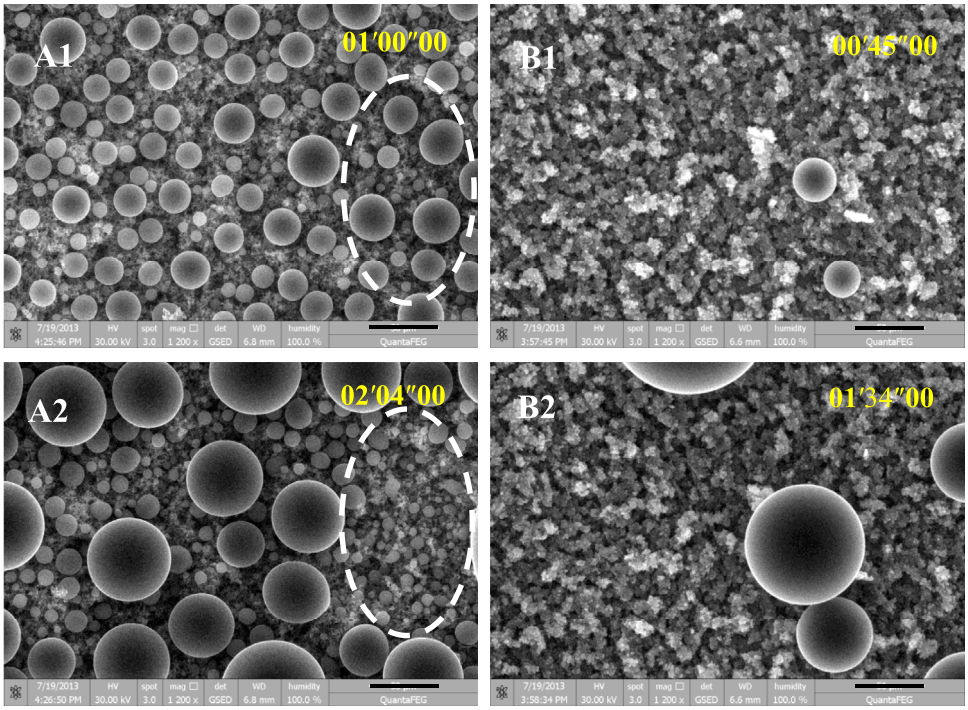

FIGURE 3 | Time-lapse ESEM images of vapor condensation on SHSs with submicron rectangle structures (A1-2) and with coral-like micro/nano-structures (B1-2), respectively. The scale bar is 50 μm. The temperature of the sample stage was fixed at ~1°C. The vapor pressure was gradually increased to ~800 Pa, at which the vapor started to nucleate on the sample surface, and then maintained at ~800 Pa during imaging. The images were taken every 1.6 s. The time scale in the images is minute, second, and millisecond.

nucleation and growth. Nucleation is the process of vapor molecules clustering together. It was generally triggered by supersaturation and with or without preferential sites such as dust and surface nanostructures (so called homogeneous or heterogeneous nucleation). Critical nucleation radius is the minimum size that must be formed by vapor molecules clustering before a droplet is stable and begins to grow. It mainly depends on supersaturation caused by dew point, supercooling temperature, and RH. According to the classical nucleation theory (Liu, 1999), the radius of the critical nucleus (r_c) in vapor condensation can be estimated from:

$$RT \ln \frac{P_r}{P} = -\frac{2\gamma V_m}{r}$$

Where R is ideal gas constant (8.314 $J \cdot mol^{-1}K^{-1}$), T is the temperature of condensation (273.15 K), P_r is the vapor pressure over a curved interface of a droplet with radius r, P is the equilibrium vapor pressure above a flat surface of the condensed phase at T (P is 0.61129 kPa at 0°C), $\gamma \approx 7.56 \times 10^{-2}$ J/m^2 is the water (0°C) interfacial tension, and $v \approx 1.8 \times 10^{-5}$ m^3/mol is the water molar volume. When the $P_r \leq$ P (28°C) (3.7818 kPa) × 80 % (RH at 28°C), nucleation occurs and the corresponding radius is at an equilibrium or critical radius (here named r_c, which is 0.75 nm after calculation).

The critical radius is the minimum droplet radius for the formation of stable nuclei. However, it is a concept suitable to homogeneous nucleation. In most cases, nucleation occurs at nucleation sites on surfaces contacting the vapor, and thus results in heterogeneous nucleation. Comparing with critical radius, the free energy barrier of nucleation is another index being developed to describe the difficulty of nucleation especially those that occur on the surfaces with nano or micro-structures (heterogeneous nucleation). According to the classical heterogeneous nucleation theory (Liu, 1999), the effect of the surface structure on the free energy barrier of heterogeneous formation of condensate droplet (ΔG_c) can be readily estimated as:

$$\Delta G_c = \Delta G_c^{homo} f(m, x)$$

Where ΔG_c^{homo} is the free energy barrier forming a droplet in a homogeneous way, $f(m, x)$ is the ratio of free energy barrier for nucleation around a spherical particle relative to that in the bulk, e.g., a factor that reduces the energy barrier of heterogeneous nucleation. $m = \cos\theta_{flat}$ with $\theta_{flat} = 108^\circ$ for FAS treatment (Feng et al., 2012a), and $x = R_s/r_c$. Since r_c is certain (0.75 nm), $f(m, x)$ only changes with the radius of nucleating substrate structures (R_s). As Liu et al. (1999) derived, the $f(m, x)$ ascends dramatically as the nanostructure diameter decreases till it approaches 1. When the condensation conditions (RH, supercooling, et al.) are same, the smaller nanostructure on SHS would bring a more difficult nucleation.

On the SHS with coral-like micro/nano-structures (**Figure 1B**), the average width of the nano-flakes is ~10 nm and the average space is ~100 nm. This means that the corresponding apparent radius of nucleating structures (R_s)

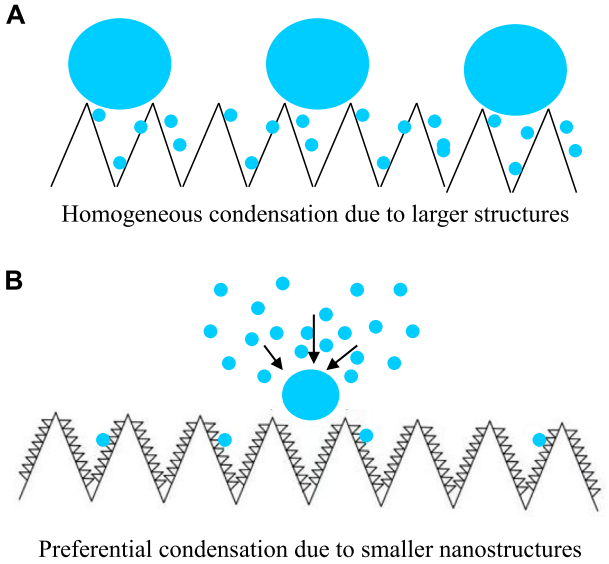

FIGURE 4 | Scheme of water vapor condensation on SHS with submicron rectangle structures **(A)**, condensate droplets appeared immediately, continuously, and densely, and on the SHS with much smaller nanostructures **(B)**, condensate droplets appeared tardily, randomly, and sparsely, and the subsequent condensation preferentially occurred on the nuclei formed earlier, respectively.

are ~5 nm and ~50 nm, respectively, both larger than the critical nucleus r_c (0.75 nm). However, on SHS with submicron rectangle structures, the average apparent radius of nucleating structures (R_s) are ~0.5–1 μm, which is much larger than the critical nucleus r_c (0.75 nm). This means that the ΔG_c on the submicron rectangle structures should be lower than that on the coral-like micro/nano-structures. A similar result had also been obtained by Lo et al. (2014) , where they found that water vapor preferentially condenses on the designed microgrooves on the Si nanowire surface (both with CA~145°).

The structure of the SHS has a strong effect on the nucleation rate J *via* the inverse exponential dependence on ΔG_c, $J = J_0 \exp(-\Delta G/kT)$ (Varanasi et al., 2009). As a result, on the SHS with coral-like micro/nano-structures, due to higher vapor–liquid nucleation energy barrier caused by the finer nano-structures, vapor nucleation is difficult (~50 s delaying) comparing with that on SHS with submicron rectangle structures (immediately, continuously, and densely). However, difficulty does not mean impossible. Vapor nucleation may also occur at some gaps of the surfaces. Once the primary nucleation is completed on the SHS with coral-like micro/nano-structures, the subsequent nucleation preferentially occurs on these primary nuclei (**Figure 4** This is because they are hydrophilic, which dramatically decreases the ΔG_c (Liu, 1999; Varanasi et al., 2009). As a result, the condensation occurred tardily, randomly, and sparsely. The condensation proceeded along the typical Matthew effect, e.g., always occurred on special sites (primary nuclei or defects). If we could fabricate SHS with homogeneous hydrophilic nano sites, a new type of condensation would be expected (Xing et al., 2020).

CONCLUSION

In summary, we found an interesting phenomenon, e.g., "Matthew effect condensation" or "anti-condensation", on SHS with much smaller nanostructures. Different to the classical self-propelled motion or "jumping" behavior of condensate droplets on SHS with relatively larger structures, condensate droplets on SHS with smaller nanoflakes appear slowly (~50 s delay), dispersedly, and sparsely in the whole condensation procedure. Condensation started from random nucleation and the subsequent nucleation preferentially occurred on these primary nuclei. As a result, most of the SHS area appears dry during the condensation procedure. A much higher vapor–liquid nucleation energy barrier caused by much smaller nanostructures should be responsible for such a unique "anti-condensation" property. This study would be helpful in designing new SHSs and moving their application in anti-icing, anti-fogging, air humidity control, and other relative fields.

DATA AVAILABILITY STATEMENT

The original contributions presented in the study are included in the article/**Supplementary Material**, further inquiries can be directed to the corresponding author.

AUTHOR CONTRIBUTIONS

KL contributed to investigation and the original draft. YZ contributed to data curation and investigation. JY supervised the writing. JF administrated the project, conceptualized the idea, supervised the writing, reviewed and edited the draft.

FUNDING

This study is financially supported by the National Natural Science Foundation of China (Grant No. 51172206) and the Zhejiang Provincial Natural Science Foundation of China (Grant No. LQ18E010005).

SUPPLEMENTARY MATERIAL

The Supplementary Material for this article can be found online at: https://www.frontiersin.org/articles/10.3389/fbioe.2022.887902/full#supplementary-material

REFERENCES

Barthlott, W., and Neinhuis, C. (1997). Purity of the Sacred lotus, or Escape from Contamination in Biological Surfaces. *Planta* 202, 1–8. doi:10.1007/s004250050096

Caldona, E. B., de Leon, A. C. C., Thomas, P. G., Naylor, D. F., Pajarito, B. B., and Advincula, R. C. (2017). Superhydrophobic Rubber-Modified Polybenzoxazine/SiO2 Nanocomposite Coating with Anticorrosion, Anti-ice, and Superoleophilicity Properties. *Ind. Eng. Chem. Res.* 56, 1485–1497. doi:10.1021/acs.iecr.6b04382

Chen, R., Jiao, L., Zhu, X., Liao, Q., Ye, D., Zhang, B., et al. (2018). Cassie-to-Wenzel Transition of Droplet on the Superhydrophobic Surface Caused by Light Induced Evaporation. *Appl. Therm. Eng.* 144, 945–959. doi:10.1016/j.applthermaleng.2018.09.011

Feng, J., Pang, Y., Qin, Z., Ma, R., and Yao, S. (2012a). Why Condensate Drops Can Spontaneously Move Away on Some Superhydrophobic Surfaces but Not on Others. *ACS Appl. Mater. Inter.* 4, 6618–6625. doi:10.1021/am301767k

Feng, J., Qin, Z., and Yao, S. (2012b). Factors Affecting the Spontaneous Motion of Condensate Drops on Superhydrophobic Copper Surfaces. *Langmuir* 28, 6067–6075. doi:10.1021/la300609f

Geyer, F., D'Acunzi, M., Sharifi-Aghili, A., Saal, A., Gao, N., Kaltbeitzel, A., et al. (2020). When and How Self-Cleaning of Superhydrophobic Surfaces Works. *Sci. Adv.* 6, eaaw9727. doi:10.1126/sciadv.aaw9727

Hao, Q., Pang, Y., Zhao, Y., Zhang, J., Feng, J., and Yao, S. (2014). Mechanism of Delayed Frost Growth on Superhydrophobic Surfaces with Jumping Condensates: More Than Interdrop Freezing. *Langmuir* 30, 15416–15422. doi:10.1021/la504166x

Hao, T., Wang, K., Chen, Y., Ma, X., Lan, Z., and Bai, T. (2018). Multiple Bounces and Oscillatory Movement of a Microdroplet in Superhydrophobic Minichannels. *Ind. Eng. Chem. Res.* 57, 4452–4461. doi:10.1021/acs.iecr.7b04613

He, M., Zhou, X., Zeng, X., Cui, D., Zhang, Q., Chen, J., et al. (2012). Hierarchically Structured Porous Aluminum Surfaces for High-Efficient Removal of Condensed Water. *Soft Matter* 8, 6680–6683. doi:10.1039/C2SM25828E

Jiang, S., Zhang, H., Jiang, C., and Liu, X. (2020). Antifrosting Performance of a Superhydrophobic Surface by Optimizing the Surface Morphology. *Langmuir* 36, 10156–10165. doi:10.1021/acs.langmuir.0c01618

Kreder, M. J., Alvarenga, J., Kim, P., and Aizenberg, J. (2016). Design of Anti-icing Surfaces: Smooth, Textured or Slippery? *Nat. Rev. Mater.* 1, 15003. doi:10.1038/natrevmats.2015.3

Liu, X. Y. (1999). A New Kinetic Model for Three-Dimensional Heterogeneous Nucleation. *J. Chem. Phys.* 111, 1628–1635. doi:10.1063/1.479391

Lo, C.-W., Wang, C.-C., and Lu, M.-C. (2014). Spatial Control of Heterogeneous Nucleation on the Superhydrophobic Nanowire Array. *Adv. Funct. Mater.* 24, 1211–1217. doi:10.1002/adfm.201301984

Mohammadian, B., Annavarapu, R. K., Raiyan, A., Nemani, S. K., Kim, S., Wang, M., et al. (2020). Delayed Frost Growth on Nanoporous Microstructured Surfaces Utilizing Jumping and Sweeping Condensates. *Langmuir* 36, 6635–6650. doi:10.1021/acs.langmuir.0c00413

Neinhuis, C., and Barthlott, W. (1997). Characterization and Distribution of Water-Repellent, Self-Cleaning Plant Surfaces. *Ann. Bot.* 79, 667–677. doi:10.1006/anbo.1997.0400

Orejon, D., Askounis, A., Takata, Y., and Attinger, D. (2019). Dropwise Condensation on Multiscale Bioinspired Metallic Surfaces with Nanofeatures. *ACS Appl. Mater. Inter.* 11, 24735–24750. doi:10.1021/acsami.9b06001

Sarode, A., Raj, R., and Bhargav, A. (2020). On the Role of Confinement Plate Wettability on Pool Boiling Heat Transfer. *Int. J. Heat Mass Transfer* 156, 119723. doi:10.1016/j.ijheatmasstransfer.2020.119723

Varanasi, K. K., Hsu, M., Bhate, N., Yang, W., and Deng, T. (2009). Spatial Control in the Heterogeneous Nucleation of Water. *Appl. Phys. Lett.* 95, 094101. doi:10.1063/1.3200951

Wang, R., Wu, F., Xing, D., Yu, F., and Gao, X. (2020). Density Maximization of One-step Electrodeposited Copper Nanocones and Dropwise Condensation Heat-Transfer Performance Evaluation. *ACS Appl. Mater. Inter.* 12, 24512–24520. doi:10.1021/acsami.0c05224

Wang, R., Wu, F., Yu, F., Zhu, J., Gao, X., and Jiang, L. (2021). Anti-vapor-penetration and Condensate Microdrop Self-Transport of Superhydrophobic Oblique Nanowire Surface under High Subcooling. *Nano Res.* 14, 1429–1434. doi:10.1007/s12274-020-3196-8

Wu, X., Yang, F., Lu, G., Zhao, X., Chen, Z., and Qian, S. (2021). A Breathable and Environmentally Friendly Superhydrophobic Coating for Anti-condensation Applications. *Chem. Eng. J.* 412, 128725. doi:10.1016/j.cej.2021.128725

Xing, D., Wang, R., Wu, F., and Gao, X. (2020). Confined Growth and Controlled Coalescence/Self-Removal of Condensate Microdrops on a Spatially Heterogeneously Patterned Superhydrophilic-Superhydrophobic Surface. *ACS Appl. Mater. Inter.* 12, 29946–29952. doi:10.1021/acsami.0c04922

Xue, Y., Wang, S., Xue, Y., Cao, L., Nie, M., and Jin, Y. (2020). Robust Self-Cleaning and Marine Anticorrosion Super-Hydrophobic Co-Ni/CeO 2 Composite Coatings. *Adv. Eng. Mater.* 22, 2000402. doi:10.1002/adem.202000402

Yang, J., Zhang, Z., Xu, X., Men, X., Zhu, X., and Zhou, X. (2011). Superoleophobic Textured Aluminum Surfaces. *New J. Chem.* 35, 2422–2426. doi:10.1039/C1NJ20401G

Yin, L., Wang, Y., Ding, J., Wang, Q., and Chen, Q. (2012). Water Condensation on Superhydrophobic Aluminum Surfaces with Different Low-Surface-Energy Coatings. *Appl. Surf. Sci.* 258, 4063–4068. doi:10.1016/j.apsusc.2011.12.100

Zhao, Y., and Yang, C. (2017). Frost Spreading on Microscale Wettability/morphology Patterned Surfaces. *Appl. Therm. Eng.* 121, 136–145. doi:10.1016/j.applthermaleng.2017.04.063

Zhao, Y., Zhang, H., Wang, W., and Yang, C. (2018). Wetting Transition of Sessile and Condensate Droplets on Copper-Based Superhydrophobic Surfaces. *Int. J. Heat Mass Transfer* 127, 280–288. doi:10.1016/j.ijheatmasstransfer.2018.07.153

Zheng, Y., Bai, H., Huang, Z., Tian, X., Nie, F.-Q., Zhao, Y., et al. (2010). Directional Water Collection on Wetted Spider Silk. *Nature* 463, 640–643. doi:10.1038/nature08729

Zhu, T., Cheng, Y., Huang, J., Xiong, J., Ge, M., Mao, J., et al. (2020). A Transparent Superhydrophobic Coating with Mechanochemical Robustness for Anti-icing, Photocatalysis and Self-Cleaning. *Chem. Eng. J.* 399, 125746. doi:10.1016/j.cej.2020.125746

Conflict of Interest: The authors declare that the research was conducted in the absence of any commercial or financial relationships that could be construed as a potential conflict of interest.

Publisher's Note: All claims expressed in this article are solely those of the authors and do not necessarily represent those of their affiliated organizations, or those of the publisher, the editors, and the reviewers. Any product that may be evaluated in this article, or claim that may be made by its manufacturer, is not guaranteed or endorsed by the publisher.

frontiers | Frontiers in Bioengineering and Biotechnology

ORIGINAL RESEARCH
published: 28 April 2022
doi: 10.3389/fbioe.2022.909187

Three-Phases Interface Induced Local Alkalinity Generation Enables Electrocatalytic Glucose Oxidation in Neutral Electrolyte

Yangru Chen[1], Jun Zhang[1], Zhenyao Ding[1], Liping Chen[1], Haili Wang[1], Man Zhang[1] and Xinjian Feng[1,2]**

[1]College of Chemistry, Chemical Engineering and Materials Science, Soochow University, Suzhou, China, [2]Innovation Center for Chemical Science, Soochow University, Suzhou, China

Electrocatalytic glucose oxidation is crucial to the development of non-enzymatic sensors, an attractive alternative for enzymatic biosensors. However, due to OH^- consumption during the catalytic process, non-enzymatic detection generally requires electrolytes having an alkaline pH value, limiting its practical application since biofluids are neutral. Herein, *via* interfacial microenvironment design, we addressed this limitation by developing a non-enzymatic sensor with an air–solid–liquid triphase interface electrodes that synergistically integrates the functions of local alkalinity generation and electrocatalytic glucose oxidation. A sufficiently high local pH value was achieved *via* oxygen reduction reaction at the triphase interface, which consequently enabled the electrochemical oxidation (detection) of glucose in neutral solution. Moreover, we found that the linear detection range and sensitivity of triphase non-enzymatic sensor can be tuned by changing the electrocatalysts of the detection electrode. The triphase electrode architecture provides a new platform for further exploration and promotes practical application of non-enzymatic sensors.

Keywords: hydrophobicity, three-phase interfaces, local microenvironment, electrocatalytic glucose oxidation, non-enzymatic detection

OPEN ACCESS

Edited by:
Jingxin Meng,
Technical Institute of Physics and Chemistry (CAS), China

Reviewed by:
Zhiqiang Niu,
Tsinghua University, China
Lizeng Gao,
Institute of Biophysics (CAS), China

****Correspondence:***
Xinjian Feng
xjfeng@suda.edu.cn
Jun Zhang
jzhang2017@suda.edu.cn

Specialty section:
This article was submitted to Bionics and Biomimetics, a section of the journal Frontiers in Bioengineering and Biotechnology

Received: *31 March 2022*
Accepted: *08 April 2022*
Published: *28 April 2022*

Citation:
Chen Y, Zhang J, Ding Z, Chen L, Wang H, Zhang M and Feng X (2022) Three-Phases Interface Induced Local Alkalinity Generation Enables Electrocatalytic Glucose Oxidation in Neutral Electrolyte. Front. Bioeng. Biotechnol. 10:909187. doi: 10.3389/fbioe.2022.909187

INTRODUCTION

Diabetes is a chronic disease that threatens human health across the world. Notably, over 420 million adults worldwide diabetic (Rubino, 2016; Lu et al., 2016; Ohayon et al., 2020; Zhou Y et al., 2020; Zhang et al., 2021). Reliable glucose monitoring facilitates better blood glucose control and prevents complications. Enzymatic electrochemical biosensors have been widely used for glucose detection; however, biological enzymes are susceptible to factors, such as temperature, pH, and ions, hindering the stability and scope of enzymatic biosensors (Yang et al., 2014; Sun and James, 2015; Johnston et al., 2021). Non-enzymatic sensor based on direct electrocatalytic glucose oxidation reaction, is highly attractive as it avoids the use of biological enzymes (Zhang et al., 2018; Teymourian et al., 2020). In the past decades, great efforts have been devoted to the development of electrocatalysts, and a variety of electrocatalytic materials including noble metal (Lang et al., 2013; Bae et al., 2019), metal alloys (Yamauchi et al., 2012; Bag et al., 2020), metal oxides (Cheng et al., 2016; Mondal et al., 2017) and carbon-related materials (Bao et al., 2017; Dung et al., 2013) have been reported. Unfortunately, due to OH^- consumption during the electrochemical glucose oxidation process, $C_6H_{12}O_6$ (glucose) +

$2OH^- \rightarrow C_6H_{10}O_6$ (glucolactone) + $2H_2O$+ $2e^-$, non-enzymatic sensors generally require solutions with high pH value for acceptable sensitivity and linear detection range (Wei et al., 2020). In addition, serious electrode fouling will occur during the oxidation reaction, due to the lack of sufficient OH^- supply (Adeel et al., 2021; Chen et al., 2019). With these restrictions, the development and practical application of non-enzymatic sensors has been limited since biofluids are neutral.

Besides the electrocatalytic materials, the reaction interface microenvironment that governs the diffusion, adsorption and reaction of reactants is also crucial to the performance of catalytic reaction, but has received limited attentions (Sheng et al., 2017; Song et al., 2018; Zhou H et al., 2020; Kim et al., 2021; Yang and Gao, 2022). In this work, we addressed this limitation by developing a novel non-enzymatic sensing system with an air–solid–liquid triphase interface as illustrated in Figure 1. This electrode architecture synergistically integrates the functions of interfacial local alkalinity generation and electrocatalytic glucose oxidation. Two electrodes that were used for local OH^- production and glucose detection, respectively, and they were deposited on a hydrophobic porous substrate in an interdigitated shape. When the sensing system was immersed in an aqueous solution, water contacted the electrode surface but did not enter the inner porous substrate, due to its surface hydrophobicity (Wen et al., 2015; Liu et al., 2017). This led to the formation of an air–solid–liquid triphase interface where sufficient oxygen can be supplied directly from the air phase. Oxygen can be readily reduced to OH^- at the surface of electrocatalysts, O_2+ $2H_2O$+ $4e^- \rightarrow 4OH^-$, leading to an increase in the local pH. Using the triphase electrode architecture, sufficient oxygen was utilized to generate OH^- and form a sufficient high local alkaline microenvironment, enabling the electrocatalytic glucose oxidation in neutral solution.

MATERIALS AND METHODS

Materials

The hydrophobic porous polyethylene (PE) membrane was purchased from Entek International LLC and the hydrophilic flat (pore-free) polyethylene terephthalate (PET) membrane was purchased from Membrane solutions. Sodium sulfate, sodium hydroxide, sulfuric acid, phenolphthalein, chloroauric acid, sodium chloride, lactic acid, galactose, glucose, ascorbic acid and acetaminophen were purchased from Sinopharm Chemical Reagent. All reagents are analytical grade. Nafion perfluorinated resin solution (5 wt% in lower aliphatic alcohols and water, contained 15–20% water) was purchased from Sigma-Aldrich. The high purity platinum target material (99.95%) was purchased from Shijiazhuang Dongming New Material Technology Co., Ltd. All of our experiments used deionized water. All reagents are used as received reagents without further purification.

Fabrication of Triphase/Diphase Electrode

1) The hydrophobic porous PE membrane was cut into a rectangle, cleaned with alcohol 3–4 times and dried with Ar, then was tightly against an interdigital electrode mask and directly deposited by automatic sputter coater (GVC-2000, Hezao) of a platinum target for 300 s at 30 mA. Thus, a triphase Pt-Pt electrode was prepared. (2) Au electrocatalysts were electrodeposited onto the Pt detection electrode at 0 V *vs.* Ag/AgCl for 100, 200, 400 and 600 s in 5 mM chloroauric acid solution (10 g/L in DI water), respectively. Then, a triphase Pt-Au electrode was prepared. (3) The 50 μL mixed solution of Nafion (5 wt% in DI water) drop cast onto the triphase Pt-Au electrode with an area of 0.7 cm × 1.0 cm and dried in an oven for 0.5 h at 60°C. For controlled experiment, a diphase Pt-Pt electrode was also prepared in a similar way using a hydrophilic non-porous PET membrane as substrate.

Characterization

The morphology was characterized by FE-SEM (SU8010, Hitachi) and the element mapping distribution is characterized by Evo-SEM (EVO18, Zeiss). The water contact angle was measured by a contact angle goniometer (Jc 2000d6, Poareach). Electrochemical measurements were carried out at room temperature using the CHI 660E workstation (CH Instruments, Inc.).

Measurement Methods

Electrochemical measurements were performed using a CHI 660E electrochemical workstation with a three-electrode system. The triphase/diphase electrode consisting of an OH^- production electrode and a glucose detection electrode was used as the working electrode. A Pt wire was as the counter electrode and an Ag/AgCl (3 M KCl) was as the reference electrode. Na_2SO_4 solution was used as the electrolyte. 1) The potential of OH^- production was determined by linear sweep voltammetry in Ar or O_2 atmosphere, at a scan rate of 50 mV s^{-1}. 2) The pH-potential curve measurement was conducted using chronopotentiometer with a current of 5 μA for 30 s in solutions with different pH. The dynamic surface pH of the detection electrode was carried out using chronopotentiometer as mentioned above after the OH^- production step. 3) Two steps to the working electrode were used to measure glucose concentrations, including a negative potential of −0.6 V *vs.* Ag/AgCl for 20 s on the OH^- production electrode and 0.4 V *vs.* Ag/AgCl for 10 s on the detection electrode. 4) Selectivity tests were performed by amperometric measurement at 0.4 V after OH^- production step. A series of interferents (50 μM of ascorbic acid, lactic acid, galactose, acetaminophen and sodium chloride) were added to the solution after the addition of 0.5 mM glucose using the triphase Nafion-coated Pt-Au electrode.

RESULTS AND DISCUSSION

The triphase electrode illustrated in **Figure 1** was constructed by choosing a hydrophobic porous polyethylene (PE) membrane (**Figure 2A**) as the substrate. The PE membrane has an average pore size of about 200 nm (**Figure 2B**) and a thickness of about 25 μm (**Figure 2C**). Contact angle (CA) analysis of the PE membrane shows a CA of about 120 ± 2° (inset of **Figure 2B**),

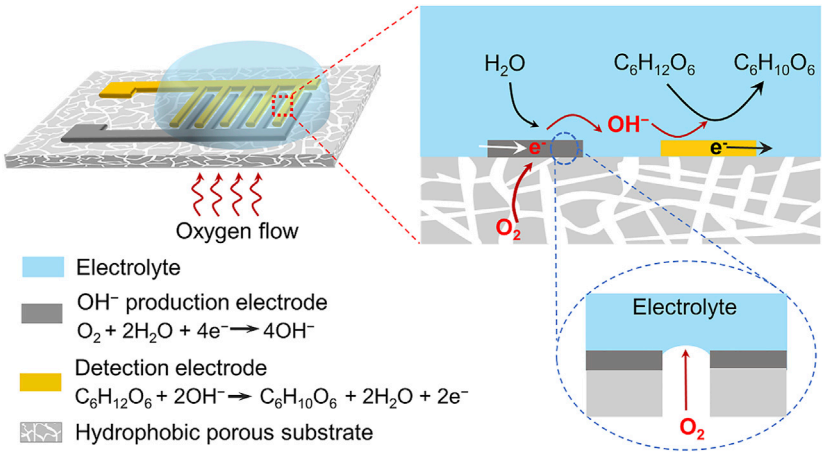

FIGURE 1 | Schematic illustration of the triphase non-enzymatic sensor. The sensor consists of a hydrophobic porous substrate, an electrode for local alkalinity generation *via* oxygen reduction reaction, and an electrode for electrocatalytic glucose oxidation reaction. Sufficient oxygen supplied from the air phase was reduced to OH^- at the triphase interface, leading to a high interface pH for electrocatalytic glucose oxidation. The electrode architecture makes the non-enzymatic glucose detection independent of the solution pH. During the experiment, a negative potential was first applied to the OH^- production electrode to generate a local alkaline microenvironment, and then a positive potential was applied to the detection electrode for electrochemical glucose oxidation.

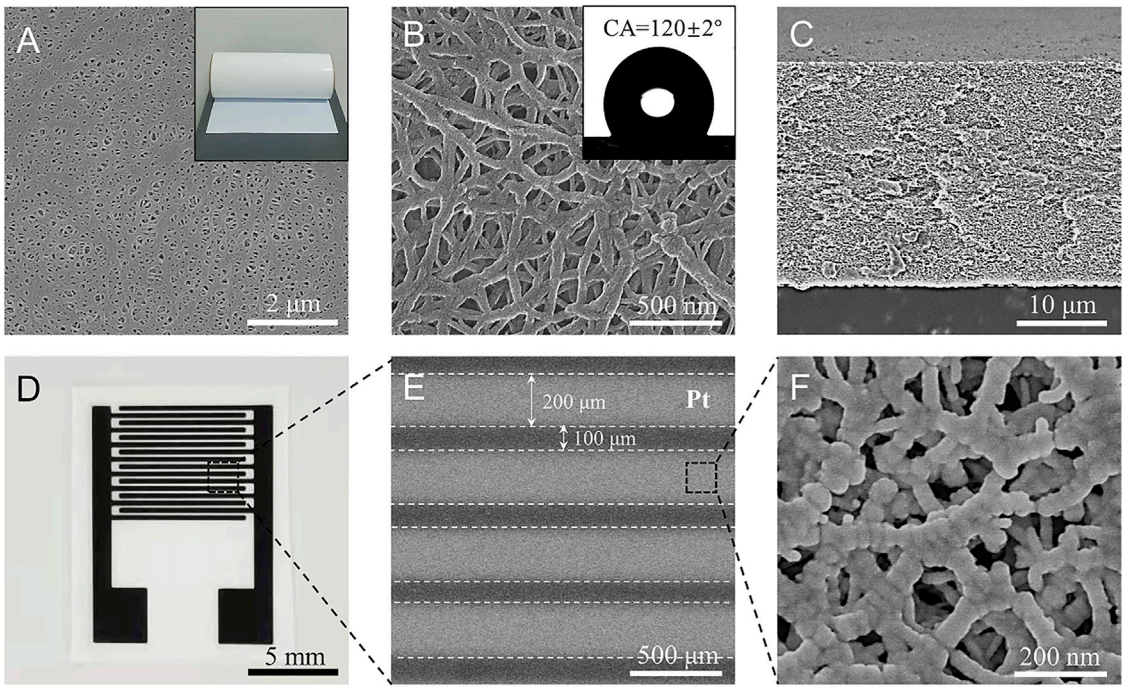

FIGURE 2 | (A,B) Scanning electron microscopy (SEM) images of the porous polyethylene membrane substrate at low and high magnification, respectively. Insets in **(A,B)** show photographs of the membrane and water droplets on it with a contact angle of about 120 ± 2°. **(C)** Cross-section SEM image of the membrane with a thickness of about 25 μm. **(D)** Photograph of Pt-Pt electrodes sputtered on the porous substrate with eight pairs of electrodes. **(E,F)** are SEM images of the Pt electrode at low and higher magnifications. The electrode band-width is 200 μm, the gap between the interdigitated electrodes is 100 μm. The Pt electrode also has a porous structure.

indicating a hydrophobic surface property. Platinum (Pt) metal, with good oxygen reduction and electrochemical glucose oxidation capabilities (Briega-Martos et al., 2017; Lee et al., 2018), was chosen as a model electrocatalyst to prepare the Pt-Pt electrode. As shown in **Figure 2D,E** and **Supplementary Figure S1**, the Pt-Pt electrode has eight pairs of electrodes, a width of 200 μm and a gap distance of 100 μm. After Pt deposition the porous structure of the PE substrate was maintained (**Figure 2F**), which facilitates rapid

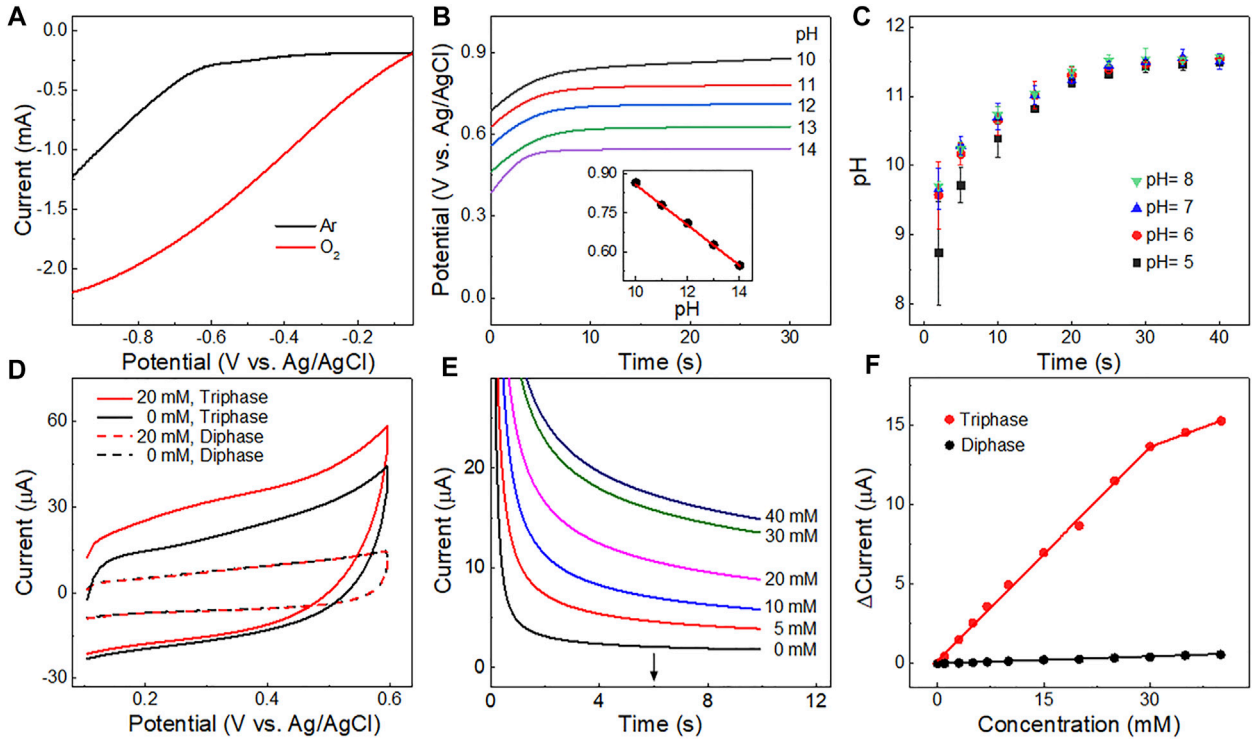

FIGURE 3 | (A) Linear sweep voltammetry curves of the Pt detection electrode in Ar and O_2 saturated 0.10 M Na_2SO_4 solution. **(B)** Potentials of the detection electrode measured in solutions of different pH with a constant current (5 μA). Inset is the linear relationship between potentials derived at 20 s and solution pH values. **(C)** Changes in pH value over time at the detection electrode upon application of a potential of –0.6 V at the OH^- production electrode in electrolyte with different pH values. The error bar represents the standard deviation for two replicated measurements. **(D)** Cyclic voltammetry curves obtained in a 0.1 M Na_2SO_4 solution with or without 20 mM glucose using a triphase or diphase Pt-Pt electrode after the OH^- production step. **(E)** Amperometric i-t curves corresponding to the triphase Pt-Pt electrode with glucose concentrations up to 40 mM. **(F)** Corresponding calibration plots of triphase and diphase electrodes derived from **(E)** and **Supplementary Figure S5** at 6 s ΔCurrent = $Current_s$ - $Current_0$; $Current_0$ is the background current; and $Current_s$ is the current measured in the solution with different glucose concentrations.

oxygen transport from the free space of the porous hydrophobic PE membrane to the electrode surface. For the control experiment, a conventional solid–liquid diphase electrode was also fabricated on a non-porous flat hydrophilic polyethylene terephthalate (PET) substrate (**Supplementary Figure S2**).

The performance of the triphase electrode for local alkalinity generation was first investigated. **Figure 3A** shows linear sweep voltammetry (LSV) of Pt electrode in 0.1 M sodium sulfate (Na_2SO_4) solution saturated with Ar or O_2. Water reduction was apparent when the potential was negative than approximately −0.6 V *vs.* Ag/AgCl (black cure in **Figure 3A**), while a much higher potential was sufficient for O_2 reduction to OH^- (red curve in **Figure 3A**; **Supplementary Figure S3**). In order to obtain the high OH^- production capacity and avoid the hydrogen evolution reaction to generate hydrogen bubbles, which would affect glucose transmission and the accuracy of detection, a potential of −0.6 V (*vs.* Ag/AgCl) was chosen for OH^- production in this work. The OH^- ions produced diffused outwards and led to an increase in pH near the surface of the adjacent glucose detection electrode.

To determine the pH value at the surface of the detection electrode after OH^- production, a chronopotentiometer was used to apply a constant current (5 μA) at the detection electrode in solutions with different pH values (10.0–14.0) (**Figure 3B**). The relationship between the pH values and the potentials was recorded (inset of **Figure 3B**) according to the effect of OH^- concentration on the potential of the oxygen evolution reaction ($4OH^- \rightarrow 2H_2O + O_2 + 4e^-$) (Dresp et al., 2021; Maruthapandian et al., 2017; Yin and Liu, 2020). Thus, the dynamic pH value near the surface of the Pt detection electrode was measured after OH^- production. As shown in **Figure 3C**, the measured interfacial pH values were all above 11 for solutions with bulk pH of 5–8.0 when the time course of OH^- production step is longer than 20 s. Thus, to ensure the reproducibility for further experiments a time course of 20 s was chosen for the OH^- production step.

The triphase Pt-Pt electrode was then used for glucose detection (**Supplementary Figure S4**). The cyclic voltammograms of the triphase or diphase detection electrodes in 0.10 M Na_2SO_4, with or without 20 mM glucose after OH^- production step, are shown in **Figure 3D**. The anodic current increased upon the addition of glucose for the triphase electrode (red solid curve), while a negligible anodic current increase was recorded (red dotted curve) for the diphase electrode, due to the lack of sufficient oxygen and the insufficient alkalinity needed for electrocatalytic glucose oxidation. **Figure 3E** shows that the anodic current response of the triphase

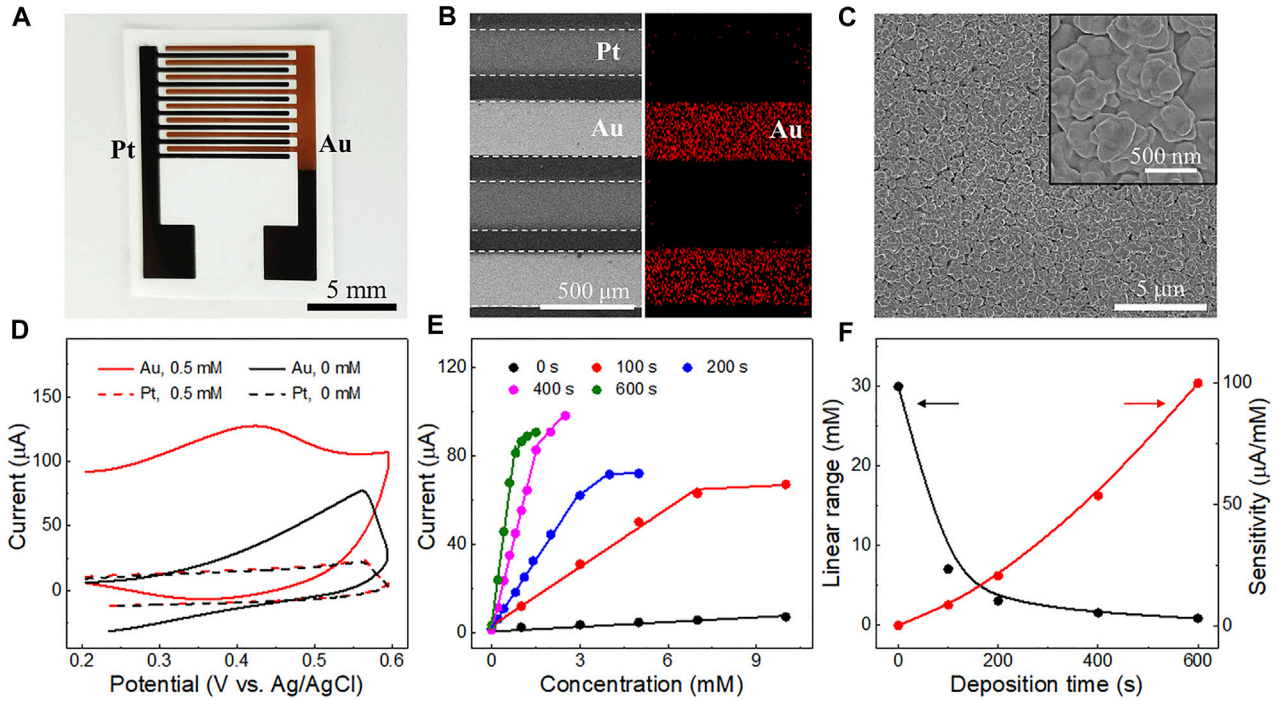

FIGURE 4 | (A) Photograph of the triphase electrodes after 400 s Au electrocatalyst deposition on the Pt detection electrode. **(B)** SEM image of the triphase Pt-Au electrodes (left) and the corresponding Au elemental mapping distribution (right). **(C)** SEM images of the Au nanoparticles with diameter ranging from 200 to 500 nm. The inset is an enlarged SEM view of the Au nanoparticles. **(D)** Cyclic voltammetry curves of the Pt-Pt and Pt-Au electrodes obtained in solutions with or without glucose (0.5 mM). **(E)** Corresponding calibration plots of the electrodes with different Au electrodeposition times (100, 200, 400 and 600 s) derived from their amperometric i-t curves (**Supplementary Figure S7**) at 6 s. **(F)** Relationship between the linear detection range (black curve) and the sensitivity (red curve) of electrodes with different Au electrodeposition times.

electrode increased with glucose concentration to approximately 40 mM. The current response versus glucose concentration (**Figure 3F**) shows that the triphase electrode displayed a linear detection range to about 30 mM (red line), and the sensitivity was 2.1 μA mM^{-1} cm^{-2}. In remarkable contrast, negligible current increase was observed for the diphase electrode as the glucose concentration increased (**Figure 3F**; **Supplementary Figure S5**). These results confirm sufficient oxygen was supplied at the triphase interface, and non-enzymatic glucose detection was achieved in neutral solution.

The performance of the triphase non-enzymatic sensor can be further improved by alternating the electrocatalysts of the detection electrode. Au is a commonly used and stable electrocatalyst with high activity towards glucose oxidation in alkaline solution (Zhong et al., 2017). To improve the device performance, different amounts of Au nanoparticles were electrodeposited on the detection electrode (Pt) by adjusting deposition time. The morphologies of the Pt-Au electrode were further characterized. As shown in **Figure 4A**, the color of the detection electrode turned from black to dark yellow after Au catalyst deposition. **Figure 4B** shows SEM image of the Pt-Au electrode. The existence and distribution of the Au catalysts were confirmed by elemental mapping (**Figure 4B**, right) and energy dispersive X-ray spectroscopy (EDS) analysis (**Supplementary Figure S6**). Au particles have a diameter of 200-500 nm (**Figure 4C**) and were uniformly distributed on the surface of the detection electrode.

We then explored the performance of the triphase electrode after Au deposition. As shown in **Figure 4D**, a strong anode wave (red solid curve) is observed on the detection electrode at 0.4 V (*vs.* Ag/AgCl), due to the carbonyl oxidation of glucose. Interestingly, its glucose oxidation current was much higher than that of the detection Pt electrode without Au electrocatalyst (red dotted curve). This indicates that the introduction of Au can effectively improve the performance of glucose oxidation. Thus, the performance of Pt-Au electrodes with different Au electrodeposition times (100, 200, 400 and 600 s) was further investigated. As shown in **Figure 4E** and **Supplementary Figure S7**, with the increase in electrodeposition time, the sensitivity of the electrode for glucose detection increased, but the linear detection upper limit decreased (**Figure 4F**). We reasoned that increasing the amount of Au catalysts would increase the number of available active sites for glucose oxidation and consequently lead to a higher reaction rate and sensitivity. A higher reaction rate generally results in faster OH^- consumption at the interface microenvironment and makes the detection of glucose at high concentrations difficult. These results indicate that glucose detection with different sensitivity and linear range can be obtained by modifying the electrocatalysts on the detection electrode.

Apart from the linear dynamic range and sensitivity, selectivity is also a crucial parameter for non-enzymatic

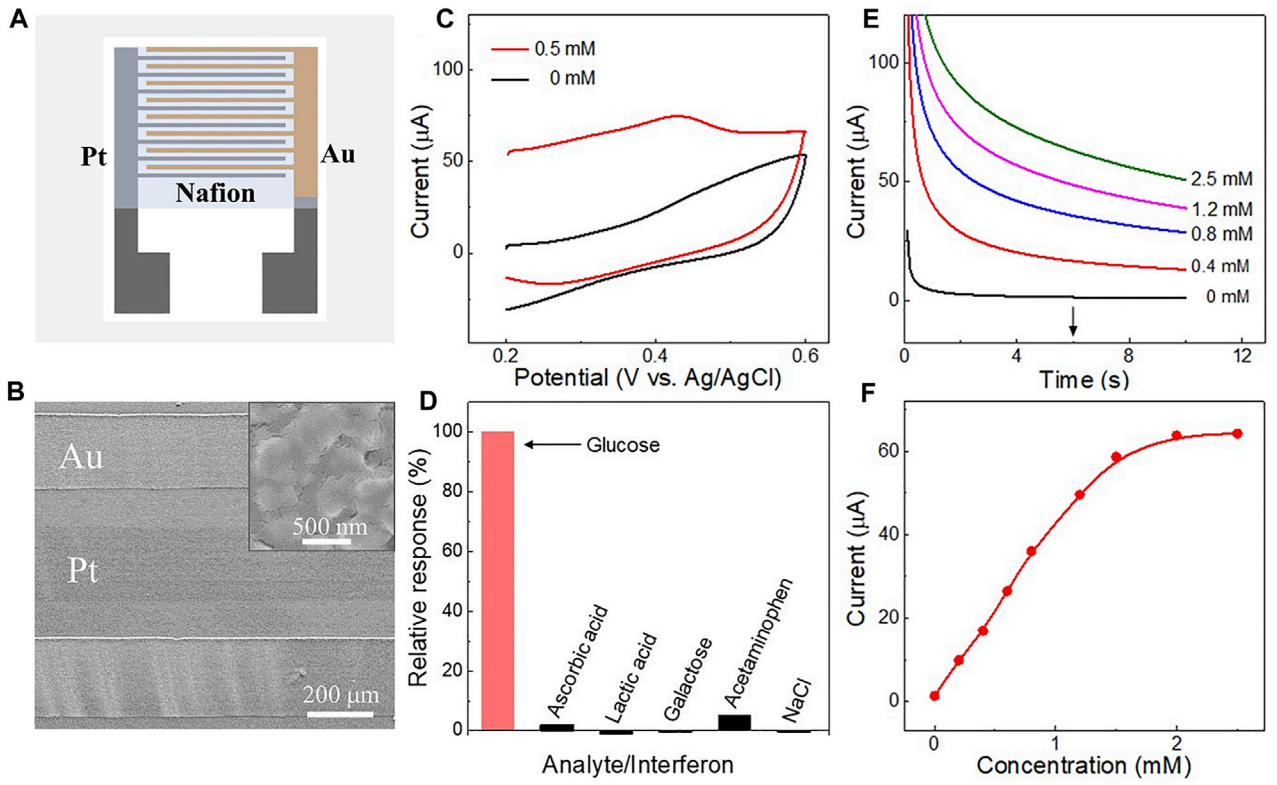

FIGURE 5 | (A) Schematic of the Nafion layer on the Pt-Au electrode surface. **(B)** SEM image of the Nafion film-coated electrode. The inset is an enlarged view of the surface of the Au electrode. **(C)** Cyclic voltammetry curves obtained in a 0.1 M Na_2SO_4 solution with or without 0.5 mM glucose, using the nafion-coated triphase Pt-Au electrode, respectively. **(D)** Histogram of the interference effects on the electrode while measuring 0.5 mM glucose at 0.4 V *vs*. Ag/AgCl. The concentration of interferents was 0.05 mM, including ascorbic acid, lactic acid, galactose, acetaminophen and sodium chloride (NaCl). **(E)** Amperometric i-t curves corresponding to the nafion-coated electrode with glucose concentrations up to 2.5 mM. **(F)** Corresponding calibration plots of nafion-coated triphase electrode derived from **(E)** at 6 s.

sensors. To reduce the influence of interferents, the surface of the Pt-Au electrode was coated with a layer of Nafion, as illustrated in **Figure 5A**. **Figure 5B** is a SEM top view of the Nafion film on the Pt-Au electrode surface. The negatively charged Nafion film can selectively restrict the diffusion of some kinds of anions from the solution to the electrode surface without affecting the detection of glucose (Cao et al., 2013; Chen et al., 2015). The performance of nafion-coated Pt-Au electrode was evaluated after the OH^- production step. As shown in **Figure 5C**, the glucose oxidation current of the nafion-coated triphase Pt-Au electrode significantly increased after 0.5 mM glucose addition (red curve).

Interfering compounds, including ascorbic acid, lactic acid, galactose, acetaminophen, and sodium chloride (NaCl), were then added into the sample matrix in large excess compared with that in human perspiration (Lu et al., 2019; Zhu et al., 2019). As shown in **Figure 5D**, negligible interferences were observed with the triphase Pt-Au electrode while measuring glucose in the presence of interfering compounds. **Figure 5E** shows the electrode responses in glucose solution with concentrations up to 2.5 mM. A linear detection upper limit of about 1.5 mM and sensitivity of 179.1 μA mM^{-1} cm^{-2} were obtained (**Figure 5F**). This result indicates that the Nafion layer on the electrode surface can not only reduce the effects of some kinds of interference but also ensure the detection of glucose. In addition, the repeatability of the nafion-coated electrode was also assessed. **Supplementary Figure S8** shows 100 successive measurements of 0.5 mM glucose using the same biosensor. A relative standard deviation of only 2.34% was observed for these measurements, indicating good repeatability.

CONCLUSION

In summary, we have fabricated a triphase electrode that enables electrocatalytic glucose oxidation and non-enzymatic sensing in neutral solution. Using the air-solid-liquid triphase electrode, sufficient oxygen was available from the air phase for the generation of a local interfacial alkaline microenvironment *via* oxygen reduction reaction. This sensor is superior to other non-enzymatic ones because it does not require an electrolyte with high pH. Moreover, the triphase non-enzymatic electrode with tunable performance including sensitivity and linearity, can be obtained by choosing suitable electrocatalysts, which endows great potential for practical applications in different scenarios.

DATA AVAILABILITY STATEMENT

The original contributions presented in the study are included in the article/**Supplementary Material**, further inquiries can be directed to the corresponding authors.

AUTHOR CONTRIBUTIONS

XF supervised the project. YC designed the devices and completed the experiments. MZ and ZD conducted SEM and CA characterizations. JZ and YC drafted the manuscript. JZ and LC discussed the data. All authors revised the manuscript.

FUNDING

This research was financially supported by National Key R&D Program of China (No. 2019YFA0709200), the National Natural Science Foundation of China (22102111 and 21988102), the Natural Science Research of Jiangsu Higher Education Institutions of China (21KJB150031) and the Jiangsu Provincial Shuangchuang Doctor Talent Program (JSSCBS20210705).

SUPPLEMENTARY MATERIAL

The Supplementary Material for this article can be found online at: https://www.frontiersin.org/articles/10.3389/fbioe.2022.909187/full#supplementary-material

REFERENCES

Adeel, M., Asif, K., Rahman, M. M., Daniele, S., Canzonieri, V., and Rizzolio, F. (2021). Glucose Detection Devices and Methods Based on Metal-Organic Frameworks and Related Materials. *Adv. Funct. Mater.* 31, 2106023. doi:10.1002/adfm.202106023

Bae, C. W., Toi, P. T., Kim, B. Y., Lee, W. I., Lee, H. B., Hanif, A., et al. (2019). Fully Stretchable Capillary Microfluidics-Integrated Nanoporous Gold Electrochemical Sensor for Wearable Continuous Glucose Monitoring. *ACS Appl. Mater. Inter.* 11 (16), 14567–14575. doi:10.1021/acsami.9b00848

Bag, S., Baksi, A., Nandam, S. H., Wang, D., Ye, X., Ghosh, J., et al. (2020). Nonenzymatic Glucose Sensing Using Ni60Nb40 Nanoglass. *ACS Nano* 14, 5543–5552. doi:10.1021/acsnano.9b09778

Bao, L., Li, T., Chen, S., Peng, C., Li, L., Xu, Q., et al. (2017). 3D Graphene Frameworks/Co_3O_4 Composites Electrode for High-Performance Supercapacitor and Enzymeless Glucose Detection. *Small* 13, 1602077. doi:10.1002/smll.201602077

Briega-Martos, V., Herrero, E., and Feliu, J. M. (2017). Effect of pH and Water Structure on the Oxygen Reduction Reaction on Platinum Electrodes. *Electrochimica Acta* 241, 497–509. doi:10.1016/j.electacta.2017.04.162

Cao, X., Wang, N., Jia, S., and Shao, Y. (2013). Detection of Glucose Based on Bimetallic PtCu Nanochains Modified Electrodes. *Anal. Chem.* 85, 5040–5046. doi:10.1021/ac400292n

Chen, D., Wang, C., Chen, W., Chen, Y., and Zhang, J. X. J. (2015). PVDF-Nafion Nanomembranes Coated Microneedles for *In Vivo* Transcutaneous Implantable Glucose Sensing. *Biosens. Bioelectron.* 74, 1047–1052. doi:10.1016/j.bios.2015.07.036

Chen, J., Zhu, X., Ju, Y., Ma, B., Zhao, C., and Liu, H. (2019). Electrocatalytic Oxidation of Glucose on Bronze for Monitoring of Saliva Glucose Using a Smart Toothbrush. *Sensors Actuators B: Chem.* 285, 56–61. doi:10.1016/j.snb.2019.01.017

Cheng, X., Zhang, J., Chang, H., Luo, L., Nie, F., and Feng, X. (2016). High Performance Cu/Cu_2O Nanohybrid Electrocatalyst for Nonenzymatic Glucose Detection. *J. Mater. Chem. B* 4, 4652–4656. doi:10.1039/c6tb01158f

Dresp, S., Dionigi, F., Klingenhof, M., Merzdorf, T., Schmies, H., Drnec, J., et al. (2021). Molecular Understanding of the Impact of Saline Contaminants and Alkaline pH on NiFe Layered Double Hydroxide Oxygen Evolution Catalysts. *ACS Catal.* 11, 6800–6809. doi:10.1021/acscatal.1c00773

Johnston, L., Wang, G., Hu, K., Qian, C., and Liu, G. (2021). Advances in Biosensors for Continuous Glucose Monitoring Towards Wearables. *Front. Bioeng. Biotechnol.* 9, 733810. doi:10.3389/fbioe.2021.733810

Kim, C., Bui, J. C., Luo, X., Cooper, J. K., Kusoglu, A., Weber, A. Z., et al. (2021). Tailored Catalyst Microenvironments for CO_2 Electroreduction to Multicarbon Products on Copper Using Bilayer Ionomer Coatings. *Nat. Energ.* 6, 1026–1034. doi:10.1038/s41560-021-00920-8

Lang, X.-Y., Fu, H.-Y., Hou, C., Han, G.-F., Yang, P., Liu, Y.-B., et al. (2013). Nanoporous Gold Supported Cobalt Oxide Microelectrodes as High-Performance Electrochemical Biosensors. *Nat. Commun.* 4, 2169. doi:10.1038/ncomms3169

Lee, S., Lee, J., Park, S., Boo, H., Kim, H. C., and Chung, T. D. (2018). Disposable Non-Enzymatic Blood Glucose Sensing Strip Based on Nanoporous Platinum Particles. *Appl. Mater. Today* 10, 24–29. doi:10.1016/j.apmt.2017.11.009

Liu, M., Wang, S., and Jiang, L. (2017). Nature-Inspired Superwettability Systems. *Nat. Rev. Mater.* 2, 17306. doi:10.1038/natrevmats.2017.36

Lu, Y., Aimetti, A. A., Langer, R., and Gu, Z. (2016). Bioresponsive Materials. *Nat. Rev. Mater.* 2, 16075. doi:10.1038/natrevmats.2016.75

Lu, Y., Jiang, K., Chen, D., and Shen, G. (2019). Wearable Sweat Monitoring System with Integrated Micro-Supercapacitors. *Nano. Energ.* 58, 624–632. doi:10.1016/j.nanoen.2019.01.084

Maruthapandian, V., Mathankumar, M., Saraswathy, V., Subramanian, B., and Muralidharan, S. (2017). Study of the Oxygen Evolution Reaction Catalytic Behavior of $Co_xNi_{1-x}Fe_2O_4$ in Alkaline Medium. *ACS Appl. Mater. Inter.* 9, 13132–13141. doi:10.1021/acsami.6b16685

Mondal, S., Madhuri, R., and Sharma, P. K. (2017). Probing the Shape-Specific Electrochemical Properties of Cobalt Oxide Nanostructures for Their Application as Selective and Sensitive Non-Enzymatic Glucose Sensors. *J. Mater. Chem. C* 5, 6497–6505. doi:10.1039/c7tc01411b

Ohayon, D., Nikiforidis, G., Savva, A., Giugni, A., Wustoni, S., Palanisamy, T., et al. (2020). Biofuel Powered Glucose Detection in Bodily Fluids with an N-Type Conjugated Polymer. *Nat. Mater.* 19, 456–463. doi:10.1038/s41563-019-0556-4

Quoc Dung, N., Patil, D., Jung, H., and Kim, D. (2013). A High-Performance Nonenzymatic Glucose Sensor Made of CuO-SWCNT Nanocomposites. *Biosens. Bioelectron.* 42, 280–286. doi:10.1016/j.bios.2012.10.044

Rubino, F. (2016). Medical Research: Time to Think Differently About Diabetes. *Nature* 533, 459–461. doi:10.1038/533459a

Sheng, X., Liu, Z., Zeng, R., Chen, L., Feng, X., and Jiang, L. (2017). Enhanced Photocatalytic Reaction at Air-Liquid-Solid Joint Interfaces. *J. Am. Chem. Soc.* 139, 12402–12405. doi:10.1021/jacs.7b07187

Song, Z., Xu, C., Sheng, X., Feng, X., and Jiang, L. (2018). Utilization of Peroxide Reduction Reaction at Air-Liquid-Solid Joint Interfaces for Reliable Sensing System Construction. *Adv. Mater.* 30, 1701473. doi:10.1002/adma.201701473

Sun, X., and James, T. D. (2015). Glucose Sensing in Supramolecular Chemistry. *Chem. Rev.* 115, 8001–8037. doi:10.1021/cr500562m

Teymourian, H., Barfidokht, A., and Wang, J. (2020). Electrochemical Glucose Sensors in Diabetes Management: An Updated Review (2010-2020). *Chem. Soc. Rev.* 49 (21), 7671–7709. doi:10.1039/d0cs00304b

Wei, M., Qiao, Y., Zhao, H., Liang, J., Li, T., Luo, Y., et al. (2020). Electrochemical Non-Enzymatic Glucose Sensors: Recent Progress and Perspectives. *Chem. Commun.* 56, 14553–14569. doi:10.1039/d0cc05650b

Wen, L., Tian, Y., and Jiang, L. (2015). Bioinspired Super-Wettability from Fundamental Research to Practical Applications. *Angew. Chem. Int. Ed.* 54, 3387–3399. doi:10.1002/anie.201409911

Yamauchi, Y., Tonegawa, A., Komatsu, M., Wang, H., Wang, L., Nemoto, Y., et al. (2012). Electrochemical Synthesis of Mesoporous Pt-Au Binary Alloys with Tunable Compositions for Enhancement of Electrochemical Performance. *J. Am. Chem. Soc.* 134, 5100–5109. doi:10.1021/ja209044g

Yang, G., Kampstra, K. L., and Abidian, M. R. (2014). High Performance Conducting Polymer Nanofiber Biosensors for Detection of Biomolecules. *Adv. Mater.* 26, 4954–4960. doi:10.1002/adma.201400753

Yang, Y. J., and Gao, Z. F. (2022). Superwettable Biosensor for Disease Biomarker Detection. *Front. Bioeng. Biotechnol.* 10, 872984. doi:10.3389/fbioe.2022.872984

Yin, F., and Liu, H. (2020). The J-pH Diagram of Interfacial Reactions Involving H+ and OH−. *J. Energ. Chem.* 50, 339–343. doi:10.1016/j.jechem.2020.03.078

Zhang, L., Ye, C., Li, X., Ding, Y., Liang, H., Zhao, G., et al. (2018). A CuNi/C Nanosheet Array Based on a Metal-Organic Framework Derivate as a Supersensitive Non-Enzymatic Glucose Sensor. *Nano-Micro Lett.* 10 (2), 28. doi:10.1007/s40820-017-0178-9

Zhang, S., Zeng, J., Wang, C., Feng, L., Song, Z., Zhao, W., et al. (2021). The Application of Wearable Glucose Sensors in Point-of-Care Testing. *Front. Bioeng. Biotechnol.* 9, 774210. doi:10.3389/fbioe.2021.774210

Zhong, S.-L., Zhuang, J., Yang, D.-P., and Tang, D. (2017). Eggshell Membrane-Templated Synthesis of 3D Hierarchical Porous Au Networks for Electrochemical Nonenzymatic Glucose Sensor. *Biosens. Bioelectron.* 96, 26–32. doi:10.1016/j.bios.2017.04.038

Zhou, H., Sheng, X., Xiao, J., Ding, Z., Wang, D., Zhang, X., et al. (2020). Increasing the Efficiency of Photocatalytic Reactions *via* Surface Microenvironment Engineering. *J. Am. Chem. Soc.* 142, 2738–2743. doi:10.1021/jacs.9b12247

Zhou, Y., Liu, C., Yu, Y., Yin, M., Sun, J., Huang, J., et al. (2020). An Organelle-Specific Nanozyme for Diabetes Care in Genetically or Diet-Induced Models. *Adv. Mater.* 32, 2003708. doi:10.1002/adma.202003708

Zhu, X., Yuan, S., Ju, Y., Yang, J., Zhao, C., and Liu, H. (2019). Water Splitting-Assisted Electrocatalytic Oxidation of Glucose with a Metal-Organic Framework for Wearable Nonenzymatic Perspiration Sensing. *Anal. Chem.* 91, 10764–10771. doi:10.1021/acs.analchem.9b02328

Conflict of Interest: The authors declare that the research was conducted in the absence of any commercial or financial relationships that could be construed as a potential conflict of interest.

Publisher's Note: All claims expressed in this article are solely those of the authors and do not necessarily represent those of their affiliated organizations, or those of the publisher, the editors and the reviewers. Any product that may be evaluated in this article, or claim that may be made by its manufacturer, is not guaranteed or endorsed by the publisher.

frontiers | Frontiers in Bioengineering and Biotechnology

REVIEW
published: 13 July 2022
doi: 10.3389/fbioe.2022.947327

Recent Advances in Multifunctional Mechanical–Chemical Superhydrophobic Materials

Qinghua Luo[1], *Jiao Peng*[1], *Xiaoyu Chen*[1], *Hui Zhang*[1], *Xia Deng*[1], *Shiwei Jin*[1]* *and Hai Zhu*[2]

[1]*Key Laboratory of Catalysis and Energy Materials Chemistry of Education, Hubei Key Laboratory of Catalysis and Materials Science, South-Central University for Nationalities, Wuhan, China,* [2]*China State Key Laboratory of Biogeology and Environmental Geology, Engineering Research Center of Nano-Geomaterials of Ministry of Education, Faculty of Materials Science and Chemistry, China University of Geosciences, Wuhan, China*

In recent years, biology-inspired superhydrophobic technology has attracted extensive attention and has been widely used in self-cleaning, anti-icing, oil–water separation, and other fields. However, the poor durability restricts its application in practice; thus, it is urgent to systematically summarize it so that scientists can guide the future development of this field. Here, in this review, we first elucidated five kinds of typical superhydrophobic models, namely, Young's equation, Wenzel, Cassie–Baxter, Wenzel–Cassie, "Lotus," and "Gecko" models. Then, we summarized the improvement in mechanical stability and chemical stability of superhydrophobic surface. Later, the durability test methods such as mechanical test methods and chemical test methods are discussed. Afterwards, we displayed the applications of multifunctional mechanical–chemical superhydrophobic materials, namely, anti-fogging, self-cleaning, oil–water separation, antibacterial, membrane distillation, battery, and anti-icing. Finally, the outlook and challenge of mechanical–chemical superhydrophobic materials are highlighted.

Keywords: superhydrophobic, mechanical stability, chemical stability, multifunctional, durability test

OPEN ACCESS

Edited by:
Pengchao Zhang,
Wuhan University of Technology, China

Reviewed by:
Meirong Song,
Henan Agricultural University, China
Moyuan Cao,
Nankai University, China

***Correspondence:**
Shiwei Jin
jinsw@mail.scuec.edu.cn

Specialty section:
This article was submitted to Bionics and Biomimetics, a section of the journal Frontiers in Bioengineering and Biotechnology

Received: *18 May 2022*
Accepted: *06 June 2022*
Published: *13 July 2022*

Citation:
Luo Q, Peng J, Chen X, Zhang H, Deng X, Jin S and Zhu H (2022) Recent Advances in Multifunctional Mechanical–Chemical Superhydrophobic Materials. Front. Bioeng. Biotechnol. 10:947327. doi: 10.3389/fbioe.2022.947327

INTRODUCTION

Nature has incubated many sophisticated superhydrophobic creatures during long-term evolution and natural selection (Sanchez et al., 2005; Liu et al., 2010). Water droplets are spherical on the lotus leaf surface and can roll away the pollution form the surface, which is caused by the chemical composition and special structure of the surface of the lotus leaf. The waterproof composition and microscopic rough structure on the surface of the lotus leaf cause the superhydrophobic phenomenon. This is known as the "Lotus Effect" confirmed by W. Barthlott and C. Neihuis. In addition, many fascinating superhydrophobic phenomena in nature have been uncovered, such as low-adhesion water striders, water-collecting beetles, high-adhesion rose petals, and gecko feet. Inspired by these natural superhydrophobic phenomena, lots of superhydrophobic materials have been developed and used in many fields, self-cleaning (Wang et al., 2022; Jung and Bhushan, 2009; Lou et al., 2020), anti-icing (Lv et al., 2014; Boinovich and Emelyanenko, 2013; Rico et al., 2020; Xie et al., 2022; Zhang et al., 2021a; Yang et al., 2022; Chen et al., 2021; Liu et al., 2019a), anti-fogging (Yoon et al., 2020a; Feng et al., 2021; Sun et al., 2014; Wen et al., 2014), antibacterial (Wu et al., 2016; Wang et al., 2020a; Ma et al., 2020; Ye et al., 2021), fluid drag reduction (Li et al., 2019a; Hu H. et al., 2017; Liu et al., 2019b), liquid separation (Lv et al., 2017; Gu et al., 2019a, b; Chen et al., 2016; Zhang et al., 2022), membrane distillation (Liao et al., 2020; Guo et al., 2021; Ji et al., 2021), fog harvest (Zhu et al., 2016a; Zhu and Guo, 2016a; Zhong et al., 2018), *etc.*

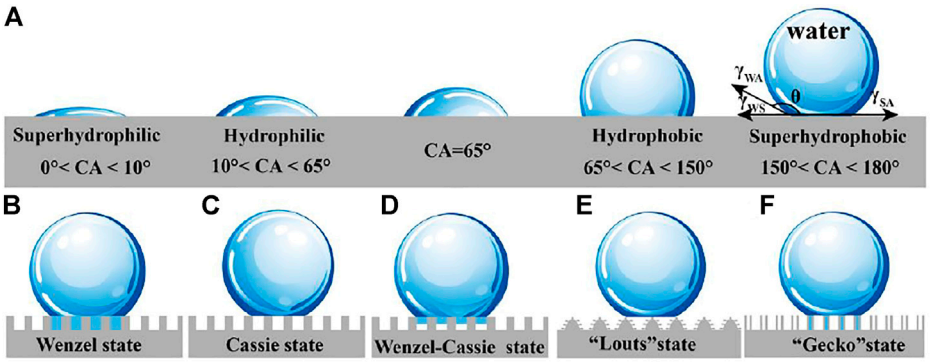

FIGURE 1 | (A) Wetting definitions. **(B)** Wenzel model. **(C)** Cassie–Baxter model. **(D)** Wenzel–Cassie model. **(E)** "Lotus" model. **(F)** "Gecko" model (Zhu et al., 2020).

The construction of superhydrophobic materials is based on the combination of micro/nano structures and low surface energy chemicals (Fu et al., 2019; Wang et al., 2020a). The micro/nano structures are vulnerable to mechanical wear and chemical corrosion in practical application (Verho et al., 2011; Milionis et al., 2016; Tian et al., 2016). Once the superhydrophobic surface is worn or impacted by external pressure, the structure collapses and the chemical substances are worn off, causing the hydrophobic properties to be partially or completely lost immediately and cannot be recovered. In addition, the superhydrophobic materials suffer from the degradation induced by UV exposure and chemical reactions with solvents. Therefore, the development of superhydrophobic materials with excellent mechanical durability and chemical stability are highly desired.

In this review, we illustrated the recent development of multifunctional mechanical–chemical superhydrophobic materials. At first, the theories about superhydrophobic surfaces including Young's equation, Wenzel model, Cassie–Baxter model, Wenzel–Cassie model, "lotus" model, "gecko" model are elucidated. Then, we summarized the improvement in mechanical stability and chemical stability of superhydrophobic surface. Later, the durability test methods such as mechanical test methods (sandpaper abrasion, tape-peeling, knife-scratch, finger wiping, Taber abrasion, impact test) and chemical test methods (solution immersion, UV irradiation, electrochemical) are discussed. Afterwards, the applications of multifunctional mechanical–chemical superhydrophobic materials are elaborated. Finally, conclusion and prospects of multifunctional mechanical–chemical superhydrophobic materials were discussed.

THEORY OF SUPERHYDROPHOBICITY

Wetting Definitions

If the interaction between liquid molecules and solid molecules is stronger than that between liquid molecules, the liquid will spread on the solid surface, which is called wetting phenomenon. Wettability is generally characterized by the contact angle of liquid on the solid surface. (**Figure 1A**) (Tuteja et al., 2007; Xia and Jiang, 2008; Bormashenko, 2019). When water contact angle (WCA) is lower than 10°, the surface is superhydrophilic. And the hydrophilicity is called at 10°–65°, hydrophobicity is denominated at 65° < CA < 150°. Especially, when the WCA is greater than 150°, the sample exhibits superhydrophobicity. Recently, through Jiang's theoretical research and experimental operation (Xia and Jiang, 2008; Zhu et al., 2021a), it is proved that CA of 65 defines non-wetting and wetting.

Young's Equation

In 1805, Thomas Young carried out force analysis on the three-phase interface and proposed a force analysis model called Young's equation (Young, 1805), which was only applicable to the contact angle value of water droplets with ideal smooth surface when they reached equilibrium state on the surface.

$$\gamma_{SV} = \gamma_{SL} + \gamma_{LV}\cos\theta,$$

where θ is the static water contact angle; γ_{SV}, γ_{SL}, and γ_{LV} represent surface tension of solid–vapor, solid–liquid, and liquid–vapor, respectively.

Wenzel Model

Based on Young's equation, Wenzel linked the roughness factor of the surface with the water contact angle by calculating the adhesion force balance in the surface wetting process (Wenzel and Robert, 1936), and the linear relationship between Young's contact angle and apparent contact angle are acquired:

$$\cos\theta_w = r\cos\theta\,,$$

where r is the roughness factor, which is determined by the ratio of the actual surface area to the projected surface area, and θ_w and θ represent the water CA in respective apparent and original states.

According to the Wenzel model (**Figure 1B**), r can be regarded as the amplification factor in a mathematical relationship, which will make the hydrophilic surface more hydrophilic; on the contrary, for a hydrophobic surface, it will make the surface more hydrophobic.

Cassie–Baxter Model

Cassie–Baxter model (Cassie and Baxter, 1944) can be used to analyze the wettability of porous hydrophobic fabric surface. On the basis of Young's equation, it is concluded that the apparent contact angle is the sum of the contributions of each contact phase (fabric and air (pore)):

$$\cos\theta_{CB} = f_{SL}\cos\theta + f_{LV}\cos\theta',$$

where f_{SL} and f_{LV}, respectively, show the fraction between the solid–liquid and liquid–vapor interface at the contacted area and air ($f_{SL}+f_{LV} = 1$). θ_{CB} and θ' are the apparent contact angle of liquid droplets on rough surface and the contact angle of liquid on ideal air surface ($\theta' = 180^{\circ}$), respectively. The wetting state described by Cassie is shown in **Figure 1C**. The droplet is suspended on the convex surface, and the contact area between the surface and the droplet is very small.

Wenzel–Cassie State

The research of Lafuma and Quéré (Lafuma and Quéré, 2003) shows that Wenzel–Cassie model is an intermediate state between Wenzel model and Cassie model (**Figure 1D**) where water droplets are semi-filled on solid surface. The Cassie state will transform to the Wenzel state under the stimulation of external energy such as droplet impact, mechanical vibration, and droplet evaporation.

"Lotus" Model

"Lotus" model (Gao and McCarthy, 2006) is a special Cassie model, lotus leaf surface microscale mastoid and surface wax to give it a repellent ability, These structures (**Figure 1E**) reduce the contact area between solid surface and liquid, and water droplets are in a semi-suspended state, so pollutants can be rolled away by the falling water droplets, which gives a self-cleaning performance on lotus leaf.

"Gecko" Model

The "gecko" model (Jin et al., 2005) comes from the classical superhydrophobic nanotube structure, and has good adhesion performance. It is similar to Wenzel model. One is in direct contact with the external atmosphere, and the other is trapped in the nanotube. Due to the change of air volume in the nanotubes, the negative pressure in the nanotubes increases, resulting in high CA, which makes the nanotubes have high adhesion to water (**Figure 1F**).

IMPROVEMENT IN THE MECHANICAL STABILITY

Self-Hardness

Cement (Song et al., 2017a), diamond (Yang et al., 2014; Wang et al., 2017; Wang et al., 2020b), and alloys (Qiao et al., 2018; Wu et al., 2018) have inherently high hardness and are thus ideal materials to develop superhydrophobic surfaces with an enhanced mechanical robustness. A superhydrophobic concrete (**Figure 2A**) was prepared by combining metal mesh covering and fluoroalkylsilane modification (Song et al., 2017a). The obtained concrete can retain its superhydrophobic property after a sandpaper wear test (a pressure of 1100 Pa, standard sandpaper of 360#, and abrasion distance of 8 m). In addition, the superhydrophobic concrete is able to endure the knife-scratch and the hammer blow tests. This effectively demonstrates the remarkable mechanical strength of as-prepared superhydrophobic concrete. For its own hard materials, his preparation method is simple and easy to obtain, but because of the lack of materials, it is not suitable for large-scale production.

Porous Materials

Sponges (Zhu et al., 2013; Cheng et al., 2019a; Dong et al., 2020), textiles (Luo et al., 2021; Zhou et al., 2021), foamed nickel (Hu et al., 2017; Eum et al., 2019; Wang et al., 2021), and other materials (Hou Y. et al., 2015) with multiple layers and porous (**Figure 2B**), due to their large specific surface area, even if part of the material surface is rubbed off, the material still remains, so it has abrasion resistance and is an excellent superhydrophobic material. Superhydrophobic textiles (Luo et al., 2021) are manufactured by decorating the textiles modified by polydopamine (PDA) with MXene ($Ti_3C_2T_x$) and then coating with polydimethylsiloxane (PDMS). The obtained superhydrophobic breathable textiles still maintain superhydrophobic properties in the sandpaper wear test (moving 2 cm with traction under the weight of 50 g), which demonstrates the robustness of the superhydrophobic textiles. Porous material is one of the recent research hotspots, which has the advantages of simple operation, low production cost, and suitable for large-scale production, while at the same time, porous materials have been widely used in separation, catalysis, and other fields.

"Paint + Adhesive" Method

In order to reduce the dependence of superhydrophobic surface on substrate and strengthen the interface bonding force, a strategy of "Paint + adhesive" was developed to prepare superhydrophobic surface. The surface superhydrophobic layer is connected with the substrate by an intermediate layer, which can not only anchor the micro-nano structure on the surface, but also serve as a shielding layer to provide additional protection for the substrate, thus obviously improving the mechanical properties of superhydrophobic surface and preparing durable superhydrophobic surfaces on various substrates. Lu et al. (Lu et al., 2015) proposed a "paint + adhesive" strategy to build a durable superhydrophobic surface for the first time. TiO_2 nanoparticles modified by fluorosilane, was dispersed in ethanol solution and sprayed on the adhesive-coated substrate. The adhesive can firmly adhere the TiO_2 nanoparticles (superhydrophobic layer) to the substrates that the obtained superhydrophobic surface shows a water CA of >160° even after wiping with fingers, impacting with water droplets, and 40 cycles of sandpaper abrasion (standard glasspaper, grit no. 240, and moved for 10 cm). Based on the above "paint + adhesive" method, many organic/inorganic adhesives and superhydrophobic materials are used to develop superhydrophobic surfaces with good durability (**Figure 2C**)

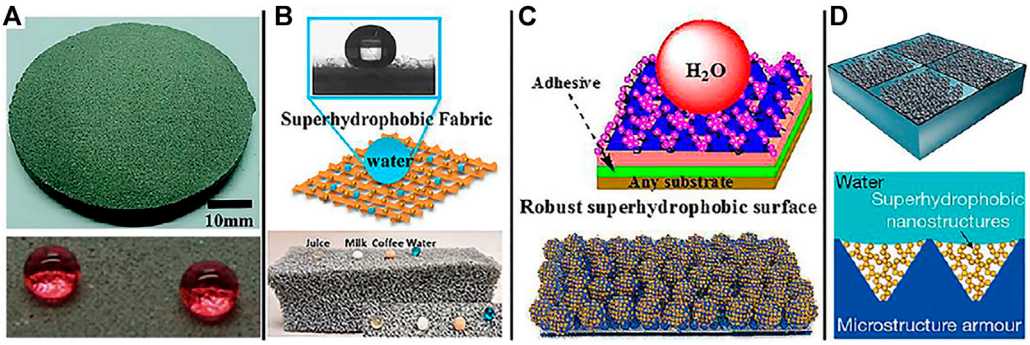

FIGURE 2 | Mechanical superhydrophobic models: **(A)** Self-hardness: the surface of cement (Song et al., 2017a). **(B)** Porous materials: the surface of textile and sponge (Shang et al., 2020; Ozkan et al., 2020). **(C)** "Paint + adhesive" method (Qing et al., 2019; Zhu et al., 2020). **(D)** Schematic diagram of a strategy to enhance the mechanical robustness of superhydrophobic surfaces by containing hydrophobic nanostructures in protective microstructures "armor" (Wang et al., 2020c).

(Zheng et al., 2021). The method can improve the binding force between the substrate and the superhydrophobic material, and can be produced on a large scale which has wide selectivity to the substrate. However, the superhydrophobic layer is affected by external mechanical friction or chemical corrosion, and its service life is greatly reduced.

"Armor"

Armoring strategy is to use materials with excellent mechanical properties to protect the surface micro-nano structures, which is similar to the function of armor. At present, nano-scale armor and microscale armor are mainly used. In 2020, Wang and coworkers (Wang et al., 2020c) fabricated a robust superhydrophobic surface *via* constructing surface texture at two different length scales, including superhydrophobic nanostructures and a microstructure frame (**Figure 2D**). The microstructure frame is made up of an array of microscale inverted-pyramidal cavities, which can house the superhydrophobic nanostructure and act as a protective "armor" to avoid the destruction of the superhydrophobic nanostructure by abradants. The combination of superhydrophobic nanostructures and the protective microstructure frame ensures that the obtained superhydrophobic surface could tolerate more than 1000 abrasion cycles and even under tape-peeling tests, Taber abrasion tests, and scratch tests. The armor model provides a new idea for the preparation of durable superhydrophobic materials, but it is still in the exploratory stage because of its complex preparation method.

IMPROVEMENT IN THE CHEMICAL STABILITY

Improving the chemical stability of superhydrophobic surface is also a research hotspot in recent years. At present, the common preparation methods to improve the chemical stability of superhydrophobic surface include chemical etching, spraying, electrochemical deposition, sol-gel method and electrostatic spinning. However, they have their own advantages and disadvantages. (**Table 1**).

Chemical Etching

Chemical etching method refers to the preparation of superhydrophobic surface by using the strong corrosiveness of strong acid/alkali solution to construct a micro/nano composite structure on the substrate, which is simple to operate and fast to react. Xu et al. (Xu et al., 2020a) used nitric acid solutions with different concentrations to etch the nickel mold, discussed the importance of etching time and chemical solution concentration, and then copied the surface pattern of the chemical etching template to obtain a large-area micro/nano-structured polydimethylsiloxane (PDMS) film with superhydrophobicity. The film shows superhydrophobicity even under high-strength friction, and also has excellent acid and alkali resistance (excellent liquid repellency even after contacting with 1 M HCl, 1 M NaOH and 1 M NaCl solutions for 96 h), ultraviolet resistance, and optical transparency.

Spraying

The spraying method uniformly disperses and overlays the raw materials of micro/nanoparticles on the surface of the base material to mode a uniform coating with a certain structure, which is not limited to the shape and size of the base material, simple and convenient to operate, low in cost, and high in coating efficiency. Yokoi et al. (Yokoi et al., 2015) deposited perfluorodecyl trichlorosilane on the surface of alkali-treated polyester, and then sprayed silica modified by fluorosilane on the surface of modified polyester to acquire a transparent superhydrophobic surface. The contact angle of the sample remained above 150° after 100 wear cycles under the pressure of 10 kPa, and the sample had strong repulsion to strong acid and alkali (the contact angle and sliding angle of acidic and alkaline aqueous solutions with pH values ranging from 2 to 14 were measured. The contact angle of all solutions was over 150°, and the sliding angle was less than 15°), which indicates that the prepared superhydrophobic polyester mesh not only had high mechanical strength, but also had good acid and alkali resistance.

Electrochemical Deposition

Electrochemical deposition (Lee et al., 2021) method refers to the preparation technology of depositing one or more materials on the workpiece surface of the anode, while the cathode undergoes a reduction reaction. She et al. (She et al., 2014) performed electroless nickel plating on the pre-treated AZ91D magnesium alloy and then electrodeposited the nickel-cobalt alloy coating, obtaining a superhydrophobic surface with a contact angle of 167.3 ± 1.3° and a rolling angle of about 1°, and the corrosion current density is three orders of magnitude lower than that of the blank sample, the corrosion rate is about 0.06% of the blank sample, which shows it has better corrosion resistance and pH stability.

Sol–Gel Method

Sol–gel method refers to the use of highly chemically active compounds as precursors, hydrolysis, and condensation reaction in the liquid phase to form a stable transparent sol system, after polymerization, gel is formed, and then by drying, sintering curing treatment to prepare micro and nano pore structure, so as to give the surface of the material hydrophobic properties. Su et al. (Su et al., 2017) prepared hydrophobic sol by teosilicate ethyl ester and polydimethylsiloxane according to a certain mass ratio. Polyester fabric absorbed sol by immersion and reacted with acid to prepare superhydrophobic polyester surface with good mechanical stability. The prepared superhydrophobic textiles have excellent durability in deionized water, various solvents (the CAs were almost unchanged and still above 150° immersed in deionized water, hexane, hexane and toluene hexane for 168 h), strong acid/alkali solutions (the superhydrophobic textiles still had water repellency after being immersed in HCl solution for 60 h or an aqueous NaOH solution for 48 h) and boiling water/ice water.

Electrostatic Spinning

Electrospinning (Wan et al., 2022) is a kind of method in which polymer solution forms a jet under the action of high-voltage electrostatic force, and finally one-dimensional nanofibers are prepared. The superhydrophobic surface can be obtained by covering the surface of the substrate with nanofiber membrane and then modifying it with low surface energy substances. It has the advantages of low spinning cost, simple manufacturing device, various kinds of spinnable substances, controllable process, *etc*. Cui et al. (Cui et al., 2018) prepared superhydrophobic anticorrosive coating on aluminum substrate by electrospinning. Polyvinylidenefluoride (PVDF)/ stearic acid nanofibers are used to construct micron/ nanometer superhydrophobic structures to provide long-term corrosion protection. After corrosion in 3.5% NaCl solution for 30 days, it still had excellent corrosion resistance.

DURABILITY TEST

Mechanical Durability Test

Inspired by lotus leaves, superhydrophobic surfaces have huge potential applications. However, their practical application is limited by poor durability. When exposed to harsh mechanical or chemical conditions, they can easily lose their functions. Scientists also try to adopt various methods to improve the durability of materials, so we need to establish a test method for superhydrophobic durability. At present, there are many testing methods of superhydrophobic durability, which can be summarized into two aspects: one is mechanical durability test, such as sandpaper abrasion, tape-peeling, knife-scratch, finger wipe, Taber abrasion, and impact test, the other is chemical durability test, such as acid-base test, solution immersion, UV irradiation, and electrochemical corrosion.

Sandpaper Abrasion Test

The sandpaper abrasion test is a common method to test the wear resistance of superhydrophobic surface at present. During the sandpaper abrasion test (**Figure 3A**) (Zhu et al., 2018a; Wang et al., 2018; Cheng et al., 2019b), a certain load is applied on the superhydrophobic material, and the material is rubbed on the sandpaper. The surface between the superhydrophobic material and the sandpaper acts as a wear surface. Sandpaper abrasion test is the most common evaluation method, which has good practicability. However, at present, the test standards are not uniform and the test error is relatively large. Li et al. (Li et al., 2019b) studied the effects of superhydrophobic coatings prepared with different filler particle sizes on surface morphology and hydrophobic properties under the same load, different abrasive particle sizes and friction distances. The results show that with the same filler content, the larger the filler particle size, the greater the wear resistance.

Tape-Peeling Test

Tape peeling (**Figure 3B**) (Wu et al., 2017a; Zhang et al., 2018; Ghasemlou et al., 2019; Ji et al., 2019) is one of the easiest ways to determine the surface abrasion resistance of superhydrophobic materials, which is to fully contact the tape with the surface of the tested material under a certain pressure, and then peel off at a certain angle and speed. This method is mainly used to test the adhesion strength of superhydrophobic coating and its rough structure to substrate. However, this method can only evaluate the firmness of coating and substrate, but not the strength of superhydrophobic surface, which has certain limitations. By observing the SEM diagram, Zhao et al. (Zhao et al., 2020) compared the number of nanoparticles per unit area before and after peeling, evaluated the binding strength of silica particles with different sizes and epoxy resin substrate, and optimized the superhydrophobic surface durability by adjusting the ratio of different particle sizes to fillers.

Knife-Scratch Test

Considering that the superhydrophobic surfaces are often subjected to scratches in practical application, such as car scratches, knife scratch is selected as a typical test to evaluate the mechanical wear resistance of superhydrophobic surfaces. This method is suitable for fields with high requirements for mechanical stability, but the current testing standards are not uniform (Carmalt et al., 2015; Wu Y. et al., 2017; Ghasemlou

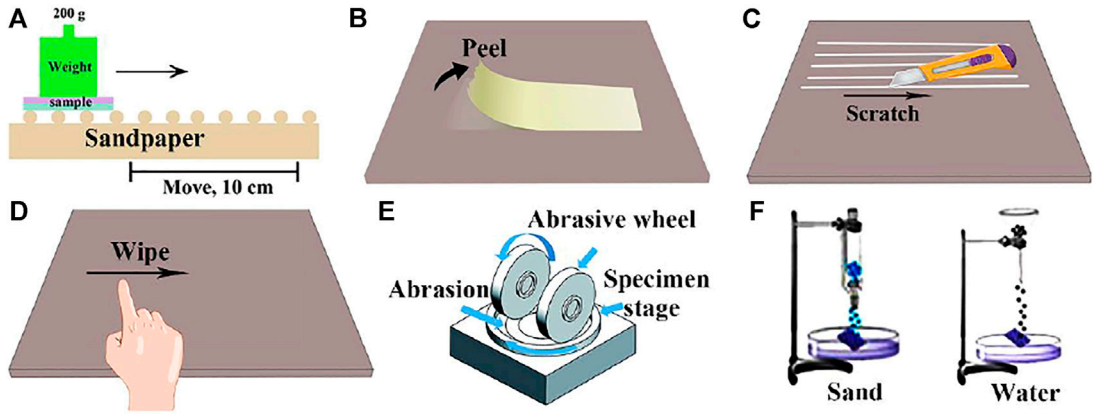

FIGURE 3 | Wear resistance test: **(A)** Sandpaper abrasion. **(B)** Tape-peel test. **(C)** Knife-scratch test. **(D)** Finger wiping test. **(E)** Taber abrasion test (Ye et al., 2017). **(F)** Sand or water impact test.

et al., 2019). As shown in **Figure 3C**, the knife is used to scrape the superhydrophobic surface, resulting in a dense array of wide and deep scars on the surface. Wu et al. (Wu et al., 2017a) used knives to form wide and deep lattice marks on the superhydrophobic wood, however, water droplets can easily roll down from it without leaving any traces, indicating that the superhydrophobicity still exists.

Finger Wiping Test

As shown in **Figure 3D**, the finger wipe test (Carmalt et al., 2015; Wu et al., 2017a) is to wipe the surface of the superhydrophobic material repeatedly with the finger in the same direction, and then test the change of the contact angle of the material surface. Finger wiping test can preliminarily evaluate the durability of superhydrophobic surface, and the experimental operation is convenient and easy. Liu et al. (Liu et al., 2019a) designed and prepared a new type of polyfluorinated organic superhydrophobic coating based on mercaptan-olefin click reaction. The coating has excellent superhydrophobicity and self-cleaning properties, and has good adhesion to the substrate, which still maintains excellent superhydrophobicity after finger wiping.

Taber Abrasion Test

Taber friction (**Figure 3E**) (Ye et al., 2017; Zhu et al., 2018b) is also a kind of friction test, which is carried out in a special Taber friction testing machine. The machine consists of three parts: a turntable that clamps the sample, a friction wheel and a load. During the experiment, the superhydrophobic material is clamped on the turntable. Then, load a certain weight of the friction wheel for rotating friction, and take out the test piece after the specified number of revolutions to test its superhydrophobic performance. This method has certain evaluation criteria, the experimental operation is convenient and the data is accurate. Peng et al. (Peng et al., 2018) observed the variation of coating contact angle and coating thickness with Taber abrasion cycles under three different loads (150, 200 and 250 g). After 100 wear cycles, the CA of PTFE coating remained above 150° under 150 and 200 g loads and decreased to 146° under 250 g loads.

Impact Test

There are two types of impact tests (**Figure 3F**). One is the water impact test (Zhu et al., 2018b), and the other is the sand impact test (Zhu T. et al., 2020). It is mainly a method to tilt the superhydrophobic surface at a certain angle, impact the surface with sand or water drops at a certain height, and evaluate the change of surface hydrophobicity. This method can effectively evaluate the outdoor durability of superhydrophobic materials. Deng et al. (Deng et al., 2012) used candle soot and silica to prepare superhydrophobic coating. To explore the mechanical properties of the coating, water drop impact and sand wear tests were carried out. Sand particles with a diameter of 100–300 mm hit the surface from a height of 10–40 cm. Although the coating surface is impacted by sand to form a cave, its microstructure has little change.

Chemical Durability Test

Solution Immersion

At present, superhydrophobic materials have been used in various industries; however, their low corrosion resistance hinders their wider application. Therefore, there is a need to, at a relatively low-cost technology, improve the corrosion resistance of these materials. At the same time, scientists used a chemical solution immersion method to test the chemical resistance of materials.

In acidic solution (Si et al., 2015; Zhu et al., 2018a), high concentration of H^+ will hydrogenate with superhydrophobic materials, which will destroy their original properties and make them lose superhydrophobic properties. In alkali solutions, the chemical properties of strong base are relatively active, with strong reducibility, easy to react with other substances, so as to achieve corrosion. In chloride-containing solutions, because the radius is small and it has strong penetration ability, chloride ions are most likely to pass through the tiny voids in the oxidation film to get to the metal surface, interact with the metal to get

soluble compounds, which changes the structure of the oxide film and causes corrosion of the metal. In aqua regia, aqua regia is a very corrosive liquid that can corrode the surface of the material. However, polytetrafluoroethylene (PTFE), the king of organic plastics, is not corroded by aqua regia, so researchers immersed a superhydrophobic material made of polytetrafluoroethylene in aqua regia to test its corrosion resistance.

Ultraviolet Light Irradiation

Ultraviolet light irradiation (Zhu et al., 2018a) is one of the common methods for testing the aging of materials, which is mainly tested by putting superhydrophobic materials under a certain wavelength and power ultraviolet lamp, evaluate the attenuation degree of the surface contact angle with the extension of irradiation time. This method is mainly used for evaluating and testing the outdoor durability of superhydrophobic materials. Huang et al. (Huang et al., 2021) used polytetrafluoroethylene (PTFE) particles to prepare powder coatings without solvent and chemical modification. Due to the high bond energy and chemical inertia of PTFE, the surface contact angle of the coating remained above 160° after UV irradiation for 84 h, showing excellent chemical durability.

Electrochemical Corrosion

Electrochemical corrosion (Yu et al., 2018) means the corrosion of metal due to electrochemical action in a conductive liquid medium, and current is generated during the corrosion process. When metal is placed in an aqueous solution or in a moist atmosphere, a microcell, also known as a corrosive cell, forms on the surface of the metal, oxidation reaction happens on the anode, so that the anode is dissolved, reduction reaction happens on the cathode, generally only play the role of electron transfer. This method can effectively evaluate the outdoor durability of metallic superhydrophobic materials.

APPLICATIONS

Anti-Fogging

Changing the wettability of the surface is a common method of anti-fogging, and two extreme cases are usually paid attention to: superhydrophilicity and superhydrophobicity. The hydrophilic anti-fogging method, which makes the surface of the substrate highly hydrophilic, the contact angle between the surface of the material and water approaches zero, and makes the water vapor quickly spread on the surface of the substrate after condensation to constitute a transparent water film, which has been deeply studied. Generally, superhydrophobic materials are able to firmly bond with the surfaces of other materials, and water droplets are easy to roll on the superhydrophobic surface. Therefore, it can be inferred that the droplets formed by condensation of water vapor on the surface can also roll off the surface of hydrophobic materials quickly, thus having anti-fogging pe rformance.

Medical endoscopes have promoted the development of medical careers, but endoscopes are prone to mirror fogging due to liquid adsorption and high humidity, which reduces visibility. Lee et al. (Lee et al., 2020) applied a laser to construct a lubricant-infused directly engraved nano/micro structured surface (LIDENS) on the lens, (**Figure 4A**), which can repel various liquids after chemical modification of the LIDENS lens (**Figure 4B**). Among them, the injection of lubricant can smoothen the rough surface structure and improve the transmittance. The low cost of LIDENS Nuclear density and dynamic coalescence can remove droplets under gravity, thereby preventing fogging (**Figure 4E**). At the same time, the mechanical durability of the LIDENS directly etched on the surface morphology was tested, after 30 times of tape peeling (**Figure 4C**), the SEM images in **Figure 3D** shows that the dentate wrapped by F-SAM has no obvious topological changes, which proves it has good mechanical properties (**Figure 4D**).

Yoon et al. (Yoon et al., 2020b) prepared a wet superhydrophobic coating, which maintained excellent anti-fogging performance. The top of the coating is a PDMS micro-well with low surface energy, which shows superhydrophobicity, and the bottom is a sacrificial oil (silicone oil) embedded polymer-silica nanocomposite as hydrophilic part, which guides the upper layer of water vapor condensation to the lower layer. The coating can prevent the formation of fog and maintain optical transparency during condensation.

Self-Cleaning

The lotus leaves that "come out of silt but do not dye" are typically natural self-cleaning surfaces. In addition, many animals and plants in nature have a superhydrophobic surface with self-cleaning property, such as rice leaves (Bixler and Bhushan, 2012; Nishimoto and Bhushan, 2013; Lee et al., 2017; Xu et al., 2020b), pitcher plants (Song et al., 2017b; Huang et al., 2017; Li et al., 2020a), cicada wings (Oh et al., 2017), butterfly wings (Nishimoto and Bhushan, 2013), gecko feet (Stark et al., 2016), snail shells (Nishimoto and Bhushan, 2013), fish scales (Waghmare et al., 2014), shark skin (Bixler and Bhushan, 2014). Water droplets can capture dust particles and roll away easily when arriving at the superhydrophobic surface, which offers the superhydrophobic surface its self-cleaning property.

Wu et al. (Wu et al., 2021) proposed an efficient solution modification method to prepare superhydrophobic F-PE/SiO_2 foam materials (**Figure 5A**), which shows a water CA of 158 ± 2° (**Figure 5D**). The polyethylene foam has an interconnected three-dimensional skeleton, which is composed of a polyethylene skeleton and irregular pores (**Figure 5C**). The interconnected three-dimensional skeleton results in an enhanced wear resistance for the polyethylene foam. The polyethylene foam still exhibits superhydrophobic property even after sandpaper friction and water impact (**Figure 5B**). In addition, F-PE/SiO_2 foam also shows excellent self-cleaning performance (**Figure 5E**).

Photocatalysis (Liu et al., 2020a; Sutar et al., 2020; Zhu et al., 2021b) can produce self-cleaning effects (Zhu et al., 2020b). Superhydrophobic materials with photocatalytic performance can convert light energy into chemical energy to decompose organic pollutants. During this process, the decomposed organic pollutants leave the surface of superhydrophobic material in the form of gas, and the residual solid particles will be taken away with the spreading of water film.

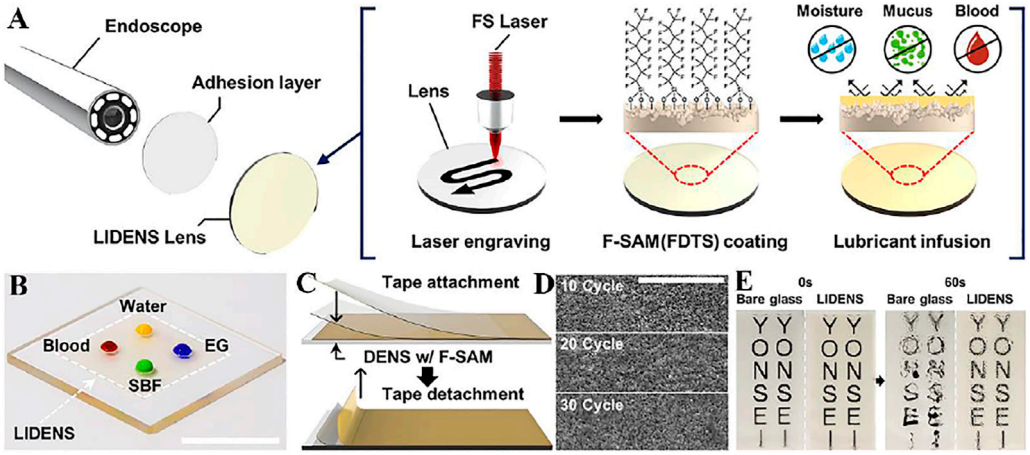

FIGURE 4 | (A) Manufacturing process diagram of anti-fogging endoscope. **(B)** Picture of various liquids on the LIDENS (scale bar: 1 cm). **(C)** Schematic diagram of tape-peeling. **(D)** SEM images after 10, 20, 30 tape-peel experiment cycles (scale bars: 20 μm). **(E)** Continuous photographic images after exposed glass (left) and LIDENS (right) are placed on distilled water (~80°C, 100% relative humidity) for about 3 cm and 60 s (Lee et al., 2020).

TABLE 1 | Advantages and disadvantages of different methods.

Method	Advantages	Shortcoming	Large-scale production
Chemical etching	Convenient preparation Cheap raw materials High success rate	High requirements on etching time, soaking time, *etc.*	Yes
Spraying	Easy to control Low cost High spraying efficiency	Poor adhesion short service life	Yes
Electrochemical deposition	Mature technology simple operation	High cost high equipment requirements	No
Sol–gel method	Heat-resistant, low-cost, simple operation	Easy to crack long preparation time	Yes
Electrostatic spinning	How spinning cost many kinds of textiles Simple operation	Need to be done at high-voltage high energy consumption	No

Our team (Zhu et al., 2021c) mixed TiO_2 NPs, epoxy resin and 1H,1H,2H,2H-perfluorooctyltriethoxysilane (FAS) through stirring and ultrasonic treatment to compose an inorganic organic superhydrophobic coating (IOS-PA) (**Figure 6A**). The presence of TiO_2 NPs enables the degradation of Nile red (**Figure 6B**). The superhydrophobicity of IOS-PA is preserved after sandpaper abrasion (**Figure 6C**) and sand impact (**Figure 6D**), indicating the excellent mechanical durability. At the same time, after being stored in acidic (pH = 1) solution for 4 h and saline (pH = 7) and alkaline (pH = 14) solutions for 8 h, the high WCA and low RA remained on the coating samples (**Figures 6E–G**). Moreover, the layer we studied had multifunctional self-cleaning ability, which can not only remove stains by gravity rolling of water, but also decompose organic dyes by ultraviolet (**Figure 6H**).

Oil–Water Separation

Frequent oil spills cause serious global water pollution (Liu et al., 2017; Zhu et al., 2020c; Huettel, 2022), which poses an urgent need for efficient solutions to oil–water separation. The traditional methods for oil–water separation include gravity separation (Saththasivam et al., 2016), filtration, centrifugation (Liu et al., 2018), flotation (Rocha e Silva et al., 2018) and electrochemical methods (Kwon et al., 2010). However, most of them have low separation efficiency and complicated operation (Wang et al., 2019). Superhydrophobic material has high separation speed and efficiency and is a promising way to solve this serious matter (Zhu and Guo, 2016b; Kong et al., 2022).

Shang and his team (Shang et al., 2020) have prepared an environmentally friendly and sustainable superhydrophobic or superoleophilic castor oil-based nanocomposite on cotton fabric using a thiol-ene chemical method initiated by ultraviolet light (**Figure 7A**). The cotton fabric has a rough surface and possesses a water CA of ~160° and a water SA of 7.5° (**Figure 7B**). The water droplets can penetrate into the pristine fabric immediately because of the capillary effect which is caused by the porosity and abundant hydroxyl groups on the fabric (**Figure 7D**). In addition, high-strength superhydrophobic cotton fabrics can withstand at least 30 sandpaper wear cycles without losing their superhydrophobicity (**Figure 7C**). At the same time, the functional cotton fabric can separate kinds oil and water mixtures and emulsions with high separation efficiency (**Figure 7E**).

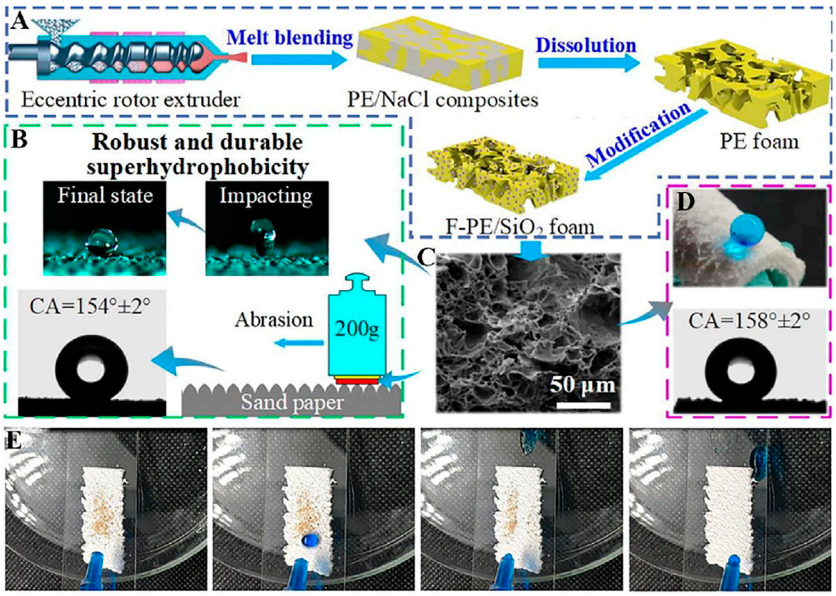

FIGURE 5 | (A) PE foam and F-PE/SiO_2 foam schematic diagram of foam plastic preparation process. **(B)** Illustration of sandpaper abrasion for the foam surface. **(C)** The SEM image of F-PE/SiO_2 foam. **(D)** Water on the surface of F-PE/SiO_2 foam. **(E)** Picture of 30° inclined F-PE/SiO_2 foam polluted by sands before and after water drop washing (Wu et al., 2021).

Tang et al. (Tang et al., 2021) proposed a cheap, environmentally friendly and pollution-free method to prepare superhydrophobic calcium carbonate ($CaCO_3$) which coated stainless steel mesh (SSM). In the experiment, the superhydrophilic $CaCO_3$-SSM was firstly prepared by using the biomineralization method induced by bacteria, and immersed in stearic acid (SA) to obtain a superhydrophobic SA/$CaCO_3$-SSM. This has regular and large-size micro-pores, and thus shows high oil flux to various oil/water mixtures ($0.2–9.12 \times 104\ L\ m^{-2}{\cdot}h^{-1}$) and high efficiency in separation (>94.8%). In addition, the SA/$CaCO_3$-SSM also exhibits outstanding wear resistance.

Zhou et al. (Zhou et al., 2016) modified the interior of the PU sponge using (3-mercaptopropyl) trimethoxysilane and graphite oxide by solvent heat treatment, resulting in a graphene layer resembling a crater that was firmly attached to the polyurethane skeleton. Graphene/PU sponges are superhydrophobic with a WCA of over 160° and can effectively separate oil and water.

The recent development of superhydrophobic materials provides a simple and inexpensive solution for oil-water separation. For example, Tudu and Kumar (Tudu and Kumar, 2019) use TiO_2 nanoparticles and perfluorodecyltriethoxysilane (PFDTS) to make superhydrophobic steel and copper mesh. Yan's group (Yan et al., 2020) prepared superhydrophobic cotton fabric by combining micro-nano-binary structure of polydopamine (PDA) with grafting of octadecyylamine (ODA).

Antibacterial Action

The adhesion and proliferation of bacteria on the surface of objects will lead to the formation of biofilms, which poses huge challenges for medical, health, and industrial applications (Monteiro et al., 2022). The antibacterial material based on superhydrophobicity is an emerging method recently (Li S. et al., 2020; Lan et al., 2021). The information of bacterial biofilm involves transportation, adhesion, firmness, and reproduction. The strategies to remove biofilms on the surface of substrates mainly include preventing bacteria from adhesion (Chung et al., 2012) and killing bacteria that have attached.

Ye et al. (Ye et al., 2021) used PDMS as the adhesive to attach fluorinated mesoporous silica nanoparticles (F-MSNS) and quaternary ammonium functionalized microporous silica nanoparticles (Q-MSNS) (**Figure 8A**) to the surface of various fabrics (**Figure 8C**), and the resulting textiles showed obvious synergistic antibacterial effects against Escherichia coli and Staphylococcus aureus by "repellent" (**Figure 8B**), which is mainly because the superhydrophobicity can repel most bacteria, and Q-MSNS on the surface of cotton fabric can effectively kill some bacteria (**Figure 8E**). At the same time, due to the surface of F/Q-MSNS coating being rough, even after 600 times of friction, the surface of the coating is still superhydrophobic (**Figure 8D**).

Ou et al. (Ou et al., 2016) selected polydopamine as an adhesive to prepare a superhydrphobic cotton coated with silver nanoparticles. The polydopamine can increase the binding between silver cotton fibers and nanoparticles, so as to prevent silver nanoparticles from dropping from the surface of cotton fibers. At the same time, the fabric composite has obvious antibacterial effect on Staphylococcus aureus and Escherichia coli.

Zhu et al. (Zhu et al., 2021d) prepared a superhydrophobic coating solution by dispersing hydrophobic silica nanoparticles

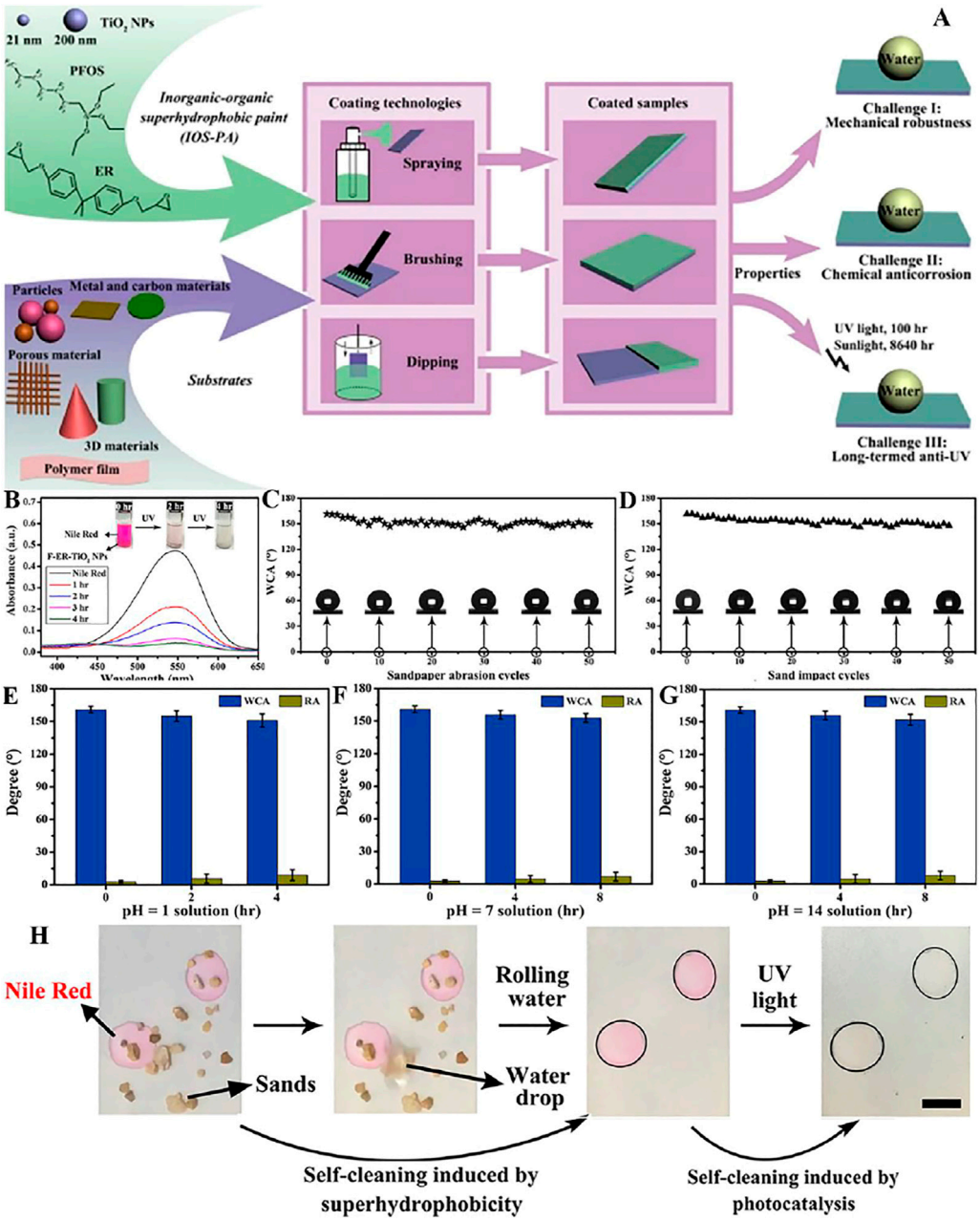

FIGURE 6 | (A) Schematic illustration of fabrication of IOS-PA. **(B)** UV–Vis spectra of Nile red solution showing decomposition by F-ER-TiO_2 NPs every 1 h. The insets are optical photos of the color variations. **(C)** The WCAs of the paint-coated surfaces were tested after each abrasion cycle, and stable superhydrophobicity was obtained with almost all WCAs larger than 150°. **(D)** After sand impact for 50 cycles, the WCAs of the coatings remained high, also showing super water repellency. When placed in pH = 1 **(E)**, pH = 7 **(F)**, and pH = 14 **(G)** solutions for 2, 4, and 8 h, respectively, the coating still manifested super water repellency with high WCAs and low RCAs. **(H)** Multifunctional self-cleaning was shown on the coating, where sand particles could be removed by rolling water, and organic dye could be decomposed by UV light (Zhu et al., 2021c).

(Aerosil® gaseous silica) in ethanol at a concentration of 2.5 w/w %. Compared with the bare surface, the attachment amount of SARS-CoV-2 on the superhydrophobic (SHPB) surface was significantly reduced, up to 99.99995%. This suggests that the as-prepared coating can effectively resist the adhesion of severe acute respiratory syndrome coronavirus 2 (SARS-CoV-2) by repelling virus-carrying droplets.

Membrane Distillation

Membrane distillation (MD) (Laqbaqbi et al., 2017; Hong et al., 2022) is a bright desalination technology because it is capable of treating highly saline water. Deng et al. (Deng et al., 2019) created a unique bilayer composite membrane using the superhydrophobic selective skin of amorphous polypropylene (APP) and the support composition of electrospun

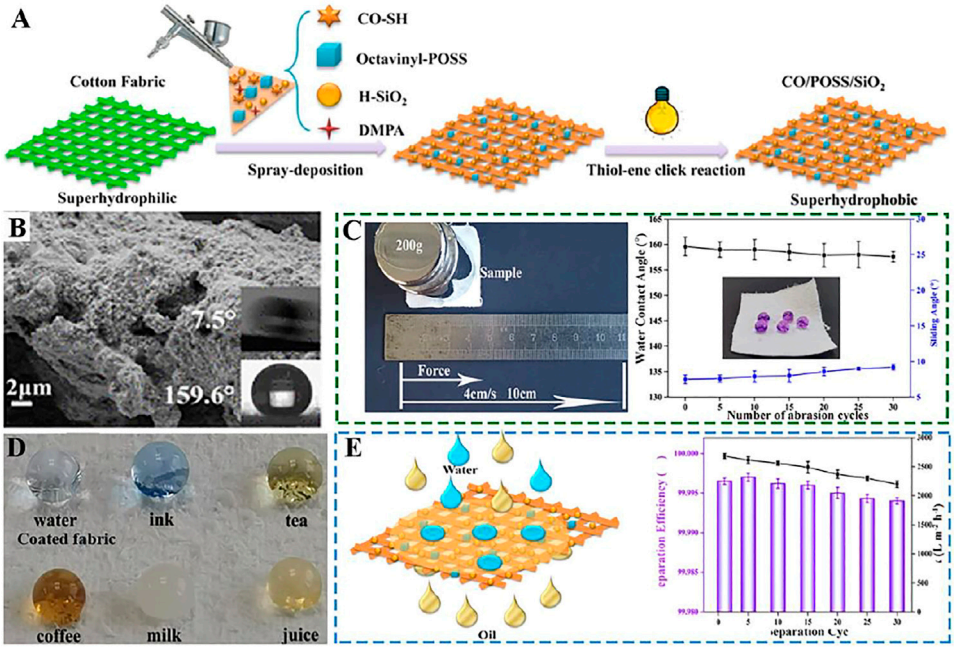

FIGURE 7 | (A) Schematic diagram of superhydrophobic cotton fabrics prepared by spray deposition of the thiol–ene resin and UV curing. **(B)** SEM images of the superhydrophobic CO/POSS/SiO_2 coated cotton fabric and the insets are the corresponding WCA and SA. **(C)** Schematic illustration of the sandpaper abrasion and CA and SA changes after different separation cycles. **(D)** Photos of different liquids on coated fabrics. **(E)** Schematic illustration of the separation process of the oil/water mixture and separation efficiency and flux of petroleum ether/water mixture after different separation cycles (Shang et al., 2020).

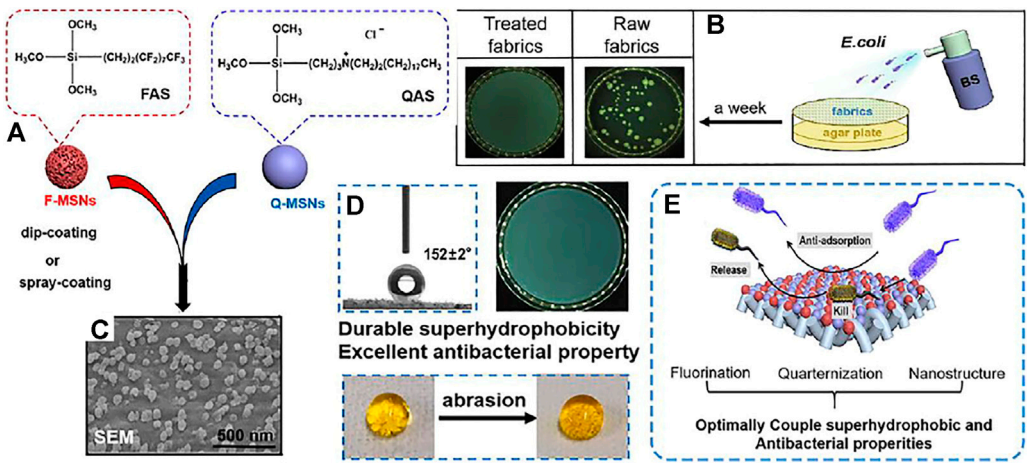

FIGURE 8 | (A) Schematic illustration of the configuring process of functionalized textiles. **(B)** Bacterial shielding experiments of cotton fabrics. **(C)** SEM images of the textiles. **(D)** Picture of a water drop (10 μl) on the treated cotton fabrics surface before and after 600 abrasion cycles. **(E)** The schematic diagram of anti-bacterial action (Ye et al., 2021);

polyvinylidene fluoride (PVDF) nanofibers. The permeable vapor flux of the superhydrophobic APP/PVDF membrane is 53.1 kg/(m^2•h), and the permeable conductivity is stable. At the same time, it has great applicability in MD desalination.

Lu et al. (Lu et al., 2016) developed a porous polyvinylidene fluoride (PVDF) three-porous hollow fiber membrane with superhydrophobicity. The three-pored hollow fiber has greater mechanical strength than traditional single-pored fibers. Under the supreme coating conditions (0.025 wt% Teflon® AF 2400, 30 s), a superhydrophobic surface was obtained which contact angle is 151°. At the same time, Teflon® AF 2400-coated membrane has higher stability,

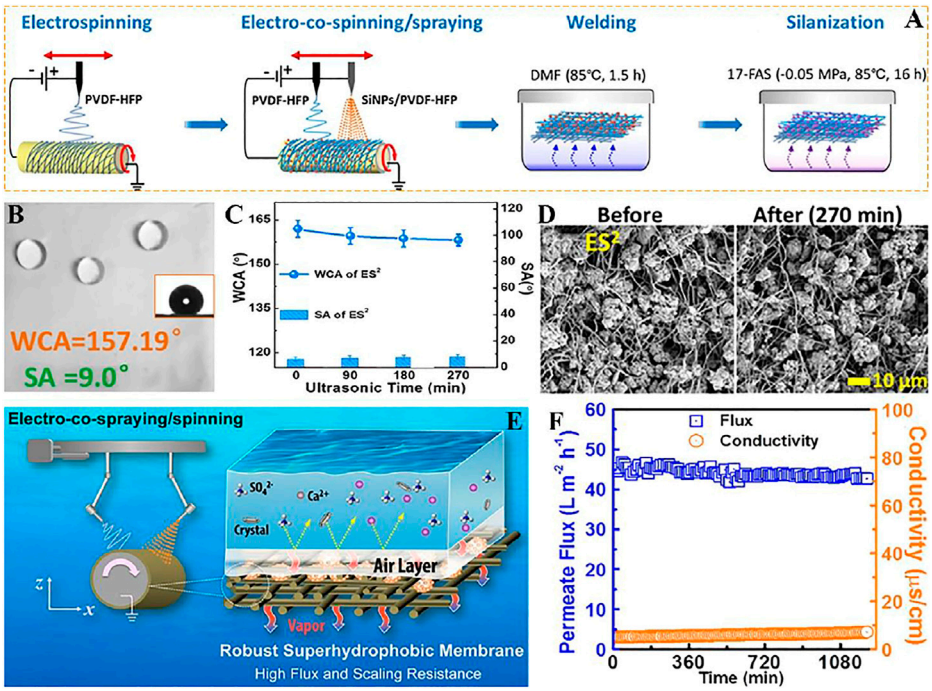

FIGURE 9 | (A) Schematic diagram of the ES2 process for fabricating robust superhydrophobic membrane. **(B)** The WCA and SA of robust superhydrophobic membrane. **(C)** WCA and SA of the r-SH membranes after different durations of ultrasonication. **(D)** SEM surface morphology of ES2-derived robust superhydrophobic membrane 270 min before (left) and after (right) ultrasound. **(E)** The mechanism of membrane distillation. **(F)** Vapor flux and conductivity of superhydrophobic electrospun fiber membrane (Su et al., 2019).

which average flux is 21 kg m^{-2} h^{-1} and rejection rate is 99.99% in 60°C desalination applications.

Distilled water is produced by the differential partial pressure of steam due to the different temperatures between hot brine and cold deionized water, which drives the transfer of steam from the feed stream to the distillate stream (**Figure 9E**). Su et al. (Su et al., 2019) used electronic co-spinning/spraying (ES2) with chemical vapor welding to produce superhydrophobic films with mechanical strength, high porosity and robustness (**Figure 9A**), which also has outstanding vapor permeability (**Figure 9F**). The prepared superhydrophobic film WCA is bigger than 150° and SA is lower than 10° (**Figure 9B**). Compared with the superhydrophobic film deposited on the surface of fluorinated nanoparticles, the superhydrophobic film has stronger wettability and wear resistance on MD, the surface of WCA and SA has little change after different ultrasonic treatment time (**Figure 9C**), and the surface morphology of the solid superhydrophobic film does not change greatly after observation on SEM (**Figure 9D**).

Battery

Solar cells (Hegazy, 2001; Liang et al., 2020) are popular because of their low-cost, friendly environment, and renewable characteristics (Syafiq et al., 2018). However, in practical application, the solar cells will affect the efficiency due to the influence of environmental temperature, dust, and wind speed. Therefore, we need to develop a solar cell board which can resist pollution. Superhydrophobic materials can be used in batteries on account of their low surface energy and surface roughness, and they have the characteristics of self-cleaning.

Wu et al. (Wu et al., 2017b) developed a viable lithium-O_2 battery with lithium metal negative electrode in a humid environment (relative humidity of 45%), which prevents H_2O by constructing a superhydrophobic quasi-solid electrolyte (SHQSE) (**Figure 10A**). In **Figure 10B**, the water contact angle is larger than 150°, which indicates that the SHQSE membrane is superhydrophobic and the SHQSE membrane has mechanical stability due to the porous substrate of nonwoven fabrics. From **Figure 10C**, it displays the classic discharge and charge profiles during cycles, which shows that the hydrophobic effects may take a vital part in the achievement of safe and permanent Li-air battery.

Liang et al. (Liang et al., 2020) used plasma-improved chemical vapor deposition (PECVD) to prepare SiO_2 as the bottom layer, and then hydrolyzed and condensed epoxy propylpropyltrimethoxysilane (KH560) at both ends to shape a network structure as an intermediate connecting layer. The hydrophilic SiO_2 modified by hexamethyldisilazane (HMDS) to obtain the top superhydrophobic layer. The structure of the superhydrophobic surface is like the double layer structure of phospholipid in the cell membrane. Compared with the bare glass panel, the glass cover plate used in solar cells greatly improves the efficiency of utilization.

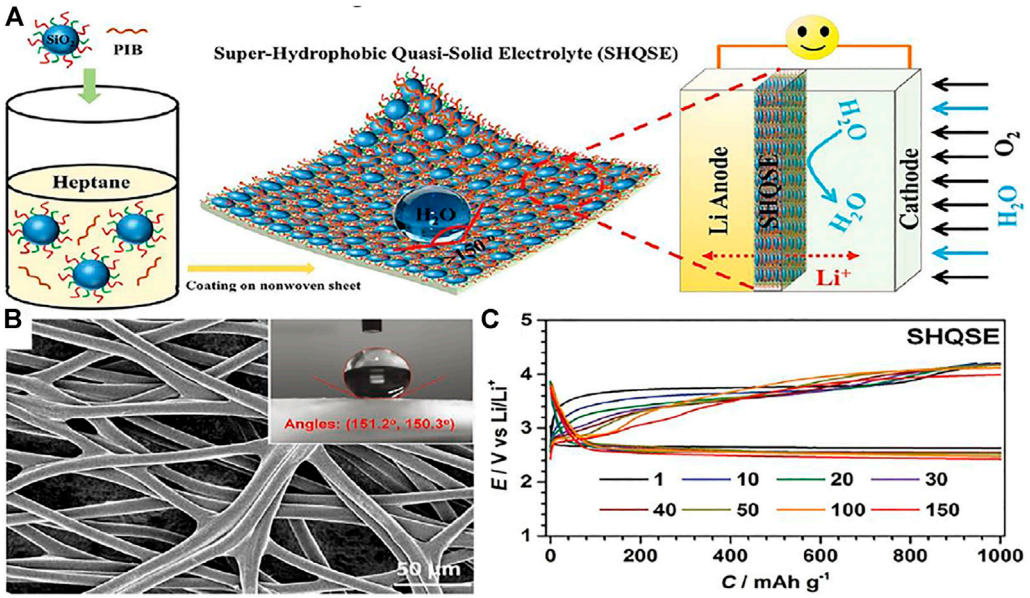

FIGURE 10 | (A) Schematic diagram of solid Li-O_2 battery in humid atmosphere on basis of the superhydrophobic quasi-solid electrolyte (SHQSE). **(B)** SEM image of the original nonwoven fabric and the insets are the corresponding water CA. **(C)** The typical discharge–charge profiles of Li-O_2 batteries when relative humidity is 45% (Wu et al., 2017b).

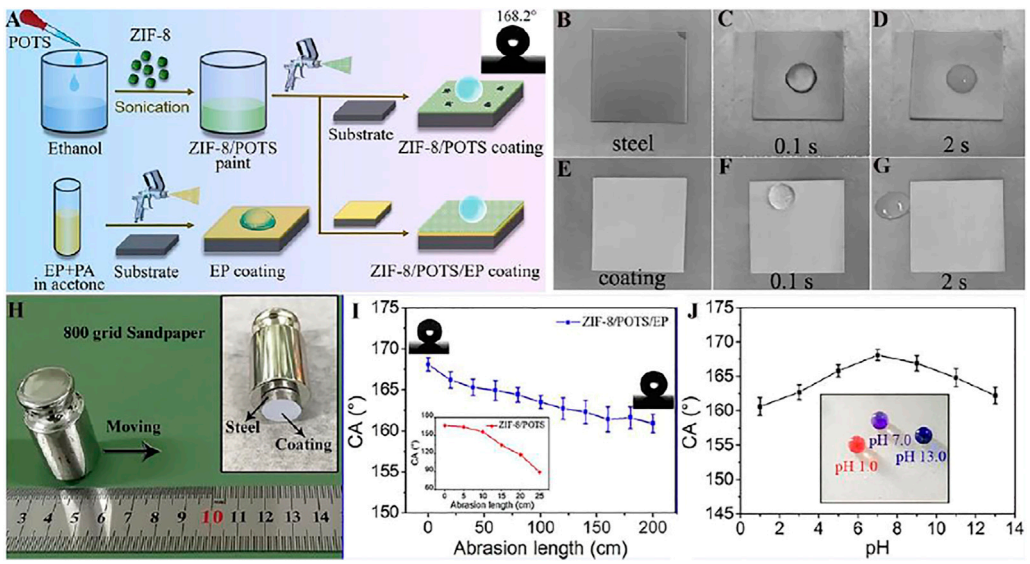

FIGURE 11 | (A) The manufacturing process of EP coating, superhydrophobic ZIF-8/POTS coating and ZIF-8/POTS/EP coating. The pictures of **(B–D)** Q235 steel sheet and **(E–G)** ZIF-8/POTS/EP coating after **(B,D)** 2 h in –20°C refrigerator, and after **(C,F)** 0.1s and **(D,G)** 2 s of dripping 0°C water droplets on their surfaces. **(H)** The schematic of sandpaper abrasion test, and **(I)** the change of abrasion length on the CA. **(J)** The change of pH values of water droplet on the CA of ZIF-8/POTS/EP coating, inset picture is the photograph of litmus colored water droplets with different pH value on ZIF-8/POTS/EP coating (Chen et al., 2021).

Zhi et al. (Zhi and Zhang, 2018) first formed three-dimensional nanopores crosslinked network by the volatilization of pore-forming agents during calcination, then make the silica nanoparticles attached on the pore structure is formed on the double scale structure, thus forming a kind of superhydrophobic coating, a coating made of surface display WCA is 157.9°, which method is simple, and low coating can be applied in the solar cell cover glass.

Others

The principle of superhydrophobic anti-icing (Maitra et al., 2014; Boinovich et al., 2015; Liu et al., 2020b) is to cut down the contact

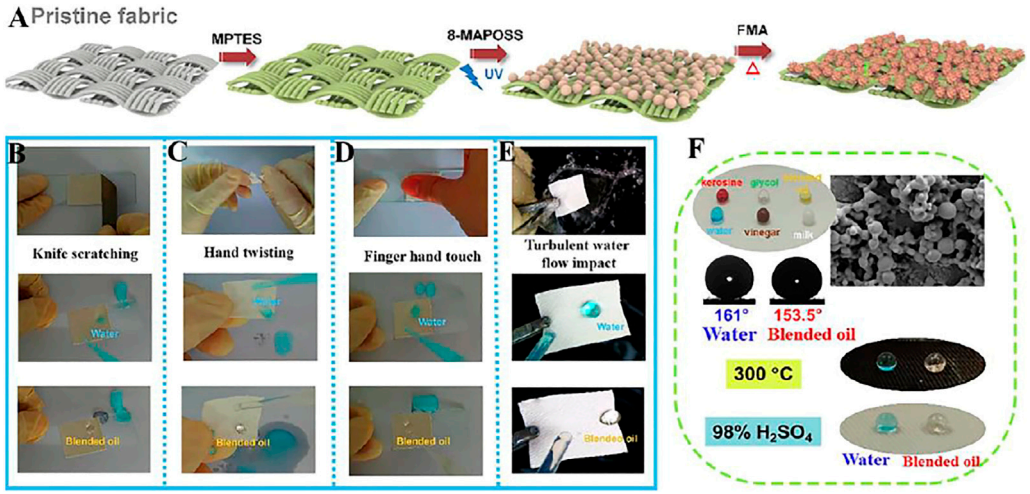

FIGURE 12 | (A) Schematic diagram of manufacturing process of Fabric-S-MAPOSS-F; Durability tests through **(B)** knife-scratching, **(C)** hand twisting, **(D)** finger hand touch, and **(E)** turbulent water flow impact. **(F)** Common droplets (kerisine, dyed with oil red dye; glycol, colorless; blended oil, yellow; water; vinegar, brown; milk, lacte) on fabric, and liquid repellency of Fabric-S-MAPOSS-F after immersion in 98% H_2SO_4 for 30 min and 300°C heating for 2 h (Luo et al., 2020).

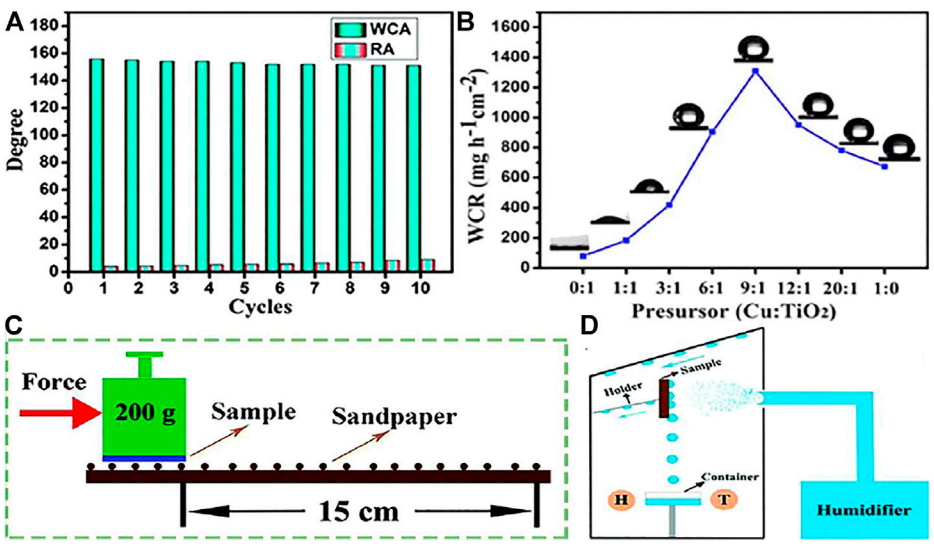

FIGURE 13 | (A) WCA and RA on the surface after abrasion test. **(B)** Water collection rate changed with the precursor of Cu and TiO_2. **(C)** Schematic of the abrasion test. **(D)** Schematic diagram of self-made fog collection system, H and T represent the humidity thermometer (Zhu and Guo, 2016a).

area between water drop and the superhydrophobic surface, and postpone the frozen time of water droplets on the surface. Meanwhile, before freezing, water droplets slide down with the help of gravity, reducing the possibility surface icing.

Chen et al. (Chen et al., 2021) structed a superhydrophobic composite coating on the basis of MOF (ZIF-8) nanoparticles and organic resins, which shows superhydrophobicity and the water contact angle is 168.2° because of the rough structure of ZIF-8 nanoparticles and the low surface energy (**Figure 11A**). After being rubbed with sandpaper or immersed in different pH value (**Figures 11H–J**), the superhydrophobicity can still be maintained, showing that the coating has excellent wear resistance and chemical stability. **Figures 11B–G** shows the freezing process of the coating surface after dripping 0°C water and the results reveal that the ZIF-8/POTS/EP superhydrophobic coating exhibits great anti-icing properties.

A superhydrophobic surface with a low rolling angle helps to reduce the resistance of the water surface, and the existence of the surface microstructure can make the liquid flow through the superhydrophobic surface to form a gas-liquid two-phase flow, resulting in a slip flow phenomenon, reducing the velocity gradient on the boundary surface, thereby reducing the resistance of the liquid flowing through the solid surface (Venkateshan et al., 2016; Zheng et al., 2020).

Luo et al. (Luo et al., 2020) prepared a sturdy and durable fluorinated 8-Methacryl polyhedral oligomeric silsesquioxane Cage Mixture-based superamphiphobic fabric (Fabrics-S-MAPOSS-F) (**Figure 12A**), which could easily float on the surface of water or mixed oil, and could resist high temperature and acid corrosion (**Figure 12F**). The navigation speed of Fabrics-S-MAPOSS-F in water and mixed oil is increased by 2.5 times, and the drag reduction rate is up to 154.7%. As shown in **Figure 12B–E**, the mechanical stability of the superamphiphobic fabric is evaluated through knife-scratching, finger hand touch, hand twisting, and turbulent water flow impact, the results show that Fabrics-S-MAPOSS-F is still superhydrophobic.

The beetle (Zhu et al., 2018c; Zhu et al., 2019; Zhu et al., 2021e) uses the special structure of the shell to collect water to provide itself with water resources. The cactus spines have a round cone-shaped wedge structure with Laplace pressure and surface energy gradient on the surface to achieve water collection (Zhu et al., 2016b). Inspired by natural creatures, lots of superhydrophobic materials are developed for water collection (Zhang et al., 2021b; Zhu et al., 2021f).

Zhu et al. (Zhu and Guo, 2016a) used copper particles and titanium dioxide particles to prepare coatings with superhydrophobic properties which can be used for water collection (**Figure 13D**). As shown in **Figure 13B**, when the molar ratio of the prepared sample precursor is 9:1, the water collection rate is the biggest water collection rate of 1309.9 mg h^{-1} cm^{-2}, and showed an approximate WCA and RA of 155.11, 4.51, respectively. After sandpaper friction (**Figure 13C**), it is observed that there is no great change in WCA and RA (**Figure 13A**) due to the excellent adhesion of epoxy resin is helpful to improve the surface firmness, indicating that the coating has excellent mechanical wear resistance.

CONCLUSION

Superhydrophobic materials with outstanding mechanical and chemical stability are highly vital in practical application. This review elaborates the progress of mechanical–chemical superhydrophobic materials in recent years. Firstly, the typical superwetting models are introduced, such as "Young's contact," "Wenzel," "Cassie," "Wenzel–Cassie," "Lotus," and "Gecko" model. Secondly, some mechanical–chemical superhydrophobic models and corresponding tests to evaluate mechanical and chemical durability are discussed. Finally, the application of these mechanical–chemical superhydrophobic materials is described. Although great scientific progress has been made in the research of durable superhydrophobic surfaces, up to now, almost no superhydrophobic surface can withstand all types of wear required by strict industrial requirements and commercial standards. Therefore, the following are some of our views and opinions:

(1) There are a great many studies to increase the mechanical properties of superhydrophobic materials, and there are many differences in the durability tests carried out. However, unified standards to measure the durability of superhydrophobic materials are lacking and should be formulated.
(2) At present, the durable superhydrophobic surface has not been widely employed in practical application, which indicates that the development of durable superhydrophobic surface should take practical application into consideration.
(3) In the preparation of superhydrophobic materials, many used organic materials are harmful to the human body and environment. Environment-friendly materials and green preparation technology are highly recommended.

We believe that a comprehensive and depth review will provide strategic guidance for the development of multifunctional durable superhydrophobic materials, and that the most challenging aspect is to create a durable superhydrophobic material without affecting wettability. We believe that a comprehensive review can provide new ideas for the development and application of superhydrophobic materials. The research of durable superhydrophobic materials is constantly developing and innovating, and its research will become a hot development direction in the next few years.

AUTHOR CONTRIBUTIONS

QL was responsible for literature retrieval and manuscript writing. HZ and SJ reviewed and edited the manuscript. JP, XC, HZ, and XD revised the manuscript.

FUNDING

This project was supported by the Fundamental Research Funds for the Central Universities (CZY19005).

REFERENCES

Bixler, G. D., and Bhushan, B. (2012). Bioinspired Rice Leaf and Butterfly Wing Surface Structures Combining Shark Skin and Lotus Effects. *Soft Matter* 8, 11271–11284. doi:10.1039/C2SM26655E

Bixler, G. D., and Bhushan, B. (2014). Rice- and Butterfly-Wing Effect Inspired Self-Cleaning and Low Drag Micro/Nanopatterned Surfaces in Water, Oil, and Air Flow. *Nanoscale* 6, 76–96. doi:10.1039/C3NR04755E

Boinovich, L. B., and Emelyanenko, A. M. (2013). Anti-Icing Potential of Superhydrophobic Coatings. *Mendeleev Commun.* 23, 3–10. doi:10.1016/j.mencom.2013.01.002

Boinovich, L. B., Emelyanenko, A. M., and Emelyanenko, K. A. (2015). Effect of Decanol Vapors on the Delay in Water Droplet Crystallization on Superhydrophobic Substrates. *J. Phys. Chem. C* 119, 8718–8724. doi:10.1021/acs.jpcc.5b00990

Bormashenko, E. (2019). Apparent Contact Angles for Reactive Wetting of Smooth, Rough, and Heterogeneous Surfaces Calculated from the Variational Principles. *J. Colloid Interface Sci.* 537, 597–603. doi:10.1016/j.jcis.2018.11.068

Cassie, A. B. D., and Baxter, S. (1944). Wettability of Porous Surfaces. *Trans. Faraday Soc.* 40, 546–551. doi:10.1039/TF9444000546

Chen, H., Wang, F., Fan, H., Hong, R., and Li, W. (2021). Construction of Mof-Based Superhydrophobic Composite Coating with Excellent Abrasion Resistance and

Durability for Self-Cleaning, Corrosion Resistance, Anti-icing, and Loading-Increasing Research. *Chem. Eng. J.* 408, 127343. doi:10.1016/j.cej.2020.127343

Chen, L., Si, Y., Zhu, H., Jiang, T., and Guo, Z. (2016). A Study on the Fabrication of Porous Pvdf Membranes by In-Situ Elimination and Their Applications in Separating Oil/Water Mixtures and Nano-Emulsions. *J. Membr. Sci.* 520, 760–768. doi:10.1016/j.memsci.2016.08.026

Cheng, Q., Liu, C., and Liu, S. (2019a). Fabrication of a Robust Superhydrophobic Polyurethane Sponge for Oil-Water Separation. *Surf. Eng.* 35, 403–410. doi:10.1080/02670844.2018.1429204

Cheng, Y., Miao, D., Kong, L., Jiang, J., and Guo, Z. (2019b). Preparation and Performance Test of the Super-hydrophobic Polyurethane Coating Based on Waste Cooking Oil. *Coatings* 9, 861. doi:10.3390/coatings9120861

Chung, J.-S., Kim, B. G., Shim, S., Kim, S.-E., Sohn, E.-H., Yoon, J., et al. (2012). Silver-Perfluorodecanethiolate Complexes Having Superhydrophobic, Antifouling, Antibacterial Properties. *J. Colloid Interface Sci.* 366, 64–69. doi:10.1016/j.jcis.2011.09.080

Cui, M., Xu, C., Shen, Y., Tian, H., Feng, H., and Li, J. (2018). Electrospinning Superhydrophobic Nanofibrous Poly(Vinylidene Fluoride)/Stearic Acid Coatings with Excellent Corrosion Resistance. *Thin Solid Films* 657, 88–94. doi:10.1016/j.tsf.2018.05.008

Deng, L., Li, P., Liu, K., Wang, X., and Hsiao, B. S. (2019). Robust Superhydrophobic Dual Layer Nanofibrous Composite Membranes with a Hierarchically Structured Amorphous Polypropylene Skin for Membrane Distillation. *J. Mat. Chem. A* 7, 11282–11297. doi:10.1039/C9TA02662B

Deng, X., Mammen, L., Butt, H.-J., and Vollmer, D. (2012). Candle Soot as a Template for a Transparent Robust Superamphiphobic Coating. *Science* 335, 67–70. doi:10.1126/science.1207115

Dong, T., Li, Q., Nie, K., Jiang, W., Li, S., Hu, X., et al. (2020). Facile Fabrication of Marine Algae-Based Robust Superhydrophobic Sponges for Efficient Oil Removal from Water. *ACS Omega* 5, 21745–21752. doi:10.1021/acsomega.0c02731

Eum, K. Y., Phiri, I., Kim, J. W., Choi, W. S., Ko, J. M., and Jung, H. (2019). Superhydrophobic and Superoleophilic Nickel Foam for Oil/Water Separation. *Korean J. Chem. Eng.* 36, 1313–1320. doi:10.1007/s11814-019-0308-9

Feng, X., Guan, H., Wang, Z., Niu, S., and Han, Z. (2021). Biomimetic Slippery Pdms Film with Papillae-like Microstructures for Antifogging and Self-Cleaning. *Coatings* 11, 238. doi:10.3390/coatings11020238

Fu, Y., Xu, F., Weng, D., Li, X., Li, Y., and Sun, J. (2019). Superhydrophobic Foams with Chemical- and Mechanical-Damage-Healing Abilities Enabled by Self-Healing Polymers. *ACS Appl. Mat. Interfaces* 11, 37285–37294. doi:10.1021/acsami.9b11858

Gao, L., and McCarthy, T. J. (2006). The "Lotus Effect" Explained: Two Reasons Why Two Length Scales of Topography Are Important. *Langmuir* 22, 2966–2967. doi:10.1021/la0532149

Ghasemlou, M., Daver, F., Ivanova, E. P., and Adhikari, B. (2019). Bio-Inspired Sustainable and Durable Superhydrophobic Materials: From Nature to Market. *J. Mat. Chem. A* 7, 16643–16670. doi:10.1039/C9TA05185F

Gu, J., Fan, H., Li, C., Caro, J., and Meng, H. (2019a). Back Cover: Robust Superhydrophobic/Superoleophilic Wrinkled Microspherical MOF@rGO Composites for Efficient Oil-Water Separation (Angew. Chem. Int. Ed. 16/2019). *Angew. Chem. Int. Ed.Angewandte Chem. Int. Ed.* 58, 5464. doi:10.1002/anie.201902736

Gu, J., Fan, H., Li, C., Caro, J., and Meng, H. (2019b). Robust Superhydrophobic/Superoleophilic Wrinkled Microspherical MOF@rGO Composites for Efficient Oil-Water Separation. *Angew. Chem. Int. Ed.* 58, 5297–5301. doi:10.1002/anie.201814487

Guo, J., Deka, B. J., Wong, P. W., Sun, J., and An, A. K. (2021). Fabrication of Robust Green Superhydrophobic Hybrid Nanofiber-Nanosphere Membrane for Membrane Distillation. *Desalination* 520, 115314. doi:10.1016/j.desal.2021.115314

Hegazy, A. A. (2001). Effect of Dust Accumulation on Solar Transmittance through Glass Covers of Plate-type Collectors. *Renew. Energy* 22, 525–540. doi:10.1016/S0960-1481(00)00093-8

Hong, S. K., Kim, H., Lee, H., Lim, G., and Cho, S. J. (2022). A Pore-Size Tunable Superhydrophobic Membrane for High-Flux Membrane Distillation. *J. Membr. Sci.* 641, 119862. doi:10.1016/j.memsci.2021.119862

Hou, Y., Wang, Z., Guo, J., Shen, H., Zhang, H., Zhao, N., et al. (2015). Facile Fabrication of Robust Superhydrophobic Porous Materials and Their Application in Oil/Water Separation. *J. Mat. Chem. A* 3, 23252–23260. doi:10.1039/C5TA05612H

Hu, H., Wen, J., Bao, L., Jia, L., Song, D., Song, B., et al. (2017). Significant and Stable Drag Reduction with Air Rings Confined by Alternated Superhydrophobic and Hydrophilic Strips. *Sci. Adv.* 3, e1603288. doi:10.1126/sciadv.1603288

Hu, Y., Zhu, Y., Wang, H., Wang, C., Li, H., Zhang, X., et al. (2017). Facile Preparation of Superhydrophobic Metal Foam for Durable and High Efficient Continuous Oil-Water Separation. *Chem. Eng. J.* 322, 157–166. doi:10.1016/j.cej.2017.04.034

Huang, J., Yang, M., Zhang, H., and Zhu, J. (2021). Solvent-Free Fabrication of Robust Superhydrophobic Powder Coatings. *ACS Appl. Mat. Interfaces* 13, 1323–1332. doi:10.1021/acsami.0c16582

Huang, Y., Stogin, B. B., Sun, N., Wang, J., Yang, S., and Wong, T. S. (2017). A Switchable Cross-Species Liquid Repellent Surface. *Adv. Mat.* 29, 1604641. doi:10.1002/adma.201604641

Huettel, M. (2022). Oil Pollution of Beaches. *Curr. Opin. Chem. Eng.* 36, 100803. doi:10.1016/j.coche.2022.100803

Ji, C., Zhu, Z., Zhong, L., Zhang, W., and Wang, W. (2021). Design of Firm-Pore Superhydrophobic Fibrous Membrane for Advancing the Durability of Membrane Distillation. *Desalination* 519, 115185. doi:10.1016/j.desal.2021.115185

Ji, Q., Xiao, X., Ye, Z., and Yu, N. (2019). Fabrication of Durable Superhydrophobic Coating on Fabrics Surface for Oil/Water Separation. *Polym. Compos.* 40, 2019–2028. doi:10.1002/pc.24982

Jin, M., Feng, X., Feng, L., Sun, T., Zhai, J., Li, T., et al. (2005). Superhydrophobic Aligned Polystyrene Nanotube Films with High Adhesive Force. *Adv. Mat.* 17, 1977–1981. doi:10.1002/adma.200401726

Jung, Y. C., and Bhushan, B. (2009). Mechanically Durable Carbon Nanotube–Composite Hierarchical Structures with Superhydrophobicity, Self-Cleaning, and Low-Drag. *ACS Nano* 3, 4155–4163. doi:10.1021/nn901509r

Kong, Y., Zhang, S., Gao, Y., Cheng, X., Kong, W., Qi, Y., et al. (2022). Low-Temperature Carbonization Synthesis of Carbon-Based Super-hydrophobic Foam for Efficient Multi-State Oil/Water Separation. *J. Hazard. Mater.* 423, 127064. doi:10.1016/j.jhazmat.2021.127064

Kwon, W.-T., Park, K., Han, S. D., Yoon, S. M., Kim, J. Y., Bae, W., et al. (2010). Investigation of Water Separation from Water-In-Oil Emulsion Using Electric Field. *J. Industrial Eng. Chem.* 16, 684–687. doi:10.1016/j.jiec.2010.07.018

Lafuma, A., and Quéré, D. (2003). Superhydrophobic States. *Nat. Mater* 2, 457–460. doi:10.1038/nmat924

Lan, X., Zhang, B., Wang, J., Fan, X., and Zhang, J. (2021). Hydrothermally Structured Superhydrophobic Surface with Superior Anti-corrosion, Anti-bacterial and Anti-icing Behaviors. *Colloids Surfaces A Physicochem. Eng. Aspects* 624, 126820. doi:10.1016/j.colsurfa.2021.126820

Laqbaqbi, M., Sanmartino, J., Khayet, M., García-Payo, C., and Chaouch, M. (2017). Fouling in Membrane Distillation, Osmotic Distillation and Osmotic Membrane Distillation. *Appl. Sci.* 7, 334. doi:10.3390/app7040334

Lee, K.-M., Ngo, C.-V., Jeong, J.-Y., Jeon, E.-c., Je, T.-J., and Chun, D.-M. (2017). Fabrication of an Anisotropic Superhydrophobic Polymer Surface Using Compression Molding and Dip Coating. *Coatings* 7, 194. doi:10.3390/coatings7110194

Lee, S. A., Yang, J. W., Choi, S., and Jang, H. W. (2021). Nanoscale Electrodeposition: Dimension Control and 3d Conformality. *Exploration* 1 (3), 20210012. doi:10.1002/EXP.20210012

Lee, Y., Chung, Y.-W., Park, J., Park, K., Seo, Y., Hong, S.-N., et al. (2020). Lubricant-Infused Directly Engraved Nano-Microstructures for Mechanically Durable Endoscope Lens with Anti-biofouling and Anti-fogging Properties. *Sci. Rep.* 10, 17454. doi:10.1038/s41598-020-74517-8

Li, J., Zhou, Y., Wang, W., Du, F., and Ren, L. (2020a). A Bio-Inspired Superhydrophobic Surface for Fog Collection and Directional Water Transport. *J. Alloys Compd.* 819, 152968. doi:10.1016/j.jallcom.2019.152968

Li, M., Li, Y., Xue, F., and Jing, X. (2019b). A Robust and Versatile Superhydrophobic Coating: Wear-Resistance Study upon Sandpaper Abrasion. *Appl. Surf. Sci.* 480, 738–748. doi:10.1016/j.apsusc.2019.03.001

Li, S., Liu, Y., Tian, Z., Liu, X., Han, Z., and Ren, L. (2020b). Biomimetic Superhydrophobic and Antibacterial Stainless-Steel Mesh via Double-Potentiostatic Electrodeposition and Modification. *Surf. Coatings Technol.* 403, 126355. doi:10.1016/j.surfcoat.2020.126355

Li, Z., Marlena, J., Pranantyo, D., Nguyen, B. L., and Yap, C. H. (2019a). A Porous Superhydrophobic Surface with Active Air Plastron Control for Drag Reduction and Fluid Impalement Resistance. *J. Mat. Chem. A* 7, 16387–16396. doi:10.1039/C9TA02745A

Liang, Z., Zhou, Z., Zhao, L., Dong, B., and Wang, S. (2020). Fabrication of Transparent, Durable and Self-Cleaning Superhydrophobic Coatings for Solar Cells. *New J. Chem.* 44, 14481–14489. doi:10.1039/D0NJ01402H

Liao, Y., Zheng, G., Huang, J. J., Tian, M., and Wang, R. (2020). Development of Robust and Superhydrophobic Membranes to Mitigate Membrane Scaling and Fouling in Membrane Distillation. *J. Membr. Sci.* 601, 117962. doi:10.1016/j.memsci.2020.117962

Liu, C., Liu, Q., Jin, R., Lin, Z., Qiu, H., and Xu, Y. (2020b). Mechanism Analysis and Durability Evaluation of Anti-icing Property of Superhydrophobic Surface. *Int. J. Heat Mass Transf.* 156, 119768. doi:10.1016/j.ijheatmasstransfer.2020.119768

Liu, J., Ye, L., Sun, Y., Hu, M., Chen, F., Wegner, S., et al. (2020a). Elastic Superhydrophobic and Photocatalytic Active Films Used as Blood Repellent Dressing. *Adv. Mat.* 32, 1908008. doi:10.1002/adma.201908008

Liu, K., Yao, X., and Jiang, L. (2010). Recent Developments in Bio-Inspired Special Wettability. *Chem. Soc. Rev.* 39, 3240–3255. doi:10.1039/B917112F

Liu, M., Chen, J., Cai, X., Han, Y., and Xiong, S. (2018). Oil-water Pre-separation with a Novel Axial Hydrocyclone. *Chin. J. Chem. Eng.* 26, 60–66. doi:10.1016/j.cjche.2017.06.021

Liu, T., Wang, J., Yang, J., Huang, Q., Chi, Y., and Yan, J. (2017). Contamination of Fresh Water by Petroleum Sludge. *Petroleum Sci. Technol.* 35, 413–418. doi:10.1080/10916466.2016.1263209

Liu, Y., Fu, K., Liu, J., Tian, Y., Zhang, H., Wang, R., et al. (2019a). Design and Preparation of a Multi-Fluorination Organic Superhydrophobic Coating with High Mechanical Robustness and Icing Delay Ability. *Appl. Surf. Sci.* 497, 143663. doi:10.1016/j.apsusc.2019.143663

Liu, Y., Gu, H., Jia, Y., Liu, J., Zhang, H., Wang, R., et al. (2019b). Design and Preparation of Biomimetic Polydimethylsiloxane (Pdms) Films with Superhydrophobic, Self-Healing and Drag Reduction Properties via Replication of Shark Skin and Si-Atrp. *Chem. Eng. J.* 356, 318–328. doi:10.1016/j.cej.2018.09.022

Lou, X., Huang, Y., Yang, X., Zhu, H., Heng, L., and Xia, F. (2020). External Stimuli Responsive Liquid-Infused Surfaces Switching between Slippery and Nonslippery States: Fabrications and Applications. *Adv. Funct. Mat.* 30, 1901130. doi:10.1002/adfm.201901130

Lu, K.-J., Zuo, J., and Chung, T.-S. (2016). Tri-Bore Pvdf Hollow Fibers with a Super-hydrophobic Coating for Membrane Distillation. *J. Membr. Sci.* 514, 165–175. doi:10.1016/j.memsci.2016.04.058

Lu, Y., Sathasivam, S., Song, J., Crick, C. R., Carmalt, C. J., Parkin, I. P., et al. (2015). Robust Self-Cleaning Surfaces that Function when Exposed to Either Air or Oil. *Science* 347 (6226), 1132–1135. doi:10.1126/science.aaa0946

Luo, G., Wen, L., Yang, K., Li, X., Xu, S., Pi, P., et al. (2020). Robust and Durable Fluorinated 8-Maposs-Based Superamphiphobic Fabrics with Buoyancy Boost and Drag Reduction. *Chem. Eng. J.* 383, 123125. doi:10.1016/j.cej.2019.123125

Luo, J., Gao, S., Luo, H., Wang, L., Huang, X., Guo, Z., et al. (2021). Superhydrophobic and Breathable Smart Mxene-Based Textile for Multifunctional Wearable Sensing Electronics. *Chem. Eng. J.* 406, 126898. doi:10.1016/j.cej.2020.126898

Lv, J., Gong, Z., He, Z., Yang, J., Chen, Y., Tang, C., et al. (2017). 3D Printing of a Mechanically Durable Superhydrophobic Porous Membrane for Oil-Water Separation. *J. Mat. Chem. A* 5, 12435–12444. doi:10.1039/C7TA02202F

Lv, J., Song, Y., Jiang, L., and Wang, J. (2014). Bio-Inspired Strategies for Anti-icing. *ACS Nano* 8, 3152–3169. doi:10.1021/nn406522n

Ma, W., Ding, Y., Zhang, M., Gao, S., Li, Y., Huang, C., et al. (2020). Nature-Inspired Chemistry toward Hierarchical Superhydrophobic, Antibacterial and Biocompatible Nanofibrous Membranes for Effective Uv-Shielding, Self-Cleaning and Oil-Water Separation. *J. Hazard. Mater.* 384, 121476. doi:10.1016/j.jhazmat.2019.121476

Maitra, T., Tiwari, M. K., Antonini, C., Schoch, P., Jung, S., Eberle, P., et al. (2014). On the Nanoengineering of Superhydrophobic and Impalement Resistant Surface Textures below the Freezing Temperature. *Nano Lett.* 14, 172–182. doi:10.1021/nl4037092

Milionis, A., Loth, E., and Bayer, I. S. (2016). Recent Advances in the Mechanical Durability of Superhydrophobic Materials. *Adv. Colloid Interface Sci.* 229, 57–79. doi:10.1016/j.cis.2015.12.007

Monteiro, A., Cardoso, J., Guerra, N., Ribeiro, E., Viegas, C., Cabo Verde, S., et al. (2022). Exposure and Health Effects of Bacteria in Healthcare Units: An Overview. *Appl. Sci.* 12, 1958. doi:10.3390/app12041958

Nishimoto, S., and Bhushan, B. (2013). Bioinspired Self-Cleaning Surfaces with Superhydrophobicity, Superoleophobicity, and Superhydrophilicity. *RSC Adv.* 3, 671–690. doi:10.1039/C2RA21260A

Oh, J., Dana, C. E., Hong, S., Román, J. K., Jo, K. D., Hong, J. W., et al. (2017). Exploring the Role of Habitat on the Wettability of Cicada Wings. *ACS Appl. Mat. Interfaces* 9, 27173–27184. doi:10.1021/acsami.7b07060

Ou, J., Wang, Z., Wang, F., Xue, M., Li, W., and Amirfazli, A. (2016). Washable and Antibacterial Superhydrophbic Fabric. *Appl. Surf. Sci.* 364, 81–85. doi:10.1016/j.apsusc.2015.12.113

Peng, C., Chen, Z., and Tiwari, M. K. (2018). All-Organic Superhydrophobic Coatings with Mechanochemical Robustness and Liquid Impalement Resistance. *Nat. Mater* 17, 355–360. doi:10.1038/s41563-018-0044-2

Qiao, J.-h., Jin, X., Qin, J.-h., Liu, H.-t., Luo, Y., and Zhang, D.-k. (2018). A Super-hard Superhydrophobic Fe-Based Amorphous Alloy Coating. *Surf. Coatings Technol.* 334, 286–291. doi:10.1016/j.surfcoat.2017.11.046

Rico, V., Mora, J., García, P., Agüero, A., Borrás, A., González-Elipe, A. R., et al. (2020). Robust Anti-icing Superhydrophobic Aluminum Alloy Surfaces by Grafting Fluorocarbon Molecular Chains. *Appl. Mater. Today* 21, 100815. doi:10.1016/j.apmt.2020.100815

Rocha e Silva, F. C. P., Rocha e Silva, N. M. P., da Silva, I. A., Ferreira Brasileiro, P. P., Luna, J. M., Rufino, R. D., et al. (2018). Oil Removal Efficiency Forecast of a Dissolved Air Flotation (DAF) Reduced Scale Prototype Using the Dimensionless Number of Damköhler. *J. Water Process Eng.* 23, 45–49. doi:10.1016/j.jwpe.2018.01.019

Sanchez, C., Arribart, H., and Giraud Guille, M. M. (2005). Biomimetism and Bioinspiration as Tools for the Design of Innovative Materials and Systems. *Nat. Mater* 4, 277–288. doi:10.1038/nmat1339

Saththasivam, J., Loganathan, K., and Sarp, S. (2016). An Overview of Oil-Water Separation Using Gas Flotation Systems. *Chemosphere* 144, 671–680. doi:10.1016/j.chemosphere.2015.08.087

Shang, Q., Liu, C., Chen, J., Yang, X., Hu, Y., Hu, L., et al. (2020). Sustainable and Robust Superhydrophobic Cotton Fabrics Coated with Castor Oil-Based Nanocomposites for Effective Oil-Water Separation. *ACS Sustain. Chem. Eng.* 8, 7423–7435. doi:10.1021/acssuschemeng.0c01469

She, Z., Li, Q., Wang, Z., Tan, C., Zhou, J., and Li, L. (2014). Highly Anticorrosion, Self-Cleaning Superhydrophobic Ni-Co Surface Fabricated on AZ91D Magnesium Alloy. *Surf. Coatings Technol.* 251, 7–14. doi:10.1016/j.surfcoat.2014.03.060

Si, Y., Zhu, H., Chen, L., Jiang, T., and Guo, Z. (2015). A Multifunctional Transparent Superhydrophobic Gel Nanocoating with Self-Healing Properties. *Chem. Commun.* 51, 16794–16797. doi:10.1039/C5CC06977G

Song, F., Wu, C., Chen, H., Liu, Q., Liu, J., Chen, R., et al. (2017b). Water-Repellent and Corrosion-Resistance Properties of Superhydrophobic and Lubricant-Infused Super Slippery Surfaces. *RSC Adv.* 7, 44239–44246. doi:10.1039/C7RA04816E

Song, J., Zhao, D., Han, Z., Xu, W., Lu, Y., Liu, X., et al. (2017a). Super-Robust Superhydrophobic Concrete. *J. Mat. Chem. A* 5, 14542–14550. doi:10.1039/C7TA03526H

Stark, A. Y., Subarajan, S., Jain, D., Niewiarowski, P. H., and Dhinojwala, A. (2016). Superhydrophobicity of the Gecko Toe Pad: Biological Optimization versus Laboratory Maximization. *Phil. Trans. R. Soc. A* 374, 20160184. doi:10.1098/rsta.2016.0184

Su, C., Horseman, T., Cao, H., Christie, K., and Lin, S. (2019). Robust Superhydrophobic Membrane for Membrane Distillation with Excellent Scaling Resistance. *Environ. Sci. Technol.* 53 (20), 11801–11809. doi:10.1021/acs.est.9b04362

Su, X., Li, H., Lai, X., Zhang, L., Wang, J., Liao, X., et al. (2017). Vapor-Liquid Sol-Gel Approach to Fabricating Highly Durable and Robust Superhydrophobic Polydimethylsiloxane@Silica Surface on Polyester Textile for Oil-Water Separation. *ACS Appl. Mat. Interfaces* 9, 28089–28099. doi:10.1021/acsami.7b08920

Sun, Z., Liao, T., Liu, K., Jiang, L., Kim, J. H., and Dou, S. X. (2014). Superhydrophobic Materials: Fly-Eye Inspired Superhydrophobic Anti-fogging Inorganic Nanostructures (Small 15/2014). *Small* 10, 3000. doi:10.1002/smll.201470089

Sutar, R. S., Manadeshi, S. D., Latthe, S. S., Kulal, S. R., Salunkhe, G. D., Rangar, K. K., et al. (2020). Superhydrophobic Coating Using TiO 2 NPs/PMHS Composite for Self-Cleaning Application. *Macromol. Symp.* 393, 2000033. doi:10.1002/masy.202000033

Syafiq, A., Pandey, A. K., Adzman, N. N., and Rahim, N. A. (2018). Advances in Approaches and Methods for Self-Cleaning of Solar Photovoltaic Panels. *Sol. Energy* 162, 597–619. doi:10.1016/j.solener.2017.12.023

Tang, S., Chang, X., Li, M., Ge, T., Niu, S., Wang, D., et al. (2021). Fabrication of Calcium Carbonate Coated-Stainless Steel Mesh for Efficient Oil-Water Separation via Bacterially Induced Biomineralization Technique. *Chem. Eng. J.* 405, 126597. doi:10.1016/j.cej.2020.126597

Tian, X., Verho, T., and Ras, R. H. A. (2016). Moving Superhydrophobic Surfaces toward Real-World Applications. *Science* 352, 142–143. doi:10.1126/science.aaf2073

Tudu, B. K., and Kumar, A. (2019). Robust and Durable Superhydrophobic Steel and Copper Meshes for Separation of Oil-Water Emulsions. *Prog. Org. Coatings* 133, 316–324. doi:10.1016/j.porgcoat.2019.04.069

Tuteja, A., Choi, W., Ma, M., Mabry, J. M., Mazzella, S. A., Rutledge, G. C., et al. (2007). Designing Superoleophobic Surfaces. *Science* 318, 1618–1622. doi:10.1126/science.1148326

Venkateshan, D. G., Amrei, M. M., Hemeda, A. A., Cullingsworth, Z., Corbett, J., and Vahedi Tafreshi, H. (2016). Failure Pressures and Drag Reduction Benefits of Superhydrophobic Wire Screens. *Colloids Surfaces A Physicochem. Eng. Aspects* 511, 247–254. doi:10.1016/j.colsurfa.2016.09.087

Verho, T., Bower, C., Andrew, P., Franssila, S., Ikkala, O., and Ras, R. H. A. (2011). Mechanically Durable Superhydrophobic Surfaces. *Adv. Mat.* 23, 673–678. doi:10.1002/adma.201003129

Waghmare, P. R., Gunda, N. S. K., and Mitra, S. K. (2014). Under-Water Superoleophobicity of Fish Scales. *Sci. Rep.* 4, 7454. doi:10.1038/srep07454

Wang, D., Sun, Q., Hokkanen, M. J., Zhang, C., Lin, F. Y., Liu, Q., et al. (2020c). Design of Robust Superhydrophobic Surfaces. *Nature* 582 (7810), 55–59. doi:10.1038/s41586-020-2331-8

Wang, F., Lei, S., Ou, J., Li, C., and Li, W. (2019). Novel All-Natural Material for Oil/Water Separation. *Ind. Eng. Chem. Res.* 58, 1924–1931. doi:10.1021/acs.iecr.8b05535

Wang, F., Pi, J., Song, F., Feng, R., Xu, C., Wang, X.-L., et al. (2020a). A Superhydrophobic Coating to Create Multi-Functional Materials with Mechanical/Chemical/Physical Robustness. *Chem. Eng. J.* 381, 122539. doi:10.1016/j.cej.2019.122539

Wang, Q., Bai, J., Dai, B., Yang, Z., Guo, S., Yang, L., et al. (2017). Robust Superhydrophobic Diamond Microspheres for No-Loss Transport of Corrosive Liquid Microdroplets. *Chem. Commun.* 53, 2355–2358. doi:10.1039/C6CC09806A

Wang, T., Huang, L., Liu, Y., Li, X., Liu, C., Handschuh-Wang, S., et al. (2020b). Robust Biomimetic Hierarchical Diamond Architecture with a Self-Cleaning, Antibacterial, and Antibiofouling Surface. *ACS Appl. Mat. Interfaces* 12, 24432–24441. doi:10.1021/acsami.0c02460

Wan, X., Zhao, Y., Li, Z., and Li, L. (2022). Emerging Polymeric Electrospun Fibers: From Structural Diversity to Application in Flexible Bioelectronics and Tissue Engineering. *Exploration* 2 (1), 20210029. doi:10.1002/EXP.20210029

Wang, Y., Zhao, S., Guo, Z., Huang, J., and Liu, W. (2021). Multi-Layer Superhydrophobic Nickel Foam (Nf) Composite for Highly Efficient Water-In-Oil Emulsion Separation. *Colloids Surfaces A Physicochem. Eng. Aspects* 628, 127299. doi:10.1016/j.colsurfa.2021.127299

Wang, Z., Gao, X., Wen, G., Tian, P., Zhong, L., Gou, X., et al. (2018). Robust Silicon Dioxide @ Epoxy Resin Micronanosheet Superhydrophobic Omnipotent Protective Coating for Applications. *Colloids Surfaces A Physicochem. Eng. Aspects* 550, 9–19. doi:10.1016/j.colsurfa.2018.04.036

Wang, Z., Peng, S., Wu, L., and Weng, Z. (2022). Construction of Ultra-long Service Life Self-Cleaning Slippery Surface on Superhydrophobicity Functionalized by Atrp Treatment. *Chem. Eng. J.* 428, 130997. doi:10.1016/j.cej.2021.130997

Wen, M., Wang, L., Zhang, M., Jiang, L., and Zheng, Y. (2014). Antifogging and Icing-Delay Properties of Composite Micro- and Nanostructured Surfaces. *ACS Appl. Mat. Interfaces* 6, 3963–3968. doi:10.1021/am405232e

Wenzel, R. N., and Robert, N. (1936). Resistance of Solid Surfaces to Wetting by Water. *Ind. Eng. Chem.* 28, 988–994. doi:10.1021/ie50320a024

Wu, B., Lu, S., Xu, W., Cheng, Y., and Cui, S. (2018). A Robust and Repairable Superhydrophobic Co5zn21 Alloy Surface on a Zinc Substrate. *New J. Chem.* 42, 5408–5414. doi:10.1039/C7NJ04201A

Wu, M., Ma, B., Pan, T., Chen, S., and Sun, J. (2016). Silver-Nanoparticle-Colored Cotton Fabrics with Tunable Colors and Durable Antibacterial and Self-Healing Superhydrophobic Properties. *Adv. Funct. Mat.* 26, 569–576. doi:10.1002/adfm.201504197

Wu, S., Yi, J., Zhu, K., Bai, S., Liu, Y., Qiao, Y., et al. (2017b). A Super-hydrophobic Quasi-Solid Electrolyte for Li-O2Battery with Improved Safety and Cycle Life in Humid Atmosphere. *Adv. Energy Mat.* 7, 1601759. doi:10.1002/aenm.201601759

Wu, T., Xu, W.-h., Guo, K., Xie, H., and Qu, J.-p. (2021). Efficient Fabrication of Lightweight Polyethylene Foam with Robust and Durable Superhydrophobicity for Self-Cleaning and Anti-icing Applications. *Chem. Eng. J.* 407, 127100. doi:10.1016/j.cej.2020.127100

Wu, Y., Jia, S., Wang, S., Qing, Y., Yan, N., Wang, Q., et al. (2017a). A Facile and Novel Emulsion for Efficient and Convenient Fabrication of Durable Superhydrophobic Materials. *Chem. Eng. J.* 328, 186–196. doi:10.1016/j.cej.2017.07.023

Xia, F., and Jiang, L. (2008). Bio-Inspired, Smart, Multiscale Interfacial Materials. *Adv. Mat.* 20, 2842–2858. doi:10.1002/adma.200800836

Xie, H., Wei, J., Duan, S., Zhu, Q., Yang, Y., Chen, K., et al. (2022). Non-Fluorinated and Durable Photothermal Superhydrophobic Coatings Based on Attapulgite Nanorods for Efficient Anti-icing and Deicing. *Chem. Eng. J.* 428, 132585. doi:10.1016/j.cej.2021.132585

Xu, J., Hou, Y., Lian, Z., Yu, Z., Wang, Z., and Yu, H. (2020b). Bio-Inspired Design of Bi/Tridirectionally Anisotropic Sliding Superhydrophobic Titanium Alloy Surfaces. *Nanomaterials* 10, 2140. doi:10.3390/nano10112140

Xu, W., Yi, P., Gao, J., Deng, Y., Peng, L., and Lai, X. (2020a). Large-Area Stable Superhydrophobic Poly(Dimethylsiloxane) Films Fabricated by Thermal Curing via a Chemically Etched Template. *ACS Appl. Mat. Interfaces* 12, 3042–3050. doi:10.1021/acsami.9b19677

Yan, X., Zhu, X., Ruan, Y., Xing, T., Chen, G., and Zhou, C. (2020). Biomimetic, Dopamine-Modified Superhydrophobic Cotton Fabric for Oil-Water Separation. *Cellulose* 27, 7873–7885. doi:10.1007/s10570-020-03336-x

Yang, S., Chen, L., Wang, S., Liu, S., Xu, Q., Zhu, J., et al. (2022). Honeycomb-Like Cobalt Hydroxide Nanosheets Induced Basalt Fiber Fabrics with Robust and Durable Superhydrophobicity for Anti-icing and Oil-Water Separation. *J. Hazard. Mater.* 429, 128284. doi:10.1016/j.jhazmat.2022.128284

Yang, Y., Li, H., Cheng, S., Zou, G., Wang, C., and Lin, Q. (2014). Robust Diamond Meshes with Unique Wettability Properties. *Chem. Commun.* 50, 2900–2903. doi:10.1039/C4CC00258J

Ye, H., Zhu, L., Li, W., Liu, H., and Chen, H. (2017). Simple Spray Deposition of a Water-Based Superhydrophobic Coating with High Stability for Flexible Applications. *J. Mater. Chem. A* 10, 1039. doi:10.1039/c7ta02118f

Ye, Z., Li, S., Zhao, S., Deng, L., Zhang, J., and Dong, A. (2021). Textile Coatings Configured by Double-Nanoparticles to Optimally Couple Superhydrophobic and Antibacterial Properties. *Chem. Eng. J.* 420, 127680. doi:10.1016/j.cej.2020.127680

Yokoi, N., Manabe, K., Tenjimbayashi, M., and Shiratori, S. (2015). Optically Transparent Superhydrophobic Surfaces with Enhanced Mechanical Abrasion Resistance Enabled by Mesh Structure. *ACS Appl. Mat. Interfaces* 7, 4809–4816. doi:10.1021/am508726k

Yoon, J., Min, R., Kim, H., Ahn, G., and Lee, H. (2020b). WetlogTyle Superhydrophobic Antifogging Coatings for Optical Sensors. *Adv. Mater.* 32 (34), e2002710. doi:10.1002/adma.202002710

Yoon, J., Ryu, M., Kim, H., Ahn, G. N., Yim, S. J., Kim, D. P., et al. (2020a). Wet-Style Superhydrophobic Antifogging Coatings for Optical Sensors. *Adv. Mat.* 32, 2002710. doi:10.1002/adma.202002710

Young, T. (1805). Iii. An Essay on the Cohesion of Fluids. *Phil. Trans. R. Soc.* 95, 65–87. doi:10.1098/rstl.1805.0005

Yu, S. Q., Ling, Y. H., Wang, R. G., Zhang, J., Qin, F., and Zhang, Z. J. (2018). Constructing Superhydrophobic Wo3@Tio2 Nanoflake Surface beyond Amorphous Alloy against Electrochemical Corrosion on Iron Steel. *Appl. Surf. Sci.* 436, 527–535. doi:10.1016/j.apsusc.2017.11.211

Zhang, F., Qian, H., Wang, L., Wang, Z., Du, C., Li, X., et al. (2018). Superhydrophobic Carbon Nanotubes/Epoxy Nanocomposite Coating by

Facile One-step Spraying. *Surf. Coatings Technol.* 341, 15–23. doi:10.1016/j.surfcoat.2018.01.045

Zhang, F., Xu, D., Zhang, D., Ma, L., Wang, J., Huang, Y., et al. (2021a). A Durable and Photothermal Superhydrophobic Coating with Entwinned Cnts-Sio2 Hybrids for Anti-icing Applications. *Chem. Eng. J.* 423, 130238. doi:10.1016/j.cej.2021.130238

Zhang, M. C., Jing, Y., Zhang, J., Sheng, Z. Z., Hou, Y. Q., Xu, J. D., et al. (2022). Performance Prediction of Magnetorheological Fluid-Based Liquid Gating Membrane by Kriging Machine Learning Method. *Inter. Mater.* 1 (1), 157–169. doi:10.1002/idm2.12005

Zhang, Y., Wang, T., Wu, M., and Wei, W. (2021b). Durable Superhydrophobic Surface with Hierarchical Microstructures for Efficient Water Collection. *Surf. Coatings Technol.* 419, 127279. doi:10.1016/j.surfcoat.2021.127279

Zhao, X., Park, D. S., Choi, J., Park, S., Soper, S. A., and Murphy, M. C. (2020). Robust, Transparent, Superhydrophobic Coatings Using Novel Hydrophobic/Hydrophilic Dual-Sized Silica Particles. *J. Colloid Interface Sci.* 574, 347–354. doi:10.1016/j.jcis.2020.04.065

Zheng, K., Zhang, J., Dodiuk, H., Kenig, S., Barry, C., Sun, H., et al. (2020). Effect of Superhydrophobic Composite Coatings on Drag Reduction in Laminar Flow. *ACS Appl. Polym. Mat.* 2, 1614–1622. doi:10.1021/acsapm.0c00049

Zheng, Z., Liao, C., Xia, Y., Chai, W., Xie, C., Zhang, W., et al. (2021). Facile Fabrication of Robust, Biomimetic and Superhydrophobic Polymer/Graphene-Based Coatings with Self-Cleaning, Oil-Water Separation, Anti-icing and Corrosion Resistance Properties. *Colloids Surfaces A Physicochem. Eng. Aspects* 627, 127164. doi:10.1016/j.colsurfa.2021.127164

Zhi, J., and Zhang, L.-Z. (2018). Durable Superhydrophobic Surface with Highly Antireflective and Self-Cleaning Properties for the Glass Covers of Solar Cells. *Appl. Surf. Sci.* 454, 239–248. doi:10.1016/j.apsusc.2018.05.139

Zhong, L., Zhu, H., Wu, Y., and Guo, Z. (2018). Understanding How Surface Chemistry and Topography Enhance Fog Harvesting Based on the Superwetting Surface with Patterned Hemispherical Bulges. *J. Colloid Interface Sci.* 525, 234–242. doi:10.1016/j.jcis.2018.04.061

Zhou, F., Zhang, Y., Zhang, D., Zhang, Z., Fu, F., Zhang, X., et al. (2021). Fabrication of Robust and Self-Healing Superhydrophobic Pet Fabrics Based on Profiled Fiber Structure. *Colloids Surfaces A Physicochem. Eng. Aspects* 609, 125686. doi:10.1016/j.colsurfa.2020.125686

Zhou, S., Hao, G., Zhou, X., Jiang, W., Wang, T., Zhang, N., et al. (2016). One-pot Synthesis of Robust Superhydrophobic, Functionalized Graphene/polyurethane Sponge for Effective Continuous Oil-Water Separation. *Chem. Eng. J.* 302, 155–162. doi:10.1016/j.cej.2016.05.051

Zhu, H., Cai, S., Zhou, J., Li, S., Wang, D., Zhu, J., et al. (2021f). Integration of Water Collection and Purification on Cactus- and Beetle-Inspired Eco-Friendly Superwettable Materials. *Water Res.* 206, 117759. doi:10.1016/j.watres.2021.117759

Zhu, H., Duan, R., Wang, X., Yang, J., Wang, J., Huang, Y., et al. (2018c). Prewetting Dichloromethane Induced Aqueous Solution Adhered on Cassie Superhydrophobic Substrates to Fabricate Efficient Fog-Harvesting Materials Inspired by Namib Desert Beetles and Mussels. *Nanoscale* 10, 13045–13054. doi:10.1039/C8NR03277G

Zhu, H., and Guo, Z. (2016a). Hybrid Engineered Materials with High Water-Collecting Efficiency Inspired by Namib Desert Beetles. *Chem. Commun.* 52, 6809–6812. doi:10.1039/C6CC01894G

Zhu, H., Guo, Z., and Liu, W. (2016a). Biomimetic Water-Collecting Materials Inspired by Nature. *Chem. Commun.* 52, 3863–3879. doi:10.1039/C5CC09867J

Zhu, H., and Guo, Z. (2016b). Understanding the Separations of Oil/Water Mixtures from Immiscible to Emulsions on Super-wettable Surfaces. *J. Bionic Eng.* 13, 1–29. doi:10.1016/S1672-6529(14)60156-6

Zhu, H., Huang, Y., Lou, X., and Xia, F. (2019). Beetle-Inspired Wettable Materials: From Fabrications to Applications. *Mater. Today Nano* 6, 100034. doi:10.1016/j.mtnano.2019.100034

Zhu, H., Huang, Y., Lou, X., and Xia, F. (2021a). Bioinspired Superwetting Surfaces for Biosensing. *VIEW* 2, 20200053. doi:10.1002/VIW.20200053

Zhu, H., Huang, Y., Lou, X., and Xia, F. (2021e). Bioinspired Superwetting Surfaces for Biosensing. *VIEW* 2, 20200053. doi:10.1002/VIW.20200053

Zhu, H., Huang, Y., and Xia, F. (2020c). Environmentally Friendly Superhydrophobic Osmanthus Flowers for Oil Spill Cleanup. *Appl. Mater. Today* 19, 100607. doi:10.1016/j.apmt.2020.100607

Zhu, H., Huang, Y., Zhang, S., Jin, S., Lou, X., and Xia, F. (2021c). A Universal, Multifunctional, High-Practicability Superhydrophobic Paint for Waterproofing Grass Houses. *NPG Asia Mater* 13, 47. doi:10.1038/s41427-021-00315-x

Zhu, H., Tu, Y., Luo, C., Dai, L., Lou, X., Huang, Y., et al. (2021b). Temperature-Triggered Switchable Superwettability on a Robust Paint for Controllable Photocatalysis. *Cell. Rep. Phys. Sci.* 2, 100669. doi:10.1016/j.xcrp.2021.100669

Zhu, H., Wu, L., Meng, X., Wang, Y., Huang, Y., Lin, M., et al. (2020b). An Anti-uv Superhydrophobic Material with Photocatalysis, Self-Cleaning, Self-Healing and Oil/Water Separation Functions. *Nanoscale* 12, 11455–11459. doi:10.1039/D0NR01038C

Zhu, H., Yang, F., Li, J., and Guo, Z. (2016b). High-Efficiency Water Collection on Biomimetic Material with Superwettable Patterns. *Chem. Commun.* 52, 12415–12417. doi:10.1039/C6CC05857D

Zhu, K., Zhang, J., Hao, Z., Tan, H., Zhang, W., Liu, Y., et al. (2018b). Fabrication of Durable Superhydrophobic Coatings Based on a Novel Branched Fluorinated Epoxy. *Chem. Eng. J.* 351, 569–578. doi:10.1016/j.cej.2018.06.116

Zhu, K., Zhang, J., Zhang, H., Tan, H., Zhang, W., Liu, Y., et al. (2018a). Fabrication of Durable Superhydrophobic Coatings Based on a Novel Branched Fluorinated Epoxy. *Chem. Eng. J.* 351, 569–578. doi:10.1016/j.cej.2018.06.116

Zhu, P., Wang, Y., Chu, H., and Wang, L. (2021d). Superhydrophobicity Preventing Surface Contamination as a Novel Strategy against Covid-19. *J. Colloid Interface Sci.* 600, 613–619. doi:10.1016/j.jcis.2021.05.031

Zhu, Q., Chu, Y., Wang, Z., Chen, N., Lin, L., Liu, F., et al. (2013). Robust Superhydrophobic Polyurethane Sponge as a Highly Reusable Oil-Absorption Material. *J. Mat. Chem. A* 1, 5386–5393. doi:10.1039/C3TA00125C

Zhu, T., Cheng, Y., Huang, J., Xiong, J., Ge, M., Mao, J., et al. (2020a). A Transparent Superhydrophobic Coating with Mechanochemical Robustness for Anti-icing, Photocatalysis and Self-Cleaning. *Chem. Eng. J.* 399, 125746. doi:10.1016/j.cej.2020.125746

Conflict of Interest: The authors declare that the research was conducted in the absence of any commercial or financial relationships that could be construed as a potential conflict of interest.

Publisher's Note: All claims expressed in this article are solely those of the authors and do not necessarily represent those of their affiliated organizations, or those of the publisher, the editors, and the reviewers. Any product that may be evaluated in this article, or claim that may be made by its manufacturer, is not guaranteed or endorsed by the publisher.

frontiers | Frontiers in Bioengineering and Biotechnology

TYPE Review
PUBLISHED 30 August 2022
DOI 10.3389/fbioe.2022.1001616

OPEN ACCESS

EDITED BY
Feilong Zhang,
Nanyang Technological University, Singapore

REVIEWED BY
Chao Ma,
Tsinghua University, China
Jinlin Song,
Chongqing Medical University, China

*CORRESPONDENCE
Yunfan Zhang,
bdzj_yunfan@163.com
Si Chen,
elisa02@163.com
Bing Han,
kqbinghan@bjmu.edu.cn

†These authors have contributed equally to this work

SPECIALTY SECTION
This article was submitted to Bionics and Biomimetics, a section of the journal Frontiers in Bioengineering and Biotechnology

RECEIVED 23 July 2022
ACCEPTED 05 August 2022
PUBLISHED 30 August 2022

CITATION
Zhang X, Bai R, Sun Q, Zhuang Z, Zhang Y, Chen S and Han B (2022), Bio-inspired special wettability in oral antibacterial applications. *Front. Bioeng. Biotechnol.* 10:1001616. doi: 10.3389/fbioe.2022.1001616

Bio-inspired special wettability in oral antibacterial applications

Xin Zhang[1,2†], Rushui Bai[1,2†], Qiannan Sun[1,2], Zimeng Zhuang[1,2], Yunfan Zhang[1,2*], Si Chen[1,2*] and Bing Han[1,2*]

[1]Department of Orthodontics, School and Hospital of Stomatology, Peking University, Beijing, China, [2]National Engineering Laboratory for Digital and Material Technology of Stomatology & Beijing Key Laboratory of Digital Stomatology, Beijing, China

Most oral diseases originate from biofilms whose formation is originated from the adhesion of salivary proteins and pioneer bacteria. Therefore, antimicrobial materials are mainly based on bactericidal methods, most of which have drug resistance and toxicity. Natural antifouling surfaces inspire new antibacterial strategies. The super wettable surfaces of lotus leaves and fish scales prompt design of biomimetic oral materials covered or mixed with super wettable materials to prevent adhesion. Bioinspired slippery surfaces come from pitcher plants, whose porous surfaces are infiltrated with lubricating liquid to form superhydrophobic surfaces to reduce the contact with liquids. It is believed that these new methods could provide promising directions for oral antimicrobial practice, improving antimicrobial efficacy.

KEYWORDS

bio-inspired, super wettability, low-fouling surfaces, antibacterial, oral biofilm management

Introduction

Most oral diseases originate from plaque biofilms, different compositions and locations of which result in distinct diseases. Acid-producing plaques on the edges of teeth, orthodontic archwires or brackets, or restorations lead to caries; residual biofilm after root canal treatment may lead to inflammation recurrence and even apical paracentesis; subgingival plaque of teeth and implants may lead to periodontitis and periimplantitis; biofilms on dentures are associated with local and general inflammation, such as mucosal inflammation and aspiration pneumonia (Li et al., 2010; Jiao et al., 2019; Park et al., 2020). As shown in Figure 1(Ramburrun et al., 2021), biofilm forms as follows: bacteria attachment, growth, maturation, and dispersion (Jiao et al., 2019). A glycoprotein is naturally present in saliva, which makes almost all surfaces in the mouth being covered with it, and bacteria can adhere to it (Ramburrun et al., 2021). In the process of plaque biofilm formation, first bacteria attaching to teeth are called pioneer species, such as *Streptococcus spp.* and *Actinomyces spp.* These pioneer species promote the subsequent colonization and create anoxic conditions, which play a crucial role in the formation and maturation of biofilm (Lad et al., 2014). Above progresses suggest that inhibiting the adhesion of pioneer bacteria is the premise of suppressing palque formation.

Major materials used for inhibiting biofilm formation rely on bactericidal effect, including antibiotics, chlorhexidine, fluoride, etc. However, drug resistance limits the use

of antibiotics; chlorhexidine has a limited effect; antibacterial effect shows in a high concentration of fluoride, that is, difficult to achieve and accompanied by some toxicity (Autio-Gold, 2008; Rošin-Grget et al., 2013; Oh et al., 2017; Ullah et al., 2017; Zhou et al., 2021). Current limitations call for new antibacterial materials. Metal ions and polymetric antimicrobial materials are developed to eliminate bacteria but also face problems such as the toxicity of metal ions (Li et al., 2021; Ramburrun et al., 2021). Zhou et al. used programmable base pair interactions at the nanoscale to make a encapsulated quaternary ammonium group within the dense hydroxyapatite that endowed the composite with long-lasting and local antibacterial activity (Zhou et al., 2022). Now that attachment of salivary proteins and pioneer microbial species is the first step in plaque formation and intermediated by water (Lendenmann et al., 2000; Donlan and Costerton, 2002), managing surface

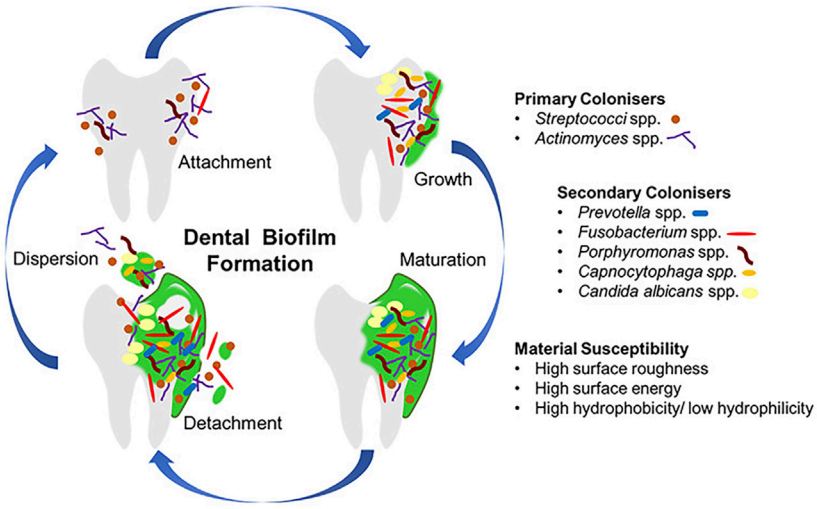

FIGURE 1
The progress of dental biofilm formation. Copyright from ref (Ramburrun et al., 2021).

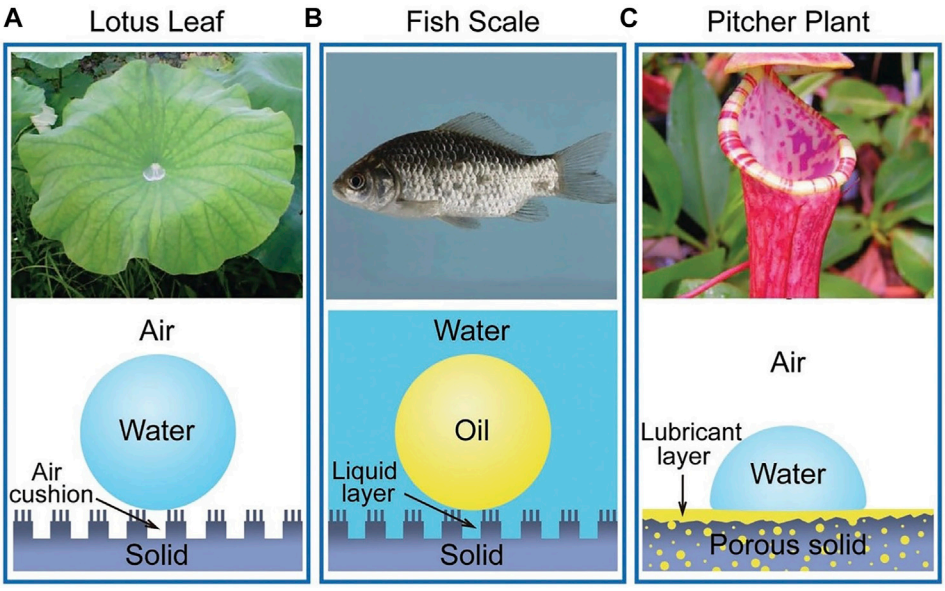

FIGURE 2
The natural anti-fouling surfaces. Copyright from ref (Cao et al., 2016).

TABLE 1 The summary of super wettable material applied in dentistry.

Material	Wettability	Character	Disadvantage
Poly ethylene glycol	Super hydrophilicity	• Form a water layer on the surface. The layer can reduce adhesion	• Poor stabilization
		• A biocompatible polymer	• Lose the anti-fouling ability at 35°
		• Be grafted to substrate or coupled to polyelectrolytes directly	
		• Use silane chemistry to combine with orthodontic wires	• Not be metabolized naturally
		• Use free radical polymerization to synthesize polymers that be grafted to resin	
Zwitterionic polymers (2-methacryloyloxyethyl phosphorylcholine, sulfobetaine methacrylate)	Super hydrophilicity	• Lock a layer of free water on the surface to form a physical or energetic barrier	• May degrade the mechanical properties of mixed materials
		• Coat teeth or enamel directly	
		• Reduce the "coat-inhibition" of other bactericidal materials	
		• Physically mix with flowable resin, inorganic salt materials et al	
		• Graft to or from metal	
Proteins (histatin 5, casein phosphor peptide, bovine serum albumin)	Super hydrophilicity	• Anti-adhesion and promote remineralization	• Need more *in vitro* studies
		• Coat teeth or enamel	
		• Coat orthodontic archwires	
Silica-based materials	Super hydrophobicity	• Supper hydrophobicity reduces the temporal window and spatial possibilities for bio-adhesion events of bacteria from a contaminated droplet.	• The anti-fouling of surfaced created by chemical modification may be not durable
		• Coat titanium implant and orthodontic archwires	
		• Introduced into the resin by branched amino silicone	
Slippery liquid-infused porous surfaces (SLIPS)	Super hydrophobicity (bioinspired slippery surfaces)	• Low-surface-energy porous solids are infiltrated by lubricating liquids to form a stable, immobilized, and smooth liquid-like omniphobic surface	• SLIPS has a little application
		• Immiscible liquids deposited on the SLIPS can be easily removed even under weak shear forces	• Need more *in vivo* and *in vitro* experiments

wettability might be a promising and simple solution to control this process.

Many biological antifouling phenomena in nature are based on special wettability. For example, lotus leaf is superhydrophobic surface to trap a stable air cushion so that outside water has less access to the surface, achieving antifouling (Figure 2A); fish scales can trap a water layer through the super hydrophilic surface to reduce the adhesion of oil in water (Figure 2B); picher plant uses the porous surfaces infiltrating with lubricating liquid to reduce contact with other liquid (Figure 2C) (Cao et al., 2016). The wettability of surface is expressed by the contact angle (CA) of a water droplet on the substrate. Young's equation of CA is

$\cos\theta_Y = \frac{\gamma SV - \gamma SL}{\gamma LV}$. γSV, γSL, and γLV are the solid-liquid, solid-vapor, and liquid-vapor interfacial energies respectively. The CA of hydrophobic surface is >90°; the CA of hydrophilic surfaces is <90°. Proteins and bacteria tend to adhere to a slightly hydrophobic or hydrophilic surface, while less adhesion occurs on the highly hydrophobic or hydrophilic surfaces. Therefore, anti-fouling effect could be achieved by changing wettability of teeth or material surfaces via increasing hydrophobicity (e.g., silica-based materials), like lotus leaves, or hydrophilicity (e.g., zwitterion), like fish scales; or via inspired slippery liquid-infused porous surfaces. In this review, we will summarize the principles and synthesis of bio-inspired materials with super wettability to prevent adhesion, and focus on their dental applications (Table 1.).

Super-hydrophilic material

The surface of fish scales is covered with a layer of hydrophilic components, as well as special nano-structures, which trap water on the surface underwater to resist oil (Liu et al., 2009). Similarly, the teeth or oral material surfaces could also be modified to be super hydrophilic to form a hydration

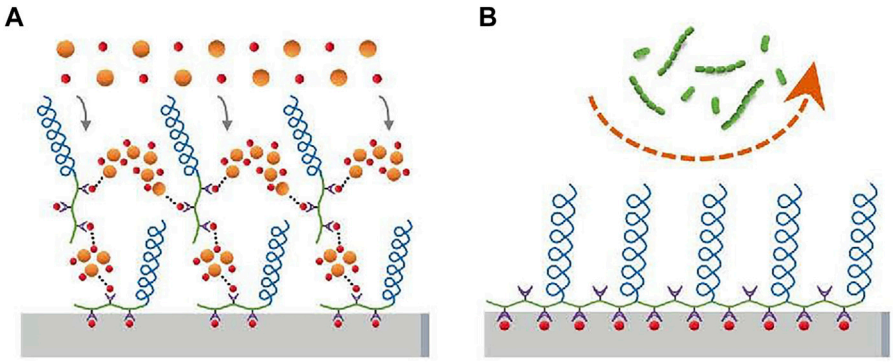

FIGURE 3
PASP-PEG on the enamel surface forms a brush-like barrier that inhibits bacterial adhesion (*S. sanguis* and *S. mutans*). Copyright from ref (Hou et al., 2020).

layer. The tightly bound water layer forms a physical or energetic barrier, making it difficult for microorganisms to adhere and penetrate (Chen et al., 2010; Cazzaniga et al., 2015; Leng et al., 2016).

Poly ethylene glycol

Poly ethylene glycol (PEG) is a biocompatible polymer. PEG has pretty hydrophilicity and can reduce the adhesion of proteins, platelets, and bacteria (Elbert and Hubbell, 1998; Park et al., 1998; Chen et al., 2000; Kenausis et al., 2000; Razatos et al., 2000; Zhu et al., 2001; Harris, 2013). Then anti-adhesion is due to the strong hydrophilicity of polyethylene glycol, which forms a water layer on the surface. The layer can reduce the adsorption of proteins (Harder et al., 1998; Feldman et al., 1999; Harris, 2013). PEG can connect with different terminal functional groups to reduce the protein adhesion to different extents. A relatively long PEG surface will have better resistance (Park et al., 1998).

PEG can be grafted to substrate or coupled to polyelectrolytes directly, such as poly (l-lysine) (PLL) or poly (acrylic acid), and then adhere to the substance as a monolayer (Boulmedais et al., 2004). The layer-by-layer self-assembly of polyelectrolytes on charged surfaces offers another possibility to deposit polyelectrolytes with grafted PEG onto substrates (Decher and Hong, 1991). PEG can be used to compound a comb-like graft copolymer (poly (l-lysine)-grafted-poly (ethylene glycol)—PLL-g-PEG), with a polycationic PLL backbone and PEG side chains. The polymers can be adsorbed to negatively charged metallic oxide spontaneously, such as titanium or niobium oxide surfaces, to form a stable, densely packed PEG monomolecular adlayer to reduce the adhesion of bacteria (Harris et al., 2004). Poly (aspartic acid)-polyethylene glycol (PASP-PEG) was synthesized by a similar method with high affinity for hydroxyapatite (HA)/tooth surfaces and low toxicity, and promoted mineralization of PASP, like mineralization protein (Hou et al., 2020). And the reason for antiadhesion is as follows (Figure 3): Firstly, a water layer is formed due to hydrophilicity (Lüsse and Arnold, 1996; Aray et al., 2004); in addition, "steric repulsion" can be obtained from the long chain of PASP-PEG, which is an entropic effect concerning the change in free energy associated with confinement and the dehydration of soft polymer chains (Hui et al., 2017). PEG can not only be coupled to polyelectrolytes but also be inserted into polyelectrolyte multilayer. It has been reached that poly (l-glutamic acid)-grafted-poly (ethylene glycol) (PGA-g-PEG) is obtained by modifying the PGA backbone by a PEG, which is inserted into polyelectrolyte multilayer to get the same anti-adhesive effect (Boulmedais et al., 2004). Cui (Cui et al., 2016) used conventional free radical polymerization and changed the feed ration of monomers to synthesize a series of copolymers containing pendants of poly (ethylene glycol) methyl ether methacrylate (PEGMA) and ethylene glycol methacrylate phosphate (Phosmer). And then the copolymer was anchored to hydroxyapatite and enamel to provide inhibition of bacterial adhesion.

Besides coating, PEG hydrogel has been applied in the field of wound dressing, drug delivery, etc (Vimala et al., 2010; Li et al., 2011; Dong et al., 2016; Nitta et al., 2017; Wang et al., 2017; Zhao et al., 2017; Bozuyuk et al., 2018; Shutava et al., 2019). Peng et al. (Peng et al., 2017) bond long-chain PEG chemically and used silane chemistry to combine it with orthodontic wires to avoid *S. mutans* adhesion. It has been demonstrated that PEG can use hydrogen bonding to form a stable water layer to resist adhesion (Figure 4). In their next study (Peng et al., 2020), they used chitosan (CS) and PEG to synthesize a hydrogel by silanization and copolymerization reaction, covering the stainless steel wire. The hydrogen consists of cross-linked PEG and CS chains. The

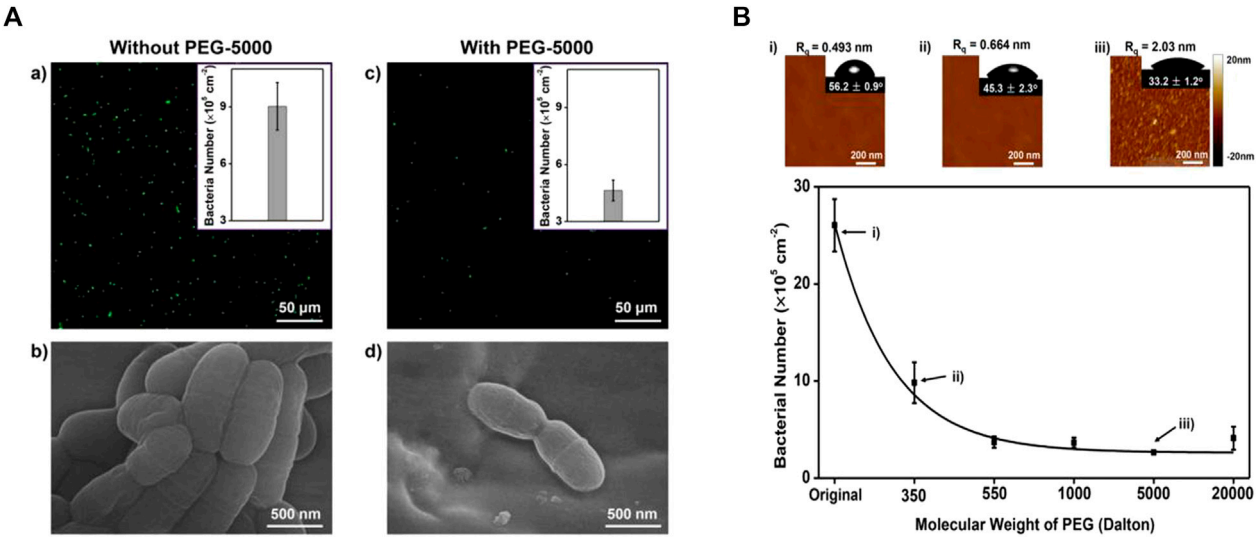

FIGURE 4
(A-a,b) For the stainless steel archwires without PEG coating, significant *S. mutans* adhesion was observed. **(A-c,d)** For the stainless steel archwires coated with PEG of molecular weight 5,000 (PEG-5000), the number of adhered *S. mutans* was greatly reduced. **(B)**When the molecular weight of PEG was increased from 350 to 20,000, the anti-adhesive property of PEG-coated stainless steel archwires increased, which may be due to the relative hydrophilicity of long-chain PEG-modified stainless steel archwires. Reprinted (adapted) with permission from (Peng et al., 2017). Copyright 2017 American Chemical Society.

cross-linked PEG can absorb water effectively through hydrogen bonds to form a thin water layer to provide a pretty anti-adhesive performance, while CS can provide bactericidal function. The antibacterial performance is best when CS/PEG. The surface charge becomes more positive when the portion of CS increased and the anti-adhesive performance will be better.

PEG can also be used in resin-based composites. Poly (ethylene glycol) methyl ether methacrylate (PEGMA) can be synthesized by PEG through free radical polymerization and has been certified to resist biological contamination (Tedjo et al., 2007; Cui et al., 2016). PEGMA can be grafted to polymethyl methacrylate (PMMA) by atmospheric pressure plasma to improve the hydrophilic and anti-adhesive properties of PMMA. It can prevent bacterial adhesion effectively, even though it is coated with salivary. However, this method exposes the alkoxy portion of the glycol chain, so that the degree of hydrophilic improvement is limited, for the hydrophilicity of the alkoxy portion is less than that of hydroxyl (Cui et al., 2016; Lee et al., 2018).

Though PEG was approved to be used in humans in 1992, and the prospects for its application are greatly enhanced, there are still many problems. The stabilization of PEG is poor. It will autoxidize and degrade during storage or handling at room temperature, especially in the presence of transition metal ions, which are present in most biological solutions (Hamburger et al., 1975; Crouzet et al., 1976; Gerhardt and Martens, 1985). Studies have shown that when the temperature rises to 35 °C, PEG brushes lose the anti-fouling ability (Leckband et al., 1999). Moreover, PEG can not be metabolized naturally. These limitations should be considered when applying PEG to oral materials.

Zwitterionic polymers

As for the disadvantages of PEG, the zwitterionic polymer has been considered to be the perfect alternative. Compared with the amphiphilicity of PEG, zwitterionic polymers are super hydrophilic due to the presence of abundant ions and subsequent strong hydration layers (Zheng et al., 2017). The main zwitterions used in dentistry are 2-methacryloyloxyethyl phosphorylcholine (MPC) and sulfobetaine methacrylate (SBMA), of which MPC is the most common.

MPC is a methacrylate with a phospholipid polar group in the side chain (Lewis, 2000). The phospholipids, as the main components of the cell membrane, consist of a hydrophilic head and a hydrophobic tail, so they can form lipid bilayers that have the hydrophilic head to the outside and the hydrophobic tail to the inside, which contribute to the super hydrophilicity of MPC (Ishihara et al., 1990; Mashaghi et al., 2013). Due to the super hydrophilicity, MPC can lock a layer of free water on the surface, which can effectively detach proteins to reduce the adsorption (Ishihara et al., 1998; Yamasaki et al., 2003). On the other hand, the water layer can form a physical or energetic barrier, making it difficult for microorganisms to penetrate or adhere (Chen et al., 2010; Cazzaniga et al., 2015; Leng et al., 2016). K. Hirota's group

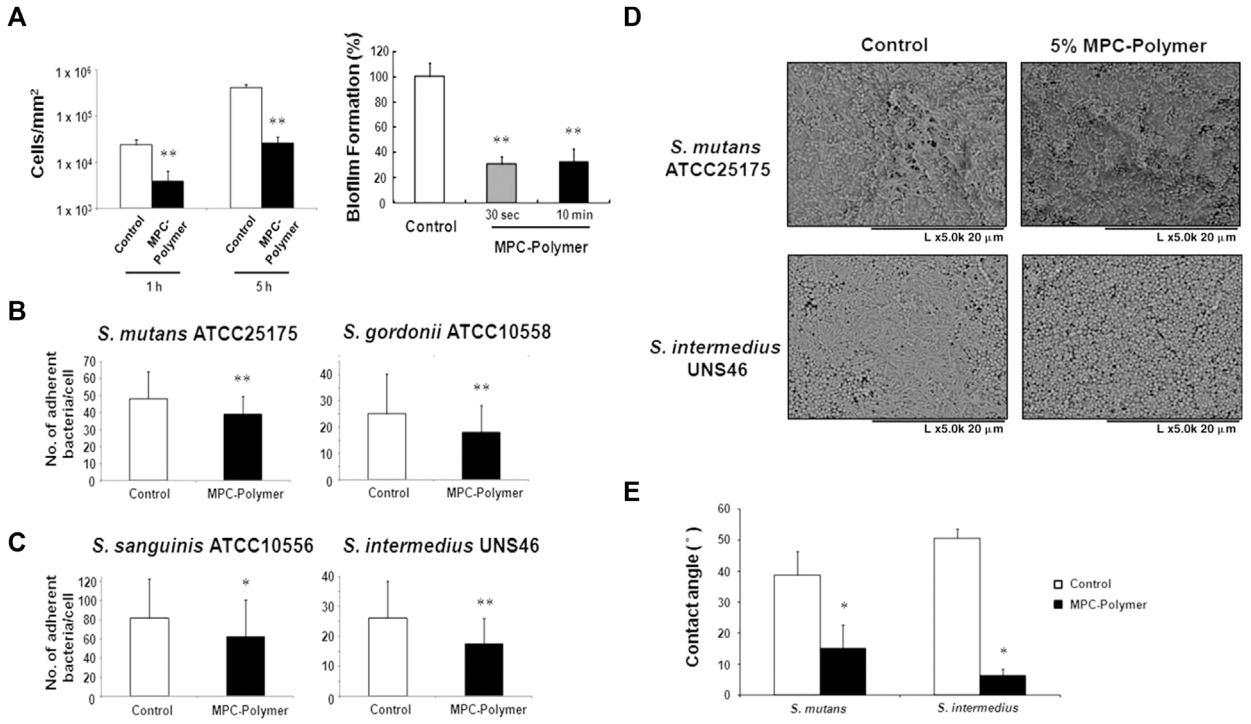

FIGURE 5
(A–C) The effects of MPC-polymer treatment on streptococcal adherence to saliva-coated hydroxyapatite and oral epithelial cells, and biofilm formation of *S. mutans* on saliva-coated hydroxyapatite. The mean number of adherent bacteria ±SD to 1 cell was calculated. $*p < 0.05$ and $**p < 0.01$ compared with the control (without MPC-polymer treatment). The results are representative of 5 different experiments demonstrating similar results. **(D, E)** The effect of MPC-polymer on the adherence of *F. nucleatum* to saliva-coated streptococcal biofilms. MPC-polymer treatment significantly inhibited the adherence of *F. nucleatum* JCM8532 to both S. mutans ATCC25175 and *S. intermedius* UNS46 biofilms when compared with the non-treated control. **(D)** After cultivation, the adhesion of *F. nucleatum* to the streptococcal biofilm was observed by SEM. The results are representative of 5 different experiments demonstrating similar results. **(E)** As an index of hydrophobicity, the surface contact angles of streptococcal biofilm were measured by the horizontal projection technique. $*p < 0.01$ compared with the control (without MPC-polymer treatment). The results are representative of 5 different experiments demonstrating similar results. Copyright from ref (Hirota et al., 2011).

(Hirota et al., 2011) first demonstrated that MPC polymers significantly inhibit the adhesion of many oral bacteria to hydroxyapatite and oral epithelial cells *in vitro*, therefore effectively reducing plaque formation (Figure5). And then it has been demonstrated that MPC can be merged with 2-methacryloyloxyethyl phosphate (MOEP) monomers. For MOEP has Ca^{2+}-binding moieties that can be combined with hydroxyapatite, the compound makes MPC bond with teeth directly, forming a pretty anti-biofouling coating (Kang et al., 2016). Besides teeth, Yumoto (Yumoto et al., 2015) showed that the interaction of butyl in MPC with hydrophobic structural domains in surface proteins of oral epithelial cells made MPC adhere to the oral epithelium and the hydrophilicity of MPC prevented *Porphyromonas gingivalis* from adhering the epithelium. In addition, while MPC adhered to the epithelium, it could prevent periodontics by blocking the binding of TLR2 to reduce producing IL-8 and the natural immune mediated by IL-8. Recent clinical trials using mouthwash containing MPC showed that MPC didinhibit the increase of oral bacteria, especially *Streptococcus pyogenes* (Fujiwara et al., 2019).

MPC can be applied not only todirect anti-adhesion, but also to provide synergistic effects in combination with other antimicrobial agents. Many current oral anti-bacterial materials face the problem that direct contact is required for these materials toinhibit bacteria. In other words, this “contact-inhibition” effect is reduced if the surfaces are covered with salivary proteins. Methacryloyloxydodecylpyridinium bromide (MDPB) is a compound of the antibacterial agent dodecyl pyridinium bromide and a methacryloyl group, and it can copolymerize with other dental monomers (Imazato et al., 1995; Imazato, 2003). MDPB has an obvious limitation of contact inhibition, and introducing MPC into it can reduce the adsorption of salivary, which is conducive to the direct release of antibacterial components to achieve a better effect (Figure 6) (Thongthai et al., 2020). Therefore, combining

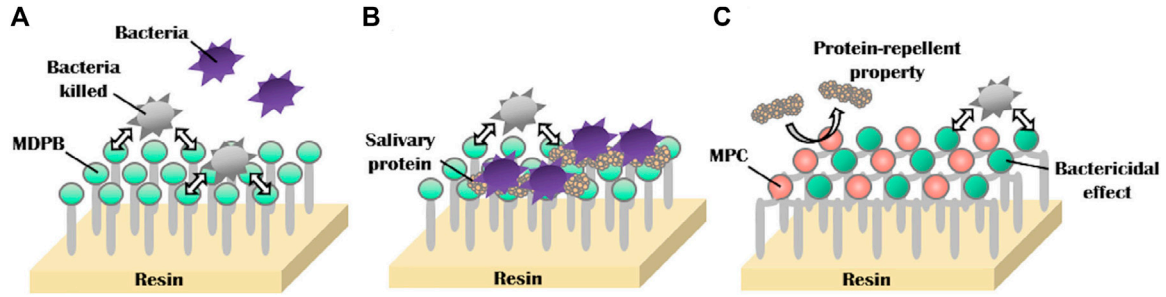

FIGURE 6
Schematic of dual functions of protein repellent property and antibacterial effect. **(A)** Dental resins with immobilized bactericides exhibit antibacterial effects, which depend on the contact inhibition of bacteria. **(B)** However, their effectiveness can be readily reduced by coverage with salivary protein. **(C)** Novel surface coating composed of 12-methacryloyloxydodecylpyrimidinium bromide and 2-methacryloyloxyethyl phosphorylcholine exhibits protein repellent ability and bactericidal effect (Thongthai et al., 2020). Copyright from ref (Thongthai et al., 2020).

hydrophilic MPC with hydrophobic dental restorative materials has become the main direction of current research. Hatsuno, Ishihara, and Nishigochi et al. found that water-soluble MPC could be combined with n-butyl methacrylate (BMA) to form an insoluble copolymer coating, which could be coated on the surface of resinous materials via hydrophobic interaction between the hydrophobic unit of BMA and resin. Pasiree Thongthai used a similar way to introduce MPC into a copolymer that was synthesized by radical polymerization of MDPB, MPC, and BMA in ethanol using 2,20azobisisobutyronitrile (AIBN) as an initiator, and MDPB, MPC, and BMA at mole ratios of 15:15:70. MPC reduced protein adhesion significantly and synergized with MDPB to enhance antibacterial ability (Thongthai et al., 2020). Referring to the experience of MDPB, MPC was subsequently combined with other antimicrobial materials, such as QAM, to overcome the problem of contact-inhibition of antimicrobial materials (Zhang et al., 2015b).

According to the above, MPC can also be combined with other materials in dentistry, e.g., with mineralization-promoting adhesives to provide antibacterial, anti-adhesive, and remineralization-promoting effects (Xie et al., 2017). MPC can be introduced into 3D printing material- PMMA - to achieve anti-adhesive 3D printing without affecting mechanical properties and printing accuracy (Kwon et al., 2021). In addition, MPC can be mixed with a variety of inorganic salt materials in the form of handmade powders to enhance the resistance of bacterial adhesion, such as light-curing fluorine coatings, root canal therapy material, and surface pre-reacted glass-ionomer (Kwon et al., 2019a; Kwon et al., 2019b; Lee et al., 2019). MPC can also be physically mixed and stirred with flowable resin, which also gives the orthodontic bonding agent an antibacterial effect (Park et al., 2020).

MPC has been approved by FDA for its good biocompatibility. But the mechanical properties of dental materials with MPC are degraded, especially when the MPC content is higher than 3% (Zhang et al., 2015a; Kwon et al., 2021).

SBMA and MPC are both amphoteric ions with similar anti-adhesive principles (Zheng et al., 2017). SBMA can be added to PMMA to achieve anti-adhesion (Kwon et al., 2021). SBMA can also be combined with metal, such as titanium and stainless steel, by methods of grafting "grafting from" or "grafting to" (Chou et al., 2017). "Grafting from" methods consist of growing a polymer from a monomer mixture at the surface of the material to modify, and bond it covalently to the surface. The "grafting to (or onto)" methods consist of bonding a polymer at the surface of the material at play and an efficient method to graft zwitterionic heads by this technique is to use glycidyl methacrylate, a biomimetic anchoring group (Zanini et al., 2007; Li et al., 2008; Gao et al., 2009; Xu et al., 2009; Huang et al., 2012; Schlenoff, 2014; Chou et al., 2016).

Peptide

Faced with the above limitations of polyethylene glycols and amphoteric compounds, new strategies have been proposed: protein.

Histatin 5(H5) is a salivary antimicrobial peptide (AMP), that is, naturally present in the salivary glands and is very effective in killing bacteria including *S. mutans* (Madhwani and McBain, 2012; Krzyściak et al., 2015). What's more, it can adhere to enamel well and inhibits demineralization (Yin et al., 2003; Siqueira et al., 2010). Compared with PEG and zwitterion, it has better biocompatibility (Zhou et al., 2021). AMP performance can be enhanced by grafting phosphoserine (S*p*)—a key component in initiating free calcium ion mineralization—to the N-terminal of H5 (Zhou et al., 2020). Later, Zhou et al. continued to set the end of S*p*S*p* (DSP) to increase the S*p* structure, which can enable enamel

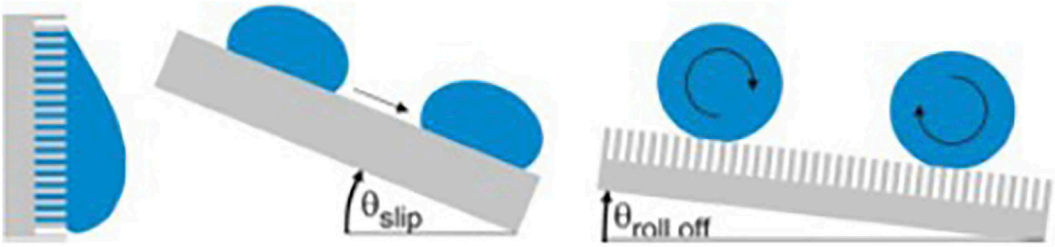

FIGURE 7
Water droplets on super-hydrophobic surfaces. Copyright from (Sterzenbach et al., 2020).

bound with modified H5 to have a pretty hydrophilicity and to resist bacterial adhesion through forming a thin layer of water on the surface (Zhou et al., 2021).

For enhancing the remineralization of teeth, another protein has been found and it can also be anti-adhesive. Casein phosphor peptide (CPP) is a natural phosphorylated peptide in milk that can be obtained by the proteolysis of casein (Meisel et al., 2003; Baum et al., 2013; Dallas et al., 2016). It can bind calcium and improve the remineralization of teeth effectively (Reynolds, 1987; Nongonierma and FitzGerald, 2012). It has been studied that CPP is a negatively charged amphiphilic polypeptide with the hydrophilic end facing outward, which can inhibit the initial adhesion of the *S. mutans* to hydroxyapatite by increasing the hydrophobicity of the HA surface and negative charge (Reynolds and Wong, 1983; Roger et al., 1994; Schüpbach et al., 1996; Fitzgerald, 1998; Colloca et al., 2000; Cross et al., 2005; Song et al., 2015; Yang et al., 2017; Wang et al., 2020).

As for the shortcomings of PEG that it tends to auto-oxidize into aldehydes in the presence of oxygen (Hucknall et al., 2009), Liu *et al.* actively explored other proteins to improve the anti-adhesive effect of orthodontic archwires. Bovine serum albumin (BSA) is an inexpensive and easily available protein with potent anti-adhesive properties to mammalian cells, platelets, and red blood cells (Cai et al., 2015; Jeoung et al., 2015). So Liu et al. chose BSA to be grafted onto orthodontic brackets, resisting the adhesion of bacteria (Liu et al., 2018).

Super-hydrophobic material

Hydrophobic surface of lotus leaf has high CA, giving it anti-fouling ability. This characteristic can be measured by the angle at which the surface tilts when the water drops on the surface begin to roll down (Figure 7). The more hydrophobic the surface is, the larger the CA is, the smaller the angle of inclined surfaces is, and the smaller the area of contact between the liquid and the surface is, which reduces the temporal window and spatial possibilities for bio-adhesion events of bacteria from a contaminated droplet. When immersed in liquid, a liquid-air interface is formed between the hydrophobic surface and the liquid as a protective layer, which is difficult for bacteria to penetrate, thus inhibiting microorganisms from settling and adhering.

Silicon based materials have good hydrophobicity and are widely used in dental materials. The silicification of titanium implants is one of the most common applications. Using silane primer to siliconize the surface of titanium can significantly reduce the surface energy and improve hydrophobicity. Previous studies demonstrated that the preparation of silane primer using 3-acryloxypropyltrimethoysilane + bis-1,2-(triethoxysilyl)ethane increased the contact angle of the titanium surface and hydrophobicity and decreased the surface free energy, without affecting the surface roughness (Matinlinna et al., 2013). It was subsequently demonstrated that these changes in properties reduced the formation of *Candida albicans* colonies (Villard et al., 2015).

Besides titanium, introducing silicon based materials into the synthetic process of resin can give it an anti-adhesive property. Yu et al. synthesized a composite resin containing branched silicone methacrylate (BSM) (Yu et al., 2020; Tong et al., 2021). BSM was synthesized through a reaction between branched amino silicone and isocyanatoethyl methacrylate, and it was incorporated into 2,2-bis [4- (2-hydroxy-3-methacryloxy-propoxy) phenyl] propane (Bis-GMA)/triethyleneglycol dimethacrylate (TEGDMA) (50 wt%/50 wt%) with a series of concentrations to form resin matrices. The experimental composites (EC) were then prepared by mixing different resin matrices with silane BaAlSiO2 fillers. BSM can reduce the volume shrinkage of the composite resin. Adding 10 wt% or more BSM into ECs can make the CA of ECs >120°. With the BSM content increasing, the CA is larger. The addition of 15 wt% or 20 wt% of BSM gives ECs adhesion resistance to *Streptococcus pyogenes* without affecting the mechanical properties, but 30 wt% of BSM reduces the flexural strength of the resin material.

For orthodontic archwires, silicon treatment can also reduce bacterial adhesion. Inspired by the superhydrophobic antifouling principle of lotus leaves, Liu *et al.* (Tong et al., 2021) electrochemically etch orthodontic archwires (AWs) to

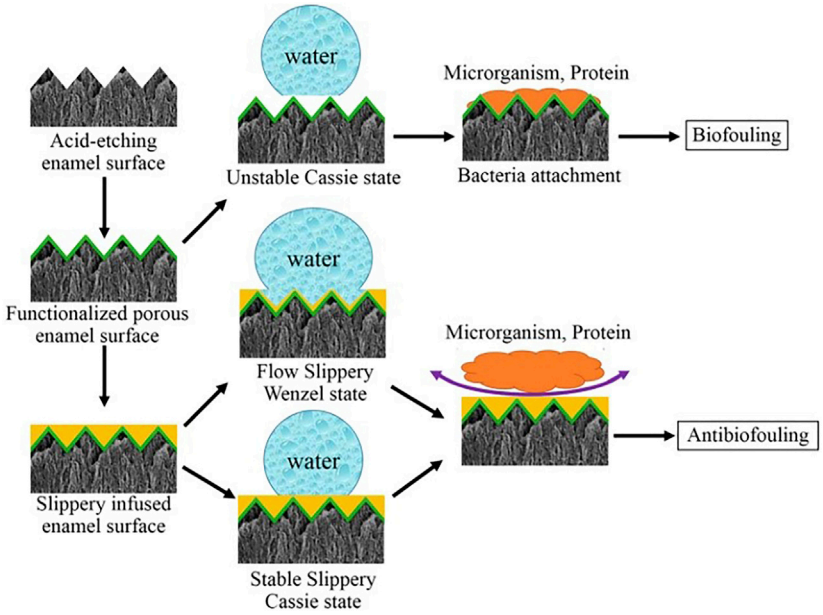

FIGURE 8
The process of anti-fouling on SLIPS. Copyright from ref (Yin et al., 2016).

improve the roughness of orthodontic archwires, after which 1H, 1H, 2H, 2H-perfluorodecyltrimethoxysilane (FAS) was deposited on the prepared AWs in a decompression environment at 80°C overnight. The CA of the treated orthodontic archwires were all above 120° and even reached 150°. Super hydrophobicity caused air to be trapped on the surface, which significantly reduced the actual contact area between the rough AWs and the bacterial suspension. It not only improved the corrosion resistance of the archwires and reduced the release of Ni ions, but also reduced the adhesion of the *S. mutans*.

However, subsequent experiments showed that superhydrophobic surfaces constructed with 1H, 1H, 2H, 2H-perfluorooctyltriethoxysilane lead to the disappearance of the air layer on the surface when it is immersed in water for a long time. The phenomenon is observed for a variety of superhydrophobic surfaces, suggesting that the anti-fouling of surfaces created by chemical modification is not durable (Hwang et al., 2018).

Bioinspired slippery surfaces

In terms of stain prevention, pitcher plants are slightly different from fish scales and lotus leaves. The surface of pitcher plants is micro/nanotextures that lock in special liquids and build a slippery surface to resist stains. From pitcher plants, researchers design slippery liquid-infused porous surfaces (SLIPS), whose low-surface-energy porous solids are infiltrated by lubricating liquids to form a stable, immobilized, and smooth liquid-like omniphobic surface. Immiscible liquids deposited on the SLIPS can be easily removed even under weak shear forces, thus providing great promising for the resistance of fouling organisms (Zhang et al., 2017). The anti-fouling of hydrophobic interfaces created by SLIPS are stronger and more durable than those created by chemical modifications (Epstein et al., 2012; Howell et al., 2014; Amini et al., 2017).

Three important criteria for the design of a stable SLIPS are as follows: 1) the surface prefers to be rough to increase the adhesion of the lubricant and its immobilized surface area; 2) the chemical affinity between the lubricant and the solid should be higher than that between the surrounding fluid and the solid; 3) the lubricant and the surrounding fluid must be largely incompatible (Epstein et al., 2012). Based on the above criteria, Yin *et al.* (Yin et al., 2016) synthesized a SLIPS. Firstly, they use 37% phosphoric acid to etch enamel surfaces to obtain micro/nanoporous surfaces. Then, the surface is functionalized by hydrophobic low-surface energy heptadecafluoro-1,1,2,2-tetra- hydrodecyltrichlorosilane. Subsequent infusion of fluorocarbon lubricants (Fluorinert FC-70) into the polyfluoroalkyl-silanized rough surface results in an enamel surface with the slippery liquid-infused porous surface (SLIPS). The hydrophobic surface has been demonstrated to have an excellent anti-adhesive effect on *S. mutans in vivo* and in rabbits' oral. The mechanism is that functionalized porous enamel surface is slightly hydrophobic which is easy for bacteria to adhere,

while the lippery infused enamel surface has two states and both states is so super hydrophobic that microorganism and proteins are hard to adhere (Figure 8). And then, during simple dipping process, researchers used crystal violets to produce a crystal violet-impregnated slippery so that SLIPS has bactericidal feature (Patir et al., 2021).

SLIPS, as a new anti-fouling method, has few application in the oral field, and the corresponding *in vivo* and *in vitro* experiments need to be enriched, especially the stability in the oral cavity under special conditions.

Conclusion

Inspired by biological anti-fouling phenomena in nature, super hydrophilic, super hydrophobic, and smooth surfaces have been successfully applied in dentistry to resist bacteria effectively. And preventing bacterial adhesion is achieved by an energy barrier or a trapped layer of water/air, that is, difficult for bacteria to penetrate through. However, super wettability dental materials still face the following problems: firstly, materials applied in human body need to be biocompatibility. Secondly, mechanical properties of materials may change when various components are mixed together, so more researches are needed to achieve anti-adhesion without reducing the mechanical properties of materials, or even improving them. Finally, the oral cavity is in a constant temperature and humidity environment, stability and durability of super wettable materials under such condition also need to be futher investigated. Most of the existing experiments are *in vitro* or *in vivo* in animal. Whether it is harmless to human need to be further explored. Super wettability materials with their unique physicochemical anti-adhesion mechanisms will become an increasing area for oral antimicrobial practice and provide a new direction for solving drug resistance.

Author contributions

XZ and RB contributed equally to this review. YZ, SC, and BH designed and supervised the manuscript. XZ and RB wrote and revised the manuscript. QS, YZ, and ZZ modified and polished the manuscript. All authors contributed to the article and approved the submitted version.

Funding

This work was funded by the National Key R&D Program of China (2021YFC2400403), the National Natural Science Foundation of China (51972005,U21A2055,82101074), Ningxia Hui Autonomous Region key Research and Development program (2022BEG02031), and Beijing Key Program for Research and Application of Clinical Diagnosis and Technology (Z211100002921066).

Conflict of interest

The authors declare that the research was conducted in the absence of any commercial or financial relationships that could be construed as a potential conflict of interest.

Publisher's note

All claims expressed in this article are solely those of the authors and do not necessarily represent those of their affiliated organizations, or those of the publisher, the editors and the reviewers. Any product that may be evaluated in this article, or claim that may be made by its manufacturer, is not guaranteed or endorsed by the publisher.

References

Amini, S., Kolle, S., Petrone, L., Ahanotu, O., Sunny, S., Sutanto, C. N., et al. (2017). Preventing mussel adhesion using lubricant-infused materials. *Science* 357, 668–673. doi:10.1126/science.aai8977

Aray, Y., Marquez, M., Rodríguez, J., Vega, D., Simón-Manso, Y., Coll, S., et al. (2004). Electrostatics for exploring the nature of the hydrogen bonding in polyethylene oxide hydration. *J. Phys. Chem. B* 108, 2418–2424. doi:10.1021/jp036921o

Autio-Gold, J. (2008). The role of chlorhexidine in caries prevention. *Oper. Dent.* 33, 710–716. doi:10.2341/08-3

Baum, F., Ebner, J., and Pischetsrieder, M. (2013). Identification of multiphosphorylated peptides in milk. *J. Agric. Food Chem.* 61, 9110–9117. doi:10.1021/jf401865q

Boulmedais, F., Frisch, B., Etienne, O., Lavalle, P., Picart, C., Ogier, J., et al. (2004). Polyelectrolyte multilayer films with pegylated polypeptides as A new type of anti-microbial protection for biomaterials. *Biomaterials* 25, 2003–2011. doi:10.1016/j.biomaterials.2003.08.039

Bozuyuk, U., Dogan, N. O., and Kizilel, S. (2018). Deep insight into pegylation of bioadhesive chitosan nanoparticles: Sensitivity study for the key parameters through artificial neural network model. *ACS Appl. Mat. Interfaces* 10, 33945–33955. doi:10.1021/acsami.8b11178

Cai, B., Hu, K., Li, C., Jin, J., and Hu, Y. (2015). Bovine serum albumin bioconjugated graphene oxide: Red blood cell adhesion and hemolysis studied by qcm-D. *Appl. Surf. Sci.* 356, 844–851. doi:10.1016/j.apsusc.2015.08.178

Cao, M., Guo, D., Yu, C., Li, K., Liu, M., and Jiang, L. (2016). Water-repellent properties of superhydrophobic and lubricant-infused "slippery" surfaces: A brief study on the functions and applications. *ACS Appl. Mat. Interfaces* 8, 3615–3623. doi:10.1021/acsami.5b07881

Cazzaniga, G., Ottobelli, M., Ionescu, A., Garcia-Godoy, F., and Brambilla, E. (2015). Surface properties of resin-based composite materials and biofilm formation: A review of the current literature. *Am. J. Dent.* 28, 311–320.

Chen, S., Li, L., Zhao, C., and Zheng, J. (2010). Surface hydration: Principles and applications toward low-fouling/nonfouling biomaterials. *Polymer* 51, 5283–5293. doi:10.1016/j.polymer.2010.08.022

Chen, Y., Kang, E. T., Neoh, K. G., Wang, P., and Tan, K. L. (2000). Surface modification of polyaniline film by grafting of poly(ethylene glycol) for reduction in protein adsorption and platelet adhesion. *Synth. Met.* 110, 47–55. doi:10.1016/s0379-6779(99)00257-x

Chou, Y.-N., Wen, T.-C., and Chang, Y. (2016). Zwitterionic surface grafting of epoxylated sulfobetaine copolymers for the development of stealth biomaterial interfaces. *Acta Biomater.* 40, 78–91. doi:10.1016/j.actbio.2016.03.046

Chou, Y. N., Venault, A., Cho, C. H., Sin, M. C., Yeh, L. C., Jhong, J. F., et al. (2017). Epoxylated zwitterionic triblock copolymers grafted onto metallic surfaces for general biofouling mitigation. *Langmuir* 33, 9822–9835. doi:10.1021/acs.langmuir.7b02164

Colloca, M. E., Ahumada, M. C., López, M. E., and Nader-Macías, M. E. (2000). Surface properties of lactobacilli isolated from healthy subjects. *Oral Dis.* 6, 227–233. doi:10.1111/j.1601-0825.2000.tb00118.x

Cross, K. J., Huq, N. L., Palamara, J. E., Perich, J. W., and Reynolds, E. C. (2005). Physicochemical characterization of casein phosphopeptide-amorphous calcium phosphate nanocomplexes. *J. Biol. Chem.* 280, 15362–15369. doi:10.1074/jbc.m413504200

Crouzet, C., Decker, C., and Marchal, J. (1976). Characterization of primary oxidative degradation reactions during the autoxidation of poly(ethylene oxide)S at 25°C: Study in aqueous solution with initiation by solvent irradiation. 8. Kinetic studies at ph between 1 and 13. *Makromol. Chem.* 177, 145–157. doi:10.1002/macp.1976.021770112

Cui, X., Koujima, Y., Seto, H., Murakami, T., Hoshino, Y., and Miura, Y. (2016). Inhibition of bacterial adhesion on hydroxyapatite model teeth by surface modification with pegma-phosmer copolymers. *ACS Biomater. Sci. Eng.* 2, 205–212. doi:10.1021/acsbiomaterials.5b00349

Dallas, D. C., Citerne, F., Tian, T., Silva, V. L. M., Kalanetra, K. M., Frese, S. A., et al. (2016). Peptidomic analysis reveals proteolytic activity of kefir microorganisms on bovine milk proteins. *Food Chem.* 197, 273–284. doi:10.1016/j.foodchem.2015.10.116

Decher, G., and Hong, J.-D. (1991). Buildup of ultrathin multilayer films by A self-assembly process, 1 consecutive adsorption of anionic and cationic bipolar amphiphiles on charged surfaces. *Makromol. Chem. Macromol. Symp.* 46, 321–327. doi:10.1002/masy.19910460145

Dong, R., Zhao, X., Guo, B., and Ma, P. X. (2016). Self-healing conductive injectable hydrogels with antibacterial activity as cell delivery carrier for cardiac cell therapy. *ACS Appl. Mat. Interfaces* 8, 17138–17150. doi:10.1021/acsami.6b04911

Donlan, R. M., and Costerton, J. W. (2002). Biofilms: Survival mechanisms of clinically relevant microorganisms. *Clin. Microbiol. Rev.* 15, 167–193. doi:10.1128/cmr.15.2.167-193.2002

Elbert, D. L., and Hubbell, J. A. (1998). Self-assembly and steric stabilization at heterogeneous, biological surfaces using adsorbing block copolymers. *Chem. Biol.* 5, 177–183. doi:10.1016/s1074-5521(98)90062-x

Epstein, A. K., Wong, T. S., Belisle, R. A., Boggs, E. M., and Aizenberg, J. (2012). Liquid-infused structured surfaces with exceptional anti-biofouling performance. *Proc. Natl. Acad. Sci. U. S. A.* 109, 13182–13187. doi:10.1073/pnas.1201973109

Feldman, K., Hähner, G., Spencer, N. D., Harder, P., and Grunze, M. (1999). Probing resistance to protein adsorption of oligo(ethylene glycol)-terminated self-assembled monolayers by scanning force microscopy. *J. Am. Chem. Soc.* 121, 10134–10141. doi:10.1021/ja991049b

Fitzgerald, R. J. (1998). Potential uses of caseinophosphopeptides. *Int. Dairy J.* 8, 451–457. doi:10.1016/s0958-6946(98)00068-5

Fujiwara, N., Yumoto, H., Miyamoto, K., Hirota, K., Nakae, H., Tanaka, S., et al. (2019). 2-Methacryloyloxyethyl phosphorylcholine (Mpc)-Polymer suppresses an increase of oral bacteria: A single-blind, crossover clinical trial. *Clin. Oral Investig.* 23, 739–746. doi:10.1007/s00784-018-2490-2

Gao, C., Li, G., Xue, H., Yang, W., Zhang, F., and Jiang, S. (2009). Functionalizable and ultra-low fouling zwitterionic surfaces via adhesive mussel mimetic linkages. *Biomaterials* 31, 1486–1492. doi:10.1016/j.biomaterials.2009.11.025

Gerhardt, W., and Martens, C. (1985). Zur oxydation von polyethylenoxiden und polyethylenoxidethern; die bildung von acetaldehyd bei der oxydation von diethylenglycol mit sauerstoff. *Z. Chem.* 25, 143. doi:10.1002/zfch.19850250412

Hamburger, R., Azaz, E., and Donbrow, M. (1975). Autoxidation of polyoxyethylenic non ionic surfactants and of polyethylene glycols. *Pharm. Acta Helv.* 50, 10–17.

Harder, P., Grunze, M., Dahint, R., Whitesides, G. M., and Laibinis, P. E. (1998). Molecular conformation in oligo(ethylene glycol)-terminated self-assembled monolayers on gold and silver surfaces determines their ability to resist protein adsorption. *J. Phys. Chem. B* 102, 426–436. doi:10.1021/jp972635z

Harris, J. M. (2013). *Poly(Ethylene glycol) chemistry: Biotechnical and biomedical applications*. New York, Ny: Springer.

Harris, L. G., Tosatti, S., Wieland, M., Textor, M., and Richards, R. G. (2004). Staphylococcus aureus adhesion to titanium oxide surfaces coated with non-functionalized and peptide-functionalized poly(L-lysine)-grafted- poly(ethylene glycol) copolymers. *Biomaterials* 25, 4135–4148. doi:10.1016/j.biomaterials.2003.11.033

Hirota, K., Yumoto, H., Miyamoto, K., Yamamoto, N., Murakami, K., Hoshino, Y., et al. (2011). Mpc-polymer reduces adherence and biofilm formation by oral bacteria. *J. Dent. Res.* 90, 900–905. doi:10.1177/0022034511402996

Hou, A., Luo, J., Zhang, M., Li, J., Chu, W., Liang, K., et al. (2020). Two-in-one strategy: A remineralizing and anti-adhesive coating against demineralized enamel. *Int. J. Oral Sci.* 12, 27. doi:10.1038/s41368-020-00097-y

Howell, C., Vu, T. L., Lin, J. J., Kolle, S., Juthani, N., Watson, E., et al. (2014). Self-replenishing vascularized fouling-release surfaces. *ACS Appl. Mat. Interfaces* 6, 13299–13307. doi:10.1021/am503150y

Huang, C.-J., Brault, N. D., Li, Y., Yu, Q., and Jiang, S. (2012). Controlled hierarchical architecture in surface-initiated zwitterionic polymer brushes with structurally regulated functionalities. *Adv. Mat.* 24, 1834–1837. doi:10.1002/adma.201104849

Hucknall, A., Rangarajan, S., and Chilkoti, A. (2009). In pursuit of zero: Polymer brushes that resist the adsorption of proteins. *Adv. Mat.* 21, 2441–2446. doi:10.1002/adma.200900383

Hui, N., Sun, X., Niu, S., and Luo, X. (2017). Pegylated polyaniline nanofibers: Antifouling and conducting biomaterial for electrochemical dna sensing. *ACS Appl. Mat. Interfaces* 9, 2914–2923. doi:10.1021/acsami.6b11682

Hwang, G. B., Page, K., Patir, A., Nair, S. P., Allan, E., and Parkin, I. P. (2018). The anti-biofouling properties of superhydrophobic surfaces are short-lived. *Acs Nano* 12, 6050–6058. doi:10.1021/acsnano.8b02293

Imazato, S. (2003). Antibacterial activity of bactericide-immobilized filler for resin-based restoratives. *Biomaterials* 24, 3605–3609. doi:10.1016/s0142-9612(03)00217-5

Imazato, S., Russell, R. R., and Mccabe, J. F. (1995). Antibacterial activity of mdpb polymer incorporated in dental resin. *J. Dent. (Shiraz).* 23, 177–181. doi:10.1016/0300-5712(95)93576-n

Ishihara, K., Nomura, H., Mihara, T., Kurita, K., Iwasaki, Y., and Nakabayashi, N. (1998). Why do phospholipid polymers reduce protein adsorption? *J. Biomed. Mat. Res.* 39 (6), 323–330. doi:10.1002/(sici)1097-4636(199802)39:2<323::aid-jbm21>3.0.co;2-c

Ishihara, K., Ueda, T., and Nakabayashi, N. (1990). Preparation of phospholipid polylners and their properties as polymer hydrogel membranes. *Polym. J.* 22, 355–360. doi:10.1295/polymj.22.355

Jeoung, E., Duncan, B., Wang, L.-S., Saha, K., Subramani, C., Wang, P., et al. (2015). Fabrication of robust protein films using nanoimprint lithography. *Adv. Mat.* 27, 6251–6255. doi:10.1002/adma.201502457

Jiao, Y., Tay, F. R., Niu, L. N., and Chen, J. H. (2019). Advancing antimicrobial strategies for managing oral biofilm infections. *Int. J. Oral Sci.* 11, 28. doi:10.1038/s41368-019-0062-1

Kang, S., Lee, M., Kang, M., Noh, M., Jeon, J., Lee, Y., et al. (2016). Development of anti-biofouling interface on hydroxyapatite surface by coating zwitterionic mpc polymer containing calcium-binding moieties to prevent oral bacterial adhesion. *Acta Biomater.* 40, 70–77. doi:10.1016/j.actbio.2016.03.006

Kenausis, G. L., Vörös, J., Elbert, D. L., Huang, N., Hofer, R., Ruiz-Taylor, L., et al. (2000). Poly(L-Lysine)-G-Poly(Ethylene glycol) layers on metal oxide surfaces: Attachment mechanism and effects of polymer architecture on resistance to protein adsorption. *J. Phys. Chem. B* 104, 3298–3309. doi:10.1021/jp993359m

Krzyściak, W., Jurczak, A., Piątkowski, J., Kościelniak, D., Gregorczyk-Maga, I., Kołodziej, I., et al. (2015). Effect of histatin-5 and lysozyme on the ability of Streptococcus mutans to form biofilms in *in vitro* conditions. *Postepy Hig. Med. Dosw.* 69, 1056–1066.

Kwon, J. S., Kim, J. Y., Mangal, U., Seo, J. Y., Lee, M. J., Jin, J., et al. (2021). Durable oral biofilm resistance of 3d-printed dental base polymers containing zwitterionic materials. *Int. J. Mol. Sci.* 22, 417. doi:10.3390/ijms22010417

Kwon, J. S., Lee, M. J., Kim, J. Y., Kim, D., Ryu, J. H., Jang, S., et al. (2019a). Novel anti-biofouling bioactive calcium silicate-based cement containing 2-methacryloyloxyethyl phosphorylcholine. *Plos One* 14, E0211007. doi:10.1371/journal.pone.0211007

Kwon, J. S., Lee, M. J., Kim, J. Y., Kim, D., Ryu, J. H., Jang, S., et al. (2019b). Novel anti-biofouling light-curable fluoride varnish containing 2-methacryloyloxyethyl phosphorylcholine to prevent enamel demineralization. *Sci. Rep.* 9, 1432. doi:10.1038/s41598-018-38255-2

Leckband, D., Sheth, S., and Halperin, A. (1999). Grafted poly(ethylene oxide) brushes as nonfouling surface coatings. *J. Of Biomaterials Sci. Polym. Ed.* 10, 1125–1147. doi:10.1163/156856299x00720

Lee, B. S., Chen, Y. J., Wei, T. C., Ma, T. L., and Chang, C. C. (2018). Comparison of antibacterial adhesion when salivary pellicle is coated on both poly(2-

hydroxyethyl-methacrylate)- and polyethylene-glycol-methacrylate-grafted poly(methyl methacrylate). *Int. J. Mol. Sci.* 19, 2764. doi:10.3390/ijms19092764

Lee, M. J., Kwon, J. S., Kim, J. Y., Ryu, J. H., Seo, J. Y., Jang, S., et al. (2019). Bioactive resin-based composite with surface pre-reacted glass-ionomer filler and zwitterionic material to prevent the formation of multi-species biofilm. *Dent. Mat.* 35, 1331–1341. doi:10.1016/j.dental.2019.06.004

Lendenmann, U., Grogan, J., and Oppenheim, F. G. (2000). Saliva and dental pellicle--A review. *Adv. Dent. Res.* 14, 22–28. doi:10.1177/08959374000140010301

Leng, C., Sun, S., Zhang, K., Jiang, S., and Chen, Z. (2016). Molecular level studies on interfacial hydration of zwitterionic and other antifouling polymers *in situ*. *Acta Biomater.* 40, 6–15. doi:10.1016/j.actbio.2016.02.030

Lewis, A. L. (2000). Phosphorylcholine-based polymers and their use in the prevention of biofouling. *Colloids And Surfaces B Biointerfaces* 18, 261–275. doi:10.1016/s0927-7765(99)00152-6

Li, G., Cheng, G., Xue, H., Chen, S., Zhang, F., and Jiang, S. (2008). Ultra low fouling zwitterionic polymers with A biomimetic adhesive group. *Biomaterials* 29, 4592–4597. doi:10.1016/j.biomaterials.2008.08.021

Li, J., Song, S., Meng, J., Tan, L., Liu, X., Zheng, Y., et al. (2021). 2d mof periodontitis photodynamic ion therapy. *J. Am. Chem. Soc.* 143, 15427–15439. doi:10.1021/jacs.1c07875

Li, L., Finnegan, M. B., Özkan, S., Kim, Y., Lillehoj, P. B., Ho, C. M., et al. (2010). *In vitro* study of biofilm formation and effectiveness of antimicrobial treatment on various dental material surfaces. *Mol. Oral Microbiol.* 25, 384–390. doi:10.1111/j.2041-1014.2010.00586.x

Li, P., Poon, Y. F., Li, W., Zhu, H.-Y., Yeap, S. H., Cao, Y., et al. (2011). A polycationic antimicrobial and biocompatible hydrogel with microbe membrane suctioning ability. *Nat. Mat.* 10, 149–156. doi:10.1038/nmat2915

Liu, M., Wang, S., Wei, Z., Song, Y., and Jiang, L. (2009). Bioinspired design of A superoleophobic and low adhesive water/solid interface. *Adv. Mat.* 21, 665–669. doi:10.1002/adma.200801782

Liu, X., Peng, L., Meng, J., Zhu, Z., Han, B., and Wang, S. (2018). Protein-mediated anti-adhesion surface against oral bacteria. *Nanoscale* 10, 2711–2714. doi:10.1039/c7nr08844b

Lüsse, S., and Arnold, K. (1996). The interaction of poly(ethylene glycol) with water studied by 1h and 2h nmr relaxation time measurements. *Macromolecules* 29, 4251–4257. doi:10.1021/ma9508616

Madhwani, T., and Mcbain, A. J. (2012). Compositional modification of nascent *in vitro* dental plaques by human host-defence peptides. *FEMS Immunol. Med. Microbiol.* 64, 374–381. doi:10.1111/j.1574-695x.2011.00922.x

Mashaghi, S., Jadidi, T., Koenderink, G., and Mashaghi, A. (2013). Lipid nanotechnology. *Int. J. Mol. Sci.* 14, 4242–4282. doi:10.3390/ijms14024242

Matinlinna, J. P., Tsoi, J. K.-H., De Vries, J., and Busscher, H. J. (2013). Characterization of Novel silane coatings on titanium implant surfaces. *Clin. Oral Implants Res.* 24, 688–697. doi:10.1111/j.1600-0501.2012.02504.x

Meisel, H., Meisel, H., Fairweather-Tait, S., Fitzgerald, R. J., Hartmann, R., Lane, C. N., et al. (2003). Detection of caseinophosphopeptides in the distal ileostomy fluid of human subjects. *Br. J. Nutr.* 89, 351–358. doi:10.1079/bjn2002803

Nitta, S., Komatsu, A., Ishii, T., Ohnishi, M., Inoue, A., and Iwamoto, H. (2017). Fabrication and characterization of water-dispersed chitosan nanofiber/poly(ethylene glycol) diacrylate/calcium phosphate-based porous composites. *Carbohydr. Polym.* 174, 1034–1040. doi:10.1016/j.carbpol.2017.06.111

Nongonierma, A. B., and Fitzgerald, R. J. (2012). Biofunctional properties of caseinophosphopeptides in the oral cavity. *Caries Res.* 46, 234–267. doi:10.1159/000338381

Oh, H. J., Oh, H. W., Lee, D. W., Kim, C. H., Ahn, J. Y., Kim, Y., et al. (2017). Chronologic trends in studies on fluoride mechanisms of action. *J. Dent. Res.* 96, 1353–1360. doi:10.1177/0022034517717680

Park, K. D., Kim, Y. S., Han, D. K., Kim, Y. H., Lee, E. H., Suh, H., et al. (1998). Bacterial adhesion on peg modified polyurethane surfaces. *Biomaterials* 19, 851–859. doi:10.1016/s0142-9612(97)00245-7

Park, S. Y., Yoo, K. H., Yoon, S. Y., Son, W. S., and Kim, Y. I. (2020). *Synergetic Effect Of 2-Methacryloyloxyethyl Phosphorylcholine And Mesoporous Bioactive Glass Nanoparticles On Antibacterial And Anti-Demineralisation Properties In Orthodontic Bonding Agents*, 10.*Nanomater. (Basel).*

Patir, A., Hwang, G. B., Lourenco, C., Nair, S. P., Carmalt, C. J., and Parkin, I. P. (2021). Crystal violet-impregnated slippery surface to prevent bacterial contamination of surfaces. *ACS Appl. Mat. Interfaces* 13, 5478–5485. doi:10.1021/acsami.0c17915

Peng, L., Chang, L., Liu, X., Lin, J., Liu, H., Han, B., et al. (2017). Antibacterial property of A polyethylene glycol-grafted dental material. *ACS Appl. Mat. Interfaces* 9, 17688–17692. doi:10.1021/acsami.7b05284

Peng, L., Chang, L., Si, M., Lin, J., Wei, Y., Wang, S., et al. (2020). Hydrogel-coated dental device with adhesion-inhibiting and colony-suppressing properties. *ACS Appl. Mat. Interfaces* 12, 9718–9725. doi:10.1021/acsami.9b19873

Ramburrun, P., Pringle, N. A., Dube, A., Adam, R. Z., D'souza, S., and Aucamp, M. (2021). Recent advances in the development of antimicrobial and antifouling biocompatible materials for dental applications. *Mater. (Basel)* 14 (12), 3167. doi:10.3390/ma14123167

Razatos, A., Ong, Y. L., Boulay, F., Elbert, D. L., Hubbell, J. A., Sharma, M. M., et al. (2000). Force measurements between bacteria and poly(ethylene glycol)-coated surfaces. *Langmuir* 16, 9155–9158. doi:10.1021/la000818y

Reynolds, E. C. (1987). The prevention of sub-surface demineralization of bovine enamel and change in plaque composition by casein in an intra-oral model. *J. Dent. Res.* 66, 1120–1127. doi:10.1177/00220345870660060601

Reynolds, E. C., and Wong, A. (1983). Effect of adsorbed protein on hydroxyapatite zeta potential and Streptococcus mutans adherence. *Infect. Immun.* 39, 1285–1290. doi:10.1128/iai.39.3.1285-1290.1983

Roger, V., Tenovuo, J., Lenander-Lumikari, M., Söderling, E., and Vilja, P. (1994). Lysozyme and lactoperoxidase inhibit the adherence of Streptococcus mutans nctc 10449 (serotype C) to saliva-treated hydroxyapatite *in vitro*. *Caries Res.* 28, 421–428. doi:10.1159/000262015

Rošin-Grget, K., Peroš, K., Sutej, I., and Bašić, K. (2013). The cariostatic mechanisms of fluoride. *Acta Med. Acad.* 42, 179–188. doi:10.5644/ama2006-124.85

Schlenoff, J. B. (2014). Zwitteration: Coating surfaces with zwitterionic functionality to reduce nonspecific adsorption. *Langmuir* 30, 9625–9636. doi:10.1021/la500057j

Schüpbach, P., Neeser, J. R., Golliard, M., Rouvet, M., and Guggenheim, B. (1996). Incorporation of caseinoglycomacropeptide and caseinophosphopeptide into the salivary pellicle inhibits adherence of mutans streptococci. *J. Dent. Res.* 75, 1779–1788. doi:10.1177/00220345960750101101

Shutava, T. G., Livanovich, K. S., and Sharamet, A. A. (2019). Layer-by-layer films of polysaccharides modified with polyethylene glycol and dextran. *Colloids And Surfaces B Biointerfaces* 173, 412–420. doi:10.1016/j.colsurfb.2018.10.009

Siqueira, W. L., Margolis, H. C., Helmerhorst, E. J., Mendes, F. M., and Oppenheim, F. G. (2010). Evidence of intact histatins in the *in vivo* acquired enamel pellicle. *J. Dent. Res.* 89, 626–630. doi:10.1177/0022034510363384

Song, F., Koo, H., and Ren, D. (2015). *Effects of material properties on bacterial adhesion and biofilm formation*. Los Angeles, Ca: Sage Publications.

Sterzenbach, T., Helbig, R., Hannig, C., and Hannig, M. (2020). Bioadhesion in the oral cavity and approaches for biofilm management by surface modifications. *Clin. Oral Investig.* 24, 4237–4260. doi:10.1007/s00784-020-03646-1

Tedjo, C., Neoh, K. G., Kang, E. T., Fang, N., and Chan, V. (2007). Bacteria-surface interaction in the presence of proteins and surface attached poly(ethylene glycol) methacrylate chains. *J. Biomed. Mat. Res. A* 82, 479–491. doi:10.1002/jbm.a.31172

Thongthai, P., Kitagawa, H., Kitagawa, R., Hirose, N., Noree, S., Iwasaki, Y., et al. (2020). Development of Novel surface coating composed of mdpb and mpc with dual functionality of antibacterial activity and protein repellency. *J. Biomed. Mat. Res.* 108, 3241–3249. doi:10.1002/jbm.b.34661

Tong, H., Yu, X., Shi, Z., Liu, F., Yu, Y., Deng, F., et al. (2021). Physicochemical properties, bond strength and dual-species biofilm inhibition effect of dental resin composites with branched silicone methacrylate. *J. Mech. Behav. Biomed. Mat.* 116, 104368. doi:10.1016/j.jmbbm.2021.104368

Ullah, R., Zafar, M. S., and Shahani, N. (2017). Potential fluoride toxicity from oral medicaments: A review. *Iran. J. Basic Med. Sci.* 20, 841–848. doi:10.22038/IJBMS.2017.9104

Villard, N., Seneviratne, C., Tsoi, J. K. H., Heinonen, M., and Matinlinna, J. (2015). Candida albicans aspects of Novel silane system–coated titanium and zirconia implant surfaces. *Clin. Oral Implants Res.* 26, 332–341. doi:10.1111/clr.12338

Vimala, K., Mohan, Y. M., Sivudu, K. S., Varaprasad, K., Ravindra, S., Reddy, N. N., et al. (2010). Fabrication of porous chitosan films impregnated with silver nanoparticles: A facile approach for superior antibacterial application. *Colloids And Surfaces B Biointerfaces* 76, 248–258. doi:10.1016/j.colsurfb.2009.10.044

Wang, B., Liu, H., Wang, Z., Shi, S., Nan, K., Xu, Q., et al. (2017). A self-defensive antibacterial coating acting through the bacteria-triggered release of A hydrophobic antibiotic from layer-by-layer films. *J. Mat. Chem. B* 5, 1498–1506. doi:10.1039/c6tb02614a

Wang, X., Liu, L., Zhou, X., Huo, Y., Gao, J., and Gu, H. (2020). Casein phosphopeptide combined with fluoride enhances the inhibitory effect on initial

adhesion of Streptococcus mutans to the saliva-coated hydroxyapatite disc. *Bmc Oral Health* 20, 169. doi:10.1186/s12903-020-01158-8

Xie, X., Wang, L., Xing, D., Zhang, K., Weir, M. D., Liu, H., et al. (2017). Novel dental adhesive with triple benefits of calcium phosphate recharge, protein-repellent and antibacterial functions. *Dent. Mat.* 33, 553–563. doi:10.1016/j.dental.2017.03.002

Xu, F. J., Neoh, K. G., and Kang, E. T. (2009). Bioactive surfaces and biomaterials via atom transfer radical polymerization. *Prog. Polym. Sci.* 34, 719–761. doi:10.1016/j.progpolymsci.2009.04.005

Yamasaki, A., Imamura, Y., Kurita, K., Iwasaki, Y., Nakabayashi, N., and Ishihara, K. (2003). Surface mobility of polymers having phosphorylcholine groups connected with various bridging units and their protein adsorption-resistance properties. *Colloids Surfaces B Biointerfaces* 28, 53–62. doi:10.1016/s0927-7765(02)00130-3

Yang, X., Huang, P., Wang, H., Cai, S., Liao, Y., Mo, Z., et al. (2017). Antibacterial and anti-biofouling coating on hydroxyapatite surface based on peptide-modified tannic acid. *Colloids Surfaces B Biointerfaces* 160, 136–143. doi:10.1016/j.colsurfb.2017.09.006

Yin, A., Margolis, H. C., Grogan, J., Yao, Y., Troxler, R. F., and Oppenheim, F. G. (2003). Physical parameters of hydroxyapatite adsorption and effect on candidacidal activity of histatins. *Archives Of Oral Biol.* 48, 361–368. doi:10.1016/s0003-9969(03)00012-8

Yin, J., Mei, M. L., Li, Q., Xia, R., Zhang, Z., and Chu, C. H. (2016). Self-cleaning and antibiofouling enamel surface by slippery liquid-infused technique. *Sci. Rep.* 6, 25924. doi:10.1038/srep25924

Yu, X., He, J., Li, S., Liu, F., Yang, J., and Deng, F. (2020). Preparation of experimental resin composites with an anti-adhesion effect against S. Mutans using branched silicone methacrylate. *J. Mech. Behav. Biomed. Mat.* 101, 103414. doi:10.1016/j.jmbbm.2019.103414

Yumoto, H., Hirota, K., Hirao, K., Miyazaki, T., Yamamoto, N., Miyamoto, K., et al. (2015). Anti-inflammatory and protective effects of 2-methacryloyloxyethyl phosphorylcholine polymer on oral epithelial cells. *J. Biomed. Mat. Res. A* 103, 555–563. doi:10.1002/jbm.a.35201

Zanini, S., Müller, M., Riccardi, C., and Orlandi, M. (2007). Polyethylene glycol grafting on polypropylene membranes for anti-fouling properties. *Plasma Chem. Plasma process.* 27, 446–457. doi:10.1007/s11090-007-9094-y

Zhang, N., Chen, C., Melo, M. A., Bai, Y. X., Cheng, L., and Xu, H. H. (2015a). A Novel protein-repellent dental composite containing 2-methacryloyloxyethyl phosphorylcholine. *Int. J. Oral Sci.* 7, 103–109. doi:10.1038/ijos.2014.77

Zhang, N., Ma, J., Melo, M. A., Weir, M. D., Bai, Y., and Xu, H. H. (2015b). Protein-repellent and antibacterial dental composite to inhibit biofilms and caries. *J. Dent. (Shiraz).* 43, 225–234. doi:10.1016/j.jdent.2014.11.008

Zhang, P., Lin, L., Zang, D., Guo, X., and Liu, M. (2017). Designing bioinspired anti-biofouling surfaces based on A superwettability strategy. *Small* 13, 1503334. doi:10.1002/smll.201503334

Zhao, X., Wu, H., Guo, B., Dong, R., Qiu, Y., and Ma, P. X. (2017). Antibacterial anti-oxidant electroactive injectable hydrogel as self-healing wound dressing with hemostasis and adhesiveness for cutaneous wound healing. *Biomaterials* 122, 34–47. doi:10.1016/j.biomaterials.2017.01.011

Zheng, L., Sundaram, H. S., Wei, Z., Li, C., and Yuan, Z. (2017). Applications of zwitterionic polymers. *React. And Funct. Polym.* 118, 51–61. doi:10.1016/j.reactfunctpolym.2017.07.006

Zhou, L., Li, Q. L., and Wong, H. M. (2021). A Novel strategy for caries management: Constructing an antibiofouling and mineralizing dual-bioactive tooth surface. *ACS Appl. Mat. Interfaces* 13, 31140–31152. doi:10.1021/acsami.1c06989

Zhou, L., Wong, H. M., Zhang, Y. Y., and Li, Q. L. (2020). Constructing an antibiofouling and mineralizing bioactive tooth surface to protect against decay and promote self-healing. *ACS Appl. Mat. Interfaces* 12, 3021–3031. doi:10.1021/acsami.9b19745

Zhou, Y., Deng, J., Zhang, Y., Li, C., Wei, Z., Shen, J., et al. (2022). Engineering dna-guided hydroxyapatite bulk materials with high stiffness and outstanding antimicrobial ability for dental inlay applications. *Adv. Mat.* 34, E2202180. doi:10.1002/adma.202202180

Zhu, B., Eurell, T., Gunawan, R., and Leckband, D. (2001). Chain-length dependence of the protein and cell resistance of oligo(ethylene glycol)-terminated self-assembled monolayers on gold. *J. Biomed. Mat. Res.* 56 (6), 406–416. doi:10.1002/1097-4636(20010905)56:3<406::aid-jbm1110>3.0.co;2-r

frontiers | Frontiers in Bioengineering and Biotechnology

TYPE Original Research
PUBLISHED 08 September 2022
DOI 10.3389/fbioe.2022.989729

OPEN ACCESS

EDITED BY
Jingxin Meng,
Chinese Academy of Sciences (CAS), China

REVIEWED BY
Hiroshi Yabu,
Tohoku University, Japan
Pengfei Li,
Sichuan University, China

*CORRESPONDENCE
Nadja Rohr,
nadja.rohr@unibas.ch
Neha Sharma,
neha.sharma@usb.ch

†These authors have contributed equally to this work and share first authorship

SPECIALTY SECTION
This article was submitted to Bionics and Biomimetics, a section of the journal Frontiers in Bioengineering and Biotechnology

RECEIVED 08 July 2022
ACCEPTED 19 August 2022
PUBLISHED 08 September 2022

CITATION
Chi M, Li N, Cui J, Karlin S, Rohr N, Sharma N and Thieringer FM (2022), Biomimetic, mussel-inspired surface modification of 3D-printed biodegradable polylactic acid scaffolds with nano-hydroxyapatite for bone tissue engineering.
Front. Bioeng. Biotechnol. 10:989729.
doi: 10.3389/fbioe.2022.989729

Biomimetic, mussel-inspired surface modification of 3D-printed biodegradable polylactic acid scaffolds with nano-hydroxyapatite for bone tissue engineering

Minghan Chi[1†], Na Li[1†], Junkui Cui[2], Sabrina Karlin[3], Nadja Rohr[3,4]*, Neha Sharma[1,5]* and Florian M. Thieringer[1,5]

[1]Medical Additive Manufacturing Research Group (Swiss MAM), Department of Biomedical Engineering, University of Basel, Allschwil, Switzerland, [2]Department of Earth and Environmental Studies, Montclair State University, Montclair, NJ, United States, [3]Biomaterials and Technology, Department of Research, University Center for Dental Medicine Basel UZB, University of Basel, Basel, Switzerland, [4]Biomaterials and Technology, Department of Reconstructive Dentistry, University Center for Dental Medicine Basel UZB, University of Basel, Basel, Switzerland, [5]Oral and Cranio-Maxillofacial Surgery, University Hospital Basel, Basel, Switzerland

Polylactic acid (PLA) has been widely used as filaments for material extrusion additive manufacturing (AM) to develop patient-specific scaffolds in bone tissue engineering. Hydroxyapatite (HA), a major component of natural bone, has been extensively recognized as an osteoconductive biomolecule. Here, inspired by the mussel-adhesive phenomenon, in this study, polydopamine (PDA) coating was applied to the surface of 3D printed PLA scaffolds (PLA@PDA), acting as a versatile adhesive platform for immobilizing HA nanoparticles (nHA). Comprehensive analyses were performed to understand the physicochemical properties of the 3D-printed PLA scaffold functionalized with nHA and PDA for their potent clinical application as a bone regenerative substitute. Scanning electron microscopy (SEM) and element dispersive X-ray (EDX) confirmed a successful loading of nHA particles on the surface of PLA@PDA after 3 and 7 days of coating (PLA@PDA-HA3 and PLA@PDA-HA7), while the surface micromorphology and porosity remain unchanged after surface modification. The thermogravimetric analysis (TGA) showed that 7.7 % and 12.3% mass ratio of nHA were loaded on the PLA scaffold surface, respectively. The wettability test indicated that the hydrophilicity of nHA-coated scaffolds was greatly enhanced, while the mechanical properties remained uncompromised. The 3D laser scanning confocal microscope (3DLS) images revealed that the surface roughness was significantly increased, reaching Sa (arithmetic mean height) of 0.402 μm in PLA@PDA-HA7. Twenty-eight days of *in-vitro* degradation results showed that the introduction of nHA to the PLA surface enhances its degradation properties, as evidenced by the SEM images and weight loss test. Furthermore, a sustainable release of Ca^{2+} from PLA@PDA-HA3 and PLA@PDA-HA7 was recorded, during the degradation process. In contrast, the released hydroxyl group of nHA tends to neutralize the local acidic

environments, which was more conducive to osteoblastic differentiation and extracellular mineralization. Taken together, this facile surface modification provides 3D printed PLA scaffolds with effective bone regenerative properties by depositing Ca^{2+} contents, improving surface hydrophilicity, and enhancing the *in-vitro* degradation rate.

KEYWORDS

bioinspired, three-dimensional printing, hydroxyapaite, surface modication, nanocomposites

Introduction

Critical-sized bone defects are severe consequences of traumatic injury, infection, congenital defects, or surgical resection, which require clinical interventions to achieve functional restoration and complete healing (Zhang et al., 2019). Although bone autografts are the gold standard for bone reconstructive surgeries, their application is limited due to additional pain, potential infection, and donor-site morbidity (Blokhuis and Arts, 2011). Thus field of bone tissue engineering thus aims to design and develop materials that outperform bone allografts and autografts (Roseti et al., 2017). Despite many conventional approaches that have been developed for fabricating biomimetic porous scaffolds (Chen et al., 2018; Grenier et al., 2019; Sola et al., 2019), challenges remain to optimize the shape and porosity of patient-specific customized scaffolds. Nowadays, with the advancement of materials and medical technology, additive manufacturing (AM), also known as three-dimensional (3D) printing, has attracted significant attention to producing predictable bone regenerative scaffolds with customized shapes and structures (Brien, 2011; Madrid et al., 2019).

Polylactic acid (PLA), one of the most intriguing polymeric materials, has recently received much attention in the food and medical fields due to its excellent biodegradability, biocompatibility, bioresorbability, and ductility (Senatov et al., 2016; Tyler et al., 2016). However, PLA also has the disadvantages of being bioinert, hydrophobic, low fracture toughness, and lacking osteoconduction and cell-scaffold interactions, limiting its potential clinical application (Ma et al., 2007; Mondal et al., 2020; Zaaba and Jaafar, 2020). To tackle such drawbacks, nanosized hydroxyapatite (nHA) has been widely introduced to the bone regenerative scaffolds as an additive composite or coating material to act as a cell recognition site and promote bone regeneration (Dutta et al., 2015; Ramesh et al., 2018). Various conventional fabricating methods, such as solvent casting, mechanical milling, and electrospinning, have been applied to produce PLA/nHA composite scaffolds for bone regeneration (Novotna et al., 2014; Trifol et al., 2019). However, the presence of residual organic solvents (e.g., chloroform and dichloromethane) resulted in harmful effects on cells and tissues (Chakraborty et al., 2018; Gayer et al., 2019). More importantly, the surface of scaffolds was not ideally functionalized since most of the nHA particles are entrapped in the PLA matrix, resulting in limited hydrophilicity, cell recruitment, and osteo-stimulating effects (Qiang et al., 2018; Liu et al., 2020).

In recent years, the mussel-inspired, biomimetic polydopamine (PDA) coating has received increasing attention as a universal bio-adhesive coating due to its unique adhesion ability (Lee et al., 2007; Grewal and Yabu, 2020; Grewal et al., 2021). With material-independent surface chemistry and deposition strategy, the PDA coating layer can be quickly formed at different interfaces (e.g., oil-water and air-water interfaces) by oxidation and self-polymerization of dopamine (DA) (Ryu et al., 2010) and thus can be expected promising applications in multidisciplinary fields such as energy, environmental, electrocatalysis, and biomedicine (Liu et al., 2014; Abe et al., 2020; Abe and Yabu, 2021; Yabu et al., 2022). The as-synthesized PDA layer further serves as a versatile platform for the immobilization of bionic molecules (e.g., bioactive ions and ceramics) (Shanmugam et al., 2019; Park et al., 2021; Shuai et al., 2021).

Herein, a facile approach to fabricating osteoconductive and osteoinductive nanocomposite scaffolds using material extrusion-based (commonly known as Fused Filament Fabrication, (FFF)) AM technology with surface modification strategy is presented in the present work. This study aims to comprehensively analyze additively manufactured PLA scaffolds functionalized by PDA and nHA, from surface structure to *in-vitro* degradation properties. The objectives of this study were to develop 3D printed porous scaffolds with enhanced osteogenicity by introducing PDA and nHA to their surfaces and to systematically characterize and evaluate the scaffolds' physicochemical properties, including surface hydrophilicity, roughness, mechanical behavior, and *in-vitro* biodegradability. The hypotheses were that *1*) the PDA and nHA coating result in increased hydrophilic surfaces of PLA scaffolds and *2*) the nHA and PDA coating enhances the *in-vitro* hydrolysis process of PLA scaffolds, and *3*) the mechanical properties were not compromised.

Materials and methods

Materials

Dopamine hydrochloride ($(HO)_2C_6H_3CH_2CH_2NH_2{\cdot}HCl$), tris-base ($NH_2C(CH_2OH)_3$), hydrochloric acid (HCl, 98%), and phosphate-buffered saline (PBS) at pH = 7.4 were

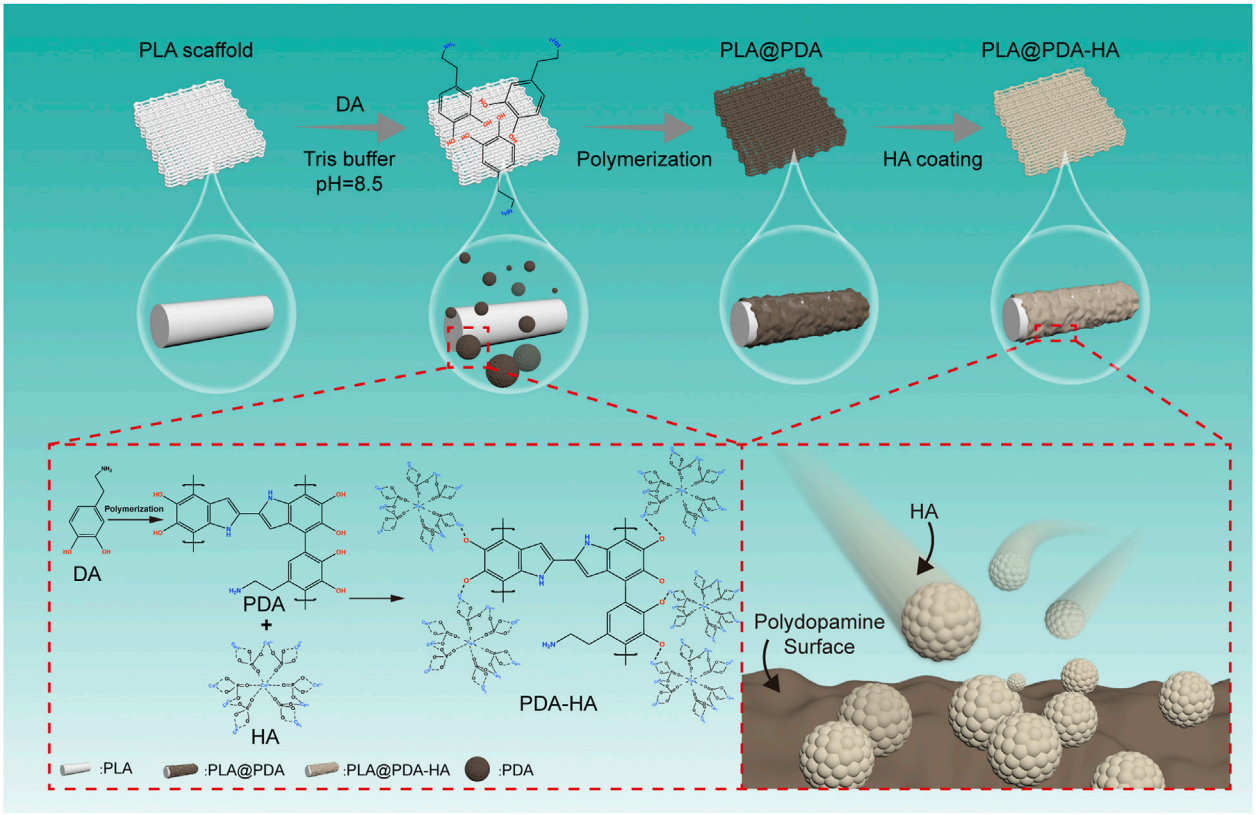

FIGURE 1
Schematic illustration of surface modification process of three-dimensional (3D)-printed PLA scaffolds. The PLA scaffold was fabricated with a rectangular porous structure using material extrusion-based 3D printing technology. Afterward, polydopamine was homogeneously coated onto the surface by immersing PLA scaffolds into the dopamine solution (tris buffer, pH = 8.5) and simultaneously stirring for 24 h, during which PDA was developed by self-polymerization of DA particles. Furthermore, nHA particles were successfully immobilized onto the surface of as-synthesized PDA coatings *via* catechol functional groups. Finally, the nHA functionalized PLA scaffolds were obtained.

purchased from Sigma-Aldrich (Merck KGaA, Darmstadt, Germany). Material extrusion 3D printing PLA filaments were purchased from 3DJake GmbH (Paldau, Austria). Nano hydroxyapatite (nHA) powders (≥97%, <200 nm particle size-BET) were obtained from Shanghai Aladdin Biochemical Technology (Shanghai, China). Ultrapure water (>18.2 MΩ·cm) was provided using a Milli-Q ® EQ water purification system (Basel, Switzerland).

Fabrication of material extrusion 3D printed PLA scaffolds

3D scaffolds (10 mm × 10 mm × 3 mm) were designed using a computer-aided design modeling software (3ds Max, v. 2022, Autodesk Inc., San Francisco, CA, United States) and exported in a standard tessellation language (STL) file format. The printing path of the scaffolds was then generated using the 3D printer's compatible slicing software (MakerBot Print software, v. 3.10.1, NY, United States) and saved in a g-code file. Specifically, the parameters of g-code were set at a printing temperature of 215°C, layer height of 0.2 mm, infill density of 90%, infill rotation angle of 90°, and travel speed of 150 mm/s. Subsequently, the g-code was imported to the material extrusion-based 3D printer (Makerbot Replicator +, Makerbot Industries, NY, United States) with a nozzle of 400 μm and printed using a diameter of 1.75 mm PLA filament. After production, all scaffolds were stored at room temperature in a desiccator before further surface modification and characterization.

Surface modification of material extrusion 3D printed PLA scaffolds

The overview of the surface modification process was depicted in the schematic illustration (Figure 1). The PLA scaffolds were fabricated using material extrusion-based 3D printing technology. Subsequently, simple and direct coating

methods were applied to obtain PDA and nHA functionalized PLA 3D scaffolds. The surface functionalization of material extrusion 3D printed PLA scaffolds with PDA was carried out as illustrated by Lee et al. (Lee et al., 2020). Briefly, the spontaneous formation of a thin adherent PDA film on PLA scaffolds was achieved *via* direct immersion into a dopamine solution (2 mg/ml in 10 mM Tris buffer, pH 8.5) under a 25 rpm shaker (Agilent Technologies, CA, United States) at room temperature (25°C) for 24 h. The solution was continuously stirred during the coating process to avoid the aggregation of self-polymerizing PDA nanoparticles formed in the solution. The resultant PLA scaffolds, denoted as PLA@PDA, were rinsed with deionized water three times to remove the residual solvent and dried at 60°C in a conventional oven. Immobilization of HA nanoparticles was achieved by immersing PLA@PDA scaffolds into nHA solution (50 mg/ml) for 3 and 7 days. Finally, the scaffolds were washed with deionized water three times, dried overnight at 60°C, and hereafter referred to as PLA@PDA-HA3 and PLA@PDA-HA7. Native 3D printed PLA scaffolds without surface modification served as the control group (henceforth referred to as PLA).

Microstructure characterization

The micromorphologies and chemical composition of scaffolds were investigated using scanning electron microscopy (SEM, Phillips XL30, Eindhoven, Netherlands) equipped with energy-dispersive X-ray spectroscopy (EDX). The scaffolds were sputtered with gold and observed at an accelerating voltage of 10 kV at different magnifications. EDX analysis was conducted using an accelerating voltage of 20 kV. The porosity of 3D-printed PLA scaffolds was obtained using the following equation:

$$\text{Porosity}\,(\%) = 1 - \left(\rho\text{scaffolds}/\rho\text{pla}\right) \times 100\% \qquad (1)$$

The ρ scaffolds was defined as the ratio of weight and volume of the scaffolds, while the ρ pla was 1.25 g/cm3 according to previously reported (Van der Walt et al., 2019).

The phase composition of scaffolds was studied using X-ray diffraction (XRD). The XRD patterns were recorded in the 2θ range 5°–40°, with a step size of 0.02°. Specifically, the XRD test specimens were printed in a cylindrical shape (D: 10 mm; H: 1 mm), followed by surface modification procedures. The functional groups of scaffolds with or without surface modification were identified using Fourier transform infrared spectroscopy with attenuated accessory (FTIR-ATR) in the range of 500–4000 cm^{-1}. The surface roughness of each specimen was visualized and studied using Keyence Laser Microscope (VK-X3000 series, Keyence Corporation, Osaka, Japan).

Water absorption ability and surface wettability

To determine the water absorption ability of scaffolds, using a contact angle system, a drop shape analyzer (DSA 100, Krüss, Hamburg, Germany) tested the surface wettability (hydrophilic or hydrophobic) of the scaffolds. The samples were placed on a microscope glass slide, and three 2 μl ultrapure water droplets were applied to each sample at room temperature. Moreover, the water uptake ability of 3D printed porous samples was measured. Briefly, the dried scaffolds were first weighed and then immersed in a 5 ml PBS solution for 10, 30, and 60 s. The samples were weighed using filter paper after removing the residual water on the surface at each predetermined time point. The water absorption ability or water uptake (%) of the scaffolds was calculated according to the equation:

$$\text{Water Uptake}\,(\%) = [W\,(s) - W\,(i)]/W\,(i) \times 100\%$$

Where W (s) is the weight of the scaffold after immersion, and W (i) is the initial dry mass. All tests were performed in three replicates.

Mechanical tests

To identify the mechanical properties of scaffolds, tensile strength and compressive strength were studied using a universal testing machine (Z020, Zwick/Roell, Ulm, Germany). Briefly, the 3D model of a tensile bar was designed and created based on the International Organization for Standardization (ISO) 527-1 (2012) standard (detailed dimension and print patterns refer to Supplementary Figure S1) (Iof, 2012). All specimens used in tensile tests were sliced and printed under the previously described condition. The grip distance was 25.4 mm, and the speed was 5 mm/min. The compressive tests were performed on the fabricated scaffold samples (10 mm × 10 mm × 3 mm) with and without surface modification at a crosshead speed of 1 mm/min. All mechanical tests were performed in three replicates, and the mean values of each group were reported.

Thermogravimetric analysis

To investigate the amount of HA nanoparticles immobilized on PLA scaffolds, thermogravimetric analysis (TGA) was performed (TGA 5500, TA Instruments, New Castle, DE, United States). The samples were first cut into small pieces (3 mg) and placed in aluminum pans. Samples were then heated to 800°C at a ramp rate of 10°C min^{-1} under nitrogen flow. The residues were considered the inorganic contents. The experiments were conducted in three replicates.

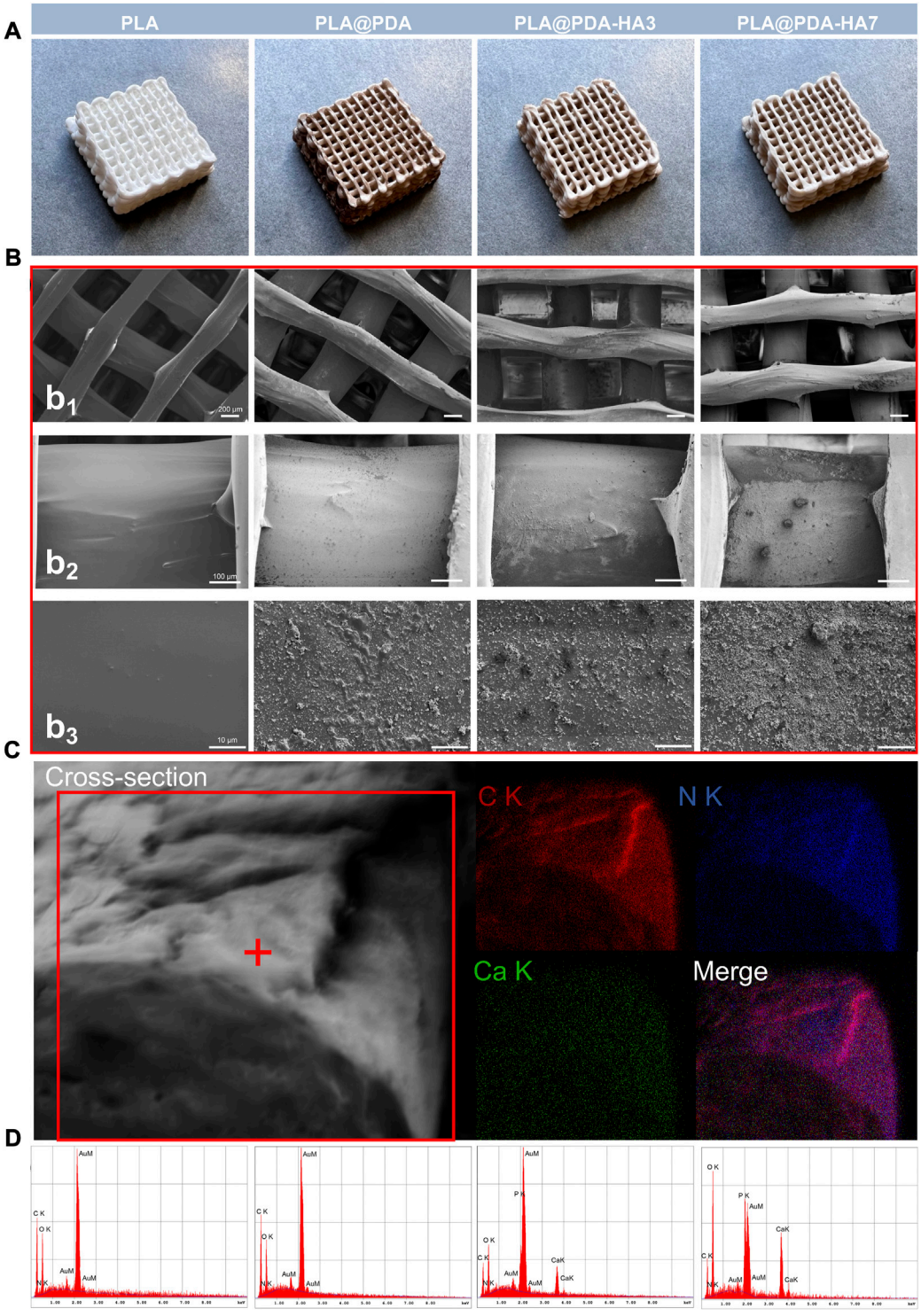

FIGURE 2
(A) Representative optical images of 3D printed PLA, PLA@PDA, PLA@PDA-HA3, and PLA@PDA-HA7 scaffolds; **(B)** Corresponding SEM images of surface topography of the fabricated scaffold within each group. Scale bar: Figure $2b_1$ = 200 μm, Figure $2b_2$ = 100 μm, Figure $2b_3$ = 10 μm; **(C)** Cross-sectional micromorphology of PLA@PDA-HA7 specimen and the corresponding EDX mapping. (Red: Carbon; Blue: Nitrogen; Green: Calcium). **(D)** Corresponding EDX analysis of each scaffold.

In-vitro biodegradable properties

In-vitro degradation ratios of the study groups' samples were measured *via* the mass loss method. In short, the dried scaffolds were initially weighed and immersed in PBS solution and kept at 37°C for 28 days. At each predetermined time point, the samples were removed and dried overnight, and the dry weight was recorded and compared with the initial weight to determine the degradation rate. At the end of each time point, the pH variation of PBS solution was detected utilizing a pH meter (AE150, ThermoFisher Scientific, MA, United States). At 14 and 28 days, the degradation micro-morphologies of samples were observed by SEM. Furthermore, calcium ion release rates of PLA@PDA-HA3 and PLA@PDA-HA7 scaffolds were studied. The release of calcium ions was determined at predetermined time intervals of 7, 14, 21, and 28 days. The immersion solution was collected and renewed with fresh PBS at each time point. The collected solutions were stored at 4°C until measurements. Finally, each collected supernatant's calcium ion concentration (ppm) was investigated *via* inductively coupled plasma mass spectrometry (ICP-MS, ICAP Q, ThermoFisher Scientific, MA, United States).

Statistical analysis

The data were expressed as means ± standard deviation (SD) of independent replicates. The results of the experiments were statistically analyzed using a one-way analysis of variances (ANOVA) using the GraphPad Prism software package (GraphPad, San Diego, CA, United States). Significant differences among mean values, where applicable, were determined using ANOVA and by Tukey's *post hoc* test for multiple comparisons. The level of significance was set to $\alpha = 0.05$.

Results

Fabrication and characterization of nHA-coated scaffolds

The fabricated scaffolds' representative photographs and surface micro-morphology are shown in Figures 2A,B, respectively. Representative macrostructure digital photographs (Figure 2A) revealed that the overall architecture of 3D-printed PLA (native and functionalized nanocomposite) scaffolds was with a well-designed rectangular subunit depicting lattice periodicity, and no fabrication defects associated with the spreading of the coatings on polymer were observed. In contrast to the native 3D-printed PLA scaffolds, the PDA functionalized PLA scaffolds turned from white to dark brown, indicating the successful oxidative self-polymerization of DA with the production of eumelanin on the surface of PLA scaffolds. Similarly, after coating with the HA nanoparticles, the PDA functionalized PLA scaffolds exhibited a creamy-white color, indirectly demonstrating the successful loading of nHA. SEM images at different magnifications further confirm the abovementioned findings. The lower magnification SEM images (Figure $2b_1$) show the struts and pores' morphology of the fabricated scaffolds. The struts of scaffolds with a diameter of ~600 μm were printed neatly, and a ~400 μm interconnected pores were shown, and they remained unchanged with the surface modification process.

TABLE 1 Elements obtained with EDX on the surface of each specimen in Wt%.

	Element (wt%)					
Group	**C K**	**O K**	**N K**	**Ca K**	**P K**	**Total**
PLA	40.0	46.4	13.6	—	—	100
PLA@PDA	38.6	43.0	18.4	—	—	100
PLA@PDA-HA3	26.0	33.0	10.2	21.2	9.6	100
PLA@PDA-HA7	9.8	33.5	4.6	34.7	17.4	100

Moreover, highly interconnected porosity was also observed, following the pre-modeled design. High magnification SEM images (Figures $2b_2$ and $2b_3$) clearly showed the fabricated scaffolds' different surface morphology and topography. The PLA scaffolds exhibited smooth and uniform surfaces, while lumps of PDA deposits were coated homogeneously all over the surfaces, indicating PDA was successfully deposited to the surface. For the PLA@PDA-HA3 scaffolds, there were some relatively small amounts of nHA distributed on the surface. However, it can be observed that apart from the area coated with nHA, a large portion of PLA surfaces was not covered, leaving it exposed. In contrast, with the extension of immersion time to 7 days, thicker and more visible nHA coatings were formed evenly on the surface of PLA@PDA-HA7. Additionally, the surfaces of PLA@PDA-HA7 were covered by different sizes of nHA aggregates, suggesting that 7 days of immobilization were sufficient to achieve high loading of HA nanoparticles.

Figure 2C shows the cross-sectional micromorphology of the PLA@PDA-HA7 scaffold. The surface of the strut appeared rougher due to the coating of nHA and PDA. The corresponding EDX-mapping analysis showed a homogeneous element distribution on the fracture surface, with strong signals of C (red) and N (blue) signals on the interior part of the strut. In contrast, relatively weak Ca (green) signals were concentrated on the surface area due to the nHA coating.

EDX was carried out to verify these results further and determine the chemical composition of different scaffold surfaces (Figure 2D and Table 1). As shown in Table 1, the nitrogen (N) content (wt%) increased from 13.6 to 18.4 wt% in

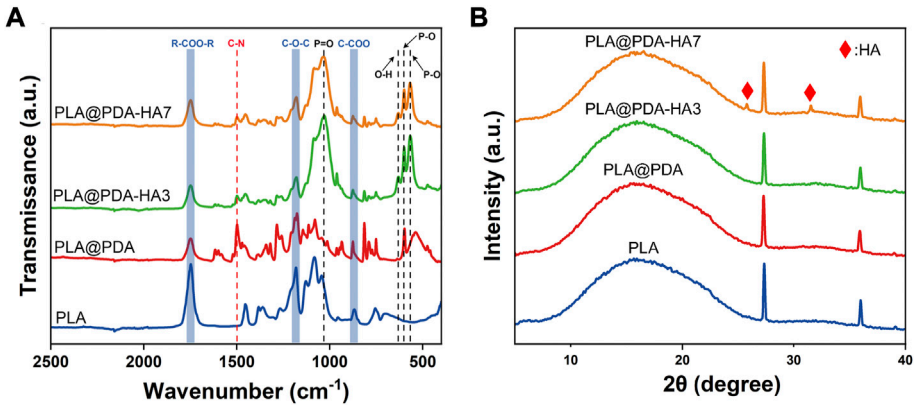

FIGURE 3
FTIR-ATR spectrum **(A)** and XRD pattern **(B)** of PLA, PLA@PDA, PLA@PDA-HA3, and PLA@PDA-HA7 scaffolds.

PLA@PDA scaffolds indicating successful coating of PDA layers on the PLA scaffold surface. Elements Ca and P were distributed on the surfaces after immersing scaffolds in nHA solution for 3 and 7 days, with a concomitant increase. Moreover, the resulting Ca/P ratios of PLA@PDA-HA3 and PLA@PDA-HA7 were 1.69 and 1.54, respectively (Table 1), which is close to the theoretical Ca/P ratio of HA 1.67. Additionally, the porosity rate of 3D printed PLA scaffolds showed a minor oscillation rate (Supplementary Table S1), with 36% ± 0.005 ($p < 0.05$), which was within the range of cancellous bone (Bose et al., 2012).

Chemical and phase composition of scaffolds

The chemical composition of the specimens was studied using FTIR-ATR analysis. As shown in Figure 3A, all four groups showed typical peaks at 1750 cm^{-1}, 1181 cm^{-1}, and 869 cm^{-1}, which were assigned to the carboxyl group stretch vibration ($V_{R\text{-}COO\text{-}R}$), and ether group stretch vibration ($V_{C\text{-}O\text{-}C}$), reflecting the carbon backbone of the PLA. For the PLA@PDA sample, a new peak at 1498 cm^{-1} corresponding to the C-N group stretch vibration appeared. Additionally, the intensity of this peak decreased significantly after introducing nHA to the surface. In PLA@PDA-HA3 and PLA@PDA-HA7 scaffold samples, multiple new peaks at 1040 cm^{-1} ($V_{P=O}$), 600 cm^{-1}, 566 cm^{-1} ($V_{P\text{-}O}$), and 631 cm^{-1} (OH^-) were found, indicating the presence of PO_4^{3-} and thus confirming the successful immobilization of HA.

The XRD tests were also carried out to confirm the phase composition of the 3D printed scaffold samples. Figure 3B shows the diffraction peaks of PLA, PLA@PDA, PLA@PDA-HA3, and PLA@PDA-HA7 scaffolds. For the PLA scaffolds, it offers a typical broad peak at 2θ ≈ 17°, which was the characteristic peak of PLA, and two sharp peaks at 2θ ≈ 27.8° and 35.4°, respectively, corresponding to the (200) and (110) plane of the orthorhombic crystal. Compared with PLA scaffolds, no new Bragg peaks were detected in the PLA@PDA scaffold samples due to the amorphous structure of PDA. After immobilizing nHA on the surface of PLA@PDA for 3 days, no new typical diffraction peaks of crystalline HA were observed. When nHA coating was extended to 7 days, two characteristic diffraction peaks at around 25.9° and 31.8° arose, corresponding to the (002) and (211) crystal planes of HA nanoparticles.

Surface roughness and 3D topography of scaffolds

Surface 3D topography and roughness of different scaffold samples (scanning area of 94.1 × 70.6 μm rectangle) are illustrated in Figure 4. Unlike PLA and PLA@PDA scaffolds, apparent peaks and valleys were noticed in nHA-coated samples representing HA nanoparticles and aggregates (Figure 4A). Figures 4B,C illustrates the surface roughness variation trends of Sa (arithmetical mean height) and Sz (maximum height). Following SEM images, Sa and Sz increase with the extension of nHA coating time. Precisely, compared with the Sa of native PLA scaffolds (ca. 0.03 μm), it can be calculated that the Sa of PLA@PDA, PLA@PDA-HA3, and PLA@PDA-HA7 increased to 0.14, 0.29, and 0.40 μm respectively. Similarly, the Sz value increased correspondingly and reached the highest level of 3.33 μm in PLA@PDA-HA7 scaffold samples.

Water contact angle and wettability tests

Figures 5A,B shows the water contact angle test (WCA) result. Compared with PLA scaffolds, the hydrophilicity of the

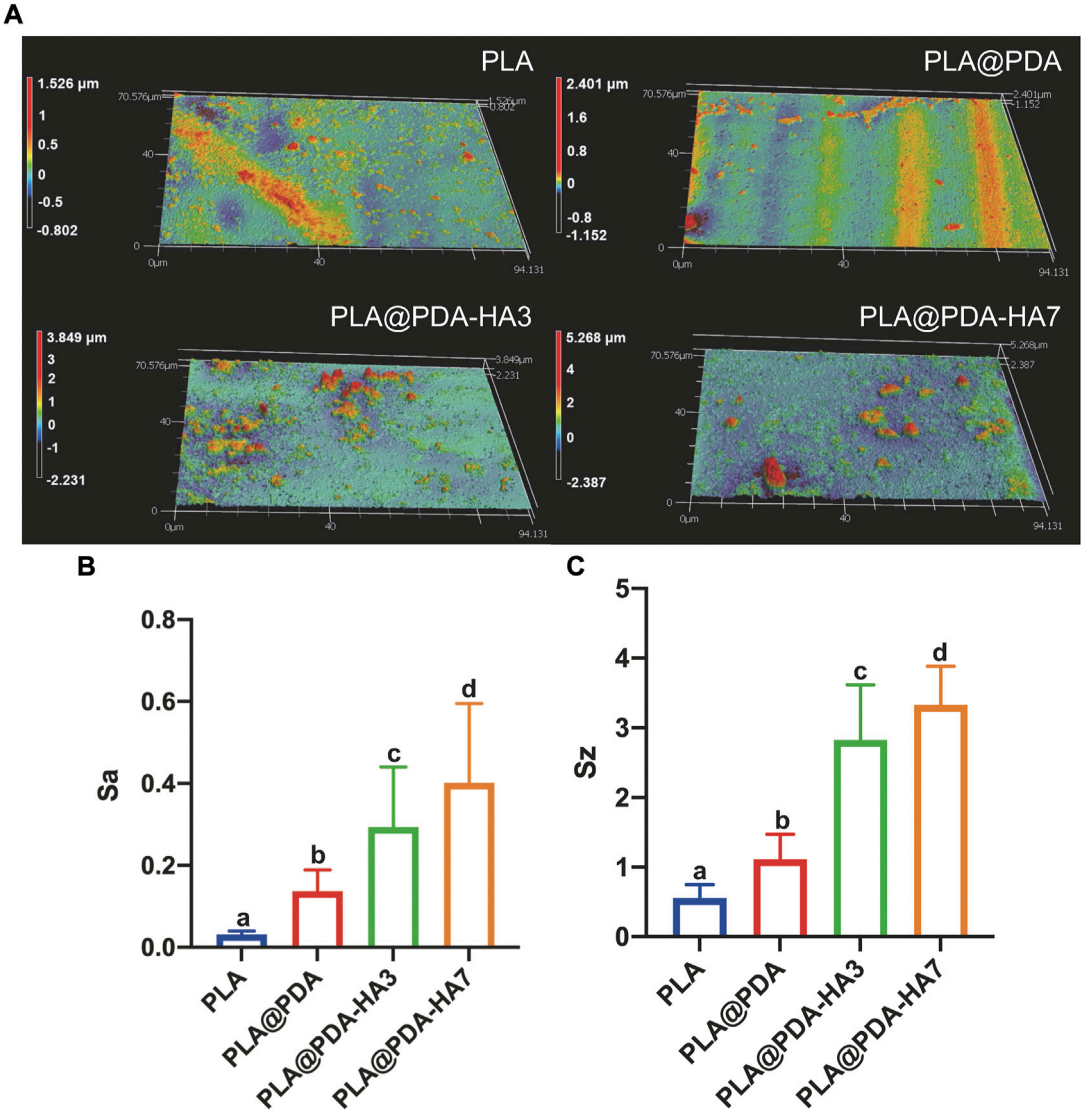

FIGURE 4
Surface roughness evaluation of PLA, PLA@PDA, PLA@PDA-HA3, and PLA@PDA-HA7 scaffolds. **(A)** Representative 3D surface topography of each scaffold. **(B)** Corresponding Sa (arithmetic mean height) and **(C)** Sz (maximum height). Dissimilar letters indicate statistical differences between groups (n = 3, p < 0.05).

PLA@PDA scaffold surface improved significantly, evidenced by a decrease in WCA from 92.7° to 52.5°. Interestingly, after functionalizing the PLA scaffold with nHA, the surface became completely hydrophilic and absorbed the water drops as soon as they fell onto the surface. Consequently, the WCA of PLA@PDA-HA3 and PLA@PDA-HA7 could be either 0° or undetectable. Figure 5C shows the water uptake rate of each scaffold during the time of 60 s. PLA scaffold showed an inferior water uptake ability, only achieving 4.7% after 60 s immersion. In contrast, the surface modification process enabled the scaffolds to absorb higher water. The PLA@PDA scaffold absorbed water more rapidly and significantly (p < 0.05), reaching 31.2% at 10 s and the maximum water absorption rose to 46.1% after 60 s. This trend became more evident with nHA coating, with 55.4% and 57% water absorption rates for PLA@PDA-HA3 and PLA@PDA-HA7 scaffold samples. However, no statistical significance was found between these two groups (p = 0.950). Additionally, during the water uptake tests, it was found that the surface-modified scaffolds sank immediately after placing them in PBS solution, whereas the PLA scaffold was floating on the solution during the 60 s experiment duration (*see* Supplementary Figure S2).

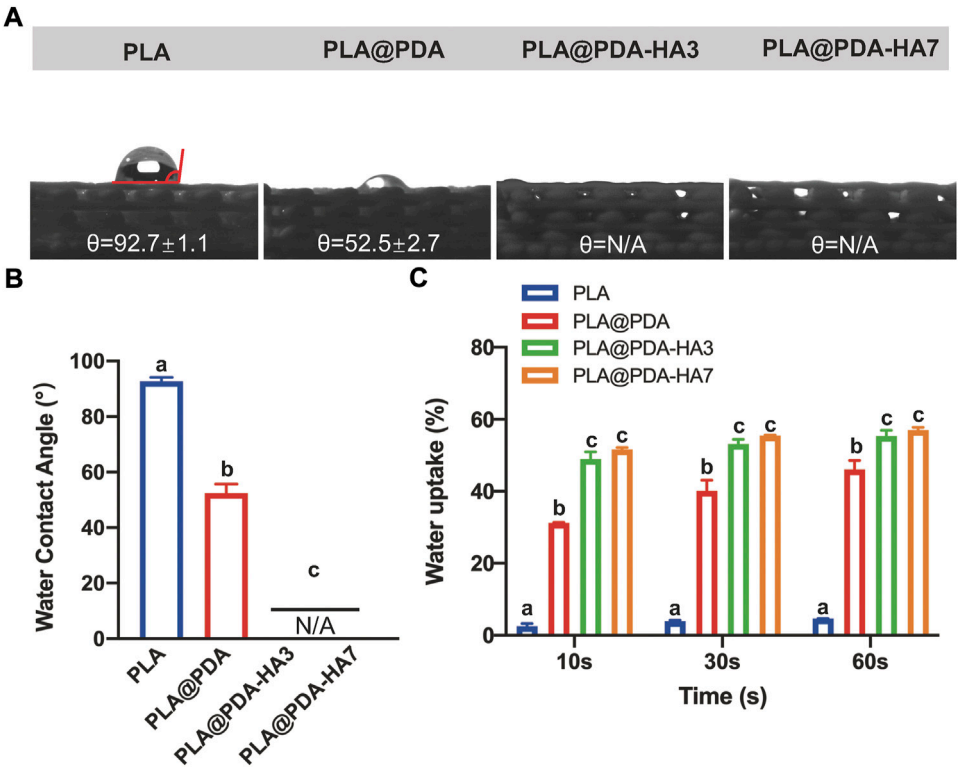

FIGURE 5
Hydrophilicity assay of PLA, PLA@PDA, PLA@PDA-HA3, and PLA@PDA-HA7 scaffolds. **(A)** Representative photographs of water droplets on the surface of each scaffold. **(B)** The water contact angle within each group. **(C)** Wettability analysis of each scaffold immersed in PBS for 10, 30, and 60 s. Dissimilar letters indicate statistically significant differences between groups (n = 6, p < 0.05).

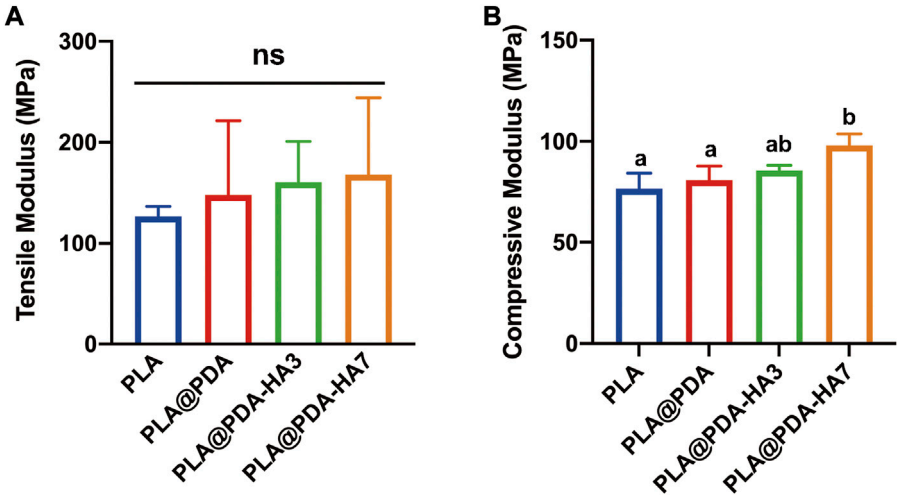

FIGURE 6
Mechanical properties of PLA, PLA@PDA, PLA@PDA-HA3, and PLA@PDA-HA7 scaffolds. **(A)** Tensile modulus and **(B)** compressive modulus of each specimen. Dissimilar letters indicate statistical differences between groups (n = 3, p < 0.05).

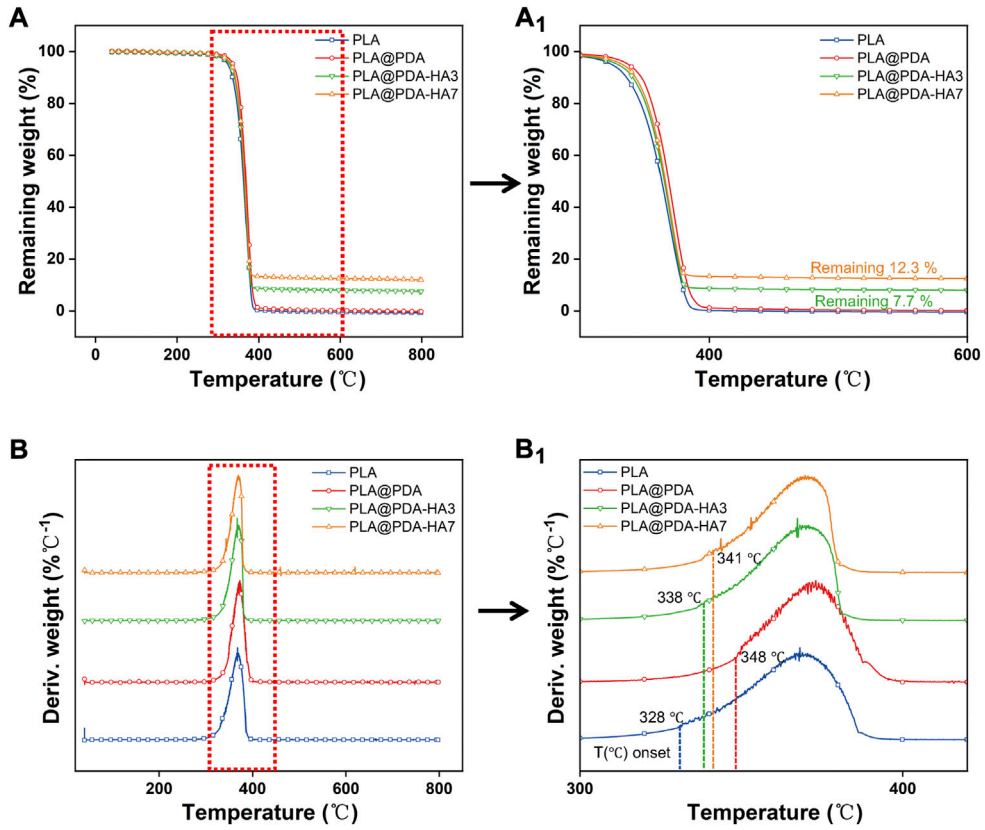

FIGURE 7
Thermal gravimetric curves (TGA) **(A)** and derivative thermal gravimetric curves (DTG) **(B)** of PLA, PLA@PDA, PLA@PDA-HA3, and PLA@PDA-HA7 scaffolds. Close-up views of TGA **(a_1)** and DTG **(b_1)** curves.

Mechanical behaviors of scaffolds

The mechanical properties of each scaffold were determined *via* tensile and compressive strength tests, and the corresponding young's modulus was calculated from the stress-strain curves obtained from the textxpert® III software (Zwick Roell, Ulm, Germany). Figure 6 shows the fabricated scaffold samples' representative mechanical properties (tensile and compressive modulus). It was seen that the elastic modulus of specimens was increased after surface modification, yet no statistical significance was found between groups. Statistically, the tensile modulus of PLA was 126.9 MPa, while the surface-modified group (PLA@PDA, PLA@PDA-HA3, and PLA@PDA-HA7) increased slightly to 148.1, 160.7, and 168.1 MPa respectively. On the other hand, the compressive modulus of scaffolds was significantly enhanced after immobilizing HA nanoparticles for 7 days. In detail, the compressive modulus of the PLA scaffold was 30.7 MPa, and it increased slightly to 32.4 MPa after introducing PDA to the surface. After surface functionalization with nHA for 3 days, the compressive modulus reached 34.2 MPa. More importantly, the compressive modulus of PLA@PDA-HA7 further increased to 39.2 MPa, significantly higher than the other three groups. However, it should be noted that no significant difference was recorded between PLA, PLA@PDA, and PLA@PDA-HA3 groups.

Thermal gravimetric analysis (TGA)

The thermal decomposition test was carried out to quantitatively determine the amount of HA nanoparticles deposited on the surface of PLA scaffolds. Figure 7 represents the TGA and DTG curves of different samples. According to Figure 7A, all samples showed a one-step thermolysis process at 328–380°C, which was evident by one peak from DTG curves (Figure 7B). The thermal degradation onset temperature for the PLA, PLA@PDA, PLA@PDA-HA3, and PLA@PDA-HA7 specimens were 328°C, 348°C, 338°C, and 341°C, respectively. For PLA and PLA@PDA specimens, no solid inorganic residues were found after the thermal decomposition, indicating that the tested samples were composed of pure organic components. After surface modification with nHA for 3 and 7 days, the mass ratio of 7.7

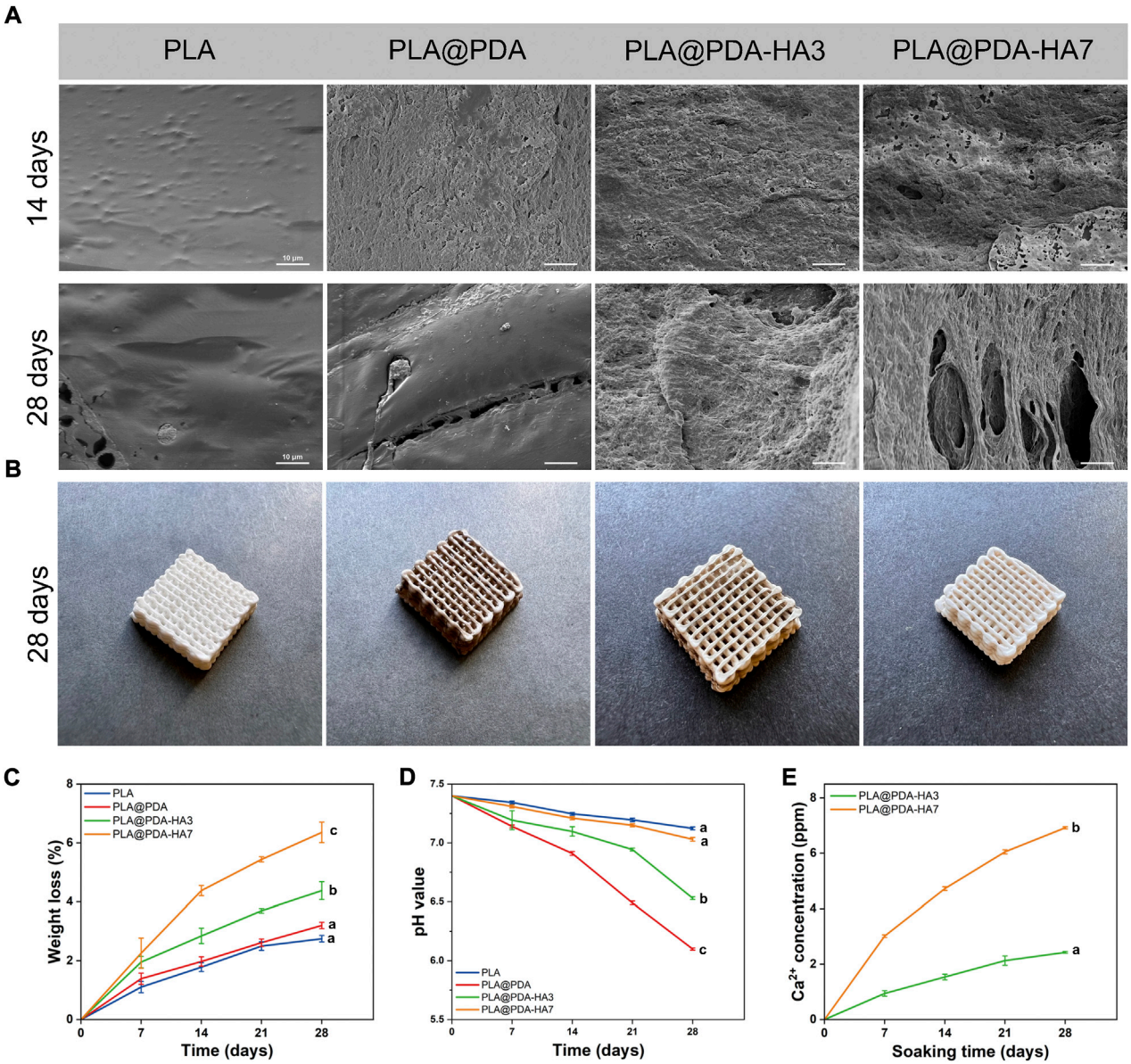

FIGURE 8
In-vitro degradation behavior of PLA, PLA@PDA, PLA@PDA-HA3, and PLA@PDA-HA7 scaffolds after immersing in PBS for 28 days. **(A)** SEM images of surface morphology of each scaffold after soaking in PBS for 14 and 28 days; **(B)** Representative optical photographs of each scaffold after 28 days of immersing; **(C)** Weight loss ratio of each scaffold for 28 days of degradation; **(D)** pH variation of immersing solution for 28 days; **(E)** 28 days' Ca^{2+} release profile of PLA@PDA-HA3 and PLA@PDA-HA7 scaffolds.

% and 12.3% inorganic residues was reported, corresponding to the amount of coated nHA on PLA@PDA-HA3, PLA@PDA-HA7 scaffolds, respectively.

In-vitro degradation behavior of scaffolds

The specimens were immersed in PBS solution for 28 days for *in-vitro* degradation analysis. According to Figure 8B, PLA@PDA, PLA@PDA-HA3, and PLA@PDA-HA7 scaffolds lightened in color after being soaked in PBS for 28 days, and all scaffolds showed no noticeable changes in their macrostructure, suggesting that the scaffolds were stable during 28 days of the degradation process. Figure 8A depicts the microstructure changes of different scaffolds on days 14 and 28. It can be seen that after 14 days of soaking in PBS, the microstructure of the PLA scaffold remained unchanged, exhibiting a relatively smooth and continuous surface with some tiny protuberances. In

PLA@PDA scaffolds, visible eroded surfaces with tiny pits were observed after 14 days. After surface modification with nHA, degradation signs were visible. For the PLA@PDA-HA3 scaffold sample, an irregular surface with considerably large-sized pits was evenly distributed, and this trend became more evident in the PLA@PDA-HA7 scaffolds. After 28 days of soaking, the surfaces of PLA scaffolds were relatively intact, and only a few small-sized pits were formed.

Similarly, shallow cracks and minor holes were generated on the surface of PLA@PDA scaffolds. Interestingly, in contrast to the PLA and PLA@PDA scaffolds, nHA modification accelerated the degradation process for continuous immersion after 14 days. In the case of PLA@PDA-HA3, large-sized cracks and holes were easily observed. More importantly, PLA@PDA-HA7 exhibits large fractures that connect the surface to the inner side, indicating the highest degradation rate of all scaffolds after 28 days of immersion.

Accordingly, weight changes of scaffolds were recorded along with the degradation test. As depicted in Figure 8C, all scaffolds exhibited a continuous weight loss during 28 days of immersion. In detail, PLA showed the lowest mass loss, reaching 2.7% at 14 and 28 days, respectively. While PLA@PDA, PLA@PDA-HA3, and PLA@PDA-HA7 scaffold samples, exhibited a gradual increase in mass loss, reaching 3.2%, 4.4%, and 6.4% at 28 days, respectively. These results were in accordance with their degradation behavior.

Moreover, the pH variations of PBS solution for 28 days immersion period were recorded to understand the degradation behavior of all scaffolds. According to Figure 8D, the pH of all sample solutions gradually lowered with the extension of soaking time, indicating the formation of acidic by-products during the degradation process of PLA scaffolds. Specifically, the pH value for the PLA group tended to be more stable than the other three groups, reducing slightly to 7.1 during 28 days of immersion. On the other hand, the PLA@PDA specimen exhibited the most significant reduction in pH value, decreasing from 7.4 to 6.1 after 28 days of degradation. Interestingly, with the introduction of nHA to the surface, less reduction in pH value was observed, and such a tendency became clearer when nHA coating time was extended to 7 days. The pH value for PLA@PDA-HA3 decreased from 7.4 to 6.5, whereas the pH for PLA@PDA-HA7 was 7.0 at the end of the 28th day of incubation.

The calcium ion release properties of PLA@PDA-HA3 and PLA@PDA-HA7 scaffold samples were also measured at the various soaking period (Figure 8E). As expected, the PLA@PDA-HA7 exhibits the highest amount of Ca^{2+} releasing profile, almost three times that of PLA@PDA-HA3 samples. In detail, at the end of 7 days, the Ca^{2+} concentration for the PLA@PDA-HA7 sample reached 3.01 ppm, followed by 4.72, 6.05, and 6.92 ppm for 14, 21, and 28 days respectively. For the PLA@PDA-HA3 sample, the calcium ion concentration was 0.94, 1.53, 2.13, and 2.43 ppm at 7, 14, 21, and 27 days.

Discussion

The present study aimed to comprehensively understand the physicochemical properties of surface bioactivated osteogenic PLA scaffolds fabricated using AM technology. The first hypothesis that the nHA and PDA layer would increase its hydrophilicity was proved by water uptake analysis and WCA measurement. The second hypothesis that the nHA and PDA coating would stimulate *in-vitro* hydrolysis of PLA scaffold was testified by SEM, mass loss study. Finally, the third hypothesis that the surface modification of the scaffolds would not lead to compromised mechanical strength was demonstrated by tensile and compressive strength tests.

In the last decade, PLA-based scaffolds produced by 3D printing technology had widespread uses in bone tissue engineering owing to their good biocompatibility, biodegradability, and printability (Kao et al., 2015; Hassanajili et al., 2019; Yao et al., 2020). However, the major drawbacks of PLA, such as hydrophobicity, slow degradation behavior, and lack of abundant cell-recognition functional group, limit further clinical application (Chen et al., 2021a). Until recently, researchers have proposed various approaches to optimize the osteogenic properties of the PLA to promote adequate cell interactions with its surface (Feng et al., 2018; Shuai et al., 2021). One of the promising approaches was integrating bioactive molecules and/or ceramics with PLA at the initial stage to optimize filaments for subsequent 3D printing. Generally, solvent-evaporation and mechanical-milling methods are typical approaches to fabricating PLA composites (Schliephake et al., 2015; Gayer et al., 2019). However, these approaches may result in undesirable outcomes, such as remaining toxic organic solvents and non-homogeneous composites with unpredictable biological performances (Gayer et al., 2019; Govindrao et al., 2019; Yu et al., 2019; Brounstein et al., 2021).

In the present study, HA nanoparticles were successfully introduced to the surface of 3D printed PLA scaffolds by organic solvent-free polydopamine coating. The present work studied the macrostructure and microstructure of 3D printed PLA scaffolds modified with PDA and nHA (Figure 2). After surface coating with PDA, the PLA scaffold's color darkened significantly, ascribed to the formation of eumelanin on the surface. Similar color changes were also detected in PLA@PDA-HA3 and PLA@PDA-HA7 groups. Moreover, this result was further supported by the EDX, XRD, FTIR-ATR, and TGA tests. Specifically, as mentioned above, regarding the XRD result, the PLA@PDA-HA3 did not show the typical diffraction peaks of nHA particles, which is most probably ascribed to the low content of nHA. To meet the XRD test requirements, the PLA samples were printed in the shape of cylinders (D: 10 mm; H: 1 mm) before coating with PDA and nHA according to previously reported literature (Kim et al., 2021). Due to the small-size and porous-free structure of the specimens, a relatively lower amount of nHA was

immobilized onto the surface after 3 days of immersion, which was under the lower limit of detection of XRD analysis. Regarding the microstructure of PLA scaffolds, SEM tests confirmed that the interconnected pore size was ~400 μm, which was in accordance with the previously described optimal pore size for bone regeneration (200–500 μm) (Thavornyutikarn et al., 2014). Additionally, controlled porosity (36% ± 0.005 ($p < 0.05$)), which was within the range of cancellous bone, of the 3D-printed PLA scaffolds was detected (Bose et al., 2012).

Another major limitation of the 3D-printed PLA scaffold is its hydrophobic properties, which were not conducive for osteoblasts to promote bone formation (Mohsenimehr et al., 2020). Indeed, the hydrophilicity of biomaterials is a pivotal factor affecting initial cell adhesion (Boyan et al., 2017). The present study achieved significantly improved surface hydrophilicity by PDA coating (WCA from 92.7° to 52.5°). Previous studies have pointed out that the PDA contains many hydrophilic functional groups, such as amino groups, which enhance surface wettability by promoting hydrogen bonding (Li et al., 2019). More interestingly, after immobilizing nHA on the PLA@PDA surface, the water droplet was absorbed instantly after it touched the surface, demonstrating that the nHA coating could further turn its surface into a superhydrophilic surface (WCA = 0°). It should be noted that apart from the abundant hydroxyl groups from HA that enhance the surface hydrophilicity to a further extent, nanosized HA particles with increased specific areas exposed to the surface were also reportedly contributing to the results above (Crisan et al., 2015). As a result, by achieving a hydrophilic surface, the nHA-coated PLA scaffolds are expected to be covered by serum more rapidly to provide bioactive molecular factors that can further stimulate cells to proliferate and osteogenic differentiate at an initial stage.

The micro-topography of the scaffold surface is another decisive factor for their osteogenic behavior since it is the first site for surrounding cells and tissues in contact (Cai et al., 2020). There have been controversial reports regarding the correlation between surface roughness and osteogenic behavior. For instance, literature has demonstrated that the optimal osteogenic properties were realized on micro-scale surface roughness (Sa = 3–4 μm) (Costa et al., 2013). In contrast, Wong et al. reported that a relatively smooth surface roughness (Sa = 0.22 μm) provided a good platform for osteoblastic MG63 cell attachment and proliferation (Wong et al., 2020). However, most preclinical studies focused on elucidating the mechanism of how surface roughness directly affects (pre-) osteoblastic cell behavior solely. Apart from osteoblasts, osteoclasts have a remarkable impact on bone formation since they reportedly initiate the bone remodeling process earlier than osteoblastic cells (Orsini et al., 2012). A recent study by Zhang et al. revealed the relationship between surface roughness and bone formation by uncovering the mechanism of cross-talk between osteoblasts and osteoclasts (Zhang et al., 2018). The results showed that surface roughness is an essential factor for osteogenesis and osteoclastogenesis, which positively affects the osteogenic differentiation of osteoblastic cells far more obviously than osteoblast itself. Accordingly, although osteoblastic cell differentiation was optimized on micro rough surfaces (ca. Sa = 3–4 μm), the authors suggested smooth surfaces were more suitable for bone formation (Zhang et al., 2018). In the present study, the surface roughness of PLA scaffolds gradually increased with the extension of nHA coating time. As a result, the Sa of PLA@PDA-HA7 reached 0.40 μm, however, it could still be regarded as a relatively smooth surface (<1 μm) compared to micro-scale rough surfaces. Further studies are needed to clarify the desired surface roughness for different cell and tissue types to achieve the desired outcomes.

The mechanical properties of 3D printed scaffolds are important factors determining their *in vivo* performance for bone regeneration in the long term (Prasadh and Wong, 2018). They typically undergo different mechanical stress such as compression and tension from surrounding bone tissues, affecting their stability and osseointegration properties (Little et al., 2011). Therefore, the mechanical properties of scaffolds should be tailored to match the native bone to be repaired (Little et al., 2011). After surface modification, the mechanical behaviors of scaffolds should be characterized before implantation to avoid possible implant failure. In the present study, the tensile and compressive tests were carried out for all scaffolds to determine the changes in their mechanical properties before and after surface modification. Regarding tensile tests, although there was no statistical significance among all four groups, the tensile modulus increased slightly after surface modification and reached its highest level of 168 MPa in the PLA@PDA-HA7 group. On the other hand, the compressive strength of PLA@PDA-HA7 scaffolds was significantly higher than PLA and PLA@PDA groups; however, not statistically significant compared to the PLA@PDA-HA3 group. Taking all results together, it can be concluded that the PDA and nHA coating on the surface of PLA scaffolds would grant them enhanced resistance and were less prone to deformation. These results could be attributed to two reasons. First, the nHA and PDA coating acts as an adhesive transition layer, resulting in a favorable stress buffer between the coating layer and scaffold surface (Guan et al., 2018). Second, the uniformly dispersed nanosized HA particles with a high modulus act as a buffer zone that consumes more fracture energy (Meng et al., 2019).

Generally, biodegradation of bone grafting substitutes is achieved during the repair of bone defects, which requires a consistent rate between new bone formation and artificial implant scaffold degradation (Bose et al., 2012). Although 3D-printed PLA-based scaffolds are biodegradable, the degradation process is deemed to be too slow (2–3 years) to match the rate of *in vivo* new bone formation (8–12 weeks) (Feng et al., 2021). Theoretically, in a physiological environment, the PLA-based implant scaffold is mainly degraded by the action of water

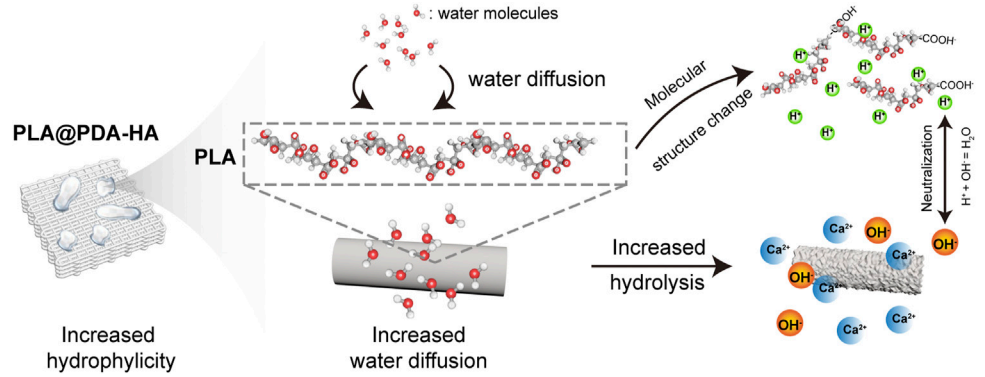

FIGURE 9
Schematic illustration of hydrolysis process of PLA@PDA-HA scaffolds. The increased surface wettability of nHA-modified PLA scaffolds enhances water diffusion, by which PLA chains are "attacked" by a more significant number of water molecules. As a result, an accelerated hydrolysis process, namely the cleavage of the ester bond, took place, and in turn, a local acidic environment was formed due to the exposure of the carboxyl group. The hydroxyl group from nHA and PDA neutralized the local acids greatly.

molecules (Feng et al., 2021). In the present study, enhanced biodegradable properties were achieved by introducing HA nanoparticles to the surface of 3D printed PLA scaffolds, as evidenced by Figure 7. As discussed above, the primary mechanism of PLA scaffold degradation is hydrolysis. Thus, it was speculated that the improved hydrophilicity of the PLA scaffold surface increased water intake and initiated the corrosion of the surface, which in turn promoted the immersion of water molecules. Apart from increased hydrophilicity of scaffold surface, nHA coating is another important factor that accelerates the degradation. According to previous literature (Yuan et al., 2002), the PLA-based scaffolds degrade much faster in an alkaline environment than in an acidic solution. As illustrated in Figure 9, Ca^{2+} released from the PLA@PDA-HA3 and PLA@PDA-7 scaffold formed hydroxide, thereby creating a local micro-alkaline environment, further accelerating the degradation of PLA scaffolds. The results suggested that the PLA@PDA-HA7 possesses the fastest degradation rate among all scaffolds, mainly due to its superior hydrophilicity and nHA coating. Notably, after 28 days of immersion, the mass loss ratio of PLA@PDA-HA3 and PLA reached 4.4 % and 6.4%, respectively; however, the macrostructure remains unchanged, indicating the degradation was mainly confined to the surface area of the scaffold and did not affect the overall stability during the initial degradation process.

Meanwhile, the pH variation during 28 days of immersion time was recorded. Proverbially, the acidic environments produced during the biodegradation of PLA scaffolds might cause a local immune response, which is a detrimental factor for bone regeneration (Feng et al., 2021; Shuai et al., 2021). The results from the present immersion test revealed that the nHA coating layer greatly neutralized the acidic by-products produced during the degradation process of the PLA scaffold, and such trends became more evident with the increasing amount of HA nanoparticles on the surface. A plausible explanation for this result is that the nHA possesses weak alkalinity, and the hydroxyl group of nHA acts as a buffer to suppress the acidic environment (Wang et al., 2021). In contrast, the PDA coating layer seems to "accelerate" the acidic formation, as the pH decreased to 6.1 after 28 days of immersion. On the one hand, as discussed above, the increased hydrophilicity of the PLA scaffolds achieved by the PDA coating layer would enhance their hydrolysis, which promotes the formation of acidic degradation products of the PLA. On the other hand, the acidic functional group of PDA, namely, the catechol group, is exposed while the degradation progress, resulting in a decrease in the local pH value (Chen et al., 2021b).

Moreover, according to the calcium ion release profile (Figure 8E), both nHA-modified PLA scaffolds showed a "fast followed by slow" trend during 28 days of immersion. At the end of 28 days of soaking, the accumulated Ca^{2+} concentration released by PLA@PDA-HA3 and PLA@PDA-HA7 reached 2.43 ppm (0.06 mM) and 6.92 ppm (0.173 mM), respectively. Previous studies have demonstrated the correlation between extracellular Ca^{2+} concentration and osteogenic behavior. For instance, upregulated alkaline phosphatase (ALP) and osteocalcin (OCN) expression of MC3T3-E1 cells was detected when local Ca^{2+} concentration reached 8 ppm (Park et al., 2010), with similar Ca^{2+} concentration reported in the present study. More importantly, Park et al. previously reported that the scaffold's ability to increase local Ca^{2+} concentration is more critical than its surface's roughness and hydrophilicity, promoting osteogenic differentiation. Other studies have also revealed that the surface functionalization with bioactive molecules such as Ca^{2+} could greatly enhance early cellular response and subsequent osteogenic behavior such as extracellular mineralization (Kim et al., 2016). Thus,

considering all these results, the nHA coating layer could provide surrounding cells and tissues with a conducive environment for bone formation by neutralizing the pH of the local environment and providing sufficient Ca^{2+} to optimize their osteoconductive and osteoinductive properties.

Generally, additively manufactured 3D scaffolds for bone tissue engineering have a wide range of advantages over conventional fabrication methods in terms of cost, time effectiveness, and flexibility in designing patient-specific implants (Zhang et al., 2019). Nevertheless, limited material resources for 3D printing make it hard to pick specific materials for the desired application. On the other hand, traditionally available biomaterials are not feasible for 3D printing, while the best performing AM materials, in terms of printability and accuracy, are often not osteoconductive and hard to biodegrade (Zhang et al., 2019; Qu, 2020). In this study, we provide a facile approach by combining the traditionally available techniques of surface modification with the cutting-edge technology of AM to better engineer patient-specific bone regenerative scaffolds. The findings presented in this study, physiochemical properties of biomimicry produced PLA@PDA-HA scaffolds, would grant effective application both in bone regenerative medicine and biomedical engineering. Furthermore, considering the relatively low costs of PLA and nHA materials, the present study provided, for the first time, a comprehensive understanding and evaluation of the effects of nHA functionalized 3D printed PLA scaffolds, from their design, fabrication, and post-process to mechanical behavior, surface physicochemical properties, and biodegradability. These findings provide insights into how AM methods could improve the application potential in bone tissue engineering. The authors believe that such a multidisciplinary technology of post-processing additively manufactured scaffolds would foresee a hopeful paradigm shift in the field of regenerative medicine. Further studies, both *in-vitro* and *in-vivo* biological performance, should be carried out in the near future to determine osteogenic efficacy before clinical application.

Conclusion

In the present study, PDA mediated coating method was applied to successfully immobilize HA nanoparticles onto the surface of PLA scaffolds fabricated by material extrusion-based 3D printing technology. Such a facile, mussel-inspired post-processing method enables nHA to be highly loaded on the PLA scaffold surface after 3 and 7 days of immersion, resulting in a 7.7 % and 12.3% mass ratio, respectively. The surface functionalization with PDA and nHA effectively increased the hydrophilicity of PLA scaffolds, which greatly enhanced the surface hydrolysis process of the PLA scaffolds. Furthermore, mechanical behavior and surface macrostructures were not compromised thanks to the post-modification method used in this research. Instead, significantly enhanced compressive modulus and surface roughness was detected in the PLA@PDA-HA7 group. With these encouraging results, nHA functionalized PLA scaffolds have great potential in bone tissue engineering.

Data availability statement

The original contributions presented in the study are included in the article/Supplementary Material, further inquiries can be directed to the corresponding authors.

Author contributions

MC and NL conceived and designed the project. JC and SK conducted the SEM and ICP-MS experiments. NR, NS, and FT supervised the project. All authors contributed to data analysis and manuscript drafting.

Acknowledgments

This study is supported by the MIRACLE (Minimally Invasive Robot-Assisted Computer-guided LaserosteomE) project. MC expresses gratitude to China Scholarship Council (CSC) for their kind support. Thanks to Sven Freimann from Constable and Housecroft research group for assistance with the TGA analysis.

Conflict of interest

The authors declare that the research was conducted in the absence of any commercial or financial relationships that could be construed as a potential conflict of interest.

Publisher's note

Supplementary material

The Supplementary Material for this article can be found online at: https://www.frontiersin.org/articles/10.3389/fbioe.2022.989729/full#supplementary-material

References

Abe, H., Nozaki, K., Sokabe, S., Kumatani, A., Matsue, T., and Yabu, H. (2020). S/N Co-doped hollow carbon particles for oxygen reduction electrocatalysts prepared by spontaneous polymerization at oil–water interfaces. *ACS omega* 5, 18391–18396. doi:10.1021/acsomega.0c02182

Abe, H., and Yabu, H. (2021). Bio-inspired incrustation interfacial polymerization of dopamine and cross-linking with gelatin toward robust, biodegradable three-dimensional hydrogels. *Langmuir* 37, 6201–6207. doi:10.1021/acs.langmuir.1c00364

Blokhuis, T., and Arts, J. C. (2011). Bioactive and osteoinductive bone graft substitutes: Definitions, facts and myths. *Injury* 42, S26–S29. doi:10.1016/j.injury.2011.06.010

Bose, S., Roy, M., and Bandyopadhyay, A. (2012). Recent advances in bone tissue engineering scaffolds. *Trends Biotechnol.* 30, 546–554. doi:10.1016/j.tibtech.2012.07.005

Boyan, B. D., Lotz, E. M., and Schwartz, Z. (2017). Roughness and hydrophilicity as osteogenic biomimetic surface properties. *Tissue Eng. Part A* 23, 1479–1489. doi:10.1089/ten.tea.2017.0048

Brien, F. (2011). Biomaterials & scaffolds Every day thousands of surgical procedures are performed to replace. *Mat. Today* 14, 88–95. doi:10.1016/S1369-7021(11)70058-X

Brounstein, Z., Yeager, C. M., and Labouriau, A. (2021). Development of antimicrobial PLA composites for fused filament fabrication. *Polymers* 13, 580. doi:10.3390/polym13040580

Cai, S., Wu, C., Yang, W., Liang, W., Yu, H., and Liu, L. (2020). Recent advance in surface modification for regulating cell adhesion and behaviors. *Nanotechnol. Rev.* 9, 971–989. doi:10.1515/ntrev-2020-0076

Chakraborty, G., Gupta, A., Pugazhenthi, G., and Katiyar, V. (2018). Facile dispersion of exfoliated graphene/PLA nanocomposites via *in situ* polycondensation with a melt extrusion process and its rheological studies. *J. Appl. Polym. Sci.* 135, 46476. doi:10.1002/app.46476

Chen, S., Zhao, X., and Du, C. (2018). Macroporous poly (l-lactic acid)/chitosan nanofibrous scaffolds through cloud point thermally induced phase separation for enhanced bone regeneration. *Eur. Polym. J.* 109, 303–316. doi:10.1016/j.eurpolymj.2018.10.003

Chen, W., Nichols, L., Brinkley, F., Bohna, K., Tian, W., Priddy, M. W., et al. (2021a). Alkali treatment facilitates functional nano-hydroxyapatite coating of 3D printed polylactic acid scaffolds. *Mater. Sci. Eng. C* 120, 111686. doi:10.1016/j.msec.2020.111686

Chen, X., Yang, W., Zhang, J., Zhang, L., Shen, H., and Shi, D. (2021b). Alkalinity triggered the degradation of polydopamine nanoparticles. *Polym. Bull. Berl.* 78, 4439–4452. doi:10.1007/s00289-020-03312-2

Costa, D. O., Prowse, P. D., Chrones, T., Sims, S. M., Hamilton, D. W., Rizkalla, A. S., et al. (2013). The differential regulation of osteoblast and osteoclast activity by surface topography of hydroxyapatite coatings. *Biomaterials* 34, 7215–7226. doi:10.1016/j.biomaterials.2013.06.014

Crisan, L., Crisan, B., Soritau, O., Baciut, M., Biris, A. R., Baciut, G., et al. (2015). In vitro study of biocompatibility of a graphene composite with gold nanoparticles and hydroxyapatite on human osteoblasts. *J. Appl. Toxicol.* 35, 1200–1210. doi:10.1002/jat.3152

Dutta, S., Passi, D., Singh, P., and Bhuibhar, A. (2015). Ceramic and non-ceramic hydroxyapatite as a bone graft material: A brief review. *Ir. J. Med. Sci.* 184, 101–106. doi:10.1007/s11845-014-1199-8

Feng, J., Yang, G., Zhang, S., Liu, Q., Jafari, S. M., and Mcclements, D. J. (2018). Fabrication and characterization of β-cypermethrin-loaded PLA microcapsules prepared by emulsion-solvent evaporation: Loading and release properties. *Environ. Sci. Pollut. Res.* 25, 13525–13535. doi:10.1007/s11356-018-1557-6

Feng, P., Jia, J., Liu, M., Peng, S., Zhao, Z., and Shuai, C. (2021). Degradation mechanisms and acceleration strategies of poly (lactic acid) scaffold for bone regeneration. *Mater. Des.* 210, 110066. doi:10.1016/j.matdes.2021.110066

Gayer, C., Ritter, J., Bullemer, M., Grom, S., Jauer, L., Meiners, W., et al. (2019). Development of a solvent-free polylactide/calcium carbonate composite for selective laser sintering of bone tissue engineering scaffolds. *Mater. Sci. Eng. C* 101, 660–673. doi:10.1016/j.msec.2019.03.101

Govindrao, P., Ghule, N., Haque, A., and Kalaskar, M. (2019). Journal of drug delivery science and technology metal nanoparticles synthesis: An overview on methods of preparation, advantages and disadvantages, and applications. *J. Drug Deliv. Sci. Technol.* 53, 101174. doi:10.1016/j.jddst.2019.101174

Grenier, J., Duval, H., Barou, F., Lv, P., David, B., and Letourneur, D. (2019). Mechanisms of pore formation in hydrogel scaffolds textured by freeze-drying. *Acta biomater.* 94, 195–203. doi:10.1016/j.actbio.2019.05.070

Grewal, M. S., Abe, H., Matsuo, Y., and Yabu, H. (2021). Aqueous dispersion and tuning surface charges of polytetrafluoroethylene particles by bioinspired polydopamine–polyethyleneimine coating via one-step method. *R. Soc. Open Sci.* 8, 210582. doi:10.1098/rsos.210582

Grewal, M. S., and Yabu, H. (2020). Biomimetic catechol-based adhesive polymers for dispersion of polytetrafluoroethylene (PTFE) nanoparticles in an aqueous medium. *RSC Adv.* 10, 4058–4063. doi:10.1039/c9ra10606e

Guan, X., Hwang, K., Lee, D., Kim, T., and Kim, N. (2018). Applied Surface Science Enhanced mechanical properties of self-polymerized polydopamine-coated recycled PLA filament used in 3D printing. *Appl. Surf. Sci.* 441, 381–387.

Hassanajili, S., Karami-Pour, A., Oryan, A., and Talaei-Khozani, T. (2019). Preparation and characterization of PLA/PCL/HA composite scaffolds using indirect 3D printing for bone tissue engineering. *Mater. Sci. Eng. C* 104, 109960. doi:10.1016/j.msec.2019.109960

Iof, S. (2012). *ISO 527-1: 2012 plastics–determination of tensile properties*. Geneva, Switzerland: Standardization IOF.

Kao, C.-T., Lin, C.-C., Chen, Y.-W., Yeh, C.-H., Fang, H.-Y., and Shie, M.-Y. (2015). Poly (dopamine) coating of 3D printed poly (lactic acid) scaffolds for bone tissue engineering. *Mater. Sci. Eng. C* 56, 165–173. doi:10.1016/j.msec.2015.06.028

Kim, C. G., Han, K. S., Lee, S., Kim, M. C., Kim, S. Y., and Nah, J. (2021). Fabrication of biocompatible polycaprolactone–hydroxyapatite composite filaments for the FDM 3D printing of bone scaffolds. *Appl. Sci.* 11, 6351. doi:10.3390/app11146351

Kim, H.-S., Kim, Y.-J., Jang, J.-H., and Park, J.-W. (2016). Surface engineering of nanostructured titanium implants with bioactive ions. *J. Dent. Res.* 95, 558–565. doi:10.1177/0022034516638026

Lee, H. A., Park, E., and Lee, H. (2020). Polydopamine and its derivative surface chemistry in material science: A focused review for studies at KAIST. *Adv. Mat.* 32, 1907505. doi:10.1002/adma.201907505

Lee, H., Dellatore, S. M., Miller, W. M., and Messersmith, P. B. (2007). Mussel-inspired surface chemistry for multifunctional coatings. *science* 318, 426–430. doi:10.1126/science.1147241

Li, R., Liu, J., Shi, A., Luo, X., Lin, J., Zheng, R., et al. (2019). A facile method to modify polypropylene membrane by polydopamine coating via inkjet printing technique for superior performance. *J. colloid interface Sci.* 552, 719–727. doi:10.1016/j.jcis.2019.05.108

Little, C. J., Bawolin, N. K., and Chen, X. (2011). Mechanical properties of natural cartilage and tissue-engineered constructs. *Tissue Eng. Part B Rev.* 17, 213–227. doi:10.1089/ten.teb.2010.0572

Liu, S., Zheng, Y., Liu, R., and Tian, C. (2020). Preparation and characterization of a novel polylactic acid/hydroxyapatite composite scaffold with biomimetic micro-nanofibrous porous structure. *J. Mat. Sci. Mat. Med.* 31, 74–11. doi:10.1007/s10856-020-06415-4

Liu, Y., Ai, K., and Lu, L. (2014). Polydopamine and its derivative materials: Synthesis and promising applications in energy, environmental, and biomedical fields. *Chem. Rev.* 114, 5057–5115. doi:10.1021/cr400407a

Ma, Z., Mao, Z., and Gao, C. (2007). Surface modification and property analysis of biomedical polymers used for tissue engineering. *Colloids Surfaces B Biointerfaces* 60, 137–157. doi:10.1016/j.colsurfb.2007.06.019

Madrid, A. P. M., Vrech, S. M., Sanchez, M. A., and Rodriguez, A. P. (2019). Advances in additive manufacturing for bone tissue engineering scaffolds. *Mater. Sci. Eng. C* 100, 631–644. doi:10.1016/j.msec.2019.03.037

Meng, K., Wang, X., Xu, Q., Li, Z., Liu, Z., Wu, L., et al. (2019). *In situ* observation of crystallization dynamics and grain orientation in sequential deposition of metal halide perovskites. *Adv. Funct. Mat.* 29, 1902319. doi:10.1002/adfm.201902319

Mohsenimehr, S., Khani, M. R., Fani, N., Eslaminejad, M. R. B., Shokri, B., and Ghassami, A. (2020). Surface modification of PLA scaffold using radio frequency (RF) nitrogen plasma in tissue engineering application. *Surf. Topogr.* 8, 015012. doi:10.1088/2051-672x/ab7c30

Mondal, S., Nguyen, T. P., Hoang, G., Manivasagan, P., Kim, M. H., Nam, S. Y., et al. (2020). Hydroxyapatite nano bioceramics optimized 3D printed poly lactic acid scaffold for bone tissue engineering application. *Ceram. Int.* 46, 3443–3455. doi:10.1016/j.ceramint.2019.10.057

Novotna, K., Zajdlova, M., Suchy, T., Hadraba, D., Lopot, F., Zaloudkova, M., et al. (2014). Polylactide nanofibers with hydroxyapatite as growth substrates for osteoblast-like cells. *J. Biomed. Mat. Res. A* 102, 3918–3930. doi:10.1002/jbm.a.35061

Orsini, E., Salgarello, S., Martini, D., Bacchelli, B., Quaranta, M., Pisoni, L., et al. (2012). Early healing events around titanium implant devices with different surface

microtopography: A pilot study in an in vivo rabbit model. *Sci. World J.*, 2012, 1–9. doi:10.1100/2012/349842

Park, J., Lee, S. J., Jung, T. G., Lee, J. H., Kim, W. D., Lee, J. Y., et al. (2021). Surface modification of a three-dimensional polycaprolactone scaffold by polydopamine, biomineralization, and BMP-2 immobilization for potential bone tissue applications. *Colloids Surfaces B Biointerfaces* 199, 111528. doi:10.1016/j.colsurfb.2020.111528

Park, J. W., Kim, Y. J., Jang, J. H., and Song, H. (2010). Osteoblast response to magnesium ion-incorporated nanoporous titanium oxide surfaces. *Clin. oral implants Res.* 21, 1278–1287. doi:10.1111/j.1600-0501.2010.01944.x

Prasadh, S., and Wong, R. C. W. (2018). Unraveling the mechanical strength of biomaterials used as a bone scaffold in oral and maxillofacial defects. *Oral Sci. Int.* 15, 48–55. doi:10.1016/s1348-8643(18)30005-3

Qiang, L., Zhang, C., Qu, F., Wu, X., and Wang, H. (2018). Electrospun porous PDLLA Fiber membrane coated with nHA. *Appl. Sci.* 8, 831. doi:10.3390/app8050831

Qu, H. (2020). Additive manufacturing for bone tissue engineering scaffolds. *Mater. Today Commun.* 24, 101024. doi:10.1016/j.mtcomm.2020.101024

Ramesh, N., Moratti, S. C., and Dias, G. J. (2018). Hydroxyapatite–polymer biocomposites for bone regeneration: A review of current trends. *J. Biomed. Mat. Res.* 106, 2046–2057. doi:10.1002/jbm.b.33950

Roseti, L., Parisi, V., Petretta, M., Cavallo, C., Desando, G., Bartolotti, I., et al. (2017). Scaffolds for bone tissue engineering: State of the art and new perspectives. *Mater. Sci. Eng. C* 78, 1246–1262. doi:10.1016/j.msec.2017.05.017

Ryu, J., Ku, S. H., Lee, H., and Park, C. B. (2010). Mussel-inspired polydopamine coating as a universal route to hydroxyapatite crystallization. *Adv. Funct. Mat.* 20, 2132–2139. doi:10.1002/adfm.200902347

Schliephake, H., Boven, J., Backhaus, S., Annen, T., and Epple, M. (2015). Solvent free production of porous PDLLA/calcium carbonate composite scaffolds for controlled release of rhBMP2 and rhVEGF165. *Oral Maxillofac. Surg.* 19, 133–141.

Senatov, F. S., Niaza, K. V., Zadorozhnyy, M. Y., Maksimkin, A., Kaloshkin, S., and Estrin, Y. (2016). Mechanical properties and shape memory effect of 3D-printed PLA-based porous scaffolds. *J. Mech. Behav. Biomed. Mater.* 57, 139–148. doi:10.1016/j.jmbbm.2015.11.036

Shanmugam, L., Feng, X., and Yang, J. (2019). Enhanced interphase between thermoplastic matrix and UHMWPE fiber sized with CNT-modified polydopamine coating. *Compos. Sci. Technol.* 174, 212–220. doi:10.1016/j.compscitech.2019.03.001

Shuai, C., Zan, J., Deng, F., Yang, Y., Peng, S., and Zhao, Z. (2021). Core–shell-structured ZIF-8@ PDA-HA with controllable Zinc ion release and superior bioactivity for improving a poly-l-lactic acid scaffold. *ACS Sustain. Chem. Eng.* 9, 1814–1825. doi:10.1021/acssuschemeng.0c08009

Sola, A., Bertacchini, J., D'Avella, D., Anselmi, L., Maraldi, T., Marmiroli, S., et al. (2019). Development of solvent-casting particulate leaching (SCPL) polymer scaffolds as improved three-dimensional supports to mimic the bone marrow niche. *Mater. Sci. Eng. C* 96, 153–165. doi:10.1016/j.msec.2018.10.086

Thavornyutikarn, B., Chantarapanich, N., Sitthiseripratip, K., Thouas, G. A., and Chen, Q. (2014). Bone tissue engineering scaffolding: Computer-aided scaffolding techniques. *Prog. Biomater.* 3, 61–102. doi:10.1007/s40204-014-0026-7

Trifol, J., Van Drongelen, M., Clegg, F., Plackett, D., Szabo, P., and Daugaard, A. (2019). Impact of thermal processing or solvent casting upon crystallization of PLA nanocellulose and/or nanoclay composites. *J. Appl. Polym. Sci.* 136, 47486. doi:10.1002/app.47486

Tyler, B., Gullotti, D., Mangraviti, A., Utsuki, T., and Brem, H. (2016). Polylactic acid (PLA) controlled delivery carriers for biomedical applications. *Adv. drug Deliv. Rev.* 107, 163–175. doi:10.1016/j.addr.2016.06.018

Van Der Walt, M., Crabtree, T., and Albantow, C. (2019). PLA as a suitable 3D printing thermoplastic for use in external beam radiotherapy. *Australas. Phys. Eng. Sci. Med.* 42, 1165–1176. doi:10.1007/s13246-019-00818-6

Wang, W., Zhang, B., Li, M., Li, J., Zhang, C., Han, Y., et al. (2021). 3D printing of PLA/n-HA composite scaffolds with customized mechanical properties and biological functions for bone tissue engineering. *Compos. Part B Eng.* 224, 109192. doi:10.1016/j.compositesb.2021.109192

Wong, P.-C., Song, S.-M., Tsai, P.-H., Nien, Y.-Y., Jang, J. S.-C., Cheng, C.-K., et al. (2020). Relationship between the surface roughness of biodegradable mg-based bulk metallic glass and the osteogenetic ability of mg63 osteoblast-like cells. *Materials* 13, 1188. doi:10.3390/ma13051188

Yabu, H., Ishibashi, K., Grewal, M. S., Matsuo, Y., Shoji, N., and Ito, K. (2022). Bifunctional rare metal-free electrocatalysts synthesized entirely from biomass resources. *Sci. Technol. Adv. Mater.* 23, 31–40. doi:10.1080/14686996.2021.2020597

Yao, C. H., Lai, Y. H., Chen, Y. W., and Cheng, C. H. (2020). Bone morphogenetic protein-2-activated 3D-printed polylactic acid scaffolds to promote bone regrowth and repair. *Macromol. Biosci.* 20, 2000161. doi:10.1002/mabi.202000161

Yu, B., Zhao, Z., Fu, S., Meng, L., Liu, Y., Chen, F., et al. (2019). Fabrication of PLA/CNC/CNT conductive composites for high electromagnetic interference shielding based on Pickering emulsions method. *Compos. Part A Appl. Sci. Manuf.* 125, 105558. doi:10.1016/j.compositesa.2019.105558

Yuan, X., Mak, A. F., and Yao, K. (2002). Comparative observation of accelerated degradation of poly (l-lactic acid) fibres in phosphate buffered saline and a dilute alkaline solution. *Polym. Degrad. Stab.* 75, 45–53. doi:10.1016/s0141-3910(01)00203-8

Zaaba, N. F., and Jaafar, M. (2020). A review on degradation mechanisms of polylactic acid: Hydrolytic, photodegradative, microbial, and enzymatic degradation. *Polym. Eng. Sci.* 60, 2061–2075. doi:10.1002/pen.25511

Zhang, L., Yang, G., Johnson, B. N., and Jia, X. (2019). Three-dimensional (3D) printed scaffold and material selection for bone repair. *Acta biomater.* 84, 16–33. doi:10.1016/j.actbio.2018.11.039

Zhang, Y., Chen, S., Shao, J., and van den Beucken, J. J. J. P. (2018). Combinatorial surface roughness effects on osteoclastogenesis and osteogenesis. *ACS Appl. Mat. Interfaces* 10, 36652–36663. doi:10.1021/acsami.8b10992

frontiers | Frontiers in Bioengineering and Biotechnology

TYPE Review
PUBLISHED 08 September 2022
DOI 10.3389/fbioe.2022.952523

OPEN ACCESS

EDITED BY
Jun-Bing Fan,
Southern Medical University, China

REVIEWED BY
Shan He,
Flinders University, Australia
Debao Niu,
Guangxi University, China

*CORRESPONDENCE
Chunbo Chen,
gghccm@163.com

†These authors have contributed equally to this work and share first authorship

SPECIALTY SECTION
This article was submitted to Bionics and Biomimetics, a section of the journal Frontiers in Bioengineering and Biotechnology

RECEIVED 25 May 2022
ACCEPTED 13 July 2022
PUBLISHED 08 September 2022

CITATION
Wu G, Hui X, Hu L, Bai Y, Rahaman A, Yang X-F and Chen C (2022), Recent advancement of bioinspired nanomaterials and their applications: A review.
Front. Bioeng. Biotechnol. 10:952523.
doi: 10.3389/fbioe.2022.952523

Recent advancement of bioinspired nanomaterials and their applications: A review

Gang Wu[1], Xiaodan Hui[1†], Linhui Hu[1,2], Yunpeng Bai[1,2], Abdul Rahaman[3], Xing-Fen Yang[4] and Chunbo Chen[1,5,6,7*]

[1]Department of Critical Care Medicine, Maoming People's Hospital, Maoming, Guangdong Province, China, [2]Center of Scientific Research, Maoming People's Hospital, Maoming, Guangdong Province, Guangdong Province, China, [3]School of Food Science and Engineering, South China University of Technology, Guangzhou, China, [4]School of Public Health, Southern Medical University, Guangzhou, China, [5]Department of Intensive Care Unit of Cardiovascular Surgery, Guangdong Cardiovascular Institute, Guangdong Provincial People's Hospital, Guangdong Academy of Medical Sciences, Guangzhou, China, [6]Department of Critical Care Medicine, Guangdong Provincial People's Hospital, Guangdong Academy of Medical Sciences, Guangzhou, China, [7]The Second School of Clinical Medicine, Southern Medical University, Guangzhou, China

With the advancement in the field of nanotechnology, different approaches for the synthesis of nanomaterials have been formulated, among which the bioinspired or biomimetic nanoplatforms have been utilized for different biomedical applications. In this context, bioinspired or biomimetic nanoparticles (NPs) have been synthesized in which the inspiration for synthesis is taken from nature or its components. Innovations in bioengineering tools and bio-conjugation chemistry have enabled scientists to develop novel types of such nanoplatforms. They have several advantages over normal synthesis protocols. In this review, we 1) summarized nanomaterial types and their advancements in bioinspired nanotechnology therapies; 2) discussed the major types, novel preparation methods, and synthesis progress of NPs in current biomedical fields; 3) gave a brief account of the need for synthesizing NPs via a bioinspired route rather than their common route; 4) highlighted the updated information on the biomimetic synthesis of different types of NPs; and 5) provided future perspectives in the synthesis of novel NPs for their potential applications in biomedical sciences.

KEYWORDS

bioinspired nanoparticles, biomimetic nanoparticles, natural nanoparticles, quantum dots, camouflage nanoparticles

Abbreviations: EPR, enhanced permeation and retention; AgNPs, silver nanoparticles; DLS, dynamic light scattering; SPION, superparamagnetic iron oxide NPs; PLGA, poly (lactic-co-glycolic acid; PSMA, prostate-specific membrane antigen; PSA, prostate-specific antigen; WFA, withaferin A; FA, folic acid; TAM, tumor-associated macrophages; CAF, cancer-associated fibroblast; ECM, extracellular matrix; HDL, high-density lipoproteins; Apo A1, apolipoprotein A1; TSM, tumor stromal microenvironment; BTV, bioinspired tumor-responsive theranostic nanovehicle; PHB/PCL, polyhydroxybutyrate/poly-3-caprolactone; C-dots, carbon quantum dots.

Introduction

In recent years, the demand for the use of nanotechnology in treating diseases such as cancer has been increasing, owing to the vast striking properties of nanomaterials that allow scientists to modify them to suit their needs. The size of therapeutically used nanoparticles (NPs) is lower than 100 nm with a specific surface area to volume ratio, which makes them a remarkable carrier for drugs as the positively charged particle is more compatible and attracted to negatively charged membranes of cells, which contributes to its higher cellular uptake. Nanomaterials tend to enhance the permeation and retention (EPR) effect, leading to good contact with cells and their compartments. Size and surface properties can be easily adjusted in these nanomaterials due to which different types of structures can be drawn, such as particles, fibers, and rods (Kim et al., 2010). NPs deliver drugs either passively or actively. In this respect, various nanomaterials have been employed to synthesize different types of NPs to apply them in the field of nanomedicine. However, due to stringent preparation methods and the use of harsh chemicals, the applicability of NPs is sometimes questionable, which leads to bioinspired methods coming into this picture. The most common members of bioinspired nanoparticles include solid lipid nanoparticles, dendrimers, aptamers, protein NPs, and viral NPs (Sivarajakumar et al., 2018) (Madamsetty et al., 2019). NPs have greatly improved the therapeutic action of many drugs and diagnostic value of various diseases due to its small size, large surface area–to-volume ratio, enhanced drug loading, easy synthetic routes, increased drug release timings, easy penetration abilities, and finally easy retention in the affected tissues.

Many diseases are caused by irregularities in the body at the molecular level or on a nanoscale, such as misfolding of important proteins, mutations in single nucleotide bases, and eventually infections induced by some pathogens (Kim et al., 2010). NPs have been given more attention due to the fact that they have the same size scale as biological molecules or components (Chan, 2017). Due to their tunable properties such as shape, size, morphology, surface charge, and surface elements, NPs can be used as therapeutic agents in the field of nanomedicine (Kim et al., 2010). Having some inspiration from biological aspects and the field of materials technology, bioinspired nanomaterials and their components, such as bioinspired nanoparticles and bioinspired nanovesicles, have received much more attention for two decades (Gaharwar et al., 2014). These materials, after mimicking nature, changed into novel generations of materials such as bacterial-inspired, mammalian cell–inspired, and virus-inspired nanosystems. Common nanosystems formed include lipid-based systems, vesicle-based nanosystems (exosomes), polysaccharide-based systems, and metallic nanosystems. The terms “biomimetic” and “bioinspired” are used interchangeably, with the same meaning but very little difference. The former states directly mimic techniques or processes that are present in nature, while the latter can be direct or indirect, with a wider range of uses and more flexibility. Figure 1 summarizes the synthetic sources and important applications of biomimetic nanomaterials.

Currently, different types of cells such as red blood cells, white blood cells, cancer cells, and platelets are extruded from the plasma membrane and coated with different types of NPs by different types of technologies, such as liposomes, metallic NPs, dendrimers, quantum dots, and polymeric NPs, to form biomimetic NPs. These have been used to evoke immune responses involved in cancer immunotherapy. Figure 2 illustrates different plasma membrane coatings on different NPs for cancer immunotherapy.

In this article, various types of nanomaterials and their advancements in bioinspired nanotechnology therapy were critically reviewed. The major types, novel preparation methods, and synthesis progress of NPs in the current biomedical field were also discussed. Furthermore, we have given a brief account of the need for synthesizing NPs *via* a bioinspired route rather than their common route. This review highlighted the updated information on the biomimetic synthesis of different types of NPs. Table 1. summarized the nanoparticles formed by bioinspired technology discussed in the review article.

Bioinspired metallic nanoparticles

Bioinspired silver nanoparticles (AgNPs)

Ali et al. (2020) used different fractions of *Elaeagnus umbellate* extract (EU) to reduce silver nitrate to silver NPs, ultimately synthesizing AgNPs. The formed NPs were morphologically controlled, and their shape/size-dependent application was evaluated. Furthermore, the shape, size, and bactericidal activity of these NPs were evaluated, and their mechanism of action was studied via atomic force microscopy (AFM) and scanning electron microscopy (SEM). They found that the NPs were around 40 nm in size and were monodisperse and non-toxic in nature. In addition, they had a good killing effect against gram-positive and gram-negative strains of *Staphylococcus aureus* (*S. aureus*) and *Escherichia coli* (*E. coli*). There was an electrostatic interaction between the bacterial cell wall and NPs. The results showed that the cell surface accumulation of NPs in *E. coli* was faster and more obvious than that in *S. aureus*, which was probably related to the different composition of cell walls of two different bacterial strains. NPs penetrated into bacteria and interacted with sulfhydryl groups to denature proteins, ultimately affecting enzyme activity.

Bioinspired gold nanoparticle

Graphene has become one of the most developed nanomaterials and has shown great scientific value for future

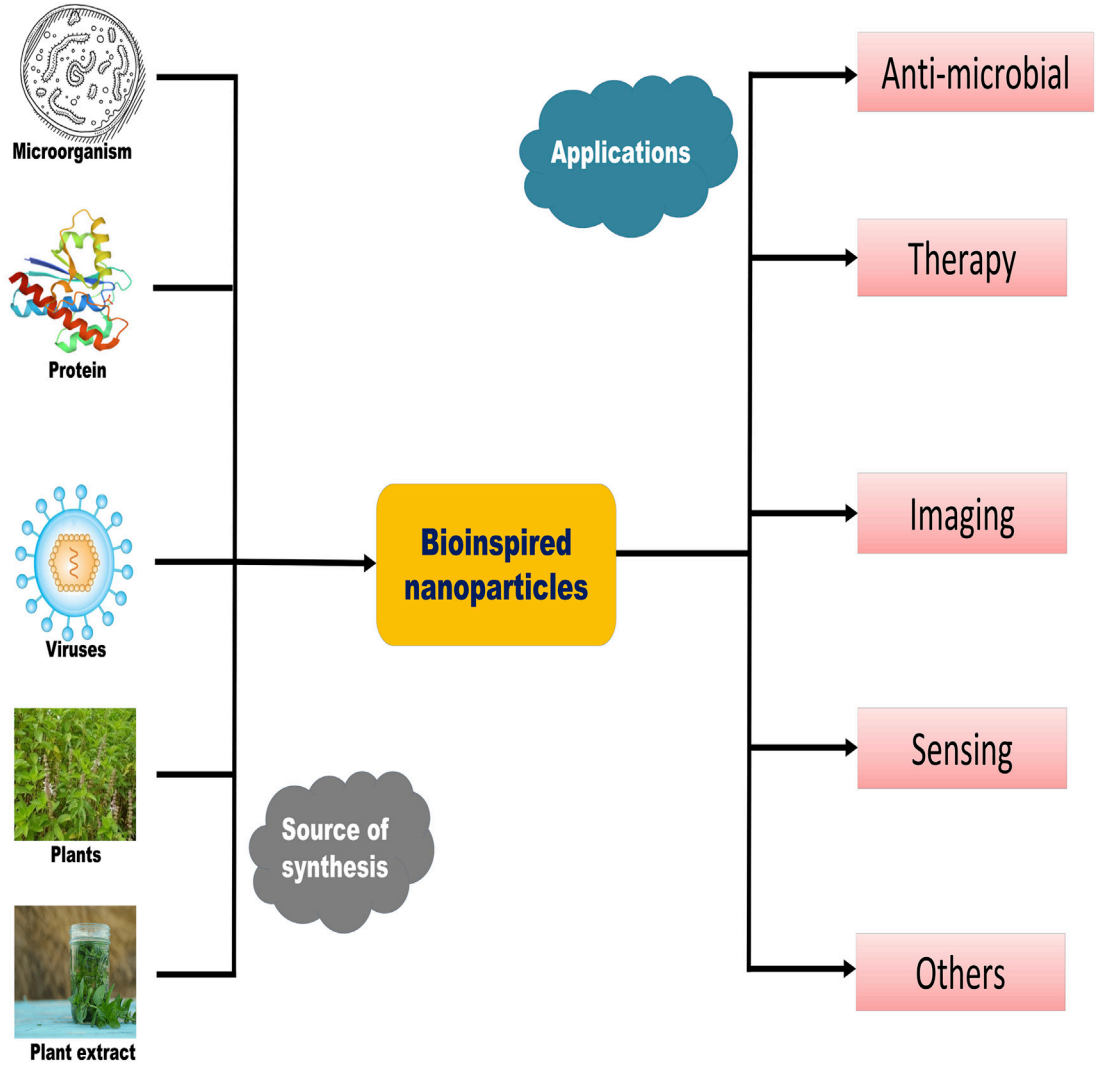

FIGURE 1
Illustrates different plasma membrane coatings on different nanoparticles for cancer immunotherapy. The plasma membranes of different types of cells like RBC, WBC, and cancer cells were extruded and coated with different types of nanoparticles (liposomes, dendrimers, carbon dots, polymeric nanoparticles, metallic nanoparticles, etc.) to form biomimetic nanoparticles which evoke immune responses (T cells, B cells, dendritic cells) to participate in the process of cancer immunotherapy.

applications of nanotechnology (Mao et al., 2013). It may be considered one of the best biocompatible nanoplatforms due to its applications in antibacterial (Akhavan and Ghaderi, 2010; Hu et al., 2010; Ma et al., 2011), antiviral materials (Akhavan et al., 2012), cancer-targeting (Yang et al., 2010), drug delivery (Zhang et al., 2010), and photothermal therapy (Yang et al., 2012). A team of scientists synthesized gold nanoparticles (AuNPs) coated with reduced graphene oxide. They used *Syzygium cumini* seed extract to reduce both chloroauric acid and graphene oxide (GO). Meticulously, biophysical techniques such as UV-Vis spectroscopy (UV-Vis), dynamic light scattering (DLS), and Fourier transform infrared spectroscopy (FTIR) were employed to characterize its physicochemical properties. The results showed AuNPs were successfully synthesized and coated with graphene oxide. The antibacterial and anticancerous activities were performed on the strain of gram-negative bacteria, *E. coli*, and on the strains of gram-positive bacteria, *S. aureus* and *Bacillus subtilis*, and on the human colorectal cancer cell line (HCT 116) and lung (A549) cancer cell line, respectively. The cytotoxicity and antibacterial toxicological assays revealed that the synthesized nanocomposite showed significant anticancer activity against the A549 cell line and gram-negative bacterial strain *E. coli* compared to the rest of the strains (Kadiyala et al., 2018).

TABLE 1 Summarizes the nanoparticles formed by bioinspired technology discussed in the review article.

Type of nanoparticle	Name of nanoparticle	Synthesis protocol	Application	References
Silver nanoparticle	Bioinspired AgNPs	*Elaeagnus umbellate* extract (EU) for reducing silver nitrate to silver nanoparticles.	Good killing effect against gram-positive and gram-negative strains of *Staphylococcus aureus* (*S. aureus*) and *Escherichia coli* (*E. coli*)	Ali et al., 2020
Gold nanoparticle	AuNPs coated with reduced graphene oxide.	*Syzygium cumini* seed extract (SCSE) to simultaneously reduce chloroauric acid and graphene oxide (GO).	Enhanced antibacterial and anticancerous activity on *Staphylococcus aureus* and *Bacillus subtilis* and human colorectal cancer cell line (HCT 116) and lung (A549) cancer cell line, respectively.	Kadiyala et al., 2018
Iron oxide nanoparticle	SPION-loaded silica nanocapsules	SPION-loaded silica nanocapsules based on a bimodal catalytic peptide surfactant stabilized nanoemulsion template method	Encapsulating iron oxide into silica nanocapsules simply signifies the drug delivery ability.	Wilson et al., 2021
Poly (lactic-co-glycolic acid) (PLGA) nanoparticles	Polymeric nanoparticles coated with programmed cancer cell membrane (BiNPs)	Stimulated cancer cells for over-expression of integrin expression on the outermost surface of cells and then coated polymeric nanoparticles membranes.	Enhanced circulation time, escape from immune system, and improved biocompatibility	Hu et al., 2011
Alginate NPs	Bioinspired alginate NPs	Microbubble-bursting method	Improvement in size and dispersity of formed NPs	Elsayed et al., 2015
Nanovesicle	PSMA-targeted "Hybrid" nanoparticles	Hybrid nanoparticles in which they loaded PSA cleavable prodrug doxorubicin (DOX-PSA).	Increased specificity, decreased tumor growth in *in vitro* and *in vivo* models compared to free forms	Ma et al., 2021
Nanovesicle	Polymeric nanovesicle (TPZ/AI-NV)	Used diblock copolymers for the synthesis of nanovesicle: one was chlorine e6 (Ce6)–modified PEG-polyserine, another one was PEG-poly (Ser-S-NI	Precise drug delivery and finally synergistic therapeutic effect was observed	Qian et al., 2017
Nanovesicle	Biomimetic nanovesicle coated by PD-1 receptors	First, they transfected HEK 293 T cells with plasmid to express PD-1 on the surface of cell membrane and secondly they synthesized nanovesicles by dialysis method using repeated extrusion process	Nanovesicles accumulate near the tumor regions and retard the tumor growth through the filtration of $CD8^+$ T cells.	Zhang et al., 2018a
Exosomes	Melanoma (cancer of skin)-derived exosomes	Loaded with immunomodulatory CpG DNA displayed *antigens* on their surface	Better in eradicating tumor than either exosomes or DNA alone	Morishita et al., 2016
Exosomes	Withaferin A (WFA)–loaded exosomes targeted by conjugated it with folic acid	Bioinspired exosomes derived from bovine milk	Enhanced antitumor effect (74%) when compared to non-targeted exosomes (50%)	Munagala et al., 2016
Lipoproteins	Bioinspired lipoprotein particle bLP	Loaded both a photothermal agent ($DiOC_{18}$ (Hu et al., 2010) (DiR) producing D-bLP NPs and an anticancer drug, namely, mertansine forming M-bLP	D-bLP remodeled the tumor stromal microenvironment (TSM) and M-bLP killed the tumor cells and inhibited tumor relapse and metastasis	Tan et al., 2019
Nanovehicle based particle	Bioinspired tumor-responsive theranostic nanovehicle (BTV)	A theranostic probe of photochlor (HPPH), a tumor-activated melittin pro-peptide (TM), and a ROS-responsive prodrug gemcitabine (RG) was loaded into a lipoprotein-based bioinspired nanovehicle	Drastic elimination of multiple immunosuppressive cells and enhanced infiltration of cytotoxic lymphocytes in tumor	Wang et al., 2021
Chitosan or calcium phosphate–based Nanoparticles	VitB12 was conjugated on chitosan or calcium phosphate–based NPs	Ionic gelation method	Oral absorption of insulin was highly enhanced	Ke et al., 2015, Verma et al., 2016
Polycaprolactone nanoparticles	Polyhydroxybutyrate/poly-3-caprolactone (PHB/PCL) mats	Process of electrospinning	Significant antimicrobial activity toward both the strains of bacteria (gram-positive/gram-negative), very good water holding capacity, hydrophilicity, and *in vitro* activity which clearly indicates its interaction and attachment	Avossa et al., 2021
Quantum dots	Fluorescent C-quantum dots	By the process known as hydrothermal approach using *Citrus limetta* juice.	Enhanced *in vitro* activity clearly indicates its anti-adhesion and anti–biofilm production ability of *Candida albicans*	Shaikh et al., 2019

Bioinspired iron oxide nanoparticles

Superparamagnetic iron oxide NPs (SPIONs) have been extensively used owing to their unique properties. However, their use in the biomedical field is hampered by the fact that these NPs are more toxic, less magnetic, and expensive due to the harsh chemical reagents used for the synthesis of these NPs. Russell J. Wilson bioengineered SPION-loaded silica nanocapsules based on a bimodal catalytic peptide surfactant stabilized nanoemulsion template. SPIONs were preloaded into the oil phase of nanoemulsions, and the surface property of the peptide and its electrostatic repulsion resulted in the stability of nanoemulsions. Catalytic peptides lead to biosilification and promote the formation of silica shell nanocapsules containing iron oxide. In conclusion, the encapsulating of iron oxide into silica nanocapsules simply signifies the drug delivery capabilities of these formed nanoplatforms (Wilson et al., 2021).

Bioinspired green synthesis of metallic nanoparticles

Inspired by nature, there is a growing opportunity for bioinspired synthesis of metallic nanoparticles due to its ease and low cost of biosynthesis, and they can be easily modified by many proteins, lipids, carbohydrates, and antibodies to enhance their biological effects (Gurunathan, 2019). This is attributed to the toxic effects and high energy inputs provided by the use of harsh chemicals and stabilizers in the synthesis and processes of these metallic NPs. From the point of view of industrial preparation, it is necessary to ensure that the NPs are well dispersed and their size is controlled. Various attempts have been made to utilize many food by-products such as orange peels (Castro et al., 2013) and banana peels (Ibrahim, 2015). In addition to their use in synthesis as reducing agents, they can be easily recovered into some useful products through these processes. Inspired by these facts, a group of workers synthesized silver (Ag), gold (Au), and platinum (Pt), using an aqueous extract of the rind of the fruit *Garcinia mangostana*, used against inflammation, cholera, and diarrhea (Pedraza-Chaverri et al., 2008), to check for their antimicrobial activity with or without their attachment to several classes of antibiotics. The results showed that AgNPs had a better antimicrobial effect than AuNPs and PtNPs against gram-negative strains of bacteria, and all groups of NPs showed synergistic activity with different classes of antibiotics, indicating a certain correlation between antibiotics and NPs. Additionally, *Bacillus spp.*, previously found to be resistant to streptomycin, was now susceptible to the combination of AuNPs and antibiotics. Collectively, metallic NPs increased the susceptibility of bacterial strains to antibiotics (Nishanthi et al., 2019).

Polymeric bioinspired nanoparticles

Poly (lactic-co-glycolic acid) nanoparticles

Organ-specific drug targeting remains a challenging task in the fields of drug delivery and nanomedicine. A team of scientists has synthesized programmable bioinspired NPs (P-BiNPs) that can deliver cargo to homotypic cancer cells while targeting bone localization in animal models. First of all, they stimulated cancer cells to over-express integrin on the outermost surface of cells. They then coated the polymeric NPs with these programmed cancer cell membranes, which were absorbed by prostate cancer cells to improve the therapeutic ability of drugs, enhance their imaging quality, and ultimately reduce side effects. Coating these NPs in biologically inspired nanomaterials enhanced their circulation time, escaped from the immune system, and improved biocompatibility (Hu et al., 2011).

Alginate nanoparticles

In the field of nanotechnology, natural and synthetic NPs have been extensively synthesized and characterized for drug delivery. It comprises poly (D,L-lactide), poly (D,L-glycolide), poly (lactic acid), poly (lactide-co-glycolide) acid, alginate, chitosan, gelatin, and collagen (Soppimath et al., 2001). Alginate NPs are an important class of polymeric drug delivery carriers that enhance bioavailability and finally the efficacy of many drugs (Kulkarni Vishakha et al., 2012). Alginate, a natural sugar polysaccharide, is mucoadhesive in nature due to the cationic nature of the polymer so that it can adhere to the plasma membrane (Malafaya et al., 2007).

Synthesis schemes have been developed from time to time to obtain proper alginate NPs. However, these conventional methods lack proper regulation, require dispersion and size of NPs, and finally require the use of harsh organic solvents that might be toxic to the *in vivo* environment. Bubble bursting is a natural phenomenon occurring in the marine medium virtue, which forms nano-sized and micro-sized particles (Fitzgerald, 1991). It is mainly caused by wave breaking *via*, namely, bubble film disintegration and jetting (Spiel, 1998). Hence, alginate NPs have been synthesized using the microbubble-bursting method with a size range of 80–200 nm. A device, which is T junction microfluidic, was used by the researcher group to form microbubbles with varying sizes in the best possible controlled manner. The size produced was directly related to the viscosity of the alginate solution used in this process (Elsayed et al., 2015).

Bioinspired nanovesicle

Nanovesicles

Nanovesicles based on lipids have been widely used as important drug delivery carriers in the field of nanomedicine due to their good biocompatibility and sample preparation protocols. In nanovesicles, the outer layer is covered with two lipids and the inner part is composed of an aqueous cavity. The first and foremost characterized lipid nanovesicle was liposomes, and they have been used as drug delivery carriers to deliver genes and drugs (Grimaldi et al., 2016). Bioinspired nanovesicles include biomimetics and cell-derived nanovesicles, which form a new class of drug delivery carriers (Goh et al., 2017; Zhao et al., 2020). The construction of these vesicles involves extrusion of intact cells and then synthesis of nanoparticles with a coating of cell-derived membranes and fusing exosomes with lipid-derived particles (Ma et al., 2021). This ensures a high loading capability and mimics many natural particles so that it may not evoke any type of immune response. Finally, they are also highly biocompatible, finding application in drug delivery, immunotherapy, tumor targeting, and gene delivery (Ilahibaks et al., 2019; Park et al., 2019).

Ma et al. (2021) simultaneously targeted two specific components of prostate cancer (PC). In PC, prostate-specific membrane antigen (PSMA) and prostate-specific antigen (PSA) are found to be highly upregulated in advanced stages of PC, and there was no evidence that they are both targeted. Hence, they designed PSMA-targeted "Hybrid" NPs and loaded them with the PSA cleavable prodrug, doxorubicin (DOX-PSA). The specificity of *in vitro* and *in vivo* models increased and tumor growth decreased compared to free forms and untargeted PSA hybridization, indicating an enhanced efficacy of the formed nanovesicle loaded with the prodrugs.

Inspired by anaerobic bacteria and their metabolism under hypoxia, Qian et al. (2017) synthesized the nanovesicle system. Under hypoxia, external light irradiation delivered the material to the tumor microenvironment, resulting in a reaction. They used diblock copolymers for the synthesis of nanovesicles: one was chlorine e6 (Ce6)–modified PEG-polyserine, and the other was PEG-poly (Ser-S-NI). When the light irradiates the photosensitizer Ce6, oxygen is converted to singlet oxygen, which is further consumed by oxidizing the thioether on PEGpoly (Ser-S-NI) to a hydrophilic oxidized state, resulting in an anoxic atmosphere. This low oxygen concentration atmosphere could bring out the bioreduction of NI pendants into hydrophilic units and eventually the disassociation of the nanovesicles. Additionally, by encapsulating the hypoxia-activated prodrug tirapazamine into the cavity of nanovesicles, automated, precise drug delivery and finally synergistic therapeutic effect between the two main processes, namely, photodynamic therapy and chemotherapy could thus be achieved.

Nanovesicles derived from cell membranes can be directly used for biomimetic nanomedicines. Taking advantage of genetic engineering technology and nanotechnology, Zhang and co-workers recently developed a biomimetic nanovesicle that represents the PD-1 receptor on its surface for cancer immunotherapy. First, HEK 293 T cells were transfected with a plasmid to express PD-1 on the surface of the cell membrane, and then nanovesicles were synthesized by the dialysis method using a repeated extrusion process. The blockade of PD-1 or PD-L1 is an emerging trend in cancer immunotherapy as it suppresses the host antitumor immune response. Data from their experiments revealed that vesicles carrying PD-L1 bind to PD-L1 receptors on cancer cell membranes. In addition, *in vivo* studies have shown that these nanovesicles accumulate near tumor regions and retard tumor growth through filtration of $CD8^+$ T cells. This system was boosted by the use of drugs such as 1-methyl-tryptophan, which was proved to be an effective inhibitor of the immunosuppressive enzyme indoleamine 2, 3-dioxygenase (IDO) (Pardoll, 2012). By encapsulating it in the core of a nanovesicle, they have increased the efficacy of formed particles by blocking two important pathways (Zhang et al., 2018a).

Extracellular vesicles

Extracellular vesicles are heterogeneous entities released by cells and play a key role in cell-to-cell communications. Exosomes are the smallest of all kinds of extracellular vesicles, with a size ranging from 50 to 150 nm (Stremersch et al., 2016). They are used as drug delivery agents as they can be moved from one location to another and in some cases, as a diagnostic marker. However, it is sometimes difficult to use it as a sole drug delivery agent due to challenges faced by many scientists, such as low loading capacity and obtaining a lower amount of exosomes in normal conditions. Hence, bioinspired exosomes come into play as an alternative to naturally derived exosomes, and it proved to be an effective therapy against many issues, as mentioned previously (Lu and Huang, 2020).

Exosomes

It has been reported that exosomes from different types of cells, such as those derived from immune cells and mesenchymal stem cells (MSCs) in particular conditions, possess different therapeutic responses (Buschow et al., 2010; Sun et al., 2018). In this regard, exosomes derived from B cells present a major histocompatibility complex on their heads, so the induction of T-cell responses (Clayton et al., 2003) indicates that exosomes could be used as an immunomodulatory agent, which was proved by dendritic cell (DC)–derived exosomes added with tumor antigens, evoking immune responses and inhibiting the survival of established tumors (Zitvogel et al., 1998). Taking these effects as an immunomodulatory and immunotherapy agent, exosomes are used to load cargo, in addition to displaying antigens on their surface. For example, melanoma (cancer of the skin)-derived exosomes from murine models loaded with immunomodulatory CpG DNA displayed antigens on their surface which proved to be

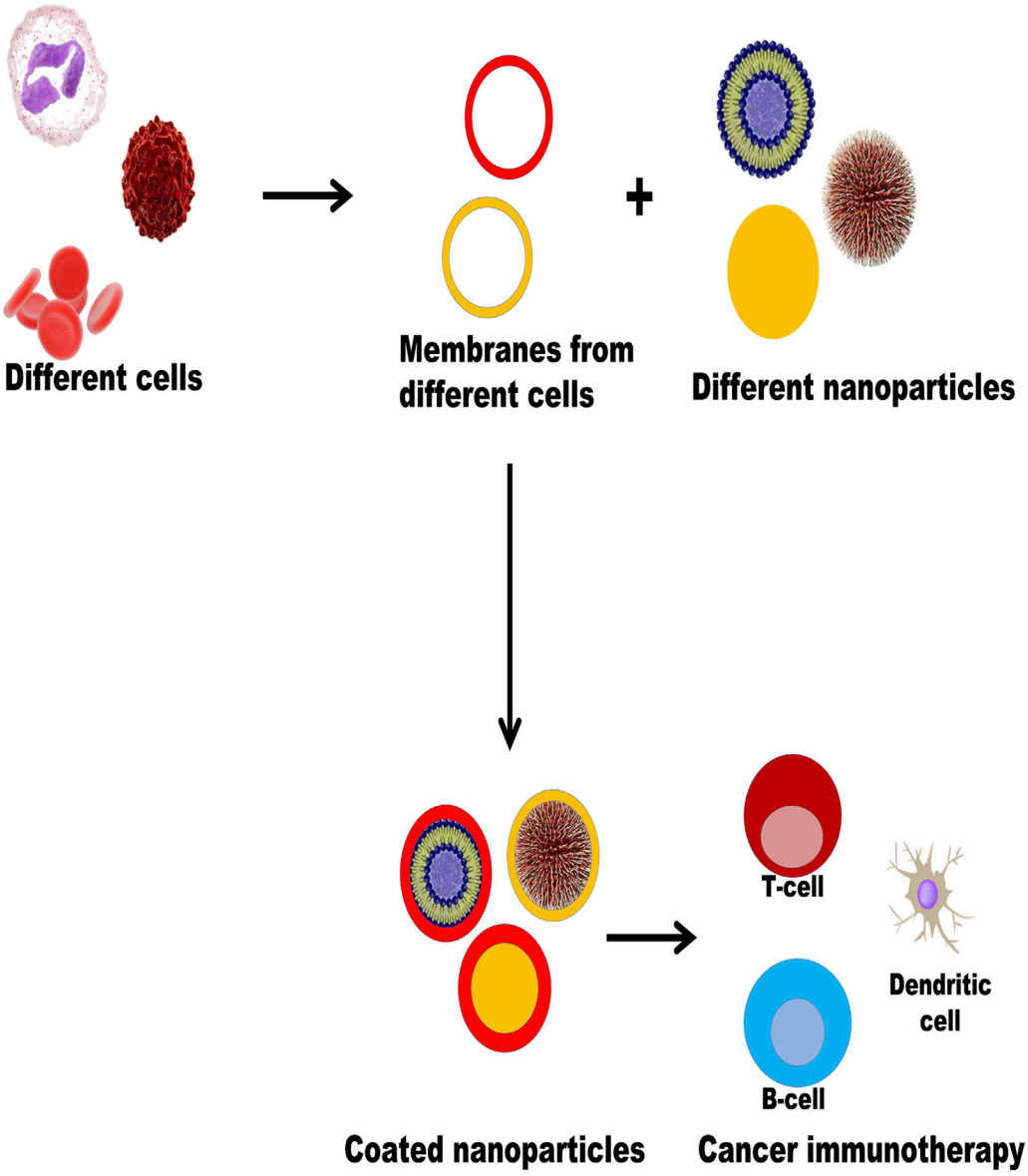

FIGURE 2
Illustrates different plasma membrane coating on different nanoparticles for cancer immunotherapy.

better in eradicating tumors than either exosomes or DNA alone (Morishita et al., 2016).

Bovine milk is used for the synthesis of cost-effectiveness and for the large-scale production of exosomes in a bioinspired manner. When withaferin A (WFA) was administered three times per week, enhanced antitumor activity was found in xenograft mice bearing A549 lung cancer. When exosomes were modified with the ligand folic acid (FA), the antitumor effect was enhanced (74%) when compared to non-targeted exosomes (50%) (Munagala et al., 2016). Other groups also successfully loaded different drugs, such as anthocyanidins and paclitaxel, for oral administration of milk-derived exosomes (Agrawal et al., 2017; Munagala et al., 2017).

Miscellaneous

Bioinspired lipoproteins

In a cancer environment, several nanosystems are not effective in providing a therapeutic response due to the inability of many nanosystems to access cancer cells (Minchinton and Tannock,

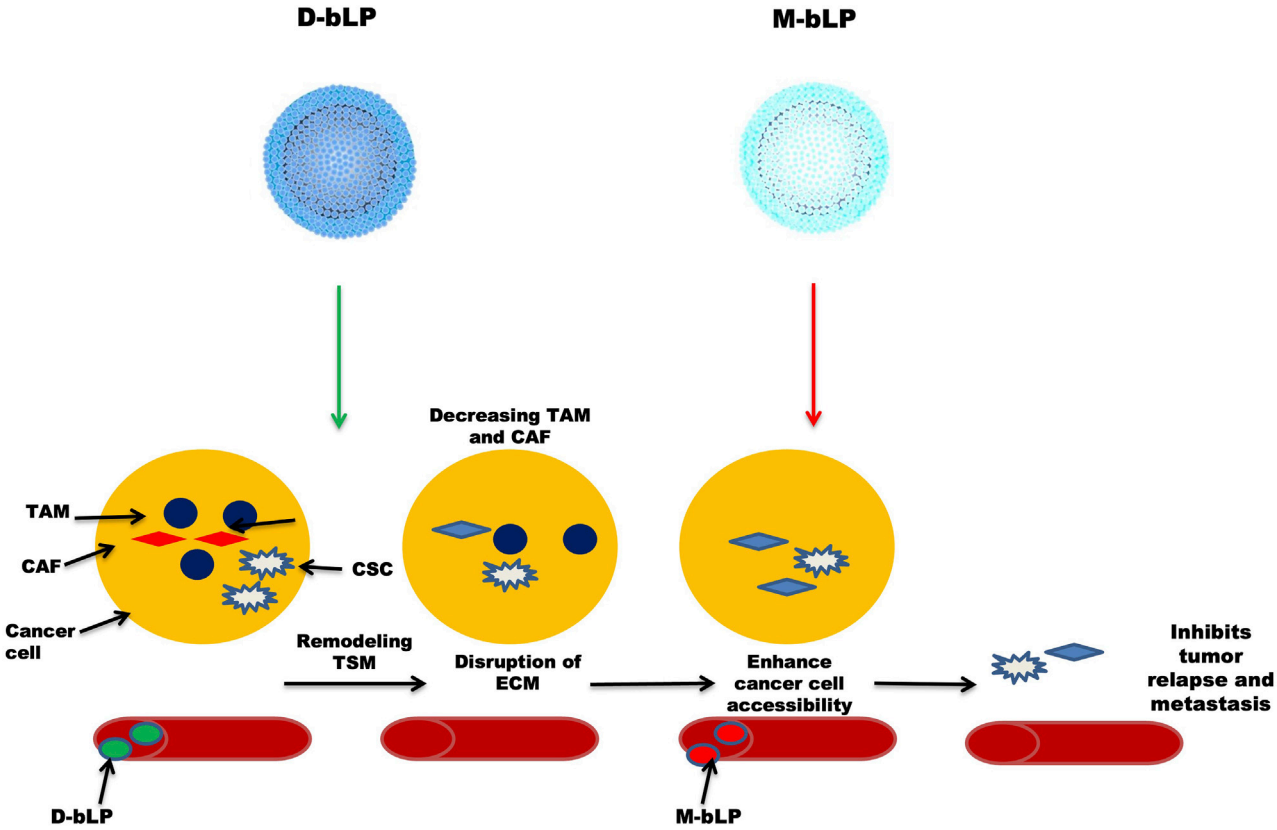

FIGURE 3
Illustrates D-bLP-mediates photothermal remodelling of tumor stroma which increases the accessibility of second wave of nanoparticles M-bLP near cancer cells.

2006; Dewhirst and Secomb, 2017). NPs passively accumulate near the tumor microenvironment, but only a few (around 5%) NPs actually reach the tumor site (Wilhelm et al., 2016; Dai et al., 2018). Researchers found that a large number of stromal cells, such as cancer-associated fibroblasts (CAF) and tumor-associated macrophages (TAM), are needed during the development of cancer (Kitamura et al., 2015; Kalluri, 2016). By forming an extracellular matrix (ECM), they play a pivotal role in shaping the morphology and the whole environment of tumor tissue. NPs are actually hijacked by ECM, preventing them from penetrating into tumor tissue and eventually lowering their efficacy in cancer therapeutics (Zhang et al., 2018b; Overchuk and Zheng, 2018). Lipoproteins, notably, the high-density lipoproteins (HDL) are endogenous nanoscale particles composed of a variety of proteins (e.g., apolipoprotein A1, Apo A1) and some lipids (e.g., phospholipids and cholesterol esters), making them an ideal platform for sustained delivery of many therapeutic agents and in biological imaging of tumor tissues. Tan et al. (2019) synthesized the bioinspired lipoprotein particle, bLP, which was loaded with a photothermal agent ($DiOC_{18}$) (Hu et al., 2010) (DiR) to produce D-bLP NPs and the anti-cancer drug, namely, mertansine, to form M-bLP. These two were used one by one to ensure proper management of the disease. First, they administered D-bLP using a photothermic pulse in the infrared (IR) range to reshape the tumor stromal microenvironment (TSM), and then actively enhanced the second wave of M-bLP to kill the tumor cells and inhibit tumor relapse and metastasis, as done in two breast cancer models. Figure 3 illustrates D-bLP–mediated photothermal remodeling of tumor stroma which increases the accessibility of the second wave of M-bLP nanoparticles near cancer cells.

Bioinspired theranostic tumor permeated nanovehicle

In addition to the challenges facing cancer treatment, there are several obstacles to effective therapy in the oncology field. This is probably due to the presence of certain types of immunosuppressive cells, namely, myeloid-derived suppressor cells (MDSCs), M2-like tumor-associated macrophages (TAMs), regulatory T cells (Tregs), and immature/tolerogenic dendritic cells (DCs), in the context of the tumor cell region that is considered immunosuppressive (Alizadeh

and Larmonier, 2014; Shaked, 2019; Togashi et al., 2019). Cancer cells have also evolved a natural tendency to suppress the immune response of immunosuppressive cells that function as $CD8^+$ T cells and natural killer (NK) cells in tumors through multiple mechanisms, thereby hampering the antitumor immunity (Binnewies et al., 2018; Shaked, 2019). Undoubtedly, there is a need to cope with this situation in which immunosuppression is relieved, enhancing the antitumor response of cancer cells.

Wang et al. (2021) synthesized a bioinspired tumor-responsive theranostic nanovehicle (BTV) with tumor-penetrating ability to cope with immunosuppression of cancer cells for effective anti-cancer therapy. In this nanovehicle, a theranostic probe of photochlor (HPPH), a tumor-activated melittin pro-peptide (TM), and an ROS-responsive prodrug gemcitabine (RG) were loaded into a lipoprotein-based bioinspired nanovehicle. The functions of different compounds are as follows: TM enhances tumor penetration and accumulation capacity and was enzymatically restored to active melittin at the specific sites, thereby increasing the activities of pharmacological drugs. RG (prodrug), as an active immunomodulator, was degraded into active gemcitabine. HPPH acted as a theranostic probe in BTN for systemic tumor tracking *in vivo* and generated singlet oxygen upon irradiation to enhance the overall antitumor activity of the formed nanovehicle. Remarkably, this combinational treatment significantly eliminated multiple immunosuppressive cells and enhanced the infiltration of cytotoxic lymphocytes in tumors, which is the essential key element in relieving tumor immunosuppression and also strikingly decreasing tumor growth. In a nutshell, this novel design provides a pathway to deliver a nanoplatform with striking immunosuppression-relieving capacity that could be used for effective anti-cancer therapies.

Bioinspired VitB12-coated NPs

Receptor-mediated endocytosis, a process by which VitB12 is absorbed, has been reported by several groups (Seetharam, 1999). Hence, this vitamin is utilized for coating NPs to improve their oral bioavailability. Conjugation of this vitamin on insulin-encapsulated dextran NPs improved insulin availability (26.5%) in chemically induced diabetic rats (streptozotocin-induced) compared with control rats (10.3%) without any coating (Chalasani et al., 2007a; Chalasani et al., 2007b). Similar trends were observed when VitB12 was conjugated on chitosan or calcium phosphate–based NPs; oral insulin absorption was greatly enhanced (Ke et al., 2015; Verma et al., 2016), while poor oral availability of some drugs like cyclosporine A and scutellarin was also improved when NPs were coated with VitB12 (Francis et al., 2005; Wang et al., 2017).

Bioinspired wound healing dressing mat

Wound treatment is challenging as some diseases, such as diabetes and cardiovascular diseases, make it more chronic (Qu et al., 2018). Wound dressing plays a key role in the healing process by mimicking ECM, adhesion, and eventually migrating to the wound, aiding in the process of healing and skin regeneration (Chhabra et al., 2016). Polycaprolactone (PCL) has been widely used in wound healing due to its good biocompatibility, biodegradability, and easy availability (Ravichandran et al., 2019). It can be blended with other polymers to improve its mechanical properties and tissue regeneration abilities (Sawadkar et al., 2020). In this regard, biodegradable and eco-friendly polyhydroxybutyrate/poly-3-caprolactone (PHB/PCL) mats were developed by electrospinning to imitate the extracellular matrix (ECM) and to provide structural and biochemical evidence for tissue regeneration. Inspired by the natural component melanin, which is highly exploited as a tool against microbial infection, the above-developed mats were modified by melanin–TiO_2 nanostructures. These coated mats had significant antimicrobial activity toward both the strains of bacteria (gram-positive/gram-negative). They had good water holding capacity, hydrophilicity, as well as *in vitro* activity, indicating their interaction and attachment (Avossa et al., 2021).

Bioinspired carbon dots

As a powerful carrier, quantum dots have been widely used in the biomedicine field due to their optical properties based on their size. The preparation methods are quite difficult, take a lot of time, and have low reproducibility; among these, the hydrothermal approach is one of the green chemistry approaches for producing fluorescent carbon quantum dots (C-dots) (Kasibabu et al., 2015) on a large scale by using waste material and natural resources (like fruit juice of orange, ginger, and sugarcane) as carbon starting materials. Additionally, watermelon peel, milk, lignin, sugarcane juice, coffee grounds, chicken eggs, food waste, banana, hair, ginger, onion waste, honey, bread, candle soot, chitosan, and gelatine have been utilized as carbon sources (Zhou et al., 2012; Li et al., 2014; Liu et al., 2014; Mehta et al., 2014; Wang and Zhou, 2014; Bandi et al., 2016). Considering these specialties of natural resources, Asiya F. Shaikh synthesized rapid, highly fluorescent C-dots using a hydrothermal approach, using *Citrus limetta* juice, commonly known as Mausambi in the Indian subcontinent. It contains a high amount of sugar as carbohydrate, which is the starting source of carbon for C-dot production. *In vitro* activity studies have shown that they have anti-adhesion and anti–biofilm production ability of *Candida albicans* grown on polystyrene surfaces. In a nutshell, this novel approach provides a new way to synthesize C-dots using natural sources of carbon (Shaikh et al., 2019).

Viral nanoparticle

Nowadays, viruses are being employed in the synthesis of bioinspired/biomimetic nanoplatforms due to their unique properties. Viral nanomaterials can be synthesized using virus nanoparticles (VNPs) and virus-like particles (VLPs). The latter is being utilized for the synthesis of inorganic NPs and the delivery of drugs and bio-imaging agents (Allen et al., 2005; Liepold et al., 2007). A virus consists of a protein coat called the capsid, which is considered a smart material because of its monodispersity, symmetry, and polyvalency. Among the various types of viruses, the helical virus is a prefabricated scaffold with a unique structure and a high surface area–to-volume ratio that enables it to form various types of nanostructures (Narayanan and Han, 2017a). Plant virus capsids provide the best platform for the synthesis of novel nanomaterials that combine inorganic or organic moieties in a very specific and controllable way. In addition, the capsid proteins of spherical plant viruses are assembled into well-defined 3D structures called icosahedral three-dimensional architectures with structural symmetry. They can be employed for a wide range of biomedical applications with simple manipulations (Narayanan and Han, 2017b). Taking inspiration from this, TMV, a helical virus that causes tobacco mosaic virus disease in tobacco plants, is used to synthesize bioinspired nanomaterials. Due to its elongated hollow tube-like structure (4 nm in diameter), it can be easily turned into nanorods. The central hollow space is utilized for the synthesis of cobalt and nickel nanowires (3 nm in diameter). Tsukamoto and co-workers developed a novel formula to produce bimetallic Co-Pt and Fe-Pt alloy nanowires in the hollow channel of the TMV. The process of nucleation and the growth of Co-Pt and Fe-Pt nanowires were successfully examined and characterized in detail (Tsukamoto et al., 2007).

Conclusion and future prospects

The present work describes the biosynthesis of NPs using approaches derived from natural sources or inspired by nature. Bioinspired NPs avoid several disadvantages of conventionally used protocols, including the use of harsh chemicals in their preparations. These NPs are less toxic, easy to prepare, and cost-effective. Novel types of bioinspired nanoplatforms have potential applications in the field of nanomedicine. Currently, they have various applications in the biomedicine field, such as cancer therapy, antimicrobial, immunotherapy, biosensing, and diagnosis. In the case of membrane coating, the membranes of cancer cells are coated with NPs so that the natural defense system is activated to produce cancer immunotherapies much like nano-vaccines. They may also benefit from increased blood circulation time, reticuloendothelial system escaping, and tumor-specific active targeting.

With the advancement of material science and nanotechnology, proper care should be taken to avoid any uncontrolled reactions leading to the formation of polydisperse and larger NPs, thus affecting their therapeutic effectiveness. Novel methods should be devised for the proper synthesis of bioinspired nanomaterials so as to formulate novel NPs with higher loading efficiency and better efficacy. In the future, antibodies, proteins, and peptides can be inserted into the plasma membrane of NPs to achieve targeted and improved therapeutic effects. Research should focus on translating the synthesis of NPs into clinical applications and mass production at a lower cost.

Author contributions

GW: conceptualization, methodology, investigation, software, validation, resources, writing—original draft, writing—review and editing, and project administration. XH: methodology, investigation, validation, and writing—review and editing. LH: investigation and methodology. YB: writing—review and editing. AR: writing—review and editing. X-FY: funding acquisition, project administration, supervision, and writing—review and editing. CC: funding acquisition, project administration, supervision, and writing—review and editing.

Funding

The project is supported by the “High-level Hospital Construction Research Project of Maoming People’s Hospital” and a research Fund for International Young Scientists funded by the National Natural Science Foundation of China (32150410363).

Conflict of interest

The authors declare that the research was conducted in the absence of any commercial or financial relationships that could be construed as a potential conflict of interest.

Publisher’s note

References

Agrawal, A. K., Aqil, F., Jeyabalan, J., Spencer, W. A., Beck, J., Gachuki, B. W., et al. (2017). Milk-derived exosomes for oral delivery of paclitaxel. *Nanomedicine Nanotechnol. Biol. Med.* 13 (5), 1627–1636. doi:10.1016/j.nano.2017.03.001

Akhavan, O., Choobtashani, M., and Ghaderi, E. (2012). Protein degradation and RNA efflux of viruses photocatalyzed by graphene–tungsten oxide composite under visible light irradiation. *J. Phys. Chem. C* 116 (17), 9653–9659. doi:10.1021/jp301707m

Akhavan, O., and Ghaderi, E. (2010). Toxicity of graphene and graphene oxide nanowalls against bacteria. *ACS Nano* 4 (10), 5731–5736. doi:10.1021/nn101390x

Ali, S., Perveen, S., Ali, M., Jiao, T., Sharma, A. S., Hassan, H., et al. (2020). Bioinspired morphology-controlled silver nanoparticles for antimicrobial application. *Mater. Sci. Eng. C* 108, 110421. doi:10.1016/j.msec.2019.110421

Alizadeh, D., and Larmonier, N. (2014). Chemotherapeutic targeting of cancer-induced immunosuppressive cells. *Cancer Res.* 74 (10), 2663–2668. doi:10.1158/0008-5472.can-14-0301

Allen, M., Bulte, J. W. M., Liepold, L., Basu, G., Zywicke, H. A., Frank, J. A., et al. (2005). Paramagnetic viral nanoparticles as potential high-relaxivity magnetic resonance contrast agents. *Magn. Reson. Med.* 54 (4), 807–812. doi:10.1002/mrm.20614

Avossa, J., Pota, G., Vitiello, G., Macagnano, A., Zanfardino, A., Di Napoli, M., et al. (2021). Multifunctional mats by antimicrobial nanoparticles decoration for bioinspired smart wound dressing solutions. *Mater. Sci. Eng. C* 123, 111954. doi:10.1016/j.msec.2021.111954

Bandi, R., Gangapuram, B. R., Dadigala, R., Eslavath, R., Singh, S. S., and Guttena, V. (2016). Facile and green synthesis of fluorescent carbon dots from onion waste and their potential applications as sensor and multicolour imaging agents. *RSC Adv.* 6 (34), 28633–28639. doi:10.1039/c6ra01669c

Binnewies, M., Roberts, E. W., Kersten, K., Chan, V., Fearon, D. F., Merad, M., et al. (2018). Understanding the tumor immune microenvironment (TIME) for effective therapy. *Nat. Med.* 24 (5), 541–550. doi:10.1038/s41591-018-0014-x

Buschow, S. I., Balkom, B. W. M., Aalberts, M., Heck, A. J. R., Wauben, M., and Stoorvogel, W. (2010). MHC class II-associated proteins in B-cell exosomes and potential functional implications for exosome biogenesis. *Immunol. Cell Biol.* 88 (8), 851–856. doi:10.1038/icb.2010.64

Castro, L., Blázquez, M. L., González, F., Muñoz, J. A., and Ballester, A. (2013). "Gold, silver and platinum nanoparticles biosynthesized using orange peel extract," in *Advanced materials research* Trans Tech Publ Ltd, 825, 556–559. doi:10.4028/www.scientific.net/amr.825.556

Chalasani, K. B., Russell-Jones, G., Yandrapu, S. K., Diwan, P. V., and Jain, S. K. (2007). A novel vitamin B12-nanosphere conjugate carrier system for peroral delivery of insulin. *J. Control. release* 117 (3), 421–429. doi:10.1016/j.jconrel.2006.12.003

Chalasani, K. B., Russell-Jones, G. J., Jain, A. K., Diwan, P. V., and Jain, S. K. (2007). Effective oral delivery of insulin in animal models using vitamin B12-coated dextran nanoparticles. *J. Control. release* 122 (2), 141–150. doi:10.1016/j.jconrel.2007.05.019

Chan, W. C. (2017). Nanomedicine 2.0. *Acc. Chem. Res.* 50 (3), 627–632. doi:10.1021/acs.accounts.6b00629

Chhabra, H., Deshpande, R., Kanitkar, M., Jaiswal, A., Kale, V. P., and Bellare, J. R. (2016). A nano zinc oxide doped electrospun scaffold improves wound healing in a rodent model. *RSC Adv.* 6 (2), 1428–1439. doi:10.1039/c5ra21821g

Clayton, A., Harris, C. L., Court, J., Mason, M. D., and Morgan, B. P. (2003). Antigen-presenting cell exosomes are protected from complement-mediated lysis by expression of CD55 and CD59. *Eur. J. Immunol.* 33 (2), 522–531. doi:10.1002/immu.200310028

Dai, Q., Wilhelm, S., Ding, D., Syed, A. M., Sindhwani, S., Zhang, Y., et al. (2018). Quantifying the ligand-coated nanoparticle delivery to cancer cells in solid tumors. *ACS Nano* 12 (8), 8423–8435. doi:10.1021/acsnano.8b03900

Dewhirst, M. W., and Secomb, T. W. (2017). Transport of drugs from blood vessels to tumour tissue. *Nat. Rev. Cancer* 17 (12), 738–750. doi:10.1038/nrc.2017.93

Elsayed, M., Huang, J., and Edirisinghe, M. (2015). Bioinspired preparation of alginate nanoparticles using microbubble bursting. *Mater. Sci. Eng. C* 46, 132–139. doi:10.1016/j.msec.2014.09.036

Fitzgerald, J. W. (1991). Marine aerosols: A review. *Atmos. Environ. Part A. General Top.* 25 (3-4), 533–545. doi:10.1016/0960-1686(91)90050-H

Francis, M. F., Cristea, M., and Winnik, F. M. (2005). Exploiting the vitamin B12 pathway to enhance oral drug delivery via polymeric micelles. *Biomacromolecules* 6 (5), 2462–2467. doi:10.1021/bm0503165

Gaharwar, A. K., Peppas, N. A., and Khademhosseini, A. (2014). Nanocomposite hydrogels for biomedical applications. *Biotechnol. Bioeng.* 111 (3), 441–453. doi:10.1002/bit.25160

Goh, W. J., Lee, C. K., Zou, S., Woon, E., Czarny, B., and Pastorin, G. (2017). Doxorubicin-loaded cell-derived nanovesicles: An alternative targeted approach for anti-tumor therapy. *Int. J. Nanomedicine* 12, 2759–2767. doi:10.2147/ijn.s131786

Grimaldi, N., Andrade, F., Segovia, N., Ferrer-Tasies, L., Sala, S., Veciana, J., et al. (2016). Lipid-based nanovesicles for nanomedicine. *Chem. Soc. Rev.* 45 (23), 6520–6545. doi:10.1039/c6cs00409a

Gurunathan, S. (2019). Rapid biological synthesis of silver nanoparticles and their enhanced antibacterial effects against Escherichia fergusonii and Streptococcus mutans. *Arabian J. Chem.* 12 (2), 168–180. doi:10.1016/j.arabjc.2014.11.014

Hu, C-M. J., Zhang, L., Aryal, S., Cheung, C., Fang, R. H., and Zhang, L. (2011). Erythrocyte membrane-camouflaged polymeric nanoparticles as a biomimetic delivery platform. *Proc. Natl. Acad. Sci. U. S. A.* 108 (27), 10980–10985. doi:10.1073/pnas.1106634108

Hu, W., Peng, C., Luo, W., Lv, M., Li, X., Li, D., et al. (2010). Graphene-based antibacterial paper. *ACS Nano* 4, 4317–4323. doi:10.1021/nn101097v

Ibrahim, H. M. (2015). Green synthesis and characterization of silver nanoparticles using banana peel extract and their antimicrobial activity against representative microorganisms. *J. Radiat. Res. Appl. Sci.* 8 (3), 265–275. doi:10.1016/j.jrras.2015.01.007

Ilahibaks, N. F., Lei, Z., Mol, E. A., Deshantri, A. K., Jiang, L., Schiffelers, R. M., et al. (2019). Biofabrication of cell-derived nanovesicles: A potential alternative to extracellular vesicles for regenerative medicine. *Cells* 8 (12), 1509. doi:10.3390/cells8121509

Kadiyala, N. K., Mandal, B. K., Ranjan, S., and Dasgupta, N. (2018). Bioinspired gold nanoparticles decorated reduced graphene oxide nanocomposite using Syzygium cumini seed extract: Evaluation of its biological applications. *Mater. Sci. Eng. C* 93, 191–205. doi:10.1016/j.msec.2018.07.075

Kalluri, R. (2016). The biology and function of fibroblasts in cancer. *Nat. Rev. Cancer* 16 (9), 582–598. doi:10.1038/nrc.2016.73

Kasibabu, B. S. B., D'souza, S. L., Jha, S., Singhal, R. K., Basu, H., and Kailasa, S. K. (2015). One-step synthesis of fluorescent carbon dots for imaging bacterial and fungal cells. *Anal. Methods* 7 (6), 2373–2378. doi:10.1039/c4ay02737j

Ke, Z., Guo, H., Zhu, X., Jin, Y., and Huang, Y. (2015). Efficient peroral delivery of insulin via vitamin B12 modified trimethyl chitosan nanoparticles. *J. Pharm. Pharm. Sci.* 18 (2), 155. doi:10.18433/j3j88q

Kim, B., Rutka, J., and Chan, W. (2010). Nanomedicine. *N. Engl. J. Med. Overseas. Ed.* 363, 2434–2443. doi:10.1056/nejmra0912273

Kitamura, T., Qian, B-Z., and Pollard, J. W. (2015). Immune cell promotion of metastasis. *Nat. Rev. Immunol.* 15 (2), 73–86. doi:10.1038/nri3789

Kulkarni Vishakha, S., Butte Kishor, D., and Rathod Sudha, S. (2012). Natural polymers–A comprehensive review. *Int. J. Res. Pharm. Biomed. Sci.* 3 (4), 1597–1613.

Li, C-L., Ou, C. M., Huang, C. C., Wu, W. C., Chen, Y. P., Lin, T. E., et al. (2014). Carbon dots prepared from ginger exhibiting efficient inhibition of human hepatocellular carcinoma cells. *J. Mat. Chem. B* 2 (28), 4564. doi:10.1039/c4tb00216d

Liepold, L., Anderson, S., Willits, D., Oltrogge, L., Frank, J. A., Douglas, T., et al. (2007). Viral capsids as MRI contrast agents. *Magn. Reson. Med.* 58 (5), 871–879. doi:10.1002/mrm.21307

Liu, S-S., Wang, C. F., Li, C. X., Wang, J., Mao, L. H., and Chen, S. (2014). Hair-derived carbon dots toward versatile multidimensional fluorescent materials. *J. Mat. Chem. C* 2 (32), 6477–6483. doi:10.1039/c4tc00636d

Lu, M., and Huang, Y. (2020). Bioinspired exosome-like therapeutics and delivery nanoplatforms. *Biomaterials* 242, 119925. doi:10.1016/j.biomaterials.2020.119925

Ma, G., Severic, M., Barker, M., Pereira, S., Ruiz, A., Cheung, C. C., et al. (2021). Dually targeted bioinspired nanovesicle delays advanced prostate cancer tumour growth *in vivo*. *Acta Biomater.* 134, 559–575. doi:10.1016/j.actbio.2021.07.021

Ma, J., Zhang, J., Xiong, Z., Yong, Y., and Zhao, X. (2011). Preparation, characterization and antibacterial properties of silver-modified graphene oxide. *J. Mat. Chem.* 21 (10), 3350–3352. doi:10.1039/c0jm02806a

Madamsetty, V. S., Mukherjee, A., and Mukherjee, S. (2019). Recent trends of the bio-inspired nanoparticles in cancer theranostics. *Front. Pharmacol.* 10, 1264. doi:10.3389/fphar.2019.01264

Malafaya, P. B., Silva, G. A., and Reis, R. L. (2007). Natural–origin polymers as carriers and scaffolds for biomolecules and cell delivery in tissue engineering applications. *Adv. drug Deliv. Rev.* 59 (4-5), 207–233. doi:10.1016/j.addr.2007.03.012

Mao, H. Y., Laurent, S., Chen, W., Akhavan, O., Imani, M., and Ashkarran, A. A. (2013). Graphene: Promises, facts, opportunities, and challenges in nanomedicine. *Chem. Rev.* 113 (5), 3407–3424. doi:10.1021/cr300335p

Mehta, V. N., Jha, S., and Kailasa, S. K. (2014). One-pot green synthesis of carbon dots by using Saccharum officinarum juice for fluorescent imaging of bacteria (*Escherichia coli*) and yeast (*Saccharomyces cerevisiae*) cells. *Mater. Sci. Eng. C* 38, 20–27. doi:10.1016/j.msec.2014.01.038

Minchinton, A. I., and Tannock, I. F. (2006). Drug penetration in solid tumours. *Nat. Rev. Cancer* 6 (8), 583–592. doi:10.1038/nrc1893

Morishita, M., Takahashi, Y., Matsumoto, A., Nishikawa, M., and Takakura, Y. (2016). Exosome-based tumor antigens–adjuvant co-delivery utilizing genetically engineered tumor cell-derived exosomes with immunostimulatory CpG DNA. *Biomaterials* 111, 55–65. doi:10.1016/j.biomaterials.2016.09.031

Munagala, R., Aqil, F., Jeyabalan, J., and Gupta, R. C. (2016). Bovine milk-derived exosomes for drug delivery. *Cancer Lett.* 371 (1), 48–61. doi:10.1016/j.canlet.2015.10.020

Munagala, R., Aqil, F., Jeyabalan, J., Agrawal, A. K., Mudd, A. M., Kyakulaga, A. H., et al. (2017). Exosomal formulation of anthocyanidins against multiple cancer types. *Cancer Lett.* 393, 94–102. doi:10.1016/j.canlet.2017.02.004

Narayanan, K. B., and Han, S. S. (2017). Helical plant viral nanoparticles—bioinspired synthesis of nanomaterials and nanostructures. *Bioinspir. Biomim.* 12 (3), 031001. doi:10.1088/1748-3190/aa6bfd

Narayanan, K. B., and Han, S. S. (2017). Icosahedral plant viral nanoparticles-bioinspired synthesis of nanomaterials/nanostructures. *Adv. Colloid Interface Sci.* 248, 1–19. doi:10.1016/j.cis.2017.08.005

Nishanthi, R., Malathi, S., Palani, P., and P., P. (2019). Green synthesis and characterization of bioinspired silver, gold and platinum nanoparticles and evaluation of their synergistic antibacterial activity after combining with different classes of antibiotics. *Mat. Sci. Eng. C Mat. Biol. Appl.* 96, 693–707. doi:10.1016/j.msec.2018.11.050

Overchuk, M., and Zheng, G. (2018). Overcoming obstacles in the tumor microenvironment: Recent advancements in nanoparticle delivery for cancer theranostics. *Biomaterials* 156, 217–237. doi:10.1016/j.biomaterials.2017.10.024

Pardoll, D. M. (2012). The blockade of immune checkpoints in cancer immunotherapy. *Nat. Rev. Cancer* 12 (4), 252–264. doi:10.1038/nrc3239

Park, K-S., Svennerholm, K., Shelke, G. V., Bandeira, E., Lasser, C., Jang, S. C., et al. (2019). Mesenchymal stromal cell-derived nanovesicles ameliorate bacterial outer membrane vesicle-induced sepsis via IL-10. *Stem Cell Res. Ther.* 10 (1), 231. doi:10.1186/s13287-019-1352-4

Pedraza-Chaverri, J., Cárdenas-Rodríguez, N., Orozco-Ibarra, M., and Pérez-Rojas, J. M. (2008). Medicinal properties of mangosteen (Garcinia mangostana). *Food Chem. Toxicol.* 46 (10), 3227–3239. doi:10.1016/j.fct.2008.07.024

Qian, C., Feng, P., Yu, J., Chen, Y., Hu, Q., Sun, W., et al. (2017). Innentitelbild: Anaerobe-Inspired anticancer nanovesicles (angew. Chem. 10/2017). *Angew. Chem. Int. Ed. Engl.* 129 (10), 2558. doi:10.1002/ange.201701131

Qu, X., Liu, H., Zhang, C., Lei, Y., Lei, M., Xu, M., et al. (2018). Electrofabrication of functional materials: Chloramine-based antimicrobial film for infectious wound treatment. *Acta Biomater.* 73, 190–203. doi:10.1016/j.actbio.2018.02.028

Ravichandran, S., Radhakrishnan, J., Jayabal, P., and Venkatasubbu, G. D. (2019). Antibacterial screening studies of electrospun Polycaprolactone nano fibrous mat containing Clerodendrum phlomidis leaves extract. *Appl. Surf. Sci.* 484, 676–687. doi:10.1016/j.apsusc.2019.04.150

Sawadkar, P., Mohanakrishnan, J., Rajasekar, P., Rahmani, B., Kohli, N., Bozec, L., et al. (2020). A synergistic relationship between polycaprolactone and natural polymers enhances the physical properties and biological activity of scaffolds. *ACS Appl. Mat. Interfaces* 12 (12), 13587–13597. doi:10.1021/acsami.9b19715

Seetharam, B. (1999). Receptor-mediated endocytosis of cobalamin (vitamin B12). *Annu. Rev. Nutr.* 19, 173–195. doi:10.1146/annurev.nutr.19.1.173

Shaikh, A. F., Tamboli, M. S., Patil, R. H., Bhan, A., Ambekar, J. D., and Kale, B. B. (2019). Bioinspired carbon quantum dots: an antibiofilm agents. *J. Nanosci. Nanotechnol.* 19 (4), 2339–2345. doi:10.1166/jnn.2019.16537

Shaked, Y. (2019). The pro-tumorigenic host response to cancer therapies. *Nat. Rev. Cancer* 19 (12), 667–685. doi:10.1038/s41568-019-0209-6

Sivarajakumar, R., Mallukaraj, D., Kadavakollu, M., Neelakandan, N., Chandran, S., Bhojaraj, S., et al. (2018). Nanoparticles for the treatment of lung cancers. *J. Young Pharm.* 10 (3), 276–281. doi:10.5530/jyp.2018.10.62

Soppimath, K. S., Aminabhavi, T. M., Kulkarni, A. R., and Rudzinski, W. E. (2001). Biodegradable polymeric nanoparticles as drug delivery devices. *J. Control. release* 70 (1-2), 1–20. doi:10.1016/s0168-3659(00)00339-4

Spiel, D. E. (1998). On the births of film drops from bubbles bursting on seawater surfaces. *J. Geophys. Res.* 103 (C11), 24907–24918. doi:10.1029/98jc02233

Stremersch, S., De Smedt, S. C., and Raemdonck, K. (2016). Therapeutic and diagnostic applications of extracellular vesicles. *J. Control. release* 244, 167–183. doi:10.1016/j.jconrel.2016.07.054

Sun, Y., Shi, H., Yin, S., Ji, C., Zhang, X., Zhang, B., et al. (2018). Human mesenchymal stem cell derived exosomes alleviate type 2 diabetes mellitus by reversing peripheral insulin resistance and relieving β-cell destruction. *ACS Nano* 12 (8), 7613–7628. doi:10.1021/acsnano.7b07643

Tan, T., Hu, H., Wang, H., Li, J., Wang, Z., Wang, J., et al. (2019). Bioinspired lipoproteins-mediated photothermia remodels tumor stroma to improve cancer cell accessibility of second nanoparticles. *Nat. Commun.* 10 (1), 3322. doi:10.1038/s41467-019-11235-4

Togashi, Y., Shitara, K., and Nishikawa, H. (2019). Regulatory T cells in cancer immunosuppression—implications for anticancer therapy. *Nat. Rev. Clin. Oncol.* 16 (6), 356–371. doi:10.1038/s41571-019-0175-7

Tsukamoto, R., Muraoka, M., Seki, M., Tabata, H., and Yamashita, I. (2007). Synthesis of CoPt and FePt3 nanowires using the central channel of tobacco mosaic virus as a biotemplate. *Chem. Mat.* 19 (10), 2389–2391. doi:10.1021/cm062187k

Verma, A., Sharma, S., Gupta, P. K., Singh, A., Teja, B. V., Dwivedi, P., et al. (2016). Vitamin B12 functionalized layer by layer calcium phosphate nanoparticles: A mucoadhesive and pH responsive carrier for improved oral delivery of insulin. *Acta Biomater.* 31, 288–300. doi:10.1016/j.actbio.2015.12.017

Wang, H., Li, J., Wang, Z., Wang, Y., Xu, X., Gong, X., et al. (2021). Tumor-permeated bioinspired theranostic nanovehicle remodels tumor immunosuppression for cancer therapy. *Biomaterials* 269, 120609. doi:10.1016/j.biomaterials.2020.120609

Wang, J., Tan, J., Luo, J., Huang, P., Zhou, W., Chen, L., et al. (2017). Enhancement of scutellarin oral delivery efficacy by vitamin B12-modified amphiphilic chitosan derivatives to treat type II diabetes induced-retinopathy. *J. Nanobiotechnology* 15 (1), 18. doi:10.1186/s12951-017-0251-z

Wang, L., and Zhou, H. S. (2014). Green synthesis of luminescent nitrogen-doped carbon dots from milk and its imaging application. *Anal. Chem.* 86 (18), 8902–8905. doi:10.1021/ac502646x

Wilhelm, S., Tavares, A. J., Dai, Q., Ohta, S., Audet, J., Dvorak, H. F., et al. (2016). Analysis of nanoparticle delivery to tumours. *Nat. Rev. Mat.* 1 (5), 16014. doi:10.1038/natrevmats.2016.14

Wilson, R. J., Hui, Y., Whittaker, A. K., and Zhao, C-X. (2021). Facile bioinspired synthesis of iron oxide encapsulating silica nanocapsules. *J. Colloid Interface Sci.* 601, 78–84. doi:10.1016/j.jcis.2021.05.021

Yang, K., Wan, J., Zhang, S., Tian, B., Zhang, Y., and Liu, Z. (2012). The influence of surface chemistry and size of nanoscale graphene oxide on photothermal therapy of cancer using ultra-low laser power. *Biomaterials* 33 (7), 2206–2214. doi:10.1016/j.biomaterials.2011.11.064

Yang, K., Zhang, S., Zhang, G., Sun, X., Lee, S. T., and Liu, Z. (2010). Graphene in mice: ultrahigh *in vivo* tumor uptake and efficient photothermal therapy. *Nano Lett.* 10 (9), 3318–3323. doi:10.1021/nl100996u

Zhang, L., Xia, J., Zhao, Q., Liu, L., and Zhang, Z. (2010). Functional graphene oxide as a nanocarrier for controlled loading and targeted delivery of mixed anticancer drugs. *small* 6 (4), 537–544. doi:10.1002/smll.200901680

Zhang, X., Wang, C., Wang, J., Hu, Q., Langworthy, B., Ye, Y., et al. (2018). Cancer immunotherapy: PD-1 blockade cellular vesicles for cancer immunotherapy (adv. Mater. 22/2018). *Adv. Mat.* 30 (22), 1870152. doi:10.1002/adma.201870152

Zhang, Z., Wang, H., Tan, T., Li, J., Wang, Z., and Li, Y. (2018). Rational design of nanoparticles with deep tumor penetration for effective treatment of tumor metastasis. *Adv. Funct. Mat.* 28 (40), 1801840. doi:10.1002/adfm.201801840

Zhao, Q., Hai, B., Zhang, X., Xu, J., Koehler, B., and Liu, F. (2020). Biomimetic nanovesicles made from iPS cell-derived mesenchymal stem cells for targeted therapy of triple-negative breast cancer. *Nanomedicine Nanotechnol. Biol. Med.* 24, 102146. doi:10.1016/j.nano.2019.102146

Zhou, J., Sheng, Z., Han, H., Zou, M., and Li, C. (2012). Facile synthesis of fluorescent carbon dots using watermelon peel as a carbon source. *Mater. Lett.* 66 (1), 222–224. doi:10.1016/j.matlet.2011.08.081

Zitvogel, L., Regnault, A., Lozier, A., Wolfers, J., Flament, C., Tenza, D., et al. (1998). Eradication of established murine tumors using a novel cell-free vaccine: dendritic cell derived exosomes. *Nat. Med.* 4 (5), 594–600. doi:10.1038/nm0598-594

frontiers | Frontiers in Bioengineering and Biotechnology

TYPE Mini Review
PUBLISHED 09 September 2022
DOI 10.3389/fbioe.2022.1013217

OPEN ACCESS

EDITED BY
Pengchao Zhang,
Wuhan University of Technology, China

REVIEWED BY
Xin Han,
Nanjing University of Chinese Medicine, China
Chunmei Ding,
Sichuan University, China

*CORRESPONDENCE
Tian Xia,
xiatian76@163.com
Yanting Liu,
dr.yantingliu@foxmail.com

SPECIALTY SECTION
This article was submitted to Biomaterials, a section of the journal Frontiers in Bioengineering and Biotechnology

RECEIVED 06 August 2022
ACCEPTED 22 August 2022
PUBLISHED 09 September 2022

CITATION
Dong R, Ma S, Zhao X, Wang B, Roy M, Yao L, Xia T and Liu Y (2022), Recent progress of Bioinspired Hydrogel-based delivery system for endometrial repair. *Front. Bioeng. Biotechnol.* 10:1013217. doi: 10.3389/fbioe.2022.1013217

Recent progress of Bioinspired Hydrogel-based delivery system for endometrial repair

Rong Dong[1], Saihua Ma[1], Xiaoli Zhao[1], Baojuan Wang[1], Mridul Roy[2], Lu Yao[3], Tian Xia[1]* and Yanting Liu[2]*

[1]First Teaching Hospital of Tianjin University of Traditional Chinese Medicine, National Clinical Research Center for Chinese Medicine Acupuncture and Moxibustion, Tianjin, China, [2]Department of Oncology, The First Affiliated Hospital of Xinxiang Medical University, Weihui, China, [3]Hemay Zhihui Science and Technology Co. Ltd, Tianjin, China

Endometrial injury is the main fact leading to infertility. Current treatments of endometrial injury present many problems, such as unable to achieve desired effects due to low retention and the inherent potential risk of injury. Besides, it is important to the development of bioinspired material that can mimic the natural tissue and possess native tissue topography. Hydrogel is a kind of bioinspired superhydrophilic materials with unique characteristics, such as excellent biocompatibility, biodegradability, porosity, swelling, and cross-linkage. These unique physiochemical properties of bioinspired hydrogels enable their promising application as novel delivery platform and alternative therapies for endometrial injury. In this mini review, we summarize the recent advances in bioinispred hydrogel-based delivery system for endometrial repair, including as a post-operative physical barrier and therapeutic delivery system. In addition, present status, limitations, and future perspectives are also discussed.

KEYWORDS

bioinspired, hydrogel, uterine, endometrial, reproductive

1 Introduction

Endometrium is the innermost layer of the uterus. This layer comprises epithelial and stroma components that are responsible for cell proliferation, differentiation, and shedding—which is deterministic of a woman's viability for embryo implantation (Lessey, 2000). The normal endometrium can repair and regenerate itself and plays a pivotal role in female physiology and reproductive function. However, severe endocrine disorders, intrauterine infection and intrauterine surgery can lead to endometrial injury. When the uterine cavity lacks endometrial coverage, fibrosis, scarring and adhesion may occur, which result in decreased reception, loss, or reduced regenerative ability (Deans and Abbott, 2010; Liao et al., 2021; Lv et al., 2021), and those are the common cause of infertility worldwide (Ma et al., 2021).

Traditionally, there are three main treatments for endometrium repair, including surgical separation of the adherent endometrium, estrogen and cytokines therapy, and stem cell therapy (Yu et al., 2008; Evans-Hoeker and Young, 2014; Hooker et al., 2016)).

TABLE 1 The physiochemical properties of hydrogels.

Characteristic	Physiochemical property	Function
1. Swelling property	The presence of hydrophilic, carboxyl and hydroxyl groups	Serve as therapeutic cargo or scaffold for delivery
2. Pore containing structure	Incorporation of porogens	Provide rapid cellular infiltration with maintaining structural integrity
3. Self-healing	Polymeric networks within the hydrogel matrix are mediated by either weak sacrificial noncovalent ionic, hydrogen or hydrophobic interactions or dynamic chemical covalent bonds	Repair structural damages to recover original functions applied for wound healing, tissue engineering, surface coating, or drug/cell delivery
4. Biocompatibility	Incorporation of polymeric substances, the internal water content and appropriate viscosity	Helps adhere to the injured site, often used as artificial ECM that mimics the tissue environment

For surgical treatment, the re-adhesion rate is high. For drug and stem cell therapy, the retention to the sites of endometrium is quite low (Abomaray et al., 2016; Liu et al., 2016; Xie et al., 2017; Mao et al., 2020). Moreover, the stem cells easily flow with blood and body fluids, making them difficult to be delivered to the damaged endometrium (Ma et al., 2021). Contrary, recent study shed light on the potential efficiency of constructed uterus-inspired niche for the efficient developmental events during the early stage of organogenesis (Gu et al., 2022). Knowledge of the above assertion prompts a need for a bio-material to provide a favorable environment for stem cell adhesion, controlled drug release and post-operation anti-adhesive barrier for effective repair of the endometrium.

Hydrogel is a kind of bioinspired superhydrophilic materials, which have similar compositional and structural features with natural tissues (Chen et al., 2021). Their polymeric three-dimentional (3D) network enables them to absorb and retain a significant amount of water. The water content of hydrogel can be as high as 90% (Zhang et al., 2019). Moreover, bioinspired hydrogel possesses excellent properties, such as high water absorbability, biocompatibility, low interfacial tension and degradability (Table 1). What's more, the above mentional properties of bioinspired hydrogel can be tuned both physically and chemically, gaining great interests in a variety of applications such as tissue engineering, drug release, and 3D cell culture (Lim et al., 2014). All in all, hydrogel is a perfect platform for encapsulating and delivery of novel intrauterine therapies (Ma et al., 2018; Tang et al., 2018; Marycz et al., 2019), and serve as a promising biomaterial for endometrium repair (Townsend et al., 2019).

2 Application of bioinspired hydrogel in endometrium injury

Hydrogels have unique properties that make them enable for application in regenerative medicine. These properties include excellent biocompatibility and biodegradability, strong water-binding capacity, which enables them to double their size while swelling, an ability to incorporate therapeutic components for controlled release as well as, the ability to encapsulate seed cells at optimum physiological conditions (Wang et al., 2021). For endometrial injury, hydrogels are applied as a physical anti-adhesion barrier and as a delivery mechanism for therapeutics. The physical and biological properties of hydrogels enable them to influence the uterine microenvironment, biological behaviors, proliferation and angiogenesis. Swelling property makes hydrogel capable of compressing the bleeding point. The interactions between blood cells and the charged amino groups on the hydrogels confer aggregation, adhesion and blood clotting (Gu et al., 2010; Wen et al., 2016). The amino group, in association with the hydroxyl group of hydrogels also reacts with the oxygen free radicals to reduce the reactive oxygen-mediated damage of endometrium (Castro Marin et al., 2019; Wei et al., 2019). In addition, hydrogels can inhibit the release of TNF-α and IL-6 and increase the production of IL-8. These IL-8 induce an anti-inflammatory response on one hand and also combine with the neutral granulocytes surface receptors CXCR1/2 to produce active components against bacteria.

2.1 Application of bioinspired hydrogel as a post operative Physical Barrier

Conventional post-transcervical resection of adhesion (TCRA) anti-adhesion physical barriers such as intrauterine devices (IUD) and Foley catheter balloons pose the risk of recurring adhesion owing to a limited surface area (Bhandari et al., 2015; Chi et al., 2018). This implies that they are unable to cover the anterior and posterior walls of the uterus effectively. Another underlying issue is the risk of infection during their removal and their inability to promote pregnancy. Biomedical researches indicate the application of optimized hydrogels to be efficient in this regard (Xiao et al., 2015). Hyaluronic acid (HA) hydrogel is biocompatible, biodegradable as well as non-toxic to the cells and tissues. In fact, HA hydrogels were proven to reduce the risk of the reformation of intrauterine adhesions (IUAs) in women with

an endometrial injury who undergo resection surgery (Can et al., 2018; Lee et al., 2020a; Tafti et al., 2021). However, studies found that hydrogel combined treatment strategy with the insertion of a urinary catheter or IUD had a more satisfactory effect in regaining an adhesion-free uterine cavity (Xiao et al., 2015; Li et al., 2019; Pabuccu et al., 2019). A meta-analysis indicated that Hyaluronic acid (HA) hydrogel platforms and chitosan platforms used after TCRA facilitate excellent tissue repair, and reduce adhesion recurrence but did not affect on postoperative pregnancy rate among patients (Fei et al., 2019). The latter is consistent with the research findings of Mao et al. (2020) which suggest HA hydrogels could enhance endometrial receptivity and clinical pregnancy rates in moderate IUA patients. Although many studies proved IUD combined with hydrogels reduce IUA recurrence, in some cases, the pregnancy rate remains lower in these patients. Furthermore, due to rapid degradation, it cannot stay for a prolonged duration inside the uterine cavity (Azumaguchi et al., 2019). Also, following hysteroscopic adhesiolysis, auto-cross-linked HA gel was found inefficient to reduce the recurrence rate of adhesion (Zhou et al., 2021b). This can be explained by, the use of concurrent adjuvant therapy which can mask the beneficial effect of hydrogels in reducing adhesion recurrence. Furthermore, the severity of pre-existing adhesions and the types of the gel used in different studies were also different. Whatever, the results suggesting the necessity of in-depth studies to explore the appropriate application of hydrogels to improve patients outcomes.

2.2 Application of bioinspired hydrogel as a Therapeutic Delivery System

Novel treatment emerged as a postoperative mechanism after TCRA and hysteroscopic adhesiolysis to facilitate the repair and regeneration of the endometrium and reduce the recurrence of adhesion. In the case of drug treatment for endometrial injuries, drugs may be administered via oral means, transvaginal or intravenous injections. Albeit, complications resulting from these drug administration methods, such as damage to liver and blood tissues (Lin et al., 2020), claim the requirement of other efficient modes of delivery of the drugs to the injured site. Also, stem therapy options facilitated the possibility of substitution or replacement of injured cells to aid in endometrium regeneration (Tan et al., 2016; Gan et al., 2017; Yin et al., 2019). Both therapies result in limited therapeutic effect due to the low retention to the sites of injury (Abomaray et al., 2016). For optimum therapeutic effect, the materials (drug or 3D stem cells) should be delivered and retained to the injured site to prevent bacterial infection. Hydrogel used in endometrial regeneration and repair is highly biocompatible, biodegradable and has a porous structure for encapsulation as well as the sustained release of materials. Therapeutic materials to be delivered include; estrogen, cytokines, stem cells and exosomes.

2.2.1 Application of Hydrogel as a Drug Delivery System

Hydrogel presents distinctive properties that interest its application for drug delivery in the repair and regeneration of endometrial injury. First, the porous structure enables the loading and control release of treatment drugs. Drugs such as β-estradiol can be delivered by hydrogel scaffolds for various purposes including endometrial regeneration (Zhang et al., 2017). Furthermore, the use of stimuli-responsive hydrogels brings many possibilities to drug delivery systems. Poloxamer hydrogel is a thermosensitive hydrogel with better fluidity. When optimized via a polycondensation reaction into heparin-modified poloxamer hydrogel, the half-life of its growth factors is extended and fluidity improved. It covers the injured site completely and perfectly becomes solid at equilibrium temperature (normal body temperature). This prevents bacterial infection and loss of the drug. Thus, injecting the thermosensitive hydrogel (E2-HPhydrogel) with the encapsulation of 17β-estradiol into the injured uterine cavity eliminates the weaknesses of exogenous administration of 17β-estradiol including water solubility, limited half-life time, and low concentrations at the injured area (Baghersad et al., 2018). Hormones such as estrogen, cytokine, exosomes, etc. could also be delivered efficiently and effectively while capitalizing on hydrophilic polymer chain linkage in hydrogels. With regards to estrogen release, the application of poloxamer hydrogel as a carrier does not prolong retention time. Aloe has traits that make it an ideal organic component to mix with poloxamer to form a more biologically friendly thermosensitive hydrogel system (Baghersad et al., 2018; Yao et al., 2020). Aloe-poloxamer (AP) hybrid hydrogel has been fabricated for treating endometrial injury and achieved a better therapeutic effect with a prolonged retention time (Figure 1A). Yao et al. designed a nano-composite aloe/poloxamer hydrogel containing E2 with an additional benefit to enhance the therapeutic effects of estrogen on endometrial regeneration by upregulating estrogen receptors, reducing the likelihood that high-dose estrogen would increase the risk of thrombosis and malignancy. Hydrogel as drug delivery system may be applied as *in situ* vaginal administration in a low viscous form at room temperature, further functionalization, such as with amino group, of poloxamer-based hydrogel prolong intravaginal residence (Figure 1B). Studies suggested that the large surface area and high vascularized nature of the vaginal area enable excellent drug absorption (Liu et al., 2017b; Ci

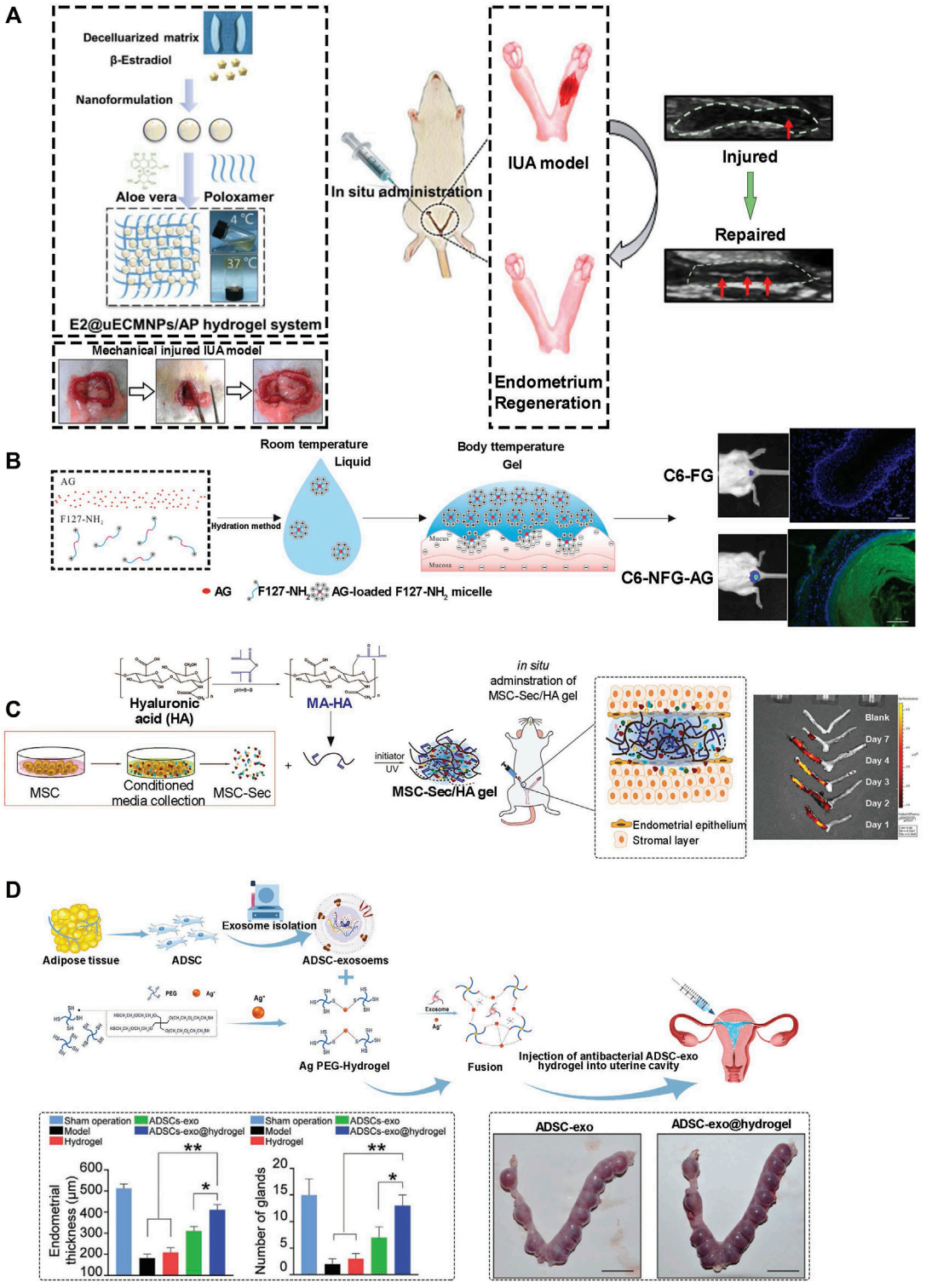

FIGURE 1
Application of hydrogel in endometrium injury. **(A)** E2@uECMNPs/AP hydrogel system for B-estradiol. Following establishment of rat intrauterine adhesion (IUA) model, and treatment the theragnostic ultrasound test was employed to compare the images of the injured IUA with or without E2@uECMNPs treatment (Yao et al., 2020). **(B)** Poloxamer 407 (F127)-based *in situ* hydrogel for the delivery of acetate gossypol (AG) as a model drug. Intravaginal retention of NFG (acetate gossypol-loaded aminated poloxamer 407-based temperature-sensitive hydrogel) and FG (F127 gel) was evaluated. Photographs and fluorescence microscopy showed NFG prolonged intravaginal residence (Ci et al., 2017). **(C)** HA-Hydrogel
(*Continued*)

FIGURE 1 (Continued)
integrated with mesenchymal stem cell (MSC) to treat endometrial injury in a rat model. Schematic showing the synthesis of MSC-Sec-loaded, crosslinked HA gel. MSC-Sec/HA gel was injected in rodent model of endometrium injury and *ex vivo* fluorescent imaging of rat uteri showed the crosslinked HA can stay in the uterine cavity for roughly two estrous cycles (Liu et al., 2019). **(D)** Schematic overview of the development of an exosome secreted by adipose-derived stem cell (ADSC-exo) hydrogel for endometrial regeneration. Increase of endothelial thickness with a concomitant increase of gland numbers affirmed the ability of ADSC-exo hydrogel to promote tissue regeneration. Beside, no significantly higher pregnancy and implantation rates in the ADSC-exo and ADSC-exo hydrogel groups evidant normal endometrial formation and function (Lin et al., 2021).

et al., 2017). Again, vaginal administration has no first-pass effect and has low enzyme activity; therefore, drugs can perform a localized activity, and can also enter the systemic circulation. When thermosensitive hydrogel is administered vaginally, the hydrogel spreads rapidly into the folded area of the vaginal mucosa and forms a gel at body temperature (Andrzejewska et al., 2019). Drug delivery system through injectable hydrogels, as another option, provides other benefits including shortened duration of treatment, decreased risk of infection and prevention of scarring (Asai et al., 2012).

2.2.2 Application of bioinspired Hydrogel as a Three-dimensional Cell Delivery and Culture System

Recent advances in the treatment of endometrium injury suggest cell therapy as a promising alternative to drug therapy. For example, Yi et al. stated that similar to normal rats, rats with injured uterus achieve nearly complete recovery, following treatment with uterus-derived extracellular matrix and seeded chorionic villi mesenchymal stem cells-combined reconstructable uterus-derived materials (RUMs) (Yi et al., 2022). Transplanting Mesenchymal Stem Cells (MSC) via hydrogel as a delivery system showed good potential for endometrial repair (Figure 1C) (Nelson et al., 2009). There have been several sources of stem cells that have been proposed for tissue regeneration. Bone marrow-derived MSC (BM-MSC) has been the most promising cell source of regeneration due to ease in acquisition, self-renewal ability, multi potential differentiation and weak immunogenicity (Ding et al., 2014; Zhou et al., 2021a). Other sources of stem cells include; Human umbilical cord mesenchymal stem cell (UCMSC), Endometrial stromal cell (EMSC), Endometrial perivascular cell (ENPSC) and Bone mononuclear cell (BMNC). Interestingly, hydrogels can be designed as culture systems with a tunable stiffness that encompasses a physiological range owing to their distinguishable properties. Normally hydrogels used for such applications have high-water content, excellent porosity and soft consistency. Also, such hydrogels can closely simulate natural living tissue. Collagen, a natural hydrogel, is widely used in conjunction with the BM-MSC for healing wounds and tissue regeneration as evidence shown in a research study by Ding et al. (Liu et al., 2017a). Again, other synthetic hydrogels used in conjunction with the stem cells include Pluronic F-127 (PF-127). However, it has been found that these synthetic models may have toxic side effects on the cells and thus, there is a need for antioxidants within the scaffold. Commonly, Vitamin C reduces the cytotoxic effect of PF127, and promotes the survival and growth of cells by influencing ECM and collagen homeostasis, exerting anti-inflammatory functions by downregulating the secretion of proinflammatory cytokines such as TNF-a and interleukin-6 (IL-6). Another high-quality carrier for BM-MSC is the photo-crosslinked PRP hydrogel (HNPRP) (Wenbo et al., 2020). The material can be quickly prepared *in situ* to form a strong scaffold and was demonstrated to achieve controlled release of growth factors and reduce tissue adhesion. All the above exogenous substances have potential safety problems such as immunoreaction risk. As such other research studies choose endogenous stem cell migration (Han et al., 2016). *In situ* delivery of stromal cell derivative-1α (SDF-1α) in a controlled release could accelerate the regeneration of multiple tissues.

2.2.3 Application of bioinspired Hydrogel as Exosome Delivery System

Exosomes are extracellular vesicles with a size range of 40–160 nm in diameter. Exosomes, both on their surfaces or inside of them, mainly contain cargo, such as lipids, proteins and nucleic acids, including DNA, mRNA and miRNA (Mathivanan et al., 2010; D'Asti et al., 2012). Under normal physiological conditions, exosomes can originate from endothelial cells, immune cells, tumor cells and mesenchymal stem cells (MSCs) and mimic the extracellular matrix or act as regulators of intercellular communication and immune response (Huang et al., 2021). Exosomes from MSCs are capable of functions similar to MSCs including tissue regeneration and repair (Askenase, 2020). However, exosomes showed several advantages over MSCs, including reduced risk of immune rejection and malignant growth, longer stability and readily circulatory capacity through capillaries (Wang et al., 2021). Owing to all these advantageous characteristics which make exosomes a current research hotspot, the use of purified exosomes can be limited by their rapid clearance from the host after being absorbed by the endothelial system. This limitation can be overcome by hydrogels that can protect exosomes acting as a carrier and delivery depot at the target site to achieve well-regulated cellular secretions more stable therapeutic effect (Figure 1D). Because of the unique physiochemical

characteristic of hydrogel and the ability to controlled-release its embedded molecule, encapsulation of exosomes with hydrogel provide an outstanding candidate in plenty of treatments including bone and cartilage regeneration, cardiovascular diseases, spinal cord injury, periodontal and corneal repairs (Xie et al., 2022). Exosome has immense potential of treating injured endometrium by regulating EMT (Yao et al., 2019; Feng et al., 2020), miRNA (Tan et al., 2020; Shi et al., 2021), proliferation (Lv et al., 2020) and endometrium angiogenesis (Zhang et al., 2022). However, all these effects are achieved *via* the suboptimal approach of direct injection which restricts the activity of exosomes by local tissue irritation or reduced self-life. The ideal repair of endometrium by exosomes can be achieved by using the biocompatibility and physically tunable properties of hydrogels. The exosome-hydrogel system proved to be a safe, noninvasive and convenient method for repairing injured endometrium and can exert excellent effects by promoting angiogenesis, inhibiting local tissue fibrosis and increasing endometrial receptivity (Lin et al., 2021). Although the results were promising, the exosome-hydrogel also has the disadvantage that the bioscaffolds lack the native tissue topography to mimic the natural tissues.

3 Present status and future outlook

Although the damaged endometrium cells can be self-healing and self-regenerated in patients, treatment options such as drugs (estrogen, cytokines, 17β-estradiol, cytokines, etc.) and stem cell therapy aid in the repair and regenerative process. However, it has been found that these therapies usually have low retention to the sites of injury and thus, the desired therapeutic effect is not achieved (Zhao et al., 2021). Bioinspired hydrogel is a 3D hydrophilic polymer with excellent biocompatibility and biodegradability features. It have been identified as having the ability to transport and deliver these therapeutics to the sites of injury owing to their porous, biodegradable and biocompatible features. Coupled with its other distinct features, the material finds varied applications in endometrial regeneration and repair. It serves as an excellent anti-adhesion physical barrier, drug delivery system, three-dimensional cell delivery, and exosome delivery system. While multiresponsive hydrogels that respond to redox, pH and temperature are being proved effective in physiological environments (Lou et al., 2015). Hence, the development of multiresponsive hydrogels to adapt to the intrauterine environment is a future meaningful subject. In addition to physiologically relevant stimuli, the response of these polymers needs to measure in the presence of prevalent biomedical external stimuli such as magnetic field and UV light. To develop an innovative delivery system with excellent biocompatibility, the future direction of research needs compilation of the responsive properties of hydrogels in nearly every conceivable arrangement and minimize the synthesis complexity of these multi-responsive hydrogels. Hydrogels may be optimized to be sensitive to physiological environmental changes to facilitate their specificity and controlled release of treatment. This demonstrates the potential benefits of the encapsulation of cells or other therapeutic substances and underlines the importance of hydrogels in endometrial repair and regeneration. However, to achieve desired and effective therapeutic effects, it is recommended that future studies consider the extending application of multiresponsive hydrogel delivery system to endometrial injury treatment.

The hydrophobic and electrostatic interactions in hydrogels aid the supramolecular assembly of amphiphiles that hold a large amount of water. As a result, hydrogels are potential drug reservoirs and capable of maintaining slow and sustained release. Utilizing this property, researches entrapped two or more drugs in a biodegradable hydrogel to produce a synergistic effect against different ailments including cancer (Medatwal et al., 2020). Therefore, optimization of hydrogels by using rational molecular design to carry multiple drugs for emdometrium regeneration should be considered as this would improve the overall repair and regenerative process of the injured endometrium (An et al., 2021). This will aid in resolving infertility in patients.

Gene editing technology is considered as the driver of modifying genes in fundamental research and facilitating gene therapies in clinical developments. The invention of CRISPR (clustered regularly interspaced short palindromic repeats) Cas (CRISPR-associated) toolbox is a remarkable breakthrough for gene editing. The system contains a complex of the guide RNA (gRNA) that recognizes its complementary target DNA and the Cas nuclease that cut the dsDNA (Knott and Doudna, 2018; Es et al., 2019). Though the system is simple and flexible, the efficiency for targeted delivery of both gRNA and Cas9 needs thoughtful consideration (Lindsay-Mosher and Su, 2016). Biocompatible DNA hydrogels, harboring the crosslinked structure and programmable property, can be harnessed for the targeted transport of CRISPR biomaterials. Although gene therapy is not common for IUA, future research may be directed to using a CRISPR-DNA hydrogel system for the improvement of endometrium recovery. In recent years, bioprinting has gained significant attention not only for the fabrication of biomimetic tissue constructs but also in pharmaceuticals, improving drug screening, disease research, and controlled drug-delivery systems. Hydrogels, being the most common bioink for bioprinting, provide a supportive hydrated environment for cells and preserve the shape of printed materials (Wang et al., 2017). Through various crosslinking, hydrogels are capable of achieving different tissue engineering applications as bioinks and

support baths (Zhou et al., 2022). Hydrogel bioinks that can respond to external stimuli, such as gelatin methacrylate (GelMA) polymer, photo-cross linked HA-hydrogels or polyethylene glycol and alginate hydrogel, proved to be outstanding materials for 3D bioprinting of human organoid including vascularized soft tissues, cardiac muscle, cartilage-like tissue constructs and components of the human heart (de Melo et al., 2019; Lee et al., 2019; Lee et al., 2020b; Kupfer et al., 2020). On the other hand, cell-laden hydrogels are the most frequently used and attractive choice to mimic the native niche (Mirdamadi et al., 2019; Spencer et al., 2019; Mancha Sanchez et al., 2020). Possible applications of cross-linked hydrogels as bioink of bath for bioprinting in IUA are foreseen for the repair of damaged endometrium, regenerative drugs or cell delivery. However, bioinspired hydrogels cannot become the first-line therapy in endometrial regeneration mainly because, the use of hydrogels as a single without a traditional IUD anti-adhesion barrier is less satisfactory. Increasing the mechanical strength can make hydrogel capable to meet the requirement of a culture system for the formation of normal functional endometrium for embryo implantation. In addition, for the clinically relevant applications, focus is needed toward possible chemical crosslinking and mechanical intigrety to withstand the conventional sterilization methods as terminal sterilization is difficult and time-consuming because of the hydrated nature of hydrogels (Lima et al., 2020). All these questions are still worth the continued efforts in the future.

Author contributions

RD, SM, and XZ prepared the manuscript, BW, MR, and LY prepared the Figures and Tables, TX and YL revised the manuscript, All authors approve the version of the manuscript to be published.

Funding

This work was financially supported by the Joint Fund Project of Xinxiang Medical University (No. LHGJ20200505).

Acknowledgments

We would like to thank Lily Zhang for her kindly support.

Conflict of interest

LY was employed by Hemay Zhihui Science and Technology Co. Ltd.

The remaining authors declare that the research was conducted in the absence of any commercial or financial relationships that could be construed as a potential conflict of interest.

Publisher's note

References

Abomaray, F. M., Al Jumah, M. A., Alsaad, K. O., Jawdat, D., Al Khaldi, A., Alaskar, A. S., et al. (2016). Phenotypic and functional characterization of mesenchymal stem/multipotent stromal cells from decidua basalis of human term placenta. *Stem Cells Int.* 2016, 5184601–5184618. doi:10.1155/2016/5184601

An, H. W., Mamuti, M., Wang, X., Yao, H., Wang, M. D., Zhao, L., et al. (2021). "Rationally designed modular drug delivery platform based on intracellular peptide self-assembly," in *Exploration* (Wiley Online Library). 20210153.

Andrzejewska, A., Lukomska, B., and Janowski, M. (2019). Concise review: Mesenchymal stem cells: From roots to boost. *Stem Cells* 37, 855–864. doi:10.1002/stem.3016

Asai, D., Xu, D., Liu, W., Garcia Quiroz, F., Callahan, D. J., Zalutsky, M. R., et al. (2012). Protein polymer hydrogels by *in situ*, rapid and reversible self-gelation. *Biomaterials* 33, 5451–5458. doi:10.1016/j.biomaterials.2012.03.083

Askenase, P. W. (2020). COVID-19 therapy with mesenchymal stromal cells (MSC) and convalescent plasma must consider exosome involvement: Do the exosomes in convalescent plasma antagonize the weak immune antibodies? *J. Extracell. Vesicles* 10, e12004. doi:10.1002/jev2.12004

Azumaguchi, A., Henmi, H., and Saito, T. (2019). Efficacy of silicone sheet as a personalized barrier for preventing adhesion reformation after hysteroscopic adhesiolysis of intrauterine adhesions. *Reprod. Med. Biol.* 18, 378–383. doi:10.1002/rmb2.12294

Baghersad, S., Hajir Bahrami, S., Mohammadi, M. R., Mojtahedi, M. R. M., and Milan, P. B. (2018). Development of biodegradable electrospun gelatin/aloe-vera/poly(ε-caprolactone) hybrid nanofibrous scaffold for application as skin substitutes. *Mater. Sci. Eng. C* 93, 367–379. doi:10.1016/j.msec.2018.08.020

Bhandari, S., Bhave, P., Ganguly, I., Baxi, A., and Agarwal, P. (2015). Reproductive outcome of patients with asherman's syndrome: A saims experience. *J. Reprod. Infertil.* 16, 229–235.

Can, S., Kirpinar, G., Dural, O., Karamustafaoglu, B. B., Tas, I. S., Yasa, C., et al. (2018). Efficacy of a new crosslinked hyaluronan gel in the prevention of intrauterine adhesions. *JSLS* 22, e201800036. doi:10.4293/jsls.2018.00036

Castro Marin, A., Culcasi, M., Cassien, M., Stocker, P., Thetiot-Laurent, S., Robillard, B., et al. (2019). Chitosan as an antioxidant alternative to sulphites in oenology: EPR investigation of inhibitory mechanisms. *Food Chem. x.* 285, 67–76. doi:10.1016/j.foodchem.2019.01.155

Chen, Z., Lv, Z., Zhang, Z., Weitz, D. A., Zhang, H., Zhang, Y., et al. (2021). "Advanced microfluidic devices for fabricating multi-structural hydrogel microsphere," in *Exploration* (Wiley Online Library). 20210036.

Chi, Y., He, P., Lei, L., Lan, Y., Hu, J., Meng, Y., et al. (2018). Transdermal estrogen gel and oral aspirin combination therapy improves fertility prognosis via the promotion of endometrial receptivity in moderate to severe intrauterine adhesion. *Mol. Med. Rep.* 17, 6337–6344. doi:10.3892/mmr.2018.8685

Ci, L., Huang, Z., Liu, Y., Liu, Z., Wei, G., and Lu, W. (2017). Amino-functionalized poloxamer 407 with both mucoadhesive and thermosensitive properties: Preparation, characterization and application in a vaginal drug delivery system. *Acta Pharm. Sin. B* 7, 593–602. doi:10.1016/j.apsb.2017.03.002

D'asti, E., Garnier, D., Lee, T. H., Montermini, L., Meehan, B., and Rak, J. (2012). Oncogenic extracellular vesicles in brain tumor progression. *Front. Physiol.* 3, 294. doi:10.3389/fphys.2012.00294

De Melo, B. a. G., Jodat, Y. A., Mehrotra, S., Calabrese, M. A., Kamperman, T., Mandal, B. B., et al. (2019). 3D printed tissues: 3D printed cartilage-like tissue constructs with spatially controlled mechanical properties (adv. Funct. Mater. 51/2019). *Adv. Funct. Mat.* 29, 1970350. doi:10.1002/adfm.201970350

Deans, R., and Abbott, J. (2010). Review of intrauterine adhesions. *J. Minim. Invasive Gynecol.* 17, 555–569. doi:10.1016/j.jmig.2010.04.016

Ding, L., Li, X., Sun, H., Su, J., Lin, N., Peault, B., et al. (2014). Transplantation of bone marrow mesenchymal stem cells on collagen scaffolds for the functional regeneration of injured rat uterus. *Biomaterials* 35, 4888–4900. doi:10.1016/j.biomaterials.2014.02.046

Es, I., Gavahian, M., Marti-Quijal, F. J., Lorenzo, J. M., Mousavi Khaneghah, A., Tsatsanis, C., et al. (2019). The application of the CRISPR-Cas9 genome editing machinery in food and agricultural science: Current status, future perspectives, and associated challenges. *Biotechnol. Adv.* 37, 410–421. doi:10.1016/j.biotechadv.2019.02.006

Evans-Hoeker, E. A., and Young, S. L. (2014). Endometrial receptivity and intrauterine adhesive disease. *Semin. Reprod. Med.* 32, 392–401. doi:10.1055/s-0034-1376358

Fei, Z., Bin, Z., Xin, X., Fei, H., and Yuechong, C. (2019). Meta-analysis on the use of hyaluronic acid gel to prevent recurrence of intrauterine adhesion after hysteroscopic adhesiolysis. *Taiwan. J. Obstet. Gynecol.* 58, 731–736. doi:10.1016/j.tjog.2019.09.002

Feng, Y., Zhan, F., Zhong, Y., and Tan, B. (2020). Effects of human umbilical cord mesenchymal stem cells derived from exosomes on migration ability of endometrial glandular epithelial cells. *Mol. Med. Rep.* 22, 715–722. doi:10.3892/mmr.2020.11137

Gan, L., Duan, H., Xu, Q., Tang, Y. Q., Li, J. J., Sun, F. Q., et al. (2017). Human amniotic mesenchymal stromal cell transplantation improves endometrial regeneration in rodent models of intrauterine adhesions. *Cytotherapy* 19, 603–616. doi:10.1016/j.jcyt.2017.02.003

Gu, R., Sun, W., Zhou, H., Wu, Z., Meng, Z., Zhu, X., et al. (2010). The performance of a fly-larva shell-derived chitosan sponge as an absorbable surgical hemostatic agent. *Biomaterials* 31, 1270–1277. doi:10.1016/j.biomaterials.2009.10.023

Gu, Z., Guo, J., Zhai, J., Feng, G., Wang, X., Gao, Z., et al. (2022). A uterus-inspired niche drives blastocyst development to the early organogenesis. *Adv. Sci.*, e2202282. doi:10.1002/advs.202202282

Han, Y., Liu, S., Mao, H., Tian, L., and Ning, W. (2016). Synthesis of novel temperature- and pH-sensitive ABA triblock copolymers P(DEAEMA-co-MEO(2)MA-co-OEGMA)-b-PEG-b-P(DEAEMA-co-MEO(2)MA-co-OEGMA): Micellization, Sol(-)Gel transitions, and sustained BSA release. *Polym. (Basel)* 8, 367. doi:10.3390/polym8110367

Hooker, A., Fraenk, D., Brolmann, H., and Huirne, J. (2016). Prevalence of intrauterine adhesions after termination of pregnancy: A systematic review. *Eur. J. Contracept. Reprod. Health Care* 21, 329–335. doi:10.1080/13625187.2016.1199795

Huang, J., Xiong, J., Yang, L., Zhang, J., Sun, S., and Liang, Y. (2021). Cell-free exosome-laden scaffolds for tissue repair. *Nanoscale* 13, 8740–8750. doi:10.1039/d1nr01314a

Knott, G. J., and Doudna, J. A. (2018). CRISPR-Cas guides the future of genetic engineering. *Science* 361, 866–869. doi:10.1126/science.aat5011

Kupfer, M. E., Lin, W. H., Ravikumar, V., Qiu, K., Wang, L., Gao, L., et al. (2020). *In situ* expansion, differentiation, and electromechanical coupling of human cardiac muscle in a 3D bioprinted, chambered organoid. *Circ. Res.* 127, 207–224. doi:10.1161/circresaha.119.316155

Lee, A., Hudson, A. R., Shiwarski, D. J., Tashman, J. W., Hinton, T. J., Yerneni, S., et al. (2019). 3D bioprinting of collagen to rebuild components of the human heart. *Science* 365, 482–487. doi:10.1126/science.aav9051

Lee, D. Y., Lee, S. R., Kim, S. K., Joo, J. K., Lee, W. S., Shin, J. H., et al. (2020a). A new thermo-responsive hyaluronic acid sol-gel to prevent intrauterine adhesions after hysteroscopic surgery: A randomized, non-inferiority trial. *Yonsei Med. J.* 61, 868–874. doi:10.3349/ymj.2020.61.10.868

Lee, S., Sani, E. S., Spencer, A. R., Guan, Y., Weiss, A. S., and Annabi, N. (2020b). Human-recombinant-elastin-based bioinks for 3D bioprinting of vascularized soft tissues. *Adv. Mat.* 32, e2003915. doi:10.1002/adma.202003915

Lessey, B. A. (2000). The role of the endometrium during embryo implantation. *Hum. Reprod.* 15 (6), 39–50.

Li, X., Wu, L., Zhou, Y., Fan, X., Huang, J., Wu, J., et al. (2019). New crosslinked hyaluronan gel for the prevention of intrauterine adhesions after dilation and curettage in patients with delayed miscarriage: A prospective, multicenter, randomized, controlled trial. *J. Minim. Invasive Gynecol.* 26, 94–99. doi:10.1016/j.jmig.2018.03.032

Liao, Z., Liu, C., Wang, L., Sui, C., and Zhang, H. (2021). Therapeutic role of mesenchymal stem cell-derived extracellular vesicles in female reproductive diseases. *Front. Endocrinol.* 12, 665645. doi:10.3389/fendo.2021.665645

Lim, H. L., Hwang, Y., Kar, M., and Varghese, S. (2014). Smart hydrogels as functional biomimetic systems. *Biomater. Sci.* 2, 603–618. doi:10.1039/c3bm60288e

Lima, C. S. A., Balogh, T. S., Varca, J., Varca, G. H. C., Lugao, A. B., Bucio, E., et al. (2020). An updated review of macro, micro, and nanostructured hydrogels for biomedical and pharmaceutical applications. *Pharmaceutics* 12, 970. doi:10.3390/pharmaceutics12100970

Lin, J., Wang, Z., Huang, J., Tang, S., Saiding, Q., Zhu, Q., et al. (2021). Fertility restoration: Microenvironment-protected exosome-hydrogel for facilitating endometrial regeneration, fertility restoration, and live birth of offspring (small 11/2021). *Small* 17, 2170049. doi:10.1002/smll.202170049

Lin, Y., Dong, S., Zhao, W., Hu, K. L., Liu, J., Wang, S., et al. (2020). Application of hydrogel-based delivery system in endometrial repair. *ACS Appl. Bio Mat.* 3, 7278–7290. doi:10.1021/acsabm.0c00971

Lindsay-Mosher, N., and Su, C. (2016). Cancer gene therapy: Innovations in therapeutic delivery of CRISPR-cas9. *Drug Discov. Today Dis. Models* 21, 17–21. doi:10.1016/j.ddmod.2017.02.009

Liu, A. Z., Zhao, H. G., Gao, Y., Liu, M., and Guo, B. Z. (2016). Effectiveness of estrogen treatment before transcervical resection of adhesions on moderate and severe uterine adhesion patients. *Gynecol. Endocrinol.* 32, 737–740. doi:10.3109/09513590.2016.1160375

Liu, F., Hu, S., Yang, H., Li, Z., Huang, K., Su, T., et al. (2019). Hyaluronic acid hydrogel integrated with mesenchymal stem cell-secretome to treat endometrial injury in a rat model of asherman's syndrome. *Adv. Healthc. Mat.* 8, e1900411. doi:10.1002/adhm.201900411

Liu, X., Yang, Y., Niu, X., Lin, Q., Zhao, B., Wang, Y., et al. (2017a). An *in situ* photocrosslinkable platelet rich plasma - complexed hydrogel glue with growth factor controlled release ability to promote cartilage defect repair. *Acta Biomater.* 62, 179–187. doi:10.1016/j.actbio.2017.05.023

Liu, Y., Yang, F., Feng, L., Yang, L., Chen, L., Wei, G., et al. (2017b). *In vivo* retention of poloxamer-based *in situ* hydrogels for vaginal application in mouse and rat models. *Acta Pharm. Sin. B* 7, 502–509. doi:10.1016/j.apsb.2017.03.003

Lou, S., Gao, S., Wang, W., Zhang, M., Zhang, J., Wang, C., et al. (2015). Galactose-functionalized multi-responsive nanogels for hepatoma-targeted drug delivery. *Nanoscale* 7, 3137–3146. doi:10.1039/c4nr06714b

Lv, C. X., Duan, H., Wang, S., Gan, L., and Xu, Q. (2020). Exosomes derived from human umbilical cord mesenchymal stem cells promote proliferation of allogeneic endometrial stromal cells. *Reprod. Sci.* 27, 1372–1381. doi:10.1007/s43032-020-00165-y

Lv, H., Wu, B., Song, J., Wu, W., Cai, W., and Xu, J. (2021). Hydrogel, a novel therapeutic and delivery strategy, in the treatment of intrauterine adhesions. *J. Mat. Chem. B* 9, 6536–6552. doi:10.1039/d1tb01005k

Ma, J., Zhan, H., Li, W., Zhang, L., Yun, F., Wu, R., et al. (2021). Recent trends in therapeutic strategies for repairing endometrial tissue in intrauterine adhesion. *Biomater. Res.* 25, 40. doi:10.1186/s40824-021-00242-6

Ma, Y., Lin, M., Huang, G., Li, Y., Wang, S., Bai, G., et al. (2018). 3D spatiotemporal mechanical microenvironment: A hydrogel-based platform for guiding stem cell fate. *Adv. Mat.* 30, e1705911. doi:10.1002/adma.201705911

Mancha Sanchez, E., Gomez-Blanco, J. C., Lopez Nieto, E., Casado, J. G., Macias-Garcia, A., Diaz Diez, M. A., et al. (2020). Hydrogels for bioprinting: A systematic review of hydrogels synthesis, bioprinting parameters, and bioprinted structures behavior. *Front. Bioeng. Biotechnol.* 8, 776. doi:10.3389/fbioe.2020.00776

Mao, X., Zhang, J., Cai, R., Tao, Y., Gao, H., Kuang, Y., et al. (2020). Therapeutic role of granulocyte macrophage colony-stimulating factor (GM-CSF) in patients with persistent thin endometrium: A prospective and randomized study. *Int. J. Gynecol. Obstet.* 150, 194–199. doi:10.1002/ijgo.13152

Marycz, K., Smieszek, A., Trynda, J., Sobierajska, P., Targonska, S., Grosman, L., et al. (2019). Nanocrystalline hydroxyapatite loaded with resveratrol in colloidal suspension improves viability, metabolic activity and mitochondrial potential in human adipose-derived mesenchymal stromal stem cells (hASCs). *Polym. (Basel)* 11, 92. doi:10.3390/polym11010092

Mathivanan, S., Ji, H., and Simpson, R. J. (2010). Exosomes: Extracellular organelles important in intercellular communication. *J. Proteomics* 73, 1907–1920. doi:10.1016/j.jprot.2010.06.006

Medatwal, N., Ansari, M. N., Kumar, S., Pal, S., Jha, S. K., Verma, P., et al. (2020). Hydrogel-mediated delivery of celastrol and doxorubicin induces a synergistic effect on tumor regression via upregulation of ceramides. *Nanoscale* 12, 18463–18475. doi:10.1039/d0nr01066a

Mirdamadi, E., Muselimyan, N., Koti, P., Asfour, H., and Sarvazyan, N. (2019). Agarose slurry as a support medium for bioprinting and culturing freestanding cell-laden hydrogel constructs. *3D Print. Addit. Manuf.* 6, 158–164. doi:10.1089/3dp.2018.0175

Nelson, T. J., Behfar, A., Yamada, S., Martinez-Fernandez, A., and Terzic, A. (2009). Stem cell platforms for regenerative medicine. *Clin. Transl. Sci.* 2, 222–227. doi:10.1111/j.1752-8062.2009.00096.x

Pabuccu, E. G., Kovanci, E., Sahin, O., Arslanoglu, E., Yildiz, Y., and Pabuccu, R. (2019). New crosslinked hyaluronan gel, intrauterine device, or both for the prevention of intrauterine adhesions. *JSLS* 23, e201800108. doi:10.4293/jsls.2018.00108

Shi, Q., Wang, D., Ding, X., Yang, X., and Zhang, Y. (2021). Exosome-shuttled miR-7162-3p from human umbilical cord derived mesenchymal stem cells repair endometrial stromal cell injury by restricting APOL6. *Arch. Biochem. Biophys.* 707, 108887. doi:10.1016/j.abb.2021.108887

Spencer, A. R., Shirzaei Sani, E., Soucy, J. R., Corbet, C. C., Primbetova, A., Koppes, R. A., et al. (2019). Bioprinting of a cell-laden conductive hydrogel composite. *ACS Appl. Mat. Interfaces* 11, 30518–30533. doi:10.1021/acsami.9b07353

Tafti, S. Z. G., Javaheri, A., Firoozabadi, R. D., Ashkezar, S. K., and Abarghouei, H. F. (2021). Role of hyaluronic acid intrauterine injection in the prevention of Asherman's syndrome in women undergoing uterine septum resection: An RCT. *Int. J. Reprod. Biomed.* 19, 339–346. doi:10.18502/ijrm.v19i4.9060

Tan, J., Li, P., Wang, Q., Li, Y., Li, X., Zhao, D., et al. (2016). Autologous menstrual blood-derived stromal cells transplantation for severe Asherman's syndrome. *Hum. Reprod.* 31, 2723–2729. doi:10.1093/humrep/dew235

Tan, Q., Xia, D., and Ying, X. (2020). miR-29a in exosomes from bone marrow mesenchymal stem cells inhibit fibrosis during endometrial repair of intrauterine adhesion. *Int. J. Stem Cells* 13, 414–423. doi:10.15283/ijsc20049

Tang, J. N., Cores, J., Huang, K., Cui, X. L., Luo, L., Zhang, J. Y., et al. (2018). Concise review: Is cardiac cell therapy dead? Embarrassing trial outcomes and new directions for the future. *Stem Cells Transl. Med.* 7, 354–359. doi:10.1002/sctm.17-0196

Townsend, J. M., Beck, E. C., Gehrke, S. H., Berkland, C. J., and Detamore, M. S. (2019). Flow behavior prior to crosslinking: The need for precursor rheology for placement of hydrogels in medical applications and for 3D bioprinting. *Prog. Polym. Sci.* 91, 126–140. doi:10.1016/j.progpolymsci.2019.01.003

Wang, J., Yang, C., Xie, Y., Chen, X., Jiang, T., Tian, J., et al. (2021). Application of bioactive hydrogels for functional treatment of intrauterine adhesion. *Front. Bioeng. Biotechnol.* 9, 760943. doi:10.3389/fbioe.2021.760943

Wang, X., Ao, Q., Tian, X., Fan, J., Tong, H., Hou, W., et al. (2017). *Gelatin-Based Hydrogels for Organ 3D Bioprinting*, 9.*Polym. (Basel)*

Wei, L., Tan, W., Wang, G., Li, Q., Dong, F., and Guo, Z. (2019). The antioxidant and antifungal activity of chitosan derivatives bearing Schiff bases and quaternary ammonium salts. *Carbohydr. Polym.* 226, 115256. doi:10.1016/j.carbpol.2019.115256

Wen, J., Weinhart, M., Lai, B., Kizhakkedathu, J., and Brooks, D. E. (2016). Reversible hemostatic properties of sulfabetaine/quaternary ammonium modified hyperbranched polyglycerol. *Biomaterials* 86, 42–55. doi:10.1016/j.biomaterials.2016.01.067

Wenbo, Q., Lijian, X., Shuangdan, Z., Jiahua, Z., Yanpeng, T., Xuejun, Q., et al. (2020). Controlled releasing of SDF-1α in chitosan-heparin hydrogel for endometrium injury healing in rat model. *Int. J. Biol. Macromol.* 143, 163–172. doi:10.1016/j.ijbiomac.2019.11.184

Xiao, S., Wan, Y., Zou, F., Ye, M., Deng, H., Ma, J., et al. (2015). Prevention of intrauterine adhesion with auto-crosslinked hyaluronic acid gel: A prospective, randomized, controlled clinical study. *Zhonghua Fu Chan Ke Za Zhi* 50, 32–36.

Xie, Y., Guan, Q., Guo, J., Chen, Y., Yin, Y., and Han, X. (2022). Hydrogels for exosome delivery in biomedical applications. *Gels* 8, 328. doi:10.3390/gels8060328

Xie, Y., Zhang, T., Tian, Z., Zhang, J., Wang, W., Zhang, H., et al. (2017). Efficacy of intrauterine perfusion of granulocyte colony-stimulating factor (G-CSF) for infertile women with thin endometrium: A systematic review and meta-analysis. *Am. J. Reprod. Immunol.* 78, e12701. doi:10.1111/aji.12701

Yao, Q., Zheng, Y. W., Lan, Q. H., Wang, L. F., Huang, Z. W., Chen, R., et al. (2020). Aloe/poloxamer hydrogel as an injectable beta-estradiol delivery scaffold with multi-therapeutic effects to promote endometrial regeneration for intrauterine adhesion treatment. *Eur. J. Pharm. Sci.* 148, 105316. doi:10.1016/j.ejps.2020.105316

Yao, Y., Chen, R., Wang, G., Zhang, Y., and Liu, F. (2019). Exosomes derived from mesenchymal stem cells reverse EMT via TGF-β1/Smad pathway and promote repair of damaged endometrium. *Stem Cell Res. Ther.* 10, 225. doi:10.1186/s13287-019-1332-8

Yi, X., Liu, F., Gao, K., Chen, F., Wang, Y., Li, H., et al. (2022). Reconstructable uterus-derived materials for uterus recovery toward efficient live births. *Adv. Mat.* 34, e2106510. doi:10.1002/adma.202106510

Yin, M., Zhou, H. J., Lin, C., Long, L., Yang, X., Zhang, H., et al. (2019). CD34(+) KLF4(+) stromal stem cells contribute to endometrial regeneration and repair. *Cell Rep.* 27, 2709–2724.e3. e2703. doi:10.1016/j.celrep.2019.04.088

Yu, D., Wong, Y. M., Cheong, Y., Xia, E., and Li, T. C. (2008). Asherman syndrome--one century later. *Fertil. Steril.* 89, 759–779. doi:10.1016/j.fertnstert.2008.02.096

Zhang, L., Yu, Z., Qu, Q., Li, X., Lu, X., and Zhang, H. (2022). Exosomal lncRNA HOTAIR promotes the progression and angiogenesis of endometriosis via the miR-761/HDAC1 Axis and activation of STAT3-mediated inflammation. *Int. J. Nanomedicine* 17, 1155–1170. doi:10.2147/ijn.s354314

Zhang, P., Zhao, C., Zhao, T., Liu, M., and Jiang, L. (2019). Recent advances in bioinspired gel surfaces with superwettability and special adhesion. *Adv. Sci. (Weinh).* 6, 1900996. doi:10.1002/advs.201900996

Zhang, S. S., Xia, W. T., Xu, J., Xu, H. L., Lu, C. T., Zhao, Y. Z., et al. (2017). Three-dimensional structure micelles of heparin-poloxamer improve the therapeutic effect of 17β-estradiol on endometrial regeneration for intrauterine adhesions in a rat model. *Int. J. Nanomedicine* 12, 5643–5657. doi:10.2147/ijn.s137237

Zhao, Y., Zhang, Z., Pan, Z., and Liu, Y. (2021). Advanced bioactive nanomaterials for biomedical applications. *Exploration* 1, 20210089. doi:10.1002/exp.20210089

Zhou, J., Zhang, Z., Joseph, J., Zhang, X., Ferdows, B. E., Patel, D. N., et al. (2021a). Biomaterials and nanomedicine for bone regeneration: Progress and future prospects. *Exploration* 1, 20210011. doi:10.1002/exp.20210011

Zhou, K., Sun, Y., Yang, J., Mao, H., and Gu, Z. (2022). Hydrogels for 3D embedded bioprinting: A focused review on bioinks and support baths. *J. Mat. Chem. B* 10, 1897–1907. doi:10.1039/d1tb02554f

Zhou, Q., Shi, X., Saravelos, S., Huang, X., Zhao, Y., Huang, R., et al. (2021b). Auto-cross-linked hyaluronic acid gel for prevention of intrauterine adhesions after hysteroscopic adhesiolysis: A randomized controlled trial. *J. Minim. Invasive Gynecol.* 28, 307–313. doi:10.1016/j.jmig.2020.06.030

frontiers | Frontiers in Bioengineering and Biotechnology

TYPE Original Research
PUBLISHED 13 September 2022
DOI 10.3389/fbioe.2022.1002853

OPEN ACCESS

EDITED BY
Jingxin Meng,
Technical Institute of Physics and Chemistry (CAS), China

REVIEWED BY
Youfeng Zhu,
Guangzhou Red Cross Hospital, China
Xue Li,
Jinan University, China

*CORRESPONDENCE
Chunbo Chen,
gghccm@163.com,
orcid.org/0000-0001-5662-497X

‡These authors have contributed equally to this work

SPECIALTY SECTION
This article was submitted to Bionics and Biomimetics, a section of the journal Frontiers in Bioengineering and Biotechnology

RECEIVED 25 July 2022
ACCEPTED 29 August 2022
PUBLISHED 13 September 2022

CITATION
Bai Y, Li Y, Tang Z, Hu L, Jiang X, Chen J, Huang S, Wu K, Xu W and Chen C (2022), Urinary proteome analysis of acute kidney injury in post-cardiac surgery patients using enrichment materials with high-resolution mass spectrometry. *Front. Bioeng. Biotechnol.* 10:1002853. doi: 10.3389/fbioe.2022.1002853

Urinary proteome analysis of acute kidney injury in post-cardiac surgery patients using enrichment materials with high-resolution mass spectrometry

Yunpeng Bai [1,2‡], Ying Li [3‡], Zhizhong Tang [4‡], Linhui Hu [2‡], Xinyi Jiang [3,5], Jingchun Chen [3,5], Sumei Huang [1,6,7], Kunyong Wu [1,7], Wang Xu [3,8,9] and Chunbo Chen [6,8,10,9*]

[1]Center of Scientific Research, Maoming People's Hospital, Maoming, China, [2]Department of Critical Care Medicine, Maoming People's Hospital, Maoming, China, [3]Department of Intensive Care Unit of Cardiovascular Surgery, Guangdong Cardiovascular Institute, Guangdong Provincial People's Hospital, Guangdong Academy of Medical Sciences, Guangzhou, China, [4]Department of Urology, Maoming People's Hospital, Maoming, China, [5]School of Medicine, South China University of Technology, Guangzhou, China, [6]Department of Emergency, Maoming People's Hospital, Maoming, China, [7]Biological Resource Center of Maoming People's Hospital, Maoming, China, [8]Department of Critical Care Medicine, Guangdong Provincial People's Hospital, Guangdong Academy of Medical Sciences, Guangzhou, China, [9]The Second School of Clinical Medicine, Southern Medical University, Guangzhou, China, [10]Guangdong Provincial Key Laboratory of Renal Failure Research, Southern Medical University, Guangzhou, China

Background: Cardiac surgery-associated acute kidney injury (CSA-AKI) may increase the mortality and incidence rates of chronic kidney disease in critically ill patients. This study aimed to investigate the underlying correlations between urinary proteomic changes and CSA-AKI.

Methods: Nontargeted proteomics was performed using nano liquid chromatography coupled with Orbitrap Exploris mass spectrometry (MS) on urinary samples preoperatively and postoperatively collected from patients with CSA-AKI. Gemini C18 silica microspheres were used to separate and enrich trypsin-hydrolysed peptides under basic mobile phase conditions. Differential analysis was conducted to screen out urinary differential expressed proteins (DEPs) among patients with CSA-AKI for bioinformatics. Kyoto Encyclopedia of Genes and Genomes (KEGG) database analysis was adopted to identify the altered signal pathways associated with CSA-AKI.

Results: Approximately 2000 urinary proteins were identified and quantified through data-independent acquisition MS, and 324 DEPs associated with AKI were screened by univariate statistics. According to KEGG enrichment analysis, the signal pathway of protein processing in the endoplasmic reticulum was enriched as the most up-regulated DEPs, and cell adhesion molecules were enriched as the most down-regulated DEPs. In protein–protein interaction analysis, the three hub targets in the up-regulated DEPs were α-1-antitrypsin, β-2-microglobulin and angiotensinogen, and the three key down-regulated DEPs

were growth arrest-specific protein 6, matrix metalloproteinase-9 and urokinase-type plasminogen activator.

Conclusion: Urinary protein disorder was observed in CSA-AKI due to ischaemia and reperfusion. The application of Gemini C18 silica microspheres can improve the protein identification rate to obtain highly valuable resources for the urinary DEPs of AKI. This work provides valuable knowledge about urinary proteome biomarkers and essential resources for further research on AKI.

KEYWORDS

urinary proteome, acute kidney injury, high-resolution mass spectrometry, differential analysis, gemini C18

Introduction

As a serious life-threatening syndrome, acute kidney injury (AKI) can lead to the imbalance of renal excretory metabolites and the impaired regulation of electrolytes and acid–base balance (Lameire et al., 2013). Given that AKI may be caused by many reasons (such as major surgery, ischaemia, sepsis and drugs), it has a relatively high incidence among patients in intensive care units and has become a common complication in critically ill patients (Santos et al., 2019). Although great progress has been achieved in the supportive therapy of AKI, this condition is still diagnosed following the previous standards: an increase in serum creatinine (sCr) and a decrease in urine volume (Kellum and Lameire., 2013). However, both are not the best early diagnostic indicators of AKI because they may frequently change after renal dysfunction (Bennett and Devarajan., 2011). Therefore, early AKI diagnosis has become one of the research hotspots in recent years.

As a sensitive indicator of renal glomerular and tubular injury, the quantitative proteinuria spectrum has always been important in predicting kidney injury. Some AKI protein biomarkers with potential clinical value have been recently investigated, including the serum/urine levels of cystatin C to reflect the glomerular filtration rate (Liang et al., 2020; Deng et al., 2019; Hou et al., 2021; Deng et al., 2020; Zhang et al., 2019) and the relationship between renal tubular epithelial cell damage and inflammatory factors, such as kidney injury molecule-1, liver type fatty acid binding protein and neutrophil gelatinase-associated lipocalin (Hu et al., 2022; Liang et al., 2022; Zdziechowska et al., 2020). Previous studies on proteomics and early pathobiological events demonstrated that urinary angiotensinogen (AGT) and urinary matrix metalloproteinase-7 (MMP-7) could be used as AKI biomarkers for clinical applications (Chen C et al., 2016; Yang et al., 2017).

Urine contains the whole excreted products from the kidneys, so the proteomic changes in renal disease can be reflected by the urinary proteomic profiles of patients (Kim et al., 2011). As a non-invasive source, urine samples can be readily obtained in large quantities with expected participant compliance and a low risk of infection to researchers (Bai et al., 2022). Thus, urinary profile analysis is an attractive option for the discovery of proteomic biomarkers, especially for the diagnosis of renal diseases and the molecular mechanisms of renal pathology (Nkuipou-Kenfack et al., 2020). For example, steroid-resistant and steroid-sensitive nephrotic syndromes can be distinguished by urinary proteome for paediatric patients (Khurana et al., 2006). Additionally, the aetiology and pathogenesis of AKI are extremely complex due to the highly heterogeneous clinical syndrome for severe patients, so a single biomarker cannot comprehensively and accurately reflect the overall pathophysiological changes of renal injury (Liang et al., 2012). Therefore, highly sensitive and specific urinary proteomic spectra can help improve the diagnosis, classification and treatment of AKI.

Given that AKI may be involved in many different types of molecules with a large dynamic concentration range, the pre-treatment of urine samples is an important step in the study of low-abundance protein biomarkers, especially when using functional materials with separation and enrichment functions. Porous polymer materials can separate target molecules from complex matrices and can be applied in various fields, from liquid purification to biomolecular fractionation (Liu et al., 1999). Heterogenous pore polymer particles, synthesised by double emulsion interfacial polymerisation, can effectively enrich the low-abundance glycopeptides (Song et al., 2018) and rapidly separate the proteins with similar sizes (Song et al., 2019). In this study, we performed the comparative proteomic analysis of urine samples from six patients with cardiac surgery-associated (CSA)-AKI using Gemini C18 column and high-resolution mass spectrometry (HRMS). The results of this urinary proteome study may help clarify the mechanisms of CSA-AKI and the application of enrichment materials in bioseparation. This work also provides valuable knowledge about urinary proteome biomarkers.

Materials and methods

Chemicals and reagents

MS-grade acetonitrile (ACN) was purchased from Thermo Fisher Scientific, United States, and ultrapure water was filtered through the Milli-Q system (Millipore, Billerica, MA). Formic acid

(FA) was obtained from DIMKA, and ammonium bicarbonate was purchased from Fluka (Honeywell Fluka, United States). Sodium dodecyl sulfate (SDS), SDS-free protein lysate, dithiothreitol (DTT), iodoacetamide (IAM), Coomassie brilliant blue G-250, trypsin and acetone were obtained from Aladdin, China.

Patients and urinary proteins extraction

This investigation was carried out according to the World Medical Association Declaration of Helsinki and approved by the ethics committee of Maoming People's Hospital. All patients had completed written informed consents before cardiac surgery, and six patients were enrolled in the urinary proteomics study after the diagnosis of AKI which was defined in accordance with the KDIGO Clinical Practice Guidelines based on sCr criteria: the increase in sCr ≥ 50% within 7 days, or the increase in sCr ≥ 0.3 mg/dl (≥ 26.5 μmol/L) within 48 h, or oliguria (Khwaja, 2012). Patients were excluded if they were age under 18 years, had preexisting chronic renal disease or undergoing renal replacement therapy, a history of renal transplantation or nephrectomy. In order to explore the effect of CSA-AKI on kidney, spot urine samples were prospectively collected at two time points, preoperative (Before_AKI) and postoperative-the first day of diagnosed CSA-AKI (AKI-Day1), which was used to compare the changes in urinary proteomic profiles. Serum creatinine was measured before cardiac surgery, at least twice a day for the first 3 days after cardiac surgery, and then daily thereafter.

Approximate 5 ml of urine sample from Biological Resource Center of Maoming People's Hospital, was transferred into a 50 ml centrifuge tube, and 25 ml (5 times the volume of urine sample) of precooled acetone was added into the tube. After placing at -20°C overnight, the urine samples were centrifuged at 25,000 *g* and 4°C for 15 min, and the supernatant of each sample were discarded. Then, an appropriate amount of SDS-free protein lysate was added into the drying urine sample, and an automatic grinder was used to promote protein dissolution. The supernatants were collected after centrifuging at 25,000 *g* at 4°C for another 15 min. Final concentration (10 mM) of DTT was added into the supernatant and bathed in water at 37°C. After 30 min water bath, final concentration (55 mM) of IAM was added into the reduced samples and kept for another 45 min in the dark at room temperature. Protein solution could be obtained from the supernatant of alkylated samples by centrifuging at 25,000 *g* at 4°C for 15 min. At last, the Bradford assay kit (Bio-Rad, Hercules, CA, United States) was used to determine the concentration of the protein solution.

Protein enzymatic digestion and high pH column separation

As for protein enzymatic digestion, 100 μg of protein solution per sample was transferred and diluted with 4 times volumes of 50 mM NH_4HCO_3 solution. According to the ratio of 40: 1 (protein to enzyme), 2.5 μg of trypsin was added into the diluted protein solution for enzymatic digestion at 37°C. After 4 h, enzymatic peptides were desalted using a Strata X column and vacuumed to dryness.

In Shimadzu LC-20AB high performance liquid chromatography (HPLC) system, the Gemini C18 00G-4435-E0 column (5 μm, 4.6 mm internal diameter×250 mm length) was used for peptide separation with mobile phase A (5% ACN, pH 9.8) and mobile phase B (95% ACN). Equal amount of peptides were mixed from all urinary proteome samples, which was further diluted with mobile phase A and eluted at a flow rate of 1 ml/min by the following gradient: 0–10 min 95% A, 5% B; 10–50 min, 95%–65% A, 5%–35% B; 50–51 min 65%–5% A, 35%–95% B; 51–54 min, 5%–0% A, 95%–100% B; finally 95% A and 5% B eluting 10 min to re-equilibrate the column. The elution peaks were monitored at 214 nm and the fractions were collected every minute. At last, the peptide components were combined into a total of 10 fractions for lyophilization and Data Dependent Acquisition (DDA) analysis.

Characterization of gemini C18 silica microspheres

The morphology of Gemini C18 silica microspheres was characterized by a JSM-6700F scanning electron microscope (SEM, JEOL, Japan) at 3.0 kV, and element analysis was performed on an energy dispersive spectrometer (EDS) of the SEM. The particle size distribution was measured by ImageJ software through SEM image, and the zeta potential of the particles (dispersed in ethanol) was measured by a nanosize and zeta potential analyzer (Malvern, United Kingdom). The water contact angles (CAs) on the coating composed of the silica microspheres were measured on a CA system (OCA20, Dataphysics, Germany) at ambient temperature, and the average CA value was obtained by measuring three different positions of the particles.

Urinary proteome analysis by nano-LC-MS/MS

An Orbitrap Exploris 480 (Thermo Fisher Scientific, San Jose, CA) system equipped was used to analyze urinary proteome for peptide sequencing and protein quantification. A Thermo Ultimate 3000 UHPLC liquid chromatography with the trap column and a tandem self-packed C18 column (150 μm internal diameter, 1.8 μm of silica microspheres diameter, 35 cm column length), were coupled online to the mass spectrometer through a nanoESI ion source.

DDA Library Construction: The segmented dried peptide samples were reconstituted with mobile phase A (2% ACN, 0.1%

FA aqueous solution), and the supernatants were collected for injection after centrifuging at 20,000 *g* for 10 min. Enriched peptides were separated at a flow rate of 500 nL/min by the following effective gradient for DDA mode detection: 0–5 min, 5% mobile phase B (98% ACN, 0.1% FA); 5–120 min, 5%–25% B; 120–160 min, 25%–35% B; 160–170 min, 35%–80% B; 170–175 min, 80% B; 175–175.5 min, 80%–5% B; 175.5–180 min, 5% B. The main parameters of Orbitrap MS were set as follows: ion source voltage 1.9kV; MS1 scanning range *m/z* 350~1,650; MS1 resolution 120,000; maximal injection time (MIT) 90 ms; MS/MS collision type HCD; collision energy NCE 30; MS/MS resolution 30,000; auto mode for MIT; dynamic exclusion duration 120 s. The start *m/z* for MS/MS was fixed to auto mode, and AGC was set as MS 300% and MS/MS 100%. Precursor peptide ions for MS/MS scan were satisfied: charge range from 2 + to 6+, top 30 precursors with intensity over 2E4.

Data Independent Acquisition (DIA) Protein Quantification: The dried enzymatic urinary proteome samples were reconstituted with mobile phase A (2% ACN, 0.1% FA aqueous solution) and centrifuged at 20,000 *g* for 10 min. The supernatants were injected into the nanoLC-MS system and separated at a flow rate of 500 nL/min by the following gradient program: 0–5 min, 5% mobile phase B (98% ACN, 0.1% FA); 5–90 min, 5%–25% B; 90–100 min, 25%–35% B; 100–108 min, 35%–80% B; 108–113 min, 80% B; 113–113.5 min, 80%–5% B; 113.5–120 min, 5% B. The main parameters of MS in DIA mode were set as follows: ion source voltage 1.9 kV, MS1 scanning range *m/z* 400~1,250; MS1 resolution 120,000; MIT 90 ms. For MS/MS scan, the scanning range *m/z* 400~1,250 was equally divided to 50 continuous windows, and fragment ions were scanned in Orbitrap with resolution of 30,000. MS/MS collision type was also selected as HCD, collision energy NCE was set to 30, MIT was auto mode, and AGCs were separately set as MS 300% and MS/MS 1000%.

Protein identification and quantitative analysis

In the DDA library construction, the software MaxQuant (version 1.5.3.30) was used for peptide identification, and the retrieved database was uniprot_homosapiens_irt.fasta (20,303 sequences). Trypsin was used for proteins cutting and up to two missed cuts were allowed. Methyl carbamate was used for the fixed modification at cysteine (C) site, while oxidized of methionine (M), acetyl groups (N-terminal of protein), glutamine (Q) to pyro-glutamate (N-terminal of Q) and deamidated (NQ) were used for variable modification. The error rate for peptide mapping matching with protein was set as 1%, and the shortest peptide length was seven amino acids. The DIA MS data were analyzed by the software Spectronaut, and the retention time (RT) was corrected by iRT peptides. Based on the target-decoy model suitable for sequential window acquisition of theoretical fragment ion mass spectrometry (SWATH-MS), the false positive control was set as 1%. Finally, the significant differences of urinary proteome were statistically evaluated by the MSstats software package. After error correction and normalization were performed on each sample, the differential expressed proteins (DEPs) were screened out according to the absolute value of fold change ($|FC| \geq 2$ and p value < 0.05 as the judgment criteria for significant differences.

Bioinformatic and statistical analysis

Gene ontology (GO) annotation of urinary proteome was analyzed using the online Database for Annotation, Visualization and Integrated Discovery (DAVID) software. The software Cluster 3.0 was used for hierarchical clustering and visualization on the urinary DEPs. Kyoto Encyclopedia of Genes and Genomes (KEGG) is a database collection referring to genomes, diseases, biological pathways, drugs and chemical materials, which was used for pathway analysis of the identified urinary proteins using the online software. The possible functions of urinary proteins were predicted by Eukaryoyic Orthologous Groups (KOG) software, and the online WoLF PSORT software was used to predict the possible subcellular locations of proteins. Finally, Search Tool for the Retrieval of Interacting Genes (STRING, 11.0) software was used to analyze the protein-protein interaction (PPI) network, which is important to understand cell physiology under normal and disease conditions.

Results

Characterisation of patients and silica particles

The basic information of six patients with CSA-AKI, such as age, body mass index (BMI), sCr levels and urinary protein amounts, is displayed in Supplementary Table S1. The urine samples were collected from patients with CSA-AKI and divided into two groups: Before_AKI (uninjured kidney) and AKI_Day1 (injured kidney). The sCr levels and urinary protein amounts of the AKI_Day1 group were significantly increased compared with those of the Before_AKI group. According to the 2012 KDIGO clinical practice guideline, AKI can be divided into three stages based on sCr elevation: stage 1A as an absolute increase in sCr of 0.3 mg/dl (or 26.5 μmol/L) within 48 h, stage 1B as a 50% relative increase in sCr within 7 days, stage 2 as a 100% relative increase in sCr over a 7-days window of observation, and stage 3 as a 200% relative sCr increase

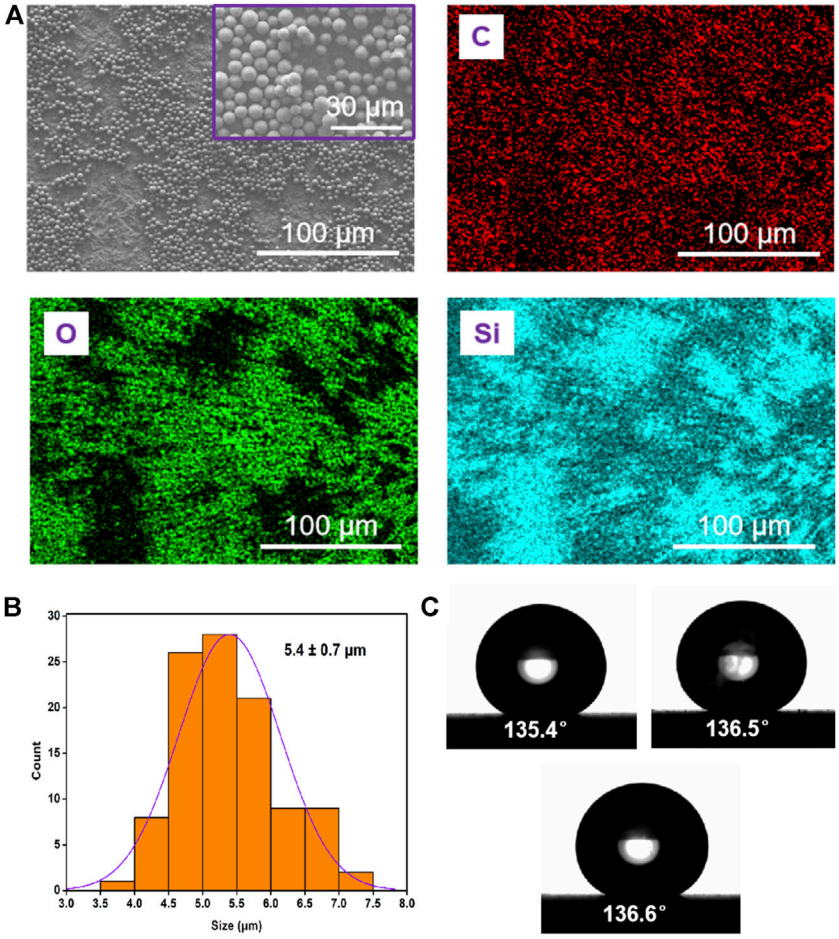

FIGURE 1
Characterisation of Gemini C18 silica microspheres. **(A)** SEM image and elemental analysis (C, O, and Si) of the particles. **(B)** Size distribution of the particles. **(C)** Photograph of a water droplet on the coating of silica microspheres surface; the water CA is about 136.1° ± 0.6°.

within 7 days. In total, the severity of six AKI patients separately belonged to three patients in stage 1A, two patients in stage 1B, and one patient in stage 2.

The high-magnification SEM image in Figure 1A showed the uniform particle size distribution of the silica microspheres. EDS mapping of the particles showed that carbon (C), oxygen (O) and silicon (Si) were only detected in the exterior region, suggesting the hydrophobicity of the surface of silica microspheres due to the grafted layer of alkane chains. The silica particles exhibited uniform size distribution with an average diameter of 5.4 ± 0.70 μm (mean ± SD, Figure 1B). The average zeta potential of these silica particles in ethanol was 13.70 ± 0.97 mV (three test values: 13.83, 12.73 and 14.53 mV), indicating that these particles could easily aggregate. Furthermore, the contact angle (CA, θ) of the three phases of the silica microspheres was measured to study their surface wettability (Figure 1C). The value of 136.1° ± 0.6° (mean ± SD, n = 3) was obtained, further proving the hydrophobic properties of the silica microsphere coating.

Identification and quantification of urinary proteomes

DDA MS was used to identify and construct the peptide library of urinary proteomes from the Gemini column enriched samples (Supplementary Table S2). A total of 10,869 peptides and 1,942 proteins were identified from the preoperative and postoperative urine samples using DIA MS as listed in Supplementary Table S3 and Supplementary Table S4, respectively. The cysteine sites in the samples can be reduced and alkylated through the classical carbamidomethylated reaction with DTT and IAM prior to tandem MS analysis. A total of 1,781 peptide segments contained cysteines with

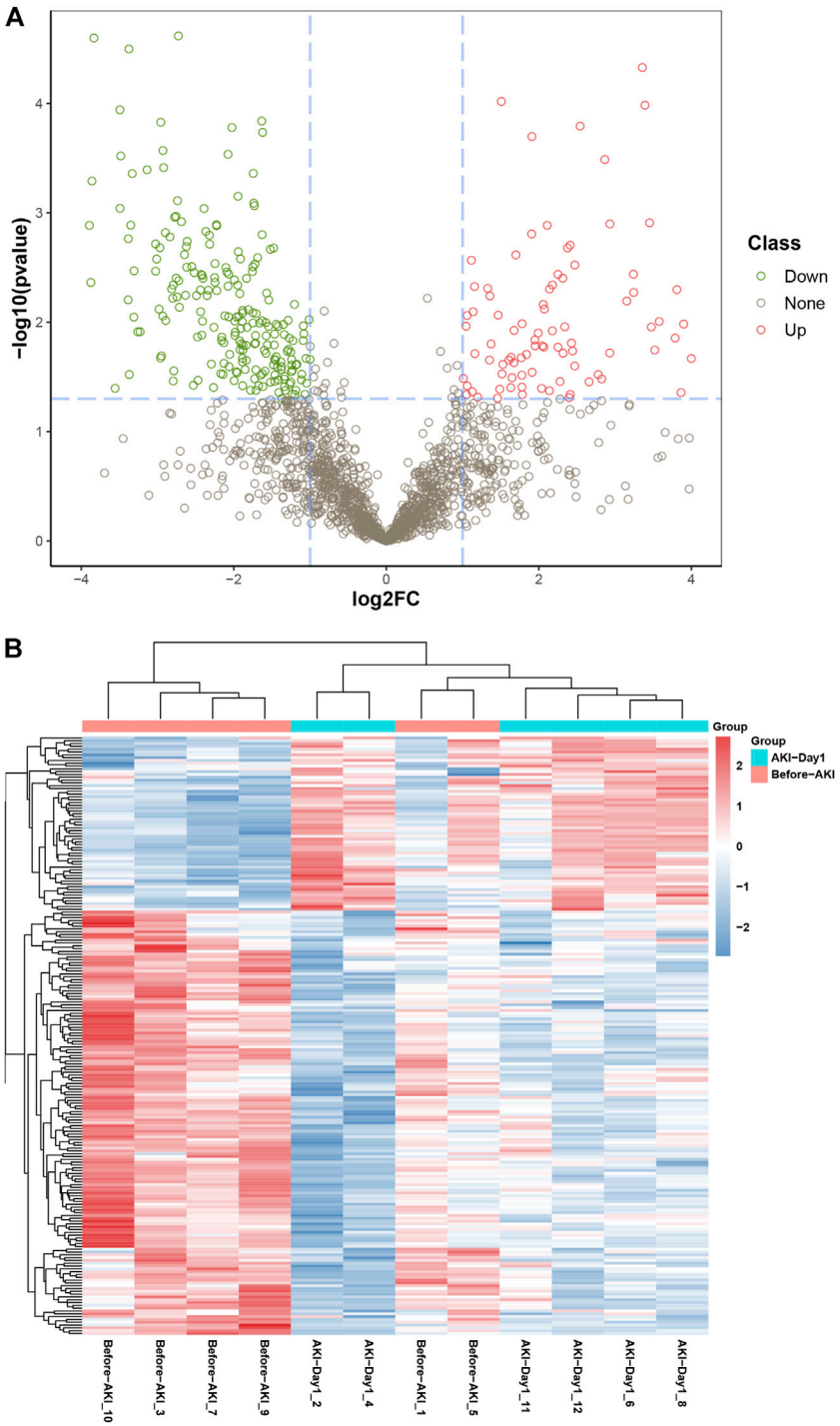

FIGURE 2
Differential expression of urinary proteins between groups. **(A)** Volcano plot for visually displaying the differential expressed proteins (DEPs): the red circles are the up-regulated DEPs, the green ones are the down-regulated DEPs, and the grey ones are the non-significant proteins. **(B)** Cluster analysis of DEPs from patients with AKI. The red part represents the proteins with high expression, and the blue part indicates the proteins with low expression.

carbamidomethylation. With the development of tandem MS, the number of posttranslational modifications (PTMs) identified on proteins has increased rapidly, providing valuable information on the signal pathways and cellular processes regulated by PTMs. In the study, the PTMs on the peptides included 961 oxidation of M, 105 acetylation of N-terminal, 218 of pyroglutamalytion on Q and 856 deamidation. The annotated data of the urinary proteomes of patients with AKI are listed in Supplementary Table S5.

The basic statistical results of the urinary proteins are shown in Supplementary Figure S1 and comprise unique peptide distribution, protein mass distribution and protein coverage distribution. According to the unique peptide distribution in Supplementary Figure S1A, 1,004 proteins had the number of unique peptides ≥ 3, accounting for 51.70% of all identified urinary proteins. Bar charts in Supplementary Figure S1B showed that the molecular masses of urinary proteins were mostly distributed in the range of 10–60 KDa. Therefore, most urinary proteins were medium proteins. For protein coverage distribution, the length of the identified sequence was divided by the total length of the protein sequence. Supplementary Figure S1C shows that the identification rate was mainly concentrated within the range of 40%.

The urinary proteome differences between groups were compared using univariate analysis to investigate the significant DEPs before and after AKI. The results were visualised through the volcano plot in Figure 2A. Changes in urinary proteins were determined by the combination of FC and p value; FC ≥ 2 and p value < 0.05 were expressed as up-regulation, and FC ≤ −2 and p value < 0.05 were expressed as down-regulation. Compared with the Before-AKI group, 324 proteins were differentially expressed in the AKI-Day1 group, with 96 up-regulated DEPs and 228 down-regulated DEPs. Furthermore, Figure 2B shows the cluster analysis chart of DEPs to visually reflect the expressed differences between the two groups.

Gene ontology annotation and enrichment analysis

GO is an international standard gene function classification system with three categories: biological process (BP), cellular component (CC) and molecular function (MF). It can provide a timely updated standard vocabulary to comprehensively describe the characteristics of genes and gene products in organisms. Blast2GO software was used for GO annotation analysis to evaluate the functional significance of all identified proteins. As shown in Supplementary Figure S2A, the most enriched BP (out of 29 GO terms) were “cellular process”, “biological regulation”, “regulation of biological process”, “metabolic process” and “response to stimulus”. Meanwhile, the most enriched CC (out of 19 GO terms) were “cell”, “cell part”, “organelle”, “extracellular region” and “extracellular region part”. The most enriched MF (out of 13 GO items) were “binding”, “catalytic activity”, “molecular function regulator”, “molecular transducer activity” and “signal transducer activity”.

GO enrichment analysis was also carried out for the identified DEPs (Supplementary Table S6). Supplementary Figure S2B shows the GO functional classification maps of all DEPs, and Figure 3 displays the GO classification of up-regulated and down-regulated differential proteins. The up-regulated and down-regulated DEPs can interfere with common structural or functional processes. However, unique enrichments were detected for some GO terms, including the up-regulated proteins (e.g., detoxification, presynaptic processes involved in chemical synaptic transmission, protein tag and transcription regulator activity) and down-regulated proteins (e.g., cell aggregation, pigmentation, nucleoid, virion and virion part).

Kyoto encyclopedia of genes and genomes enrichment analysis of differential expressed proteins

The biological functions of the identified DEPs were further characterised *via* KEGG enrichment analysis (Supplementary Table S7). The results showed that the up-regulated proteins were annotated as 29 major pathways and the most enriched pathways were “protein processing in endoplasmic reticulum” and “pathway in cancer”. Meanwhile, the down-regulated proteins were annotated to 27 major pathways, and the most enriched ones were “cell adhesion molecules”, “pathways in cancer” and “phagosome” (Figure 4A). The 19 highest ranked biological functions for the DEPs set are shown in Figure 4B. Among these pathways, “cell adhesion molecules” was enriched in ICOS ligand, poliovirus receptor, platelet endothelial cell adhesion molecule, cadherin-2, tumour necrosis factor receptor superfamily member 5, receptor-type tyrosine-protein phosphatase mu, cadherin-5, contactin-1, mucosal addressin cell adhesion molecule 1, CD276 antigen, vasorin, neuronal growth regulator 1, neogenin, golgi apparatus protein 1, junctional adhesion molecule C, cell adhesion molecule one and neurexin-3 (Supplementary Table S8).

Eukaryoyic orthologous groups annotation, subcellular localisation and protein-protein interaction of differential expressed proteins

The potential functions of the identified DEPs were predicted using KOG, a database for the classification of protein orthologs (Supplementary Figure S3). The most representative KOG category was ‘cell processes and signalling’, which indicated that the DEPs were closely associated with signal transduction mechanisms, posttranslational modification, protein turnover and chaperones. Meanwhile, WoLF PSORT software was used to predict the

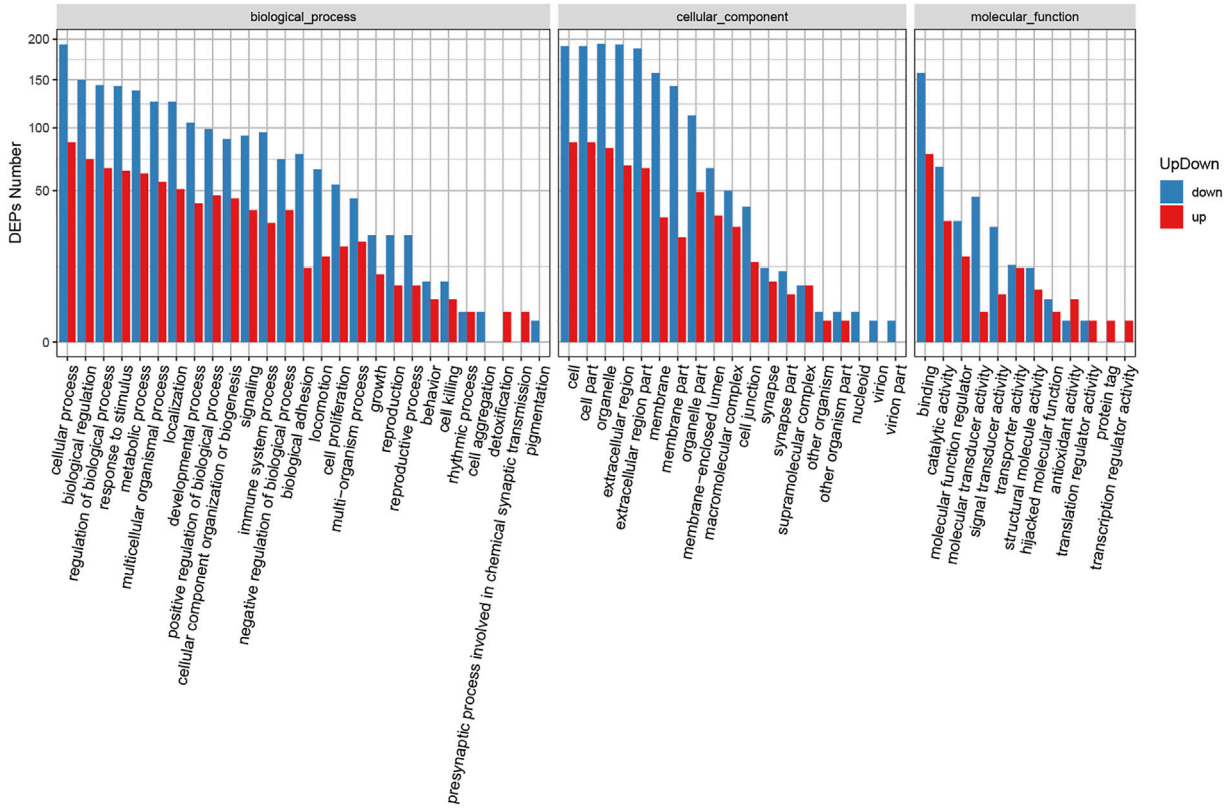

FIGURE 3
GO classification of up-regulated and down-regulated DEPs.

subcellular localisation of the identified DEPs (Supplementary Figure S4). The most represented structures were located in extracellular, plasma membrane compartments, intracellular and mitochondria.

Proteins often carry out a specific function after combining with a complex through PPI. For the top 100 confidence intervals, the STRING database was used for network interaction analysis of the DEPs to construct protein–protein relationships (Figure 5 and Supplementary Table S9). The hub eight central nodes were identified as vitamin K-dependent protein S (PROS), α-1-antitrypsin (A1AT), aggrecan core protein (PGCA), β-2-microglobulin (B2MG), AGT, matrix metalloproteinase-9 (MMP-9), growth arrest-specific protein 6 (GAS6) and urokinase-type plasminogen activator (PLAU). Among these central nodes, A1AT, B2MG, AGT and PROS belonged to the up-regulated DEPs, and the down-regulated DEPs included GAS6, MMP-9, PLAU and PGCA.

Discussion

This study aimed to generate a high-quality resource of urinary proteomic datasets from patients with CSA-AKI and compare the alterations of urinary proteome profiles to reflect the renal status. The use of MS-based proteomic strategy provides a fresh perspective to understand the pathway mechanisms of CSA-AKI by determining the changes in the signal pathways of protein processing in the endoplasmic reticulum and cell adhesion molecules in patients with CSA-AKI. Gemini C18 column belongs to the new generation silica-based hybrid column, which introduces saturated hydrocarbons on the particle surface (Benhaim Grushka, 2008; Samuelsson et al., 2007). For the stationary phase of the Gemini C18 column, saturated carbons are inserted into the silica surface to form superhydrophobic systems, which can be used to characterise acidic and basic molecules in their neutral form due to the pH stability. Such a superhydrophobic surface can expand the pH range (pH 2–12) and maintain the superior column efficiency and mechanical strength of silica gel particles. In this case, the basic peptides hydrolysed by trypsin can be efficiently separated and enriched in the alkaline mobile phase (Supplementary Figure S5), providing abundant peptide sequencing information for DDA library construction and DIA quantitative proteomics. Additionally, Orbitrap Exploris HRMS has ultrahigh sensitivity and can accurately determine the composition of

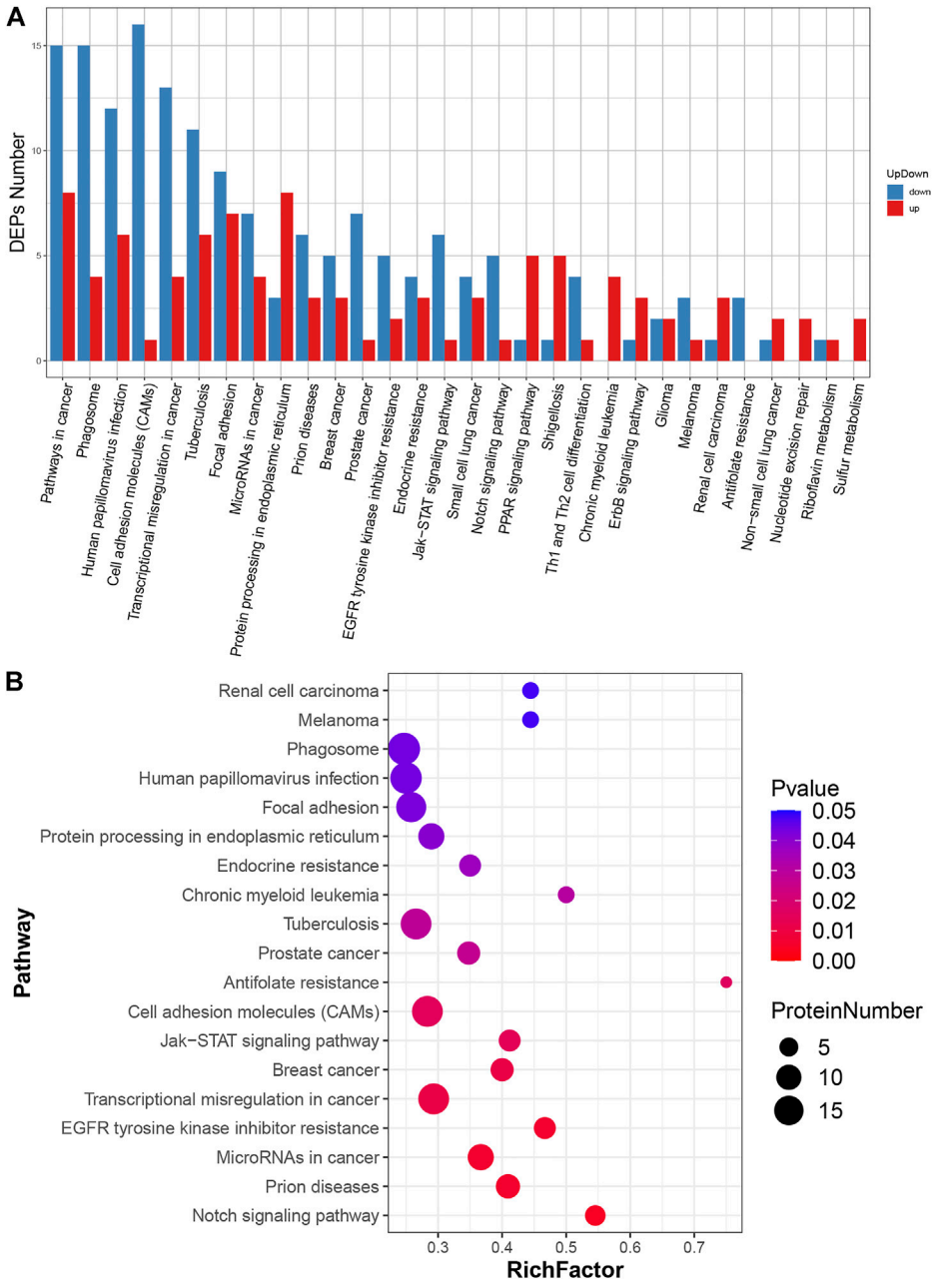

FIGURE 4
KEGG pathway analysis of DEPs. **(A)** Classification of DEPs. The x-axis represents pathway annotation entries, and the y-axis represents the number of DEPs enriched in each pathway term. **(B)** Significant enrichment pathways of DEPs. The size of the dot represents the number of DEPs annotated to the pathways, and the colour of the dot represents the *p*-value.

peptide ions. DIA quantitative proteomics has relatively high detection efficiency for low-abundance proteins and is suitable for exploring the relative expression changes of urinary proteins before and after AKI (Zi et al., 2014). Therefore, the use of enriched functional materials and Orbitrap HRMS can provide convenient conditions for the quantitative analysis of low levels of urinary proteins.

As a relatively common complication of cardiac surgery, AKI has an approximately 5%–42% incidence rate and has short-term and long-term survival implications for patients (Ostermann et al., 2021). Owing to the lack of effective AKI treatment methods, clinicians usually focus on prevention and risk factor management to reduce the incidence of AKI (Breilh et al., 2019; Goepfert et al., 2013; Khan et al., 2014). Thus,

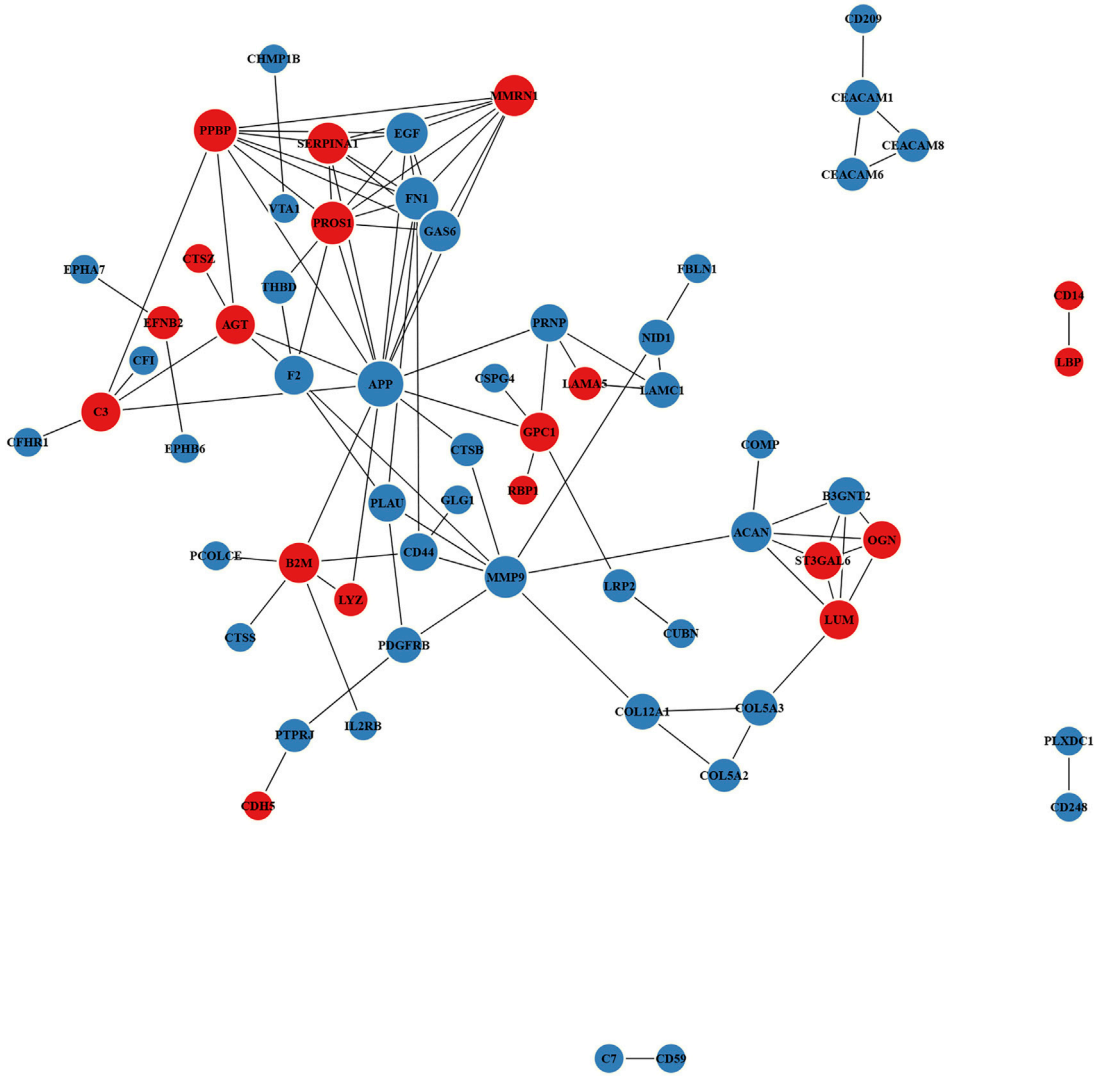

FIGURE 5
Protein–protein interaction (PPI) network of DEPs. Red and blue nodes separately represent up-regulated and down-regulated proteins. The size of the circles represents node degree.

efforts have been exerted to identify biomarkers with high specificity and sensitivity relevant to CSA-AKI, including cardiac functional biomarkers, inflammation biomarkers and renal tubule-associated biomarkers (Wu et al., 2019). Global proteomic alterations in the sepsis-induced AKI model have also been investigated to reflect the systematic responses and identify a valuable resource for sepsis biomarker discovery (Lin et al., 2020). Patients with contrast-induced AKI also showed proteomic changes in urine, revealing the potential role of urinary proteomics in the assessment of early renal injury (Zhu et al., 2021). Therefore, the urinary proteome has become an important field for the discovery of non-invasive biomarkers and can also be used to distinguish subtle proteomic differences caused by specific diseases or therapeutic interventions.

KEGG analysis showed that "protein processing in endoplasmic reticulum" was the most enriched pathway for up-regulated DEPs, and "cell adhesion molecules" was the most enriched pathway for down-regulated DEPs. According to current evidence for ischaemia–reperfusion (IR) injury, endoplasmic reticulum (ER) stress has become an essential signal event of cell stress due to the accumulation of a large number of unfolded proteins in ER (Xu et al., 2016). These unfolded proteins might be eliminated *via* autophagy to alleviate the impact of protein misfolding in kidney diseases (Cybulsky, 2017). Therefore, ER stress may play a role in the pathogenesis of

AKI, and early ER stress intervention and ER homeostasis restoration may help prevent or reduce the injury of renal cells (Tang et al., 2020). Cell adhesion molecules can mediate inflammatory processes through endothelial cells to amplify the immune response. The decrease in intercellular adhesion and the change of adhesion molecules may lead to renal function loss in AKI (Nürnberger et al., 2010). Furthermore, serum cell adhesion molecule levels, such as E-selectin levels, can be powerful predictors for early septic AKI (Su et al., 2016).

The PPI target networks of urinary DEPs were constructed using the STRING online database, and three hub DEPs with up-regulation and down-regulation were separately and comprehensively considered for AKI. Among the up-regulated DEPs, A1AT is a hepatic stress protein with protease inhibitor activity and can improve the binding efficiency with hemin to prevent the formation of hemin-induced reactive oxygen species in neutrophils (Zager et al., 2014). As a potential marker of neutrophil activation, serum A1AT can be used to predict AKI in patients with IR injury (Du et al., 2019). B2MG, a protein homologous to histocompatibility antigens, can be freely filtered into primary urine by the glomerulus. Owing to its increasing concentrations in the early stage of kidney failure, serum B2MG has already been proposed as a candidate biomarker to assess kidney function in AKI and CKD (Argyropoulos et al., 2017). Furthermore, the increased B2MG concentrations in urine have also been associated with hypoxia caused by cardiac surgery or kidney transplantation (Beitland et al., 2019). AGT is the parent polypeptide for the formation of angiotensin II, which can activate pro-inflammatory pathways in the renin–angiotensin–aldosterone system and may contribute to the progression of AKI (Ba et al., 2017). Clinical studies showed that urinary AGT can dynamically monitor the recovery of renal status after an AKI attack and may predict the progression of AKI-CKD and treatment response of patients with AKI (Chen C et al., 2016; Cui et al., 2018).

Among the down-regulated DEPs, GAS6 plays a role in leukocyte sequestration and migration, platelet aggregation and haematopoiesis, proliferation, apoptosis and phagocytosis as a member of the vitamin K-dependent protein family. Given that GAS6 is usually related to injury, inflammation and repair conditions, its contribution to AKI is closely associated with biological functions, including anti-apoptotic effect and survival-promoting capability (Xiao et al., 2021). GAS6 can exert protective roles by decreasing serum urea nitrogen, creatinine and renal apoptosis, reducing the sepsis-induced pathological damage and improving the survival rate of AKI mice (Chen L et al., 2016). MMP-9, a multi-domain zinc metalloproteinase released from inflammatory cells, can degrade the endothelial basement membrane and increase the permeability of capillaries (Bengatta et al., 2009). In addition to extracellular matrix remodelling, MMP-9 also regulates the activities of a variety of cytokines, receptors, chemokines, growth factors and cell adhesion molecules necessary for inflammation. The tissue inhibitor of matrix metalloproteinase-1 (TIMP-1) and MMP-9 can be used as potential diagnostic biomarkers for sepsis-associated AKI in clinical assessment (Bojic et al., 2015). As the soluble form of membrane-bound urokinase plasminogen activator receptor, PLAU is expressed in various cell types, such as neutrophils, monocytes, lymphocytes, endothelial cells and tumour cells (Hahm et al., 2017). Several clinical studies showed that PLAU has predictive and prognostic values in different kinds of AKI (Qin et al., 2021; Rasmussen et al., 2021). Thus, the present work can provide valuable knowledge on AKI-related urinary biomarkers for prediction and diagnosis of renal injury and signal pathways for potential therapeutic targets.

The major limitations of this study were the small sample size and fewer detection time points; hence, individual factors may affect the results of statistical analysis compared to the urinary metabolomics (Bai et al., 2022). A large number of patients in multicentre cohorts for rigorous algorithm analysis are needed in future studies of CSA-AKI urinary proteomics to minimise batch effects and confirm our results. Moreover, additional time points, such as constinuously recording kidney functional alteration before AKI, could facilitate the identification of differential substances and provide a new prospect for the discovery of potential biomarkers.

Conclusion

The results indicated that renal signal pathways, including protein processing in ER and cell adhesion molecules, dramatically changed in patients with AKI. Such an MS-based proteomics strategy can help us obtain valuable resources to improve the understanding of the significant DEPs and pathway mechanisms of patients with CSA-AKI. This study will broaden our understanding of urinary proteome profiles reflecting the kidney status, promote the development of renal disease biomarkers and provide new insights into preventive treatments for CSA-AKI.

Data availability statement

The datasets presented in this study can be found in online repositories. The names of the repository/repositories and accession number(s) can be found in the article/Supplementary Material.

Ethics statement

The studies involving human participants were reviewed and approved by the ethics committee of Maoming People's Hospital. The patients/participants provided their written informed consent to participate in this study.

Author contributions

CC, YB, YL, ZT, and LH equally contributed to the design of the research. YB and YL equally contributed to analyze and interpret the data. CC, ZT, and LH contributed to the conception and experiments of the research and critically revised the manuscript. XJ, WX, and JC performed the research and collected data. SH and KW contributed to collect the urine samples and analyze the data. All authors contributed to draft the manuscript and agreed to be fully accountable for ensuring the integrity and accuracy of the work. All authors read and approved the final manuscript.

Funding

CC is currently receiving a grant (Project No. 202101) from the Open Project of Guangdong Key Laboratory of Renal Failure Research, a grant (Project No. KJ012019445) from the Outstanding Young Medical Talents in Guangdong Province, and a grant (Project No. DFJH2020028) from the Major Program of Summit Project, Guangdong Province High-level Hospital Construction Project of Guangdong Provincial People's Hospital, Guangdong Academy of Medical Sciences. YB was funded by a grant (Project No. A2021390) from Medical Scientific Research Foundation of Guangdong Province of China, a grant (Project No. 2021S0024) from Science and Technology Planning Project of Guangdong Province of China, a grant (Project No. 2020KJZX003) from the Maoming Science and Technology Program, a grant (Project No. zx2020016) from the High-level Hospital Construction Research Project of Maoming People's Hospital, and a grant (Project No. BS2020002) from the Doctoral Research Project of Maoming People's Hospital. BGI Life Science Research Institution is acknowledged for support with HRMS data acquisition.

Conflict of interest

The authors declare that the research was conducted in the absence of any commercial or financial relationships that could be construed as a potential conflict of interest.

Publisher's note

Supplementary material

The Supplementary Material for this article can be found online at: https://www.frontiersin.org/articles/10.3389/fbioe.2022.1002853/full#supplementary-material

References

Argyropoulos, C. P., Chen, S. S., Ng, Y. H., Roumelioti, M. E., Shaffi, K., Singh, P. P., et al. (2017). Rediscovering beta-2 microglobulin as a biomarker across the spectrum of kidney diseases. *Front. Med.* 4, 73. doi:10.3389/fmed.2017.00073

Ba, A. S., Sanchez, A., and Batlle, D. (2017). Angiotensinogen as a biomarker of acute kidney injury. *Clin. Kidney J.* 10 (6), 759–768. doi:10.1093/ckj/sfx087

Bai, Y., Zhang, H., Wu, Z., Huang, S., Luo, Z., Wu, K., et al. (2022). Use of ultra high performance liquid chromatography with high resolution mass spectrometry to analyze urinary metabolome alterations following acute kidney injury in post-cardiac surgery patients. *J. Mass Spectrom. Adv. Clin. Lab.* 24, 31–40. doi:10.1016/j.jmsacl.2022.02.003

Beitland, S., Nakstad, E. R., Berg, J. P., Trøseid, A. S., Brusletto, B. S., Brunborg, C., et al. (2019). Urine β-2-microglobulin, osteopontin, and trefoil factor 3 may early predict acute kidney injury and outcome after cardiac arrest. *Crit. Care Res. Pract.* 2019, 1–9. doi:10.1155/2019/4384796

Bengatta, S., Arnould, C., Letavernier, E., Monge, M., de Préneuf, H. M., Werb, Z., et al. (2009). MMP9 and SCF protect from apoptosis in acute kidney injury. *J. Am. Soc. Nephrol.* 20 (4), 787–797. doi:10.1681/ASN.2008050515

Benhaim, D., and Grushka, E. (2008). Effect of n-octanol in the mobile phase on lipophilicity determination by reversed-phase high-performance liquid chromatography on a modified silica column. *J. Chromatogr. A* 1209 (1-2), 111–119. doi:10.1016/j.chroma.2008.08.118

Bennett, M. R., and Devarajan, P. (2011). Proteomic analysis of acute kidney injury: Biomarkers to mechanisms. *Prot. Clin. Appl.* 5 (1-2), 67–77. doi:10.1002/prca.201000066

Bojic, S., Kotur-Stevuljevic, J., Kalezic, N., Stevanovic, P., Jelic-Ivanovic, Z., Bilanovic, D., et al. (2015). Diagnostic value of matrix metalloproteinase-9 and tissue inhibitor of matrix metalloproteinase-1 in Sepsis-Associated acute kidney injury. *Tohoku J. Exp. Med.* 237 (2), 103–109. doi:10.1620/tjem.237.103

Breilh, D., Honore, P. M., De Bels, D., Roberts, J. A., Gordien, J. B., Fleureau, C., et al. (2019). Pharmacokinetics and pharmacodynamics of anti-infective agents during continuous veno-venous hemofiltration in critically ill patients: Lessons learned from an ancillary study of the IVOIRE trial. *J. Transl. Int. Med.* 7 (4), 155–169. doi:10.2478/jtim-2019-0031

Chen, C., Yang, X., Lei, Y., Zha, Y., Liu, H., Ma, C., et al. (2016). Urinary biomarkers at the time of AKI diagnosis as predictors of progression of AKI among patients with acute cardiorenal syndrome. *Clin. J. Am. Soc. Nephrol.* 11 (9), 1536–1544. doi:10.2215/CJN.00910116

Chen, L. W., Chen, W., Hu, Z. Q., Bian, J. L., Ying, L., Hong, G. L., et al. (2016). Protective effects of growth arrest-specific protein 6 (Gas6) on sepsis-induced acute kidney injury. *Inflammation* 39 (2), 575–582. doi:10.1007/s10753-015-0282-2

Cui, S., Wu, L., Feng, X., Su, H., Zhou, Z., Luo, W., et al. (2018). Urinary angiotensinogen predicts progressive chronic kidney disease after an episode of experimental acute kidney injury. *Clin. Sci. (Lond).* 132 (19), 2121–2133. doi:10.1042/CS20180758

Cybulsky, A. V. (2017). Endoplasmic reticulum stress, the unfolded protein response and autophagy in kidney diseases. *Nat. Rev. Nephrol.* 13 (11), 681–696. doi:10.1038/nrneph.2017.129

Deng, Y., Ma, J., Hou, Y., Zhou, D., Hou, T., Li, J., et al. (2020). Combining serum cystatin c and urinary N-Acetyl-Beta-D-Glucosaminidase improves the precision for acute kidney injury diagnosis after resection of intracranial Space-Occupying lesions. *Kidney Blood Press. Res.* 45 (1), 142–156. doi:10.1159/000504599

Deng, Y., Wang, L., Hou, Y., Ma, J., Chi, R., Ye, H., et al. (2019). The influence of glycemic status on the performance of cystatin C for acute kidney injury detection in the critically ill. *Ren. Fail.* 41 (1), 139–149. doi:10.1080/0886022X.2019.1586722

Du, S., Tian, J., Xiao, Z., Luo, Z., Lin, T., Zheng, S., et al. (2019). Serum alpha 1-antitrypsin predicts severe acute kidney injury after cardiac surgery. *J. Thorac. Dis.* 11 (12), 5053–5062. doi:10.21037/jtd.2019.12.17

Goepfert, M. S., Richter, H. P., Zu, E. C., Gruetzmacher, J., Rafflenbeul, E., Roeher, K., et al. (2013). Individually optimized hemodynamic therapy reduces complications and length of stay in the intensive care unit: A prospective, randomized controlled trial. *Anesthesiology* 119 (4), 824–836. doi:10.1097/ALN.0b013e31829bd770

Hahm, E., Wei, C., Fernandez, I., Li, J., Tardi, N. J., Tracy, M., et al. (2017). Bone marrow-derived immature myeloid cells are a main source of circulating suPAR contributing to proteinuric kidney disease. *Nat. Med.* 23 (1), 100–106. doi:10.1038/nm.4242

Hou, Y., Deng, Y., Hu, L., He, L., Yao, F., Wang, Y., et al. (2021). Assessment of 17 clinically available renal biomarkers to predict acute kidney injury in critically ill patients. *J. Transl. Int. Med.* 9 (4), 273–284. doi:10.2478/jtim-2021-0047

Hu, L., Gao, L., Zhang, D., Hou, Y., He, L. L., Zhang, H., et al. (2022). The incidence, risk factors and outcomes of acute kidney injury in critically ill patients undergoing emergency surgery: A prospective observational study. *BMC Nephrol.* 23 (1), 42. doi:10.1186/s12882-022-02675-0

Kellum, J. A., and Lameire, N. (2013). Diagnosis, evaluation, and management of acute kidney injury: A KDIGO summary (Part 1). *Crit. Care (Houten).* 17 (1), 204. doi:10.1186/cc11454

Khan, U. A., Coca, S. G., Hong, K., Koyner, J. L., Garg, A. X., Passik, C. S., et al. (2014). Blood transfusions are associated with urinary biomarkers of kidney injury in cardiac surgery. *J. Thorac. Cardiovasc. Surg.* 148 (2), 726–732. doi:10.1016/j.jtcvs.2013.09.080

Khurana, M., Traum, A. Z., Aivado, M., Wells, M. P., Guerrero, M., Grall, F., et al. (2006). Urine proteomic profiling of pediatric nephrotic syndrome. *Pediatr. Nephrol.* 21 (9), 1257–1265. doi:10.1007/s00467-006-0165-8

Khwaja, A. (2012). KDIGO clinical practice guidelines for acute kidney injury. *Nephron Clin. Pract.* 120 (4), c179–c184. doi:10.1159/000339789

Kim, M. J., Frankel, A. H., and Tam, F. W. (2011). Urine proteomics and biomarkers in renal disease. *Nephron Exp. Nephrol.* 119 (1), e1–e7. doi:10.1159/000324223

Lameire, N. H., Bagga, A., Cruz, D., De Maeseneer, J., Endre, Z., Kellum, J. A., et al. (2013). Acute kidney injury: An increasing global concern. *Lancet* 382 (9887), 170–179. doi:10.1016/S0140-6736(13)60647-9

Liang, S., Luo, D., Hu, L., Fang, M., Li, J., Deng, J., et al. (2022). Variations of urinary N-acetyl-β-D-glucosaminidase levels and its performance in detecting acute kidney injury under different thyroid hormones levels: A prospectively recruited, observational study. *BMJ Open* 12 (3), e055787. doi:10.1136/bmjopen-2021-055787

Liang, S., Shi, M., Bai, Y., Deng, Y., Fang, M., Li, J., et al. (2020). The effect of glucocorticoids on serum cystatin C in identifying acute kidney injury: A propensity-matched cohort study. *BMC Nephrol.* 21 (1), 519. doi:10.1186/s12882-020-02165-1

Liang, X., Chen, Y., Zhuang, J., Zhang, M., Xiong, W., Guo, H., et al. (2012). Advanced oxidation protein products as prognostic biomarkers for recovery from acute kidney injury after coronary artery bypass grafting. *Biomarkers* 17 (6), 507–512. doi:10.3109/1354750X.2012.690103

Lin, Y. H., Platt, M. P., Fu, H., Gui, Y., Wang, Y., Gonzalez-Juarbe, N., et al. (2020). Global proteome and phosphoproteome characterization of sepsis-induced kidney injury. *Mol. Cell. Proteomics* 19 (12), 2030–2047. doi:10.1074/mcp.RA120.002235

Liu, L., Li, P., and Asher, S. A. (1999). Entropic trapping of macromolecules by mesoscopic periodic voids in a polymer hydrogel. *Nature* 397 (6715), 141–144. doi:10.1038/16426

Ma, J., Chen, T., Wu, S., Yang, C., Bai, M., Shu, K., et al. (2019). IProX: An integrated proteome resource. *Nucleic Acids Res.* 47 (D1), D1211–D1217. doi:10.1093/nar/gky869

Nkuipou-Kenfack, E., Latosinska, A., Yang, W. Y., Fournier, M. C., Blet, A., Mujaj, B., et al. (2020). A novel urinary biomarker predicts 1-year mortality after discharge from intensive care. *Crit. Care (Houten).* 24 (1), 10. doi:10.1186/s13054-019-2686-0

Nürnberger, J., Feldkamp, T., Kavapurackal, R., Opazo, S. A., Becker, J., Hörbelt, M., et al. (2010). N-cadherin is depleted from proximal tubules in experimental and human acute kidney injury. *Histochem. Cell. Biol.* 133 (6), 641–649. doi:10.1007/s00418-010-0702-1

Ostermann, M., Kunst, G., Baker, E., Weerapolchai, K., and Lumlertgul, N. (2021). Cardiac surgery associated AKI prevention strategies and medical treatment for CSA-AKI. *J. Clin. Med.* 10 (22), 5285. doi:10.3390/jcm10225285

Qin, Y., Qiao, Y., Wang, D., Yan, G., Tang, C., and Ma, G. (2021). The predictive value of soluble Urokinase-Type plasminogen activator receptor in Contrast-Induced acute kidney injury in patients undergoing percutaneous coronary intervention. *Int. J. Gen. Med.* 14, 6497–6504. doi:10.2147/IJGM.S339075

Rasmussen, S. R., Nielsen, R. V., Møgelvang, R., Ostrowski, S. R., and Ravn, H. B. (2021). Prognostic value of suPAR and hsCRP on acute kidney injury after cardiac surgery. *BMC Nephrol.* 22 (1), 120. doi:10.1186/s12882-021-02322-0

Samuelsson, J., Franz, A., Stanley, B. J., and Fornstedt, T. (2007). Thermodynamic characterization of separations on alkaline-stable silica-based C18 columns: Why basic solutes may have better capacity and peak performance at higher pH. *J. Chromatogr. A* 1163 (1-2), 177–189. doi:10.1016/j.chroma.2007.06.026

Santos, R., Carvalho, A., Peres, L., Ronco, C., and Macedo, E. (2019). An epidemiologic overview of acute kidney injury in intensive care units. *Rev. Assoc. Med. Bras.* 65 (8), 1094–1101. doi:10.1590/1806-9282.65.8.1094

Song, Y., Fan, J. B., Li, X., Liang, X., and Wang, S. (2019). PH-Regulated heterostructure porous particles enable similarly sized protein separation. *Adv. Mat.* 31 (16), e1900391. doi:10.1002/adma.201900391

Song, Y., Li, X., Fan, J. B., Kang, H., Zhang, X., Chen, C., et al. (2018). Interfacially polymerized particles with heterostructured nanopores for glycopeptide separation. *Adv. Mat.* 30 (39), e1803299. doi:10.1002/adma.201803299

Su, C. M., Cheng, H. H., Hung, C. W., Hsiao, S. Y., Tsai, N. W., Chang, W. N., et al. (2016). The value of serial serum cell adhesion molecules in predicting acute kidney injury after severe sepsis in adults. *Clin. Chim. Acta* 457, 86–91. doi:10.1016/j.cca.2016.04.008

Tang, C., Hu, Y., Gao, J., Jiang, J., Shi, S., Wang, J., et al. (2020). Dexmedetomidine pretreatment attenuates myocardial ischemia reperfusion induced acute kidney injury and endoplasmic reticulum stress in human and rat. *Life Sci.* 257, 118004. doi:10.1016/j.lfs.2020.118004

Wu, B., Chen, J., and Yang, Y. (2019). Biomarkers of acute kidney injury after cardiac surgery: A narrative review. *Biomed. Res. Int.* 2019, 1–11. doi:10.1155/2019/7298635

Xiao, H., Chen, J., Duan, L., and Li, S. (2021). Role of emerging vitamin K-dependent proteins: Growth arrest-specific protein 6, Gla-rich protein and periostin (Review). *Int. J. Mol. Med.* 47 (3), 2. doi:10.3892/ijmm.2020.4835

Xu, Y., Guo, M., Jiang, W., Dong, H., Han, Y., An, X. F., et al. (2016). Endoplasmic reticulum stress and its effects on renal tubular cells apoptosis in ischemic acute kidney injury. *Ren. Fail.* 38 (5), 831–837. doi:10.3109/0886022X.2016.1160724

Yang, X., Chen, C., Teng, S., Fu, X., Zha, Y., Liu, H., et al. (2017). Urinary matrix metalloproteinase-7 predicts severe AKI and poor outcomes after cardiac surgery. *J. Am. Soc. Nephrol.* 28 (11), 3373–3382. doi:10.1681/ASN.2017020142

Zager, R. A., Johnson, A. C., and Frostad, K. B. (2014). Rapid renal alpha-1 antitrypsin gene induction in experimental and clinical acute kidney injury. *PLoS One* 9 (5), e98380. doi:10.1371/journal.pone.0098380

Zdziechowska, M., Gluba-Brzózka, A., Poliwczak, A. R., Franczyk, B., Kidawa, M., Zielinska, M., et al. (2020). Serum NGAL, KIM-1, IL-18, L-FABP: New biomarkers in the diagnostics of acute kidney injury (AKI) following invasive cardiology procedures. *Int. Urol. Nephrol.* 52 (11), 2135–2143. doi:10.1007/s11255-020-02530-x

Zhang, D., Gao, L., Ye, H., Chi, R., Wang, L., Hu, L., et al. (2019). Impact of thyroid function on cystatin C in detecting acute kidney injury: A prospective, observational study. *BMC Nephrol.* 20 (1), 41. doi:10.1186/s12882-019-1201-9

Zhu, H., Chu, W., Han, S., Gao, B., and Wang, X. (2021). Urinary proteomics investigations into contrast-induced acute kidney injury. *PLoS One* 16 (10), e0258736. doi:10.1371/journal.pone.0258736

Zi, J., Zhang, S., Zhou, R., Zhou, B., Xu, S., Hou, G., et al. (2014). Expansion of the ion library for mining SWATH-MS data through fractionation proteomics. *Anal. Chem.* 86 (15), 7242–7246. doi:10.1021/ac501828a

frontiers | Frontiers in Bioengineering and Biotechnology

TYPE Original Research
PUBLISHED 20 September 2022
DOI 10.3389/fbioe.2022.1026911

OPEN ACCESS

EDITED BY
Jingxin Meng,
Technical Institute of Physics and Chemistry, Chinese Academy of Sciences (CAS), China

REVIEWED BY
Jun Yang,
Beijing Forestry University, China
Chunxiong Luo,
Peking University, China

*CORRESPONDENCE
Shengjie Jiang,
jiangshengjiejsj@163.com
Yan Wei,
kqweiyan@126.com

†These authors have contributed equally to this work and share first authorship

SPECIALTY SECTION
This article was submitted to Biomaterials, a section of the journal Frontiers in Bioengineering and Biotechnology

RECEIVED 24 August 2022
ACCEPTED 05 September 2022
PUBLISHED 20 September 2022

CITATION
Yang Y, Huang C, Zheng H, Meng Z, Heng BC, Zhou T, Jiang S and Wei Y (2022), Superwettable and injectable GelMA-MSC microspheres promote cartilage repair in temporomandibular joints. *Front. Bioeng. Biotechnol.* 10:1026911. doi: 10.3389/fbioe.2022.1026911

Superwettable and injectable GelMA-MSC microspheres promote cartilage repair in temporomandibular joints

Yue Yang[1,2†], Chenyan Huang[1†], Huimin Zheng[1†], Zhaoqiang Meng[1†], Boon Chin Heng[1], Tuanfeng Zhou[2], Shengjie Jiang[1*] and Yan Wei[1*]

[1]Beijing Laboratory of Biomedical Materials, Department of Geriatric Dentistry, Peking University School and Hospital of Stomatology, Beijing, China, [2]Department of Prosthodontics, The First Clinical Division, Peking University School and Hospital of Stomatology, Beijing, China

Temporomandibular disorders (TMD) can be treated by promoting cartilage regeneration with biomaterials. However, there are deficiencies in the infiltration function of bone filler biological materials. In this study, stems cells were loaded onto gelatin methacryloyl (GelMA) hydrogel microspheres endowed with superwettable properties and TGF-β sustained-release function, which can quickly infiltrate the irregular surface of the temporomandibular joint (TMJ) bone defect area and accelerate cartilage healing. First, to improve cell adhesion and spreading function, the BMSCs-coated GelMA microspheres were endowed with superwetting property. At the same time, the swelling adsorption characteristics of gelatin microspheres could be used to load recombinant TGF-β within the microspheres, which could in turn promote the chondrogenic differentiation of multi-potent bone marrow mesenchymal stem cells. The SEM imaging demonstrated that BMSCs-coated GelMA microsphere has superwettable and superhydrophilic property, which enabled rapid adaptation to the bone defect surface morphology, which is conducive to tissue repair. Furthermore, the cartilage defect model showed that rBMSCs-coated GelMA microspheres promote temporomandibular joint arthritis repair. In conclusion, our study established that BMSC-coated GelMA microspheres endowed with superwetting properties, can colonize the bone defect repair site better with sustained release of growth factors, thus providing an innovative strategy for promoting cartilage regeneration.

KEYWORDS

superwettable, microspheres, temporomandibular disorder, chondrogenesis, spheroids

1 Introduction

Currently, tissue engineering approaches for treatment of temporomandibular joint disorders (TMD) are a much needed alternative to the limited efficacy of routinely-used clinical treatment modalities (Acri et al., 2019; Tarafder et al., 2016). Inducing differentiation of stem cells into chondrocytes within the condylar cartilage is a possible treatment strategy for TMD (Kim et al., 2023; Wadhwa and Kapila, 2008). However, biomaterials for cartilage regeneration within the temporomandibular joint (TMJ) is still in the developmental pipeline. The design of restorative materials with active infiltration capacity together with bio-inspired and biomimetic properties would be of great significance for the treatment of TMD.

The aim of biomimetic modification is to impart good biocompatibility to the base material, which facilitates good cytocompatibility and favorable osseointegration during the early stages of implantation (Del Bakhshayesh et al., 2019). However, current tissue repair materials often do not possess such properties, but often only provide early spatial occupancy and are usually not biologically permeable to the bone defect area. Most studies of supperwetting bioimplant materials focus on the infiltration characteristics of the base material (Jiang et al., 2022). As a natural extracellular-derived proteinaceous material, gelatin has been widely studied and applied in various biomedical fields, due to its implantability, biocompatibility and degradable properties (Stevens et al., 2002). However, gelatin itself as well as GelMA does not possess a biological infiltration capacity after implantation in the defect area, which limits its repair efficacy of bone defects (Lukin et al., 2022). Therefore, enhancing the bio-infiltration function of gelatin through surface modifications is expected to improve the biocompatibility and regeneration efficacy of implant materials.

Some studies have found that upon contact of mesenchymal stem cells (MSCs) with extracellular matrix (ECM) substrate, the infiltration and diffusion effect was similar to that of droplets touching the substrate (Douezan et al., 2011; Jiang et al., 2021). Combining the biological functions of MSCs with biomaterials to endow biomaterial with bio-inspired features is of great value for improving biocompatibility and optimizing the repair effect (Sulaiman et al., 2020). Stem cell microspheres have been extensively studied in recent years (Langhans, 2018). MSCs are a promising alternative for regenerative therapy because their lineage fate could be procisely regulated with specific growth factors (Han et al., 2019). Additionally, spheroid MSCs have shown higher therapeutic potential than MSCs monolayers through better spreading ability and increased secretion of growth factors (Cesarz and Tamama, 2016). On the other hand, there are also various difficulties in constructing cell spheroids, which often require the utilization of hydrogel scaffolds (Neto et al., 2016). Biomaterial microspheres can be used as individual cell culture units, or assembled into porous scaffolds or simulated biomimetic microenvironments, and have been widely applied in cell culture, tissue engineering, and regenerative medicine studies (Dhamecha et al., 2019). Hydrogels are good hydrophilic substrates, which are conducive to cell adhesion, and the hydrogel core can also promote the formation of MSCs spheroids (Cui et al., 2020; He et al., 2020). Surface wettability is an intrinsic but complex property of phospholipid bilayers, which can compensate for the deficiencies of artificial materials in adapting to the complex ultrastructural surface of irregular bone defects. Upon MSCs loading onto hydrogel microspheres, the cell membrane can serve as a natural substrate with strong affinity for endogenous stem cells, thereby optimizing the adaptability of the hydrogel to the TMJ defect surface ultrastructure. Being incorporated with the surface phospholipid bilayer and various cell membrane surface functional proteins, biomaterial based stem cell spheroids thus present superwetting and biological infiltration properties.

Additionally, the sustained-release of growth factors from hydrogels are also of great interest to tissue repair, in particular TGF-β (Bello et al., 2021). Previous studies have also found that sustained-release of growth factors (including TGF-β, FEGF, etc.) is an effective strategy to promote cartilage repair and treat TMD (Zheng et al., 2018). Moreover, one of the key reasons for the failure of 3D stem cell spheroid culture is the inability of growth factors to fully penetrate the spheroid core (Langhans, 2018). Using TGF-β-releasing microspheres as implantable scaffolds for the formation of cell spheroids is beneficial for maintaining the biological activity of spheroids, and directing chondrocyte differentiation, thus providing a promising strategy for tissue engineering-based treatment of TMD. Maintaining the sustained release of specific cytokines from the hydrogel internal core is a good strategy to guide the differentiation of stem cell spheroids.

Here, we exploited the infiltration characteristics of MSCs by placing these cells on the surface of TGFβ-loaded GelMA microspheres, leading to active infiltration of biomaterial. The modified gelatin-MSCs microspheres can then more efficiently colonize the bone defect repair site, releasing cytokines at specific locations, and accelerating the healing of the TMJ defect area. Figure 1 depicts a schematic representation of the superwettable gelatin-MSCs microspheres for TMJ cartilage repair.

2 Materials and methods

2.1 Cell culture

Rat Bone Marrow-derived mesenchymal stem cells (rBMSCs) were cultured at 37°C under 5% CO_2 atmosphere in

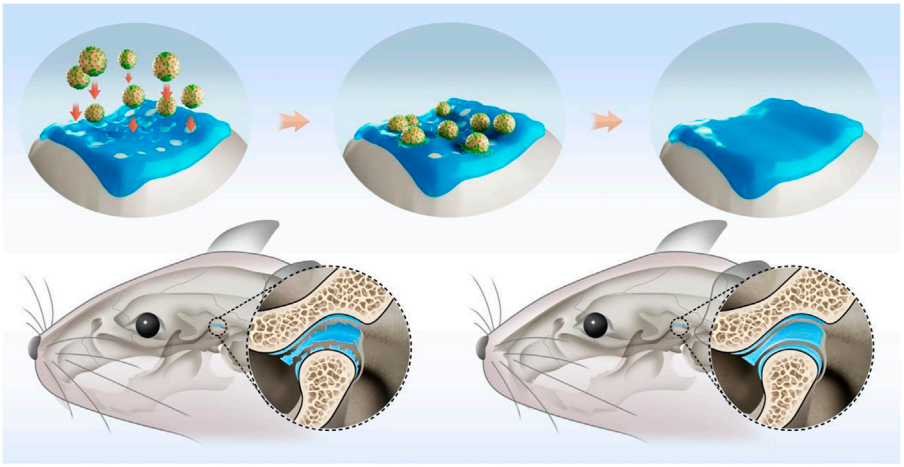

FIGURE 1
Schematic illustration of rBMSCs-coated GelMA microspheres promoting temporomandibular joint arthritis healing. GelMA: gelatin methacrylate; rBMSCs: rat bone marrow mesenchymal stem cells.

αMEM enriched with 10% Fetal bovine serum (Procell). Upon reaching 80% confluency, cells were digested by 0.25% trypsin-EDTA (Procell) for 5 min. The cell suspension was centrifuged at 1,000 rpm for 10 min. After removing the supernatant, gently resuspend the cell and obtain a cell suspension.

2.2 *In vivo* animal experiment

All animal care and experiments were conducted under guidelines stipulated by the Animal Care and Use Committee of Peking University (LA2022175). 6-weeks-old male SD rats were randomly assigned into three groups: the BMSC-coated microspheres group, microspheres group and the control group. Rats were subjected to bilateral temporomandibular joint (TMJ) cavity injection of 50 μl complete adjuvant (Complete Freund's Adjuvant) combined with 10 ng/ml IL-1β (Sigma) to establish the TMJ arthritis model. A week later, 200 μl BMSCs-coated microspheres, 200 μl blank microspheres or 200 μl saline were injected into the TMJ cavity. On day 7 and 14, rats were sacrificed and the defect lesions of condylar cartilage were extracted and fixed in 4% (w/v) paraformaldehyde for 24 h.

2.3 Fabrication of the rBMSCs coated microspheres

2 mg of GelMA microspheres (EFL, Suzhou, China) were added to each well of a 24-well culture plates, and the culture plate was sterilized by ultraviolet light in a biological safety cabinet. 30 min later, 500 μl of culture medium was added to each well of the culture plate. The microspheres in a 37°C incubator for 30 mins for swelling. The morphology of swelling GelMA microspheres were confirmed. (Supplementary Figure S1, Supporting Information). rBMSCs suspension was added to each well and mixed with the microspheres. Observations under optical microscopy showed that rBMSCs were uniformly adherent to the surface of GelMA microspheres after 24 h incubation (Supplementary Figure S2, Supporting Information).

2.4 Scanning electron microscope

2.4.1 Microspheres sample preparation

As described above, rBMSCs coated microspheres were obtained and then wash three times with 4°C prechilled PBS for 5 min each. After aspirating PBS, add 2.5% isopropanol at 4°C for 2 h. Wash three times at 4°C pre-chilled PBS for 5 min each. The microspheres were dehydrated with alcohol gradient (20 mins each in 50, 60, 70, 80, 90% and 30 mins in 100%). Finally, critical point drying was performed. The Hitachi MC1000 Ion Sputter Coater was used to spray gold on the surface of the material for 120 s. Scanning electron microscopy (SEM) images were captured in the field-emission mode using a FEI Quanta 450FEG (USA) at an acceleration voltage of 5 kV.

2.4.2 Animal samples

Extracted temporomandibular joints were dehydrated in an alcohol gradient followed by drying in vacuum. Images were captured in the field-emission mode using a FEI Quanta 450FEG (USA) at an acceleration voltage of 10 kV.

TABLE 1 Primer sequences utilized for qRT-PCR.

Gapdh	TCTCTGCTCCTCCCTGTTC	ACACCGACCTTCACCATCT
Sox9	GAAAGACCACCCCGATTAC	TGAAGATGGCGTTAGGAGA
Col2α1	GACGCCACGCTCAAGTC	TCTCCGCTCTTCCACTCTG
Aggrecan	CCCAAACAGCAGAAACAGC	GGTGGCTCCATTCAGACAA

2.5 Immunocytochemistry

The microspheres coated with BMSCs were seeded in matrigel (Corning) for 12 h, fixed in a 10% (w/v) formalin solution for 10 min, washed with PBS, and permeabilized with 0.1% (w/v) Triton X-100 in PBS for 10 min. Then, the cells were incubated with rabbit anti-SOX9 (ab185966, Abcam) and rhodamine-phalloidin in PBS with 0.3% (w/v) Triton X-100 and 3% (v/v) donkey serum for 2 h. Cell nuclei were stained with 1 μM DAPI for 10 min.

2.6 ELISA

2.6.1 Sample collection

GelMA microspheres were incubated in αMEM or chondrogenesis induction medium for 24 h and then the supernatant was aspirated. 500 μl of PBS was added to each well, and the supernatant was collected for 1, 3, and 6 h, respectively.

2.6.2 ELISA assays

The rat TGF-β ELISA kit (MEIMIAN, Jiangsu, China) was used to assay the TGF-β levels in the sample. 50 μl aliquots of standards with different concentrations of TGF-β were added to each well of a 96-well plate; Then 10 μl of the sample to be tested were added to each well, together with 40 μl of buffer for sample dilution. And the reaction wells were sealed with sealing plates and incubated at 37°C for 30 min. After incubation, the supernatant liquid was then discarded and the sample wells were patted dry on an absorbent paper. Washing with washing solution was repeated five times. In addition to the blank wells, 100 μl of HRP-conjugated reagent was added to each well. Washing was repeated five times. Then, 50 μl of chromogen solution A and 50 μl of chromogen solution B were added into each well and incubated at 37°C for 10 min, in the dark. Then 50 μl of the stop solution was added to each well, and the OD value of each sample was measured at 450 nm with microplate reader (LP400).

2.7 Real-time quantitative reverse transcription PCR

Total RNA was extracted using TRIzol (Thermo Fisher), chloroform and isopropyl alcohol. Reverse transcription was performed using a PCR thermal cycler (Takara). Optical 96-well reaction plates (Thermo Fisher Scientific) and optical adhesive films (Thermo Fisher Scientific) were used for the PCR. The PCR mixture loaded in each well had a final volume of 10 μl, and included 5 μl FastStart Universal SYBR Green Master Mix (Rox), 3 μl RNase-free water, 1 μl template cDNA, and 1 μl primer. PCR amplification was conducted with the following cycling parameters: 15 min at 95°C (heat activation step), followed by 40 cycles of 15 s at 95°C and 1 h at 60°C. Data were analyzed using the standard curve method and normalized to GAPDH mRNA levels.

2.8 Immunohistochemical staining

The dissected temporomandibular joints were embedded in paraffin after decalcification. Serial sections subjected to immunohistochemistry staining by using rabbit anti-rat Sox9 mAb, hematoxylin and eosin. For SOX9 staining, a biotinylated anti-rabbit IgG secondary antibody and streptavidin-Horseradish peroxidase (HRP), followed by colorimetric detection using DAB.

2.9 Microcomputed tomography analysis

After the macro evaluation, the specimens were examined using a Viva40 micro-CT (Scanco Medical AG®). After scanning, the appropriate sagittal and coronal cross-sections of temporomandibular joints were adjusted in the software, and 3D reconstruction was performed on each femur sample. Then a columnar region of interest (ROI) (diameter 3.5 mm, height 1 mm) was selected at the sample defect regeneration area. All analyses were performed on the digitally extracted callus tissue using 3D distance techniques (Scanco® software).

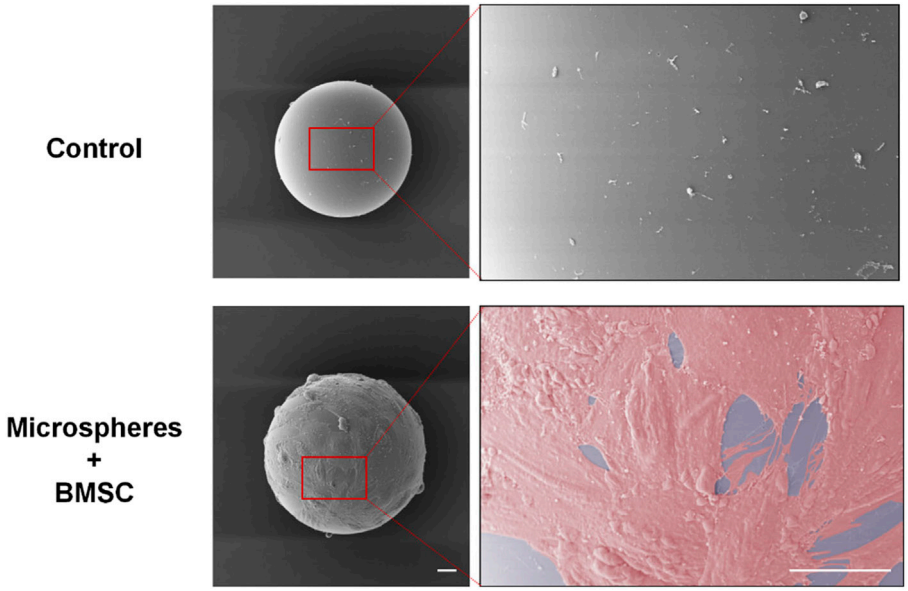

FIGURE 2
The rBMSCs cultured with swelled and disinfected microspheres for 24 h. SEM imaging results showed that BMSCs adhered to the surface of the microspheres and spread well on the hydrogel surface. Scale bars = 20 μm. rBMSCs, Rat bone marrow mesenchymal stem cells.

2.10 Statistical analysis

Numerical data were presented as mean ± SD. To evaluate the significance of observed differences between the experimental groups, the one-way analysis of variance (ANOVA) and Student t-test were used. A value of $p < 0.05$ was considered to be statistically significant.

3 Results and Discussion

3.1 Fabrication of superwettable BMSC-coated microspheres

First, we constructed the GelMA microspheres coated with rBMSCs. GelMA microspheres swelling and the adherent of rBMSCs to the microspheres surface were confirmed (Supplementary Figure S1–3, supporting information). The SEM imaging results showed that BMSCs could tightly adhere to the surface of the microspheres and spread well on the hydrogel surface (Figure 2). The cell spreading also suggested that the GelMA microspheres have good biocompatibility, which could contribute to the formation of BMSC spheroids. The complete coating of microspheres with BMSCs provided a stable phospholipid bilayer at the outermost layer of the microsphere, and its hydrophilic properties are beneficial for adapting to the ultrastructure of the defect surface, thereby enhancing the repair of complex cartilage dysfunction caused by friction, inflammation, and other reasons. It was found that upon contacting the ECM substrate, the diffusion and spreading of stem cell loaded microspheres were similar to that of droplets touching the substrate (Chatzinikolaidou, 2016; Dhamecha et al., 2019). Compared to conventional cell culture methodology, the microspheres have a higher specific surface area, and the multi-microsphere assembly scaffold has an interconnected porous structure, which provides more space for cells to proliferate and differentiate, thereby accurately simulating the natural tissue microenvironment (He et al., 2020; Wang et al., 2023). In our study, by fabricating the BMSC-coated hydrogel microsphere, the biomaterial incorporated with the cell phospholipid bilayer attains superwetting property that facilitates tissue spreading at the ultrastructural level. Furthermore, based on their regulatable and injectable properties, they can be utilized for minimally-invasive treatment of irregular wounds at the ultrastructural level.

3.2 Characterization of the superwettable GelMA microspheres

The molecular and biological characteristics of BMSCs-coated microspheres were analyzed to verify the chondrogenic differentiation potential. GelMA microspheres coated with rat BMSCs were transferred to six-well plates for culture. Observations under optical microscopy showed that after 7 days of culture, the BMSCs-coated microspheres tended to spread on

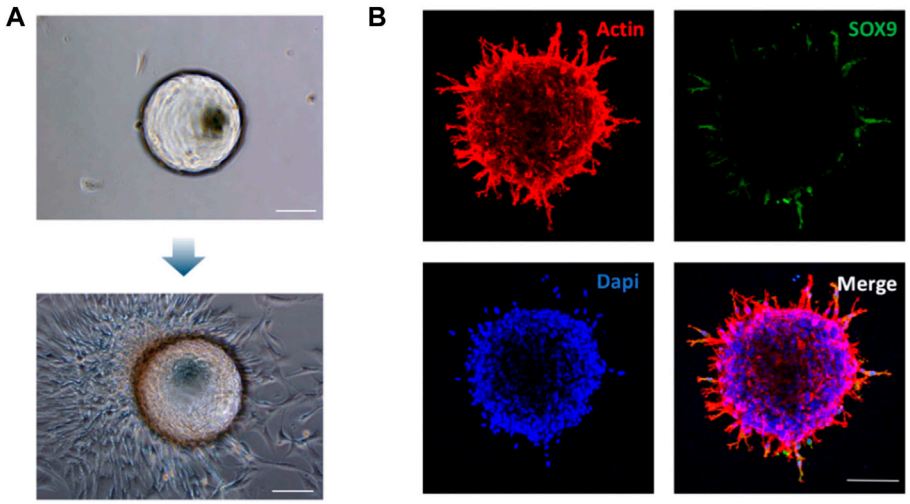

FIGURE 3
Morphological and phenotypic characterization of the rBMSCs-coated GelMA microspheres. **(A)** Identification of rBMSCs spheroid morphology coated on Gelatin Microspheres on day 7. **(B)** Immunocytochemical staining showing the expression of chondrogenic marker Sox9 on the rBMSCs spheroid at 72 h. Scale bars = 100 μm.

the bottom of the culture plates, which resulted in tight adhesion of the microspheres to the bottom of the culture plates (Figure 3A). It is well-known that SOX9 transcription factor is required for chondrocyte differentiation and cartilage formation (Behringer et al., 1999; Lefebvre and Dvir-Ginzberg, 2016). The immunocytochemistry results showed that the chondrogenic marker SOX9 was highly expressed (Figure 3B). These results thus indicated that the rBMSC-coated GelMA microspheres presented good adhesion potential, which could provide a biological basis for the subsequent repair of the tissue defect area. The expression of Sox9 suggested that the rBMSCs-coated GelMA microspheres exhibit chondrogenic potential for cartilage defect repair. The above results thus showed that promotion of the formation of superwettable spheroids by microspheres is an effective and innovative bioengineering strategy to facilitate TMJ cartilage regeneration and treatment of related disorders.

3.3 Sustained release of TGF-β and chondrogenic potential of BMSC-coated gelatin methacryloyl microspheres

There are many technical difficulties faced in the cultivation of cell spheroids (Baraniak and McDevitt, 2012; Chatzinikolaidou, 2016). Microspheres can be assembled into porous scaffolds or simulated biomimetic microenvironments, and have been widely used in cell spheroid formation for tissue engineering and regenerative medicine applications (He et al., 2020). Furthermore, microspheres can be used extensively as delivery vehicles for cells and drugs, particularly in providing more conducive proliferation and differentiation conditions for cellular spheroids, by accurately simulating natural tissue microenvironments. It has been reported that the cell growth factor TGF-β can act synergistically with various cell types to promote the healing of defect sites (Bello et al., 2021). The swelling capacity of GelMA microspheres facilitates the loading and continuous sustained release of cytokines, thereby enabling the cell spheroids to regulate differentiation and tissue repair (Nii, 2021). In this study, similar to the use of PBS, microsphere swelling can also be achieved by soaking GelMA microspheres in culture medium containing recombinant TGFβ. Then the TGF-β release profile was characterized by placing the swelled microspheres into blank PBS. The ELISA results showed that the TGF-β concentration was linearly positively correlated with the OD value (Figure 4A). The OD values corresponding to TGF-β concentrations in the two groups were basically similar during the first 3 h, as compared to the aMEM group, while the concentration of TGF-β released from microspheres in the chondrogenic induction medium group increased significantly by the 6 h timepoint. This results demonstrated that prior to loading with BMSCs, the gelatin-microspheres can be endowed with TGF-β releasing capacity by incubating them with culture medium containing TGF-β. The sustained release of TGF-β from GelMA microspheres would be more conducive to the repair of tissue defects. In order to investigate the sustained TGF-β release effects on the promotion of chondrogenesis, the cell phenotype was examined. The microspheres were assigned to three groups: chondrogenesis-induced adhesion group, αMEM adhesion group and αMEM suspension group. The results showed that the chondrogenesis-

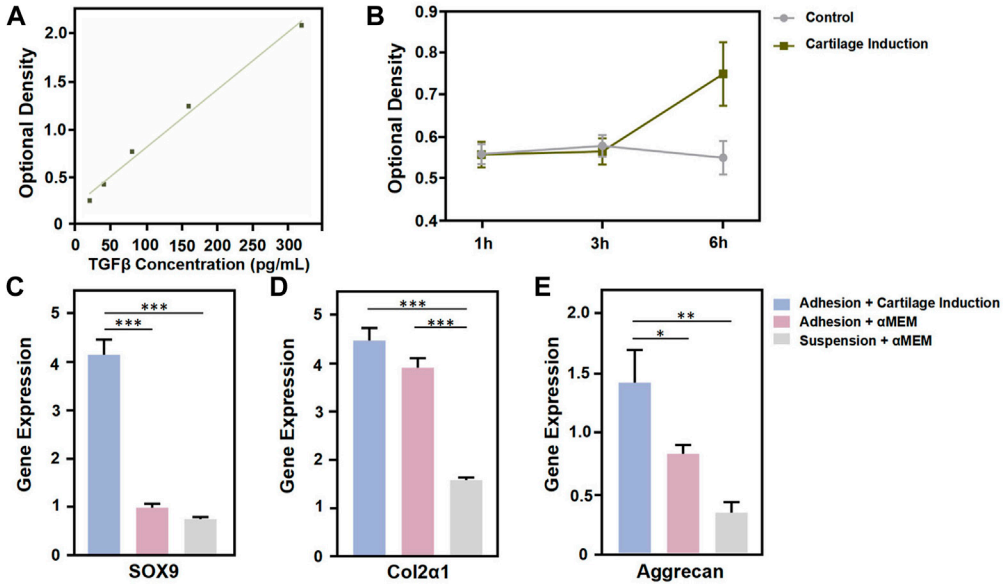

FIGURE 4
Functional characterization of GelMA Microspheres. **(A)** TGF-β concentration was determined using an ELISA kit. **(B)** Detection of TGF-β release in the control and chondrogenic induction medium group at 1 h, 3 h and 6 h. **(C, D, E)** Total RNA from cells coated to microspheres of each group was subjected to quantitative real-time PCR after 72 h culture. Relative expression of the indicated genes against GAPDH is shown. $n = 4$ for each group. (*$p < 0.05$, **$p < 0.01$, ***$p < 0.001$). All the results were repeated three times and represents means ± SD.

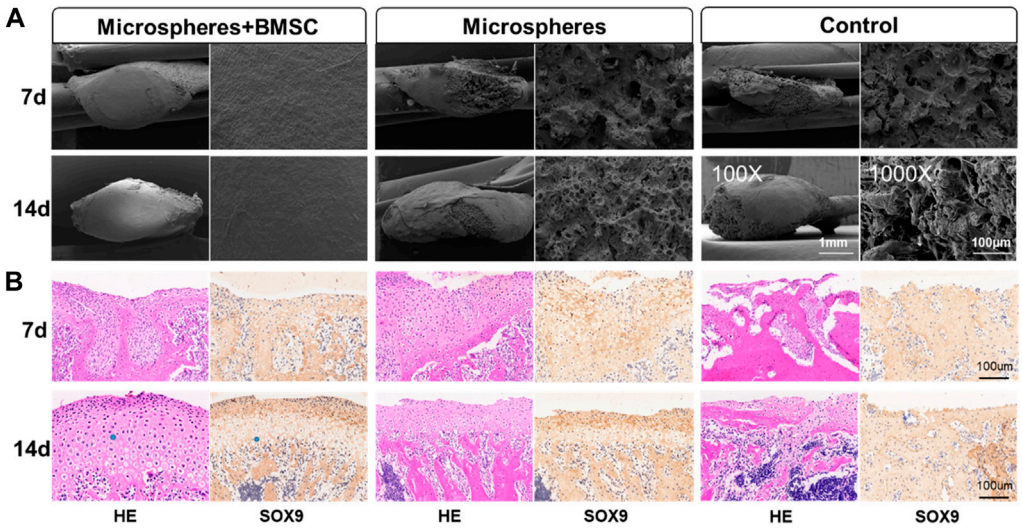

FIGURE 5
rBMSCs-coated GelMA microspheres promote temporomandibular joint arthritis repair. **(A)** SEM of condyle articular surface of TMJ. The microstructure of TMJs were detected by a scanning electron microscope (SEM) under the magnifications: ×100, and ×1,000. **(B)** HE and immunohistochemical staining of TMJ defect area. Data are representative from each group of six rats and all the results were repeated three times. SEM, scanning electron microscope; TMJ, temporomandibular joint.

related gene markers SOX9, Col2α1, and Aggrecan were all highly expressed in the chondrogenesis-induced adhesion group after 72 h culture (Figures 4C–E). These results thus demonstrated that the BMSCs-gelatin microspheres enabled rapid cell spreading, as well as the loading and sustained release of bioactive factors that can contribute to cartilage healing.

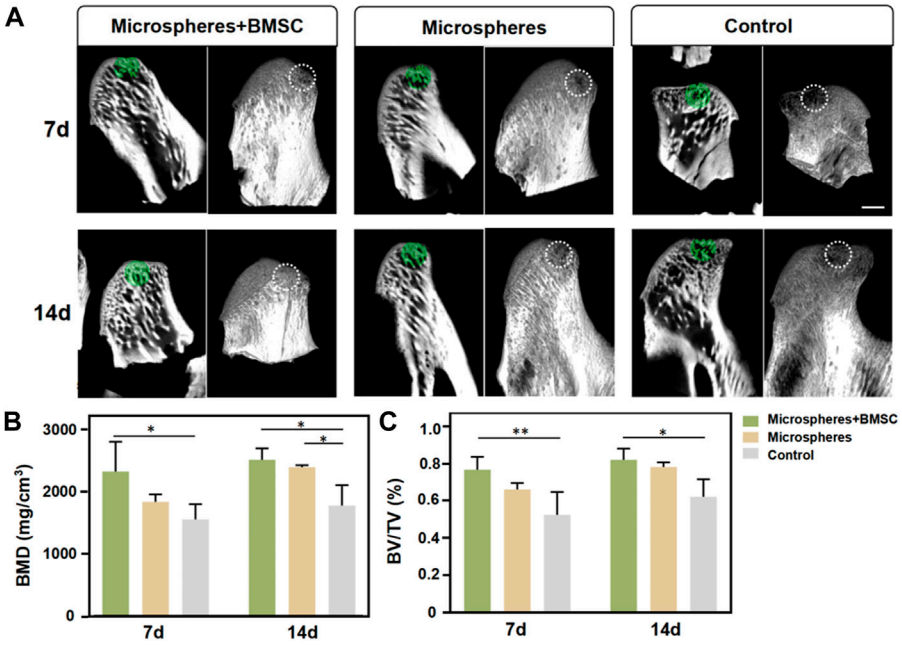

FIGURE 6
Micro-computed tomography (micro-CT) evaluation. **(A)** Micro-CT of temporomandibular joint defect area. **(B)** BMD and **(C)** BV/TV within the ROI were determined. Scale bar = 1 mm. Data are representative from each group of six rats. (*$p < 0.05$, **$p < 0.01$, ***$p < 0.001$).

3.4 rBMSC-coated gelatin methacryloyl microspheres promote cartilage repair in a rat temporomandibular defect model

Utilizing a rat TMJ cartilage defect model, we further verified the function of BMSCs-coated GelMA microspheres in promoting cartilage repair *in vivo*. As shown in Figure 5A, the SEM imaging results indicated that the temporomandibular joint defect in the rBMSCs-coated GelMA microsphere group was almost completely healed, with the healed surface being smoother than the other two groups. HE and immunohistochemical staining results of the tissue sections showed that the formation of new bone and cartilage within the temporomandibular joint of the rBMSCs-coated GelMA microsphere group was significantly better than that of the other two groups (Figure 5B). The results of the Micro-CT also indicated that the rBMSCs-coated GelMA microsphere group had more complete bone cortex and denser trabecular bone within the temporomandibular joint (Figures 6A,B). Overall, chondrogenesis-induced rBMSCs-coated GelMA microspheres displayed positive efficacy in promoting cartilage repair in temporomandibular arthritis. Future research will further explore the underlying mechanisms to lay a solid foundation for clinical applications.

4 Conclusion

In summary, we established cell spheroids with superwetting properties *via* coating of GelMA microspheres with BMSCs. The formation of cell spheroids was better facilitated by using a biocompatible hydrogel as the core. After the cells have spread and were tightly adherent to the surface of the hydrogel sphere, the phospholipid bilayer of the cell membrane conferred on the cell-coated microsphere better hydrophilicity and tissue adhesion properties, thereby facilitating the repair of irregular cartilage defects *in vivo*. At the same time, the inner GelMA microspheres can also be utilized for continuous and sustained release of recombinant TGF-β, which enhanced spheroid differentiation and chondrogenesis. The *in vitro* results showed that the cell spheroids strongly expressed gene markers related to cartilage differentiation. Additionally, the *in vivo* TMJ cartilage defect repair experiments also demonstrated that BMSCs-coated microspheres can effectively promote the repair and reconstruction of irregular cartilage defects within the TMJ area. This study thus provides a novel strategy for fabricating biomaterial-cell construct systems with superwetting microstructures that is beneficial for tissue repair in TMD and other related diseases.

Data availability statement

The original contributions presented in the study are included in the article/Supplementary Material, further inquiries can be directed to the corresponding authors.

Ethics statement

The animal study was reviewed and approved by Animal Care and Use Committee of Peking University.

Author contributions

YY contributed to administrate the project, data curation, investigation, and the original draft. CH contributed to investigation and the original draft. HZ and ZM contributed to data curation, investigation, and the original draft. BH contributed to language editing. TZ contributed to data curation. SJ conceptualized the idea. YW administrated the project, conceptualized the idea, supervised the writing, reviewed, and edited the draft.

Funding

This work was supported by the National Key R&D Program of China (2020YFA0710401), the National Natural Science Foundation of China (82225012, 81922019, 82071161, 82100979) and China Postdoctoral Science Foundation (2022T150024).

Conflict of interest

The authors declare that the research was conducted in the absence of any commercial or financial relationships that could be construed as a potential conflict of interest.

The reviewer CL declared a shared parent affiliation with the authors to the handling editor at the time of review.

Publisher's note

All claims expressed in this article are solely those of the authors and do not necessarily represent those of their affiliated organizations, or those of the publisher, the editors and the reviewers. Any product that may be evaluated in this article, or claim that may be made by its manufacturer, is not guaranteed or endorsed by the publisher.

Supplementary material

The Supplementary Material for this article can be found online at: https://www.frontiersin.org/articles/10.3389/fbioe.2022.1026911/full#supplementary-material

References

Acri, T. M., Shin, K., Seol, D., Laird, N. Z., Song, I., Geary, S. M., et al. (2019). Tissue engineering for the temporomandibular joint. *Adv. Healthc. Mat.* 8 (2), 1801236. doi:10.1002/adhm.201801236

Baraniak, P. R., and McDevitt, T. C. (2012). Scaffold-free culture of mesenchymal stem cell spheroids in suspension preserves multilineage potential. *Cell Tissue Res.* 347 (3), 701–711. doi:10.1007/s00441-011-1215-5

Behringer, R. R., de Crombrugghe, B., Bi, W., Deng, J. M., and Zhang, Z. (1999). Sox9 is required for cartilage formation. *Nat. Genet.* 22 (1), 85–89. doi:10.1038/8792

Bello, A. B., Kim, Y., Park, S., Muttigi, M. S., Kim, J., Park, H., et al. (2021). Matrilin3/TGFβ3 gelatin microparticles promote chondrogenesis, prevent hypertrophy, and induce paracrine release in MSC spheroid for disc regeneration. *npj Regen. Med.* 6 (1), 50. doi:10.1038/s41536-021-00160-0

Cesarz, Z., and Tamama, K. (2016). Spheroid culture of mesenchymal stem cells. *Stem Cells Int.* 2016, 1–11. doi:10.1155/2016/9176357

Chatzinikolaidou, M. (2016). Cell spheroids: The new frontiers in *in vitro* models for cancer drug validation. *Drug Discov. Today* 21 (9), 1553–1560. doi:10.1016/j.drudis.2016.06.024

Cui, H., Wang, W., Shi, L., Song, W., and Wang, S. (2020). Superwettable surface engineering in controlling cell adhesion for emerging bioapplications. *Small Methods* 4 (12), 2000573. doi:10.1002/smtd.202000573

Del Bakhshayesh, A. R., Asadi, N., Alihemmati, A., Tayefi Nasrabadi, H., Montaseri, A., Davaran, S., et al. (2019). An overview of advanced biocompatible and biomimetic materials for creation of replacement structures in the musculoskeletal systems: Focusing on cartilage tissue engineering. *J. Biol. Eng.* 13 (1), 85. doi:10.1186/s13036-019-0209-9

Dhamecha, D., Movsas, R., Sano, U., and Menon, J. U. (2019). Applications of alginate microspheres in therapeutics delivery and cell culture: Past, present and future. *Int. J. Pharm. X.* 569, 118627. doi:10.1016/j.ijpharm.2019.118627

Douezan, S., Guevorkian, K., Naouar, R., Dufour, S., Cuvelier, D., and Brochard-Wyart, F. (2011). Spreading dynamics and wetting transition of cellular aggregates. *Proc. Natl. Acad. Sci. U. S. A.* 108 (18), 7315–7320. doi:10.1073/pnas.1018057108

Han, Y., Li, X., Zhang, Y., Han, Y., Chang, F., and Ding, J. (2019). Mesenchymal stem cells for regenerative medicine. *Cells* 8 (8), 886. doi:10.3390/cells8080886

He, Q., Zhang, J., Liao, Y., Alakpa, E. V., Bunpetch, V., Zhang, J., et al. (2020). Current advances in microsphere based cell culture and tissue engineering. *Biotechnol. Adv.* 39, 107459. doi:10.1016/j.biotechadv.2019.107459

Jiang, S., Li, H., Zeng, Q., Xiao, Z., Zhang, X., Xu, M., et al. (2021). The dynamic counterbalance of RAC1-YAP/OB-cadherin coordinates tissue spreading with stem cell fate patterning. *Adv. Sci. (Weinh).* 8 (10), 2004000. doi:10.1002/advs.202004000

Jiang, X., Yang, F., and Guo, Z. (2022). Superwetting surfaces for filtration separation of high-viscosity raw petroleum/water mixtures. *J. Mat. Chem. A Mat.* 1 (27), 14273–14292. doi:10.1039/d2ta03444a

Kim, W., Gwon, Y., Park, S., Kim, H., and Kim, J. (2023). Therapeutic strategies of three-dimensional stem cell spheroids and organoids for tissue repair and regeneration. *Bioact. Mat.* 19, 50–74. doi:10.1016/j.bioactmat.2022.03.039

Langhans, S. A. (2018). Three-Dimensional *in vitro* cell culture models in drug discovery and drug repositioning. *Front. Pharmacol.* 9, 6. doi:10.3389/fphar.2018.00006

Lefebvre, V., and Dvir-Ginzberg, M. (2016). SOX9 and the many facets of its regulation in the chondrocyte lineage. *Connect. Tissue Res.* 58 (1), 2–14. doi:10.1080/03008207.2016.1183667

Lukin, I., Erezuma, I., Maeso, L., Zarate, J., Desimone, M. F., Al-Tel, T. H., et al. (2022). Progress in gelatin as biomaterial for tissue engineering. *Pharmaceutics* 14 (6), 1177. doi:10.3390/pharmaceutics14061177

Neto, A. I., Demir, K., Popova, A. A., Oliveira, M. B., Mano, J. F., and Levkin, P. A. (2016). Fabrication of hydrogel particles of defined shapes using Superhydrophobic-Hydrophilic micropatterns. *Adv. Mat.* 28 (35), 7613–7619. doi:10.1002/adma.201602350

Nii, T. (2021). Strategies using gelatin microparticles for regenerative therapy and drug screening applications. *Molecules* 26 (22), 6795. doi:10.3390/molecules26226795

Stevens, K. R., Einerson, N. J., Burmania, J. A., and Kao, W. J. (2002). *In vivo* biocompatibility of gelatin-based hydrogels and interpenetrating networks. *J. Biomaterials Sci. Polym. Ed.* 13 (12), 1353–1366. doi:10.1163/15685620260449741

Sulaiman, S. B., Idrus, R. B. H., and Hwei, N. M. (2020). Gelatin microsphere for cartilage tissue engineering: Current and future strategies. *Polym. (Basel).* 12 (10), 2404. doi:10.3390/polym12102404

Tarafder, S., Koch, A., Jun, Y., Chou, C., Awadallah, M. R., and Lee, C. H. (2016). Micro-precise spatiotemporal delivery system embedded in 3D printing for complex tissue regeneration. *Biofabrication* 8 (2), 025003. doi:10.1088/1758-5090/8/2/025003

Wadhwa, S., and Kapila, S. (2008). TMJ disorders: Future innovations in diagnostics and therapeutics. *J. Dent. Educ.* 72 (8), 930–947. doi:10.1002/j.0022-0337.2008.72.8.tb04569.x

Wang, Z., Zhang, X., Ding, Y., Ren, Z., and Wei, D. (2023). Natural biopolyester microspheres with diverse structures and surface topologies as micro-devices for biomedical applications. *Smart Mater. Med.* 4, 15–36. doi:10.1016/j.smaim.2022.07.004

Zheng, L., Pi, C., Zhang, J., Fan, Y., Cui, C., Zhou, Y., et al. (2018). Aberrant activation of latent transforming growth factor-beta initiates the onset of temporomandibular joint osteoarthritis. *Bone Res.* 6, 26. doi:10.1038/s41413-018-0027-6

frontiers | Frontiers in Bioengineering and Biotechnology

TYPE Mini Review
PUBLISHED 29 September 2022
DOI 10.3389/fbioe.2022.1032640

OPEN ACCESS

EDITED BY
Jingxin Meng,
Technical Institute of Physics and Chemistry (CAS), China

REVIEWED BY
Fan Xia,
The Seventh Affiliated Hospital of Sun Yat-sen University, China
Zhuo Wang,
Beijing University of Chemical Technology, China

*CORRESPONDENCE
Li-Ping Xu,
xuliping@ustb.edu.cn
Xueji Zhang,
zhangxueji@szu.edu.cn

SPECIALTY SECTION
This article was submitted to Biomaterials, a section of the journal Frontiers in Bioengineering and Biotechnology

RECEIVED 31 August 2022
ACCEPTED 13 September 2022
PUBLISHED 29 September 2022

CITATION
Yang Y, Zhu Q, Xu L-P and Zhang X (2022), Bioinspired liquid-infused surface for biomedical and biosensing applications. *Front. Bioeng. Biotechnol.* 10:1032640. doi: 10.3389/fbioe.2022.1032640

Bioinspired liquid-infused surface for biomedical and biosensing applications

Yuemeng Yang[1], Qinglin Zhu[1], Li-Ping Xu[1]* and Xueji Zhang[2]*

[1]Beijing Key Laboratory for Bioengineering and Sensing Technology, School of Chemistry and Biological Engineering, University of Science and Technology Beijing, Beijing, China, [2]School of Biomedical Engineering, Health Science Center, Shenzhen University, Shenzhen, China

Nature always inspires us to develop advanced materials for diverse applications. The liquid-infused surface (LIS) inspired by Nepenthes pitcher plants has aroused broad interest in fabricating anti-biofouling materials over the past decade. The infused liquid layer on the solid substrate repels immiscible fluids and displays ultralow adhesion to various biomolecules. Due to these fascinating features, bioinspired LIS has been applied in biomedical-related fields. Here, we review the recent progress of LIS in bioengineering, medical devices, and biosensing, and highlight how the infused liquid layer affects the performance of medical materials. The prospects for the future trend of LIS are also presented.

KEYWORDS

liquid-infused surface, bioengineering, medical devices, biosensing, anti-bioadhesion, liquid-repellency, self-healing

1 Introduction

Through evolution and natural selection, many organisms can accommodate the complex living environment by developing specific wettability surfaces that have unique functions in reproduction and predation (Liu et al., 2017). For instance, benefiting from lubricating water on the peristome with highly wettable microstructure, Nepenthes pitcher plants can provide the precarious foothold, thus forcing insects to aquaplane into its pitcher-like stomach (Bohn and Federle, 2004). By mimicking the wetting phenomenon of Nepenthes pitcher plant surface, tremendous efforts have been devoted to developing the liquid-infused surface (LIS) (Wong et al., 2011). Bioinspired LIS is a promising dynamic liquid surface fabricated by infusing the barrier liquid (lubricant) into various structured substrates (Wong et al., 2011; Liu et al., 2013; Cui et al., 2015; Shi et al., 2016). Once the surface energy of substrate and barrier liquid are matched, the infused liquid can be confined on the surface through capillary and van der Waals forces, creating a stable and homogenous liquid interface (Maji et al., 2020).

According to the characteristics of solid substrate, LIS can be classified into slippery liquid-infused porous surface (SLIPS), liquid-infused organogel surface (LIOS) and patterned liquid-infused surface (PLIS) (Figure 1). SLIPS proposed by Aizenberg's group creates a molecularly slippery and omniphobic liquid interface by infusing a

low surface energy liquid into the porous substrate (Wong et al., 2011). Due to the stable yet dynamic liquid interface, SLIPS can repel most immiscible liquids, even physiological fluids. And SLIPS has exhibited stable anti-adhesion capability towards nucleic acids, proteins, bacteria, cells, and marine organisms, and can function even at high pressure (Glavan et al., 2014; Amini et al., 2017; Kovalenko et al., 2017). Another type of LIS is liquid-infused organogel surface (LIOS) (Salbaum et al., 2021). The barrier liquid swells the organogel matrix through diffusion and forms a thin liquid layer that can be replenished from the liquid-storage compartments of organogel bulk (Cui et al., 2015). Compared with SLIPS, LIOS exhibits better self-healing ability due to the self-replenishment and the intrinsic properties of organogel. Besides SLIPS and LIOS, to endow LIS with new functions, patterned liquid-infused surface (PLIS) was also developed by combining the slippery liquid-infused surface with other wetting states on the same surface. On PLIS, selective regional adhesion of biomolecules can be achieved (Shi et al., 2016; Lei et al., 2020).

No matter which solid substrates were used, the main advantages include stable liquid-repellency, excellent anti-bioadhesion and self-healing ability (Figure 1). The distinctive interface is critical to these properties of LIS. The defect-free and molecularly slippery liquid interface eliminates defects that could become nucleation sites for undesired bio-adhesion and lead to pinning liquid. Furthermore, the fluidity of the infused liquid endows the LIS with self-healing, resulting in the long-term stability of various properties of the LIS. These features make LIS an emerging function material with great potential in the healthcare-related fields, such as medical tubing or implants, surgical devices, cell culture, and biomarker detection (Wu et al., 2019; Wang et al., 2022; Yuan et al., 2022). This mini-review summarized the development of LIS with its emerging applications in healthcare-related fields, including bioengineering, medical devices, and biosensing (Figure 1). Due to the length limitations, we mainly focus on how the unique liquid interface of LIS inspires and influences the development of new medical materials rather than a comprehensive review of this wide field. Finally, the challenges and prospects of LIS in biomedical and biosensing applications are also presented.

2 Bioinspired LIS for bioengineering

Understanding the interaction mechanisms between biological systems and artificial materials is crucial to the development of bioengineering. Benefiting from the slippery liquid interface, LIS displays unique effects on manipulating interfacial behaviors of organisms, such as adhesion, growth, and migration (Mackie et al., 2019). Hence, LIS is promising to unravel the complexity of biological systems and open up new possibilities in bioengineering applications. This section presents recent studies of LIS as a laboratory platform for regulating biofilm formation, cell culture, and tissue engineering.

2.1 LIS for regulating biofilm formation

Planktonic bacteria always tend to adhere and proliferate on the interface, forming sessile biofilm, which makes eradicating bacterial infections more challenging (Dunne, 2002). Recently, LIS has been shown to significantly reduce surface biofilm coverage of various bacteria under dynamic and static culture conditions (Zhu Y. et al., 2022).

The low biofilm coverage can be ascribed to the inhibited early adhesion of bacteria on the liquid interface because firm adhesion is the first critical step in biofilm formation (Dunne, 2002). During exposure to the external environment, through maintenance of infused liquid layer at the material surface, LIS restricts the direct contact of bacteria with the material and provides a weakly adhesive interface for bacteria. (Epstein et al., 2012; Doll et al., 2019). Therefore, the integrity of infused liquid layer is crucial for the anti-biofilm properties of LIS. Doll et al. evaluated the correlation between LIS anti-adhesion performance and liquid layer stability by screening four different structures and five different lubricants (Doll et al., 2017). The effect of different LIS on biofilm coverage can be observed by confocal laser scanning microscopy (CLSM). Only the spike-structure surface with maximum roughness combined with lubricants of intermediate viscosity could maintain a stable and intact liquid layer underwater, resulting the minimal biofilm coverage. In addition, although LIS was covered with biofilm in a static culture of *Botryococcus braunii*, the biofilm did not firmly adhere to the liquid interface and can be removed easily (Howell et al., 2014).

Although LIS shows an excellent anti-biofilm adhesion effect against various bacteria, the biofilm formation process is still complex and species-dependent (Kovalenko et al., 2017). It was reported that drug-resistant *Pseudomonas aeruginosa* exhibited higher biofilm coverage on LIS (Li et al., 2013). Recently, Levkin's group has employed the PLIS for bacterial culture to investigate the mechanisms of biofilm formation at the liquid interface (Bruchmann et al., 2017; Lei et al., 2019; Lei et al., 2020). On PLIS, bacteria did not only grow on isolated hydrophilic spots but spread over the liquid-infused periphery. Biofilm bridges connecting adjacent biofilm microclusters can be observed using fluorescence microscopy. Based on this observation, Lei et al. further studied the bacterial spreading and biofilm formation process of a wide variety of bacteria on PLIS. It was demonstrated that extracellular DNA and nutrients are essential for bacteria to overcome repulsion and biofilm formation on the liquid interface (Lei et al., 2019).

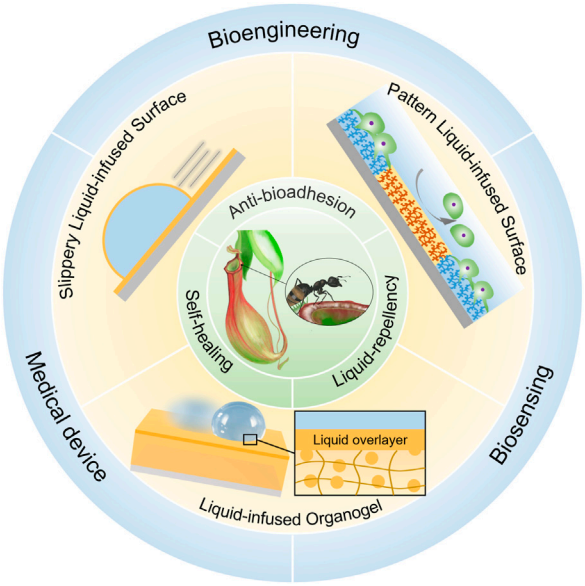

FIGURE 1
The recent progress of liquid-infused surface (LIS) inspired by Nepenthes pitcher plants. Due to their intrinsic advantages, including liquid-repellency, anti-bioadhesion, and self-healing properties, several functional LIS materials have been applied in bioengineering, medical device, and biosensing.

Due to the significant role of LIS in the formation process of bacterial biofilms, LIS provides a valuable platform for revealing structure–function relationships in biofilms and studying interactions of biofilms with various medically relevant materials.

2.2 LIS for cells and tissues regulation

Similar to bacterial adhesion, the LIS can reduce cell adhesion on materials by maintaining a stable barrier liquid layer. It was demonstrated that LIS could prevent or reduce the diverse types of cells adhering despite varying cell properties (Yao et al., 2014; Schlaich et al., 2018; Yong et al., 2018). In addition, a small number of cells settled on the LIS have a rounder morphology that can be removed by weak shear forces, indicating that cells do not firmly adhere to LIS and remain resting (Ueda and Levkin, 2013; Leslie et al., 2014; Yuan et al., 2015). It is worth noting that LIS is not cytotoxic and has no effect on external cell viability by examining macrophage viability, phagocytosis, and bactericidal activity (Chen et al., 2017). Based on these features, LIS has displayed potential for spatially and temporally controlling the behaviors of cells.

PLIS which combines the different functional domains on the same surface has been used to create cell microarrays. Our group fabricated PLIS on superhydrophilic–superhydrophobic patterned substrate by infusing silicone oil on the hydrophobic part (Shi et al., 2016). Stable NIH/3T3 cell arrays formed even after incubating under water for 12 h, which demonstrated that the silicone oil-infused barrier exhibited the long-term cell repellency (Figure 2A). While under the same culture condition, cell migration could be observed on superhydrophobic regions due to the poor stability of the air-assisted superhydrophobic barrier. Moreover, the co-culture of multiple cells can be realized on PLIS, since silicone oil-infused barrier can effectively avoid cells cross-contamination.

In addition to repelling individual cells, LIS is effective in preventing the adhesion of cell tissues (Zhang et al., 2018). The strategy used for cell sheet tissue engineering *via* LIS has been revealed (Juthani et al., 2016). The mesenchymal stem cells can grow and proliferate to form cell sheets on LIS by depositing the fibronectin layer. In the presence of excess silicone oil on LIS, the cell sheets can be easily detached due to the negligible adhesion of the cell sheet to the underlying substrate.

LIS has been validated as a controllable medium for manipulating organism behaviors at the liquid-liquid interface. In addition, by further careful design, this system also could emerge as a promising laboratory tool to study cell-to-cell interactions, tissue engineering, cell propagation, drug evaluation and other applications.

3 Bioinspired LIS for medical devices

Biological fouling on medical device surfaces has become a severe and persistent issue, which often causes device failure and severe clinical complications. However, most materials with anti-biofouling properties cannot meet the requirements of long-time use in complex environments, which can be ascribed to the decomposition or damage of functional molecules that buttress anti-adhesion properties (Banerjee et al., 2011; Falde et al., 2016; Erathodiyil et al., 2020).

Recently, bioinspired LIS has been investigated and used in medical devices to resist the fouling of undesired proteins, cells, platelets, and pathogens. As discussed in Section 2, biofouling cannot attach to LIS and can be subject to passive removal. Compared with other solid antifouling surfaces, LIS demonstrates its superiority in long-term stability. Epstein et al. presented that LIS prevents diverse biofilm accumulation over 1 week or longer under low flow conditions, which is 35 times greater than the best-case scenario for PEG surfaces (Epstein et al., 2012). And similar effects were also observed in the culture of HeLa cells (Ueda and Levkin, 2013). Long-term anti-adhesion properties of LIS can be ascribed to the self-healing of its liquid interface. Therefore, various attempts have been made to fabricate medical devices with LIS coating to relieve clinical complications caused by biofouling.

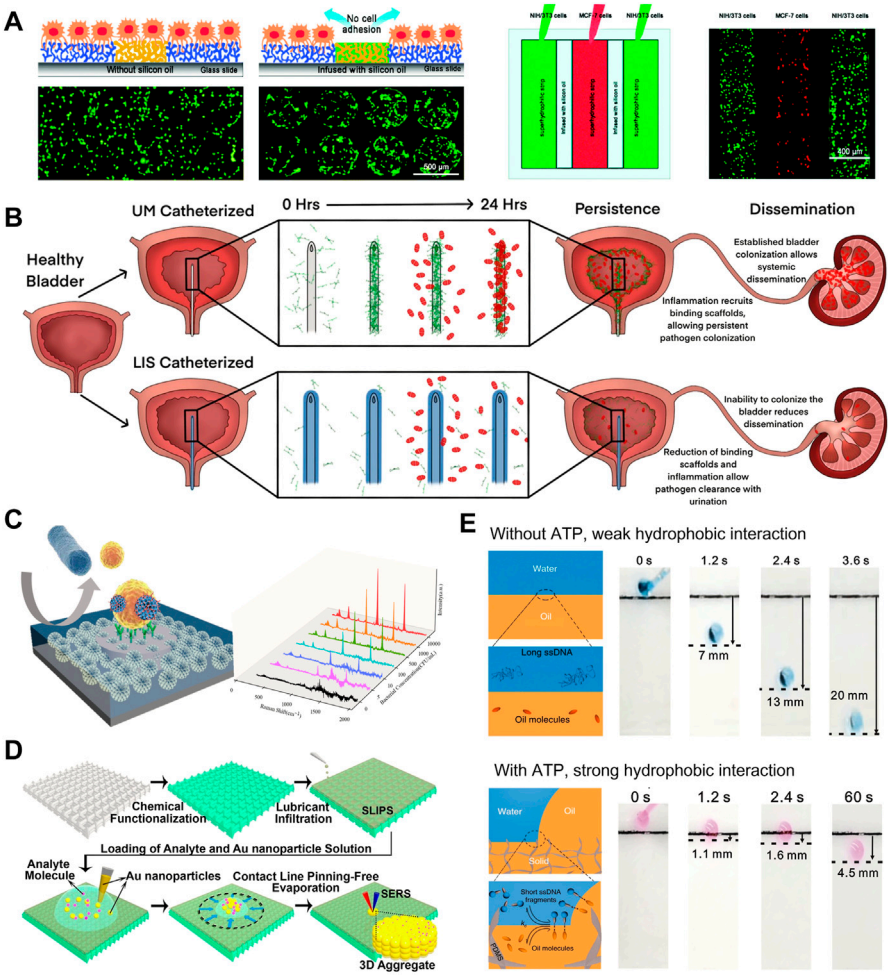

FIGURE 2
(A) The cell repellency of silicone-oil-infused barriers is superior to air-assisted superhydrophobic surfaces. PLIS can be used to culture different types of cells on the same substrate. (Shi et al., 2016). Copyright 2016, Wiley-VCH **(B)** In the mouse model of urinary tract infection, liquid-infused silicone-catheter decreased bacterial colonization on the catheter surface and within the bladder, enabling effective intervention for urinary tract infections (Andersen et al., 2022). Copyright 2022, eLife Sciences Publications Ltd **(C)** Patterned liquid-infused nanocoating that combined the hydrophobic anti-bioadhesion periphery and hydrophilic sensing regions can be used for sensitive bacterial SERS detection (Wang et al., 2022). Copyright 2022, American Chemical Society **(D)** Due to the liquid-repellency, analytes can be enriched on LIS by evaporation of droplets, enhancing subsequent SERS signal (Yang et al., 2016). Copyright 2016, The Authors, Published by the National Academy of Sciences **(E)** The sliding angle of RCA droplet on LIS can be controlled by the chain length of ssDNA. The sliding behavior of the droplet has been used as the output signal to detect ATP (Gao et al., 2020). Copyright 2020, Nature Publishing Group.

Various biomedical implants have been developed to replace a missing biological structure or support a damaged biological structure, together with multiple functions including medical monitoring and drug delivery. However, biofouling on implants in the complex human body environment leads to the failure of implants and many complications. Thus, the fabrication of biomedical devices with the stable anti-biofouling coating is urgent. Leslie et al. designed a PVC medical tubing in which the interior is immobilized with a liquid layer, which could remains patency for 8 h without heparin (anticoagulant), similar to other heparin-based coatings (Leslie et al., 2014). In another study, liquid-infused silicone-catheters reduces uropathogens colonization on the its surface by disrupting fibrinogen deposition (Andersen et al., 2022). As shown in Figure 2B, in the mouse model, LIS inhibited the colonization within bladder and systemic dissemination of uropathogens, enabling effective intervention for urinary tract infections. In addition to the remarkable results of medical tubing, the subcutaneous implants with infused liquid coating demonstrate outstanding potential *in vivo*. Upon implantation in rats, SLIPS-modified implant limits bacterial infection and vastly reduces local inflammation (Chen et al., 2017). Furthermore, the LIS has been integrated into surgical and diagnostic devices. The scalpel blades with LIS coating showed

lower blood and *E. coli* adhesions after simple washing, thus avoiding cross-contamination (Tesler et al., 2015). Constructing LIS coatings electrosurgical instruments significantly reduce the adhesion of soft tissues, leading to a much smaller charring wound (Zhang et al., 2018).

In recent years, by integrating the functional molecules on the liquid-infused surface, LIS has been endowed with the ability to intervene in outside environment actively (Manna et al., 2016; Badv et al., 2019b; Wang et al., 2021). Didar's group reported a liquid-infused vascular graft with built-in bio-functional nanoprobes that promote implant endothelialization without compromising the repellency properties of LIS (Badv et al., 2019a). In addition, LIS-coated implants combined with controlled release of anti-inflammatory or antimicrobial drugs have also been developed to increase the longevity and safety of devices (Kratochvil et al., 2016; Douglass et al., 2021).

In general, materials with LIS coating are promising candidates to enhance the anti-biofouling properties of medical devices, which reduce the risk of inflammation and infection in clinical treatment, and avoid complications caused by the systemic administration of drugs. Moreover, LIS also exhibits excellent material compatibility. It can be directly combined with many medical-grade material surfaces permitting the retention of specific material properties such as strength or transparency. Despite the promising results of LIS *in vivo*, the cytotoxicity and the detrimental downstream effects of LIS should be thoroughly evaluated in long-term practice.

4 Bioinspired LIS for emerging biosensing applications

As the crucial part of biosensors, the biosensing interface strongly influences the analytical performance of biosensors (Xu et al., 2019; Zhu Q. et al., 2022). Constructing an optimal interface to achieve sensitive detection and ultratrace analysis is one of the challenges in biosensing fabrication. Recently, leveraging the unique liquid interface, LIS has exhibited immense potential as a promising biosensing interface in detecting biomarkers in complex samples.

Undesirable nonspecific adhesion is one of the obstacles preventing the application of biosensors in the detection of real samples. The emergence of patterned liquid-infused surface (PLIS) provides an ideal approach to enhance the specific recognition of targets. Yousefi et al. used the patterned biofunctional liquid-infused surface to eliminate the adhesion of interfering substances in milk at the target recognition interface, thereby lowing the detection limits of *E. coli* by 4-fold (Yousefi et al., 2021). For more complex interference systems that accompany continuous blood clotting, LIS can effectively prevent clot formation and adhesion, directly detecting interleukin six in non-anticoagulated whole blood (Shakeri et al., 2020). PLIS was also used to enhance the identification efficiency of probes and sample enrichment. Our group developed a patterned liquid-infused nanocoating that combined the hydrophobic anti-bioadhesion periphery and hydrophilic sensing regions to achieve *Staphylococcus aureus* detection (Wang et al., 2022). As shown in Figure 2C, the hydrophobic periphery prevents bacteria adhesion by maintaining a stable liquid layer. Meanwhile, the hydrophilic sensing regions capture bacteria through specific interactions between probes and target bacteria. PLIS reduced bacterial loss in the non-detection region, enabling the ultrasensitive surface-enhanced Raman scattering (SERS) detection of *Staphylococcus aureus* with the detection limits of 2.6 CFU/ml.

In addition to the anti-adhesion, the liquid-repellency of the LIS surface has also been utilized to enhance biosensing. Taking advantage of the weakly interacting interface, the three-phase contact line of droplet/air/liquid-infused surface is almost pining-free. Yang et al. developed a perfluorinated liquid-infused slippery surface platform to control the evaporation of droplets for SERS signal enhancement (Yang et al., 2016). During the evaporation process, the droplet contact angle remains constant, while the contact area decreases gradually. Therefore, as shown in Figure 2D, LIS contributes to the enrichment of analyte molecules in a small area after droplet evaporation, thus realizing ultrasensitive SERS detection. Notably, benefiting from the omniphobicity of perfluorinated liquid, the analytes in low surface energy droplets can also be enriched on LIS. According to this strategy, LIS was also employed in the signal amplification process of aggregation-induced emission (AIE) probes (Wu et al., 2021). Furthermore, LIS can be integrated into a microfluidic system for near-lossless liquid manipulation and complex assays (Wang et al., 2018; Li et al., 2020).

The sliding behavior of droplets on LIS is very sensitive to the composition of the droplets (Wang et al., 2019; Gao et al., 2020). Gao et al. demonstrated that the sliding speed of droplets on organogel infused by n-decane can be regulated by changing the chain length of single-stranded DNA (ssDNA) within the droplets (Gao et al., 2018). This work adopted ATP-induced roll-circle amplification (RCA) to generate long ssDNA. For droplets without ATP, the short ssDNA in the droplet act as the hydrotrope to increase the hydrophobic interactions between droplet and organic liquid, thus restricting the droplet sliding (Figure 2E). On the contrary, long ssDNA produced by ATP-induced RCA does not affect the sliding of droplets owing to the reduction of exposed hydrophobic groups (Figure 2E). Based on this principle, by regulating the amount of ssDNA, the sliding behavior of the droplets has been used as the output signal for detecting ATP, miRNA, and thrombin.

According to the above discussion, the introduction of LIS facilitates the development of biosensors by leaps and bounds. The anti-bioadhesion and liquid-repellency properties of LIS offer more possibilities for detection in a wide range of biological samples. With continuous efforts in detection technology, LIS is expected to be widely used as an emerging biosensing interface to improve biosensing performance.

5 Conclusion and prospects

LIS has attracted increasing attention from the academy and industry as a liquid interface. In this mini-review, we have summarized the recent progress of LIS in biomedical-related fields, including bioengineering, biomedical devices, and biosensing. As the novel coating, numerous spin-off companies aim to translate the LIS technology into a wide range of medical products. Despite the impressive progress, LIS is still in its infancy, and some critical challenges and issues still need to be resolved.

1) The understanding of the dynamic wetting process of droplets on LIS at the molecular level is vague. The anti-adhesion process of protein, cells, and bacteria should be revealed at the microscopic scale. A comprehensive interaction mechanism is helpful in material design and will pave the way for future applications (Daniel et al., 2017).
2) The durability of the infused liquid is another challenge for LIS toward practical application. All the properties of LIS rely on the stability of the liquid layer. The loss of infused liquid through various routes is inevitable. Therefore, LIS with long-term stability under biomedical conditions is an essential direction for future research (Baumli et al., 2021).
3) Biosecurity and biocompatibility of infused liquid should be explored intensively. Although the commonly used infused liquid such as silicone oils and fluorocarbons are considered non-cytotoxic, the effects of LIS on cell metabolism, cell differentiation, and the human immune system should be thoroughly evaluated in the long-term practice (Mackie et al., 2019).
4) Finally, with the development of infused liquid, LIS with multiple functions/properties, such as stimuli-responsive liquid-infused surface and liquid crystal-infused surface, have attracted great interest. More attention should be paid to these LIS to enable the more complicated tasks in biomedical and biosensing applications (Lou et al., 2020; Xu et al., 2021).

In brief, there are still some shortcomings of LIS in practical applications. We hope this mini-review will contribute to the advancement of novel materials and sensing interfaces in medical fields.

Author contributions

YY prepared the original manuscript. YY, QZ and LX revised the manuscript. LX conceptualized and reviewed the manuscript. XZ supervised the manuscript. All authors listed have made a substantial, direct, and intellectual contribution to the work and approved it for publication.

Funding

The work is supported by National Natural Science Foundation of China (21890742), National Key Research and Development Program of China (2019YFA0709300), Beijing Municipal Science and Technology Commission (2182036).

Conflict of interest

The authors declare that the research was conducted in the absence of any commercial or financial relationships that could be construed as a potential conflict of interest.

Publisher's note

References

Amini, S., Kolle, S., Petrone, L., Ahanotu, O., Sunny, S., Sutanto, C. N., et al. (2017). Preventing mussel adhesion using lubricant-infused materials. *Science* 357 (6352), 668–673. doi:10.1126/science.aai8977

Andersen, M. J., Fong, C., La Bella, A. A., Molina, J. J., Molesan, A., Champion, M. M., et al. (2022). Inhibiting host-protein deposition on urinary catheters reduces associated urinary tract infections. *Elife* 11, e75798. doi:10.7554/eLife.75798

Badv, M., Alonso-Cantu, C., Shakeri, A., Hosseinidoust, Z., Weitz, J. I., and Didar, T. F. (2019). Biofunctional lubricant-infused vascular grafts functionalized with silanized bio-inks suppress thrombin generation and promote endothelialization. *ACS Biomater. Sci. Eng.* 5 (12), 6485–6496. doi:10.1021/acsbiomaterials.9b01062

Badv, M., Weitz, J. I., and Didar, T. F. (2019). Lubricant-infused PET grafts with built-in biofunctional nanoprobes attenuate thrombin generation and promote targeted binding of cells. *Small* 15 (51), e1905562. doi:10.1002/smll.201905562

Banerjee, I., Pangule, R. C., and Kane, R. S. (2011). Antifouling coatings: Recent developments in the design of surfaces that prevent fouling by proteins, bacteria, and marine organisms. *Adv. Mat.* 23 (6), 690–718. doi:10.1002/adma.201001215

Baumli, P., D'Acunzi, M., Hegner, K. I., Naga, A., Wong, W. S. Y., Butt, H. J., et al. (2021). The challenge of lubricant-replenishment on lubricant-impregnated surfaces. *Adv. Colloid Interface Sci.* 287, 102329. doi:10.1016/j.cis.2020.102329

Bohn, H. F., and Federle, W. (2004). Insect aquaplaning: Nepenthes pitcher plants capture prey with the peristome, a fully wettable water-lubricated anisotropic surface. *Proc. Natl. Acad. Sci. U. S. A.* 101 (39), 14138–14143. doi:10.1073/pnas.0405885101

Bruchmann, J., Pini, I., Gill, T. S., Schwartz, T., and Levkin, P. A. (2017). Patterned SLIPS for the formation of arrays of biofilm microclusters with defined geometries. *Adv. Healthc. Mat.* 6 (1), 1601082. doi:10.1002/adhm.201601082

Chen, J., Howell, C., Haller, C. A., Patel, M. S., Ayala, P., Moravec, K. A., et al. (2017). An immobilized liquid interface prevents device associated bacterial infection *in vivo*. *Biomaterials* 113, 80–92. doi:10.1016/j.biomaterials.2016.09.028

Cui, J., Daniel, D., Grinthal, A., Lin, K., and Aizenberg, J. (2015). Dynamic polymer systems with self-regulated secretion for the control of surface properties and material healing. *Nat. Mat.* 14 (8), 790–795. doi:10.1038/nmat4325

Daniel, D., Timonen, J. V. I., Li, R., Velling, S. J., and Aizenberg, J. (2017). Oleoplaning droplets on lubricated surfaces. *Nat. Phys.* 13 (10), 1020–1025. doi:10.1038/nphys4177

Doll, K., Fadeeva, E., Schaeske, J., Ehmke, T., Winkel, A., Heisterkamp, A., et al. (2017). Development of laser-structured liquid-infused titanium with strong biofilm-repellent properties. *ACS Appl. Mat. Interfaces* 9 (11), 9359–9368. doi:10.1021/acsami.6b16159

Doll, K., Yang, I., Fadeeva, E., Kommerein, N., Szafranski, S. P., Bei der Wieden, G., et al. (2019). Liquid-infused structured titanium surfaces: Antiadhesive mechanism to repel Streptococcus oralis biofilms. *ACS Appl. Mat. Interfaces* 11 (26), 23026–23038. doi:10.1021/acsami.9b06817

Douglass, M., Hopkins, S., Chug, M. K., Kim, G., Garren, M. R., Ashcraft, M., et al. (2021). Reduction in foreign body response and improved antimicrobial efficacy via silicone-oil-infused nitric-oxide-releasing medical-grade cannulas. *ACS Appl. Mat. Interfaces* 13 (44), 52425–52434. doi:10.1021/acsami.1c18190

Dunne, W. M., Jr. (2002). Bacterial adhesion: Seen any good biofilms lately? *Clin. Microbiol. Rev.* 15 (2), 155–166. doi:10.1128/CMR.15.2.155-166.2002

Epstein, A. K., Wong, T. S., Belisle, R. A., Boggs, E. M., and Aizenberg, J. (2012). Liquid-infused structured surfaces with exceptional anti-biofouling performance. *Proc. Natl. Acad. Sci. U. S. A.* 109 (33), 13182–13187. doi:10.1073/pnas.1201973109

Erathodiyil, N., Chan, H.-M., Wu, H., and Ying, J. Y. (2020). Zwitterionic polymers and hydrogels for antibiofouling applications in implantable devices. *Mat. TodayKidlingt.* 38, 84–98. doi:10.1016/j.mattod.2020.03.024

Falde, E. J., Yohe, S. T., Colson, Y. L., and Grinstaff, M. W. (2016). Superhydrophobic materials for biomedical applications. *Biomaterials* 104, 87–103. doi:10.1016/j.biomaterials.2016.06.050

Gao, Z. F., Liu, R., Wang, J., Dai, J., Huang, W.-H., Liu, M., et al. (2018). Controlling droplet motion on an organogel surface by tuning the chain length of DNA and its biosensing application. *Chem* 4 (12), 2929–2943. doi:10.1016/j.chempr.2018.09.028

Gao, Z. F., Liu, R., Wang, J., Dai, J., Huang, W. H., Liu, M., et al. (2020). Manipulating the hydrophobicity of DNA as a universal strategy for visual biosensing. *Nat. Protoc.* 15 (2), 316–337. doi:10.1038/s41596-019-0235-6

Glavan, A. C., Martinez, R. V., Subramaniam, A. B., Yoon, H. J., Nunes, R. M. D., Lange, H., et al. (2014). Omniphobic "RF paper" produced by silanization of paper with fluoroalkyltrichlorosilanes. *Adv. Funct. Mat.* 24 (1), 60–70. doi:10.1002/adfm.201300780

Howell, C., Vu, T. L., Lin, J. J., Kolle, S., Juthani, N., Watson, E., et al. (2014). Self-replenishing vascularized fouling-release surfaces. *ACS Appl. Mat. Interfaces* 6 (15), 13299–13307. doi:10.1021/am503150y

Juthani, N., Howell, C., Ledoux, H., Sotiri, I., Kelso, S., Kovalenko, Y., et al. (2016). Infused polymers for cell sheet release. *Sci. Rep.* 6 (1), 26109–9. doi:10.1038/srep26109

Kovalenko, Y., Sotiri, I., Timonen, J. V. I., Overton, J. C., Holmes, G., Aizenberg, J., et al. (2017). Bacterial interactions with immobilized liquid layers. *Adv. Healthc. Mat.* 6 (15), 1600948doi:10.1002/adhm.201600948

Kratochvil, M. J., Welsh, M. A., Manna, U., Ortiz, B. J., Blackwell, H. E., and Lynn, D. M. (2016). Slippery liquid-infused porous surfaces that prevent bacterial surface fouling and inhibit virulence phenotypes in surrounding planktonic cells. *ACS Infect. Dis.* 2 (7), 509–517. doi:10.1021/acsinfecdis.6b00065

Lei, W., Bruchmann, J., Ruping, J. L., Levkin, P. A., and Schwartz, T. (2019). Biofilm bridges forming structural networks on patterned lubricant-infused surfaces. *Adv. Sci.* 6 (13), 1900519. doi:10.1002/advs.201900519

Lei, W., Krolla, P., Schwartz, T., and Levkin, P. A. (2020). Controlling geometry and flow through bacterial bridges on patterned lubricant-infused surfaces (pLIS). *Small* 16 (52), 2004575. doi:10.1002/smll.202004575

Leslie, D. C., Waterhouse, A., Berthet, J. B., Valentin, T. M., Watters, A. L., Jain, A., et al. (2014). A bioinspired omniphobic surface coating on medical devices prevents thrombosis and biofouling. *Nat. Biotechnol.* 32 (11), 1134–1140. doi:10.1038/nbt.3020

Li, H., Shkolyar, E., Wang, J., Conti, S., Pao, A. C., Liao, J. C., et al. (2020). SLIPS-LAB-A bioinspired bioanalysis system for metabolic evaluation of urinary stone disease. *Sci. Adv.* 6 (21), eaba8535. doi:10.1126/sciadv.aba8535

Li, J., Kleintschek, T., Rieder, A., Cheng, Y., Baumbach, T., Obst, U., et al. (2013). Hydrophobic liquid-infused porous polymer surfaces for antibacterial applications. *ACS Appl. Mat. Interfaces* 5 (14), 6704–6711. doi:10.1021/am401532z

Liu, H., Zhang, P., Liu, M., Wang, S., and Jiang, L. (2013). Organogel-based thin films for self-cleaning on various surfaces. *Adv. Mat.* 25 (32), 4477–4481. doi:10.1002/adma.201301289

Liu, M., Wang, S., and Jiang, L. (2017). Nature-inspired superwettability systems. *Nat. Rev. Mat.* 2 (7), 17036. doi:10.1038/natrevmats.2017.36

Lou, X., Huang, Y., Yang, X., Zhu, H., Heng, L., and Xia, F. (2020). External stimuli responsive liquid-infused surfaces switching between slippery and nonslippery states: Fabrications and applications. *Adv. Funct. Mat.* 30 (10), 1901130. doi:10.1002/adfm.201901130

Mackie, G., Gao, L., Yau, S., Leslie, D. C., and Waterhouse, A. (2019). Clinical potential of immobilized liquid interfaces: Perspectives on biological interactions. *Trends Biotechnol.* 37 (3), 268–280. doi:10.1016/j.tibtech.2018.08.003

Maji, K., Das, A., Hirtz, M., and Manna, U. (2020). How does Chemistry influence liquid wettability on liquid-infused porous surface? *ACS Appl. Mat. Interfaces* 12 (12), 14531–14541. doi:10.1021/acsami.9b22469

Manna, U., Raman, N., Welsh, M. A., Zayas-Gonzalez, Y. M., Blackwell, H. E., Palecek, S. P., et al. (2016). Slippery liquid-infused porous surfaces that prevent microbial surface fouling and kill non-adherent pathogens in surrounding media: A controlled release approach. *Adv. Funct. Mat.* 26 (21), 3599–3611. doi:10.1002/adfm.201505522

Salbaum, T., Galvan, Y., Haumann, M., Wasserscheid, P., Zarraga, R., and Vogel, N. (2021). Enduring liquid repellency through slippery ionic liquid-infused organogels. *J. Mat. Chem. A* 9 (4), 2357–2366. doi:10.1039/d0ta10237g

Schlaich, C., Fan, Y., Dey, P., Cui, J., Wei, Q., Haag, R., et al. (2018). Universal, surfactant-free preparation of hydrogel beads on superamphiphobic and slippery surfaces. *Adv. Mat. Interfaces* 5 (7), 1701536. doi:10.1002/admi.201701536

Shakeri, A., Jarad, N. A., Terryberry, J., Khan, S., Leung, A., Chen, S., et al. (2020). Antibody micropatterned lubricant-infused biosensors enable sub-picogram immunofluorescence detection of interleukin 6 in human whole plasma. *Small* 16 (45), 2003844. doi:10.1002/smll.202003844

Shi, W., Xu, T., Xu, L. P., Chen, Y., Wen, Y., Zhang, X., et al. (2016). Cell micropatterns based on silicone-oil-modified slippery surfaces. *Nanoscale* 8 (44), 18612–18615. doi:10.1039/c6nr07498g

Tesler, A. B., Kim, P., Kolle, S., Howell, C., Ahanotu, O., and Aizenberg, J. (2015). Extremely durable biofouling-resistant metallic surfaces based on electrodeposited nanoporous tungstite films on steel. *Nat. Commun.* 6, 8649. doi:10.1038/ncomms9649

Ueda, E., and Levkin, P. A. (2013). Micropatterning hydrophobic liquid on a porous polymer surface for long-term selective cell-repellency. *Adv. Healthc. Mat.* 2 (11), 1425–1429. doi:10.1002/adhm.201300073

Wang, J., Gao, W., Zhang, H., Zou, M., Chen, Y., and Zhao, Y. (2018). Programmable wettability on photocontrolled graphene film. *Sci. Adv.* 4 (9), eaat7392. doi:10.1126/sciadv.aat7392

Wang, J., Huang, Y., You, K., Yang, X., Song, Y., Zhu, H., et al. (2019). Temperature-driven precise control of biological droplet's adhesion on a slippery surface. *ACS Appl. Mat. Interfaces* 11 (7), 7591–7599. doi:10.1021/acsami.8b21088

Wang, Y., Du, X., Wang, X., Yan, T., Yuan, M., Yang, Y., et al. (2022). Patterned liquid-infused nanocoating integrating a sensitive bacterial sensing ability to an antibacterial surface. *ACS Appl. Mat. Interfaces* 14, 23129–23138. doi:10.1021/acsami.1c24821

Wang, Z., Yi, B., Wu, M., Lv, D., He, M. L., Liu, M., et al. (2021). Bioinspired supramolecular slippery organogels for controlling pathogen spread by respiratory droplets. *Adv. Funct. Mat.* 31 (34), 2102888. doi:10.1002/adfm.202102888

Wong, T.-S., Kang, S. H., Tang, S. K. Y., Smythe, E. J., Hatton, B. D., Grinthal, A., et al. (2011). Bioinspired self-repairing slippery surfaces with pressure-stable omniphobicity. *Nature* 477 (7365), 443–447. doi:10.1038/nature10447

Wu, F., Huang, Y., Yang, X., Hu, J. J., Lou, X., Xia, F., et al. (2021). Tunning intermolecular interaction of peptide-conjugated AIEgen in nano-confined space for quantitative detection of tumor marker secreted from cells. *Anal. Chem.* 93 (48), 16257–16263. doi:10.1021/acs.analchem.1c04422

Wu, S., Zhou, L., Chen, C., Shi, L. A., Zhu, S., Zhang, C., et al. (2019). Photothermal actuation of diverse liquids on an Fe3O4-doped slippery surface for electric switching and cell culture. *Langmuir* 35 (43), 13915–13922. doi:10.1021/acs.langmuir.9b02068

Xu, T., Xu, L. P., Zhang, X., and Wang, S. (2019). Bioinspired superwettable micropatterns for biosensing. *Chem. Soc. Rev.* 48 (12), 3153–3165. doi:10.1039/c8cs00915e

Xu, Y., Rather, A. M., Yao, Y., Fang, J. C., Mamtani, R. S., Bennett, R. K. A., et al. (2021). Liquid crystal-based open surface microfluidics manipulate liquid mobility and chemical composition on demand. *Sci. Adv.* 7 (40), eabi7607. doi:10.1126/sciadv.abi7607

Yang, S., Dai, X., Stogin, B. B., and Wong, T. S. (2016). Ultrasensitive surface-enhanced Raman scattering detection in common fluids. *Proc. Natl. Acad. Sci. U. S. A.* 113 (2), 268–273. doi:10.1073/pnas.1518980113

Yao, X., Dunn, S. S., Kim, P., Duffy, M., Alvarenga, J., and Aizenberg, J. (2014). Fluorogel elastomers with tunable transparency, elasticity, shape-memory, and antifouling properties. *Angew. Chem. Int. Ed.* 53 (17), 4418–4422. doi:10.1002/anie.201310385

Yong, J., Huo, J., Yang, Q., Chen, F., Fang, Y., Wu, X., et al. (2018). Femtosecond laser direct writing of porous network microstructures for fabricating super-slippery surfaces with excellent liquid repellence and anti-cell proliferation. *Adv. Mat. Interfaces* 5 (7), 1701479. doi:10.1002/admi.201701479

Yousefi, H., Samani, S. E., Khan, S., Prasad, A., Shakeri, A., Li, Y., et al. (2021). LISzyme biosensors: DNAzymes embedded in an anti-biofouling platform for hands-free real-time detection of bacterial contamination in milk. *ACS Nano* 16 (1), 29–37. doi:10.1021/acsnano.1c05766

Yuan, S., Luan, S., Yan, S., Shi, H., and Yin, J. (2015). Facile fabrication of lubricant-infused wrinkling surface for preventing thrombus formation and infection. *ACS Appl. Mat. Interfaces* 7 (34), 19466–19473. doi:10.1021/acsami.5b05865

Yuan, S., Sun, X., Yan, S., Luan, S., Song, L., and Yin, J. (2022). Slippery 3-dimensional porous bioabsorbable membranes with anti-adhesion and bactericidal properties as substitute for vaseline gauze. *Colloids Surfaces B Biointerfaces* 212, 112341. doi:10.1016/j.colsurfb.2022.112341

Zhang, P., Liu, G., Zhang, D., and Chen, H. (2018). Liquid-infused surfaces on electrosurgical instruments with exceptional antiadhesion and low-damage performances. *ACS Appl. Mat. Interfaces* 10 (39), 33713–33720. doi:10.1021/acsami.8b13373

Zhu Q, Q., Yang, Y., Gao, H., Xu, L.-P., and Wang, S. (2022). Bioinspired superwettable electrodes towards electrochemical biosensing. *Chem. Sci.* 13 (18), 5069–5084. doi:10.1039/d2sc00614f

Zhu Y, Y., McHale, G., Dawson, J., Armstrong, S., Wells, G., Han, R., et al. (2022). Slippery liquid-like solid surfaces with promising antibiofilm performance under both static and flow conditions. *ACS Appl. Mat. Interfaces* 14 (5), 6307–6319. doi:10.1021/acsami.1c14533

frontiers | Frontiers in Bioengineering and Biotechnology

TYPE Original Research
PUBLISHED 06 October 2022
DOI 10.3389/fbioe.2022.1011851

OPEN ACCESS

EDITED BY
Hongliang Liu,
Yantai University, China

REVIEWED BY
Qiong Jia,
Jilin University, China
Baiqing Yuan,
Ludong University, China

*CORRESPONDENCE
Xiuling Li,
lixiuling@dicp.ac.cn
Xinmiao Liang,
liangxm@dicp.ac.cn

†These authors have contributed equally to this work

SPECIALTY SECTION
This article was submitted to Biomaterials, a section of the journal Frontiers in Bioengineering and Biotechnology

RECEIVED 04 August 2022
ACCEPTED 22 August 2022
PUBLISHED 06 October 2022

CITATION
Shang D, Chen C, Dong X, Cui Y, Qiao Z, Li X and Liang X (2022), Simultaneous enrichment and sequential separation of glycopeptides and phosphopeptides with poly-histidine functionalized microspheres. *Front. Bioeng. Biotechnol.* 10:1011851. doi: 10.3389/fbioe.2022.1011851

Simultaneous enrichment and sequential separation of glycopeptides and phosphopeptides with poly-histidine functionalized microspheres

Danyi Shang[1,2†], Cheng Chen[1,2†], Xuefang Dong[1], Yun Cui[1,3], Zichun Qiao[1,2], Xiuling Li[1,3*] and Xinmiao Liang[1,3*]

[1]Key Laboratory of Separation Science for Analytical Chemistry, Dalian Institute of Chemical Physics, Dalian, China, [2]University of Chinese Academy of Sciences, Beijing, China, [3]Ganjiang Chinese Medicine Innovation Center, Nanchang, China

Protein phosphorylation and glycosylation coordinately regulate numerous complex biological processes. However, the main methods to simultaneously enrich them are based on the coordination interactions or Lewis acid-base interactions, which suffer from low coverage of target molecules due to strong intermolecular interactions. Here, we constructed a poly-histidine modified silica (SiO_2@Poly-His) microspheres-based method for the simultaneous enrichment, sequential elution and analysis of phosphopeptides and glycopeptides. The SiO_2@Poly-His microspheres driven by hydrophilic interactions and multiple hydrogen bonding interactions exhibited high selectivity and coverage for simultaneous enrichment of phosphopeptides and glycopeptides from 1,000 molar folds of bovine serum albumin interference. Furthermore, "on-line deglycosylation" strategy allows sequential elution of phosphopeptides and glycopeptides, protecting phosphopeptides from hydrolysis during deglycosylation and improving the coverage of phosphopeptides. The application of our established method to HT29 cell lysates resulted in a total of 1,601 identified glycopeptides and 694 identified phosphopeptides, which were 1.2-fold and 1.5-fold higher than those obtained from the co-elution strategy, respectively. The SiO_2@Poly-His based simultaneous enrichment and sequential separation strategy might have great potential in co-analysis of PTMs-proteomics of biological and clinic samples.

KEYWORDS

poly-histidine, simultaneous enrichment, sequential elution, phosphopeptides, glycopeptides

1 Introduction

Protein post-translational modifications (PTMs) refer to covalent addition of functional groups to specific amino acid residues in a protein (Macek et al., 2019). There are 469 types of PTMs have been reported (Prabakaran et al., 2012). These PTMs not only affect protein three-dimensional structures but also jointly regulate numerous biological processes *in vivo* (Aebersold et al., 2018; Harmel and Fiedler, 2018). It is reported that multiple PTMs occurring on a protein often work interdependently, which is termed as "crosstalk" (Venne et al., 2014; Cuijpers and Vertegaal, 2018). Protein phosphorylation and glycosylation, two of the most ubiquitous and important PTMs, undergo crosstalk and play crucial roles in numerous cellular processes (Vu et al., 2018). Deregulation of crosstalk between phosphorylation and glycosylation has been implicated in many severe human diseases, such as autoimmune disease, Alzheimer's disease and cancers (Jennewein and Alter, 2017; Aasen et al., 2018; Wu et al., 2019). The PTMs crosstalk is regulated in an antagonistic or synergetic manner. For example, the glycosylation of epidermal growth factor receptor (EGFR) inhibits the abnormal phosphorylation of EGFR in TKI-resistant lung cancer cell line (Yen et al., 2015); the N-glycosylation at N359 ameliorated the hyperphosphorylated and aggregated of tau (Losev et al., 2021). Shedding light on PTMs crosstalk will help us better understand etiology and provide novel targets for drug therapy. Therefore, it is necessary to simultaneously study the protein glycosylation and phosphorylation and reveal the crosstalk between them at the molecular level.

Mass spectrometry (MS) is a mainstreamed analysis method in proteomics (Calderon-Celis et al., 2018; Xiao et al., 2018). However, direct analysis of protein PTMs crosstalk on the proteome level is quite challenging owing to the low abundance of PTM peptides, as well as significant background interference deriving from complex mixture in the biosamples. Besides, some clinic or biological samples are too precious to suffer from more than one pretreatment and co-analyze different types of protein PTMs is required to obtain as much information as possible in one sample pretreatment. Hence, it is urgently needed to develop strategies to simultaneously and selectively enrich PTM peptides prior to MS analysis.

In recent years, several methods have been developed to simultaneously enrich glycopeptides and phosphopeptides, which mainly include metal oxide affinity chromatography (MOAC, represented by TiO_2) (Luo et al., 2019; Chu et al., 2022; He et al., 2022), immobilized metal ion affinity chromatography (IMAC, typical example is Ti^{4+}-IMAC) (Wang et al., 2019; Zhang et al., 2020; Zheng et al., 2020; Huang et al., 2021) and hydrophilic interaction liquid chromatography (HILIC) (Lu et al., 2020; Luo et al., 2021). For MOAC, TiO_2 was firstly used to simultaneously enrich phosphopeptides and glycopeptides in our group, based on the Lewis acid-base interaction between the PTM peptides and the adsorbents (Yan et al., 2010). However, the interaction between PTM peptides and TiO_2 is too strong to elute multi-phosphopeptides or multiply sialylated glycopeptides (Lu et al., 2020). In order to improve the enrichment coverage of the absorbent, other hydrophilic functional groups have been introduced to the TiO_2 surface (Sun et al., 2019; Sun et al., 2020; Yi et al., 2020). IMAC utilizes the chelation interaction between the immobilized metal cations and the PTM peptides. However, the unmodified peptides with multiple acidic amino acids could be captured by IMAC materials, interfering the PTM peptides enrichment. To improve enrichment selectivity, hydrophilic groups are combined with metal cations in the functional materials for simultaneously enriching glycopeptides and phosphopeptides, such as hydrophilic chitosan and phytic acid. (Zou et al., 2017; Hong et al., 2018). Both MOAC- and IMAC-based simultaneous enrichment materials utilize the strong interaction between materials and PTM peptides. While HILIC materials based on the multiple hydrogen bonding interactions provide an alternative for simultaneous enrichment of phosphopeptides and glycopeptides (Lu et al., 2020; Luo et al., 2021). Benefited from the multiple hydrogen bonding interactions between adsorbent and target peptides, the HILIC-based simultaneous enrichment materials have high selectivity and recovery. Encouraged by these studies, it is worthwhile to develop more tunable materials based on multi-hydrogen bonding for the simultaneous enrichment of phosphopeptides and glycopeptides.

Concerning to the routine protocol for glycosylation site analysis, the enriched N-linked glycopeptides need to be deglycosylated with PNGase F in alkaline aqueous solution before MS analysis. But phosphopeptides may be hydrolyzed under this pH condition (Li et al., 2014), which could lead to loss of some phosphorylation information. Some researchers utilized the method of sequential PTM peptides enrichment to simultaneously enrich glycopeptides and phosphopeptides (Cho et al., 2019; Andaluz Aguilar et al., 2020; Zhou et al., 2020). First, one type of PTM peptides was enriched by the first enrichment strategy from peptide mixtures, and then flow-through from the first enrichment is enriched for another type of PTM peptides using another enrichment method. Although the sequential PTM peptides enrichment methods can separate glycopeptides and phosphopeptides and avoid this problem, the large amounts of starting samples and the cumbersome operation process are required. Therefore, it will be ideal that simultaneous enrichment and sequential separation of phosphopeptides and glycopeptides can be performed with the same materials.

Histidine (His) is a naturally amphiphilic amino acid, which may interact glycopeptides through multiple hydrogen bonding and electrostatic interactions (Dong et al., 2017). Unlike other amino acids, His has a unique imidazole side chain structure, which interact glycan through CH-π interactions (Kiessling and Diehl, 2021). Moreover, the hydrogen bonding interactions between His and phosphate groups have been reported between DNA and His

(Chattopadhyay et al., 2016), between triosephosphate isomerase and His (Lodi and Knowles, 1991), and between nucleic acids and His (Chou et al., 2014). Encouraged by these reports, we prepared poly-histidine modified silica (SiO_2@Poly-His) microspheres for efficiently co-enriching glycopeptides and phosphopeptides. Meanwhile, we developed an on-line deglycosylation strategy for sequential elution of glycopeptides and phosphopeptides. Firstly, the glycopeptides and phosphopeptides were simultaneously captured by SiO_2@Poly-His microspheres; then the glycopeptides that absorbed on microspheres were on-line deglycosylated with PNGase F; the deglycosylated peptides and phosphopeptides were sequentially eluted, and analyzed by MS respectively. The enrichment performance of the SiO_2@Poly-His microspheres to glycopeptides and phosphopeptides were systematically evaluated, and the optimal conditions for the entire protocol were optimized. Finally, the SiO_2@Poly-His microspheres were used to simultaneously enrich phosphopeptides and glycopeptides from the tryptic digests of standard proteins and from a complex HT29 cell lysate.

2 Materials and methods

2.1 Reagents

Acrylated histidine (AA-His, >95%) was obtained from China-Peptides Corp. (Shanghai, China). Acetonitrile (ACN, HPLC-grade), formic acid (FA, 98%), acetic acid (AA, 99.7%), urea (>99.0%), 2,2′-azobis (2-methylpropionamide) dihydrochloride (AIBA, 97%), 4-cyano-4-(phenylcarbonothioylthio)pentanoic acid (CPADB, 97%), ammonium hydroxide ($NH_3{\cdot}H_2O$, 28%–30% NH_3), ammonium bicarbonate (NH_4HCO_3, 99.0%), iodoacetamide (IAA, 99.0%), DL-dithiothreitol (DTT, 99.0%), ammonium acetate (CH_3COONH_4, 99.0%), glycolic acid (99.0%), [Glu1]-Fibrinopeptide B human (GFB), bovine serum albumin (BSA, >98%), α-casein (>98%), bovine fetuin (>99.9%) and trypsin (>98%) were purchased from Sigma Aldrich (St Louis, United States). N-hydroxysuccinimide (NHS; 98%) and dicyclohexylcarbodiimide (DCC; 99%) were bought from Shanghai Macklin Biochemical Co., Ltd. (Shanghai, China). Acetone (≥99.7%), and ethyl alcohol (≥99.7%) was purchased from Sinopharm Chemical Reagent Co., Ltd. (Beijing, China). Standard phosphopeptide (with sequence of HS*PIAPSSPSPK) was obtained from Qiangyao Biotechnology Co., Ltd. (Shanghai, China). PNGase F was purchased from New England Biolabs (Ipswich, United States). Radioimmunoprecipitation (RIPA) lysis buffer was purchased from Beyotime Biotechnology (Shanghai, China). Bicinchoninic acid (BCA) protein assay kit was purchased from Thermo Fisher scientific (CA, United States). TiO_2 was bought from GL Sciences (Tokyo, Japan). C18HC material and amino silica (5 μm, 300 Å) materials were purchased from ACCHROM (Wenling, China). Water was purified by a Milli-Q system (Millipore, Milford, United States).

2.2 Instruments

Scanning electron microscopy (SEM) image was taken on a JEM-7800F (JEOL Company, Japan) instrument. Zeta potential was measured by Malvern Zetasizer Nano ZS (Malvern, United Kingdom) at 25°C. N_2 adsorption–desorption measurement was obtained using QUADRASORB SI (QuantaChrome, United States). Thermogravimetric analysis was performed using a STA449F5 thermostar (NETZSCH, Germany). Protein/peptide concentration was determined by a Multiskan™ FC microplate reader (Thermo Scientific, United States). Infrared spectroscopy was measured by HYPERION 3000 (Bruker Optics, Germany). Standard protein digests were qualitatively analyzed using nano-electrospray ionization quadrupole time-of-flight mass spectrometry (nano-ESI-Q-TOF MS) (Waters, United Kingdom). The peptides extracted from the HT29 cell line were qualitatively analyzed using an EASY-nLC 1,200 liquid chromatography system and an Orbitrap Exploris 480 mass spectrometer (Thermo Scientific, United States).

2.3 Synthesis of poly histidine modified silica microspheres

The CPADB functionalized silica microspheres (SiO_2-CPADB) were synthesis according to the reported literature (Khani et al., 2017). AA-His (128 mg, 0.6 mmol), SiO_2-CPADB with surface density of 0.30 mmol/g (0.1 g, 0.03 mmol), ethanol (2.2 ml), and 10 mM sodium acetate solution (2.2 ml), AIBA initiator (0.03 mmol) with a ratio between species of [monomer]:[CTA]:[initiator] = 20:1:1 were added to a round bottomed flask. The mixture was degassed through three freeze pump-thaw cycles, injected with nitrogen, and then the unit was placed in an oil bath with agitation at 55°C for 72 h. The obtained silica was washed three times with water before being centrifuged at 5,000 rpm for 3 minutes and dried for storage.

2.4 Retention of glycopeptides on SiO_2@Poly-His microspheres

1 mg of SiO_2@Poly-His or SiO_2-NH_2 pellets were packed into GELoader tips and 10 μg of the bovine fetuin digests that redissolved in 40 μl of 80% acetonitrile (ACN)/1% formic acid (FA) was loaded into the microcolumn. The microcolumn was subsequently eluted with 80% ACN/1% FA (40 μl), 70% ACN/1% FA (40 μl), 60% ACN/1% FA (40 μl), 50% ACN/1% FA (40 μl),

respectively. The eluates were collected and analyzed by nano-ESI-Q-TOF MS.

2.5 Investigation of phosphopeptides retention mechanism

2.5.1 Effect of acetonitrile content on retention of phosphopeptides

1 mg of SiO_2@Poly-His microspheres were packed into GELoader tips and 2 μg of the α-casein digests that redissolved in 40 μl of 80% ACN/1% FA was loaded into the microcolumn. The microcolumn was subsequently eluted with 80% ACN/1% FA (40 μl), 70% ACN/1% FA (40 μl), 60% ACN/1% FA (40 μl), 50% ACN/1% FA (40 μl), 40% ACN/1% FA (40 μl), respectively. The eluates were collected and analyzed by nano-ESI-Q-TOF MS.

2.5.2 Effect of FA content on retention of phosphopeptides

1 mg of SiO_2@Poly-His microspheres were packed into GELoader tips and 2 μg of the α-casein digests that redissolved in 40 μl of 70% ACN/0.1% FA was loaded into the microcolumn. The microcolumn was subsequently eluted with 70% ACN/0.1% FA (40 μl), 70% ACN/0.5% FA (40 μl), 70% ACN/1% FA (40 μl), 70% ACN/2% FA (40 μl), 70% ACN/5% FA, respectively. The eluates were collected and analyzed by nano-ESI-Q-TOF MS.

2.6 Enrichment of glycopeptides and phosphopeptides from standard proteins

2.6.1 Glycopeptides enrichment

Tryptic digests of bovine fetuin and BSA were dissolved in 200 μl binding buffer (83% ACN/1% FA) and then 1 mg of SiO_2@Poly-His microspheres were added and incubated at room temperature for 15 min. After centrifugation, the supernatant was removed and the SiO_2@Poly-His microspheres were washed with 80% ACN/1% FA and 70% ACN/1% FA to remove non-glycopeptides. The glycopeptides that adsorbed on the poly His microspheres were eluted by 40% ACN/5% FA. The eluates were collected and analyzed by nano-ESI-Q-TOF MS.

2.6.2 Phosphopeptides enrichment

Tryptic digests of α-casein and BSA were dissolved in 200 μl binding buffer (83% ACN/1% FA) and then 1 mg of SiO_2@Poly-His microspheres were added and incubated at room temperature for 15 min. After centrifugation, the supernatant was removed and the SiO_2@Poly-His microspheres were washed with 80% ACN/1% FA and 75% ACN/1% FA to remove non-phosphopeptides. The phosphopeptides adsorbed on the poly His were eluted by 40% ACN/5% FA. The eluates were collected and analyzed by nano-ESI-Q-TOF MS.

2.6.3 Glycopeptides and phosphopeptides simultaneous enrichment

Tryptic digests of bovine fetuin, α-casein and BSA were dissolved in 200 μl binding buffer (83% ACN/1% FA) and then 1 mg of SiO_2@Poly-His microspheres were added and incubated at room temperature for 15 min. After centrifugation, the supernatant was removed, and the SiO_2@Poly-His microspheres were washed with 80% ACN/1% FA and 75% ACN/1% FA to remove unmodified peptides. The glycopeptides and phosphopeptides adsorbed on the poly His were eluted by 40% ACN/5% FA. The eluates were collected and analyzed by nano-ESI-Q-TOF MS.

2.7 Hydrolysis degree of phosphopeptides during the deglycosylation process

The standard phosphopeptide was dissolved in 50 mM ammonium bicarbonate solution and 5U PNGase F was added to react at 37°C for 0, 3, 6, 9, and 12 h, respectively.

2.8 On-Line deglycosylation of the glycopeptides

The poly His microspheres adsorbed with glycopeptides and phosphopeptides were mixed with 5 μL of PNGase F (2,500 U) in 30 μl of 5 mM CH_3COONH_4. The entire suspension mixture was incubated for 1 h at 37°C. The resulting mixture was concentrated and redissolved in 80% ACN/0.1% FA. After packing the entire mixture into the tip column, the flow-through was collected and the SiO_2@Poly-His microspheres were eluted with 80% ACN/1% FA and 40% ACN/5% FA, respectively. The 80% ACN/1% FA fraction and flow-through fraction were combined, and all fractions were analyzed by nano-ESI-Q-TOF MS.

2.9 Simultaneous enrichment of glycopeptides and phosphopeptides from HT29 cell line lysate

To culture HT29 cell line, McCoy's 5A Medium and 10% fetal bovine serum were added and mixed at 37°C with 5% CO_2. The protein extraction steps were referred to the previous literature (Lu et al., 2020). HT29 cell line lysate (100 μg) was digested by trypsin and Glu C, desalted and dissolved in 100 μl of 83% ACN/1% FA, and then a poly His microsphere (1 mg) was added and incubated for 30 min at room temperature. After centrifugation, the pellet was washed with 83% ACN/1% FA and

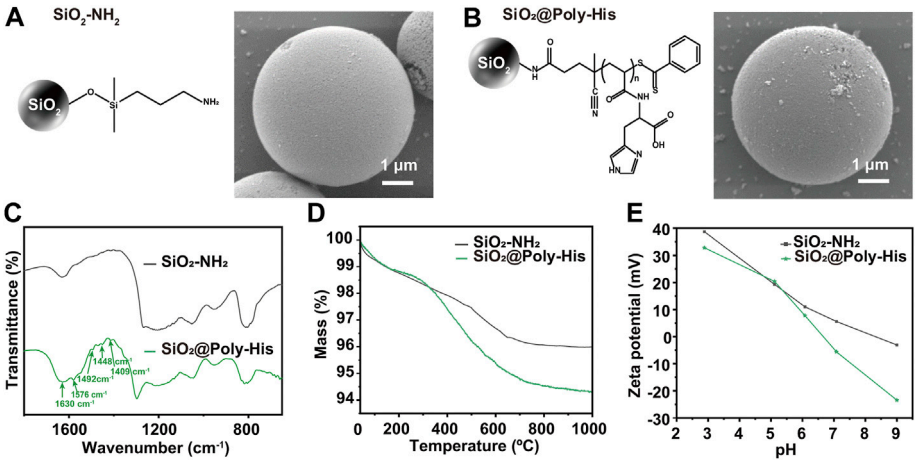

FIGURE 1
Characterization of SiO_2@Poly-His microspheres. **(A)** SEM image of SiO_2-NH_2; **(B)** SEM image of SiO_2@Poly-His microspheres; **(C)** FTIR spectra **(D)** TGA curves and **(E)** Zeta potential curves of SiO_2-NH_2 and SiO_2@Poly-His microspheres.

80% ACN/1% FA to remove unmodified peptides. The supernatant was discarded by centrifugation and the pellet was mixed with 5 μl of PNGase F (2,500 U) in 30 μl of 5 mM CH_3COONH_4, incubated for 1 h at 37°C. The resulting mixture was concentrated and redissolved in 80% ACN/0.1% FA. After packing the entire mixture into the GELoader tips, the flow-through was collected and the SiO_2@Poly-His microspheres were eluted with 80% ACN/1% FA and 40% CAN/5% FA, respectively. The 80% ACN/1% FA fraction and sample solution fraction were combined, and all fractions were analyzed by Orbitrap Exploris™ 480 Mass Spectrometer.

2.10 MS Analysis

2.10.1 Analysis of glycopeptides and phosphopeptides from standard proteins with MS

The enriched glycopeptides from bovine fetuin and phosphopeptides from α-casein were analyzed by a nano-ESI-Q-TOF MS with collision-induced dissociation in a positive mode. The source temperature was set to 100°C and the capillary voltage was set to 2.1 kV. The full scan range was from 600 to 1800 m/z.

2.10.2 Analysis of glycopeptides and phosphopeptides from HT29 cell line lysate with LC-MS

The enriched PTM-peptides were separated and identified on EASY-nLC 1,200 liquid chromatography system coupled with Orbitrap Exploris™ 480 mass spectrometer. A C18 analytical column (150 μm × 150 mm, 2 μm) was used to separate PTM-peptides. The mobile phase A was 0.1% FA and phase B was 80% ACN/0.1% FA. The gradient elution was as follows: 12–30% B, 62 min; 30%–38% B, 10 min; 38%–95% B, 8 min; and 95% B, 10 min. The flow rate was 600 nL/min. The parameter of Orbitrap Exploris™ 480 mass spectrometer was set as follows; the capillary temperature of the ion transport, 320°C; the spray voltage, 2.1 kV. The MS was operated in positive mode with the FAIMS Pro interface. Compensation voltage was set at −45 V and −65 V to remove singly charged ions. For data-dependent acquisition (DDA) experiments full MS resolution was set at 60,000 with a normalized AGC target 300%. The full scan range was from 350 to 1,500 m/z and a maximum inject time was set at 20 ms. The RF Lens was set at 50%. For MS2, resolution was set at 15,000 with a normalized AGC target of 75%. The maximum inject time was set at 30 ms. The data-dependent MS/MS was top speed mode with a cycle time of 2 s. The number of microscans to be set at 1 scan s^{-1} (charge state 2–7) within an isolation window of 1.6 m/z were considered for MS/MS analysis. Dynamic exclusion was set at 30 s. Mass tolerance of ± 10 ppm was allowed, and the precursor intensity threshold was kept at 2.5E5.

2.11 Data analysis

All the MS raw data were processed by Maxquant 3.2.0 and searched against the homo sapiens in the UniProt database. The trypsin and Glu C cleavage with a maximum of two leakage sites was allowed. Oxidation on methionine (M), acetylation of protein N terminus, deamination (N) and phospho-modification (STY) were set as the variable modifications. Carbamidomethyl (C) was set as a fixed modification, The false discovery rate (FDR) was set at 1%. The other conditions were set by default.

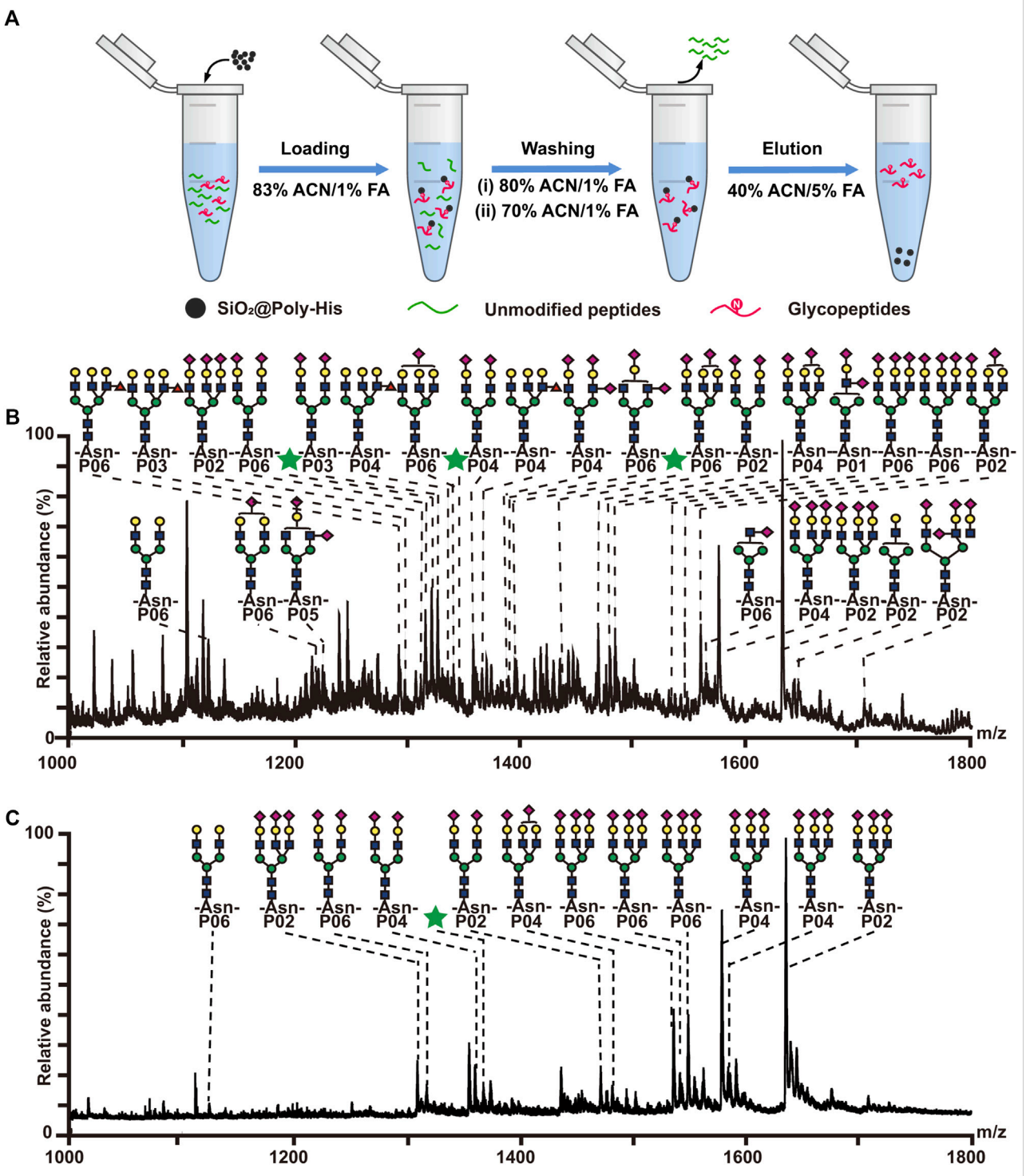

FIGURE 2
Enrichment of glycopeptides with SiO_2@Poly-His microspheres and commercial ZIC-HILIC materials. **(A)** Workflow for the glycopeptide enrichment with the SiO_2@Poly-His microspheres; **(B)** Mass spectrum of the mixture of the bovine fetuin and BSA at molar ratio of 1:5,000 enriched by SiO_2@Poly-His microspheres; **(C)** Mass spectrum of the mixture of the bovine fetuin and BSA at molar ratio of 1:5,000 enriched by ZIC-HILIC. Glycopeptides are labeled with their glycan structures or green stars (glycopeptides with unknown glycoform): ■: GlcNAc; ●: mannose; ○: galactose; ◆: Neu5Ac.

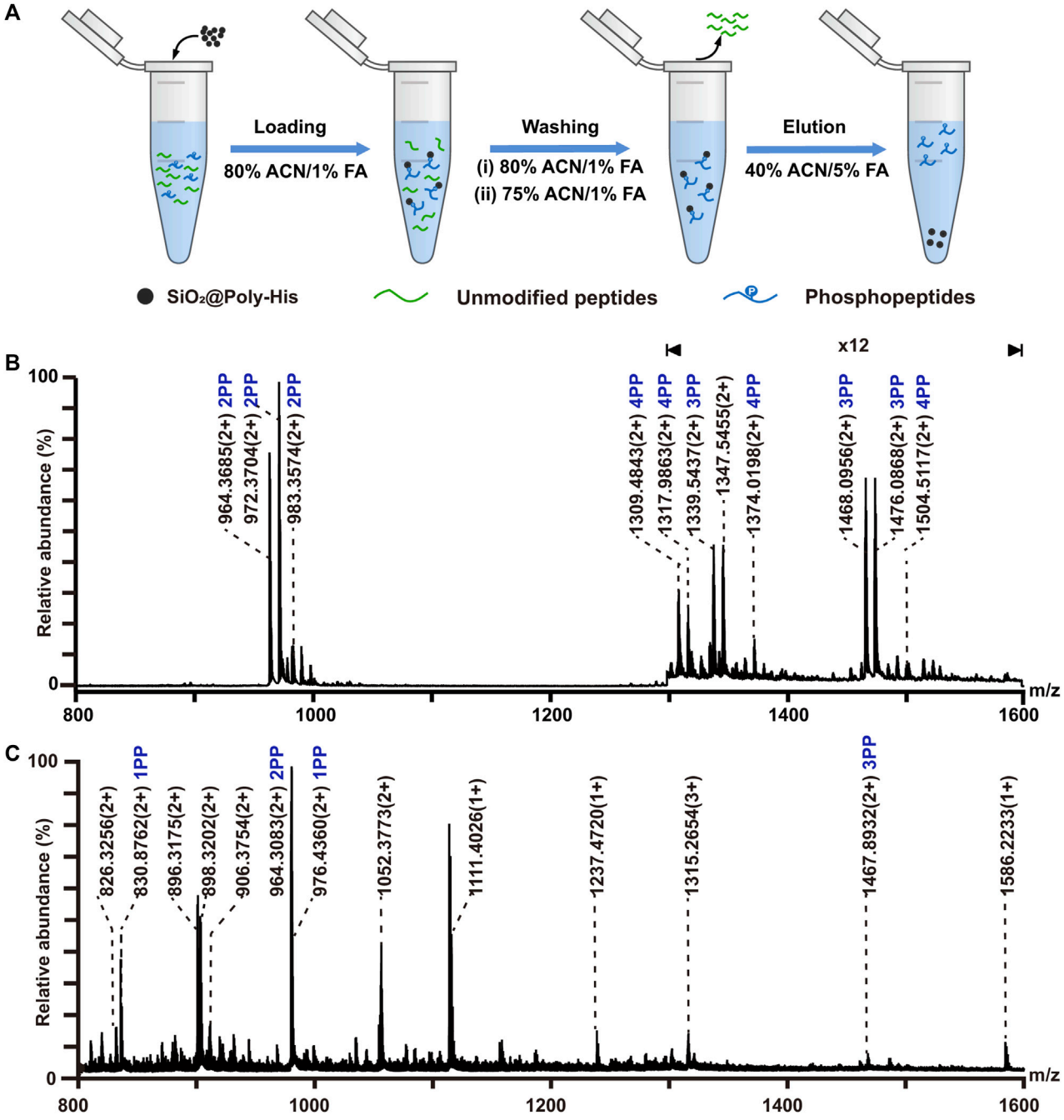

FIGURE 3
Enrichment of phosphopeptides with SiO_2@Poly-His microspheres and commercial TiO_2 materials. **(A)** Workflow for the phosphopeptides enrichment with SiO_2@Poly-His microspheres; **(B)** Mass spectrum of the mixture of the casein and BSA at molar ratio of 1:1,000 enriched by SiO_2@Poly-His microspheres; **(C)** Mass spectrum of the mixture of the casein and BSA at molar ratio of 1:1,000 enriched by TiO_2. XPP represents phosphopeptide, among which X is the number of phosphate groups in a peptide; Only mass charge ratio (m/z) represents non-phosphopeptide.

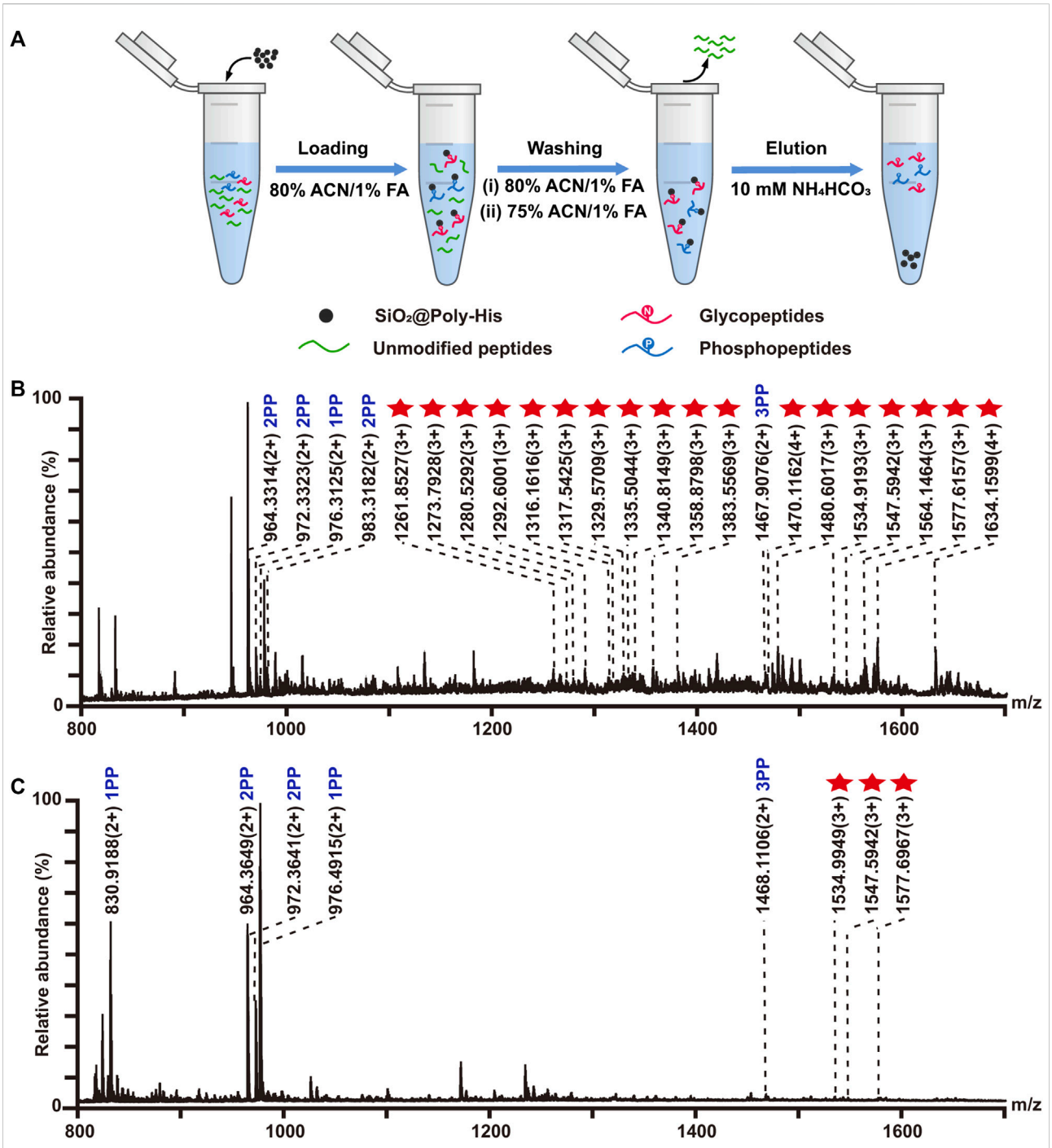

FIGURE 4
Simultaneous enrichment of glycopeptides and phosphopeptides with SiO_2@Poly-His microspheres and commercial TiO_2 materials. **(A)** Workflow for the simultaneous enrichment of glycopeptides and phosphopeptides with SiO_2@Poly-His microspheres; **(B)** Mass spectrum of the mixture of α-casein, bovine fetuin and BSA at molar ratio of 1:0.67:1,000 enriched by SiO_2@Poly-His microspheres and **(C)** Mass spectrum of the mixture of α-casein, bovine fetuin and BSA at molar ratio of 1:1:1,000 enriched by TiO_2. Red star represents glycopeptide; XPP represents phosphopeptide, among which X is the number of phosphate groups in a peptide.

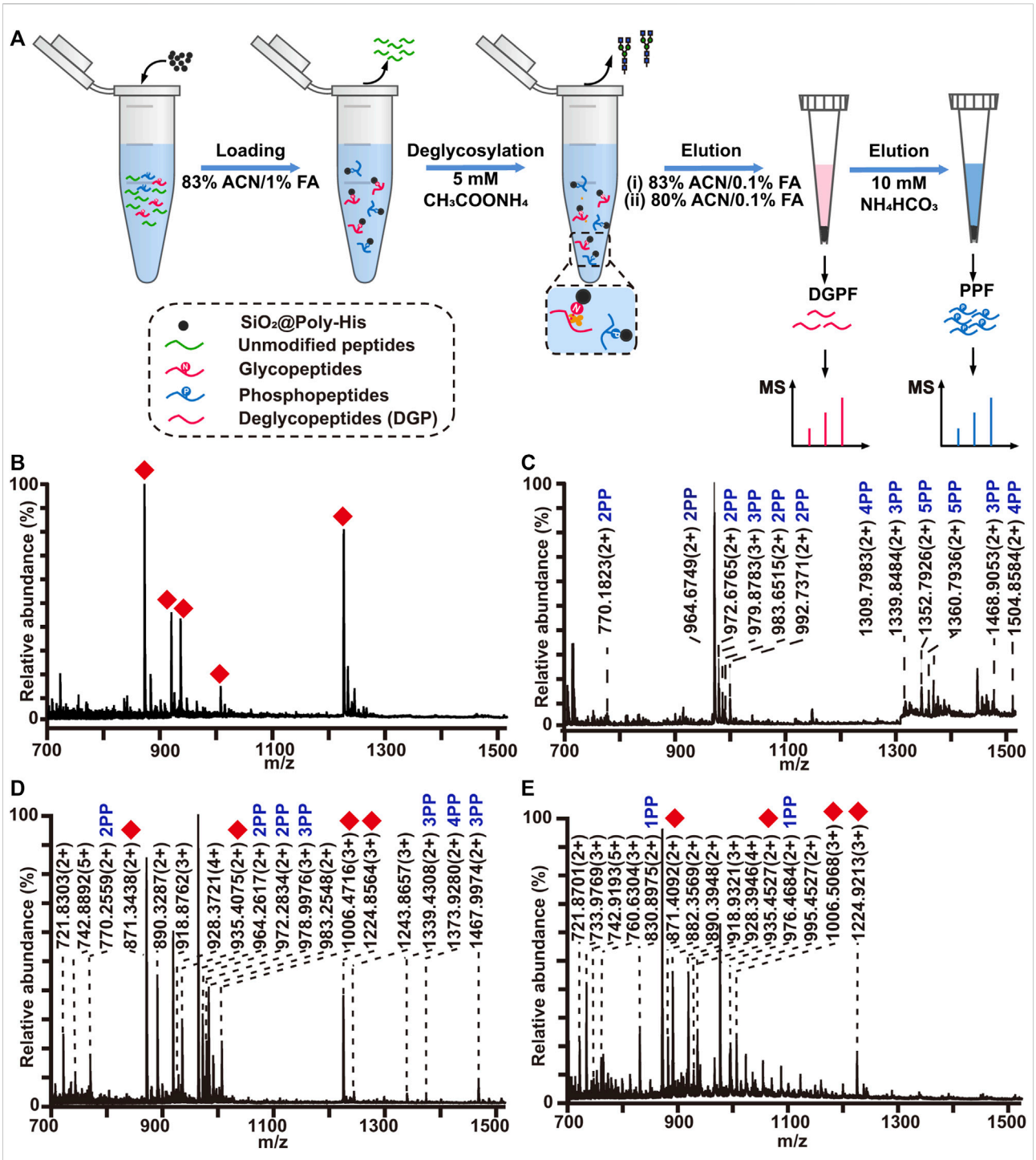

FIGURE 5
(A) Workflow the simultaneous enrichment with SiO_2@Poly-His microspheres, which consists of the sequential elution of glycopeptides and phosphopeptides. Mass spectrum of sequential elution of the deglycosylated peptides fraction **(B)** and the phosphopeptides fraction **(C)** enriched by SiO_2@Poly-His microspheres. Mass spectra of the co-elution of deglycosylated peptides and phosphopeptides that treated with SiO_2@Poly-His microspheres **(D)** and commercial TiO_2 materials **(E)**. Red diamond represents deglycosylated peptide; XPP represents phosphopeptide, among which X is the number of phosphate groups in a peptide; Only mass charge ratio (m/z) represents unmodified peptide.

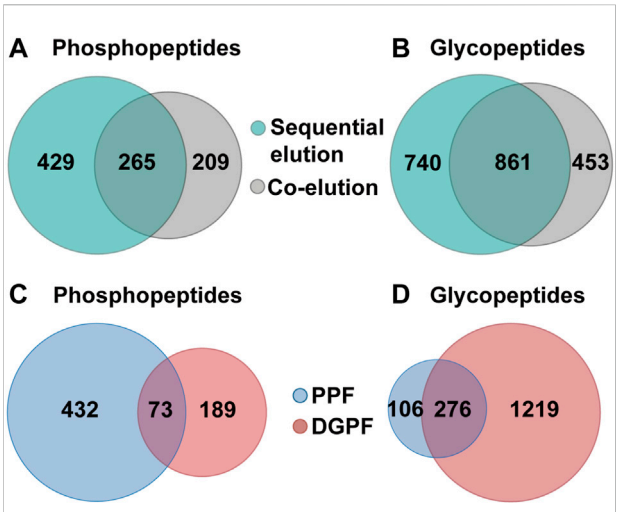

FIGURE 6
Simultaneous enrichment and sequential elution or co-elution of glycopeptides and phosphopeptides from HT29 cell lysates with SiO_2@Poly-His microspheres. **(A)** The overlap of phosphopeptides between the sequential elution strategy and co-elution strategy; **(B)** The overlap of glycopeptides between the sequential elution strategy and co-elution strategy; **(C)** The overlap of phosphopeptides between deglycosylated peptide fraction and phosphopeptide fraction; **(D)** the overlap of glycopeptides between deglycosylated peptide fraction and phosphopeptide fraction.

3 Result and discussion

3.1 Synthesis and characterization of poly His modified silica microspheres

We modified His monomer onto silica surface by surface initiated reversible addition-fragmentation transfer (SI-RAFT) polymerization (Raula et al., 2003) to obtained SiO_2@Poly-His microspheres (schematically illustrated in Supplementary Figure S1A). After synthesis, the SiO_2@Poly-His microspheres were characterized with different methods. Fourier transform interferometric radiometer (FTIR) spectrum (Figure 1C) shows that the strong adsorption at 1,630 cm^{-1} belongs to C = O group of carboxyl of His group. The peak at 1,576 cm^{-1} is attributed to the imidazole side ring stretching motions. The adsorptions around 1,409, 1,448, and 1,492 cm^{-1} are assigned to the C = C bond and the C-N bond of the imidazole ring. The morphology of SiO_2@Poly-His microspheres characterized by SEM images show the morphology of microspheres has little change after modification (Figures 1A,B). According to thermogravimetric analysis, SiO_2@Poly-His microspheres show 1.7% weight loss compared with SiO_2-NH_2 (Figure 1D) and exhibit a wider range of Zeta potential than amino silica. SiO_2@Poly-His microspheres have lower Zeta potential at high pH (Figure 1E). The pore size distribution of the silica gel before (black) and after (bule) poly-His modification was investigated by N_2 adsorption–desorption measurement. Barret-Joyner-Halenda (BJH) model was used for pore size distribution assessment. The result indicates that the film thickness of histidine polymer on SiO_2 is ~6 nm (Supplementary Figure S2). These results indicate that the SiO_2@Poly-His microspheres were successfully prepared.

Subsequently, the SiO_2@Poly-His microspheres with different initial feed molar ratio of His monomer to chain transfer reagent (CTA) were synthesized, their characterizations are shown in Supplementary Figure S1. Then we investigated the effect of the initial feed molar ratio of His monomer to CTA on the retention behavior and adsorption capacity of glycopeptides. When the initial feed molar ratio of His to CTA for SiO_2@Poly-His microspheres increases from 5:1, 10:1 to 20:1, the retention behavior (Supplementary Figure S3) and adsorption capacity (Supplementary Figure S4) of glycopeptides increases accordingly. Therefore, the SiO_2@Poly-His microspheres synthesized with an initial molar ratio of His to CTA of 20:1 were chosen for subsequent study.

3.2 Enrichment of glycopeptides with SiO_2@Poly-His microspheres

Furthermore, the performance of SiO_2@Poly-His microspheres for glycopeptides enrichment was tested using tryptic digests of bovine fetuin and bovine serum albumin (BSA) with different molar ratios. The procedure is shown in Figure 2A. After enrichment with SiO_2@Poly-His microspheres, 30 glycopeptides (detailed information of glycopeptides in Supplementary Table S1, Supplementary Figure S5) are detected with high signal intensity from tryptic digests of bovine fetuin and BSA with the molar ratio of 1:100, in sharp contrast to none detected glycopeptide signal before SiO_2@Poly-His treatment (Supplementary Figure S5). Even the molar ratio of bovine fetuin/BSA is dramatically decrease to 1:5,000, 29 glycopeptides could still be found dominating the spectrum (Figure 2B). As a comparison, the commercial ZIC-HILIC materials could only enrich 13 glycopeptides from the digests of bovine fetuin and BSA with the molar ratio of 1:200 (Figure 2C). Above results fully demonstrate that SiO_2@Poly-His microspheres have higher selectivity toward glycopeptides than ZIC-HILIC

3.3 Enrichment of phosphopeptides with SiO_2@Poly-His microspheres

According to literature reports (Chou et al., 2014; Chattopadhyay et al., 2016), His can interact with phosphate groups *via* multi-hydrogen bonding interactions. To investigate the interaction between SiO_2@Poly-His microspheres and

phosphopeptides, we investigated the retention of phosphopeptides on SiO_2@Poly-His microspheres under step-wise ACN and FA content conditions, respectively (Supplementary Figure S6 and Supplementary Figure S7). The results indicate that hydrophilic interactions and hydrogen bonding interactions contribute to the retention of phosphopeptides on SiO_2@Poly-His microspheres. Next, we investigated the performance of SiO_2@Poly-His microspheres on phosphopeptides enrichment. The enrichment procedure is shown in Figure 3A. Eleven phosphopeptides (1 monophosphopeptide, 4 diphosphopeptides and 6 multi-phosphopeptides) dominating the spectrum (detailed information of phosphopeptides in Supplemntary Table S2) could be enriched from digests of α-casein (phosphoprotein) and BSA with the molar ratio of 1:100, in sharp contrast to none phosphopeptide before enrichment (Supplementary Figure S8). With decreasing the molar ratio of α-casein and BSA to 1:1,000, 10 phosphopeptides (3 diphosphopeptides and 7 multi-phosphopeptides) could still be observed (Figure 3B). So far, there was no report on the phosphopeptides enrichment by using any kind of amino acid modified materials, which could resist such high fold interference. As a comparison, the commercial TiO_2 materials could enrich 4 phosphopeptides (2 monophosphopeptides, 1 diphosphopeptides and only 1 multi-phosphopeptide) from the same sample (Figure 3C). Besides, the number of multi-phosphopeptides enriched by SiO_2@Poly-His microspheres is 7 times that of TiO_2, demonstrating the preference of SiO_2@Poly-His in enriching multi-phosphopeptides. In addition, the recovery toward phosphopeptides and sialylated glycopeptide were evaluated by SiO_2@Poly-His microspheres based method, showing the preference of SiO_2@Poly-His for di- and multi-phosphopeptides (Supplementary Figure S9). These results may be explained that the hydrophilic interactions and hydrogen bonding interactions between SiO_2@Poly-His microspheres and phosphopeptides are more tunable than the Lewis acid-base interactions between TiO_2 and phosphopeptides. These results demonstrate that SiO_2@Poly-His microspheres have high selectivity and coverage toward phosphopeptides and are complementary to the TiO_2, suggesting that these two methods can be used in combination in future.

3.4 Simultaneous enrichment of glycopeptides and phosphopeptides

On the basis of above results, we attempted to employ SiO_2@Poly-His microspheres to simultaneously enrich phosphopeptides and glycopeptides. The enrichment procedure is shown in Figure 4A. The protein digests of α-casein, bovine fetuin and BSA with the molar ratio of 1:0.67:1,000 are applied to simulate complex sample. The enrichment result shows that 20 glycopeptides and 5 phosphopeptides could be simultaneously detected (Figure 4B). It achieves simultaneous enrichment of phosphopeptides and glycopeptides at the highest fold of BSA interference reported to date (Supplementary Table S7), implying the outstanding selectivity of SiO_2@Poly-His microspheres toward phosphopeptides and glycopeptides. When the sample of alpha-casein and BSA with the molar ratio of 1:1:1,000 is treated with TiO_2 only 3 glycopeptides and 5 phosphopeptides are identified (Figure 4C). These results demonstrate that SiO_2@Poly-His microspheres possess excellent performance for simultaneous enrichment of phosphopeptides and glycopeptides.

3.5 Investigating the hydrolysis degree of phosphopeptides during the deglycosylation process

In the reported protocols, the simultaneously enriched phosphopeptides and glycopeptides are always co-eluted and the co-eluates are deglycosylated by PNGase F to analyze glycosylation sites. Deglycosylation usually takes 10–16 h in ammonium bicarbonate aqueous (pH–8.0) solution (Palmisano et al., 2012; Boersema et al., 2013). During this deglycosylation process, the coexisted phosphopeptides were assumed to be hydrolyzed (Li et al., 2014), but no experimental data were reported. To investigate hydrolysis degree of phosphopeptides under deglycosylation process, standard monophosphopeptide (1 PP), diphosphopeptide (2 PP) and triphosphopeptide (3 PP) with the same peptide sequence (HSPIAPSSPSPK) are selected as model samples. To relatively quantify the hydrolysis of phosphopeptides in alkaline conditions, Glu-Fibrinopeptide B (GFP) is used as an internal standard. As the enzymolysis time became longer, the content of phosphopeptides decreased linearly, and the degree of phosphorylation status was positively correlated with its hydrolysis rate. After 12 h of enzymolysis, the content of 3 pp, 2 pp, 1 pp are dramatically reduce by 40%, 30%, 20%, respectively (Supplementary Figure S10). This result demonstrates that the phosphopeptides could be hydrolyzed during deglycosylation and multi-phosphopeptides are more labile for hydrolysis. To reduce/avoid the hydrolysis of the phosphopeptides in free solution, there are three ways to do: separating glycopeptides and phosphopeptides before deglycosylation, shortening deglycosylation time of co-eluates, and confining the phosphopeptides onto materials instead of in free solution.

3.6 On-line de-glycosylation and sequential elution of deglycosylated peptides and phosphopeptides

To reduce the phosphopeptides hydrolysis during the process of deglycosylation treatment, we developed a strategy based on on-line

deglycosylation and sequential elution of glycopeptides and phosphopeptides. Firstly, glycopeptides and phosphopeptides are co-enriched with SiO_2@Poly-His microspheres; Then, the captured glycopeptides on the SiO_2@Poly-His microspheres are deglycosylated with PNGase F and deglycopeptides are separated while phosphopeptides are still bound on the adsorbents. Finally, the bound phosphopeptides on SiO_2@Poly-His microspheres are subsequently eluted (Figure 5A). To test this method, the digests of bovine fetuin and α-casein are used as samples. After treatment by as-described method, 5 deglycopeptides and 12 phosphopeptides (5 diphosphopeptides and 7 multi-phosphopeptides) are detected, respectively (Figures 5B,C). As comparison, 4 deglycopeptides and 7 phosphopeptides (3 diphosphopeptides and 4 multi-phosphopeptides) are detected by using SiO_2@Poly-His microspheres with co-elution strategy (Figure 5D). Obviously, the former one identifies more target PTM peptides, which means that more information could be obtained by our established strategy. Meanwhile, the commercial materials of TiO_2 are also chosen as a comparison. Only 4 deglycopeptides and 2 monophosphopeptides are detected by using co-elution strategy (Figure 5E). Therefore, this strategy could not only achieve the sequential elution of glycopeptides and phosphopeptides, but also detect more target peptides, especially multi-phosphopeptides.

3.7 Analysis of phosphopeptides and glycopeptides from HT29 cell lysate

We further applied the SiO_2@Poly-His microspheres based on-line deglycosylation strategy to simultaneously enrich and sequentially separate phosphopeptides and glycopeptides from HT-29 cell lysates. Deglycosylated peptide fraction and phosphopeptide fraction were obtained. For comparison, the same samples are treated with SiO_2@Poly-His microspheres and the target peptides are co-eluted and further deglycosylated (co-elution strategy). By using our established strategy, 1,601 glycopeptides (Figure 6A, Supplementary Table S3) and 694 phosphopeptides (Figure 6B, Supplementary Table S4) are identified from 100 μg HT29 cell lysate. Among the identified phosphopeptides, the proportions of monophosphopeptides, diphosphopeptides and multi-phosphopeptides are 53.5%, 35.7%, and 10.8%, respectively (Supplementary Figure S11). The numbers of the phosphopeptides in deglycosylated peptide and phosphopeptide fractions are 262 and 505, respectively (Figure 6C). The overlap of phosphopeptides between these fractions is 10%. In deglycosylated peptide fraction, the proportions of monophosphopeptides, diphosphopeptides and multi-phosphopeptides are 78.4%, 20.5%, and 1.1%, respectively. While in phosphopeptide fraction, the proportions of monophosphopeptides, diphosphopeptides and multi-phosphopeptides are 41.5%, 43.1%, and 15.4%, respectively. Meanwhile, the numbers of the glycopeptides in deglycosylated peptide fraction and phosphopeptide fraction are 1,555 and 382, respectively (Figure 6D). The overlap of glycopeptides between deglycosylated peptide fraction and phosphopeptide fraction is 17%. These results suggest a low degree of overlap between deglycosylated peptide fraction and phosphopeptide fraction in sequential elution strategy. In contrast to these, only 1,314 glycopeptides (Supplementary Table S5) and 474 phosphopeptides (Supplementary Table S6) are identified from the identical sample using the co-elution strategy, among which the proportions of monophosphopeptides, diphosphopeptides and multi-phosphopeptides are 56.7%, 34.6%, and 8.7%, respectively (Supplementary Figure S12). The total number of phosphopeptides and glycopeptides identified by the sequential elution strategy is 1.5-fold and 1.2-fold higher than that of the co-elution strategy, respectively. These results demonstrate that our established strategy could simultaneously capture as well as sequentially separate glycopeptides and phosphopeptides, and increase the identified number of target peptides.

4 Conclusion

In summary, we developed one strategy to simultaneously enrich, on-line deglycosylate and sequentially elute phosphopeptides and glycopeptides based on SiO_2@Poly-His microspheres. First, SiO_2@Poly-His microspheres exhibit excellent selectivity for glycopeptides and phosphopeptide, providing a prerequisite for high coverage in global PTMs-proteomics. Second, the tunable interaction between the SiO_2@Poly-His microspheres and PTM peptides will provide versatile candidates for the highly effective separation of various specific PTM peptides, especially for multi-phosphopeptides. Third, the on-line deglycosylation strategy reduces the hydrolysis loss of phosphopeptides and the suppression of low-abundance PTM peptides during MS analysis. We believe that the biomimetic SiO_2@Poly-His microspheres may shed light on widespread applications ranging from biomolecule adsorption, biomarker and drug target discovery, and other biomedical fields.

Data availability statement

The raw data supporting the conclusions of this article will be made available by the authors, without undue reservation, to any qualified researcher.

Author contributions

DS and CC carried out the experiments and wrote the draft of the manuscript. XD and YC contributed to the optimization of the enrichment method. ZQ participated in the MS method optimization of the parameters of the MS identification method. XLL and XML secured funding and contributed to the experimental design and manuscript revision.

Funding

This work was financially supported by the National Natural Science Foundation of China (21974135, 2197040522, 22274115, and 22174140) and Dalian Institute of Chemical Physics Innovation Funding (DICP I202030 and DICP I202114).

Conflict of interest

The authors declare that the research was conducted in the absence of any commercial or financial relationships that could be construed as a potential conflict of interest.

Publisher's note

Supplementary material

The Supplementary Material for this article can be found online at: https://www.frontiersin.org/articles/10.3389/fbioe.2022.1011851/full#supplementary-material

References

Aasen, T., Johnstone, S., Vidal-Brime, L., Lynn, K. S., and Koval, M. (2018). Connexins: Synthesis, post-translational modifications, and trafficking in health and disease. *Int. J. Mol. Sci.* 19 (5), 1296. doi:10.3390/ijms19051296

Aebersold, R., Agar, J. N., Amster, I. J., Baker, M. S., Bertozzi, C. R., Boja, E. S., et al. (2018). How many human proteoforms are there? *Nat. Chem. Biol.* 14 (3), 206–214. doi:10.1038/nchembio.2576

Andaluz Aguilar, H., Iliuk, A. B., Chen, I. H., and Tao, W. A. (2020). Sequential phosphoproteomics and N-glycoproteomics of plasma-derived extracellular vesicles. *Nat. Protoc.* 15 (1), 161–180. doi:10.1038/s41596-019-0260-5

Boersema, P. J., Geiger, T., Wisniewski, J. R., and Mann, M. (2013). Quantification of the N-glycosylated secretome by super-SILAC during breast cancer progression and in human blood samples. *Mol. Cell. Proteomics* 12 (1), 158–171. doi:10.1074/mcp.M112.023614

Calderon-Celis, F., Ruiz Encinar, J., and Sanz-Medel, A. (2018). Standardization approaches in absolute quantitative proteomics with mass spectrometry. *Mass Spectrom. Rev.* 37 (6), 715–737. doi:10.1002/mas.21542

Chattopadhyay, A., Esadze, A., Roy, S., and Iwahara, J. (2016). NMR scalar couplings across intermolecular hydrogen bonds between zinc-finger histidine side chains and DNA phosphate groups. *J. Phys. Chem. B* 120 (41), 10679–10685. doi:10.1021/acs.jpcb.6b08137

Cho, K.-C., Chen, L., Hu, Y., Schnaubelt, M., and Zhang, H. (2019). Developing workflow for simultaneous analyses of phosphopeptides and glycopeptides. *ACS Chem. Biol.* 14 (1), 58–66. doi:10.1021/acschembio.8b00902

Chou, S. T., Hom, K., Zhang, D., Leng, Q., Tricoli, L. J., Hustedt, J. M., et al. (2014). Enhanced silencing and stabilization of siRNA polyplexes by histidine-mediated hydrogen bonds. *Biomaterials* 35 (2), 846–855. doi:10.1016/j.biomaterials.2013.10.019

Chu, H., Zheng, H., Sun, N., and Deng, C. (2022). Simultaneous analysis of cellular glycoproteome and phosphoproteome in cervical carcinoma by one-pot specific enrichment. *Anal. Chim. Acta X.* 1195, 338693. doi:10.1016/j.aca.2021.338693

Cuijpers, S. A. G., and Vertegaal, A. C. O. (2018). Guiding mitotic progression by crosstalk between post-translational modifications. *Trends biochem. Sci.* 43 (4), 251–268. doi:10.1016/j.tibs.2018.02.004

Dong, X., Qin, H., Mao, J., Yu, D., Li, X., Shen, A., et al. (2017). In-depth analysis of glycoprotein sialylation in serum using a dual-functional material with superior hydrophilicity and switchable surface charge. *Anal. Chem.* 89 (7), 3966–3972. doi:10.1021/acs.analchem.6b04394

Harmel, R., and Fiedler, D. (2018). Features and regulation of non-enzymatic post-translational modifications. *Nat. Chem. Biol.* 14 (3), 244–252. doi:10.1038/nchembio.2575

He, Y., Zheng, Q., Huang, H., Ji, Y., and Lin, Z. (2022). Synergistic synthesis of hydrophilic hollow zirconium organic frameworks for simultaneous recognition and capture of phosphorylated and glycosylated peptides. *Anal. Chim. Acta X.* 1198, 339552. doi:10.1016/j.aca.2022.339552

Hong, Y., Zhao, H., Pu, C., Zhan, Q., Sheng, Q., and Lan, M. (2018). Hydrophilic phytic acid-coated magnetic graphene for titanium(iv) immobilization as a novel hydrophilic interaction liquid chromatography-immobilized metal affinity chromatography platform for glyco- and phosphopeptide enrichment with controllable selectivity. *Anal. Chem.* 90 (18), 11008–11015. doi:10.1021/acs.analchem.8b02614

Huang, J., Liu, X., Wang, D., Cui, Y., Shi, X., Dong, J., et al. (2021). Dual-functional ti(iv)-imac material enables simultaneous enrichment and separation of diverse glycopeptides and phosphopeptides. *Anal. Chem.* 93 (24), 8568–8576. doi:10.1021/acs.analchem.1c01324

Jennewein, M. F., and Alter, G. (2017). The immunoregulatory roles of antibody glycosylation. *Trends Immunol.* 38 (5), 358–372. doi:10.1016/j.it.2017.02.004

Khani, M. M., Abbas, Z. M., and Benicewicz, B. C. (2017). Well-defined polyisoprene-grafted silica nanoparticles via the RAFT process. *J. Polym. Sci. Part A Polym. Chem.* 55 (9), 1493–1501. doi:10.1002/pola.28514

Kiessling, L. L., and Diehl, R. C. (2021). CH-π interactions in glycan recognition. *ACS Chem. Biol.* 16 (10), 1884–1893. doi:10.1021/acschembio.1c00413

Li, J., Jiang, W., and Xu, X. (2014). Novel method coupled TiO_2 with ultrafiltration membrane to enrich and separate phosphopeptides and sialic acid-containing glycopeptides from saliva of cancer patient. *Chem. J. Chin. U.* 35 (10), 2073–2077. doi:10.7503/cjcu20140659

Lodi, P. J., and Knowles, J. R. (1991). Neutral imidazole is the electrophile in the reaction catalyzed by triosephosphate isomerase - structural origins and catalytic implications. *Biochemistry* 30 (28), 6948–6956. doi:10.1021/bi00242a020

Losev, Y., Frenkel-Pinter, M., Abu-Hussien, M., Viswanathan, G. K., Elyashiv-Revivo, D., Geries, R., et al. (2021). Differential effects of putative N-glycosylation sites in human Tau on Alzheimer's disease-related neurodegeneration. *Cell. Mol. Life Sci.* 78 (5), 2231–2245. doi:10.1007/s00018-020-03643-3

Lu, Q., Chen, C., Xiong, Y., Li, G., Zhang, X., Zhang, Y., et al. (2020). High-efficiency phosphopeptide and glycopeptide simultaneous enrichment by hydrogen bond-based bifunctional smart polymer. *Anal. Chem.* 92 (9), 6269–6277. doi:10.1021/acs.analchem.9b02643

Luo, B., Chen, Q., He, J., Li, Z., Yu, L., Lan, F., et al. (2019). Boronic acid-functionalized magnetic metal-organic frameworks via a dual-ligand strategy for highly efficient enrichment of phosphopeptides and glycopeptides. *ACS Sustain. Chem. Eng.* 7 (6), 6043–6052. doi:10.1021/acssuschemeng.8b06171

Luo, B., Yan, S., Zhang, Y., Zhou, J., Lan, F., and Wu, Y. (2021). Bifunctional magnetic covalent organic framework for simultaneous enrichment of phosphopeptides and glycopeptides. *Anal. Chim. Acta X.* 1177, 338761. doi:10.1016/j.aca.2021.338761

Macek, B., Forchhammer, K., Hardouin, J., Weber-Ban, E., Grangeasse, C., and Mijakovic, I. (2019). Protein post-translational modifications in bacteria. *Nat. Rev. Microbiol.* 17 (11), 651–664. doi:10.1038/s41579-019-0243-0

Palmisano, G., Parker, B. L., Engholm-Keller, K., Lendal, S. E., Kulej, K., Schulz, M., et al. (2012). A novel method for the simultaneous enrichment, identification, and quantification of phosphopeptides and sialylated glycopeptides applied to a temporal profile of mouse brain development. *Mol. Cell. Proteomics* 11 (11), 1191–1202. doi:10.1074/mcp.M112.017509

Prabakaran, S., Lippens, G., Steen, H., and Gunawardena, J. (2012). Post-translational modification: nature's escape from genetic imprisonment and

the basis for dynamic information encoding. *WIREs Mech. Dis.* 4 (6), 565–583. doi:10.1002/wsbm.1185

Raula, J., Shan, J., Nuopponen, M., Niskanen, A., Jiang, H., Kauppinen, E. I., et al. (2003). Synthesis of gold nanoparticles grafted with a thermoresponsive polymer by surface-induced reversible-addition-fragmentation chain-transfer polymerization. *Langmuir* 19 (8), 3499–3504. doi:10.1021/la026872r

Sun, N., Wang, J., Yao, J., Chen, H., and Deng, C. (2019). Magnetite nanoparticles coated with mercaptosuccinic acid-modified mesoporous titania as a hydrophilic sorbent for glycopeptides and phosphopeptides prior to their quantitation by LC-MS/MS. *Microchim. Acta* 186 (3), 159. doi:10.1007/s00604-019-3274-3

Sun, N., Wu, H., and Shen, X. (2020). Magnetic titanium dioxide nanomaterial modified with hydrophilic dicarboxylic ligand for effective enrichment and separation of phosphopeptides and glycopeptides. *Microchim. Acta* 187 (3), 195. doi:10.1007/s00604-020-4161-7

Venne, A. S., Kollipara, L., and Zahedi, R. P. (2014). The next level of complexity: Crosstalk of posttranslational modifications. *Proteomics* 14 (4-5), 513–524. doi:10.1002/pmic.201300344

Vu, L. D., Gevaert, K., and De Smet, I. (2018). Protein language: Post-translational modifications talking to each other. *Trends Plant Sci.* 23 (12), 1068–1080. doi:10.1016/j.tplants.2018.09.004

Wang, Z., Wang, J., Sun, N., and Deng, C. (2019). A promising nanoprobe based on hydrophilic interaction liquid chromatography and immobilized metal affinity chromatography for capture of glycopeptides and phosphopeptides. *Anal. Chim. Acta X.* 1067, 1–10. doi:10.1016/j.aca.2019.04.010

Wu, Z., Huang, R., and Yuan, L. (2019). Crosstalk of intracellular post-translational modifications in cancer. *Arch. Biochem. Biophys.* 676, 108138. doi:10.1016/j.abb.2019.108138

Xiao, H., Suttapitugsakul, S., Sun, F., and Wu, R. (2018). Mass spectrometry-based chemical and enzymatic methods for global analysis of protein glycosylation. *Acc. Chem. Res.* 51 (8), 1796–1806. doi:10.1021/acs.accounts.8b00200

Yan, J., Li, X., Yu, L., Jin, Y., Zhang, X., Xue, X., et al. (2010). Selective enrichment of glycopeptides/phosphopeptides using porous titania microspheres. *Chem. Commun.* 46 (30), 5488–5490. doi:10.1039/c000094a

Yen, H. Y., Liu, Y. C., Chen, N. Y., Tsai, C. F., Wang, Y. T., Chen, Y. J., et al. (2015). Effect of sialylation on EGFR phosphorylation and resistance to tyrosine kinase inhibition. *Proc. Natl. Acad. Sci. U. S. A.* 112 (22), 6955–6960. doi:10.1073/pnas.1507329112

Yi, L., Yan, Y., Tang, K., and Ding, C.-F. (2020). Facile preparation of polymer-grafted ZIF-8-modified magnetic nanospheres for effective identification and capture of phosphorylated and glycosylated peptides. *Anal. Methods* 12 (38), 4657–4664. doi:10.1039/d0ay01412e

Zhang, Y., Li, J., Yu, Y., Xie, R., Liao, H., Zhang, B., et al. (2020). Coupling hydrophilic interaction chromatography materials with immobilized Fe(3+)for phosphopeptide and glycopeptide enrichment and separation. *RSC Adv.* 10 (37), 22176–22182. doi:10.1039/d0ra01048k

Zheng, H., Jia, J., Li, Z., and Jia, Q. (2020). Bifunctional magnetic supramolecular-organic framework: A nanoprobe for simultaneous enrichment of glycosylated and phosphorylated peptides. *Anal. Chem.* 92 (3), 2680–2689. doi:10.1021/acs.analchem.9b04691

Zhou, Y., Lih, T.-S. M., Yang, G., Chen, S.-Y., Chen, L., Chan, D. W., et al. (2020). An integrated workflow for global, glyco-and phospho-proteomic analysis of tumor tissues. *Anal. Chem.* 92 (2), 1842–1849. doi:10.1021/acs.analchem.9b03753

Zou, X., Jie, J., and Yang, B. (2017). Single-step enrichment of n-glycopeptides and phosphopeptides with novel multifunctional Ti(4+)-immobilized dendritic polyglycerol coated chitosan nanomaterials. *Anal. Chem.* 89 (14), 7520–7526. doi:10.1021/acs.analchem.7b01209

frontiers | Frontiers in Bioengineering and Biotechnology

TYPE Mini Review
PUBLISHED 17 October 2022
DOI 10.3389/fbioe.2022.1033514

OPEN ACCESS

EDITED BY
Hongliang Liu,
Yantai University, China

REVIEWED BY
Jiale Yong,
University of Science and Technology of China, China

*CORRESPONDENCE
Mingbo Song,
songmb@126.com

†These authors have contributed equally to this work

SPECIALTY SECTION
This article was submitted to Biomaterials, a section of the journal Frontiers in Bioengineering and Biotechnology

RECEIVED 31 August 2022
ACCEPTED 27 September 2022
PUBLISHED 17 October 2022

CITATION
Ge-Zhang S, Cai T, Yang H, Ding Y and Song M (2022), Biology and nature: Bionic superhydrophobic surface and principle.
Front. Bioeng. Biotechnol. 10:1033514.
doi: 10.3389/fbioe.2022.1033514

Biology and nature: Bionic superhydrophobic surface and principle

Shangjie Ge-Zhang†, Taoyang Cai†, Hong Yang, Yuyang Ding and Mingbo Song*

Northeast Forestry University, Harbin, China

Nature is the source of human design inspiration. In order to adapt to the environment better, creatures in nature have formed various morphological structures during billions of years of evolution, among which the superhydrophobic characteristics of some animal and plant surface structures have attracted wide attention. At present, the preparation methods of bionic superhydrophobic surface based on the microstructure of animal and plant body surface include vapor deposition, etching modification, sol-gel method, template method, electrostatic spinning method and electrostatic spraying method, etc., which have been used in medical care, military industry, shipping, textile and other fields. Based on nature, this paper expounds the development history of superhydrophobic principle, summarizes the structure and wettability of superhydrophobic surfaces in nature, and introduces the characteristics differences and applications of different superhydrophobic surfaces in detail. Finally, the challenge of bionic superhydrophobic surface is discussed, and the future development direction of this field is prospected.

KEYWORDS

nature, bionics, superhydrophobic principle, wettability, review

1 Introduction

During the long evolution of the earth, it is not difficult to find that many unrelated organisms, such as lotus leaves (aquatic plants) (Yu et al., 2007; Bai et al., 2018; Han et al., 2019; Yun et al., 2020; Ghasemlou et al., 2021), roses (terrestrial plants) (Bhushan, 2018; Chen et al., 2019; Dai et al., 2019; Zong et al., 2019; Kang et al., 2021), butterflies (insects) (Qian et al., 1900; Saison et al., 2008; Wang and Guo, 2013; Bixler and Bhushan, 2014; Han et al., 2017), geckos (terrestrial animals) (Li et al., 2011; Darmanin and Guittard, 2015; Stark et al., 2016; Wang et al., 2019a; Weng et al., 2022) and sharks (fish) (Chen et al., 2018; Gose et al., 2018; Jiaqiang et al., 2018; Bilgiç and Bilgiç, 2019; Zhao et al., 2021), have evolved superhydrophobic properties. Researchers determine whether the surface is super-hydrophobic according to the contact angle of water droplets on the solid surface, that is, when the contact angle of water on the solid surface is greater than 150°, the surface is called super-hydrophobic (Huang and Guo, 2018; Shahabadi and

Brant, 2019; Hasan and Nosonovsky, 2020; Hu et al., 2022). In fact, due to the difference in microstructure of each organism's body surface, apart from superhydrophobic properties, different structures also give them different additional properties, such as self-cleaning (Dalawai et al., 2020; Wang et al., 2021a), anti-icing (Lin et al., 2018; Li et al., 2021a; Wu et al., 2021a), anti-fogging (Varshney et al., 2018; Varshney and Mohapatra, 2018; Domke et al., 2019; Fromel et al., 2021), resistance reduction (Li and Guo, 2018; Li et al., 2019) and so on. In the past few decades, superhydrophobic surfaces, as an extreme surface non-wetting state, have attracted great attention in the scientific and technological circles because of their potential applications in many fields, such as self-cleaning, anti-fouling, anti-corrosion, anti-icing and drag reduction. Inspired by these creatures, modern researchers have prepared special superhydrophobic surfaces suitable for different fields by using bionics (Ahmad and Kan, 2016; Shang et al., 2019a; Shang et al., 2019b; Wang et al., 2020a; Lin et al., 2022).

The earliest basic theory to systematically describe the phenomenon of superhydrophobic surface wetting comes from Young's work (Young, 1805). However, in the real world, few surfaces meet the assumptions of Young's equation, so Wenzel (uniform wetting) (Wenzel, 1949) and Cassie–Baxter (non-uniform wetting) (Cassie, 1948) respectively established new models to further improve and optimize this problem. In the later period, many scientists also put forward methods to optimize the superhydrophobic model according to different situations (Nosonovsky and Bhushan, 2005; Bhushan et al., 2007; Bittoun and Marmur, 2009; Xie et al., 2018; Jiang et al., 2020). As a hot spot in the field of material research, with the development of bionic superhydrophobic surface theory, the preparation methods of superhydrophobic surface are gradually diversified. Commonly used methods include sol-gel method (Yang et al., 2018; Vidal et al., 2019; Mahadik and Mahadik, 2021), vapor deposition method (Aljumaily et al., 2018; Pour et al., 2019; Mosayebi et al., 2020; Bayram et al., 2021; Zheng et al., 2022), etching modification method (Zhang et al., 2019a; Ma et al., 2020; Wei et al., 2021), electrochemical deposition method (Zhou et al., 2018; Xue et al., 2019a; Xue et al., 2019b; Wang et al., 2020b; Li et al., 2021b) and template pressing method (Xu et al., 2011; Victor et al., 2012). Among them, the template method can completely copy the microstructure of the biological surface, while other methods can imitate the existing structures in nature or create new structures.

In our previous review (Ge-Zhang et al., 2022), various preparation methods of bionic superhydrophobic surfaces, especially etching modification methods, were compared and described in detail. Therefore, in this mini-review, we will follow the course of human development, from using the primitive things of nature to imitating and transforming all things of nature, and then to realizing self-creation. This article focuses on the exploration and discovery of nature by human beings before self-creation. Starting from the essence, it introduces in detail the development process of superhydrophobic principle and superhydrophobic of natural organisms. This review reviews the development of superhydrophobic principle (Part 2), summarizes the structure and wettability of superhydrophobic surfaces of different animals and plants in nature (Part 3), and lists the differences and applications of different superhydrophobic surfaces. Finally, the function and application of bionic superhydrophobic surface are summarized, and the next research direction of bionic superhydrophobic surface is put forward. The current difficulties and future development directions are summarized and prospected (Part 4).

2 Basic principle of superhydrophobic surface

To explore the bionic superhydrophobic surface, we must first have a deep understanding of the principle. This chapter will introduce the concepts and principles of various superhydrophobic surfaces and physical models closely related to superhydrophobic properties.

2.1 Angle

The static wetting performance of droplets on superhydrophobic surface is usually expressed by contact angle (Voronov et al., 2008), while the rolling angle can be used to evaluate the dynamic performance of droplets on superhydrophobic surface (Hao et al., 2010).

2.2 Superhydrophobic model

In order to describe the relationship between the static contact angle of droplets on solid surface and the surface tension of liquid, solid and gas systems, T. Young established Young's equation of ideal smooth solid surface state, which set a theoretical precedent for studying the wettability of materials. After that, Wensel and Cassie summarized Wensel model (Wenzel, 1949) and Cassie–Baxter model (Cassie, 1948) by studying the relationship between surface roughness and wettability, and pointed out that superhydrophobicity increased with the decrease of surface free energy and the increase of surface roughness. In modern times, more models have been optimized and pointed out (Miljkovic et al., 2013; Jiang et al., 2020; Mohseni et al., 2021; Shen et al., 2021).

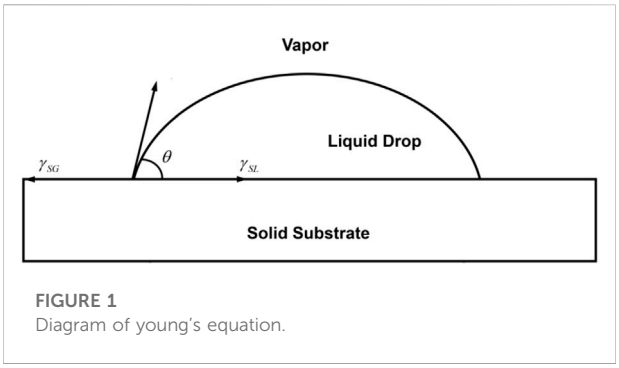

FIGURE 1
Diagram of young's equation.

2.2.1 Young's equation

For an ideal solid surface which is uniform, smooth and rigid, Young put forward Young's equation by means of the thermodynamic equilibrium equation in order to explain the quantitative relationship between contact angle and solid-liquid-gas interface (Figure 1):

$$cos\,\theta = \frac{\gamma_{SG} - \gamma_{SL}}{\gamma_{LG}}$$

Where γ_{SG}, γ_{SL}, γ_{LG} are the surface tensions between the solid-gas, solid-liquid and liquid-gas interfaces, respectively, then it is easy to know that the magnitude of the contact angle$\theta$is jointly determined by the surface tensions of solid, liquid and gas, that is, the hydrophobic properties of solid materials increase with the decrease of their surface free energy.

However, it is found that even the smooth surface constructed by the lowest surface energy substance (fluoride) has a contact angle of only 119°, which is far lower than the superhydrophobic surface with rough surface microstructure in nature. This is because the surface roughness will also affect the contact angle. In reality, many surfaces often have a certain degree of roughness, which is not completely smooth, undistorted and uniform. Therefore, Young's equation can only be applied to ideal surfaces, but not to realistic rough solid surfaces (Marmur, 1983). There are many modifications to Young's equation to deal with the shortcoming that the contact angle cannot be explained and predicted for rough surfaces (White, 1977; Dobbs, 1999; Butt et al., 2007; Alizada and Sofiyev, 2011; Makkonen, 2016; Liu et al., 2020). Starov and Velarde. (2009) considered the influence of absorption liquid layer and liquid vapor, and made the following modifications and improvements to Young's equation:

$$cos\,\theta \approx 1 + \frac{1}{\gamma}\int_{e}^{\infty} \Pi(e)de$$

They defined the contact angle in this case as an angle between the horizontal axis and the tangent to the droplet cap profile at the point where it touches the absorbed layer of molecules (also called the precursor film). Where e is the thickness of the absorbing liquid molecules overlaid on the solid substrate, $\Pi(e)$ is the disjoining pressure. Letellier et al. (2007) considered the influence of solid liquid vapor three-phase line under the condition of system equilibrium, and established a more extensive Young's relationship. It includes a term inversely proportional to the radius of the circle defined by the triphase line, where σ is the line tension of the three-phase contact circle:

$$cos\,\theta = \frac{\gamma^{SV} - \gamma^{SL}}{\gamma^{LV}} - \frac{\sigma}{\gamma^{LV} R^{SLV}}$$

In order to further expand the application range of Young's equation, Lin and Hong. (2019) further deduced the Young's equation considering the contact between oil droplets and ideal smooth solid surface:

$$cos\theta_{OW(Y)} = \frac{\gamma_{OV}\,cos\,\theta_{OV} - \gamma_{WV}\,cos\,\theta_{WV}}{\gamma_{OW}}$$

Among them, the underwater oil contact angle ($\theta_{OW(Y)}$) is related to the interfacial tension or interfacial energy of oil-steam ($\theta_{OW(Y)}$), water-steam (γ_{WV}) and oil-water (γ_{OW}) interfaces. The θ_{OV} is the contact angle of oil droplets in air, and θ_{WV} is the contact angle of water droplets in air.

2.2.2 Wenzel model

In 1936 (Wenzel, 1949), Wenzel hypothesized that droplets in contact with a rough solid surface would produce a complete wetting phenomenon, that is, filling the grooves of the surface so that the actual contact area of solid-liquid on the rough surface is larger than the apparent contact area. Because the surface energy of rough surface is low, the contact angle of droplets is high, while the surface energy of smooth surface is high and the contact angle of droplets is low, Wenzel introduced the surface roughness (i.e., the ratio of the real surface area of the solid to the apparent geometric area, whose value is usually greater than 1):

$$\gamma = \frac{S}{S_0}$$

where denotes the actual surface area of the solid surface and denotes the apparent surface area of the solid surface. Then the Wenzel model can be expressed as:

$$cos\,\theta_\gamma = \gamma\,cos\,\theta$$

Whereθ_γ is the apparent contact angle of the droplet on the rough surface, and is the intrinsic contact angle of Young's equation. By studying the Wenzel model, the following conclusions can be confirmed: under the $\gamma > 1$ usual conditions of hydrophobic surfaces, increasing the surface roughness γ will increase the apparent contact angle θ_γ of droplets under the usual hydrophobic surface conditions, which indicates that the surface hydrophobic effect will increase; For hydrophilic surface, increasing the surface roughnessγ will decrease the apparent contact angle θ_γ of droplets, which indicates that the hydrophilic effect of the surface increases. This model provides a theoretical basis for

the preparation of super hydrophobic surface materials. However, the applicability of Wenzel model to homogeneous solid surfaces (solid surfaces composed of homogeneous chemical substances) is still limited, and it is not suitable for heterogeneous solid surfaces, nor can it explain the phenomenon that some hydrophilic surface materials can be converted into hydrophobic surfaces after being treated (Herminghaus, 2007; Chen et al., 2021a). At the same time, under the assumption that the droplets are completely wetted, the large energy barrier formed by the chemical composition and geometry will make it difficult for the droplets to roll. This contradicts the phenomenon that droplets are easy to roll on the superhydrophobic surfaces such as lotus leaves in nature (Nuraje et al., 2013; Rius-Ayra et al., 2018).

Seo and Kim. (2015) derived the modified Wenzel equation by considering the constant volume of droplets as an auxiliary condition and a transverse condition:

$$cos\,\theta = K\frac{\gamma_{SO} - \gamma_{SL}}{\gamma} = K\,cos\,\theta_Y$$

where θ_Y is the equilibrium contact angle on a smooth solid surface and θ is an apparent.

In order to solve the problem that the Wenzel model is only suitable for ordered arrays or uniform porous media with uniform characteristics, Han et al. (2007) proposed a modified Wenzel model to describe heterogeneous surfaces as follows:

$$cos\,\theta = \frac{cos\,\theta}{S}\int_{X_{min}}^{X_{max}} \frac{W_0}{\delta\sqrt{2\pi}}\frac{1}{X}\left[-\frac{(X_0 - X)^2}{2\delta^2}\right]dX$$

where W is the cumulative micropore volume, $W_0$is the totalmicropore volume determined from the D–R equation, X_0 is themicropore half width at the distribution curve maximum, andδ is the dispersion parameter.

2.2.3 Cassie–Baxter model

In 1944, Cassie and Baxter (Cassie, 1948) considered the influence of surface tension, and put forward the concept of compound contact. Because the size of the roughened surface structural unit is smaller than that of the droplet, the droplet on the surface can not completely penetrate into the groove on the surface, which results in air staying in the groove. Therefore, the Cassie–Baxter model of solid-liquid-gas three-phase composite contact is established:

$$cos\,\theta_c = f_1\,cos\,\theta_1 + f_2\,cos\,\theta_2$$

where θ_c is the apparent contact angle of the droplet on the rough surface, θ_1 and θ_2 are the intrinsic contact angles on the two media, f_1 and f_2 are the proportional fractions of the solid-liquid and air-liquid contact surfaces at the composite interface, respectively, and $f_1 + f_2 = 1$. Because the inherent contact angle between droplet and air is 180°, the model can be simplified as follows:

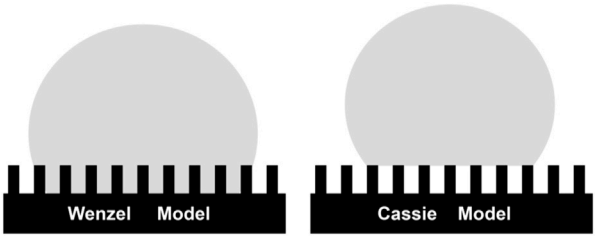

FIGURE 2
Microscopic diagram of droplets on the Wenzel model (left) and Cassie–Baxter model (right).

$$cos\,\theta_c = f_1\,cos\,\theta_1 - f_2$$

From this model, it can be clearly seen that the smaller the solid-liquid contact area ratio, the larger the contact angle of the rough surface and the better the hydrophobicity. This model explains some phenomena, for example, droplets on super-hydrophobic surfaces such as lotus leaves and rice leaves show very small rolling angle and hysteresis angles, which is difficult to be explained by Wenzel model. Figure 2 shows the difference between Wenzel model and Cassie–Baxter model.

It is worth noting that Wenzel model and Cassie–Baxter model have their respective applicable scopes. The Cassie–Baxter model is applicable to the highly hydrophobic region where the surface adhesion force is small, while the Wenzel model is applicable to the moderately hydrophobic region where the surface adhesion force is large. As a practical matter, if the droplet overcomes the energy barrier between the two modes and reaches the corresponding energy state under the action of an external force, its wettable viscous state can be transformed between the two models. That is, the wetting state of a droplet on a rough solid surface may then be transformed between both Wenzel and Cassie–Baxter.

In addition, Wang and Jiang. (2007) further refined the existence of five superhydrophobic surfaces based on the previous work (Figure 3): the Wenzel state (droplets are embedded on the surface in a fully wetted state and contact angle hysteresis can be observed), the Cassie state (droplets are independently in contact with the surface in a non-wetted state, with low surface adhesion and easy roll-off), the Lotus state (Cassie state special case, similar to the microscopic raised structure on the surface of lotus leaf, which is important for the design and construction of bionic superhydrophobic surfaces with self-cleaning properties), the Wenzel- Cassie transition state (the state that mainly exists in reality), and Gecko state (the state where droplets on polystyrene nanotube films have extremely high surface adhesion). Ideally, the contact angle of the droplet in Wenzel state is close to 0°, while droplets in the Cassie state

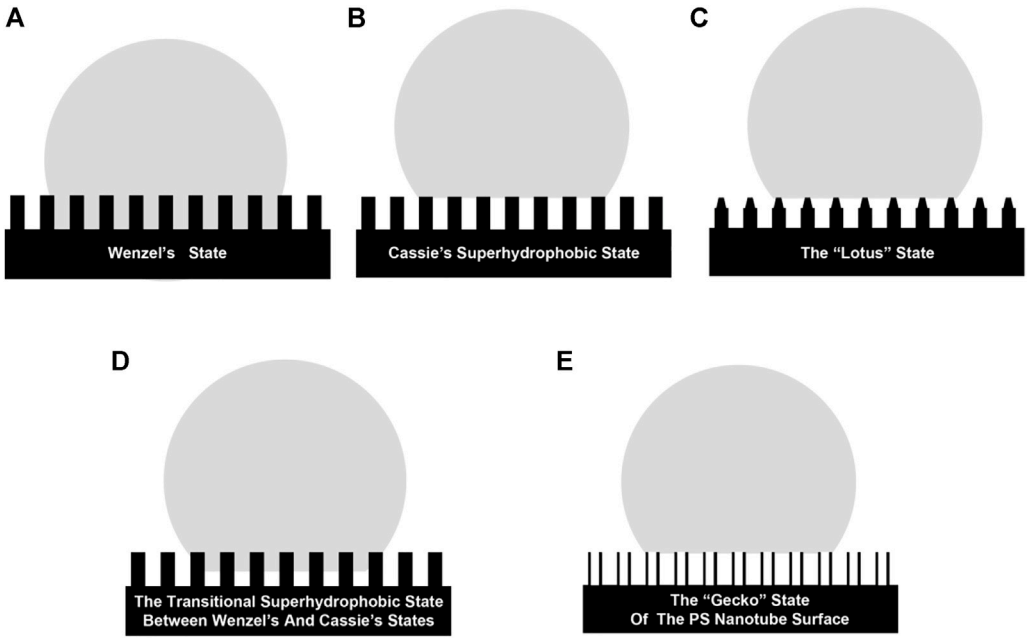

FIGURE 3
Diagram of the existence state of droplets on five superhydrophobic surfaces: Wenzel's state **(A)**, Cassie state **(B)**, Lotus state **(C)**, Wenzel- Cassie transition state **(D)**, Gecko state **(E)**.

TABLE 1 The surface structures of typical plants.

Plant surface	Properties	References
Lotus leaf	Superhydrophobic, self-cleaning, low adhesion	Cheng and Rodak. (2005); Teodorescu. (2014); Khandavalli et al. (2018); Xu et al. (2021a)
Rose petal	Superhydrophobic, high surface adhesion	Feng et al. (2008); Bhushan and Her. (2010); Lai et al. (2019)
Sunflower	Superhydrophobic, high surface adhesion	Hoefnagels et al. (2007); He et al. (2018); Liang et al. (2020)
Rice leaf	Superhydrophobic, directional transport	Wu et al. (2011); Lian et al. (2019)
Nepenthes	Directional transport, water harvesting	Wong et al. (2011); Zhang and Xu. (2021)
Purple setcreasea	Double-sided superhydrophobic	Guo and Liu (2007); Wolfs et al. (2013); Cai. (2019)
Watermelon leaf	Single-order scale hydrophobic structure	Zhang et al. (2012a); Gou and Guo. (2018); Sharma. (2021); Behera. (2022)
Peanut leaf	Superhydrophobic, high surface adhesion	Yang et al. (2014a); Yang et al. (2014b); Long et al. (2015)
Bamboo leaf	Anti-icing, high surface adhesion	Yuan et al. (2014); Zhang et al. (2019b); Gao et al. (2020)
Taro leaf	Superhydrophobic, self-cleaning	Verbanic et al. (2014); Kumar and Bhardwaj. (2020); Wu et al. (2020); Pieniazek et al. (2021)

would form perfect spheres (ignoring gravity), with the contact angle close to 180°.

3 Nature's biological superhydrophobic surfaces

Through 3.7 billion years of evolution and species selection, most of the creatures in nature have survived with various unique biological functions and structures, which enable them to quickly adapt to changes in the ecosystem and surrounding environment. According to the order of research objectives in the history of superhydrophobic surface development, this chapter follows the order from plants to animals, and lists many surface structures and multifunctional applications. In addition, according to the relationship between the multifunction of superhydrophobic surfaces from simple to complex, the representative examples of plants and animals are introduced in detail.

TABLE 2 Bionic product with lotus leaf as template.

Main materials	Technologies	Advantages	Ref
poly-ε-caprolactone	Needle-free electrospray	Adhesion resistance	Klicova et al. (2022)
Hexamethyldisiloxane	Electrospinning		
	Plasma-assisted chemical vapor deposition		
Zinc oxide	Chemical vapor deposition	No need for metal catalysts	Li et al. (2008)
Porous anodic			
Alumina			
Perchloric acid			
Ethanol			
Acetone			
Aniline		Favorable surface-to-volume ratio	
4.4- diaminodiphenylamine sulfate hydrate	Nano casting technology	Excellent anticorrosion performance	Chang et al. (2013)
4'-(4.4′- isopropylidene-diphenoxy) bis (phthalic anhydride)		Good electrical activity, mechanical properties and high temperature stability	
N,N- dimethylacetamide			
Ammonium persulfate			
Dimethyl silicone polymer			
Rubber sponge	Ultrasonic treatment	High temperature stability	Wang et al. (2021b)
Tetrahydrofuran		Stable conductivity, high compression ratio and linear working range	
MWCNTs		Excellent sensing stability and durability	
		Self-cleaning	
Copper foil	Chemical deposition method	Adhesion resistance	Wu et al. (2014)
Silver nitrate		Strong mechanical properties	
Octadecyl mercaptan			
Fresh lotus leaves			
Polymethylhydrosiloxane			
Phenyl substituted silica	Casting method	Multi-purpose	Nagappan et al. (2013)
Ammonium hydroxide solution	Dip coating method	Environmentally friendly	
Oxalic acid	Solvent evaporation method	Low price	
Polyvinylidene fluoride		Good thermal stability and mesoporous structure	
Polytetrafluoroethylene			
Medical gauze	Physical deposition	Good blood compatibility	Li et al. (2020a)
Dopamine	Chemical deposition	Adhesion resistance	
Perfluorocarbon		Antibacterial	
Silver nanoparticles			
Alumina film	—	Good blood compatibility	Mao et al. (2009)
Sodium hydroxide		Anti-platelet	
		Anti-blood cell adhesion	

3.1 The surface structures of typical plants

Table 1 lists the superhydrophobic phenomena and characteristics of many plants in nature. In fact, the first study of superhydrophobic surface by human beings started with the structure of plant surface. From dust and dirt on lotus leaves easily taken away by dew and rain, to small water drops firmly attached to rose petals on the surface, to water drops on rice leaves easily rolling towards the growth direction of leaves, natural plants have inspired us in many aspects.

3.1.1 Lotus leaves

The lotus leaf was described by the ancient Chinese as "dirt-free plant rising from soil", which is the most typical super-hydrophobic surface of plants (Latthe et al., 2014), and it is also one of the earliest research goals of human beings, which is why the "lotus leaf effect" is still synonymous with

TABLE 3 Bionic product with rose petals as template.

Main materials	Technologies	Advantages	Ref
Polyurethane Polycaprolactone glycol-400; 4-butanediol Triethylamine Dimethylformamide 4-diphenylmethane diisocyanate; Nano-fumed hydrophobic silica; Glycerol	A combination of replica molding and hydrophobic particle deposition	Reversibly transformed between Cassie–Baxter state and Cassie immersion state	Shao et al. (2020)
Dimethylol propionic acid PDMS NdFeB CIPs	Template method	Real-time wetting and adhesion behavior changes in response to magnetism	Drotlef et al. (2014); Chen et al. (2021b)
Red rose petals Acetone Polyvinyl butyral Polydimethylsiloxane Curing agent Octadecyl trichlorosilane Anhydrous ethanol Ethyl silicate GO	One-step solvothermal method Nanoimprint lithography method	Strong mechanical properties High thermal stability High buoyancy	Yang et al. (2019)
Latex balloon; (heptadecafluoro-1.1,2,2-tetrahydrodecyl) trichlorosilane	3D shrinking method	Tunable adhesion (39.2–129.4 μN) Ultralarge liquid capacity	Tan et al. (2019)
Cuprum $FeCl_3$	Chemical etching method	Simple, fast, cheap Controllable adhesion	Bahrami et al. (2017)
Stearic acid Rose petals Chloroform; n-hexadecane	Two-step molding process Wax evaporation method	Controllable adhesion	Bhushan and Her, (2010)
Cuprum Hydrochloric acid Sodium hydroxide Cerium myristate	Electrodeposition method	Excellent stability and corrosion resistance Fast and easy Low cost	Liu et al. (2014)

superhydrophobic characteristics. Later, Jiang et al. (Barthlott and Neinhuis, 1997) determined that the surface of lotus leaves is a hierarchical structure formed by micron-sized papillae and nanoscale wax crystals covering the surface, and they also explained the relationship between superhydrophobicity and self-cleaning. It is worth mentioning that in the water condensation experiment, water is hydrophilic on lotus leaves that have experienced water condensation, which shows that lotus leaves can be hydrophobic or hydrophilic, depending on how the water reaches their surface (Cheng and Rodak, 2005). Considering the characteristics of the lotus leaf and the bionic means of scientists, it has a rich and broad application prospect in production and life (Table 2).

One of the more common is the application of lotus leaf in the medical field (Lim et al., 2013; Yang et al., 2014c; Wu et al., 2021b; Huang et al., 2022). Klicova et al., (2022) developed a biocompatible nanofiber pad with anti-adhesion surface by imitating the nanostructure on the lotus leaf by using needle-free electrospraying and polycaprolactone electrospinning technology, which not only shortens the operation time but also greatly reduces the postoperative risk. At the same time, inspired by the self-cleaning characteristics of lotus leaves, Li et al. (2020a) developed a new type of anti-adhesion and antibacterial gauze through three simple dipping steps. With its excellent anti-adhesion and bactericidal activity, it can promote infectious wound regeneration and meet clinical needs. Due to the increasing demand for blood compatibility of biomaterials, Mao et al. (2009) focused on the preparation of an anticoagulant biomaterial-polystyrene nanotube film, which can prevent thrombosis and tissue capsule, and is of great significance in organ transplantation. In addition, the application of super hydrophobicity of biomimetic lotus leaf is also involved in the field of gas sensors (Li et al., 2008) and meteorology (Wang et al., 2021b).

TABLE 4 Bionic product with rice leaves as template.

Main materials	Technologies	Advantages	Ref
poly [6-(4-methoxy-4′-oxyazobenzene)hexyl methacrylate]	Reverse Breath Figure	Effective and convenient water collection	Gao et al. (2018)
Gold nanoparticles	Self-assembly		
1H,1H,2H,2H-perfluorodecanethiol			
Aluminum	Femtosecond laser grating scanning	Fast	Yang et al. (2021)
		Anisotropic superhydrophobic	
		Self-cleaning	
TiO_2	3D printing technology of stereolithography	Drag reduction	Barraza et al. (2022)
Hexadeciltrimethylsiloxane		Anisotropy	
Samples of each of the rice leaf, butterfly wing, rainbow trout fish scales, and Mako shark skin	Template method	Self-cleaning	Bixler and Bhushan, (2012)
Liquid platinum silicon		Drag reduction	
Isopropanol			
Liquid carbamate polymer			
Green rice leaf			
Polydimethylsiloxane	Femtosecond laser method	Three-dimensional anisotropy	Fang et al. (2018)
Fluoroalkyl silane			
Silicon substrate			
Dimethyl siloxane			
Heptafluorodecyl trimethoxysilane	Laser etching method	Switchable isotropy-anisotropy	Cheng et al. (2018)
Bisphenol A diglycidyl ether	Chemical etching method		
N-octylamine	Template method		
M-xylylenediamine			

3.1.2 Rose petals

In contrast to the lotus leaf, the rose petal is the canonical example in the Wenzel model. As its petal fibers have a micro-nano double-order structure scale larger than that of the lotus leaf surface, the droplets tend to completely wet the larger scale surface grooves, resulting in increased surface roughness, high surface adhesion, and strong contact angle hysteresis. This shows that even if the petals are inverted, the droplets on the surface will not fall off. Jiang et al. first discovered this phenomenon in 2008 and called it the "petal effect" (Feng et al., 2008). Subsequently, Zheng et al. (2019) studied the dynamic wetting law of viscous superhydrophobic substrates for the first time by comparing and analyzing simple artificial petal-like substrates and superhydrophobic substrates. As shown in Table 3 is bionic product with rose petals as template.

It can be predicted that the self-cleaning functional surface with the "lotus leaf effect" has played an important role in drag reduction, cell culture, dust control (Nosonovsky and Bhushan, 2009; Ueda and Levkin, 2013), while the application prospect of "petal effect" is much broader for non-destructive fluid transfer and biotechnology (Sun et al., 2005; Lai et al., 2013; Yue et al., 2020).

It is worth noting that because the super-hydrophobic rose petals have different surface microstructure and nanostructure, the adhesion of different petals is also different. On the basis of studying two kinds of super-hydrophobic rose petals with high and low adhesion, Bhushan and Her. (2010) prepared artificial super-hydrophobic surfaces with high and low adhesion by wax evaporation, in which the droplets with high adhesion will not fall when the substrate is vertically inclined or inverted.

In addition, since rose petals and lotus leaves are natural examples of the Wenzel-Cassie transition state and the Cassie–Baxter model, respectively, an increasing number of scholars have compared the two with the intention of exploring the relationship and transition between them (Zhang et al., 2012b). The researchers realized the reversible transition between the Cassie–Baxter state and the Cassie impregnation state of the superhydrophobic surface by adjusting the micro/nanostructure of the shape memory polymer SMP. This surface controls the adhesion behavior of liquids and has an important impact on rewritable patterns and the transport and collection of controlled droplets (Shao et al., 2020). In order to apply the superhydrophobic surface to droplet microfluidic chip and microfluidic transmission, Drotlef et al. (2014) Chen et al., 2021b) focused on the magnetic response surface, and proposed a magneto rheological elastomer superhydrophobic surface with magnetic response, which can be quickly and reversibly replaced between "lotus effect" and "rose petal effect". For large general conductor materials, Liu

et al. (2014) developed a one-step electrodeposition method to prepare controllable superhydrophobic surface with excellent stability and corrosion resistance.

3.1.3 Rice leaves

Compared with the former two, rice leaves show another interesting new feature: by macroscopic observation, droplets on rice leaves are easier to slide down in the growth direction of rice leaf (from the stem to the petiole or from the stem to the tip). Microscopically, the surface of rice leaves is also a super hydrophobic surface suitable for the Cassie–Baxter model, but the arrangement of its surface structure is quite different from that of lotus leaves and rose petals. Micro-nano double-stage structures are arranged orderly along the growth direction of rice leaves, but randomly in the vertical direction (Bhushan et al., 2009; Wu et al., 2011), just like the roof tile structure in ancient China. The geometric structure of micro-grooves arranged in order along the same direction makes the energy barrier overcome by liquid droplets rolling along the parallel direction of leaves and stems much smaller than the energy barrier perpendicular to the direction of leaves and stems, resulting in anisotropy of surface adhesion. The rolling angles measured by experiments are 3°–5° along the direction parallel to leaves and stems and 9°–15° in the vertical direction (Feng et al., 2002). As shown in Table 4 is bionic product with rice leaves as template.

With the intensive study of the unique anisotropic (also called liquid-oriented) superhydrophobicity of rice leaves, once again, the field of liquid-oriented drag reduction, water collection and transport has been promoted (Gleiche et al., 2000; Higgins and Jones, 2000; Chen et al., 2005).

Therefore, the researchers are committed to constructing an anisotropic hierarchical structure based on the unidirectional sliding of water droplets in rice leaves (Zhang et al., 2012b; Gao et al., 2018; Xu et al., 2020). Yang et al. (2021) transformed the bionic superhydrophobic surface from isotropic to anisotropic by laser grating scanning, and obtained an anisotropic superhydrophobic aluminum surface with rice leaf shape. Inspired by the microstructure of lotus leaf and rice leaf, Cheng et al. (2018) proposed a new functional material. By repeatedly controlling the surface microstructure shape between lotus leaf structure and rice leaf structure, the reversible transition between isotropic and anisotropic wetting state of superhydrophobic was realized. In addition, the superhydrophobic surface has good stability, even after 1 month, intelligent transformation can be observed, and it is widely used in controlled droplet transportation. In order to highly reproduce the surface structure of rice leaves, Fang et al. Fang et al. (2018) used two-step soft transfer to develop the structure of artificial rice leaves. The structure has the sliding characteristic of anisotropy clearly. The systematic measurement shows that the sliding angles of the structure parallel to the vein direction and perpendicular to the vein direction are 25° and 40° respectively, which can be used for the rapid fabrication of large area artificial rice leaf surface without expensive instruments and complex techniques.

3.1.4 Chapter summary

By comparing the superhydrophobicity of plant surface, it can be easily found that small differences in surface morphology or characteristic size will lead to great differences in surface wetting behavior. For example, the microstructure of rose petals has a larger distance than lotus leaves, which brings a completely different phenomenon, and the micro-morphology of rice leaves arranged regularly will limit the rolling direction of droplets, and so on. Therefore, when constructing and preparing superhydrophobic biomimetic materials, researchers often not only take one organism as a reference, but also combine different structures of various organisms according to the target field to achieve the purpose of meeting the application requirements.

3.2 The surface structures of typical animals

Plants are not the only creatures with superhydrophobic properties. Superhydrophobicity can also be found in different animals, some of which are listed in Table 5, and typical ones will be selected to be elaborated in more detail.

3.2.1 Gecko feet

Gecko has the ability to crawl on smooth vertical walls, which has aroused researchers' interest. With the strengthening of research in the past century, the description of the gecko crawling instincts has expanded from macroscopic grasping and suction cup to microscopic Van der Waals forces, which is more and more correct and rigorous. As shown in Table 6 is bionic product with gecko feet as template.

Different from the self-cleaning ability of lotus leaf in wet environment, gecko foot has good hydrophobicity, but also has high surface adhesion and self-cleaning performance in dry environment, which provides a direction for the research of dry self-cleaning materials.

Its microscopic state applies to the Gecko state among the five superhydrophobic surface existence states, due to the growth of about half a million micron-level extremely fine bristles on the gecko foot, each bristle end also exists a large number of nanoscale villi branches, which makes the distance between the micro-nano double-order array and the contact surface further reduced and the contact area further increased, so that the sum of the weak Van der Waals forces is sufficient to generate a strong surface adhesion force. The energy barrier for droplet movement increases, so it has the ability to climb walls (Autumn et al., 2000; Autumn et al., 2002; Wang et al., 2012).

As for the mechanism of drying self-cleaning,Xu et al. (2015) showed that geckos used a unique toe-off action in rapid movement, and this dynamic process resulted in a very large

TABLE 5 The surface structures of typical animals.

Animal surface	Properties	References
Gecko foot	High surface adhesion, self-cleaning	Wang et al. (2012); Darmanin and Guittard. (2015); Watson et al. (2015); Sethi et al. (2019)
Cicada wing	Self-cleaning, anti-reflective	Zhang et al. (2006); Xie et al. (2017); Teisala and Butt. (2018); Oh et al. (2019); Román Kustas et al. (2020)
Shark skin	Self-cleaning, underwater drag reduction, self-reparing	Walsh. (1983); Liu et al. (2019); Monfared et al. (2019); Xiang and Liu. (2021)
Penguin feather	Anti-icing, liquid guidance	Wang et al. (2016); Ma et al. (2017); Alizadeh-Birjandi et al. (2020)
Butterfly wings	Self-cleaning, liquid-directed	Zheng et al., 2007; Fang et al., 2008; Tuo et al., 2019)
Spider silk	Water collector	Zheng et al. (2010); Wang et al. (2017); Gustafsson et al. (2018); Si et al. (2018)
Earthworm	Drag reduction, lubrication	Zhao et al. (2018); Xu et al. (2021b); Carmichael. (2021)
Mosquito compound eye	Superhydrophobic, anti-fog	Gao et al. (2007); Wang et al. (2019b); Liu et al. (2021)
Dragonfly wings	Self-cleaning,Superhydrophobic	Nguyen et al. (2013); Nguyen et al. (2014a); Cheeseman et al. (2018)

TABLE 6 Bionic product with gecko feet as template.

Main materials	Technologies	Advantages	Ref
Choline chloride	Template-free electrodeposition	High adhesion	Li et al. (2020b)
Ethylene glycol			
$ZnCl_2$			
Stearic acid			
1H, 1H, 2H, 2 H-perfluorooctane triethoxy silane	Two-step template method	Switching adhesion	Zhang et al. (2021)
Hydrogen peroxide			
Sulfuric acid			
Silicone template			
Castor oil			
Diphenylmethane diisocyanate; Bisphenol An epoxy resin			
Diglycidyl ether			
Dodecylamine			
M- dimethylamine			
N- polyethylene terephthalate			
O- Polyurethane			
Acrylate			
Adhesive			
Polystyrene	Hot pressing	Strong adhesion	Sauer. (2010); Tan et al. (2020)
Aluminum plate	Shear pressing technology		
	Oxygen plasma treatment		
Anodic alumina	—	Strong adhesion	Liu et al. (2012)
4.4′-Oxydianiline			
N,N-dimethylacetamide			
Pyromellitic dianhydride powder; hydrochloric acid			
Fluoroalkylsilane ethanol solution			
Polystyrene			
Alumina membrane	Tmplate-wetting method	Strong adhesion	Jin et al. (2005)
Xylene			
Sodium hydroxide			

TABLE 7 Bionic product with cicada wings as template.

Main materials	Technologies	Advantages	Ref
Cicada wings	—	Antibacterial	Ivanova et al. (2012)
Polydimethylsiloxane	Template method	Anti-reflection	Liu et al. (2016)
Ethyl orthosilicate		Self-cleaning	
Silicon wafer	Deep reactive ion etching	Self-cleaning	Hasan et al. (2015)
C_4F_8		Antibacterial	
SF_6			
O_2			
Cicada wing	High speed wire electrical discharge machining	Simple, low cost	Liang et al. (2017)
7075 aluminum alloy		Strong mechanical properties	
Molybdenum wire		Environmental friendliness	
Silica microspheres; (Tridecafluoro-1.1,2,2-tetrahydrooctyl)-trichlorosilane;	Self-assembly method	Broadband anti-reflection	Chen et al. (2015)
PET	Chemical etching method		
Ethoxylated trimethylolpropane triacrylate monomer			
Photoinitiator			

TABLE 8 Bionic product with penguin feathers as template.

Main materials	Technologies	Advantages	Ref
Steel	One step precipitation polymerization	Effectively delay the icing process	Yang et al. (2016); Latthe et al. (2019)
Hydrogen peroxide		Durable	
Strong acid			
Heptadecafluorodecyl tripropoxy silane			
Body hair of Humboldt cocktail			
1.2,4,5-benzenetetracarboxylic anhydride	Electrospinning	Excellent mechanical strength at low temperature	Wang et al. (2016)
4.4′-diaminodiphenyl ether			
Polyvinylidene fluoride	Electrospinning	Excellent mechanical strength, thermal stability and excellent corrosion resistance	Vicente et al. (2021)
Dimethyl formamide			
Acetone			
Silicon substrate			
Nickel chloride hexahydrate			
Nickel sulfamate tetrahydrate	Lithography	Ice-proof; Wear-resistant	Li et al. (2021c)
Boric acid			
2- ethylhexyl sodium sulfate			
Saccharin sodium hydrate			
Chemical etching method			

instantaneous separation rate of their bristles and contact surfaces. Due to the bristle and shovel-like tentacle system with micro-nano dual-stage structure, the surface adhesion between the foot walls has little to do with the detachment speed, while the detachment force of the microsphere increases with the increase of detachment speed. It is this subtle difference that makes it easy to achieve dry self-cleaning effect during the rapid movement of the gecko. The research results not only provide new design ideas for the long-standing industrial particle manipulation, but also provide a new research direction for the preparation of functional surfaces that can be used repeatedly and have self-cleaning and particle manipulation properties (Kamperman et al., 2010; Liu et al., 2010; Darmanin and Guittard, 2015).

According to the characteristics of geckos, researchers have produced various adhesive materials with high surface adhesion (Li et al., 2011; Liu et al., 2012). In order to design a new type of adhesive film, Zhang et al. (2021) proposed a shape memory film with adhesion to solids and liquids. With high water repellency and low adhesion (about 51 N), this film provides a new idea for the design of different adhesives. Sauer et al. (Tan et al., 2020) prepared nanotube arrays (Eiof~3 GP) with similar size to gecko bristles from hydrophobic polystyrene, which provided guidance for adhesives designed in wet or underwater environments. In addition, the researchers also used AAO template to prepare multi-scale structure of gecko-like polyimide film. On the basis of stable superhydrophobicity, the film has a high adhesion to water (about 66 μN), and can be used as a manipulator to capture water droplets from a low-adhesion superhydrophobic surface (Liu et al., 2012).

3.2.2 Cicada wings

Compared with the century-old research of gecko, the discovery of super-hydrophobic cicada wings is much later. The Chinese idiom "as thin as a cicada's wing" is used to describe the extremely small thickness of an object. The scanning electron microscope shows that the thickness of a cicada's wing is only 8–10 μm, but the self-cleaning and anti-reflection characteristics of cicada's wings provide another way to discover the superhydrophobic characteristics (Zhang et al., 2006; Dellieu et al., 2014). As shown in Table 7 is bionic product with cicada wings as template.

Similar to the liquid thin layer at the mouth of pitcher plant, the regular hexagonal micro-nano two-level structure on the surface of cicada wings makes cicada wings have better superhydrophobic performance and self-cleaning ability, especially the micro-nano structure composed of three-dimensional waxy structure is easier to adsorb the air thin layer (Lee et al., 2004; Nguyen et al., 2014b).

Because of its different characteristics, cicada wing is widely used in medical treatment, optoelectronic devices and other fields, mainly due to its antibacterial and anti-reflection properties.

First of all, there are some similarities between cicada wings and lotus leaves in antimicrobial activity (Hasan et al., 2013; Kelleher et al., 2016). In order to limit the spread of infection without antibiotics, Ivanova et al. (2012) used anodization, lithography, micellar lithography and self-assembly to simulate the penetration of nanotube arrays on the surface of cicada wings. They solved the huge losses caused by antibiotic resistance and antibiotic action of pathogens by preparing antibacterial surfaces. The researchers prepared a nanostructured 'hypersurface' based on the deep reactive ion etching of silicon wafers. The surface is sustainably antibacterial, kills mammalian cells (mouse osteoblasts), and is used in surgical instruments (Hasan et al., 2015).

In addition, Watson and Watson. (2004) found that compared with plants such as lotus leaves, the hexagonal array of cicada wings has a circular tip extending outward about 150–350 nm. To some extent, this unique structure can be regarded as a kind of gradient refractive index material, which leads to the change of photoimpedance, the decrease of light reflection and the enhancement of antireflectivity (Stoddart et al., 2006; Xie et al., 2017). Inspired by the cicada wing structure, the researchers successfully prepared antireflective films with an average transmittance of 98% and nano-solar cells with strong absorptivity in a wide spectral range. Similarly, Liu et al. (2016) used PDMS to replicate the nano-cone structure of cicada wings to prepare the multi-functional surface of artificial cicada wings. Not only the antireflection effect is outstanding, but also the contact angle of the forward PDMS replica can reach 152°. It has a broad application prospect in many optical equipment.

3.2.3 Penguin feathers

Penguins living in the Antarctic often go to sea to feed, but their feathers do not get wet and are extremely difficult to freeze, which has aroused the interest of researchers. Penguin feathers, as a super hydrophobic material with high ice resistance, which has aroused the interest of researchers and become a hot research object in recent years. In view of the waterproof and ice resistance of penguins, Alizadeh-Birjandi explained the main mechanism of delayed solidification of waterproof materials by developing a heat transfer model, which was extended to general superhydrophobic surfaces (Alizadeh-Birjandi et al., 2020). As shown in Table 8 is bionic product with penguin feathers as template.

(Bormashenko et al. (2012) found that hook-like structures with a diameter of about 3 μm and a spacing of about 20 μm are arranged in an orderly manner on the feather branches parallel to penguin micro-scale and sub-micron feathers. The micro-nano double-stage structure has good hydrophobicity and liquid guiding property, so that the droplets falling on it slide down along the growth direction of the feather.

Further research by Wang et al. (2016) found that the surfaces of feather twigs and feather hooks are not smooth, but lined with grooves with a depth of about 100 nm. These grooves can save air, so that droplets cannot be completely wetted, but exist in Cassie state among five super-hydrophobic surface states, that is, droplets can be regarded as spherical on feather surface, which is easier to slide down and slower in heat dissipation. This multi-stage structure reduces the adhesion between ice and makes penguin feathers have excellent anti-icing performance. In addition, the penguin tail evolved a gland that can secrete oil. Penguin use their beaks to spread oil on feathers, which can play a role in waterproof.

According to the excellent anti-icing and anti-condensation properties of penguin feathers, many applications in heavy industries such as aerospace and ships have been derived. Inspired by the three-dimensional microstructure network of penguin body hair, Wang et al. fabricated a novel polyimide nanofiber film on asymmetric electrodes by electrospinning. The film has good mechanical strength at low temperature (no brittle fracture in liquid nitrogen), which prevents the accumulation of

pinning droplets and realizes hydrophobicity. It can be used in the aerospace field to avoid the great danger caused by aircraft icing during flight in extreme weather (Wang et al., 2016). Vicente et al. (2021) used electrospinning technology to prepare functional polyvinylidene fluoride (PVDF) fibers for the excellent hydrophobicity and anti-stickiness of penguin feathers. It can not only prevent the aircraft from drift and resistance caused by atmospheric icing caused by supercooled droplets, but also has excellent mechanical strength, thermal stability and very good corrosion resistance. In the field of ship navigation, researchers used a sprayable mixture of hydrophobic silica nanoparticles embedded in a silica gel matrix to create a bionic superhydrophobic surface that can be used for turbulent drag reduction, thus solving the problem that ships consume a lot of energy to overcome underwater resistance (Golovin et al., 2016). In addition, (Li et al. (2021c) using a simple and potentially low-cost method, a flexible hydrophobic surface was prepared by combining a mechanical durable nickel skeleton with an interconnected microwall array filled with hydrophobic polytetrafluoroethylene (PTFE). Even under the pressure of 0.12 MPa, the prepared surface can remain hydrophobic after more than 1,000 times of linear wear. Compared with the inherent hydrophilic metal surface, the good hydrophobicity also enhances the anti-ice function, and can be used as a multi-functional environmental protection coating in navigation engineering.

3.2.5 Chapter summary

Different super-hydrophobic characteristics of animals are closely related to their living environment. For example, the hydrophobic and anti-icing characteristics of warm feathers are of great significance to the survival of animals in cold regions, while underwater fish have evolved to reduce underwater resistance. People use these different properties and structures to design and manufacture many engineering materials, which provide a reliable guarantee for people's medical health, aerospace and many other fields.

4 Summary and outlook

The hierarchical structure formed by micron-scale papillae and nanoscale wax crystals covering the surface of a lotus leaf, the larger micro-nano double-ordered structure and grooves of rose petal fibres, the geometry of micro-grooves ordered along the same direction in a rice leaf, the bristles and spatula-like tentacle system of the micro-nano double-ordered structure of a gecko foot, the micro-nano structure consisting of regular hexagonal micro-nano two-stage structures and three-dimensional wax structures on the surface of a cicada wing, the micron-scale and The ordered arrangement of the feather branches of sub-micron feathers. All these excellent structures and functions in nature are achieved through multi-level and multi-scale assembly from simple to complex and from disorder to order, which also provides good inspiration for intelligent bionanism in humans. The rich diversity of nature and the adaptive changes of organisms inspire us to think endlessly, and the inventions using the surface hydrophobicity of animals and plants are unique and diverse. From daily necessities to heavy equipment, superhydrophobic materials have attracted people's unremitting pursuit and exploration for their high performance, low cost and simple preparation process. Based on the principle and concept of superhydrophobic surfaces, this paper mainly introduces the superhydrophobic properties of various animals and plants in nature and their great practical application value, and summarizes the differences and application fields of different superhydrophobic surfaces. Finally, we will put forward a reasonable assumption and plan for the future development prospect of bionic superhydrophobic technology. In view of the achievements and efforts made by our predecessors in constantly exploring the principles and methods of bionic superhydrophobicity, it has laid a solid foundation for us to further develop bionic superhydrophobic materials with simpler, more environmentally friendly materials and lower cost. At present, part of the bionic superhydrophobic technology is gradually changing from the laboratory scale to large-scale industrial production, which has a broad prospect, but the existing problems and shortcomings are also gradually emerging, such as low production efficiency, high production cost, unfriendly to the environment and so on. In this paper, the following ideas are put forward for the future bionic superhydrophobic from natural organism to artificial functional surface:

1) Green, environmentally friendly and sustainable materials make what we are looking for. At present, the Main materials used in the manufacture of superhydrophobic materials are mainly harmful reagents, such as fluorinated superhydrophobic materials, which successfully reduce the surface free energy, but are challenging to the growing environmental and human health problems. We should further develop biodegradable, nontoxic and environmentally friendly new materials into the process of preparing superhydrophobic surfaces, so as to avoid biological pollution and environmental pollution, resulting in irreversible consequences.
2) In light of the fact that the structure and function of these excellent superhydrophobic properties of natural organisms are achieved through multi-level and multi-scale assemblies from simple to complex and from disordered to ordered. Therefore, the development of novel high-performance nanocomposite structures and materials can be achieved by drawing on multiple structures and models.
3) How to make the application materials have sustainable durability has become a big problem. At present, the durability of nanostructure coating on mechanical wear and impact caused by flowing fluid is lower than expected. On the one hand, we need to make some exquisite surface structures,

such as micro-nano hierarchical structures or nanostructures, in order to obtain the final superhydrophobic properties. On the other hand, we require the surface to have good surface mechanical properties to meet the requirements of the application. The two are opposing in nature. Therefore, it will be an important research direction in the future that how to achieve a balance or improve its surface mechanical properties on the premise of keeping its surface super-hydrophobic.

4) Compared with the traditional micro-nano processing methods (ion etching, chemical vapor deposition, template method, etc.), femtosecond laser technology has the advantages of high precision, good controllability and applicability to different materials. Therefore, intelligent bionic design with the help of advanced manufacturing technologies and tools such as femtosecond laser machining is also a focus of future research (Yong et al., 2015; Zhang et al., 2020; Fang et al., 2022; Yong et al., 2022; Zhang et al., 2022).
5) The structural and functional design can be coherent and consistent, and the functional design can be considered in conjunction with the natural optical properties of the creature, thus imparting a more aesthetic character.

Author contributions

SG-Z: writing—original draft, writing—review and editing, visualization, methodology; TC: visualization, methodology, investigation, writing—review and editing; HY: writing—review and editing, investigation; YD: writing—review and editing; MS: supervision, writing—review and editing.

Funding

This research was funded by the Project Fund of Resource Value Evaluation of Important Wild Economic Plants in Natural Forests in Prohibited Logging Areas of Northeast China (2019FY100505).

Conflict of interest

The authors declare that the research was conducted in the absence of any commercial or financial relationships that could be construed as a potential conflict of interest.

Publisher's note

References

Ahmad, I., and Kan, C. (2016). A review on development and applications of bio-inspired superhydrophobic textiles. *Materials* 9 (11), 892. doi:10.3390/ma9110892

Alizada, A. N., and Sofiyev, A. H. (2011). Modified Young's moduli of nano-materials taking into account the scale effects and vacancies. *Meccanica* 46 (5), 915–920. doi:10.1007/s11012-010-9349-1

Alizadeh-Birjandi, E., Tavakoli-Dastjerdi, F., Leger, J. S., Faull, K. F., Davis, S. H., Rothstein, J. P., et al. (2020). Delay of ice formation on penguin feathers. *Eur. Phys. J. Spec. Top.* 229 (10), 1881–1896. doi:10.1140/epjst/e2020-900273-x

Aljumaily, M. M., Alsaadi, M. A., and Das, R. (2018). Optimization of the synthesis of superhydrophobic carbon nanomaterials by chemical vapor deposition [J]. *Sci. Rep.* 8 (1), 1–12.

Autumn, K., Liang, Y. A., Hsieh, S. T., Zesch, W., Chan, W. P., Kenny, T. W., et al. (2000). Adhesive force of a single gecko foot-hair. *Nature* 405 (6787), 681–685. doi:10.1038/35015073

Autumn, K., Sitti, M., Liang, Y. A., Peattie, A. M., Hansen, W. R., Sponberg, S., et al. (2002). Evidence for van der Waals adhesion in gecko setae. *Proc. Natl. Acad. Sci. U. S. A.* 99 (19), 12252–12256. doi:10.1073/pnas.192252799

Bahrami, H. R. T., Ahmadi, B., and Saffari, H. (2017). Preparing superhydrophobic copper surfaces with rose petal or lotus leaf property using a simple etching approach[J]. *Mater. Res. Express* 4 (5), 055014.

Bai, H., Zhang, L., and Gu, D. (2018). Micrometer-sized spherulites as building blocks for lotus leaf-like superhydrophobic coatings. *Appl. Surf. Sci.* 459, 54–62. doi:10.1016/j.apsusc.2018.07.183

Barraza, B., Olate-Moya, F., Montecinos, G., Ortega, J. H., Rosenkranz, A., Tamburrino, A., et al. (2022). Superhydrophobic SLA 3D printed materials modified with nanoparticles biomimicking the hierarchical structure of a rice leaf. *Sci. Technol. Adv. Mater.* 23 (1), 300–321. doi:10.1080/14686996.2022.2063035

Barthlott, W., and Neinhuis, C. (1997). Purity of the sacred lotus, or escape from contamination in biological surfaces. *Planta* 202, 1–8. doi:10.1007/s004250050096

Bayram, F., Mercan, E. S., and Karaman, M. (2021). One-step fabrication of superhydrophobic-superoleophilic membrane by initiated chemical vapor deposition method for oil–water separation. *Colloid Polym. Sci.* 299 (9), 1469–1477. doi:10.1007/s00396-021-04870-1

Behera, A. (2022). *Self-cleaning materials[M]//Advanced materials*. Cham: Springer, 359–394.

Bhushan, B., and Her, E. K. (2010). Fabrication of superhydrophobic surfaces with high and low adhesion inspired from rose petal. *Langmuir* 26 (11), 8207–8217. doi:10.1021/la904585j

Bhushan, B., Nosonovsky, M., and Chae Jung, Y. (2007). Towards optimization of patterned superhydrophobic surfaces. *J. R. Soc. Interface* 4 (15), 643–648. doi:10.1098/rsif.2006.0211

Bhushan, B. (2018). *Characterization of rose petals and fabrication and characterization of superhydrophobic surfaces with high and low adhesion[M]// Biomimetics*. Cham: Springer, 259–287.

Bhushan, B., Jung, Y. C., and Koch, K. (2009). Micro-nano- and hierarchical structures for superhydrophobicity, self-cleaning and low adhesion. *Phil. Trans. R. Soc. A* 367, 1631–1672. doi:10.1098/rsta.2009.0014

Bilgiç, C., and Bilgiç, Ş. (2019). Innovative superhydrophobic materials designed with inspiration from nature[J]. *Theory Res. Eng. II* 163.

Bittoun, E., and Marmur, A. (2009). Optimizing super-hydrophobic surfaces: Criteria for comparison of surface topographies. *J. Adhesion Sci. Technol.* 23 (3), 401–411. doi:10.1163/156856108x369958

Bixler, G. D., and Bhushan, B. (2012). Bioinspired rice leaf and butterfly wing surface structures combining shark skin and lotus effects. *Soft matter* 8 (44), 11271–11284. doi:10.1039/c2sm26655e

Bixler, G. D., and Bhushan, B. (2014). Rice- and butterfly-wing effect inspired self-cleaning and low drag micro/nanopatterned surfaces in water, oil, and air flow. *Nanoscale* 6 (1), 76–96. doi:10.1039/c3nr04755e

Bormashenko, E., Gendelman, O., and Whyman, G. (2012). Superhydrophobicity of Lotus leaves versus birds wings: Different physical mechanisms leading to similar phenomena. *Langmuir* 28 (42), 14992–14997. doi:10.1021/la303340x

Butt, H. J., Golovko, D. S., and Bonaccurso, E. (2007). On the derivation of young's equation for sessile Drops: nonequilibrium effects due to evaporation. *J. Phys. Chem. B* 111 (19), 5277–5283. doi:10.1021/jp065348g

Cai, Y. (2019). *Design and fabrication of superhydrophobic and antimicrobial surfaces on AISI 316L stainless steel[J]*.

Carmichael, S. W. (2021). Earthworms inspire the creation of fabrics that aggressively repel water. *Micros. Today* 29 (4), 8–9. doi:10.1017/s1551929521000857

Cassie, A. B. D. (1948). Contact angles. *Discuss. Faraday Soc.* 3, 11–16. doi:10.1039/df9480300011

Chang, K. C., Lu, H. I., Peng, C. W., Lai, M. C., Hsu, S. C., Hsu, M. H., et al. (2013). Nanocasting technique to prepare lotus-leaf-like superhydrophobic electroactive polyimide as advanced anticorrosive coatings. *ACS Appl. Mat. Interfaces* 5 (4), 1460–1467. doi:10.1021/am3029377

Cheeseman, S., Owen, S., Truong, V. K., Meyer, D., Ng, S. H., Vongsvivut, J., et al. (2018). Pillars of life: Is there a relationship between lifestyle factors and the surface characteristics of dragonfly wings? *ACS Omega* 3, 6039–6046. doi:10.1021/acsomega.8b00776

Chen, C., Liu, M., Zhang, L., Hou, Y., Yu, M., and Fu, S. (2019). Mimicking from rose petal to Lotus leaf: Biomimetic multiscale hierarchical particles with tunable water adhesion. *ACS Appl. Mat. Interfaces* 11 (7), 7431–7440. doi:10.1021/acsami.8b21494

Chen, C., Pan, L., Li, H., Liu, Q., Li, F., Tu, J., et al. (2021). Conversion of superhydrophilicity to superhydrophobicity by changing the microstructure of carbon-high fly ash. *Mater. Lett.* 299, 130051. doi:10.1016/j.matlet.2021.130051

Chen, D., Liu, Y., Chen, H., and Zhang, D. (2018). Bio-inspired drag reduction surface from sharkskin. *Biosurface Biotribology* 4 (2), 39–45. doi:10.1049/bsbt.2018.0006

Chen, S., Zhu, M., Zhang, Y., Dong, S., and Wang, X. (2021). Magnetic-responsive superhydrophobic surface of magnetorheological elastomers mimicking from Lotus leaves to rose petals. *Langmuir* 37 (7), 2312–2321. doi:10.1021/acs.langmuir.0c03122

Chen, Y. C., Huang, Z. S., and Yang, H. (2015). Cicada-wing-inspired self-cleaning antireflection coatings on polymer substrates. *ACS Appl. Mat. Interfaces* 7 (45), 25495–25505. doi:10.1021/acsami.5b08743

Chen, Y., He, B., Lee, J., and Patankar, N. A. (2005). Anisotropy in the wetting of rough surfaces. *J. colloid interface Sci.* 281 (2), 458–464. doi:10.1016/j.jcis.2004.07.038

Cheng, Y. T., and Rodak, D. E. (2005). Is the lotus leaf superhydrophobic?[J]. *Appl. Phys. Lett.* 86 (14), 144101. doi:10.1063/1.1895487

Cheng, Z., Zhang, D., Lv, T., Lai, H., Zhang, E., Kang, H., et al. (2018). Superhydrophobic shape memory polymer arrays with switchable isotropic/anisotropic wetting. *Adv. Funct. Mat.* 28 (7), 1705002. doi:10.1002/adfm.201705002

Dai, S., Zhu, Y., Gu, Y., and Du, Z. (2019). Biomimetic fabrication and photoelectric properties of superhydrophobic ZnO nanostructures on flexible PDMS substrates replicated from rose petal. *Appl. Phys. A* 125 (2), 138–211. doi:10.1007/s00339-019-2438-7

Dalawai, S. P., Aly, M. A. S., Latthe, S. S., Xing, R., Sutar, R. S., Nagappan, S., et al. (2020). Recent advances in durability of superhydrophobic self-cleaning technology: A critical review. *Prog. Org. Coatings* 138, 105381. doi:10.1016/j.porgcoat.2019.105381

Darmanin, T., and Guittard, F. (2015). Superhydrophobic and superoleophobic properties in nature. *Mater. today* 18 (5), 273–285. doi:10.1016/j.mattod.2015.01.001

Dellieu, L., Sarrazin, M., Simonis, P., Deparis, O., and Vigneron, J. P. (2014). A two-in-one superhydrophobic and anti-reflective nanodevice in the grey cicada*Cicada orni*(Hemiptera). *J. Appl. Phys.* 116 (2), 024701. doi:10.1063/1.4889849

Dobbs, H. (1999). The modified Young's equation for the contact angle of a small sessile drop from an interface displacement model[J]. *Int. J. Mod. Phys. B* 13 (27), 3255–3259. doi:10.1142/s0217979299003003

Domke, M., Sonderegger, G., and Kostal, E. (2019). Transparent laser-structured glasses with superhydrophilic properties for anti-fogging applications[J]. *Appl. Phys. A* 125 (10), 1–10.

Drotlef, D. M., Blümler, P., and del Campo, A. (2014). Magnetically actuated patterns for bioinspired reversible adhesion (dry and wet). *Adv. Mat.* 26, 775–779. doi:10.1002/adma.201303087

Fang, Y., Sun, G., Cong, Q., Chen, G. h., and Ren, L. q. (2008). Effects of methanol on wettability of the non-smooth surface on butterfly wing. *J. Bionic Eng.* 5 (2), 127–133. doi:10.1016/s1672-6529(08)60016-5

Fang, Y., Yong, J., Chen, F., Huo, J., Yang, Q., Zhang, J., et al. (2018). Bioinspired fabrication of Bi/tridirectionally anisotropic sliding superhydrophobic PDMS surfaces by femtosecond laser. *Adv. Mat. Interfaces* 5 (6), 1701245. doi:10.1002/admi.201701245

Fang, Z., Cheng, Y., Yang, Q., Lu, Y., Zhang, C., Li, M., et al. (2022). Design of metal-based slippery liquid-infused porous surfaces (SLIPSs) with effective liquid repellency achieved with a femtosecond laser. *Micromachines* 13 (8), 1160. doi:10.3390/mi13081160

Feng, L., Li, S., Li, Y., Li, H., Zhang, L., Zhai, J., et al. (2002). Super-hydrophobic surfaces: From natural to artificial. *Adv. Mat.* 14 (24), 1857–1860. doi:10.1002/adma.200290020

Feng, L., Zhang, Y., Xi, J., Zhu, Y., Wang, N., Xia, F., et al. (2008). Petal Effect: A superhydrophobic state with high adhesive force. *Langmuir* 24 (8), 4114–4119. doi:10.1021/la703821h

Fromel, M., Sweeder, D. M., Jang, S., Williams, T. A., Kim, S. H., and Pester, C. W. (2021). Superhydrophilic polymer brushes with high durability and anti-fogging activity. *ACS Appl. Polym. Mat.* 3 (10), 5291–5301. doi:10.1021/acsapm.1c01090

Gao, F., Yao, Y., Wang, W., Wang, X., Li, L., Zhuang, Q., et al. (2018). Light-driven transformation of bio-inspired superhydrophobic structure via reconfigurable PAzoMA microarrays: From Lotus leaf to rice leaf. *Macromolecules* 51 (7), 2742–2749. doi:10.1021/acs.macromol.8b00059

Gao, X., Su, L., Jiang, G., Pang, J., and Lin, L. (2020). Dimensional stability of lotus leaf-like nanostructure superhydrophobic bamboo by modification using xylan. *BioResources* 15 (2), 3443–3457. doi:10.15376/biores.15.2.3443-3457

Gao, X., Yan, X., Yao, X., Xu, L., Zhang, K., Zhang, J., et al. (2007). The dry-style antifogging properties of mosquito compound eyes and artificial analogues prepared by soft lithography. *Adv. Mat.* 19 (17), 2213–2217. doi:10.1002/adma.200601946

Ge-Zhang, S., Yang, H., and Ni, H. (2022). Biomimetic superhydrophobic metal/nonmetal surface manufactured by etching methods: A mini review[J]. *Front. Bioeng. Biotechnol.*, 10. doi:10.3389/fbioe.2022.95809

Ghasemlou, M., Le, P. H., Daver, F., Murdoch, B. J., Ivanova, E. P., and Adhikari, B. (2021). Robust and eco-friendly superhydrophobic starch nanohybrid materials with engineered Lotus leaf mimetic multiscale hierarchical structures. *ACS Appl. Mat. Interfaces* 13 (30), 36558–36573. doi:10.1021/acsami.1c09959

Gleiche, M., Chi, L. F., and Fuchs, H. (2000). Nanoscopic channel lattices with controlled anisotropic wetting. *Nature* 403 (6766), 173–175. doi:10.1038/35003149

Golovin, K. B., Gose, J. W., Perlin, M., Ceccio, S. L., and Tuteja, A. (2016). Bioinspired surfaces for turbulent drag reduction. *Phil. Trans. R. Soc. A* 374 (2073), 20160189. doi:10.1098/rsta.2016.0189

Gose, J. W., Golovin, K., Boban, M., Mabry, J. M., Tuteja, A., Perlin, M., et al. (2018). Characterization of superhydrophobic surfaces for drag reduction in turbulent flow. *J. Fluid Mech.* 845, 560–580. doi:10.1017/jfm.2018.210

Gou, X., and Guo, Z. (2018). Superhydrophobic plant leaves with micro-line structures: An optimal biomimetic objective in bionic engineering. *J. Bionic Eng.* 15 (5), 851–858. doi:10.1007/s42235-018-0072-2

Guo, Z., and Liu, W. (2007). Biomimic from the superhydrophobic plant leaves in nature: Binary structure and unitary structure. *Plant Sci.* 172 (6), 1103–1112. doi:10.1016/j.plantsci.2007.03.005

Gustafsson, L., Jansson, R., Hedhammar, M., and van der Wijngaart, W. (2018). Structuring of functional spider silk wires, coatings, and sheets by self-assembly on superhydrophobic pillar surfaces. *Adv. Mat.* 30 (3), 1704325. doi:10.1002/adma.201704325

Han, K., Park, T. Y., Yong, K., and Cha, H. J. (2019). Combinational biomimicking of Lotus leaf, mussel, and sandcastle worm for robust superhydrophobic surfaces with biomedical multifunctionality: Antithrombotic, antibiofouling, and tissue closure capabilities. *ACS Appl. Mat. Interfaces* 11 (10), 9777–9785. doi:10.1021/acsami.8b21122

Han, T. Y., Shr, J. F., Wu, C. F., and Hsieh, C. T. (2007). A modified Wenzel model for hydrophobic behavior of nanostructured surfaces. *Thin Solid Films* 515 (11), 4666–4669. doi:10.1016/j.tsf.2006.11.008

Han, Z., Fu, J., Wang, Z., Wang, Y., Li, B., Mu, Z., et al. (2017). Long-term durability of superhydrophobic properties of butterfly wing scales after continuous contact with water. *Colloids Surfaces A Physicochem. Eng. Aspects* 518, 139–144. doi:10.1016/j.colsurfa.2017.01.030

Hao, P., Lv, C., Yao, Z., and He, F. (2010). Sliding behavior of water droplet on superhydrophobic surface. *EPL Europhys. Lett.* 90 (6), 66003. doi:10.1209/0295-5075/90/66003

Hasan, J., Raj, S., Yadav, L., and Chatterjee, K. (2015). Engineering a nanostructured "super surface" with superhydrophobic and superkilling properties. *RSC Adv.* 5 (56), 44953–44959. doi:10.1039/c5ra05206h

Hasan, J., Webb, H. K., Truong, V. K., Pogodin, S., Baulin, V. A., Watson, G. S., et al. (2013). Selective bactericidal activity of nanopatterned superhydrophobic cicada Psaltoda claripennis wing surfaces. *Appl. Microbiol. Biotechnol.* 97 (20), 9257–9262. doi:10.1007/s00253-012-4628-5

Hasan, M. S., and Nosonovsky, M. (2020). Lotus effect and friction: Does nonsticky mean slippery? *Biomimetics (Basel).* 5 (2), 28. doi:10.3390/biomimetics5020028

He, J., He, J., Yuan, M., Xue, M., Ma, X., Hou, L., et al. (2018). Facile fabrication of eco-friendly durable superhydrophobic material from eggshell with oil/water separation property. *Adv. Eng. Mat.* 20 (9), 1701180. doi:10.1002/adem.201701180

Herminghaus, S. (2007). Roughness-induced non-wetting. *Europhys. Lett.* 79 (5), 59901. doi:10.1209/0295-5075/79/59901

Higgins, A. M., and Jones, R. A. L. (2000). Anisotropic spinodal dewetting as a route to self-assembly of patterned surfaces. *Nature* 404 (6777), 476–478. doi:10.1038/35006597

Hoefnagels, H. F., Wu, D., De With, G., and Ming, W. (2007). Biomimetic superhydrophobic and highly oleophobic cotton textiles. *Langmuir* 23 (26), 13158–13163. doi:10.1021/la702174x

Hu, H., Eluchie, C., and Huang, W. (2022). An experimental study to compare water droplet impinging dynamics and wind-driven water runback process over laser treated surfaces with different wettability characteristics[C]. *AIAA Aviat. 2022 Forum*, 4095.

Huang, C., and Guo, Z. (2018). The wettability of gas bubbles: From macro behavior to nano structures to applications. *Nanoscale* 10 (42), 19659–19672. doi:10.1039/c8nr07315e

Huang, H., Huang, C., Xu, C., and Liu, R. (2022). Development and characterization of lotus-leaf-inspired bionic antibacterial adhesion film through beeswax. *Food Packag. Shelf Life* 33, 100906. doi:10.1016/j.fpsl.2022.100906

Ivanova, E. P., Hasan, J., Webb, H. K., Truong, V. K., Watson, G. S., Watson, J. A., et al. (2012). Natural bactericidal surfaces: Mechanical rupture of *Pseudomonas aeruginosa* cells by cicada wings. *Small* 8 (16), 2489–2494. doi:10.1002/smll.201200528

Jiang, S., Zhang, H., Jiang, C., and Liu, X. (2020). Antifrosting performance of a superhydrophobic surface by optimizing the surface morphology. *Langmuir* 36 (34), 10156–10165. doi:10.1021/acs.langmuir.0c01618

Jiaqiang, E., Jin, Y., and Deng, Y. (2018). Wetting models and working mechanisms of typical surfaces existing in nature and their application on superhydrophobic surfaces: A review[J]. *Adv. Mat. Interfaces* 5, 1701052.

Jin, M., Feng, X., Feng, L., Sun, T., Zhai, J., Li, T., et al. (2005). Superhydrophobic aligned polystyrene nanotube films with high adhesive force. *Adv. Mat.* 17 (16), 1977–1981. doi:10.1002/adma.200401726

Kamperman, M., Kroner, E., del Campo, A., McMeeking, R. M., and Arzt, E. (2010). Functional adhesive surfaces with "gecko" effect: The concept of contact splitting. *Adv. Eng. Mat.* 12 (5), 335–348. doi:10.1002/adem.201000104

Kang, F., Yi, Z., Zhao, B., and Qin, Z. (2021). Surface physical structure and durability of superhydrophobic wood surface with epoxy resin. *BioResources* 16 (2), 3235–3254. doi:10.15376/biores.16.2.3235-3254

Kelleher, S. M., Habimana, O., Lawler, J., O' Reilly, B., Daniels, S., Casey, E., et al. (2016). Cicada wing surface topography: An investigation into the bactericidal properties of nanostructural features. *ACS Appl. Mat. Interfaces* 8 (24), 14966–14974. doi:10.1021/acsami.5b08309

Khandavalli, S., Rogers, P., and Rothstein, J. P. (2018). Roll-to-roll fabrication of hierarchical superhydrophobic surfaces. *Appl. Phys. Lett.* 113 (4), 041601. doi:10.1063/1.5037946

Klicova, M., Oulehlova, Z., Klapstova, A., Hejda, M., Krejcik, M., Novak, O., et al. (2022). Biomimetic hierarchical nanofibrous surfaces inspired by superhydrophobic lotus leaf structure for preventing tissue adhesions. *Mater. Des.* 217, 110661. doi:10.1016/j.matdes.2022.110661

Kumar, M., and Bhardwaj, R. (2020). Wetting characteristics of Colocasia esculenta (Taro) leaf and a bioinspired surface thereof[J]. *Sci. Rep.* 10 (1), 1–15.

Lai, D. L., Kong, G., Li, X. C., and Che, C. S. (2019). Corrosion resistance of ZnO nanorod superhydrophobic coatings with rose petal effect or Lotus leaf effect. *J. Nanosci. Nanotechnol.* 19 (7), 3919–3928. doi:10.1166/jnn.2019.16313

Lai, Y. K., Tang, Y. X., and Huang, J. Y. (2013). Bioinspired TiO2 nanostructure films with special wettability and adhesion for droplets manipulation and patterning[J]. *Sci. Rep.* 3 (1), 1–8.

Latthe, S. S., Sutar, R. S., Bhosale, A. K., Nagappan, S., Ha, C. S., Sadasivuni, K. K., et al. (2019). Recent developments in air-trapped superhydrophobic and liquid-infused slippery surfaces for anti-icing application. *Prog. Org. Coatings* 137, 105373. doi:10.1016/j.porgcoat.2019.105373

Latthe, S. S., Terashima, C., Nakata, K., and Fujishima, A. (2014). Superhydrophobic surfaces developed by mimicking hierarchical surface morphology of Lotus leaf. *Molecules* 19 (4), 4256–4283. doi:10.3390/molecules19044256

Lee, W., Jin, M. K., Yoo, W. C., and Lee, J. K. (2004). Nanostructuring of a polymeric substrate with well-defined nanometer-scale topography and tailored surface wettability. *Langmuir* 20 (18), 7665–7669. doi:10.1021/la049411+

Letellier, P., Mayaffre, A., and Turmine, M. (2007). Drop size effect on contact angle explained by nonextensive thermodynamics. Young's equation revisited. *J. colloid interface Sci.* 314 (2), 604–614. doi:10.1016/j.jcis.2007.05.085

Li, B., Ouyang, Y., Haider, Z., Zhu, Y., Qiu, R., Hu, S., et al. (2021). One-step electrochemical deposition leading to superhydrophobic matrix for inhibiting abiotic and microbiologically influenced corrosion of Cu in seawater environment. *Colloids Surfaces A Physicochem. Eng. Aspects* 616, 126337. doi:10.1016/j.colsurfa.2021.126337

Li, D., and Guo, Z. (2018). Metal-organic framework superhydrophobic coating on Kevlar fabric with efficient drag reduction and wear resistance. *Appl. Surf. Sci.* 443, 548–557. doi:10.1016/j.apsusc.2018.03.030

Li, J., Liu, X., Ye, Y., Zhou, H., and Chen, J. (2011). Gecko-inspired synthesis of superhydrophobic ZnO surfaces with high water adhesion. *Colloids Surfaces A Physicochem. Eng. Aspects* 384 (1-3), 109–114. doi:10.1016/j.colsurfa.2011.03.024

Li, M., Chen, Y., Luo, W., and Cheng, X. (2021). Durable and flexible hydrophobic surface with a micropatterned composite metal–polymer structure. *Langmuir* 37 (19), 5838–5845. doi:10.1021/acs.langmuir.1c00227

Li, R., Gao, Q., Dong, Q., Luo, C., Sheng, L., and Liang, J. (2020). Template-free electrodeposition of ultra-high adhesive superhydrophobic Zn/Zn stearate coating with ordered hierarchical structure from deep eutectic solvent. *Surf. Coatings Technol.* 403, 126267. doi:10.1016/j.surfcoat.2020.126267

Li, S., Chen, A., Chen, Y., Yang, Y., Zhang, Q., Luo, S., et al. (2020). Lotus leaf inspired antiadhesive and antibacterial gauze for enhanced infected dermal wound regeneration. *Chem. Eng. J.* 402, 126202. doi:10.1016/j.cej.2020.126202

Li, W., Zhan, Y., and Yu, S. (2021). Applications of superhydrophobic coatings in anti-icing: Theory, mechanisms, impact factors, challenges and perspectives. *Prog. Org. Coatings* 152, 106117. doi:10.1016/j.porgcoat.2020.106117

Li, Y., Zheng, M., Ma, L., Zhong, M., and Shen, W. (2008). Fabrication of hierarchical ZnO architectures and their superhydrophobic surfaces with strong adhesive force. *Inorg. Chem.* 47 (8), 3140–3143. doi:10.1021/ic7021598

Li, Z., Marlena, J., Pranantyo, D., Nguyen, B. L., and Yap, C. H. (2019). A porous superhydrophobic surface with active air plastron control for drag reduction and fluid impalement resistance. *J. Mat. Chem. A Mat.* 7 (27), 16387–16396. doi:10.1039/c9ta02745a

Lian, Z., Xu, J., Yu, Z., Yu, P., and Yu, H. (2019). A simple two-step approach for the fabrication of bio-inspired superhydrophobic and anisotropic wetting surfaces having corrosion resistance. *J. Alloys Compd.* 793, 326–335. doi:10.1016/j.jallcom.2019.04.169

Liang, L., Liu, P., Su, H., Qian, H., and Ma, H. (2020). One-step fabrication of superhydrophobic sponge with magnetic controllable and flame-retardancy for oil removing and collecting. *J. Appl. Polym. Sci.* 137 (44), 49353. doi:10.1002/app.49353

Liang, Y., Peng, J., Li, X., Huang, J., Qiu, R., Zhang, Z., et al. (2017). Wettability and contact time on a biomimetic superhydrophobic surface. *Materials* 10 (3), 254. doi:10.3390/ma10030254

Lim, J. I., Kim, S. I., and Jung, Y. (2013). Fabrication and medical applications of lotus-leaf-like structured superhydrophobic surfaces. *Polym. Korea* 37 (4), 411–419. doi:10.7317/pk.2013.37.4.411

Lin, J., Du, J., Xie, S., Yu, F., Fang, S., Yan, Z., et al. (2022). Durable superhydrophobic polyvinylidene fluoride membranes via facile spray-coating for effective membrane distillation. *Desalination* 538, 115925. doi:10.1016/j.desal.2022.115925

Lin, X., and Hong, J. (2019). Recent advances in robust superwettable membranes for oil–water separation. *Adv. Mat. Interfaces* 6 (12), 1900126. doi:10.1002/admi.201900126

Lin, Y., Chen, H., Wang, G., and Liu, A. (2018). Recent progress in preparation and anti-icing applications of superhydrophobic coatings. *Coatings (Basel).* 8 (6), 208. doi:10.3390/coatings8060208

Liu, J., Zhang, X., Wang, R., Long, F., Zhao, P., and Liu, L. (2021). A mosquito-eye-like superhydrophobic coating with super robustness against abrasion. *Mater. Des.* 203, 109552. doi:10.1016/j.matdes.2021.109552

Liu, K., Du, J., Wu, J., and Jiang, L. (2012). Superhydrophobic gecko feet with high adhesive forces towards water and their bio-inspired materials. *Nanoscale* 4 (3), 768–772. doi:10.1039/c1nr11369k

Liu, M., Zheng, Y., Zhai, J., and Jiang, L. (2010). Bioinspired super-antiwetting interfaces with special Liquid–Solid adhesion. *Acc. Chem. Res.* 43 (3), 368–377. doi:10.1021/ar900205g

Liu, T., Liu, Z., Jagota, A., and Hui, C. Y. (2020). Droplets on an elastic membrane: Configurational energy balance and modified Young equation. *J. Mech. Phys. Solids* 138, 103902. doi:10.1016/j.jmps.2020.103902

Liu, Y., Gu, H., Jia, Y., Liu, J., Zhang, H., Wang, R., et al. (2019). Design and preparation of biomimetic polydimethylsiloxane (PDMS) films with superhydrophobic, self-healing and drag reduction properties via replication of shark skin and SI-ATRP. *Chem. Eng. J.* 356, 318–328. doi:10.1016/j.cej.2018.09.022

Liu, Y., Li, S., Zhang, J., Wang, Y., Han, Z., and Ren, L. (2014). Fabrication of biomimetic superhydrophobic surface with controlled adhesion by electrodeposition. *Chem. Eng. J.* 248, 440–447. doi:10.1016/j.cej.2014.03.046

Liu, Y., Song, Y., Niu, S., Zhang, Y., Han, Z., and Ren, L. (2016). Integrated super-hydrophobic and antireflective PDMS bio-templated from nano-conical structures of cicada wings. *RSC Adv.* 6 (110), 108974–108980. doi:10.1039/c6ra23811d

Long, J., Fan, P., Gong, D., Jiang, D., Zhang, H., Li, L., et al. (2015). Superhydrophobic surfaces fabricated by femtosecond laser with tunable water adhesion: From Lotus leaf to rose petal. *ACS Appl. Mat. Interfaces* 7 (18), 9858–9865. doi:10.1021/acsami.5b01870

Ma, L., Li, H., and Hu, H. (2017). *An experimental study on the dynamics of water droplets impingement onto a goose feather[C]//55th AIAA aerospace sciences meeting*, 0442.

Ma, N., Cheng, D., Zhang, J., Zhao, S., and Lu, Y. (2020). A simple, inexpensive and environmental-friendly electrochemical etching method to fabricate superhydrophobic GH4169 surfaces. *Surf. Coatings Technol.* 399, 126180. doi:10.1016/j.surfcoat.2020.126180

Mahadik, S. A., and Mahadik, S. S. (2021). Surface morphological and topographical analysis of multifunctional superhydrophobic sol-gel coatings. *Ceram. Int.* 47 (20), 29475–29482. doi:10.1016/j.ceramint.2021.07.115

Makkonen, L. (2016). Young's equation revisited. *J. Phys. Condens. Matter* 28 (13), 135001. doi:10.1088/0953-8984/28/13/135001

Mao, C., Zhao, W. B., and Luo, W. P. (2009). Geometric bionics: Lotus effect helps polystyrene nanotube films get good blood compatibility[J]. *Nat. Preced.*, 1.

Marmur, A. (1983). Equilibrium and spreading of liquids on solid surfaces. *Adv. Colloid Interface Sci.* 19 (1-2), 75–102. doi:10.1016/0001-8686(83)80004-9

Miljkovic, N., Enright, R., and Wang, E. N. (2013). Modeling and optimization of superhydrophobic condensation. *J. Heat Transf.* 135 (11). doi:10.1115/1.4024597

Mohseni, M., Far, H. S., Hasanzadeh, M., and Golovin, K. (2021). Non-fluorinated sprayable fabric finish for durable and comfortable superhydrophobic textiles. *Prog. Org. Coatings* 157, 106319. doi:10.1016/j.porgcoat.2021.106319

Monfared, M., Alidoostan, M. A., and Saranjam, B. (2019). Experimental study on the friction drag reduction of superhydrophobic surfaces in closed channel flow. *J. Appl. Fluid Mech.* 12 (1), 69–76. doi:10.29252/jafm.75.253.28442

Mosayebi, E., Azizian, S., and Noei, N. (2020). Preparation of robust superhydrophobic sand by chemical vapor deposition of polydimethylsiloxane for oil/water separation. *Macromol. Mat. Eng.* 305 (12), 2000425. doi:10.1002/mame.202000425

Nagappan, S., Park, J. J., Park, S. S., Lee, W. K., and Ha, C. S. (2013). Bio-inspired, multi-purpose and instant superhydrophobic–superoleophilic lotus leaf powder hybrid micro–nanocomposites for selective oil spill capture. *J. Mat. Chem. A Mat.* 1 (23), 6761–6769. doi:10.1039/c3ta00001j

Nguyen, S. H., Webb, H. K., Mahon, P. J., Crawford, R., and Ivanova, E. (2014). Natural insect and plant micro-/nanostructsured surfaces: An excellent selection of valuable templates with superhydrophobic and self-cleaning properties. *Molecules* 19 (9), 13614–13630. doi:10.3390/molecules190913614

Nguyen, S. H. T., Webb, H. K., Hasan, J., Tobin, M. J., Crawford, R. J., and Ivanova, E. P. (2013). Dual role of outer epicuticular lipids in determining the wettability of dragonfly wings. *Colloids Surfaces B Biointerfaces* 106, 126–134. doi:10.1016/j.colsurfb.2013.01.042

Nguyen, S. H., Webb, H. K., Hasan, J., Tobin, M. J., Mainwaring, D. E., Mahon, P. J., et al. (2014). Wing wettability of Odonata species as a function of quantity of epicuticular waxes. *Vib. Spectrosc.* 75, 173–177. doi:10.1016/j.vibspec.2014.07.006

Nosonovsky, M., and Bhushan, B. (2005). Roughness optimization for biomimetic superhydrophobic surfaces. *Microsyst. Technol.* 11 (7), 535–549. doi:10.1007/s00542-005-0602-9

Nosonovsky, M., and Bhushan, B. (2009). Superhydrophobic surfaces and emerging applications: Non-adhesion, energy, green engineering. *Curr. Opin. Colloid & Interface Sci.* 14 (4), 270–280. doi:10.1016/j.cocis.2009.05.004

Nuraje, N., Khan, W. S., Lei, Y., Ceylan, M., and Asmatulu, R. (2013). Superhydrophobic electrospun nanofibers. *J. Mat. Chem. A* 1 (6), 1929–1946. doi:10.1039/c2ta00189f

Oh, J., Yin, S., Dana, C. E., Hong, S., Roman, J. K., Jo, K. D., et al. (2019). Cicada-inspired self-cleaning superhydrophobic surfaces. *J. Heat Transf.* 141 (10). doi:10.1115/1.4044677

Pieniazek, F., Dasgupta, M., and Messina, V. (2021). *Differential occurrence of cuticular wax and its role in leaf tissues of three edible aroids of Northeast India[J]*.

Pour, F. Z., Karimi, H., and Avargani, V. M. (2019). Preparation of a superhydrophobic and superoleophilic polyester textile by chemical vapor deposition of dichlorodimethylsilane for Water–Oil separation[J]. *Polyhedron* 159, 54–63.

Qian, C., Guang-hua, C., and Yan, F. (1900). Super-hydrophobic characteristics of butterfly wing surface[J]. *J. Bionic Eng.* 1 (4), 249–255.

Rius-Ayra, O., Castellote-Alvarez, R., and Escobar, A. M. (2018). Superhydrophobic coating bioinspired on rice leaf: A first attempt to enhance erosion resistance properties at environmental conditions with ceramic particles [C]. *Mater. Sci. Forum* 941, 1874–1879. Trans Tech Publications Ltd. doi:10.4028/www.scientific.net/MSF.941

Román Kustas, J., Hoffman, J. B., Reed, J. H., Gonsalves, A. E., Oh, J., Li, L., et al. (2020). Molecular and topographical organization: Influence on cicada wing wettability and bactericidal properties. *Adv. Mat. Interfaces* 7 (10), 2000112. doi:10.1002/admi.202000112

Saison, T., Peroz, C., Chauveau, V., Berthier, S., Sondergard, E., and Arribart, H. (2008). Replication of butterfly wing and natural lotus leaf structures by nanoimprint on silica sol–gel films. *Bioinspir. Biomim.* 3 (4), 046004. doi:10.1088/1748-3182/3/4/046004

Sauer, R. A. (2010). A computational model for nanoscale Adhesion between deformable solids and its application to gecko adhesion. *J. adhesion Sci. Technol.* 24 (11-12), 1807–1818. doi:10.1163/016942410x507588

Seo, K., and Kim, M. (2015). *Re-derivation of Young's equation, Wenzel equation, and Cassie-Baxter equation based on energy minimization[M]//Surface energy*. IntechOpen.

Sethi, S. K., Manik, G., and Sahoo, S. K. (2019). *Fundamentals of superhydrophobic surfaces[M]//Superhydrophobic polymer coatings*. Elsevier, 3–29.

Shahabadi, S. M. S., and Brant, J. A. (2019). Bio-inspired superhydrophobic and superoleophilic nanofibrous membranes for non-aqueous solvent and oil separation from water[J]. *Sep. Purif. Technol.*, 210: 587–599.

Shang, Q. Q., Chen, J. Q., and Yang, X. H. (2019). Fabrication and oil absorbency of superhydrophobic magnetic cellulose aerogels[J]. *J. For. Eng.* 4 (6), 105–111.

Shang, Q. Q., Hu, Y., and Liu, C. G. (2019). Fabrication of superhydrophobic cellulose composite aerogels for oil/water separation[J]. *J. For. Eng.* 4 (3), 86–92.

Shao, Y., Zhao, J., Fan, Y., Wan, Z., Lu, L., Zhang, Z., et al. (2020). Shape memory superhydrophobic surface with switchable transition between "Lotus Effect" to "Rose Petal Effect". *Chem. Eng. J.* 382, 122989. doi:10.1016/j.cej.2019.122989

Sharma, S. (2021). *Droplet behaviour on metastable hydrophobic and superhydrophobic nonwoven materials[D]*. New Delhi: Indian Institute of Technology Delhi (IITD).

Shen, D., Ming, W., Ren, X., Xie, Z., and Liu, X. (2021). Progress in non-traditional processing for fabricating superhydrophobic surfaces. *Micromachines* 12 (9), 1003. doi:10.3390/mi12091003

Si, Y., Dong, Z., and Jiang, L. (2018). Bioinspired designs of superhydrophobic and superhydrophilic materials. *ACS Cent. Sci.* 4 (9), 1102–1112. doi:10.1021/acscentsci.8b00504

Stark, A. Y., Subarajan, S., Jain, D., Niewiarowski, P. H., and Dhinojwala, A. (2016). Superhydrophobicity of the gecko toe pad: Biological optimization versus laboratory maximization. *Phil. Trans. R. Soc. A* 374 (2073), 20160184. doi:10.1098/rsta.2016.0184

Starov, V. M., and Velarde, M. G. (2009). Surface forces and wetting phenomena. *J. Phys. Condens. Matter* 21, 464121. doi:10.1088/0953-8984/21/46/464121

Stoddart, P. R., Cadusch, P. J., Boyce, T. M., Erasmus, R. M., and Comins, J. D. (2006). Optical properties of chitin: Surface-enhanced Raman scattering substrates based on antireflection structures on cicada wings. *Nanotechnology* 17 (3), 680–686. doi:10.1088/0957-4484/17/3/011

Sun, T., Feng, L., Gao, X., and Jiang, L. (2005). Bioinspired surfaces with special wettability. *Acc. Chem. Res.* 38 (8), 644–652. doi:10.1021/ar040224c

Tan, D., Luo, A., Wang, X., Shi, Z., Lei, Y., Steinhart, M., et al. (2020). Humidity-modulated core–shell nanopillars for enhancement of gecko-inspired adhesion. *ACS Appl. Nano Mat.* 3 (4), 3596–3603. doi:10.1021/acsanm.0c00314

Tan, Y., Hu, B., Chu, Z., and Wu, W. (2019). Bioinspired superhydrophobic papillae with tunable adhesive force and ultralarge liquid capacity for microdroplet manipulation. *Adv. Funct. Mat.* 29 (15), 1900266. doi:10.1002/adfm.201900266

Teisala, H., and Butt, H. J. (2018). Hierarchical structures for superhydrophobic and superoleophobic surfaces. *Langmuir* 35 (33), 10689–10703. doi:10.1021/acs.langmuir.8b03088

Teodorescu, M. (2014). Applied biomimetics: A new fresh look of textiles. *J. Text.* 2014, 1–9. doi:10.1155/2014/154184

Tuo, Y., Zhang, H., Rong, W., Jiang, S., Chen, W., and Liu, X. (2019). Drag reduction of anisotropic superhydrophobic surfaces prepared by laser etching. *Langmuir* 35 (34), 11016–11022. doi:10.1021/acs.langmuir.9b01040

Ueda, E., and Levkin, P. A. (2013). Emerging applications of superhydrophilic-superhydrophobic micropatterns. *Adv. Mat.* 25 (9), 1234–1247. doi:10.1002/adma.201204120

Varshney, P., Lomga, J., Gupta, P. K., Mohapatra, S., and Kumar, A. (2018). Durable and regenerable superhydrophobic coatings for aluminium surfaces with excellent self-cleaning and anti-fogging properties. *Tribol. Int.* 119, 38–44. doi:10.1016/j.triboint.2017.10.033

Varshney, P., and Mohapatra, S. S. (2018). Durable and regenerable superhydrophobic coatings for brass surfaces with excellent self-cleaning and anti-fogging properties prepared by immersion technique. *Tribol. Int.* 123, 17–25. doi:10.1016/j.triboint.2018.02.036

Verbanic, S., Brady, O., Sanda, A., Gustafson, C., and Donhauser, Z. J. (2014). A novel general chemistry laboratory: Creation of biomimetic superhydrophobic surfaces through replica molding. *J. Chem. Educ.* 91 (9), 1477–1480. doi:10.1021/ed4007056

Vicente, A., Rivero, P. J., Palacio, J. F., and Rodriguez, R. (2021). The role of the fiber/bead hierarchical microstructure on the properties of PVDF coatings deposited by electrospinning. *Polymers* 13 (3), 464. doi:10.3390/polym13030464

Victor, J. J., Facchini, D., and Erb, U. (2012). A low-cost method to produce superhydrophobic polymer surfaces. *J. Mat. Sci.* 47 (8), 3690–3697. doi:10.1007/s10853-011-6217-x

Vidal, K., Gómez, E., Goitandia, A. M., Angulo-Ibanez, A., and Aranzabe, E. (2019). The synthesis of a superhydrophobic and thermal stable silica coating via sol-gel process. *Coatings (Basel).* 9 (10), 627. doi:10.3390/coatings9100627

Voronov, R. S., Papavassiliou, D. V., and Lee, L. L. (2008). Review of fluid slip over superhydrophobic surfaces and its dependence on the contact angle. *Ind. Eng. Chem. Res.* 47 (8), 2455–2477. doi:10.1021/ie0712941

Walsh, M. J. (1983). Riblets as a viscous drag reduction technique. *AIAA J.* 21 (4), 485–486. doi:10.2514/3.60126

Wang, B., and Guo, Z. (2013). Superhydrophobic copper mesh films with rapid oil/water separation properties by electrochemical deposition inspired from butterfly wing. *Appl. Phys. Lett.* 103 (6), 063704. doi:10.1063/1.4817922

Wang, D., Zhao, A., Jiang, R., Li, D., Zhang, M., Gan, Z., et al. (2012). Surface properties of bionic micro-pillar arrays with various shapes of tips. *Appl. Surf. Sci.* 259, 93–98. doi:10.1016/j.apsusc.2012.06.106

Wang, L., Huang, X., Wang, D., Zhang, W., Gao, S., Luo, J., et al. (2021). Lotus leaf inspired superhydrophobic rubber composites for temperature stable piezoresistive sensors with ultrahigh compressibility and linear working range. *Chem. Eng. J.* 405, 127025. doi:10.1016/j.cej.2020.127025

Wang, L., Wang, F., Huang, B., and Tang, Q. (2020). Recent advances in superhydrophobic composites based on clay minerals. *Appl. Clay Sci.* 198, 105793. doi:10.1016/j.clay.2020.105793

Wang, M., Liu, Q., Zhang, H., Wang, C., Wang, L., Xiang, B., et al. (2017). Laser direct writing of tree-shaped hierarchical cones on a superhydrophobic film for high-efficiency water collection. *ACS Appl. Mat. Interfaces* 9 (34), 29248–29254. doi:10.1021/acsami.7b08116

Wang, S., and Jiang, L. (2007). Definition of superhydrophobic states. *Adv. Mat.* 19 (21), 3423–3424. doi:10.1002/adma.200700934

Wang, S., Xue, Y., Ban, C., Taleb, A., and Jin, Y. (2020). Fabrication of robust tungsten carbide particles reinforced Co Ni super-hydrophobic composite coating by electrochemical deposition. *Surf. Coatings Technol.* 385, 125390. doi:10.1016/j.surfcoat.2020.125390

Wang, S., Yang, Z., Gong, G., Wang, J., Wu, J., et al. (2016). Icephobicity of penguins *Spheniscus humboldti* and an artificial replica of penguin feather with air-infused hierarchical rough structures. *J. Phys. Chem. C* 120 (29), 15923–15929. doi:10.1021/acs.jpcc.5b12298

Wang, X., Ding, H., Sun, S., Zhang, H., Zhou, R., Li, Y., et al. (2021). Preparation of a temperature-sensitive superhydrophobic self-cleaning SiO2-TiO2@PDMS coating with photocatalytic activity. *Surf. Coatings Technol.* 408, 126853. doi:10.1016/j.surfcoat.2021.126853

Wang, Y., Lai, H., Cheng, Z., Zhang, H., Zhang, E., Lv, T., et al. (2019). Gecko toe pads inspired *in situ* switchable superhydrophobic shape memory adhesive film. *Nanoscale* 11 (18), 8984–8993. doi:10.1039/c9nr00154a

Wang, Y., Zhang, D., Deng, J., Zhou, F., Duan, Z., Su, Q., et al. (2019). Mosquito's compound eyes as inspiration for fabrication of conductive superhydrophobic nanocarbon materials from waste wheat straw. *ACS Sustain. Chem. Eng.* 7 (4), 3883–3894. doi:10.1021/acssuschemeng.8b04906

Watson, G. S., Green, D. W., Schwarzkopf, L., Li, X., Cribb, B. W., Myhra, S., et al. (2015). A gecko skin micro/nano structure – a low adhesion, superhydrophobic, anti-wetting, self-cleaning, biocompatible, antibacterial surface. *Acta biomater.* 21, 109–122. doi:10.1016/j.actbio.2015.03.007

Watson, G. S., and Watson, J. A. (2004). Natural nano-structures on insects—Possible functions of ordered arrays characterized by atomic force microscopy. *Appl. Surf. Sci.* 235 (1-2), 139–144. doi:10.1016/j.apsusc.2004.05.129

Wei, D., Wang, J., Liu, Y., Li, S., and Wang, H. (2021). Controllable superhydrophobic surfaces with tunable adhesion on Mg alloys by a simple etching method and its corrosion inhibition performance. *Chem. Eng. J.* 404, 126444. doi:10.1016/j.cej.2020.126444

Weng, W., Tenjimbayashi, M., Hu, W. H., and Naito, M. (2022). Evolution of and disparity among biomimetic superhydrophobic surfaces with gecko, petal, and Lotus effect. *Small* 18 (18), 2200349. doi:10.1002/smll.202200349

Wenzel, R. N. (1949). Surface roughness and contact angle. *J. Phys. Colloid Chem.* 53 (9), 1466–1467. doi:10.1021/j150474a015

White, L. R. (1977). On deviations from Young's equation. *J. Chem. Soc. Faraday Trans. 1.* 73, 390–398. doi:10.1039/f19777300390

Wolfs, M., Darmanin, T., and Guittard, F. (2013). Superhydrophobic fibrous polymers. *Polym. Rev.* 53 (3), 460–505. doi:10.1080/15583724.2013.808666

Wong, T. S., Kang, S. H., Tang, S. K. Y., Smythe, E. J., Hatton, B. D., Grinthal, A., et al. (2011). Bioinspired self-repairing slippery surfaces with pressure-stable omniphobicity. *Nature* 477, 443–447. doi:10.1038/nature10447

Wu, B., Cui, X., Jiang, H., Wu, N., Peng, C., Hu, Z., et al. (2021). A superhydrophobic coating harvesting mechanical robustness, passive anti-icing and active de-icing performances. *J. Colloid Interface Sci.* 590, 301–310. doi:10.1016/j.jcis.2021.01.054

Wu, D., Wang, J. N., Wu, S. Z., Chen, Q. D., Zhao, S., Zhang, H., et al. (2011). Three-level biomimetic rice-leaf surfaces with controllable anisotropic sliding. *Adv. Funct. Mat.* 21 (15), 2927–2932. doi:10.1002/adfm.201002733

Wu, W., Liang, R., Lu, L., Wang, W., Ran, X., and Yue, D. (2020). Preparation of superhydrophobic laser-induced graphene using taro leaf structure as templates. *Surf. Coatings Technol.* 393, 125744. doi:10.1016/j.surfcoat.2020.125744

Wu, X. H., Liew, Y. K., Mai, C. W., and Then, Y. Y. (2021). Potential of superhydrophobic surface for blood-contacting medical devices. *Int. J. Mol. Sci.* 22 (7), 3341. doi:10.3390/ijms22073341

Wu, Y., Hang, T., Yu, Z., Xu, L., and Li, M. (2014). Lotus leaf-like dual-scale silver film applied as a superhydrophobic and self-cleaning substrate. *Chem. Commun.* 50 (61), 8405–8407. doi:10.1039/c4cc03878a

Xiang, S., and Liu, W. (2021). Self-Healing superhydrophobic surfaces: Self-healing superhydrophobic surfaces: Healing principles and applications (adv. Mater. Interfaces 12/2021). *Adv. Mat. Interfaces* 8 (12), 2170065. doi:10.1002/admi.202170065

Xie, H., Huang, H. X., and Peng, Y. J. (2017). Rapid fabrication of bio-inspired nanostructure with hydrophobicity and antireflectivity on polystyrene surface replicating from cicada wings. *Nanoscale* 9 (33), 11951–11958. doi:10.1039/c7nr04176d

Xie, J., Xu, J., Shang, W., and Zhang, K. (2018). Dropwise condensation on superhydrophobic nanostructure surface, part II: Mathematical model. *Int. J. Heat Mass Transf.* 127, 1170–1187. doi:10.1016/j.ijheatmasstransfer.2018.07.008

Xu, J., Hou, Y., Lian, Z., Yu, Z., Wang, Z., and Yu, H. (2020). Bio-inspired design of bi/tridirectionally anisotropic sliding superhydrophobic titanium alloy surfaces. *Nanomater. (Basel).* 10 (11), 2140. doi:10.3390/nano10112140

Xu, L., Yang, L., Yang, S., Xu, Z., Lin, G., Shi, J., et al. (2021). Earthworm-inspired ultradurable superhydrophobic fabrics from adaptive wrinkled skin. *ACS Appl. Mat. Interfaces* 13 (5), 6758–6766. doi:10.1021/acsami.0c18528

Xu, Q. F., Mondal, B., and Lyons, A. M. (2011). Fabricating superhydrophobic polymer surfaces with excellent abrasion resistance by a simple lamination templating method. *ACS Appl. Mat. Interfaces* 3 (9), 3508–3514. doi:10.1021/am200741f

Xu, Q., Wan, Y., and Hu, T. S. (2015). Robust self-cleaning and micromanipulation capabilities of gecko spatulae and their bio-mimics[J]. *Nat. Commun.* 6 (1), 1–9.

Xu, S., Wang, Q., and Wang, N. (2021). Chemical fabrication strategies for achieving bioinspired superhydrophobic surfaces with micro and nanostructures: A review. *Adv. Eng. Mat.* 23 (3), 2001083. doi:10.1002/adem.202001083

Xue, Y., Wang, S., Bi, P., Zhao, G., and Jin, Y. (2019). Super-hydrophobic Co–Ni coating with high abrasion resistance prepared by electrodeposition. *Coatings* 9 (4), 232. doi:10.3390/coatings9040232

Xue, Y., Wang, S., Zhao, G., Taleb, A., and Jin, Y. (2019). Fabrication of Ni Co coating by electrochemical deposition with high super-hydrophobic properties for corrosion protection. *Surf. coatings Technol.* 363, 352–361. doi:10.1016/j.surfcoat.2019.02.056

Yang, H., You, W., Shen, Q., Wang, X., Sheng, J., Cheng, D., et al. (2014). Preparation of lotus-leaf-like antibacterial film based on mesoporous silica microcapsule-supported Ag nanoparticles. *RSC Adv.* 4 (6), 2793–2796. doi:10.1039/c3ra45382k

Yang, L., Shen, X., Yang, Q., Liu, J., Wu, W., Li, D., et al. (2021). Fabrication of biomimetic anisotropic super-hydrophobic surface with rice leaf-like structures by femtosecond laser. *Opt. Mater.* 112, 110740. doi:10.1016/j.optmat.2020.110740

Yang, M., Liu, W., Jiang, C., He, S., Xie, Y., and Wang, Z. (2018). Fabrication of superhydrophobic cotton fabric with fluorinated TiO2 sol by a green and one-step sol-gel process. *Carbohydr. Polym.* 197, 75–82. doi:10.1016/j.carbpol.2018.05.075

Yang, Q., Luo, Z., Jiang, F., Luo, Y., Tan, S., Lu, Z., et al. (2016). Air cushion convection inhibiting icing of self-cleaning surfaces. *ACS Appl. Mat. Interfaces* 8 (42), 29169–29178. doi:10.1021/acsami.6b10165

Yang, S., Ju, J., Qiu, Y., He, Y., Wang, X., Dou, S., et al. (2014). Peanut leaf inspired multifunctional surfaces. *Small* 10 (2), 294–299. doi:10.1002/smll.201301029

Yang, S., Ju, J., Qiu, Y., He, Y., Wang, X., Dou, S., et al. (2014). Superhydrophobic materials: Peanut leaf inspired multifunctional surfaces (small 2/2014). *Small* 10 (2), 214. doi:10.1002/smll.201470010

Yang, Y., He, H., Li, Y., and Qiu, J. (2019). Using nanoimprint lithography to create robust, buoyant, superhydrophobic PVB/SiO2 coatings on wood surfaces inspired by red roses petal. *Sci. Rep.* 9 (1), 9961–9969. doi:10.1038/s41598-019-46337-y

Yong, J., Chen, F., Yang, Q., and Hou, X. (2015). Femtosecond laser controlled wettability of solid surfaces. *Soft Matter* 11 (46), 8897–8906. doi:10.1039/c5sm02153g

Yong, J., Yang, Q., and Hou, X. (2022). Nature-inspired superwettability achieved by femtosecond lasers[J]. *Ultrafast Sci.* 2022.

Young, T., III (1805). An essay on the cohesion of fluids[J]. *Philosophical Trans. R. Soc. Lond.* 95, 65–87.

Yu, Y., Zhao, Z. H., and Zheng, Q. S. (2007). Mechanical and superhydrophobic stabilities of two-scale surfacial structure of Lotus leaves. *Langmuir* 23 (15), 8212–8216. doi:10.1021/la7003485

Yuan, Z., Bin, J., Wang, X., Peng, C., Wang, M., Xing, S., et al. (2014). Fabrication of superhydrophobic surface with hierarchical multi-scale structure on copper foil. *Surf. Coatings Technol.* 254, 151–156. doi:10.1016/j.surfcoat.2014.06.004

Yue, G., Wang, Y., Li, D., Hou, L., Cui, Z., Li, Q., et al. (2020). Bioinspired surface with special wettability for liquid transportation and separation. *Sustain. Mater. Technol.* 25, e00175. doi:10.1016/j.susmat.2020.e00175

Yun, X., Xiong, Z., He, Y., and Wang, X. (2020). Superhydrophobic lotus-leaf-like surface made from reduced graphene oxide through soft-lithographic duplication. *RSC Adv.* 10 (9), 5478–5486. doi:10.1039/c9ra10373b

Zhang, B., and Xu, W. (2021). Superhydrophobic, superamphiphobic and SLIPS materials as anti-corrosion and anti-biofouling barriers[J]. *New J. Chem.*

Zhang, G., Zhang, J., Xie, G., Liu, Z., and Shao, H. (2006). Cicada wings: A stamp from nature for nanoimprint lithography. *Small* 2 (12), 1440–1443. doi:10.1002/smll.200600255

Zhang, H., Lai, H., Cheng, Z., Zhang, D., Wang, W., Liu, P., et al. (2021). Superhydrophobic shape memory film with switchable adhesion to both water and solid. *Chem. Eng. J.* 420, 129862. doi:10.1016/j.cej.2021.129862

Zhang, J., Yang, Q., and Cheng, Y. (2022). Slippery liquid-infused porous surface on metal material with excellent ice resistance fabricated by femtosecond bessel laser[J]. *Adv. Eng. Mater.*, 2101738. doi:10.1002/adem.202101738

Zhang, K., Li, H., Yin, X., and Wang, Z. (2019). Oil/water separation on structure-controllable Cu mesh: Transition of superhydrophilic-superoleophilic to superhydrophobic-superoleophilic without chemical modification. *Surf. Coatings Technol.* 358, 416–426. doi:10.1016/j.surfcoat.2018.11.061

Zhang, X., Zhao, J., Mo, J., Sun, R., Li, Z., and Guo, Z. (2019). Fabrication of superhydrophobic aluminum surface by droplet etching and chemical modification. *Colloids Surfaces A Physicochem. Eng. Aspects* 567, 205–212. doi:10.1016/j.colsurfa.2019.01.046

Zhang, Y., Chen, Y., Shi, L., Li, J., and Guo, Z. (2012). Recent progress of double-structural and functional materials with special wettability. *J. Mat. Chem.* 22 (3), 799–815. doi:10.1039/c1jm14327a

Zhang, Y., Jiao, Y., Li, C., Chen, C., Li, J., Hu, Y., et al. (2020). Bioinspired micro/nanostructured surfaces prepared by femtosecond laser direct writing for multi-functional applications. *Int. J. Extrem. Manuf.* 2 (3), 032002. doi:10.1088/2631-7990/ab95f6

Zhang, Y. L., Xia, H., Kim, E., and Sun, H. B. (2012). Recent developments in superhydrophobic surfaces with unique structural and functional properties. *Soft Matter* 8 (44), 11217–11231. doi:10.1039/c2sm26517f

Zhao, H., Sun, Q., Deng, X., and Cui, J. (2018). Earthworm-inspired rough polymer coatings with self-replenishing lubrication for adaptive friction-reduction and antifouling surfaces. *Adv. Mat.* 30 (29), 1802141. doi:10.1002/adma.201802141

Zhao, Z., Xiang, J., and Tan, Y. (2021). Preparation of superhydrophobic coating on 5083 aluminum alloy for corrosion protection in simulated marine environment containing SRB[J]. *Phys. Metals Metallogr.* 122 (14), 1581–1587.

Zheng, J., Yang, J., and Cao, W. (2022). Fabrication of transparent wear-resistant superhydrophobic SiO2 film via phase separation and chemical vapor deposition methods[J]. *Ceram. Int.* 407. doi:10.1016/j.apsusc.2017.02.207

Zheng, Y., Bai, H., Huang, Z., Tian, X., Nie, F. Q., Zhao, Y., et al. (2010). Directional water collection on wetted spider silk. *Nature* 463 (7281), 640–643. doi:10.1038/nature08729

Zheng, Y., Gao, X., and Jiang, L. (2007). Directional adhesion of superhydrophobic butterfly wings. *Soft Matter* 3 (2), 178–182. doi:10.1039/b612667g

Zheng, Y., Zhang, C., Wang, J., Liu, Y., Shen, C., and Yang, J. (2019). Robust adhesion of droplets via heterogeneous dynamic petal effects. *J. colloid interface Sci.* 557, 737–745. doi:10.1016/j.jcis.2019.09.070

Zhou, S., Zhu, X., and Yan, Q. (2018). One-step electrochemical deposition to achieve superhydrophobic cobalt incorporated amorphous carbon-based film with self-cleaning and anti-corrosion. *Surf. Interface Anal.* 50 (3), 290–296. doi:10.1002/sia.6367

Zong, C., Hu, M., Azhar, U., Chen, X., Zhang, Y., Zhang, S., et al. (2019). Smart copolymer-functionalized flexible surfaces with photoswitchable wettability: From superhydrophobicity with "rose petal" effect to superhydrophilicity. *ACS Appl. Mat. Interfaces* 11 (28), 25436–25444. doi:10.1021/acsami.9b07767

frontiers | Frontiers in Bioengineering and Biotechnology

TYPE Original Research
PUBLISHED 18 October 2022
DOI 10.3389/fbioe.2022.1029428

OPEN ACCESS

EDITED BY
Feilong Zhang,
Nanyang Technological University, Singapore

REVIEWED BY
Shuqi Wang,
Suzhou Institute of Nano-tech and Nano-bionics (CAS), China
Yongchao Song,
Qingdao University, China

*CORRESPONDENCE
Lingyan Zhang,
18819818005@163.com
Yibiao Liu,
liuyibiao12345@126.com

†These authors have contributed equally to this work

SPECIALTY SECTION
This article was submitted to Biomaterials, a section of the journal Frontiers in Bioengineering and Biotechnology

RECEIVED 27 August 2022
ACCEPTED 07 October 2022
PUBLISHED 18 October 2022

CITATION
Huang Z, Li M, Zhang L and Liu Y (2022), Electrochemical immunosensor based on superwettable microdroplet array for detecting multiple Alzheimer's disease biomarkers.
Front. Bioeng. Biotechnol. 10:1029428.
doi: 10.3389/fbioe.2022.1029428

Electrochemical immunosensor based on superwettable microdroplet array for detecting multiple Alzheimer's disease biomarkers

Zhen Huang[1,2†], Mifang Li[1†], Lingyan Zhang[1*] and Yibiao Liu[1,2*]

[1]Longgang District Central Hospital of Shenzhen, Shenzhen, China, [2]Office of Shenzhen Clinical College, Guangzhou University of Chinese Medicine, Longggang District Central Hospital, Shenzhen, China

Alzheimer's disease (AD) is a neurodegenerative disease caused by neurons damage in the brain, and it poses a serious threat to human life and health. No efficient treatment is available, but early diagnosis, discovery, and intervention are still crucial, effective strategies. In this study, an electrochemical sensing platform based on a superwettable microdroplet array was developed to detect multiple AD biomarkers containing Aβ40, Aβ42, T-tau, and P-tau181 of blood. The platform integrated a superwettable substrate based on nanoAu-modified vertical graphene (VG@Au) into a working electrode, which was mainly used for droplet sample anchoring and electrochemical signal generation. In addition, an electrochemical micro-workstation was used for signals conditioning. This superwettable electrochemical sensing platform showed high sensitivity and a low detection limit due to its excellent characteristics such as large specific surface, remarkable electrical conductivity, and good biocompatibility. The detection limit for Aβ40, Aβ42, T-tau, and P-tau181 were 0.064, 0.012, 0.039, and 0.041 pg/ml, respectively. This study provides a promising method for the early diagnosis of AD.

KEYWORDS

superwettable electrochemical biosensor, vertical graphene, gold nanoparticles, Alzheimer's disease, portable biosensors

Introduction

Alzheimer's disease (AD) is a long-term neurodegenerative disease, that places a heavy burden on individuals, families, and communities. (Scheltens et al., 2021). Up to now, no effective cure for AD is available. Early diagnosis and early intervention are still very effective and important measures. (Li et al., 2021; Scheltens et al., 2021; Alzheimer's Association 2022). At present, the gold standards for AD diagnosis are positron emission tomography (PET) and the level of biomarkers, including β-amyloid (Aβ) peptide and tau protein, in cerebrospinal fluid (CSF). (Marcus et al., 2014; Scheltens et al., 2021). However, AD diagnosis based on PET or CSF biomarkers is inapplicable to AD screening of the

general population due to its high cost and invasive nature. Early diagnosis of AD based on blood biomarkers has elicited increased attention in recent years, and many studies have shown that AD can be diagnosed by measuring quantitative blood biomarkers, such as Aβ40, Aβ42, T-tau, and P-tau181. (Nakamura et al., 2018; Startin et al., 2019; Kim et al., 2020a; Janelidze et al., 2020; Thijssen et al., 2021; Mielke et al., 2022; Moscoso et al., 2022; Rubin 2022). However, the physiological concentration of AD blood markers, such as Aβ40, Aβ42, T-tau, and P-tau181, is only at the picograms level per milliliter. This concentration exceeds the detection limit of the conventional enzyme-linked immunosorbent assay (ELISA). Therefore, developing low-cost, non-invasive, and highly-sensitive detection methods for AD blood biomarkers is essential. (Nakamura et al., 2018; Brazaca et al., 2020). Thus far, many analytical methods have been developed to measure AD biomarkers in the blood, and these include electrochemistry (Liu et al., 2015; Liu et al. 2022a; Liu et al. 2022b; Zhang et al., 2022), fluorescence (Li et al., 2018; Zhang and Tan 2022), colorimetry (Duan et al., 2020), surface enhanced Raman spectroscopy (SERS) (Ma et al., 2021; Yang et al., 2022), and field-effect transistors (Sun Sang et al., 2021). Among these methods, electrochemical biosensors have great potential for disease diagnosis due to their easy miniaturization, high sensitivity, and low cost.

Superwettable microchips integrate two extremes of superhydrophobicity and superhydrophilicity into a 2D micropatterns (Xu et al., 2019), and are widely applied in biological medicine (Popova et al., 2015; Leite et al., 2017) and biochemical analysis (Xu et al., 2015; Xu et al. 2017; Xu et al. 2018) due to their outstanding ability for patterning microdroplets. In biosensing, superwettable microchips have remarkable advantages, including good microdroplet anchoring ability, low sample usage, high throughput, and enrichment ability. In addition, superwettable microchips can be combined with various signal output approaches, such as electrochemistry (Zhang et al., 2017; Song et al., 2019; Zhu et al., 2022), fluorescence (Chen et al., 2018), colorimetry (Hou et al., 2015; Xu et al., 2017; Zhang et al., 2021), and SERS (Song et al., 2018).

In this study, we integrated a superwettable substrate into an electrochemical biosensor, and developed a portable superwettable electrochemical sensing platform for the detection of multiple AD blood biomarkers. As shown in Figure 1, this portable sensing platform is composed of a superwettable sensing substrate, an electrochemical micro-workstation, and a smartphone. The superwettable substrate contains superhydrophilic microwell regions and superhydrophobic regions. The antibody of the target protein was fixed to the superhydrophilic microwell region by Au-S. Then, BSA was used to block the nonspecific binding sites. The peak current of differential pulse voltammetry (DPV) further decreased after binding with the target antigen. The peak current of DPV was recorded, and the target protein concentration was calculated according to the peak current change value. The electrochemical micro-workstation and smartphone were used to regulate and control electrochemical signals. The superwettable electrochemical sensing platform used a two-electrode system. Ag/AgCl electrode served as the reference and counter electrodes. NanoAu-modified vertical graphene (VG) was used as the working electrode. The design of the microdroplet system significantly reduced the use of the sample. A real picture of this portable sensing platform was shown in Supplementary Figure S1. The superwettable microchip also showed an enrichment ability in some ways, and decreased the detection limit (LOD). As a result, the superwettable electrochemical sensing platform exhibited a wide linear range

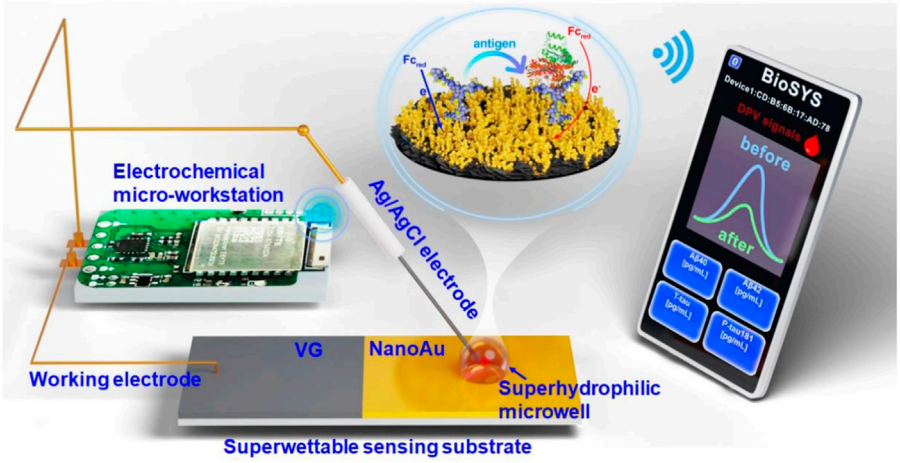

FIGURE 1
Schematic of the superwettable electrochemical sensing platform for AD biomarkers.

and low LOD. This work offers great potential for the early diagnosis of AD.

Experimental section

Chemicals and materials

Aβ peptides (including Aβ40 and Aβ42), human serum albumin (HSA), glucose (GLU), potassium chloride (KCl), potassium ferricyanide/ferrocyanide (K_3 $[Fe(CN)_6]$/K_4 $[Fe(CN)_6]$), ferrocene, and phosphate-buffered solution (PBS, pH = 7.4, 10 mM) were purchased from Sigma-Aldrich (Shanghai, China). T-tau, P-tau181 protein, bovine serum albumin (BSA) and Aβ antibody were purchased from Abcam Ltd (Hong Kong, China). The antibodies of T-tau and P-tau181 were obtained from Thermo Fisher Scientific Co., Ltd. (Beijing, China). The commercial goat serum (Gibco) was purchased from Thermo Fisher Scientific Co., Ltd. (Beijing, China). All chemical reagents were of analytical grade. All solutions were prepared with ultrapure water (Milli-Q, 18.2 MΩ).

Characterization and measurement

The morphology and elemental mapping of VG and VG modified with nanoAu were characterized through field-emission scanning electron microscopy (SEM, ThermoFisher, FEI Apreo S, Waltham, MA, United States). Water contact angles (CA) were measured at room temperature with a DSA100S system (KRUSS, Germany). All electrochemical measurements were performed on a customized electrochemical micro-workstation (Refresh AI Biosensor Co., Ltd., Shenzhen, China) at room temperature.

Construction of superwettable electrochemical substrate

First, VG on a ceramic surface was prepared through chemical vapor deposition (CVD). Second, nanoAu was modified on the VG surface through the electrodeposition of 10 mM $HAuCl_4$. The deposition voltage was -1.8 V, and deposition time was 300 s. Third, the VG substrate modified with nanoAu was immersed in a n-decanethiol solution for 24 h at room temperature, and n-decanethiol was fixed on the surface of nanoAu. Lastly, the nanoAu modified with n-decanethiol substrate was treated with 120 s O_2 plasma to obtain a superwetting electrochemical substrate containing superhydrophobic and superhydrophilic regions.

Preparation of electrochemical sensing platform based on superwettable substrate

After preparing the superwettable substrate, a superwettable electrochemical biosensor was constructed. First, 5 μL of the antibody of target protein (Aβ40, Aβ42, T-tau, and P-tau181) was dripped onto the superhydrophilic microwell region and incubated at 37°C for 1 h. Second, 5 μL of bovine serum albumin (BSA, 1%) was dropped onto the microwell, which was incubated for 1 h, and used to block the nonspecific binding sites. Third, 5 μL of different concentrations of the target protein was added to the superhydrophilic microwell surface, and incubated for 1 h at 37°C. After each step, the microwell surface was washed three times with PBS (0.01 M, pH = 7.4). Lastly, by combining the superwettable electrochemical substrate with the electrochemical micro-workstation, a superwettable electrochemical sensing platform was successfully constructed.

The target protein was measured *via* DPV by using a portable electrochemical micro-workstation. The working potential of DPV was in the range of 0–0.4 V. After incubation with different concentrations of the target protein, the corresponding peak current change value (ΔI) was recorded, and used to calculate the concentration of the target protein. The selectivity of this superwettable electrochemical sensing platform was investigated in PBS buffer containing HSA, GLU, Aβ40, Aβ42, Tau441, and P-tau181.

The application of the superwettable electrochemical sensing platform in goat serum.

The performance of the portable superwettable electrochemical sensing platform in goat serum was characterized through DPV. In brief, the antibody of the target protein (5 μL) was immobilized on the superhydrophilic microwell surface. Then 5 μL of commercial serum samples (1 μL goat serum diluted with 4 μL PBS buffer) containing different concentrations of the target protein (1, 10, and 100 pg/ml) was added to each superhydrophilic microwell surface and incubated at 37 °C for 1 h. The peak current change value of the DPV signal was monitored in this process.

Detection of clinical serum samples

5 μL clinical human sample (1 μL sample diluted with 4 μL PBS buffer) was added to the superhydrophilic microwell surface and incubated for 1 h at 37 C. The peak current value of DPV signals was recorded, and the target protein concentration was calculated according to the peak current changing value.

Results and discussion

Preparation and characterization of superwettable substrate

The fabrication of the superwettable substrate is shown in Supplementary Figure S2. NanoAu was modified on the surface by electrodeposition, which could increase the electron transfer rates and improve the sensitivity of the senor. N-decanethiol was immobilized on the nanoAu surface, and the water contact angle

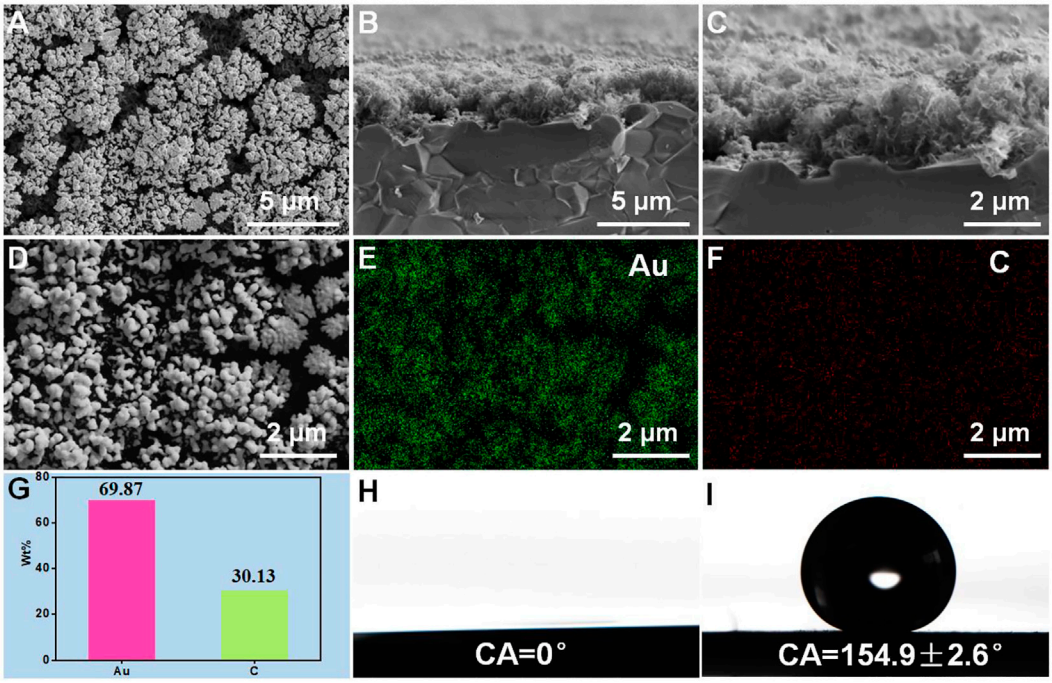

FIGURE 2
Surface **(A)** and cross-section view **(B,C)** SEM images of vertical graphene modified with nanoAu. Surface element distribution characterization **(D–G)** of vertical graphene modified with nanoAu. Water contact angles of the superhydrophilic region **(H)** and superhydrophobic region **(I)**.

was 154.9 ± 2.6°, indicating a superhydrophobic surface. After treatment by O_2 plasma for 120 s, the water contact angle became 0°, indicating that the region without photomask became superhydrophilic. (Figures 2H,I). A superwettable substrate that included superhydrophobic and superhydrophilic regions was successfully prepared.

The surface morphology of the superwettable substrate was evaluated *via* SEM, and the results are shown in Figure 2A. Many gold nanoparticles were observed on the surface of the layered vertical graphene structures. The cross-section view SEM images of vertical graphene was shown in Supplementary Figure S3. The cross-section view morphology of vertical graphene@Au is shown in Figures 2B,C. The gold nanoparticles were deposited mainly on the VG surface. In addition, the content of Au was measured through energy dispersive X-ray (EDX), and the result showed that the weight percent of Au element was 69.87%, indicating that most of the surface areas of VG were covered with Au nanoparticles (Figures 2D–G).

Construction and analytical performance of superwettable electrochemical sensing platform

The electroactive areas of VG and VG@Au were compared by cyclic voltammetrys (CVs), and the results showed that the electroactive area of the VG@Au electrode was remarkably larger than that of the VG electrode. (Figure 3A). In addition, the electrode surface dynamics process was evaluated by CV at different scan rates. As shown in Figure 3B, the peak current had a linear relation with the square root of the scan rate, indicating a diffusion-limited process. After the superwettable substrate was completed, the antibody of the target protein (Aβ40, Aβ42, T-tau, and P-tau181) was immobilized on the superhydrophilic microwell region by Au-S. After modifying the corresponding antibody, the peak current of the DPV signal decreased, which indicated that the target protein antibody was successfully fixed on the superwettable microwell region surface (Supplementary Figure. S4, lines I and II). Then, BSA was used to block the nonspecific adsorption sites, and the peak current of the DPV signals further decreased (Supplementary Figure S4, line III). Afterward, the different concentrations of the target protein were added to the superhydrophilic microwell region surface. During this period, the DPV signal was recorded, and the concentration of the target protein was calculated based on the variation of the peak current.

The concentration of the target protein antibody was optimized before the final test. As shown in Supplementary Figure S5, the optimized concentration of the target protein antibody was 10 μg/ml. Under the optimized condition, the antibody of four proteins was immobilized in the

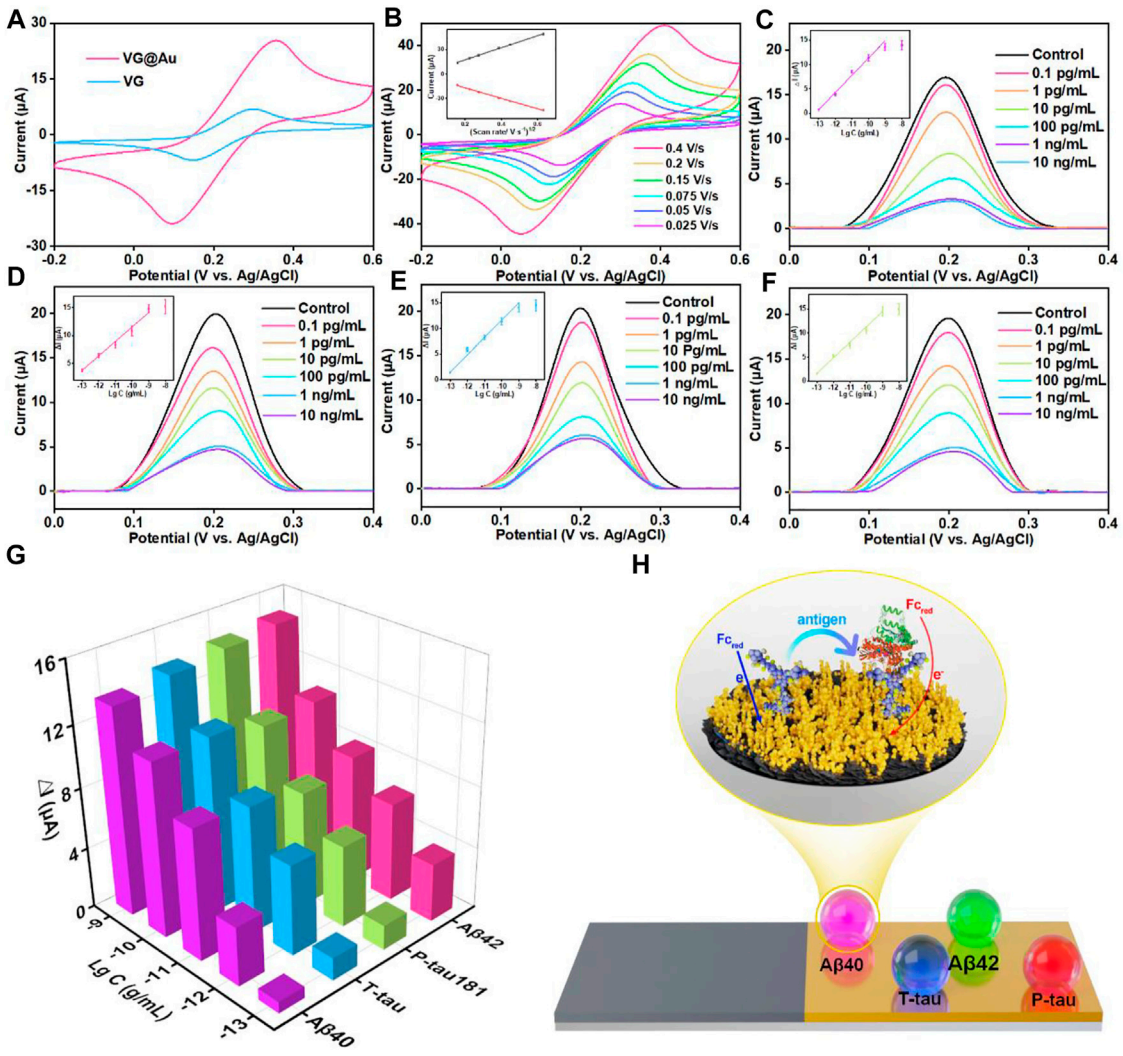

FIGURE 3
Analytical performance of the superwettable electrochemical sensing platform based on VG@Au for the detection of AD biomarkers **(A)** CVs of VG and VG@Au electrode in 5 mM $[Fe(CN)_6]^{3-}/[Fe(CN)_6]^{4-}$ solution containing 0.1 M KCl at 0.1 V/s. **(B)** CVs of the superwettable microwell electrode based on VG@Au at different scan rates. The inset is the relationship between the peak current and the square root of scan rate. DPV signals of different concentrations of Aβ40 **(C)**, Aβ42 **(D)**, T-tau **(E)**, and P-tau181 **(F)** in 1 mM ferrocene solution containing 0.1 M KCl at 0.1 V/s. **(G)** Change value (ΔI) of DPV response signals towards AD biomarkers. **(H)** Schematic of the electrochemical immunosensor based on VG@Au.

superhydrophilic microwell regions, and the concentration of the target proteins was measured by the variation in the resistance of the superhydrophilic microwell region surface, as shown in Figure 3H. The corresponding antibody specifically recognized the target protein (Aβ40, Aβ42, T-tau, and P-tau181), resulting in the increase in surface resistance, which caused signal reduction. The peak current of the DPV signals was recorded by the electrochemical micro-workstation platform, and the concentration of the target protein was calculated by the variation in peak current.

As shown in Figures 3C–G, for the target protein (Aβ40, Aβ42, T-tau, and P-tau181), the peak current of DPV signals decreased, and the variation in peak current (ΔI) increased as the concentration of the target protein increased. ΔI had a good linear relationship with the logarithm of target protein concentration from 0.1 pg/ml to 1,000 pg/ml. The detection limit of this superwettable electrochemical sensing platform for Aβ40 was about 0.064 pg/ml (S/N = 3). The LOD was calculated as three times the standard deviation of the blank. (Chiavaioli et al., 2017; Esposito et al., 2021). Similarly, the LOD for Aβ42, T-tau, and P-tau181 was 0.012, 0.039, and 0.041 pg/ml, respectively.

In blood, the physiological concentration of Aβ40, Aβ42, T-tau, and P-tau181 was about several to hundreds of picograms per

TABLE 1 Comparison between the superwettable electrochemical sensing platform and other sensors for the detection of AD biomarkers.

Method	Target	Detection limit	References
Electrochemistry	Tau, p-tau181, Aβ42, Aβ40	2.45, 2.72, 2.13, 2.20 fM	Kim et al. (2020b)
Electrochemistry	ApoE4, Tau, Aβ	5.91×10^{-11};7.1×10^{-11}; 8.6×10^{-12} mg/ml	Song et al. (2020)
Electrochemistry	T-tau, p-tau181, Aβ40, Aβ42	0.125, 0.089, 0.142, 0.176 pg/ml	Liu et al. (2022a)
Fluorescence	Aβ42, tau441, p-tau181	340.07, 669.44, 493.79 pg/ml	Chan et al. (2017)
LSPR	Aβ40, Aβ42, T-tau,	34.9, 26, 23.6 fM	Kim et al. (2018)
SERS	Tau, Aβ42 oligomers	4.2×10^{-4} pM, 3.7×10^{-2} nM	Zhang et al. (2019)
FET sensor	tau	10 fg/ml	Sun Sang et al. (2021)
Electrochemistry	T-tau, p-tau181, Aβ40, Aβ42	0.039, 0.041, 0.064, 0.012 pg/ml	This work

Selectivity and stability.

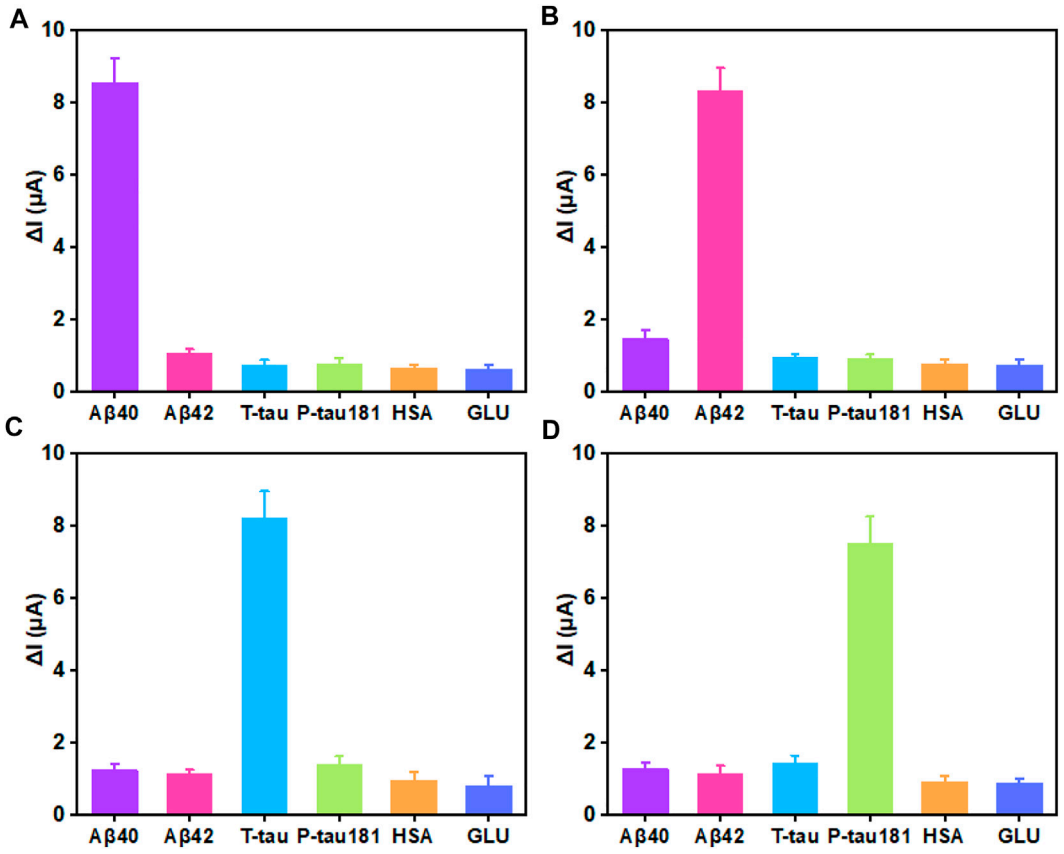

FIGURE 4
Selectivity of the superwettable electrochemical sensing platform **(A)** Variation of the peak current of 10 pg/ml Aβ40 and 1 ng/ml Aβ42, T-tau, P-tau181, GLU, and HSA. **(B)** Variation of the peak current of 10 pg/ml Aβ42 and 1 ng/ml Aβ40, T-tau, P-tau181, GLU, and HSA **(C)** Variation of the peak current of 10 pg/mL T-tau and 1 ng/ml Aβ40, Aβ42, P-tau181, GLU, and HSA. **(D)** Variation of the peak current of 10 pg/mL P-tau181 and 1 ng/ml Aβ40, Aβ42, T-tau, GLU, and HSA.

milliliter. This result shows that our developed superwettable electrochemical sensing platform satisfies the needs of detecting AD biomarkers in blood. The superwettable electrochemical sensing platform based on the VG@Au array exhibited a low LOD and a wide linear range. A comparison of this method and methods in previous reports is shown in Table 1. Our developed superwettable electrochemical sensing platform exhibited excellent analytical performance. The concentration of AD biomarkers including

Aβ40, Aβ42, T-tau, and P-tau181, was at picograms per milliliter of blood. The LOD of this superwettable electrochemical sensing platform was lower than 0.1 pg/ml, which meets the requirements for the detection of AD biomarkers.

Selectivity and stability

In biological application, selectivity and stability are important factors for biosensors. The selectivity and stability of this superwettable electrochemical sensing platform were investigated. As shown in Figure 4A, when 10 pg/ml of Aβ40 was added, an obvious signal response of 8.56 μA was obtained. On the surface of the superhydrohilic microwell sensing region, the concentration of other proteins including Aβ42, T-tau, P-tau181, GLU, and HSA was 100-fold higher than that of Aβ40, and the △I for Aβ42, T-tau, P-tau181, GLU, and HSA was 1.06, 0.73, 0.75, 0.66, and 0.62 μA, respectively, which accounted for 12.4%, 8.5%, 8.7%, 7.7%, and 7.2% of the △I for Aβ40, respectively. For Aβ42 sensing region, the signal response was about 8.33 μA. The △I for Aβ40, T-tau, P-tau181, GLU, and HSA was 1.46, 0.96, 0.89, 0.78, and 0.73 μA, respectively, which accounted for 17.5%, 11.5%, 10.6%, 9.3% and 8.7% of the △I for Aβ42, respectively (Figure 4B). Likewise, for T-tau or P-tau181, the corresponding superhydrohilic microwell sensing region also displayed excellent selectivity (Figures 4C,D). These results indicate that the selectivity of this superwettable electrochemical sensing platform for Aβ40, Aβ42, T-tau, and P-tau181 was outstanding. In addition, the stability of this superwettable electrochemical sensing platform was evaluated by detecting six times of 10 pg/ml of the target protein (Aβ40, Aβ42, T-tau, and P-tau181) As shown in Supplementary Figure S6, the sensor was stored in dry conditions at 4°C for 2 weeks. The ΔI value still remained above 90% of its initial value after 14 days, demonstrating the acceptable stability of this superwettable electrochemical sensing platform based on VG@Au. The results prove that our developed electrochemical sensing platform based on a superwettable microarray has good stability and specificity.

Application of this superwettable electrochemical sensing platform in serum sample

To further evaluate the clinical application of the superwettable electrochemical sensing platform, goat serum samples that included Aβ40, Aβ42, T-tau, and P-tau181 were detected by using the designed superwettable platform. The diluted serum samples were spiked with different concentrations of the target protein (1, 10, and 100 pg/ml) including Aβ40, Aβ42, T-tau, and P-tau181. The result was shown in Supplementary Table S1. No significant difference was observed between the detected and added values. The recovery rate ranged from 91% to 109.1%. In addition, we conduct two clinical samples and compared the results with the results from typical ELISA. As shown in Supplementary Table S2, Aβ40 and Aβ42 can be detected by this superwettable sensor and typical ELISA, there was no significant difference between the result of our sensor and that of ELISA. This result demonstrated that our developed superwettable electrochemical sensing platform based on VG@Au could be used for detecting the clinical samples. What's more, T-tau and P-tau181 were detected by this sensor, but they were not detected by typical ELISA, indicating that this superwettable electrochemical sensor has lower LOD. To sum up, the superwettable electrochemical sensing platform based on VG@Au has excellent sensitivity and reliability for the detection of AD biomarkers in clinical serum sample analysis, and could be capable of clinical diagnosis.

Conclusion

In summary, a portable superwettable electrochemical sensing platform based on the VG@Au substrate was designed and constructed to detect multiple AD biomarkers in serum. The superwettable VG@Au substrate included superhydrophobic and superhydrophilic regions on the VG@Au surface, which could be used for fixing a microdroplet sample, and used as a working electrode to generate electrochemical signals. In addition, an electrochemical micro-workstation was introduced to this superwettable electrochemical sensing platform to adjust the signal. The superwettable electrochemical sensing platform based on the superwettable VG@Au substrate showed excellent analytical performance with a low detection limit and high sensitivity due to the good properties of VG@Au, including large specific surface, outstanding electrical conductivity, and good biocompatibility. As a result, the detection limit for Aβ40, Aβ42, T-tau, and P-tau181 were 0.064, 0.012, 0.039, and 0.041 pg/ml, respectively. In blood, the AD biomarker concentration was at the ~pg/mL level. Our designed superwettable sensing platform satisfies the need for detection in blood. This work offers a new method of detecting AD biomarkers in serum. The method exhibites great potential for early diagnosis of AD.

Data availability statement

The original contributions presented in the study are included in the article/Supplementary Material, further inquiries can be directed to the corresponding authors.

Author contributions

YL and LZ provide the idea, design the experiment, and write the paper. ZH and ML mainly do the experiment and analyze data.

Funding

This work was supported by the medical and health technology plan project of special fund for economic and technological development of longgang district, Shenzhen, PR. China (Grant no. LGKCYLWS2020001), Longgang District Medical and health science and technology project (grant no. LGKCYLWS2021000003).

Acknowledgments

We thank the Instrumental Analysis Center of Shenzhen University (Xili Campus) for providing access to the instruments used in the experiments. We thank the advice of Jianbo Yu.

Conflict of interest

The authors declare that the research was conducted in the absence of any commercial or financial relationships that could be construed as a potential conflict of interest.

Publisher's note

Supplementary material

The Supplementary Material for this article can be found online at: https://www.frontiersin.org/articles/10.3389/fbioe.2022.1029428/full#supplementary-material

References

Alzheimer's Association (2022). Alzheimer's disease facts and figures. *Alzheimers Dement.* 1–90. doi:10.1002/alz.12638

Brazaca, L. C., Sampaio, I., Zucolotto, V., and Janegitz, B. C. (2020). Applications of biosensors in Alzheimer's disease diagnosis. *Talanta* 210, 120644. doi:10.1016/j.talanta.2019.120644

Chan, H. N., Xu, D., Ho, S. L., Wong, M. S., and Li, H. W. (2017). Ultra-sensitive detection of protein biomarkers for diagnosis of Alzheimer's disease. *Chem. Sci.* 8, 4012–4018. doi:10.1039/c6sc05615f

Chen, Y., Xu, L.-P., Meng, J., Deng, S., Ma, L., Zhang, S., et al. (2018). Superwettable microchips with improved spot homogeneity toward sensitive biosensing. *Biosens. Bioelectron.* 102, 418–424. doi:10.1016/j.bios.2017.11.036

Chiavaioli, F., Gouveia, C. A. J., Jorge, P. A. S., and Baldini, F. (2017). Towards a uniform metrological assessment of grating-based optical fiber sensors: From refractometers to biosensors. *Biosensors* 7, 23. doi:10.3390/bios7020023

Duan, C., Jiao, J., Zheng, J., Li, D., Ning, L., Xiang, Y., et al. (2020). Polyvalent biotinylated aptamer scaffold for rapid and sensitive detection of tau proteins. *Anal. Chem.* 92, 15162–15168. doi:10.1021/acs.analchem.0c03643

Esposito, F., Sansone, L., Srivastava, A., Baldini, F., Campopiano, S., Chiavaioli, F., et al. (2021). Long period grating in double cladding fiber coated with graphene oxide as high-performance optical platform for biosensing. *Biosens. Bioelectron.* 172, 112747. doi:10.1016/j.bios.2020.112747

Hou, J., Zhang, H., Yang, Q., Li, M., Jiang, L., and Song, Y. (2015). Hydrophilic–hydrophobic patterned molecularly imprinted photonic crystal sensors for high-sensitive colorimetric detection of tetracycline. *Small* 11, 2738–2742. doi:10.1002/smll.201403640

Janelidze, S., Mattsson, N., Palmqvist, S., Smith, R., Beach, T. G., Serrano, G. E., et al. (2020). Plasma P-tau181 in alzheimer's disease: Relationship to other biomarkers, differential diagnosis, neuropathology and longitudinal progression to alzheimer's dementia. *Nat. Med.* 26, 379–386. doi:10.1038/s41591-020-0755-1

Kim, H., Lee, J. U., Song, S., Kim, S., and Sim, S. J. (2018). A shape-code nanoplasmonic biosensor for multiplex detection of Alzheimer's disease biomarkers. *Biosens. Bioelectron. X.* 101, 96–102. doi:10.1016/j.bios.2017.10.018

Kim, K., Kim, M. J., Kim, D. W., Kim, S. Y., Park, S., and Park, C. B. (2020a). Clinically accurate diagnosis of Alzheimer's disease via multiplexed sensing of core biomarkers in human plasma. *Nat. Commun.* 11, 119. doi:10.1038/s41467-019-13901-z

Kim, K., Lee, C. H., and Park, C. B. (2020b). Chemical sensing platforms for detecting trace-level Alzheimer's core biomarkers. *Chem. Soc. Rev.* 49, 5446–5472. doi:10.1039/d0cs00107d

Leite, Á. J., Oliveira, M. B., Caridade, S. G., and Mano, J. F. (2017). Screening of nanocomposite scaffolds arrays using superhydrophobic-wettable micropatterns. *Adv. Funct. Mat.* 27, 1701219. doi:10.1002/adfm.201701219

Li, Y., Haber, A., Preuss, C., John, C., Uyar, A., Yang, H. S., et al. (2021). Alzheimer's Disease Neuroimaging, ITransfer learning-trained convolutional neural networks identify novel MRI biomarkers of Alzheimer's disease progression. *Alzheimers Dement.* 13, e12140. doi:10.1002/dad2.12140

Li, Y., Wang, K., Zhou, K., Guo, W., Dai, B., Liang, Y., et al. (2018). Novel D-A-D based near-infrared probes for the detection of beta-amyloid and Tau fibrils in Alzheimer's disease. *Chem. Commun.* 54, 8717–8720. doi:10.1039/c8cc05259j

Liu, Y., Huang, Z., Xu, Q., Zhang, L., Liu, Q., and Xu, T. (2022a). Portable electrochemical micro-workstation platform for simultaneous detection of multiple Alzheimer's disease biomarkers. *Microchim. Acta* 189, 91. doi:10.1007/s00604-022-05199-4

Liu, Y., Liu, X., Li, M., Liu, Q., and Xu, T. (2022b). Portable vertical graphene@Au-based electrochemical aptasensing platform for point-of-care testing of tau protein in the blood. *Biosensors* 12, 564. doi:10.3390/bios12080564

Liu, Y., Xu, L.-P., Wang, S., Yang, W., Wen, Y., and Zhang, X. (2015). An ultrasensitive electrochemical immunosensor for apolipoprotein E4 based on fractal nanostructures and enzyme amplification. *Biosens. Bioelectron.* 71, 396–400. doi:10.1016/j.bios.2015.04.068

Ma, H., Liu, S., Liu, Y., Zhu, J., Han, X. X., Ozaki, Y., et al. (2021). *In-situ* fingerprinting phosphorylated proteins via surface-enhanced Raman spectroscopy: Single-site discrimination of Tau biomarkers in Alzheimer's disease. *Biosens. Bioelectron.* 171, 112748. doi:10.1016/j.bios.2020.112748

Marcus, C., Mena, E., and Subramaniam, R. M. (2014). Brain PET in the diagnosis of Alzheimer's disease. *Clin. Nucl. Med.* 39, e413–e426. quiz e423-416. doi:10.1097/RLU.0000000000000547

Mielke, M. M., Dage, J. L., Frank, R. D., Algeciras-Schimnich, A., Knopman, D. S., Lowe, V. J., et al. (2022). Performance of plasma phosphorylated tau 181 and 217 in the community. *Nat. Med.* 28, 1398–1405. doi:10.1038/s41591-022-01822-2

Moscoso, A., Karikari, T. K., Grothe, M. J., Ashton, N. J., Lantero-Rodriguez, J., Snellman, A., et al. (2022). CSF biomarkers and plasma p-tau181 as predictors of

longitudinal tau accumulation: Implications for clinical trial design. *Alzheimers Dement.* doi:10.1002/alz.12570

Nakamura, A., Kaneko, N., Villemagne, V. L., Kato, T., Doecke, J., Dore, V., et al. (2018). High performance plasma amyloid-beta biomarkers for Alzheimer's disease. *Nature* 554, 249–254. doi:10.1038/nature25456

Popova, A. A., Schillo, S. M., Demir, K., Ueda, E., Nesterov-Mueller, A., and Levkin, P. A. (2015). Droplet-array (da) sandwich chip: A versatile platform for high-throughput cell screening based on superhydrophobic–superhydrophilic micropatterning. *Adv. Mat.* 27, 5217–5222. doi:10.1002/adma.201502115

Rubin, R. (2022). New test to help diagnose alzheimer disease. *JAMA* 327, 2281. doi:10.1001/jama.2022.9847

Scheltens, P., De Strooper, B., Kivipelto, M., Holstege, H., Chételat, G., Teunissen, C. E., et al. (2021). Alzheimer's disease. *Lancet* 397, 1577–1590. doi:10.1016/s0140-6736(20)32205-4

Song, Y., Xu, T., Xu, L.-P., and Zhang, X. (2019). Nanodendritic gold/graphene-based biosensor for tri-mode miRNA sensing. *Chem. Commun.* 55, 1742–1745. doi:10.1039/C8CC09586H

Song, Y., Xu, T., Xu, L.-P., and Zhang, X. (2018). Superwettable nanodendritic gold substrates for direct miRNA SERS detection. *Nanoscale* 10, 20990–20994. doi:10.1039/C8NR07348A

Song, Y., Xu, T., Zhu, Q., and Zhang, X. (2020). Integrated individually electrochemical array for simultaneously detecting multiple Alzheimer's biomarkers. *Biosens. Bioelectron. X.* 162, 112253. doi:10.1016/j.bios.2020.112253

Startin, C. M., Ashton, N. J., Hamburg, S., Hithersay, R., Wiseman, F. K., Mok, K. Y., et al. (2019). Plasma biomarkers for amyloid, tau, and cytokines in Down syndrome and sporadic Alzheimer's disease. *Alz. Res. Ther.* 11, 26. doi:10.1186/s13195-019-0477-0

Sun Sang, K., Dongwoo, K., Mijin, Y., Jeong Gon, S., and Soo Hyun, L. (2021). The role of graphene patterning in field-effect transistor sensors to detect the tau protein for Alzheimer's disease: Simplifying the immobilization process and improving the performance of graphene-based immunosensors. *Biosens. Bioelectron.* 192, 113519. doi:10.1016/j.bios.2021.113519

Thijssen, E. H., La Joie, R., Strom, A., Fonseca, C., Iaccarino, L., Wolf, A., et al. (2021). Plasma phosphorylated tau 217 and phosphorylated tau 181 as biomarkers in alzheimer's disease and frontotemporal lobar degeneration: A retrospective diagnostic performance study. *Lancet Neurology* 20, 739–752. doi:10.1016/s1474-4422(21)00214-3

Xu, L. P., Chen, Y., Yang, G., Shi, W., Dai, B., Li, G., et al. (2015). Ultratrace DNA detection based on the condensing-enrichment effect of superwettable microchips. *Adv. Mat.* 27, 6878–6884. doi:10.1002/adma.201502982

Xu, T., Li-Ping, X., Xueji, Z., and Shutao, W. (2019). Bioinspired superwettable micropatterns for biosensing. *Chem. Soc. Rev.* 48, 3153–3165. doi:10.1039/C8CS00915E

Xu, T., Shi, W., Huang, J., Song, Y., Zhang, F., Xu, L.-P., et al. (2017). Superwettable microchips as a platform toward microgravity biosensing. *ACS Nano* 11, 621–626. doi:10.1021/acsnano.6b06896

Xu, T., Song, Y., Gao, W., Wu, T., Xu, L.-P., Zhang, X., et al. (2018). Superwettable electrochemical biosensor toward detection of cancer biomarkers. *ACS Sens.* 3, 72–78. doi:10.1021/acssensors.7b00868

Yang, S. J., Lee, J. U., Jeon, M. J., and Sim, S. J. (2022). Highly sensitive surface-enhanced Raman scattering-based immunosensor incorporating half antibody-fragment for quantitative detection of Alzheimer's disease biomarker in blood. *Anal. Chim. Acta* 1195, 339445. doi:10.1016/j.aca.2022.339445

Zhang, H., Oellers, T., Feng, W., Abdulazim, T., Saw, E. N., Ludwig, A., et al. (2017). High-density droplet microarray of individually addressable electrochemical cells. *Anal. Chem.* 89, 5832–5839. doi:10.1021/acs.analchem.7b00008

Zhang, K., Zhang, J., Wang, F., and Kong, D. (2021). Stretchable and superwettable colorimetric sensing patch for epidermal collection and analysis of sweat. *ACS Sens.* 6, 2261–2269. doi:10.1021/acssensors.1c00316

Zhang, P., and Tan, C. (2022). Cross-reactive fluorescent sensor array for discrimination of amyloid beta aggregates. *Anal. Chem.* 94, 5469–5473. doi:10.1021/acs.analchem.2c00579

Zhang, X., Liu, S., Song, X., Wang, H., Wang, J., Wang, Y., et al. (2019). Robust and universal SERS sensing platform for multiplexed detection of alzheimer's disease core biomarkers using PAapt-AuNPs conjugates. *ACS Sens.* 4, 2140–2149. doi:10.1021/acssensors.9b00974

Zhang, Z.-h., Hu, J., Zhu, H., Chen, Q., Koh, K., Chen, H., et al. (2022). A facile and effective immunoassay for sensitive detection of phosphorylated tau: The role of flower-shaped TiO2 in specificity and signal amplification. *Sensors Actuators B Chem.* 366, 132015. doi:10.1016/j.snb.2022.132015

Zhu, Q., Yang, Y., Gao, H., Xu, L.-P., and Wang, S. (2022). Bioinspired superwettable electrodes towards electrochemical biosensing. *Chem. Sci.* 13, 5069–5084. doi:10.1039/D2SC00614F

frontiers | Frontiers in Bioengineering and Biotechnology

TYPE Original Research
PUBLISHED 07 April 2023
DOI 10.3389/fbioe.2023.999137

OPEN ACCESS

EDITED BY
Hongliang Liu,
Yantai University, China

REVIEWED BY
Jingxin Meng,
Technical Institute of Physics and Chemistry, China
Jing Du,
The Pennsylvania State University (PSU), United States

*CORRESPONDENCE
Yu-Xi Liu,
yuxiliu66@126.com
Shi-Yun Lin,
279190825@qq.com

†These authors have contributed equally to this work

SPECIALTY SECTION
This article was submitted to Bionics and Biomimetics, a section of the journal Frontiers in Bioengineering and Biotechnology

RECEIVED 20 July 2022
ACCEPTED 27 March 2023
PUBLISHED 07 April 2023

CITATION
Liu Y-X, Li A-H, Lin S-Y, Sun H and Chen B (2023), Research on biomimetic design and impact characteristics of periodic multilayer helical structures.
Front. Bioeng. Biotechnol. 11:999137.
doi: 10.3389/fbioe.2023.999137

Research on biomimetic design and impact characteristics of periodic multilayer helical structures

Yu-Xi Liu[1*†], Ai-Hua Li[2†], Shi-Yun Lin[3*], Hong Sun[1] and Bin Chen[4]

[1]School of Smart Health, Chongqing College of Electronic Engineering, Chongqing, China, [2]Department of Gastroenterology, Chongqing University Cancer Hospital, Chongqing, China, [3]Green Aerotechnics Research Institute of Chongqing Jiaotong University and School of Aeronautics, Chongqing Jiaotong University, Chongqing, China, [4]College of Aerospace Engineering, Chongqing University, Chongqing, China

Osteons are composed of concentric lamellar structure, the concentric lamellae are composed of periodic thin and thick sub-lamellae, and every 5 sub-lamellae is a cycle, the periodic helix angle of mineralized collagen fibers in two adjacent sub-lamellae is 30°. Four biomimetic models with different fiber helix angles were established and fabricated according to the micro-nano structure of osteon. The effects of the fiber periodic helical structure on impact characteristic and energy dissipation of multi-layer biomimetic composite were investigated. The calculation results indicated that the stress distribution, contact characteristics and fiber failur during impact, and energy dissipation of the composite are affected by the fiber helix angle. The stress concentration of composite materials under external impact can be effectively improved by adjusting the fiber helix angle when the material composition and material performance parameters are same. Compared with the sample30, the maximum stress of sample60 and sample90 increases by 38.1% and 69.8%, respectively. And the fiber failure analysis results shown that the model with a fiber helix angle of 30° has a better resist impact damage. The drop-weight test results shown that the impact damage area of the specimen with 30° helix angle is smallest among the four types of biomimetic specimens. The periodic helical structure of mineralized collagen fibers in osteon can effectively improve the impact resistance of cortical bone. The research results can provide useful guidance for the design and manufacture of high-performance, impact-resistant biomimetic composite materials.

KEYWORDS

periodic helical structure, biomimetic composite, osteon, mineralized collagen fibril, impact characteristic

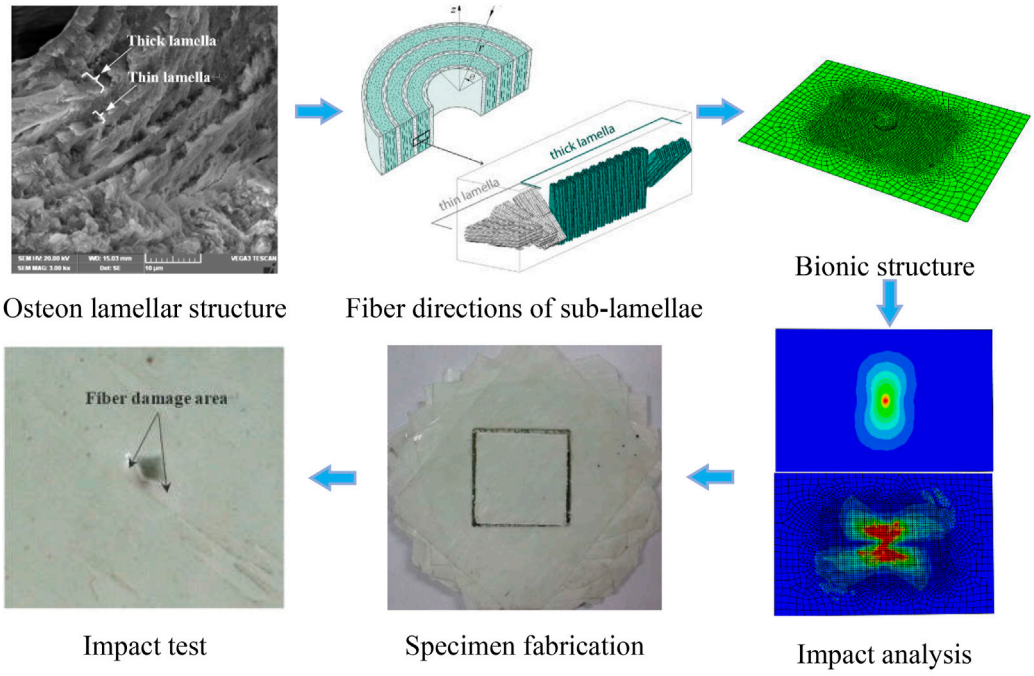

GRAPHICAL ABSTRACT

Introduction

Bone is a highly optimized composite material with outstanding mechanical properties, which has a very complex structure and is organized at different levels (Wang et al., 2020; Ingrole et al., 2021). Composite materials with high strength, light weight (Rahimizadeh et al., 2021) and impact resistance (Wang et al., 2021; Wang et al., 2022) have a wide range of needs in the fields of aerospace, military, vehicles and other fields (Dong et al., 2022; Sharma et al., 2022). Therefore, the research of biomimetic composites can provide inspiration for the design of materials with excellent mechanical properties and meet the special requirements of engineering (Bhudolia and Joshi, 2018; Jiang et al., 2019; Alizadeh and Ebrahimzadeh, 2022).

Lamellar bone is the most abundant type in the cortical bones and composed of osteonal tissue. Osteons are cylindrical shaped structural and is composed of concentric lamellar structure (Figure 1A) (Liu et al., 2017), the diameter ranges from 50 to 500 μm (Currey, 2012), and the lamella thickness is about of 3–7 μm (Giner et al., 2014a). Cortical bone is mainly composed of organic phase (Fratzl and Fratzl, 2010) and inorganic phase, and the organic phase is mainly formed by mineralized collagen fibers (Hamed et al., 2010). Xu et al. (Xu et al., 2003) characterized the micro-mechanical properties of human lamellar bone, and the results showed that the elastic modulus of thick lamellar bone was higher than that of thin lamellar bone. Gupta et al. (Gupta et al., 2006) investigated the microstructure of osteon, and the results showed that the osteon consists of a laminated cylindrical composite composed of mineralized collagen fibers. Carnelli et al. (Carnelli et al., 2013) evaluated the elastic constants of the sublayers of mineralized collagen fibrils in osteonal lamella, and the results show that the hierarchical structure of lamellar bone was the main determinant of the adjustment of tissue mechanical properties. Reznikov et al. (Reznikov et al., 2013) investigated the orientation of average collagen array and the dispersion of local collagen fibers, and three different sub-lamellar structural motifs. Varga et al. (Varga et al., 2013) investigate the 3D organization of mineralized collagen fibrils in human cortical bone, and find two specific dominant patterns, oscillating and twisted ply-woods coexisting in a single osteon, and the orientation of collagen fibrils changed periodically. Weiner et al. (Weiner et al., 1997) measured the angle between adjacent arrays of rat bone lamellae, the results shown that most of the angles were about 30°. The mineralized collagen fibers in osteons have their own uniqueness, which are periodic helical arranged and every 5 sub-lamellae constitute a lamella, the offset angle of fibers in two adjacent sub-lamellae is 30° (Giraudguille, 1988; Liu et al., 2000). Giner et al. (Giner et al., 2014a) drew a schematic diagram of the staggered structure of sub-lamellae of osteons and the fiber directions of the five sub-lamellae (Figure 1B), and the 5 sub-layers are simplified to a thin layer and a thick layer (Vercher et al., 2014).

At present, the existing literatures have reported the mechanical properties and structure bionics of multilayer fiber reinforced composites from different perspectives (Jansen et al., 2016; Rua et al., 2021), the research on osteon mainly focuses on microstructure (Giner et al., 2014b; Reznikov and Weiner, 2014; Yin et al., 2021), distribution of collagen fibers and osteocyte lacunae (Liu et al., 2017; Liu et al., 2019). However, biomimetic composite materials with periodic helical arrangement of fibers are rarely

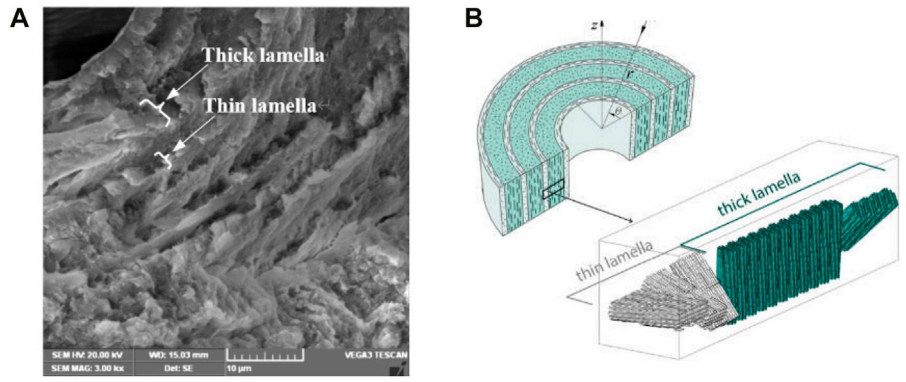

FIGURE 1
Lamella structure of osteon. **(A)** Thin and thick lamellae of osteon, **(B)** arrangement direction of fibers in adjacent lamellae.

TABLE 1 Models of multilayer fiber biomimetic composites.

Bionic models	Fiber laying mode
Small helix angle (Sample15)	[0/15/30···/165]
Medium helix angle (Sample30)	$[0/30/60\cdots/150]_{2s}$
Large helix angle (Sample60)	$[0/60/120]_{4s}$
Orthogonal m (Sample90)	$[0/90]_{6s}$

reported. Based on the distribution of fibers in osteon, four kinds of biomimetic composite model with different helix angle were constructed. In order to compare and analyze the impact characteristics of composite materials affected by the periodic helical arrangement of fibers, four biomimetic composite models were fabricated. Furthermore, the effects of the fiber periodic helical structure on impact characteristic and energy dissipation of multi-layer biomimetic composite were investigated by progressive damage analysis and drop-weight test.

Material and methods

Structure biomimetic and impact analysis

A biomimetic composite model was constructed (Table 1, Sample 30) based on the helical structure of mineralized collagen fiber in osteon, and the offset angle of periodic helix fiber is 30°. In addition, for comparing and analyzing the effects of fiber helix angle on the impact resistance of biomimetic composites, three composite material models of osteon-like with 0°/90° model and fiber helix angle of 15° and 60°models were constructed (Table 1). Then, the effects of fiber arrangement structure on the impact resistance and energy dissipation capacity of the bionic composite were investigated based on finite element (FE) analysis.

According to the periodic helical arrangement structure of the fibers in osteon, a 12-layer periodic helical structure bionic model was constructed in ABAQUS (Figure 2), and it is assumed that the thickness of each sublayer in the helical structure is same and the layers are well integrated among themselves. The geometric size of the model is 150 mm × 100 mm×6 mm (standard thickness in ASTM-D-7136: 4–6 mm), the number of layers is 12, and the thickness of each sublayer is equally distributed as shown in Table 1. The mechanical performance parameters of the composite material models used in FE analysis are shown in Table 2 (Giraudguille, 1988; Weiner et al., 1997; Hansen and Martin, 1999; Liu et al., 2000; Karakuzu et al., 2010; Giner et al., 2014b; Reznikov and Weiner, 2014; Vercher et al., 2014; Jansen et al., 2016; Liu et al., 2019; Rua et al., 2021; Yin et al., 2021; Ekhtiyari and Shokrieh, 2022).

Drop-weight impact analysis was conducted on the four bionic models. The impact energy of 20 J was selected, the mass of the drop-weight is 2kg, and the critical contact velocity is 4.47 m/s 45# steel is selected as the punch material, the elastic modulus E and Poisson's ratio ν of the punch are 210GPa and 0.3, respectively. The shape of the punch tip is hemispherical with a diameter of ϕ16 mm, and the punch is constrained as a rigid body. A reference point was chosen on the punch and a mass point was added, and impact velocity was applied on the mass point. The impact energy is applied to the punch according to formula $E = mv^2/2$.

The analysis model of periodic helical bionic structure with fiber helix angle of 30° is shown in Figure 2A, the distribution direction of the fibers in each layer are shown in Figure 2B. The four models constructed in this analysis are modeled by 3D shell element for obtaining higher accuracy, and the element type and size are the same. Furthermore, due to the severe mesh deformation in impact center area, the mesh in the impact center area was refined for improving the calculation accuracy. Then, the mesh size was increased gradually from the middle region to the boundary region to ensure the mesh quality and reduce the calculation time. Through grid optimization, the mesh information is 6 292 nodes and 6 275 hyperbolic shell elements (S4R) with large strain, reduced integral and sand leakage control. Full restraint was applied to the four sides of the model based on the drop-weight test requirements of ASTM-D-7136 for. Due to the hard contact between the punch and the composite plate in impact process which will cause the failure of contact mesh, thus the ordinary hard contact algorithm is adopted. The failure degradation of the mesh is based on the Hashin failure criterion, and the fiber is 0° along the 1-direction and 90° along the 2-direction (Figure 2A).

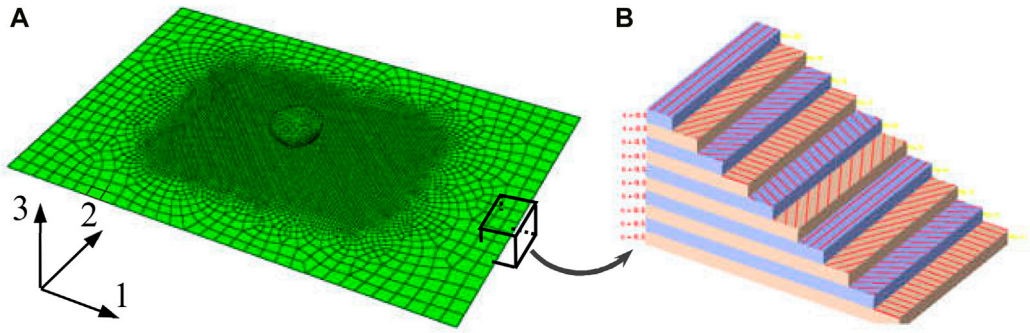

FIGURE 2
Impact analysis model of biomimetic composites. **(A)** Finite element model for impact analysis, **(B)** fiber arrangement direction of composite material (red indicates fiber).

TABLE 2 Characteristic parameters of composite material.

Material characteristics	Value	Material characteristics	Value
Densityρ/(kg/m3)	1830	Transverse compressive strengthY_c/MPa	124
Longitudinal modulusE_{11}/GPa	40.51	In-plane shear modulus G_{12}/GPa	3.1
Transverse modulusE_{22}/GPa	13.96	In-plane shear strength, S_{12}/GPa	69
Poisson's ratioν_{12}	0.22	Interlaminar shear strength, S_1/MPa	38
Longitudinal tensile strengthX_t/MPa	783.3	Longitudinal critical energy release rate $G_{cr,L}$/(kN·m^{-1})	40
Longitudinal compression strengthX_c/MPa	298	Transverse critical energy release rate $G_{cr,T}$/(kN·m^{-1})	0.3
Transverse tensile strengthY_t/MPa	64		

Material failure criterion of impact analysis

The damage types of multilayer composite materials are mainly divided into in-plane damage and interlaminar damage under low-speed impact load. The in-plane damage of composites mainly includes fiber fracture and matrix crack, and the interlaminar damage mainly refers to delamination failure between sublayers. Energy-based damage evolution was adopted for the interlaminar interface of the multi-layer composite. The impact process of composite materials can be roughly divided into four stages: compression stage, shear stage, fiber stretching deformation stage and penetration stage (Doddamani et al., 2023). Because the material is squeezed under impact load. Therefore, this paper focuses on the comparison and analysis of the in-plane damage of materials with different fiber arrangement methods, and the interlaminar damage of composite materials was ignored.

Damage failure criterion

The Hashin failure criterion can accurately determine various damage failure modes and is simple and effective, it has been widely used in practice. The combination of Hashin failure criterion and stiffness degradation criterion can simulate the progressive damage process of composite materials and can be easily realized. Thus, the Hashin criterion was used to simulate the impact damage of multilayer bionic composite. The expressions of Hashin failure criterion are as follows (Hashin and Rotem, 1973):

TABLE 3 Material stiffness degradation criterion.

Damage mode	Degradation criteria
Matrix tensile failure ($\sigma_{22} \geq 0$)	$Q_0 = 0.2Q$ ($Q = E_{22}$, G_{23}, ν_{12})
Matrix compression failure ($\sigma_{22} < 0$)	$Q_0 = 0.4Q$ ($Q = E_{22}$, G_{23}, ν_{12})
Fiber tensile failure ($\sigma_{11} \geq 0$)	$Q_0 = 0.07Q$ ($Q = E_{11}$, G_{23}, ν_{12})
Fiber compression failure ($\sigma_{11} < 0$)	$Q_0 = 0.2Q$ ($Q = E_{11}$, G_{23}, ν_{12})

Fiber tensile failure ($\sigma_{11} \geq 0$)

$$\left(\frac{\sigma_{11}}{X^T}\right)^2 + \left(\frac{\sigma_{12}}{S^L}\right)^2 = 1 \quad (1)$$

Fiber compression failure ($\sigma_{11} < 0$)

$$\left(\frac{\sigma_{11}}{X^C}\right)^2 = 1 \quad (2)$$

Tensile failure of matrix ($\sigma_{22} \geq 0$)

$$\left(\frac{\sigma_{22}}{Y^T}\right)^2 + \left(\frac{\sigma_{12}}{S^L}\right)^2 = 1 \quad (3)$$

Matrix compression failure ($\sigma_{22} < 0$)

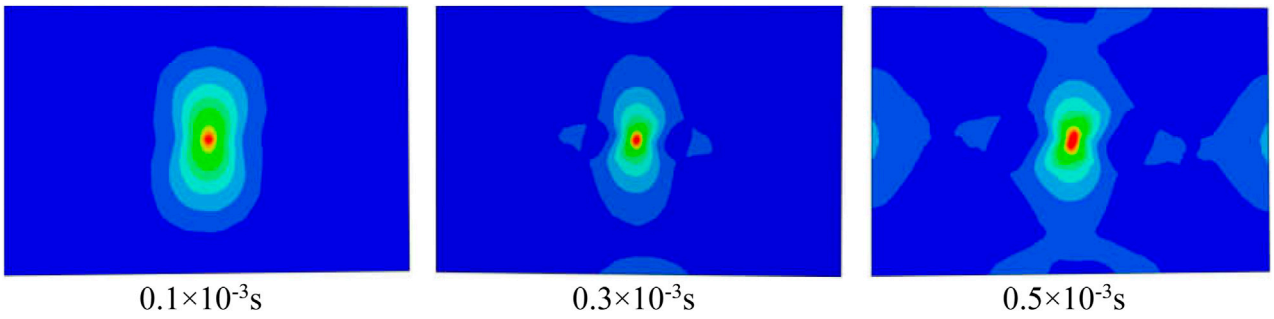

FIGURE 3
The nephogram of Mises stress distribution at the typical time moment of Sample30 when the impact energy is 20 J.

$$\left(\frac{\sigma_{22}}{2S^T}\right)^2 + \left[\left(\frac{Y^C}{2S^T}\right)^2 - 1\right] \cdot \left(\frac{\sigma_{22}}{Y^C}\right)^2 + \left(\frac{\tau_{12}}{S^L}\right)^2 = 1 \quad (4)$$

where, X^T is the longitudinal tensile strength of the single layer; X^C is the longitudinal compressive strength of the single layer; Y^T is the transverse tensile strength of the single layer; Y^C is the transverse compressive strength; S^L is the longitudinal shear strength; S^T is the transverse shear strength; σ_{11}, σ_{22} and τ_{12} are effective stress tensor components.

Material degradation criterion

The failure process of multilayer fiber reinforced composites is a complex process of progressive deterioration. At the initial stage of loading, some form of damage will occur in the weak part of the composite and cause the redistribution of load, but it may not be manifested macroscopically. With the increase of load, the damage accumulation and superposition, causing the continuous degradation of composite material properties and the continuous decrease of bearing capacity, until the whole laminates are destroyed. The progressive failure analysis method considers the local damage through the material performance degradation model, which can better simulate the failure mechanism, interaction and propagation process, and the ultimate failure load of composite laminates.

Material degradation means that when the mesh satisfies certain failure criteria in the FE models, the meshes in the model will be damaged. According to these different damage modes, the material properties of the damage element in the model need to be given new values according to certain rules, so as to obtain a new material model. In the FE progressive damage analysis, there are many methods to degrade the stiffness of the mesh. The material parameter degradation mode (Zhang and Chen, 2021) was used to degrade the stiffness of damaged area in this research, and different in-plane damage modes correspond to different degradation schemes, as shown in Table 3.

Biomimetic composite fabrication and test

Specimen fabrication

Unidirectional glass fiber prepreg (glass fiber/epoxy resin, model: G 12,500) was used to fabricate bionic spiral structure composite laminates. The fiber ratio of unidirectional glass fiber prepreg is 125 g/m^2, the resin content is 33% (included 33wt% - of resin), and the thickness of single layer is 0.1 mm. The fabrication processes of the composite laminate with fiber periodic helix ply structure are as follows.

(1) The prepreg was cut into a square of 120 mm × 120 mm.
(2) The prepreg was arranged periodically at the angles of 15°, 30°, 60° and 90°. The number of layers is 12.
(3) The prepreg lamination is put into the hot press mold, and the hot press (hot press model: hy61zf) is used for hot press curing.

The hot-pressing process is as follows.

(1) The initial pressure is 2t, and the temperature is raised to 200 °C;
(2) After holding the pressure for 5 min, the pressure dropped to 1t;
(3) The four kinds of bionic composite laminate can be obtained by keeping the pressure for 120 min and cooling naturally.

Drop-weight test

The biomimetic composite laminates were cut into drop-weight impact test specimens (size: 50 mm × mm). Then, the drop-weight impact tests were conducted according to the test method of ASTM-D-7136. The model of impact testing machine is XH-2000, and the manufacturer is Yangzhou Xinhong Test Machine Factory. The diameter of rigid body punch is 8.5 mm and the dimension of punch tip is 4mm, the mass of the drop-weight is 2kg, the drop-height is 1 m. The total impact energy (J) of a specimen was computed by the equation $E= MgH$, where M is the weight of the hammer (kg), g is 9.8 m/s^2, and H is drop-height (m).

Results and discussion

Effects of laying mode on stress distribution

Figure 3 shows the nephogram of Mises stress distribution at the typical time moment of Sample30 biomimetic model under the impact energy of 20 J. From this stress distribution nephogram can be seen, the stress wave is transmitted in the direction of the flat plate surface and the direction perpendicular to the flat plate surface from

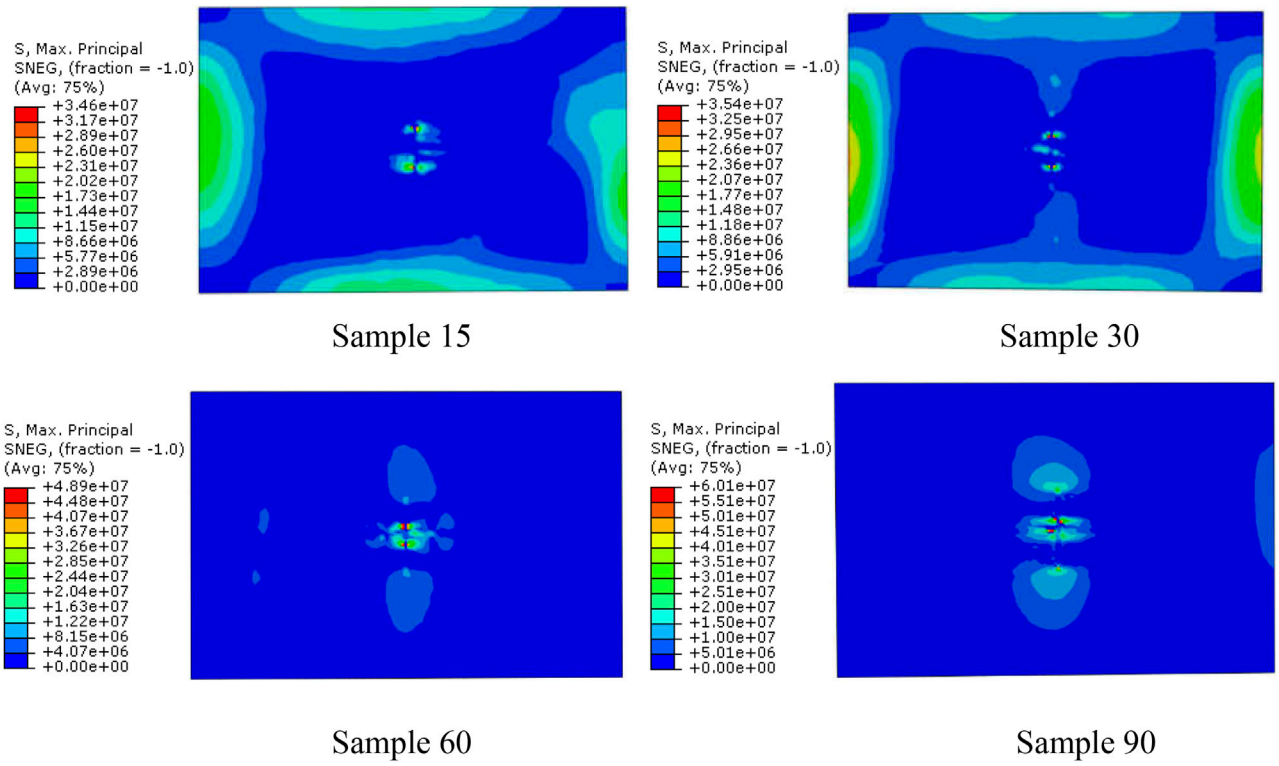

FIGURE 4
Nephogram of the maximum principal stress distribution of four biomimetic composite models when the impact energy is 20 J.

the impact center area in the composite laminate. When the stress exceeds its limit value, the mesh will fail and be destroyed. In addition, from the stress distribution of the biomimetic model with helix angle of 30° (Sample30), the Mises stress contour line roughly shows a "peanut" shape, which is consistent with the results of the general composite impact test (Chang and Lessard, 1991), which indicates the correctness of the numerical model and analysis calculation established in this paper.

Figure 4 shows the maximum stress distribution clouds of four biomimetic models based on the node maximum principal stress principle when the impact energy is 20 J. It can be seen from the analysis results that with the increase of the fiber helix angle, the shape of the stress contours and the maximum stress have obvious differences. The maximum stresses of Sample15, Sample30, Sample60, and Sample90 are 34.6 MPa, 35.4 MPa, 48.9 MPa, and 60.1 MPa, respectively. The maximum stresses of Sample15 and Sample30 are similar, but with the increase of the helix angle, the concentration of stress obviously increases. Compared with the Sample30 model, the maximum stress of Sample60 and Sample90 models increases by 38.1% and 69.8%, respectively.

The above analysis results indicated that for fiber-reinforced composite materials, when the material composition and material performance parameters are same, the mechanical properties of the material can be effectively improved and the stress concentration of the composite material when subjected to external impact can be reduced by adjusting the laying way of the fibers. For periodic fiber helical lamination composite materials, a smaller helix angle helps to reduce the stress concentration.

Effects of laying mode on impact characteristics

The maximum contact force and damage behavior are significantly different when the multi-layer composites with different fiber arrangement are subjected to external impact. For comparing and analyzing the effects of fiber arrangement methods on impact characteristics, the same boundary conditions were used in the four models and the impact damage analysis was conducted.

Contact characteristics during impact

When the impact energy is 20J, the impact load variation history of the four biomimetic composite models with time are shown in Figure 5. According to the analysis results, during the impact process, the time history of the impact load can generally be divided into two stages: the first stage is stamping stage, where the impact load continuously increases and finally reaches the peak point of the impact load; the other stage is rebound stage, in which the impactor is rebounded and gradually detaches from the composite laminate. The impact load gradually attenuates until the impactor completely detaches from the surface of the plate, and the impact load decreases to 0.

By comparing and analyzing the change history of contact load over time of four biomimetic models (Figure 5), it is can be seen that there are significant differences in the change process and peak value

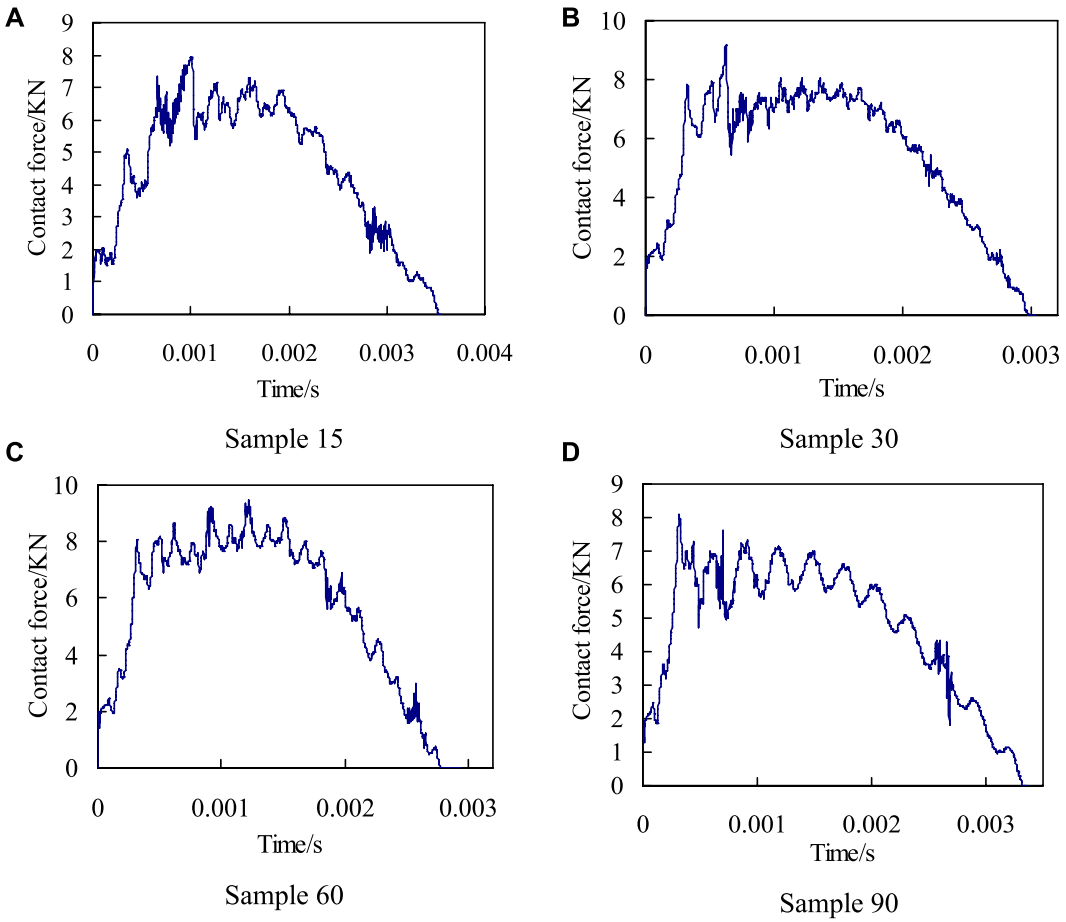

FIGURE 5
The curves of impact force-time history when the impact energy is 20 J. **(A)** Sample 15, **(B)** Sample 30, **(C)** Sample 60, and **(D)** Sample 90.

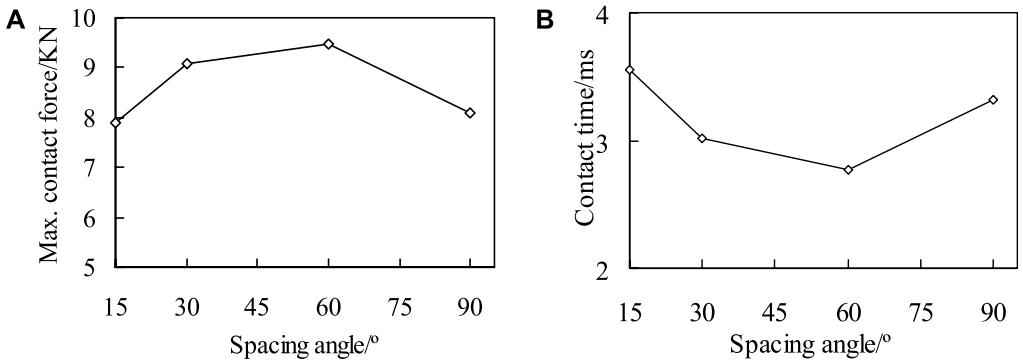

FIGURE 6
The maximum contact force **(A)** and contact time **(B)** of four different models when the impact energy is 20 J.

of contact load during the impact process. And there are also differences in the timing of the peak point of contact load for the four models. The Sample90 model first appears the peak point, and the Sample60 finally appears the peak point.

The contact load peak curve and impact contact time for the four models are shown in Figure 6. It can be seen from Figure 6B that with the increase of the fiber helix angle (from 15° to 60°), the contact time decreases significantly, and the impact contact

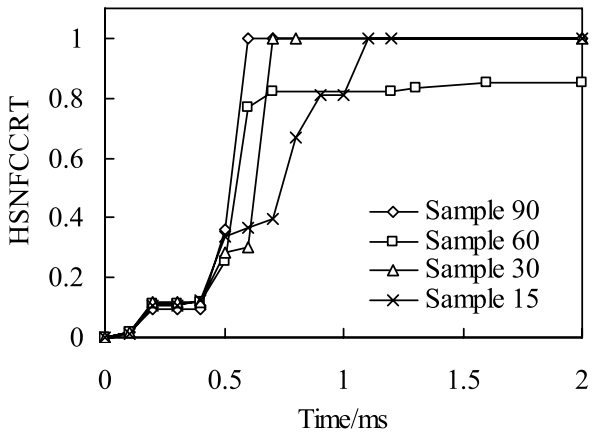

FIGURE 7
The relationship of impact time history and fiber compression failure.

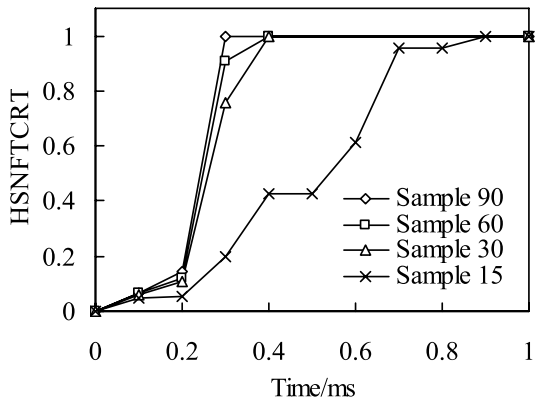

FIGURE 9
The relationship of impact time history and fiber tensile failure.

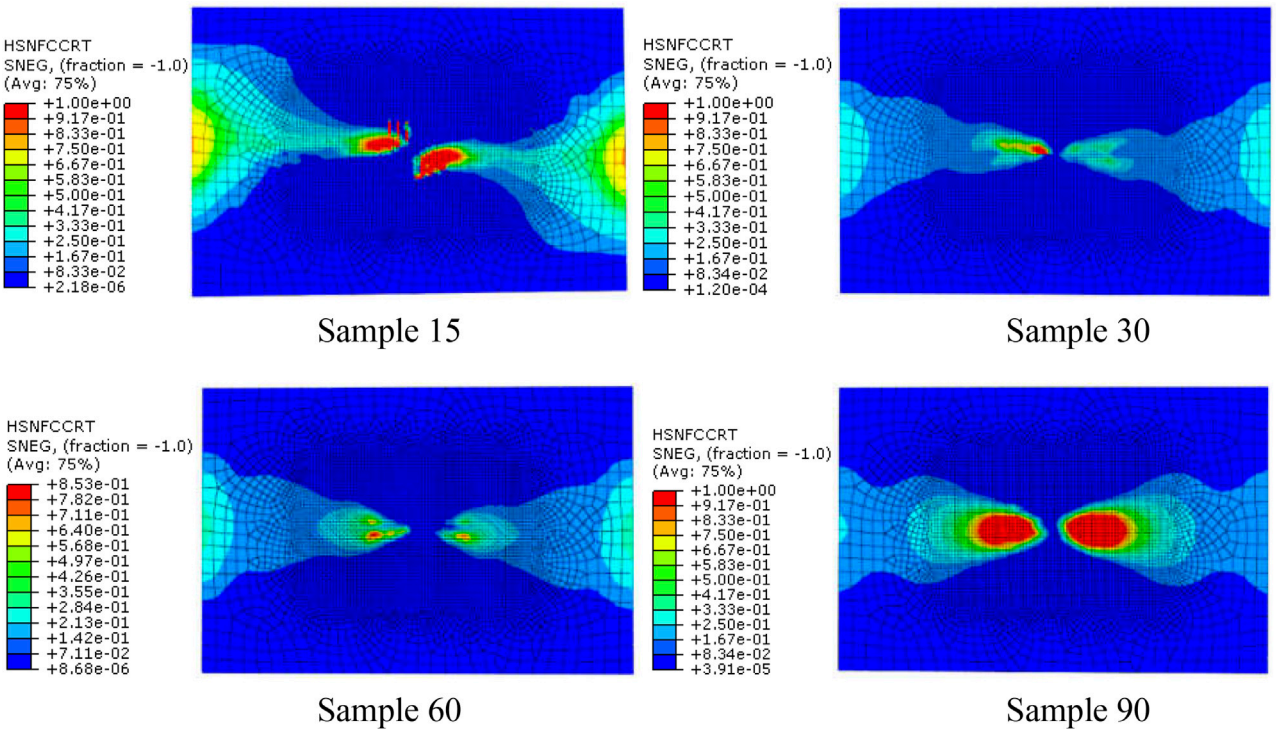

FIGURE 8
The fiber compression failure distribution when the impact energy is 20 J (the red area represents the part of fiber compression failure).

time of Sample60 decreases by 22.1% compared to Sample15. The impact contact characteristics of the four models indicate (Figure 6) that the fiber arrangement methods directly affect the peak contact load and contact time, and there are significant differences between the fiber helical structure and the orthogonal arrangement structure. In addition, according to the maximum principal stress analysis results of the four models can be known (Figure 4), the impact stress of Sample90 is the largest, and the stress concentration phenomenon is the most obvious, which means that damage occurs first during the impact process. The analysis results of the impact contact characteristics of the above four models also show that, when the material composition and performance parameters are same, the impact resistance characteristics of the composite plate can be effectively improved by adjusting the fiber laying method. With the reduction of fiber helix angles, its

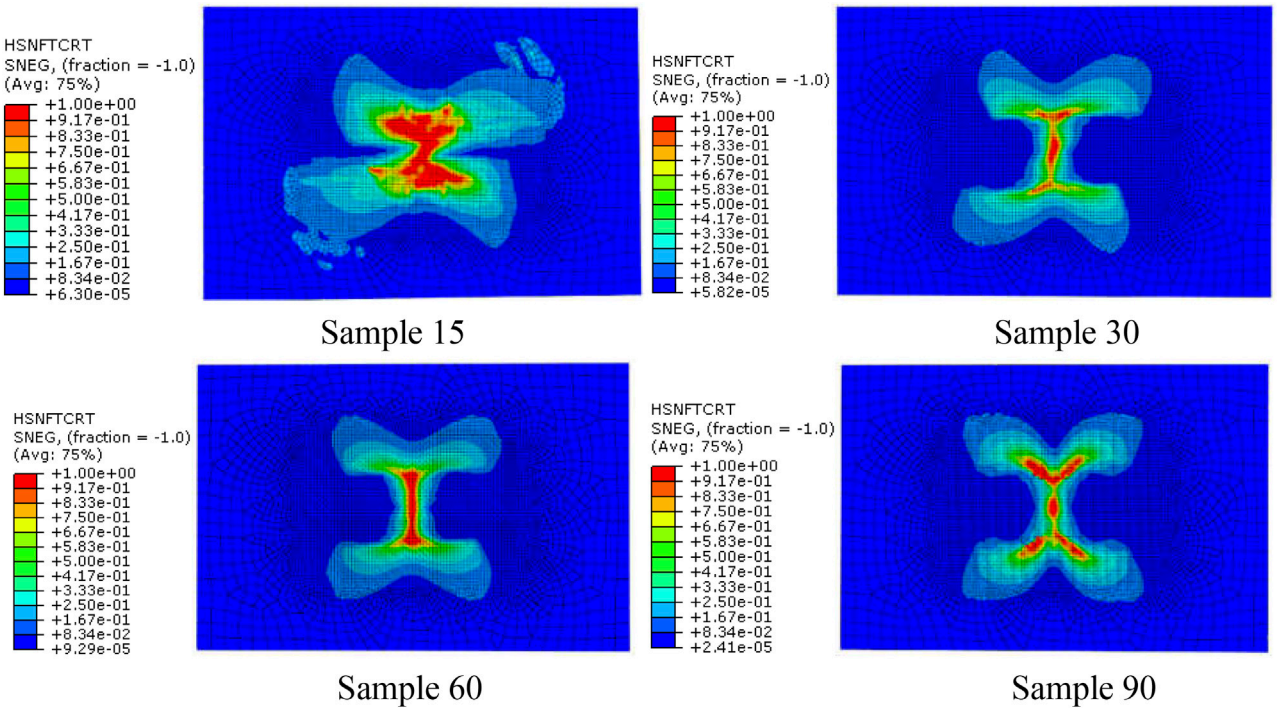

FIGURE 10
The fiber tensile failure distribution when the impact energy is 20 J.

stress distribution becomes more uniform, and the stress concentration phenomenon and impact resistance characteristics are significantly improved.

Fiber failure during impact

Fiber compression failure. When the impact energy is 20J, the initial failure of fiber compression and the failure distribution nephogram of the four kinds of bionic composites in the impact process were shown in Figures 7, 8, respectively. According to the fiber compression failure criterion, the fiber compression failure occurs when the failure criterion is greater than or equal to 1. It can be seen from the analysis results (Figure 7) that with the increase of impact energy, the fiber compression failure occurs first in the sample 90, followed by the sample 30 model, and finally the sample 15 model. However, there is no obvious fiber compression failure in the sample 60 model under the impact load. In addition, it can be seen from Figure 5 that although the fiber compression failure exists in the sample15, sample30 and sample90 models, there is a significant difference in the failure initiation time. It can be seen from the failure distribution nephogram (Figure 8) that the fiber compression failure ratio in the sample90 model is the largest, followed by the sample15 model, and the failure proportion in the sample30 model is the smallest, which indicates that the collagen fiber arrangement structure with a helix angle of 30° is helpful to enhance the compression resistance ability of osteon.

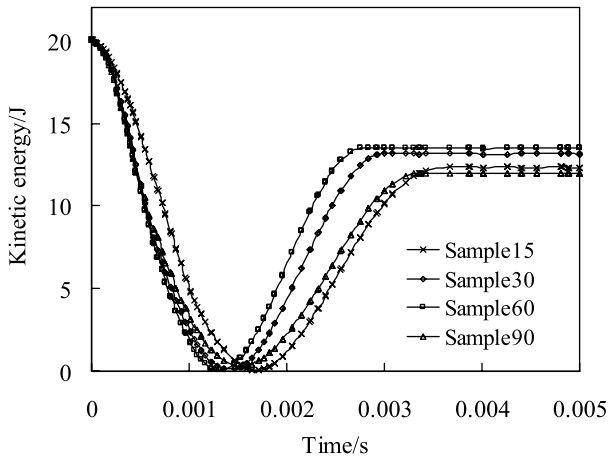

FIGURE 11
The change history of kinetic energy of the four models when the impact energy is 20 J.

The above analysis results show that the fiber stacking mode directly affects the compression failure of the fiber. By adjusting the fiber stacking mode in the multi-layer composite, the initial time of fiber compression failure and the ratio of fiber compression failure can be effectively improved.

Fiber tensile failure. The time history of fiber tensile initial failure of four bionic composite models during impact process was shown in Figure 9. It can be seen from the analysis results that under the

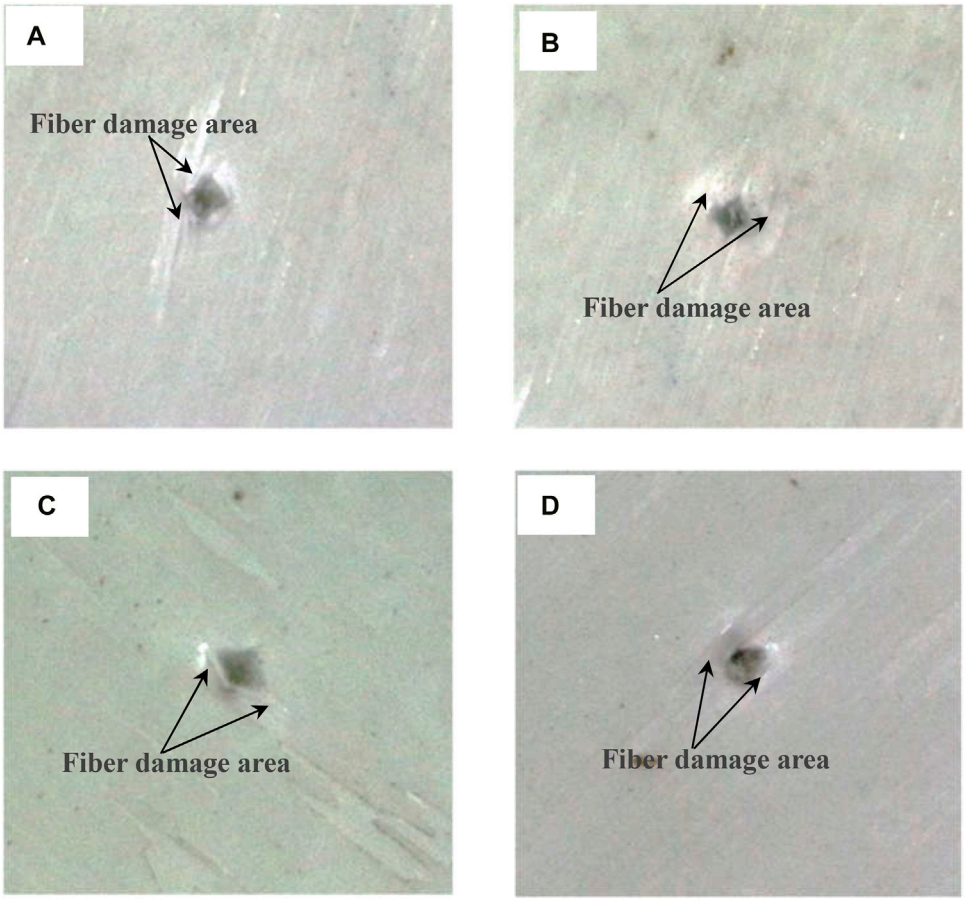

FIGURE 12
Impact damage of four biomimetic specimens. **(A)** Specimen15, **(B)** specimen30, **(C)** specimen60, **(D)** specimen90.

same impact load, the model of sample90 first appears fiber tensile failure. The second model is sample60 and sample30, but there are some differences in their time histories. Finally, the sample15 model, and the fiber tensile failure time of sample15 is much later than the first three models, which shows that the fiber has strong ability to resist tensile crack initiation in sample 15. Followed by the sample60 and sample30 models, but there are also certain differences in their time history. Finally, the sample15 model, and the fiber tensile failure time of sample15 is much later than the first three models, which shows that the fiber has strong ability to resist tensile crack initiation in model sample15.

It can be seen from the distribution nephogram of fiber tensile failure (Figure 10) that the proportion of fiber tensile failure increases in three models with fiber helix angle from 30° to 90°. However, the fiber tensile failure ratio is the largest when the helix angle is 15°, which indicates that the smaller the helix angle, the stress of the fiber in the model is more uniform. Once the failure occurs, the damage ratio will increase rapidly. The above analysis results show that the tensile strength of the multi-layer composite with fiber helix angle of 30° is stronger. Simultaneously, it also shows that the helix structure of collagen fibers with a helix angle of 30° in osteon helps to enhance the tensile strength of cortical bone.

Effects of laying mode on energy dissipation

Energy is an important factor in low-speed impact test. The difference between the impact energy and the kinetic energy of punch pin at the end of the impact is defined as the energy dissipated. The "energy dissipated" defined here also includes other energy consumption during impact process, such as strain energy released by sandwich plate, kinetic energy of sandwich plate, strain energy released by punch, consumption of viscous damping and friction. In this study, the energy dissipation capacity of impact kinetic was mainly compared and analyzed. The calculation method of impact energy as follows: the kinetic energy of the punch at the moment of contact is regarded as the impact energy. Therefore, the actual impact energy E_{impact} and the dissipated energy of composite plate $E_{dissipated}$ are defined as follows:

$$E_{impact} = \frac{1}{2}mv_0^2 \tag{5}$$

$$E_{dissipated} = \frac{1}{2}mv_0^2 - \frac{1}{2}mv_t^2 \tag{6}$$

where, m is the mass of the punch, $m = 2$ kg in this study (the mass of different sizes of punch is slightly different in actual experiment); v_0 and v_t are the velocities of the punch, at the moment of contact and

separation between the punch and the upper surface of the model, respectively.

When the impact energy is 20J, the kinetic energy change history of the four models is shown in Figure 11. It can be seen from Figure 11 that when the punch contacts with the composite plate, the velocity gradually decreases to zero, and then it is ejected and detached from the composite plate. The kinetic energy when the punch separates from the plate is the residual energy of impact. According to the kinetic energy change curve in Figure 11. The calculation results show that, as the fiber spiral angle decreases from 60° to 15°, the dissipative energy of sample 30 increases by 5.94% compared with that of sample 60, and the dissipative energy of sample 15 increases by 18.37% compared with that of sample 60. The sample 90 model consumes the most energy. According to the analysis results of the above four models, this is due to more matrix and fiber damage in sample 90, which dissipates more energy.

Bionic specimens impact test

Figure 12 shows the failure mode of layered bionic specimens after impact. It is indicated that bionic composite laminates with different helix angles have varying degrees of damage under the same impact load. A total of 20 effective samples were tested in this impact test, with 5 samples of each type. According to the measurement results of punch impact depth of the four kind samples, the average impact depths of punch of Sample15, Sample30, Sample60 and Sample90 are 4.26mm, 4.11mm, 5.14mm and 6 mm respectively, Sample 90 was penetrated. In addition, based on the impact analysis results of four bionic composites under the same impact energy, namely, stress distribution (Figure 4), fiber compression failure (Figure 8), fiber tensile failure (Figure 10). It can be seen from the comprehensive analysis that the biomimetic composite model with helix angle of 30° has better comprehensive capacity of anti-impact damage. Thus, the impact damage area of the sample with 30° helix angle is smallest among the four types of bionic composites. It can be concluded that the bionic composite laminate with fiber helix angle of 30° has a better ability to resist impact damage, which is consistent with the results of finite element impact analysis, which also shows the correctness of the FE analysis.

The model for the FE simulation analysis is rectangular, and the sample for the drop-weight test is square, the geometric size of the sample will affect its mechanical behavior. Since the focus of this study is to compare and analyze the impact resistance of different fiber helix angles on the bionic composites, a unified geometric dimension is adopted in the FE analysis process, and the impact trend of this geometric dimension on the four bionic composites is similar. In the impact test, the test standard of ASTM-D-7136 was referred to. The geometric dimensions of the four test specimens are square, and the influence trend of the geometric dimensions on the mechanical behavior of the four impact specimens is similar. Therefore, we believe that geometric dimensions of the specimen in the FEM model and in the experiments are not the same, which will not significantly affect the research results of the mechanical behavior of the four bionic composites.

Conclusion

In order to investigate the effect of fiber periodic helical structure on the impact characteristics of multilayer composites, four kinds of biomimetic composite models with different fiber helix angles were established based on the micro-nano structure of osteon, the impact characteristics and energy dissipation capacity of the four models were investigated. Then, the biomimetic structure with different helix angles were fabricated and tested. The conclusions as follows.

(1) The stress distribution and concentration of materials are affected by fiber helix angle. With the same material composition and material performance parameters, the stress concentration of composite materials under external impact can be effectively improved by adjusting the fiber arrangement method. The analysis results shown that the larger the fiber helix angle, the more serious the stress concentration phenomenon. And compared with the Sample30 model, the maximum stress of Sample60 and Sample90 models increases by 38.1% and 69.8%, respectively.
(2) The impact characteristics and energy dissipation capacity of multi-layer fiber reinforced composites are affected by the way of fiber laying. The fiber failure analysis results shown that among the four biomimetic composite models with fiber helix angles of 15°, 30°, 60° and 90°, the model with a fiber helix angle of 30° has the best resist impact damage. Moreover, in the case of without impact damage, the smaller the fiber helix angle, the more energy dissipated in impact process.
(3) The impact test results indicated that the impact damage area of the specimen with 30° helix angle is smallest among the four types of bionic specimens and has a better ability to resist impact damage, which is consistent with the results of FE impact analysis. Thus, the model with a fiber helix angle of 30° has the best comprehensive ability to resist impact damage.
(4) The helical structure of mineralized collagen fibers in osteon is the result of natural selection of biological evolution. This special structure can effectively improve the resist impact of cortical bone. The research results can provide useful guidance for the design and fabrication of high-performance biomimetic composites.

Data availability statement

The original contributions presented in the study are included in the article/Supplementary Material, further inquiries can be directed to the corresponding authors.

Author contributions

Y-XL conceived of the research. A-HL performed the design of biomimetic composite laminates and wrote the manuscript draft.

S-YL and HS contributed to the impact damage experiment and helped analyzed the data. BC provided key technical support and supervised the study. Y-XL wrote and revised manuscript. All authors read and approved the final manuscript.

Funding

This Funding was received from Science and Technology Research Program of Chongqing Municipal Education Commission (Grant No. KJQN202203110), Chongqing scientific research institutes performance incentive guidance special project (Grant No. cstc2020jxjl130017), and Key Science and Technology Research Program of Chongqing Municipal Education Commission (Grant No. KJZD-K202203104).

Conflict of interest

The authors declare that the research was conducted in the absence of any commercial or financial relationships that could be construed as a potential conflict of interest.

Publisher's note

All claims expressed in this article are solely those of the authors and do not necessarily represent those of their affiliated organizations, or those of the publisher, the editors and the reviewers. Any product that may be evaluated in this article, or claim that may be made by its manufacturer, is not guaranteed or endorsed by the publisher.

References

Alizadeh, S. R., and Ebrahimzadeh, M. A. (2022). O-substituted quercetin derivatives: Structural classification, drug design, development, and biological activities, a review. *J. Mol. Struct.* 1254, 132392. doi:10.1016/j.molstruc.2022.132392

Bhudolia, S. K., and Joshi, S. C. (2018). Low-velocity impact response of carbon fibre composites with novel liquid Methyl methacrylate thermoplastic matrix. *Compos Struct.* 203, 696–708. doi:10.1016/j.compstruct.2018.07.066

Carnelli, D., Vena, P., Dao, M., Ortiz, C., and Contro, R. (2013). Orientation and size dependent mechanical modulation within individual secondary osteons in cortical bone tissue. *J. R. Soc. Interface* 10, 20120953. doi:10.1098/rsif.2012.0953

Chang, F. K., and Lessard, L. B. (1991). Damage tolerance of laminated composites containing an open hole and subjected to compressive loadings: Part I—analysis. *J. Compos. Mater.* 25 (1), 2–43. doi:10.1177/002199839102500101

Currey, J. D. (2012). The structure and mechanics of bone. *J. Mat. Sci.* 47, 41–54. doi:10.1007/s10853-011-5914-9

Doddamani, S., Kulkarni, S. M., Joladarashi, S., Kumar T S, M., and Gurjar, A. K. (2023). Analysis of light weight natural fiber composites against ballistic impact: A review. *Int. J. Lightweight Mater. Manuf*, 1–41. doi:10.1016/j.ijlmm.2023.01.003

Dong, Y., Wang, F., Zhang, Y., Shi, X., Zhang, A., and Shuai, Y. (2022). Experimental and numerical study on flow characteristic and thermal performance of macro-capsules phase change material with biomimetic oval structure. *Energy* 238, 121830. doi:10.1016/j.energy.2021.121830

Ekhtiyari, A., and Shokrieh, M. M. (2022). A novel rate-dependent cohesive zone model for simulation of mode I dynamic delamination in laminated composites. *Compos. Struct.* 281, 114962. doi:10.1016/j.compstruct.2021.114962

Fratzl, J. W. C., and Fratzl, P. (2010). Biological composites. *Annu. Rev. Mater Res.* 40, 1–24. doi:10.1146/annurev-matsci-070909-104421

Giner, E. A., Arango, C., and Fuenmayor, F. J. (2014). Influence of the mineral staggering on the elastic properties of the mineralized collagen fibril in lamellar bone. *J. Mech. Behav. Biomed. Mat.* 42, 243–256. doi:10.1016/j.jmbbm.2014.11.022

Giner, E., Arango, C., Vercher, A., and Javier-Fuenmayor, F. (2014). Numerical modelling of the mechanical behaviour of an osteon with microcracks. *J. Mech. Behav. Biomed. Mat.* 37, 109–124. doi:10.1016/j.jmbbm.2014.05.006

Giraudguille, M. M. (1988). Twisted plywood architecture of collagen fibrils in human compact bone osteons. *Calcif. Tissue Int.* 42 (3), 167–180. doi:10.1007/bf02556330

Gupta, H. S., Stachewicz, U., Wagermaier, W., Roschger, P., Wagner, H., and Fratzl, P. (2006). Mechanical modulation at the lamellar level in osteonal bone. *J. Mat. Res.* 21 (8), 1913–1921. doi:10.1557/jmr.2006.0234

Hamed, E., Lee, Y., and Jasiuk, I. (2010). Multiscale modeling of elastic properties of cortical bone. *Acta. Mech.* 213, 131–154. doi:10.1007/s00707-010-0326-5

Hansen, P., and Martin, R. D. C. B. (1999). *4ENF and MMB delamination characterization of S2/8552 and IM7/8552*. London: European Research Office of the US Army.

Hashin, Z., and Rotem, A. A. (1973). A fatigue failure criterion for fiber reinforced materials. *J. Compos. Mater.* 7 (4), 448–464. doi:10.1177/002199837300700404

Ingrole, A., Aguirre, T. G., Fuller, L., and Donahue, S. W. (2021). Bioinspired energy absorbing material designs using additive manufacturing. *J. Mech. Behav. Biomed. Mater.* 119, 104518. doi:10.1016/j.jmbbm.2021.104518

Jansen, M. A., Singh, S. S., Chawla, N., and Franz, N. M. (2016). A multilayer micromechanical model of the cuticle of *Curculio longinasus* Chittenden,1927 (Coleoptera: Curculionidae). *J. Struct. Biol.* 195, 139–158. doi:10.1016/j.jsb.2016.05.007

Jiang, H., Ren, Y., Liu, Z., and Zhang, S. (2019). Microscale finite element analysis for predicting effects of air voids on mechanical properties of single fiber bundle in composites. *J. Mater Sci.* 54 (2), 1363–1381. doi:10.1007/s10853-018-2928-6

Karakuzu, R., Erbil, E., and Aktas, M. (2010). Impact characterization of glass/epoxy composite plates: An experimental and numerical study. *Compos. Part B* 41, 388–395. doi:10.1016/j.compositesb.2010.02.003

Liu, D., Wagner, H. D., and Weiner, S. (2000). Bending and fracture of compact circumferential and osteonal lamellar bone of the baboon tibia. *J. Mater Sci. Mater Med.* 11 (11), 49–60. doi:10.1023/a:1008989719560

Liu, Y., Chen, B., and Yin, D. (2017). Effects of direction and shape of osteocyte lacunae on resisting impact and micro-damage of osteon. *J. Mater Sci. Mater Med.* 28, 38. doi:10.1007/s10856-017-5850-6

Liu, Y., Li, A., and Chen, B. (2019). Effects of structure characteristics of osteocyte lacunae on squeeze damage resistance of osteons. *Cells Tissues Organs* 208, 142–147. doi:10.1159/000505135

Rahimizadeh, A., Sarvestani, H. Y., Li, L., Robles, J. B., Backman, D., Lessard, L., et al. (2021). Engineering toughening mechanisms in architectured ceramic-based bioinspired materials. *Mater. Des.* 198, 109375. doi:10.1016/j.matdes.2020.109375

Reznikov, N., Almany-Magal, R., Shahar, R., and Weiner, S. (2013). Three-dimensional imaging of collagen fibril organization in rat circumferential lamellar bone using a dual beam electron microscope reveals ordered and disordered sub-lamellar structures. *Bone* 52, 676–683. doi:10.1016/j.bone.2012.10.034

Reznikov, N., and Weiner, S. (2014). Bone hierarchical structure in three dimensions. *Acta Biomater.* 10 (9), 3815–3826. doi:10.1016/j.actbio.2014.05.024

Rua, J., Buchely, M. F., Monteiro, S. N., Echeverri, G. I., and Colorado, H. A. (2021). Impact behavior of laminated composites built with fique fibers and epoxy resin: A mechanical analysis using impact and flexural behavior. *J. Mater. Res. Technol.* 21, 428–438. doi:10.1016/j.jmrt.2021.06.068

Sharma, V., Borkute, G., and Gumfekar, S. P. (2022). Biomimetic nanofiltration membranes: Critical review of materials, structures, and applications to water purification. *Chem. Eng. J.* 433 (3), 133823. doi:10.1016/j.cej.2021.133823

Varga, P., Pacureanu, A., Langer, M., Suhonen, H., Hesse, B., Grimal, Q., et al. (2013). Investigation of the three-dimensional orientation of mineralized collagen fibrils in human lamellar bone using synchrotron X-ray phase nano-tomography. *Acta Biomater.* 9, 8118–8127. doi:10.1016/j.actbio.2013.05.015

Vercher, A., Giner, C., Arango, C., Tarancon, J. E., and Fuenmayor, F. J. (2014). Homogenized stiffness matrices for mineralized collagen fibrils and lamellar bone using unit cell finite element models. *Biomech. Model Mechanobiol.* 13 (2), 437–449. doi:10.1007/s10237-013-0507-y

Wang, C., Su, D., Xie, Z., Wang, H., Hazell, P. J., Zhang, Z., et al. (2022). Dynamic behaviour of Bio-inspired heterocyclic aramid Fibre-reinforced laminates subjected to Low-velocity Drop-weight impact. *Compos. Part A Appl. Sci. Manuf.* 153, 106733. doi:10.1016/j.compositesa.2021.106733

Wang, H., Wang, C., Hazell, P. J., Wright, A., Zhang, Z., Lan, X., et al. (2021). Insights into the high-velocity impact behaviour of bio-inspired composite laminates with helicoidal layups. *Polym. Test.* 103, 107348. doi:10.1016/j.polymertesting.2021.107348

Wang, Y., Naleway, S. E., and Wang, B. (2020). Biological and bioinspired materials: Structure leading to functional and mechanical performance. *Bioact. Mater.* 5 (4), 745–757. doi:10.1016/j.bioactmat.2020.06.003

Weiner, S., Arad, T., Sabanay, I., and Traub, W. (1997). Rotated plywood structure of primary lamellar bone in the rat: Orientations of the collagen fibril arrays. *Bone* 20 (6), 509–514. doi:10.1016/s8756-3282(97)00053-7

Xu, J., Rho, J. Y., Mishra, S. R., and Fan, Z. (2003). Atomic force microscopy and nanoindentation characterization of human lamellar bone prepared by microtome sectioning and mechanical polishing technique. *J. Biomed. Mater. Res.* 67A (3), 719–726. doi:10.1002/jbm.a.10109

Yin, D., Chen, B., and Lin, S. (2021). Finite element analysis on multi-toughening mechanism of microstructure of osteon. *J. Mech. Behav. Biomed. Mater.* 117, 104408. doi:10.1016/j.jmbbm.2021.104408

Zhang, Y., and Chen, P. (2021). An improved methodology of constructing inter-fiber failure criteria for unidirectional fiber-reinforced composites. *Compos. Part A Appl. Sci. Manuf.* 145, 106369. doi:10.1016/j.compositesa.2021.106369

Frontiers in
Bioengineering and Biotechnology

Accelerates the development of therapies, devices, and technologies to improve our lives

A multidisciplinary journal that accelerates the development of biological therapies, devices, processes and technologies to improve our lives by bridging the gap between discoveries and their application.

Discover the latest Research Topics

See more →

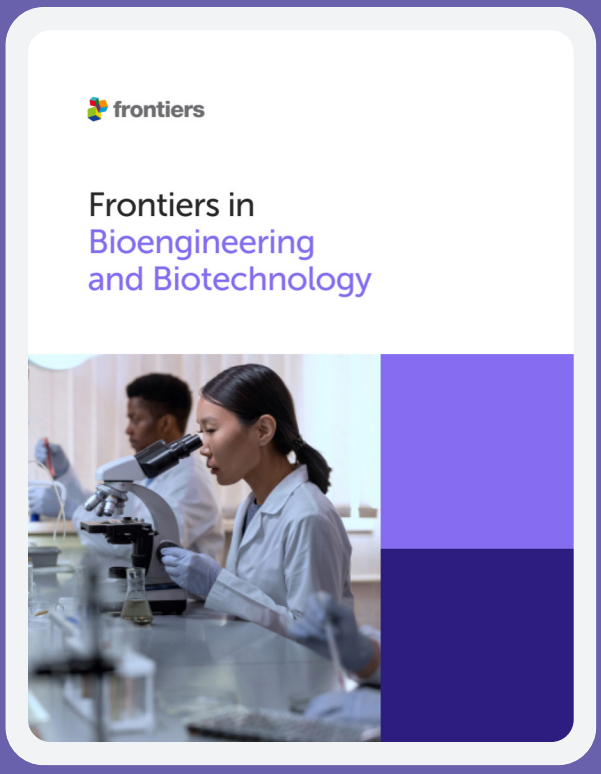

Frontiers

Avenue du Tribunal-Fédéral 34
1005 Lausanne, Switzerland
frontiersin.org

Contact us

+41 (0)21 510 17 00
frontiersin.org/about/contact